Syntheses and structures of alternative halometallate photovoltaic absorber materials

Dennington, Adam

Award date:
2019

Awarding institution:
University of Bath

Syntheses and structures of alternative halometallate photovoltaic absorber materials

Adam James Dennington

A thesis submitted for the degree of Doctor of Philosophy

University of Bath

Faculty of Science

Department of Chemistry

September 2018

University of Bath

Faculty of Science

Department of Chemistry

Doctor of Philosophy

Abstract

Syntheses and structures of alternative halometallate photovoltaic absorber materials

Adam James Dennington

The results described in this thesis concern the design, synthesis and characterisation of new candidate absorber layer sensitizer materials for photovoltaic cells; in particular exploring novel halometallate hybrid structures. Through this work, the field of iodoantimonate and iodobismuthate hybrid materials has been expanded with the discovery and analysis of many novel structures. Alternative, lead-free, antimony and bismuth metal containing hybrid structures are key and of much interest in the rapidly developing area of perovskite-based solar cell architectures. The work undertaken has added to building the database and thus further developing the understanding of hybrid absorber materials with the overarching aim of progressing towards real world thin-film and tandem solar cell designs to challenge and expand upon the industry dominant silicon-based solar cell architectures of today.

An introduction to the field and the context of the research is given in chapter 1, and the relevant experimental techniques are discussed in chapter 2. The remaining chapters of the thesis present the findings of the project as detailed below.

The particular focus of the work carried out covers the discovery and study of the structure and properties of over ten novel iodoantimonate and twenty novel iodobismuthate hybrid materials. The results of the investigations carried out are presented in an alternative thesis format with two full published papers integrated within the narrative in chapter 3. Additionally, as detailed in chapter 4 an in-situ alkylation solvothermal synthetic technique used in the formation of more complex templating agents was found and used to great effect throughout the synthesis and study of iodoantimonate and iodobismuthate novel halometallate hybrid materials. Moreover, a promising opening for a new avenue of perovskite structure potential was uncovered; triggered by the discovery and preliminary analysis of an unfamiliar novel three-dimensional superoctahedra-octahedra linked halometallate motif described in chapter 5.

Outside of this, work was undertaken on other alternative candidate material areas such as bismuth-based coordination complexes, bismuth sulphide iodide, double perovskites and related structures; contained within chapter 6. To finish, the overall results and thesis conclusions are discussed in chapter 7.

Acknowledgements

Lead Supervisor and academic support

I wish to thank Professor Mark Weller for his support and reassurance throughout the years of work on this project. I would also like to thank Dr Mary Mahon for her assistance in developing my structural solution and refinement expertise used to finalise our data to a high standard for publication.

Weller Research Group

I also wish to express my gratitude to everyone who I have worked alongside in the Weller research group, with an added thanks to Kayleigh Marshall for help in developing my knowledge and skill of solving and refining structural models assisting me greatly in finding my feet from the outset of my research project.

Funding

I would also like to thank the Engineering and Physical Sciences Research Council (EPSRC) for the three years of funding utilised to carry out the work contained within this thesis.

Special thanks

And lastly I would like to give a special thanks to friends and family for the support and the belief instilled in me throughout the years of academic study leading up to and during my PhD research.

Index

Chapter 1 – Introduction

1.1 Photovoltaic (PV) technologies

1.1.1 Introduction

In the endeavour to shape a world with an increased level of sustainability much effort and interest has been dedicated to the field of solar energy research as part of this future. To build an infrastructure of sustainable energy, the development of increasingly efficient, cheaper and more abundant solar cell material constructs is critical to the growth of this proposal of sustainability.

The sun is an understandably rich source of clean energy worth tapping into. It is by far the largest energy resource available on Earth with an average power density of 20 GW/m^2sr irradiating the surface of the planet [1]. In one year the amount of energy reaching the surface of the Earth is about twice as much as the energy that will ever be obtained from coal, oil, natural gas, and mined uranium combined [2]. With the continued depletion of currently relied upon fossil fuel resources and an ever increasing demand for energy from a mounting world population and progressively energy intensive ways of living, the drive to develop new technologies to satisfy the demand is strong. Renewable energy technologies are believed by many to be key to the future vision of providing a more stable and sustainable supply of energy. Currently, as photovoltaic (PV) technologies are being developed the cost of solar arrays are decreasing and as the efficiency of the technologies continues to grow it implies that PV generating systems will play a greater role in meeting energy demand [3].

1.1.2 The photovoltaic effect and semiconductors

Photovoltaic cells, commonly known as solar cells, convert sunlight directly into electricity. They get their name from the underlying principle of the function of a solar cell, the photovoltaic effect, which describes the process of converting light (photons) into electricity (voltage). Semiconducting materials exhibit this effect; when absorbing photons of light, if the energy of the photons is greater than that of the band gap between the valence and conduction band of the material, electrons will be promoted to a higher energy state in the conduction band.

Consequently, this means that electrons in the conduction band, as well as positive holes left in the valence band, can act as charge carriers. An electric field across the photovoltaic cell allows for an electric current to be harnessed when wires are connected to form a circuit between the positive and negative sides of the cell.

The electronic structure of solid-state materials is described by the tight-binding approximation. The orbital energies of atoms contained within the structure overlap to form a series of bands of orbitals; which in turn are separated by gaps in which orbital energy levels do not occur. Semiconducting materials, commonly crystalline inorganic solids, are materials in which the band gap between the valence band of electrons and the conduction band in the structure is small enough that thermal, and possibly photo excitation of electrons may occur and also possesses the property of increasing electrical conduction upon an increase in temperature [4].

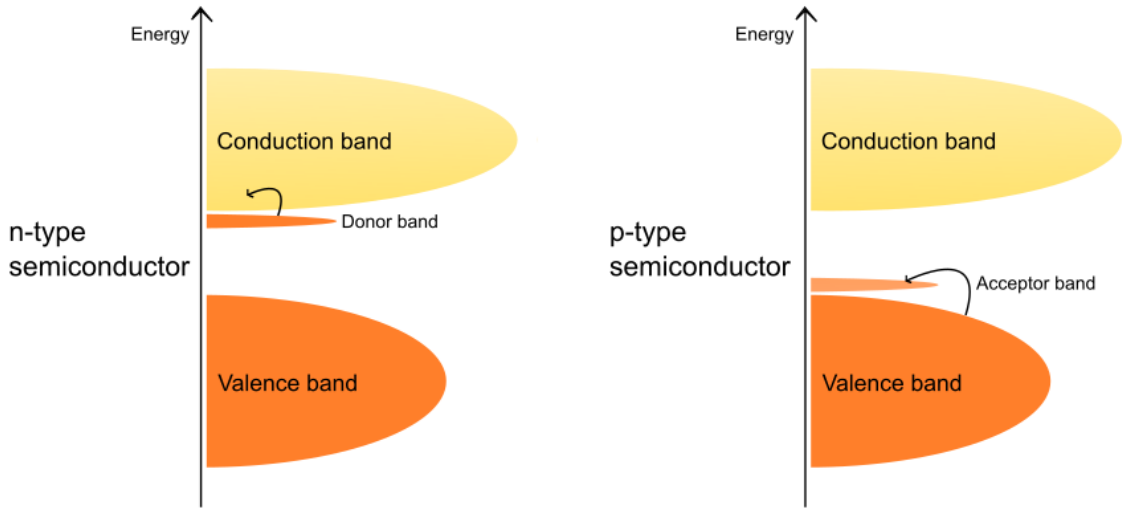

Figure 1.1 n-type/p-type semiconducting materials

Semiconducting materials fall into two main categories; intrinsic and extrinsic. Intrinsic semiconductors possess a band gap so small that thermal motion is sufficient for electrons to be promoted from the valence to conduction band. As temperature increases, the electron population in the conduction band follows an exponential Boltzmann-like dependence and as a result conductivity of the material follows from the temperature dependence. Extrinsic semiconductors are materials in which the electronic properties are changed by the addition of impurities into the bulk material. Even a low concentration of impurity (dopant) can have a significant influence on the band-gap energy and conductivity of the material. For example, if an impurity introduced is an element with a valence electron count lower than that of the bulk material, there are effectively missing electrons in the valence band structure which can be

considered as positive holes. A semiconductor doped in this way is known as a p-type semiconductor as its conductivity is more closely related to the increased number of positive hole charge carriers in the valence band (Figure 1.1). Alternatively, the impurity introduced could be an element with a valence electron count higher than that of the bulk material. Here, there is an additional band formed between the valence and conduction band of the bulk material with populated orbitals due to the increased electron count. Electrons from these orbitals can be easily promoted to the conduction band and therefore increase the number of charge carriers present. Materials of this kind are known as n-type semiconductors [4].

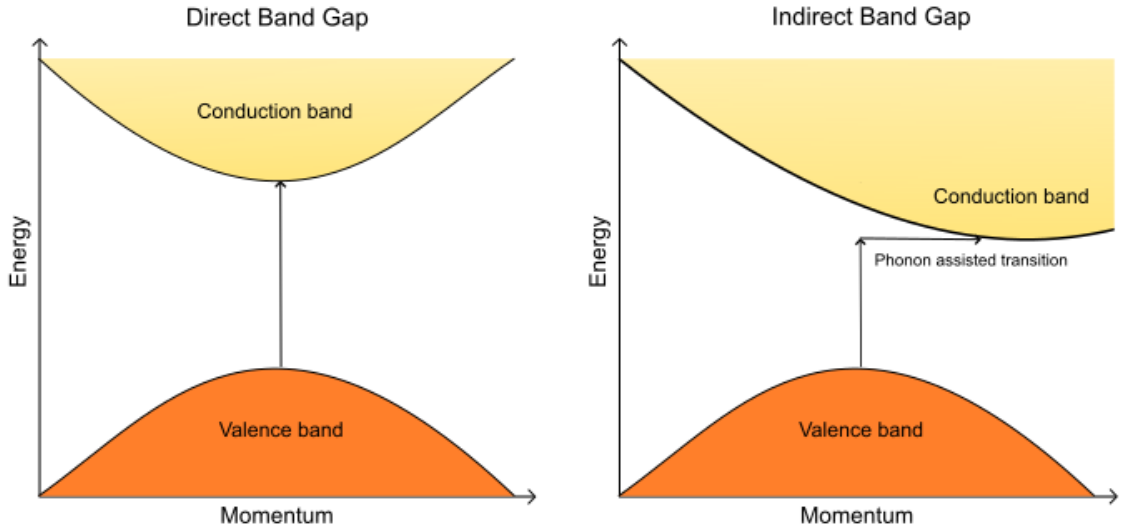

Figure 1.2 Direct/Indirect band gap semiconductor comparison

When electron excitation occurs in a semiconducting material, as previously stated, the energy of excitation must be greater than that of the minimum energy difference between the valence and conduction band. Another consideration, however, is that in some materials the bands may not be aligned at the same electron momentum for a transition to occur. For a direct band gap semiconductor, promotion of an electron to form an electron-hole pair can easily occur due to an alignment of the bands without the need for a change in momentum (Figure 1.2). Conversely, for an electron promotion to occur to form an electron-hole pair in an indirect band gap semiconductor, the electron must also undergo a more significant change in momentum to assist its transition to the conduction band. To gain or lose momentum the electron must interact with a lattice vibration, called a phonon, for the transition to occur. As a result, the process of excitation in indirect band gap semiconductors requires the interaction of an electron, a photon

and a phonon. This can result in a lower rate of formation of electron-hole pairs. Nevertheless, this also has the effect that the recombination rate of the electron-hole pairs is reduced.

As previously mentioned, in some semiconducting materials electrons can be promoted from the valence to conduction band if the photon energy (*hv*) of the light on the material is greater than the band gap energy. For this to occur, the band-gap energy must correspond to that of the incident photon energy. These types of semiconducting material are known as photoconductors and can be utilised as light-harvesting materials in solar cells. By taking account of the energy distribution of the electromagnetic spectrum when selecting the most effective light-absorbing materials for converting solar energy, obtaining a structure with a band-gap energy in the range of ~1.0-1.8 eV is most desirable. The higher the band-gap energy, the higher the voltage output, however, decreasing the band-gap energy increases the current. Power output = current x voltage, therefore, a balance of these properties can give an optimum band gap based on thermodynamic efficiency limit. For a single p-n junction-based solar cell, the maximum theoretical limit was calculated is known as the Shockley-Queisser limit. The limit, for the conditions and assumptions made, is a maximum solar efficiency of ~33.7% at 1.34 eV [5]. The most commonly known and utilised photoconductive material, silicon (Si), is an intrinsic semiconductor in its purest form with a band gap of ~1.11 eV [4]. However, multi-junction cells are theoretically capable of exceeding this limit.

Solar cells function below the maximum theoretical Shockley-Queisser limit, also known as the detailed balance limit, due to losses in the amount of electrical energy that can be obtained from the incident sunlight. The first contribution to reduction in efficiency is the effect of black-body radiation increasing the amount of electron-hole recombination in the cell. A small proportion of the background black-body radiation emitted from any given semiconductor material will have energy greater than that of the band gap. As a result, within the material photons will be generated by the electron-hole recombination process across the p-n junction even without a voltage or load across the cell. This effect is deemed to contribute to lowering the current that can be generated by an operating cell. Secondly, other effects known to contribute to the rate of recombination in the cell include the voltage across the cell and structural effects, such as grain boundaries and defects of the materials in the cell architecture. Another factor in losses contributing to the limit is the fact that a proportion of the incident sunlight energy is made up of electromagnetic radiation lower in energy that the band gap of the semiconducting absorber material and so will not contribute to the formation of electron-hole pairs within the cell and thus any power production.

1.1.3 A basic solar cell architecture

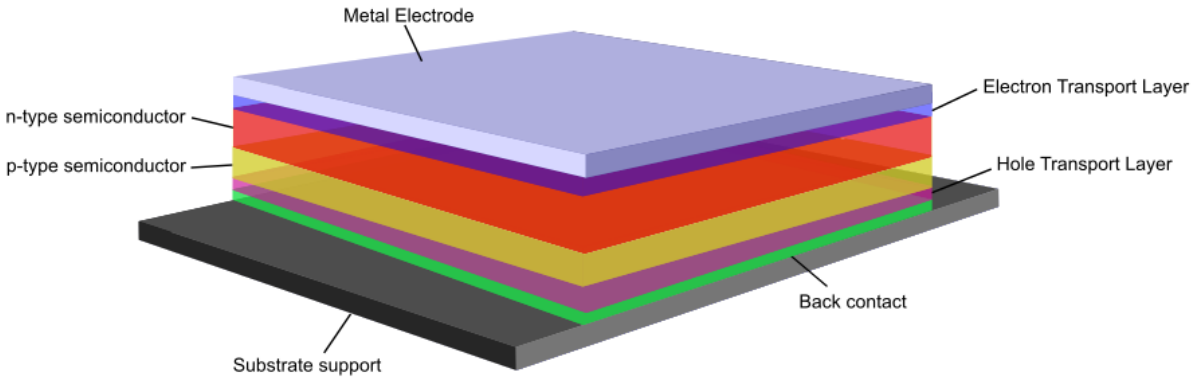

Figure 1.3 A schematic of a basic solar cell architecture design

As aforementioned, a photovoltaic cell contains at least one layer of photoactive material which upon irradiation with light will generate charge carriers, excited electrons and positive holes in the material. Figure 1.3 shows a PV cell with a single p-n junction architecture. Electron and hole transport layers are applied to assist in the separation of the photo-generated charge carriers in the n-type and p-type semiconducting layers to generate a current.

Individual PV cells are typically small and output only a few Watts of power. Therefore, to increase the power output of the cells they are interconnected to form modules. In order to meet a required output the modules can be connected to boost the power provided further. In this way, the number of PV cells employed can be designed to match a specific electrical power need, whether it is small or large (Figure 1.4).

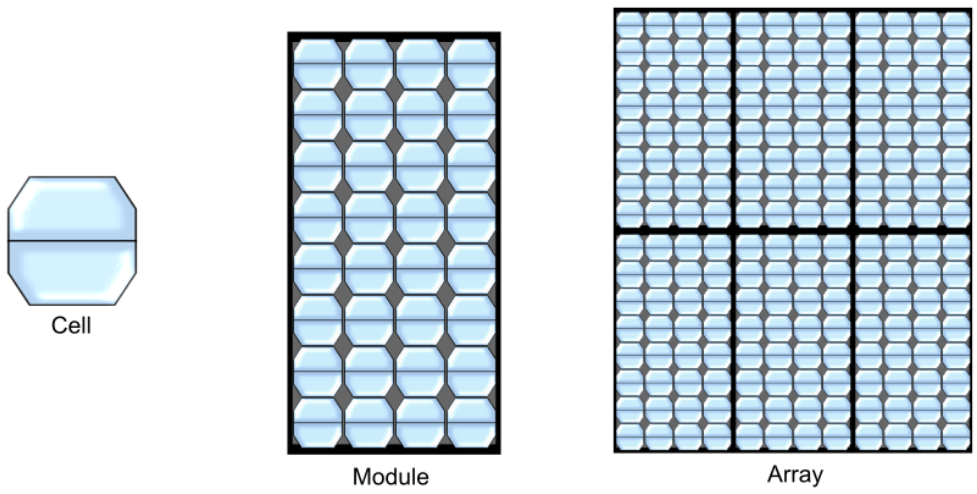

Figure 1.4 A schematic to show a solar cell module/array build

1.1.4 Meeting a growing global energy demand

Considerations for meeting the energy demand of world populations are also challenged by concern for the effects of energy technologies on the planet itself. Solar energy is a significant part of EU and international targets to increase total energy consumption from renewable energy as part of a global strategy to tackle climate change and keep global warming to below 2 ^{o}C compared to the average temperature in pre-industrial times. Targets in tandem with this ambition are to increase energy efficiency and to reduce greenhouse gas emissions [6]. Researching and developing new technologies will be key to fuelling this drive towards reducing the global dependence on current harmful gas-emitting fossil fuel technologies and increasing the efficiency of the processes used to harness and utilise energy.

1.1.5 Do solar energy technologies have potential?

Drawing upon the potential of solar energy is favourable not only because of its availability and abundance as a resource but also for its environmental impact. Although the parts and materials required for construction, transport, and installation of the panels have a negative effect on the environment this is negligible when compared to conventional sources and will improve as new technologies are developed. It is also a widely deployable technology around the world as it can be used without the need for an electrical grid system to provide energy to harder to reach or underdeveloped regions be it, for example, through solar thermal technologies providing hot water or solar photovoltaic technologies providing electricity. In addition, in more developed regions the technology is increasingly being used in partnership with national grid systems to decrease dependence on grid power and is often incentivised to people by subsidies issued by government departments [7]. Lastly, it is a resource favoured by many due to the fact that once fitted the panels require very little maintenance, function in silence without moving parts and exhibit zero emissions. As a result, they have minimal impact on people's day-to-day lives whilst contributing power.

Existing issues with harnessing the potential of this source include the current high cost of the materials used in cell architectures. The price of an energy unit generated by PV generating systems is still an order of magnitude higher than the conventional energy supplied by the grid supply [3]. Additionally, the intermittent nature of the incident light, be it from the planet's day/night cycle or from changeable cloud cover and weather conditions is an issue. Therefore,

reliance on solar power fulfilling a major part of energy demand would likely require increased utilisation of energy storage which is similarly expensive.

Furthermore, the surface area requirements for the energy it provides are a concern. Although the global mean power density for solar radiation is 170 W/m^2, more than any other renewable energy source, in reality at present a maximum of 20 W/m^2 is achieved; meaning that larger area coverage is required. To combat this, thin-film cell architectures have become increasingly popular alternatives which may hold the potential for incorporation into the materials of buildings such as the glass panels of skyscrapers, into a range of textiles [8] and into mobile screens. However, the application of transparent solar cell technologies has its difficulties as it requires the tailoring of its use in each circumstance as often a certain level of light transmission is desirable. Additionally, thickness of the cell architecture, stability and efficiency are all important considerations and challenges for the type of solar cell device to be applied in a given situation.

1.1.6 The history of photovoltaic technologies

Although the photovoltaic effect was discovered by a French physicist, Becquerel, in 1839, it took over a century to understand and utilise the effect in functional cells. One of the simplest and founding materials in photovoltaics was silicon wafers, with a functioning photovoltaic cell being built in the early 1940s and refined over the following decade to reach an efficiency of 11%. Thus, PV cells could begin to be applied for practical purposes and were employed in 1958, for example, on the Vanguard satellite [3].

The light absorbing semiconducting materials employed in photovoltaic technologies have developed and are classified into multiple generations. The history and progression of many PV cell efficiencies is displayed well by the National Renewable Energy Laboratory's (NREL) chart (Figure 1.5) which tracks the efficiencies of various PV technologies through the years. Research cell devices undergo standardised testing at independent, recognised test labs and are added to the plot if a record efficiency for their respective technology is measured.

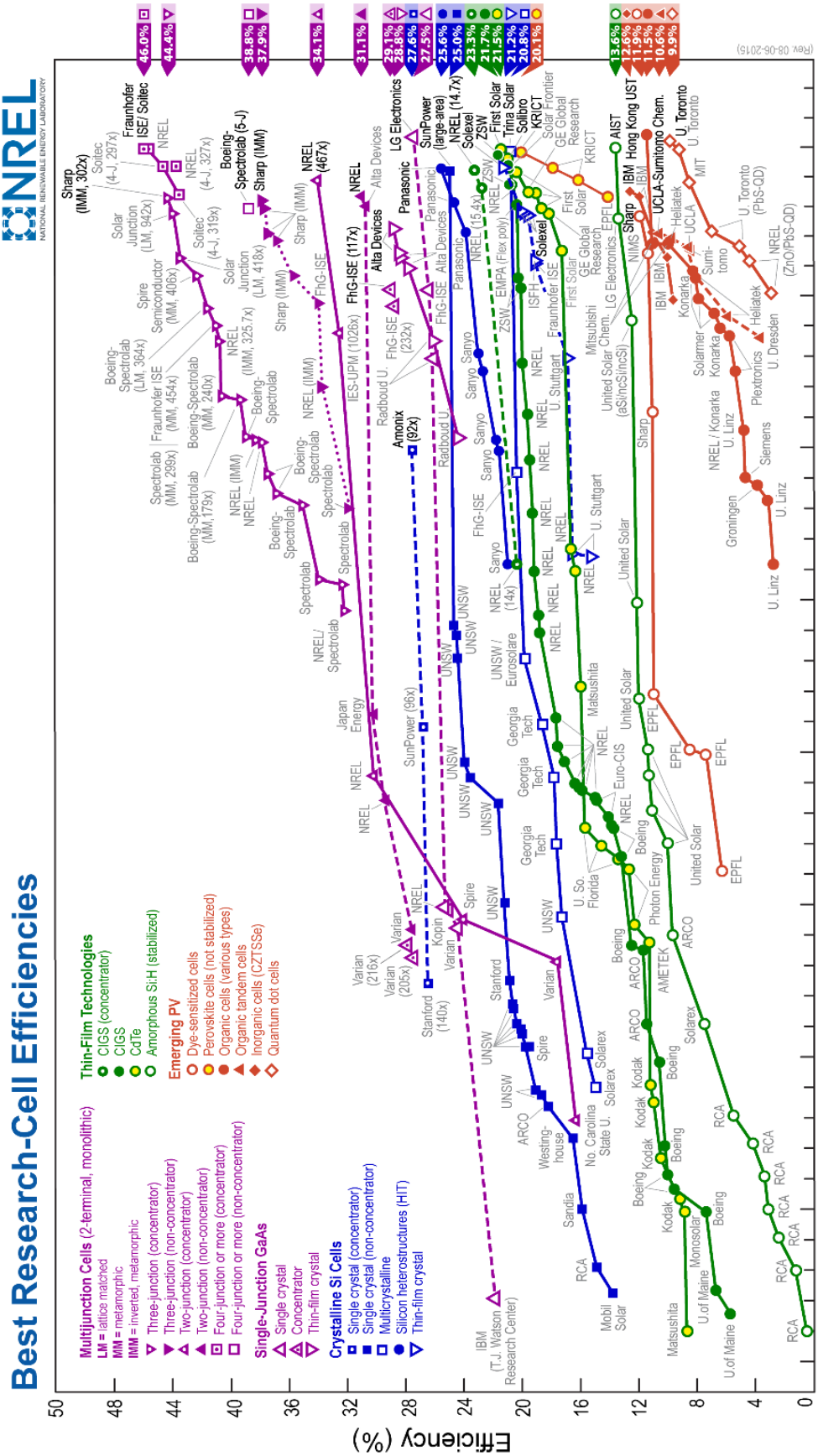
Best Research-Cell Efficiencies
NREL
NATIONAL RENEWABLE ENERGY LABORATORY
Efficiency (%)
Multijunction Cells (2-terminal, monolithic)
LM = lattice matched
MM = metamorphic
IMM = inverted, metamorphic
Three-junction (concentrator)
Three-junction (non-concentrator)
Two-junction (concentrator)
Two-junction (non-concentrator)
Four-junction or more (concentrator)
Four-junction or more (non-concentrator)
Single-Junction GaAs
Single crystal
Concentrator
Thin-film crystal
Crystalline Si Cells
Single crystal (concentrator)
Single crystal (non-concentrator)
Multicrystalline
Silicon heterostructures (HIT)
Thin-film crystal
Thin-Film Technologies
CIGS (concentrator)
CIGS
CdTe
Amorphous Si:H (stabilized)
Emerging PV
Dye-sensitized cells
Perovskite cells (not stabilized)
Organic cells (various types)
Organic tandem cells
Inorganic cells (CZTSSe)
Quantum dot cells
46.0%
44.4%
38.8%
37.9%
34.1%
31.1%
29.1%
28.8%
27.6%
27.5%
25.6%
25.0%
23.3%
21.7%
21.5%
21.2%
20.8%
20.1%
13.6%
12.6%
11.5%
10.6%
9.9%
Fraunhofer ISE/ Soitec
Boeing-Spectrolab (5-J)
Sharp (IMM)
NREL (467x)
NREL
FhG-ISE (117x)
Alta Devices
LG Electronics
Panasonic
SunPower (large-area)
NREL (14.7x)
Solexel
ZSW
First Solar
Tirna Solar
Solibro
KRICT
AIST
IBM
Hong Kong UST
UCLA-Sumitomo Chem.
U. Toronto
Sharp (IMM, 302x)
Soitec (4-J, 297x)
Solar Junction (LM, 942x)
NREL (4-J, 327x)
Soitec (4-J, 319x)
Spire Semiconductor (MM, 406x)
Boeing-Spectrolab (LM, 364x)
Fraunhofer ISE (MM, 454x)
Spectrolab (MM, 299x)
Boeing-Spectrolab (MM,179x)
Boeing-Spectrolab (MM, 240x)
NREL (IMM)
NREL (IMM, 325.7x)
Solar Junction (LM, 418x)
Boeing-Spectrolab
Sharp (IMM)
FhG-ISE
NREL (IMM)
Spectrolab
IES-UPM (1026x)
Radboud U.
FhG-ISE (232x)
Amonix (92x)
Alta Devices
Panasonic
NREL (15.4x)
EMPA (Flex poly)
ZSW
Sanyo
FhG-ISE
Fraunhofer ISE
First Solar
GE Global Research
Solar Frontier
KRICT
Mitsubishi Chem.
United Solar Chem. (aSi/nc-Si/nc-Si)
LG Electronics
EPFL
NIMS
Sharp
IBM
Konarka
Heliatek
UCLA
MIT
Sumi-tomo
U. Toronto (PbS-QD)
NREL (ZnO/PbS-QD)
U. Dresden
U. Linz
Plextronics
Siemens
Groningen
NREL / Konarka
U. Linz
Solarmer
Konarka
U. Stuttgart
NREL
United Solar
Matsushita
Japan Energy
SunPower (96x)
Georgia Tech
Euro-CIS
Photon Energy
Boeing
AMETEK
ARCO
Solarex
U. So. Florida
Varian
Stanford
Kopin
Spire
Westing-house
No. Carolina State U.
Sandia
Kodak
RCA
Mobil Solar
U.of Maine
Monosolar
IBM (T.J. Watson Research Center)
UNSW
UNSW / Eurosolare
NREL (14x)
Varian (216x)
Varian (205x)
Stanford (140x)
Varian (154x)
NREL (16.4x)
Radboud U.
Sanyo
Spectrolab
NREL/ Spectrolab
NREL (IMM)
Boeing-Spectrolab
Spectrolab
Boeing-Spectrolab
Spectrolab
NREL
Spectrolab
Spectrolab
Spectrolab

Solar cells based on silicon semiconductors remain the dominant product of the PV market. However, silicon in PV cells has developed over the decades and exists in many forms. Primarily, crystalline silicon (c-Si) and polycrystalline silicon (pc-Si) wafers are the main materials of the PV industry; at over 80% of the market [9]. Silicon is an indirect band gap semiconductor and therefore to absorb light effectively a layer (wafer), typically hundreds of micrometers thick, is required. Otherwise much of the light would pass through the cell. These traditional wafer-based technologies form the first generation. However, because of the fact that Si cell arrays are large modular systems, due to the required thickness of the wafers, and also that the higher efficiencies achieved for Si technology require much higher production costs, mean that other PV generations must penetrate and mature in the PV industry to develop photovoltaics into an increasingly favourable renewable energy provider [10].

Second generation PV solar cells include thin-film technologies, such as cadmium telluride (CdTe), copper indium gallium selenide (CIGS) and amorphous silicon (a-Si). In thin-film cell architectures the semiconducting material is applied to a backing material in thin layers; just a few micrometres thick. The reduction in the amount of material required reduces the cost of the production of the photovoltaic cells when compared to the significantly thicker silicon wafers [10]. Both CdTe and CIGS are direct band gap semiconductors with band gap energies appropriate for solar adsorption; this means that they have high adsorption coefficients and so a much thinner absorber layer can be used to absorb the photons. Amorphous silicon, in contrast to crystalline silicon, is a thin film technology in which layers tuned with doping to specific absorption wavelengths are stacked to build a functional PV cell. This involves using less silicon than a c-Si cell, however, the lower efficiency and the manufacture costs for building the multi-layer constructions is still a major drawback of the technology. a-Si technologies also suffer from light induced degradation of the material and therefore their industry tested module efficiencies are low when they had field exposure of a few months [11]. Solar conversion efficiencies of these technologies are continually progressing, yet they do not hold a significant market share due to the stabilities of the cell architectures as well as environmental concerns for CdTe, for example, due to the toxicity of cadmium as a major component; this continues to be a contentious issue.

Emerging PV technologies, with little to no market share, are classified as the third generation of photovoltaics and include nanostructured material cells, quantum dot cells [12], organic and polymer solar cells [13]. Some examples of materials currently under much attention in the research of new PV technologies include the rapid growth of perovskite solar cells based on

organo-metal halides, such as methylammonium lead iodide ($MAPbI_3$), and materials consisting of more readily available sustainable materials, like copper zinc tin sulphide (CZTS) based solar cells. Some issues which challenge these technologies include the instability of organo-metal halide materials to exposure to air and moisture [14], and improving the cell efficiencies for CZTS based cells which currently stand at below 10% by improving the phase purity and altering the stoichiometry of the structure [15].

1.1.7 Methodologies for PV material synthesis and building cell architectures

Other developments in the area of photovoltaics has come from the utilisation of various methodologies to synthesise the materials and to build the cell architectures; often simultaneously. For example, some thin film technologies use spin-coating of precursors onto a glass substrate before the layers are heated and converted into films [16]. In another example, from the area of research into perovskite light-absorbing materials, power conversion efficiencies (PCEs) of the thin-film PV cells of the methylammonium lead iodide perovskite were found to be improved by using a two-step sequential deposition technique. This involves spin-coating a PbI_2 precursor onto a substrate followed by exposure to a solution of CH_3NH_3I to form $CH_3NH_3PbI_3$ [17]. Research also goes into developing these methodologies further by controlling the crystallisation of the product to improve the film quality and thus, the PCE [18]. Additional examples of methodologies include vapour deposition [19], solution-processing [20, 21] [21] , deposition of colloidal inks [12], and spray pyrolysis [22, 23].

1.2 Bismuth chemistry

1.2.1 General bismuth chemistry

Novel hybrid sensitizers and semiconducting materials are required for the progression towards ever more efficient, cheaper and less toxic cell architectures. Although bismuth is rarer than the elements constituting CZTS, for example, bismuth compounds are nonetheless interesting candidates for further research as thin-film light absorbers for applications in photovoltaic cells [24].

Bismuth is the heaviest group 15 (pnictogen) element in the Periodic Table and also the heaviest stable element. It has an atomic number of 83 and an electron configuration of $[Xe]4f^{14}5d^{10}6s^{2}6p^{3}$. Bismuth is commonly found in compounds with a +3 oxidation state leaving an inert pair of electrons in the 6s orbital. In comparison to other members of the group 15 family due to the decreased availability and increasing diffuseness of the s orbital a +5 oxidation is less stable and accordingly is rare but useful as a strong oxidiser. Due to its high metallic character bismuth can form stoichiometric compounds with other metals for instance, MBi and M_3Bi (M = Li, Na, K), M_3Bi_2 (M = Mg, Ca), and MBi where M is a rare-earth metal. In air, the elemental form slowly oxidises to form Bi_2O_3 and when heated with sulphur can form Bi_2S_3. Furthermore, at elevated temperatures elemental bismuth can react with molecular halogens such as fluorine and chlorine to form the corresponding trivalent BiX_3 halide compounds. Bismuth metal and many bismuth inorganic compounds such as Bi_2O_3, $Bi(NO_3)_3.5H_2O$ and $BiCl_3$ are available industrially and commercially for a relatively cheap price for the elements rarity [25].

Despite its location in the Periodic Table, between lead and polonium, bismuth is a stable element with low toxicity for a heavy metal. As a result, a range of bismuth compounds have been found to have applications in cosmetics and pharmaceuticals as the bismuth does not bioaccumulate and present toxicity in the human body. Notably, the most well-known of these is pepto-bismol (bismuth subsalicylate) used as a treatment for stomach and gastrointestinal discomfort. Bismuth alloys are also being utilised as replacements for the markedly more toxic lead alloy compounds.

When designing a semiconducting material for solar energy applications, as touched upon previously, an appropriate material should be photoactive with a band gap energy in the range of ~1.0-1.8 eV. To achieve this from a compound semiconductor, commonly late transition metals/ early to main p-block metals are combined with chalcogens (group 16) and halogens (group 17). Bismuth is a heavy p-block element which can form semiconducting materials when combined with chalcogens and halogens, for example, as will be expanded upon in the following section.

1.2.2 Bismuth-based candidate semiconducting materials

Bi-containing compounds have gained more interest over recent years, in the family of Bi-VI-VII compounds BiOX (where X= Cl, Br, I) have gained attention for their photocatalytic activities [26] [27] as well as a semiconductor sensitiser for BiOI-sensitised TiO_2 [28] and photoelectric applications [29]; with BiOI having a band gap of ~1.92 eV [30]. Additionally, recently layered structures of bismuth oxysulfides have been examined for photoelectric properties, with a $Bi_9O_{7.5}S_6$ material exhibiting a direct band gap of ~1.27 eV showing potential in photovoltaic studies [31]. Previously, other bismuth oxysulphides (e.g. Bi_2O_2S) had been examined for photoelectric properties to find an indirect band gap structure (E_g = 1.12 eV). From this, research into superconductive bismuth oxysulphides (Bi_2O_2S & $Bi_4O_4S_3$) has been undertaken [32] [33] [34].

Semiconducting materials in the Bi-VI class of compounds have developed in many areas. Bismuth selenide (Bi_2Se_3) and bismuth telluride (Bi_2Te_3) materials, often doped to improve efficiency, are widely utilised for their thermoelectric properties as they exhibit high performance [35] [36] [37] [38]. Thermoelectric materials, which can convert thermal energy to electrical energy and vice versa, have applications in power generation and refrigeration processes. Moreover, bismuth sulphide (Bi_2S_3), a naturally occurring mineral known as bismuthinite, has seen much attention owing to its potential as a photoactive material with a low band-gap energy of ~1.4 eV and a high absorption coefficient for harvesting light [39]. Much work has gone into controlling the morphology of Bi_2S_3, for example, to form nanorods for incorporation into hybrid polymer-inorganic solar cells [39], various methodologies to form nanostructures [40] [41] [42], and techniques involving the decomposition of organic bismuth complex precursors, such as xanthates [43] [44] [45].

An interesting, but not extensively explored, material for its potential applications in photovoltaics is bismuth sulphide iodide (BiSI). Contained in the Bi-VI-VII class of compounds, which have been explored with interest previously owing to the coexistence of several physical properties, such as photoconductivity, ferroelectricity, electrooptical effect, electromechanical effect, piezoelectricity, and a large temperature dependence of the band gap [46]. The structure of BiSI consists of chains of the atoms in a paraelectric phase and belong to *Pnam* space group [47]. All atoms in the BiSI crystal lie on mirror planes normal to the *c*-axis. Figure 1.6 shows a projection of the *a*-*b* plane of the bismuth sulphide iodide crystal structure.

The structure contains double chains $[(BiSI)_\infty]_2$ consisting of two chains related by a twofold screw axis and linked together by a short and strong Bi-S bond. Weak van der Waals' type bonds bind the double chains [48].

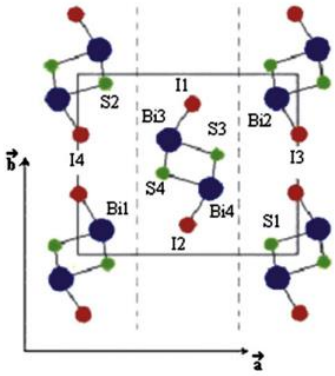

Figure 1.6 Crystal structure of bismuth sulphide iodide (BiSI) projected in the *a*-*b* plane [48]

BiSI, with a reported indirect band gap of 1.57 eV, is well suited for photovoltaic studies. The photoelectric properties of BiSI have been observed displaying anisotropic PV effects and n-type conductivity [49]. More recently, polycrystalline films of deposited BiSI have been reported which exhibit promising photoelectrochemical properties using a single-source chemical spray pyrolysis technique. The films studied show strong light absorption in the visible range and the well-crystallised layered structure exhibits excellent photoelectrochemical performance through improved electron-hole generation and separation. The structure and surface composition of these films, which varies with deposition temperature, results in significant changes in the photoelectrochemical performance [50]. BiSI and other V-VI-VII type materials, such as BiSeI, could also be of interest as a precursor reagents for developing novel photoactive semiconducting materials. In a similar vein, it may be possible to develop solution-based techniques to give phases such as $XBiSI_2$ (where X = Cs, K, Na, methylammonium (MA), formamidinium (FA)) from a BiSI precursor. In order to do this, solvothermal synthetic procedures which utilised bismuth precursors were researched and will follow this section.

Over recent years, perovskite materials have made a significant impact and continue to develop as a promising emerging photovoltaic technology [51]. The perovskite AMX_3 structure is typically a three-dimensional structurally and electronically connected anionic network of corner-sharing MX_6 octahedra with a counterbalancing organic/inorganic cation within the octahedral cavity space. At the forefront of the research are lead iodide perovskite phases such as methylammonium lead iodide ($MAPbI_3$) which can be synthesised by solution-based techniques with PbI_2 as a precursor reacting with MAI [52]. Much work has been and continues

to be undertaken into researching and producing high efficiency lead halide based perovskite solar cells to compete at a high industry standard. However, concerns over sensitivity of the absorber material to moisture and air for long-term functional stability, inherent thermodynamic instability towards dissociation and the presence of toxic lead all compound to challenge their prospects [53, 54]. Certain studies have also applied the use of pseudohalides, such as thiocyanate (SCN^-), as a dopant to substitute iodide position within $MAPbI_3$ framework materials to improve stabilisation and possibly enhance/tune the optoelectronic properties [55, 56].

To move beyond lead-based systems, the approach to designing and discovering new functional optoelectronic semiconductors within the perovskite material class is to look into interchanging the A site, M site and X site identity; and often combinations of all three. Firstly, however, it is important to understand that the impressive and desirable optoelectronic properties of the lead-based perovskites derive from the fundamental electronic structure of the semiconducting material and so the design should work to mimic these properties. From theoretical studies of lead-based perovskite structures known to exhibit the highest performance as photovoltaic absorbers it was deemed that part of the success can be attributed to the presence of partially oxidised post transition-metal ions within the materials [57]. Here, the Pb cations, with $6s^2$ lone pair of electrons, are understood to produce shallow defects and a dispersed valence band through strong antibonding coupling to iodine 5p orbitals [58, 59].

As a result, initial lead-free alternative material investigations began with halide compounds with isovalent substitution of tin (Sn^{2+}) [52, 60, 61] and germanium (Ge^{2+}) [62], but also with bismuth (Bi^{3+}) and antimony (Sb^{3+}); which possess $5s^2$ or $6s^2$ outer lone pairs of electrons in their configurations. Studies into tin-based equivalent compounds indicated that the compounds would undergo rapid oxidation by air and limited moisture-tolerance leading to decomposition of the functional materials [63, 64].

As mentioned, another group of materials deemed as possible alternative absorber materials are hybrid bismuth and antimony halometallates. Inspired by the rise of the most studied iodoplumbate $(A)PbI_3$ perovskites (Figure 1.7) where the A site is commonly occupied by organic methylammonium, formamidinium or inorganic Cs or Rb cations lead-free zero-dimensional perovskites $A_3Bi_2X_9$ ($A = Cs^+$, MA^+, FA^+, Gu^+ $X = I^-$, Br^-) [65-69] have been the initial targets for bismuth and, as discussed later, antimony-containing perovskite structures.

Reported optical band gap energies for the materials are in the range of 2.1-2.4 eV; outside the most desirable range of 1.4-1.8 eV exhibited by most of the lead-based material counterparts.

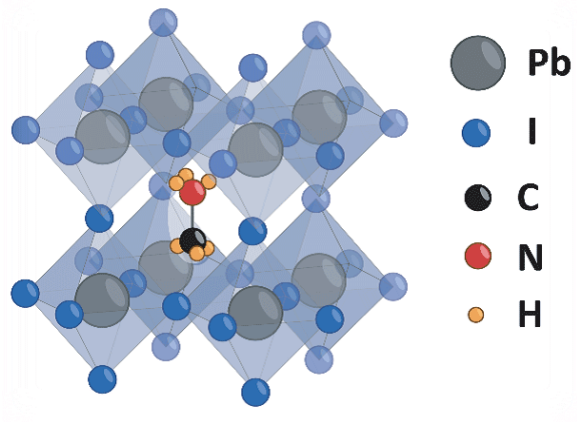

Figure 1.7 Perovskite structure of methylammonium lead iodide
(N.B. courtesy of the National Renewable Energy Laboratory, Golden, CO)

However, this class of material is shown to demonstrate a broad variety of structural types and connectivity by vertex, edge and face sharing MX_6 octahedra connections as detailed within the published and unpublished halometallate material studies undertaken in the presented research to follow.

The search for lead-free alternative materials has expanded into many areas; including double perovskite systems, also known as elpasolites, with the general formula $A_2BB'X_6$ (X = halide). B and B' sites within the structure are occupied by monovalent and trivalent cations; with Bi^{3+} and Sb^{3+} as desirable candidates. Early investigations into bismuth-based alternatives in this structural class include the hybrid double perovskite, $(MA)_2KBiCl_6$; a 3D lattice structure made up of corner-sharing KCl_6 and $BiCl_6$ octahedra counterbalanced by methylammonium cations [70]. Additionally, the inorganic double perovskites $Cs_2AgBiBr_6$ and $Cs_2AgBiCl_6$ have been synthesised and studied for their potential optoelectronic properties [71, 72] (Figure 1.8). Indirect band gap energies of 3.04, 2.19 and 2.77 eV are reported for each material respectively; slightly under the values of their equivalent $(MA)PbX_3$ analogues. Varying potential A site (Cs^+, MA^+), B site (Cu^+, Ag^+, Au^+), B' site (Bi^{3+}, Sb^{3+}) candidates in halide-based (Cl^-, Br^-, I^-) systems may yield further stable lead-free perovskite alternative materials [73].

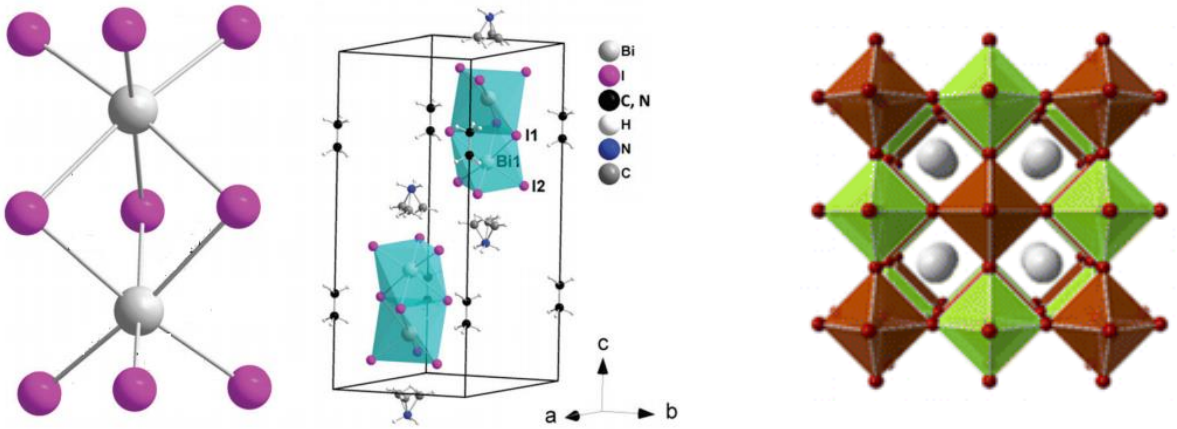

Figure 1.8 (Left) Crystal structure of methylammonium bismuth iodide (MBI) $(CH_3NH_3)_3Bi_2I_9$ showing $Bi_2I_9^{3-}$ anion and unit cell [65], (Right) Double perovskite structure Cs_2AgBiX_6 (X = Br, Cl) [71]

1.2.3 Bismuth in metal-organic framework (MOF) synthesis

Primarily, the organic linkers used in MOF synthesis contain a rigid aromatic region with multiple functional groups and/or donor atoms on the ring to bond to the metal nodes and form coordination polymers. For Bi-MOF synthesis, carboxylic acids are often used as they tend to form more stable frameworks due to the strong binding affinity of oxygen as a donor atom to bismuth; making alkoxide and carboxyl functionality favourable. Moreover, N-donor atoms bind well to Bi(III), the most common and stable oxidation state of bismuth, and therefore pyridine ring containing linkers are also favourable for forming stable structures. The organic linkers listed in Table 1.1 below were used in exploratory solvothermal synthesis procedures to find novel bismuth-carboxylic acid structures and provided a basis for further study of bismuth (III) coordinated absorber material structures with the utilisation of solvothermal synthesis.

Table 1.1 Organic linkers utilised in coordination polymer synthesis procedures

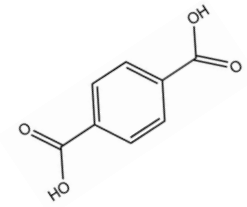	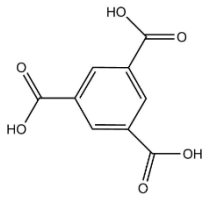	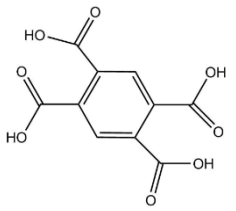
1,4-benzenedicarboxylic acid (Terephthalic acid)	1,3,5-benzenetricarboxylic acid	1,2,4,5-benzenetetracarboxylic acid
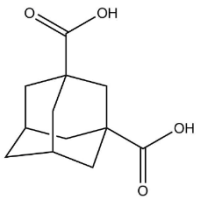	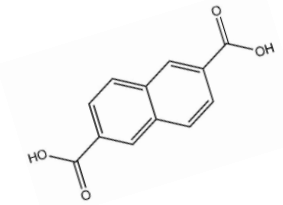	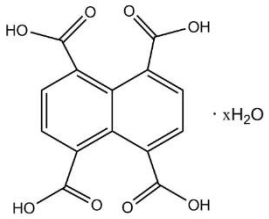
1,3-adamantanedicarboxylic acid	2,6-napthalenedicarboxylic acid	1,4,5,8-napthalenetetracarboxylic acid hydrate
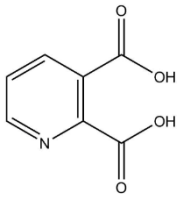	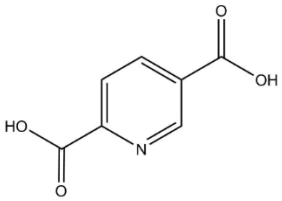	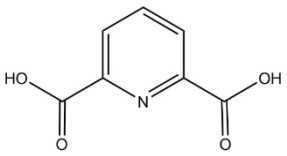
2,3-pyridinedicarboxylic acid	2,5-pyridinedicarboxylic acid	2,6-pyridinedicarboxylic acid
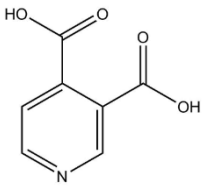	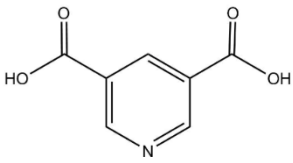	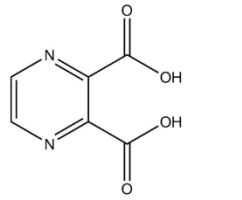
3,4-pyridinedicarboxylic acid	3,5-pyridinedicarboxylic acid	2,3-pyrazinedicarboxylic acid
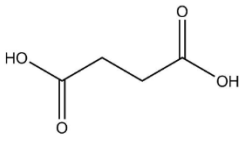	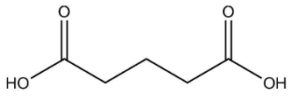	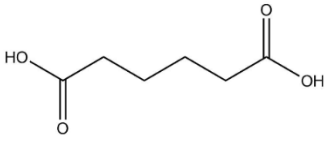
Succinic Acid (1,2-ethanedicarboxylic Acid)	Glutaric Acid (1,3-propanedicarboxylic Acid)	Adipic Acid (1,4-butanedicarboxylic Acid)

As a main group metal, with a high electron count, bismuth possesses a large coordination sphere for bonding. With electron configuration of $[Xe]4f^{14}5d^{10}6s^2$, Bi(III) ions have a stereochemically active lone pair of electrons with a possible structure directing role, however, at higher coordination with increased steric hindrance, as well as a more uniform charge distribution around the Bi(III) cation, the role of the lone pair of electrons becomes more inactive in its structural role.

1.2.4 Literature bismuth-based carboxylic acid frameworks synthesised by solvothermal methodologies

In order to investigate suitable conditions for synthesising novel bismuth-containing materials through solvothermal processes, methodologies where bismuth precursors had been used were identified from a study of the related literature. Previously, bismuth compounds such as bismuth nitrate pentahydrate, bismuth oxide and bismuth chloride have been used as reagents in hydrothermal/solvothermal processes to synthesise a range of metal-organic frameworks (MOFs)/ coordination polymers (CPs). Over the past few decades, research into these materials has grown rapidly. They are seen as promising materials for the future because they are commonly synthesised from cheap starting materials, they allow for highly adjustable and designable properties and topologies based on varying the metal centres and linkers used to form the structure and are generally structures with low framework densities but high thermal stabilities [74].

Applications for metal-organic frameworks/ coordination polymers are numerous and are continuously expanding. Examples of their properties and applications include catalysis[75], sensing [76], luminescence [77] [78], gas storage [79] [80], separations [81], drug delivery [82], removal of hazardous materials [83] and they have also gained much interest for applications in clean energy research [74]. In particular MOFs are being explored in the fields of hydrogen energy, fuel cells, lithium-ion batteries, supercapacitors and solar cells [84].

Novel MOFs are commonly synthesised by the combination of metal ions (nodes), with flexible coordination spheres, and rigid aromatic carboxylic acid based ligands (linkers) under solvothermal conditions. Owing to the fact that bismuth is a main-group metal with lone pairs and a large coordination sphere it is open to forming more distorted and unpredictable structures than when constructing MOFs with transition metals; which commonly yield

predictable topologies of coordination [85]. However, research in the area of main-group metal containing metal-organic frameworks is much more unexplored relative to transition-metal based coordination polymers.

To find novel bismuth-carboxylic acid based structures a systematic series of experiments was undertaken. Initial conditions and precursor reagents used were based on literature solvothermal routes for synthesising bismuth-based carboxylic acid coordination materials such as bismuth 1,4-benzenedicarboxylates [86 87] and bismuth 2,6-pyridinedicarboxylates [88]. Other examples include bismuth tri- and tetraarylcarboxylates [89] and bismuth 2,5-pyridine dicarboxylates [85 90 91].

1.3 Antimony chemistry

1.3.1 General antimony chemistry

Antimony (Sb) is a p-block group 15 pnictogen element in the Periodic Table situated directly above bismuth and sandwiched between tin and tellurium; all of which are elements that are prevalent in the field of semiconducting sensitiser materials. It has atomic number of 51 and an electron configuration in its ground state of $[Kr]4d^{10}5s^{2}5p^{3}$. Similarly to its heavier group 15 counterpart element, bismuth, antimony is commonly seen in compounds in either a +3 or +5 oxidation state.

Elemental antimony is not readily oxidised, however, under certain light and moisture conditions the metal can oxidise. Antimony is also found in a range of oxidised forms such as Sb_2O_3 (Valentinite – rhombic, Senarmontite - cubic) and cervantite Sb_2O_4. Also, due to its inherent affinity for sulphur, among the many mineral ores containing antimony, antimonite (Sb_2S_3) is one of the most common and commercially established. Much like bismuth, antimony reacts readily with molecular halogens, such as chlorine and iodine to form the related trivalent SbX_3 and pentavalent SbX_5 halide compounds. For this reason, as mentioned earlier, hybrid haloantimonate materials alongside hybrid halobismuthate materials have been highlighted as possible alternatives as lead-free perovskite solar absorbers. The primary application of antimony is its use in flame retardants, usually in the form of antimony trioxide, and also in alloys; typically with lead and with tin in various metallurgic applications. Other uses include being utilised in catalysis for the production of polyethyleneterephthalate (PET), paint pigment compounds and as an emetic for medical purposes.

To reiterate, when designing and directing the synthesis of photoactive compound semiconductors, much like bismuth, antimony is a p-block element which can form a broad range of potential absorber materials when combined with chalcogens (group 16 elements) and/or halogens (group 17 elements). Candidate antimony-based semiconducting materials for investigation are discussed next.

1.3.2 Antimony-based candidate semiconducting materials

Much like the bismuth-based equivalents, V-VI-VII compounds containing antimony as the group 15 pnictogen (VI = S, Se, Te) (VII = Cl, Br, I) have been an established class of known compounds for over a century. The most studied for their photoelectric properties are compounds antimony sulphiodide (SbSI) and antimony sulphobromide (SbSBr), known to be ferroelectric semiconductors, similar to BiSI and BiSBr [92]. However, the antimony equivalent semiconductors exhibit larger band gap energies of approximately 2.2 eV.

A range of synthesis and structural property studies have been undertaken for hybrid haloantimonate materials, particularly for chloro- and bromoantimonate structures over recent decades [93-99], however, iodoantimonate hybrid materials present an understudied area for further investigation. As a result, alongside iodobismuthate materials, expanding the depth and understanding of possible alternative photoactive materials in these areas provided the primary focus of the research presented here.

1.4 Solvothermal synthesis procedures using bismuth and antimony reagents

Many common commercially and industrially available bismuth and antimony precursor salts are known to be insoluble in most solvents at room temperature. Solvothermal synthesis, a synthetic method which involves heating reagents in a sealed Teflon® autoclave under increased pressure, can be used to increase the solubility of reagents, influence the reactivity for product formation and control the cooling for crystallisation. Solubility tests carried out for bismuth precursors, bismuth nitrate pentahydrate and bismuth chloride, in a range of solvents showed partial solubility in water and alcohols, almost full solubility in DMF, with limited or total insolubility in most solvents. The readily available reagent, antimony (III) chloride, readily hydrolyses in water and showed partial solubility in alcohol. Therefore, most exploratory synthesis routes developed were carried out hydrothermally or solvothermally in methanol, ethanol or DMF.

Previously, bismuth has been employed in solvothermal syntheses to synthesis a range of nanostructured materials, such as bismuth selenide nanotubes [100], nanosheets [35] and bismuth ferrites [101, 102]. Antimony has also been used in various solvothermal synthesis for a range of applications including in the one-pot synthesis of nanocrystals of copper antimony sulphide (Cu_3SbS_4) [103], antimony telluride (Sb_2Te_3) [104, 105] nanobelts and antimony selenide (Sb_2Se_3) [106] nanostructures, to name a few.

Additionally, with control over temperature changes, molar ratios, and templating agents; solvothermal synthesis has been utilised to manipulate the morphology of products such as bismuth oxychloride [107], bismuth oxyiodide [108] and bismuth/antimony sulphide iodide [109, 110]. Research in the field of bismuth metal-organic frameworks has also utilised solvothermal procedures to synthesise novel structures by combination of metal ions (nodes) and organic ligands (linkers). However, main-group metal containing metal-organic frameworks are largely unexplored in comparison to transition-metal containing frameworks.

Bismuth is of potential interest in many areas as, despite its location in the Periodic Table, it has very low toxicity, is non-carcinogenic, and is relatively inexpensive for a metal and therefore novel bismuth frameworks structures may have unique applications in the rapidly expanding fields of metal-organic framework synthesis and organic-inorganic hybrid materials. Antimony is less abundant, however, it shares similar chemical properties to bismuth being in the pnictogen group and provides an intriguing basis for structural and physical property

comparison to related metal-containing materials. As referred to earlier, both bismuth and antimony, with 3+ and 5+ oxidation states, have a tendency to bond strongly with halides to form a broad range of possible structural connectivities and therefore have been identified as target elements for further investigation in inorganic sensitizer structural research.

1.5 Research aims

The key aim of investigation was focussed on the design, synthesis and characterisation of novel inorganic sensitisers for photovoltaic cells related to the desirable properties of methylammonium lead iodide and similar emergent photovoltaic absorber materials. This would involve introducing more sustainable concepts into the reagents, metal identity and synthetic conditions utilised into the discovery of new materials.

Primarily a focus is required to be put on the expansion of the design and understanding of halometallate materials ultimately to improve upon the optimisation and tunability of the alternative absorber layer materials available in the vast family of halometallate structures.

Through unique solution-based and solvothermal procedures new structures would undergo full structural determination and where appropriate further optimisation of the synthetic conditions and analysis of the physical properties of the materials by optical and thermal analysis primarily. Each experimental technique employed within the presented research is described in chapter 2.

The first results chapter, chapter 3, introduces the published work carried out on iodoantimonate and iodobismuthate organic-inorganic hybrid material investigations; with comparisons made between materials with shared organic templates and altered metal identity. Chapter 4 expands upon the work on halometallate hybrid materials with a discussion of a useful solvothermal synthetic mechanism used to broaden the range and complexity of novel structures synthesised. Chapter 5 presents a novel three-dimensional iodoantimonate structural motif in development. Chapter 6 covers investigations into a range of areas including bismuth-based coordination polymers; which initially acted as a guide for the development of all solvothermal synthetic work to follow. In addition, bismuth chalcohalide and pseudohalide-based investigations are discussed. The overall results and conclusions are given in chapter 7.

Chapter 2 – Experimental Techniques

2.1 Introduction

The large majority of materials synthesised throughout this research were obtained by employing a solvothermal or hydrothermal synthesis procedure. Utilising this technique high quality single-crystals of each new compound could be grown in order to undertake full structural X-ray analysis and further characterisation. Other synthetic techniques included solution-based synthesis heating under reflux and solid-state synthesis, utilised to a lesser extent. Each compound has been further characterised where applicable by a range of techniques; primarily with single-crystal X-ray analysis, UV/Vis spectroscopy and thermogravimetric analysis but also with techniques such as powder X-ray diffraction, electron microscopy and energy dispersive X-ray spectroscopy.

2.2 Synthetic

2.2.1 Solvothermal/Hydrothermal Synthesis

Solvothermal/Hydrothermal synthesis is a method used to grow single-crystals in a non-aqueous (solvothermal) or aqueous (hydrothermal) solution in a sealed autoclave (a thick-walled steel vessel) at high temperature and pressure. Reagents are sealed in a Teflon® vessel and heated with a controlled procedure (Figure 2.1). Experimental parameters such as reaction temperature, reaction dwell time, temperature ramp up / ramp down rates, molar ratios of reagents, volume of solvent and solvent type can be changed to tailor product formation or manipulate the morphologies of products for example. A Lenton laboratory oven was used to carry out solvothermal synthesis experiments with a procedure control system utilised to control heating treatment and cooling processes.

Figure 2.1 Solvothermal/Hydrothermal synthesis apparatus: a Teflon® vessel and fittingly sized thick-walled steel vessel

2.2.2 Solution-based synthesis heating under reflux

Heating under reflux is a common distillation technique used to carry out chemical reactions. Reagents are heated in a solution contained in a vessel, usually a round-bottomed flask, connected to a condenser (Figure 2.2). At elevated temperatures, above the boiling point of the solvent, vapours from the solution will form a condensate in the condenser and return to the reaction solution. Thus, chemical reactions can be carried out at higher temperatures for longer periods.

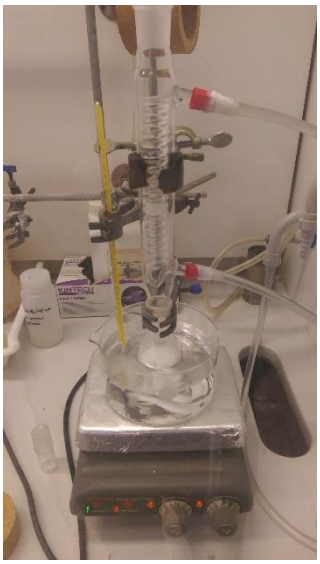

Figure 2.2 Heating under reflux synthesis apparatus: a reaction flask heated by a temperature controlled oil bath. Condenser fitted for reflux experiments

2.3 Characterisation

2.3.1 Background for X-ray diffraction characterisation

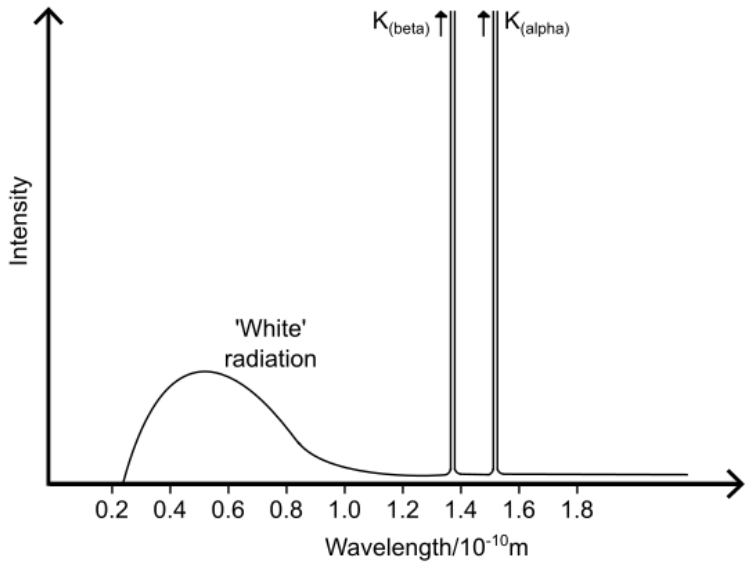

Figure 2.3 A spectrum of X-rays emitted from an X-ray tube

To undertake X-ray crystallographic studies of a solid-state material requires an X-ray source. To generate a monochromatic beam of X-rays, electrons, emitted from an electrically heated filament, are accelerated by a high potential difference (20-50 keV) towards a metal surface. When the electron stream, sometimes called the cathode stream, collides with the metal (anode) surface a continuous spectrum of 'white' radiation is emitted along with sharp X-ray peaks (K_α & K_β). The sharp K peaks occur because the accelerated electrons knock electrons out of the innermost K shell (n = 1) resulting in vacant sites which in turn leads to electrons from L shell (n = 2) and M shell (n = 3) descending to fill the sites. When the electrons descend from the higher shells to the vacant sites the energy decrease is accompanied by the emission of radiation; L→K gives the K_α peak and M→K gives the K_β peak [1, 2].

The frequencies of the K peaks are characteristic of the anode metal used as an X-ray source. Typically, the metal targets used are either copper (Cu) or molybdenum (Mo) sources, which have K_α peaks at 154.18 pm and 71.07 pm respectively. To give a monochromatic (single wavelength/ very narrow wavelength range) radiation usually K_α is selected and the 'white' radiation and K_β radiation is filtered out. This can be achieved by using a filter made of a thin metal foil of the element adjacent to that of the source (Z-1) in the Periodic Table.

Thus, for copper and molybdenum sources, foils of nickel and niobium respectively are effective filters. Alternatively, a monochromatic X-ray beam can be selected by reflecting the beam from a plane of a single crystal, commonly graphite [1].

It was noted by W.L. Bragg [3], a British physicist, that X-rays can be diffracted by planes of atoms in the solid crystalline state. The scattered X-rays from a sample with a periodic array of scattering sites can be collected by a detector and give rise to a diffraction pattern. Interpretation of the pattern can be used to give structural information such as atom positions, bond lengths, bond angles, crystal system, space group, unit cell parameters and symmetry elements present.

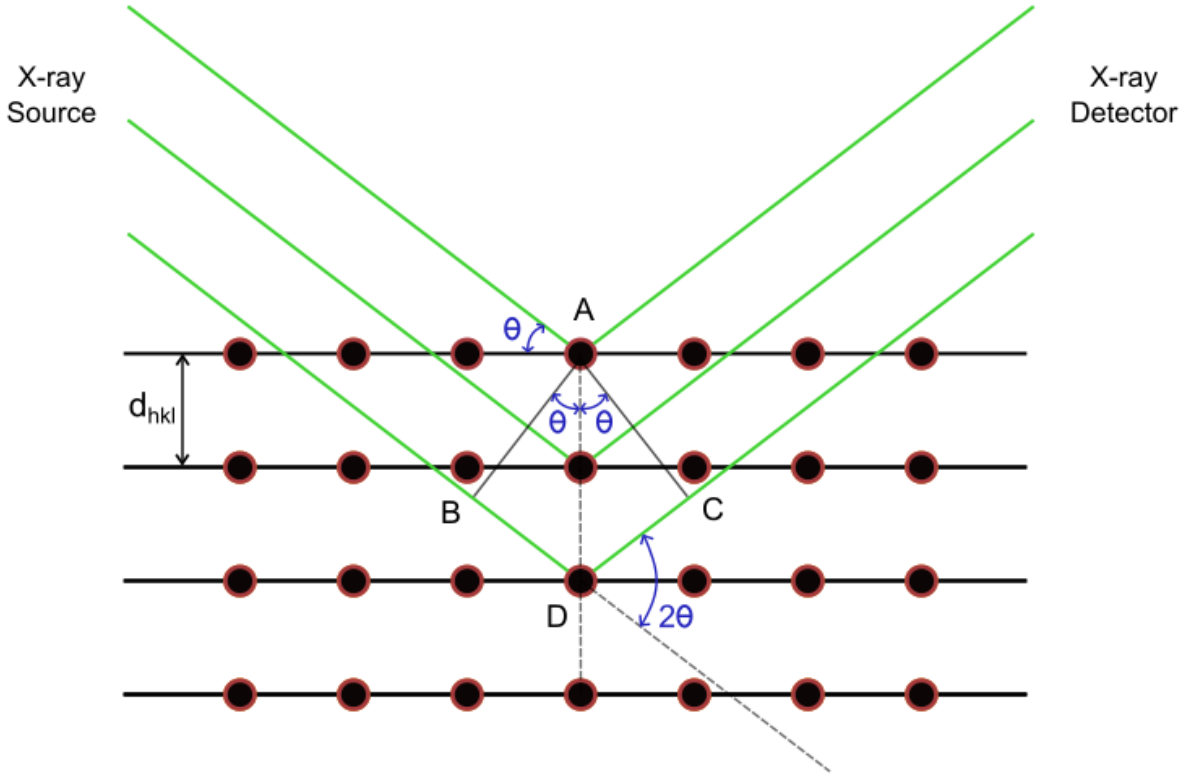

Figure 2.4 A schematic showing Bragg diffraction of X-rays on a crystalline array of atoms

A reflection can occur and be detected when X-ray beams are diffracted in phase and undergo constructive interference. For this to happen, the path lengths of the interfering X-ray beams must be separated by an integral wavelength number (nλ). The path difference of the X-rays can be described as being BD + DC when the X-ray beam is intersected at a 90° angle, as shown in Figure 2.4. The path difference of the reflection measured will be related to the Miller indices *hkl* of the lattice plane by the interlayer spacing d_{hkl} and also by the angle (θ) of the incident

X-ray beams with the relationship; BD + DC = $2.d_{hkl}.\sin\theta = n\lambda$. Thus, for an integral wavelength pathlength difference an expression can be obtained and is known as the Bragg equation; $n\lambda = 2d_{hkl}\sin\theta$ [1, 2].

2.3.2 Powder X-ray diffraction

In powder X-ray diffraction (PXRD), an analytical technique commonly used in solid-state inorganic chemistry, a crystalline powder sample is placed in the path of a monochromatic X-ray beam. Planes within the material will diffract the X-rays at the appropriate angle 2θ for constructive interference of the X-ray beams to occur with a significant intensity in relation to the Bragg equation. A recorded pattern can be used as fingerprint of the crystalline sample and therefore can be checked against a database of other recorded patterns to identify known compounds and phases. Furthermore, the technique can be used to assess phase purity of the sample, measure crystallite size and even structural determination for high symmetry systems; to name a few applications [4].

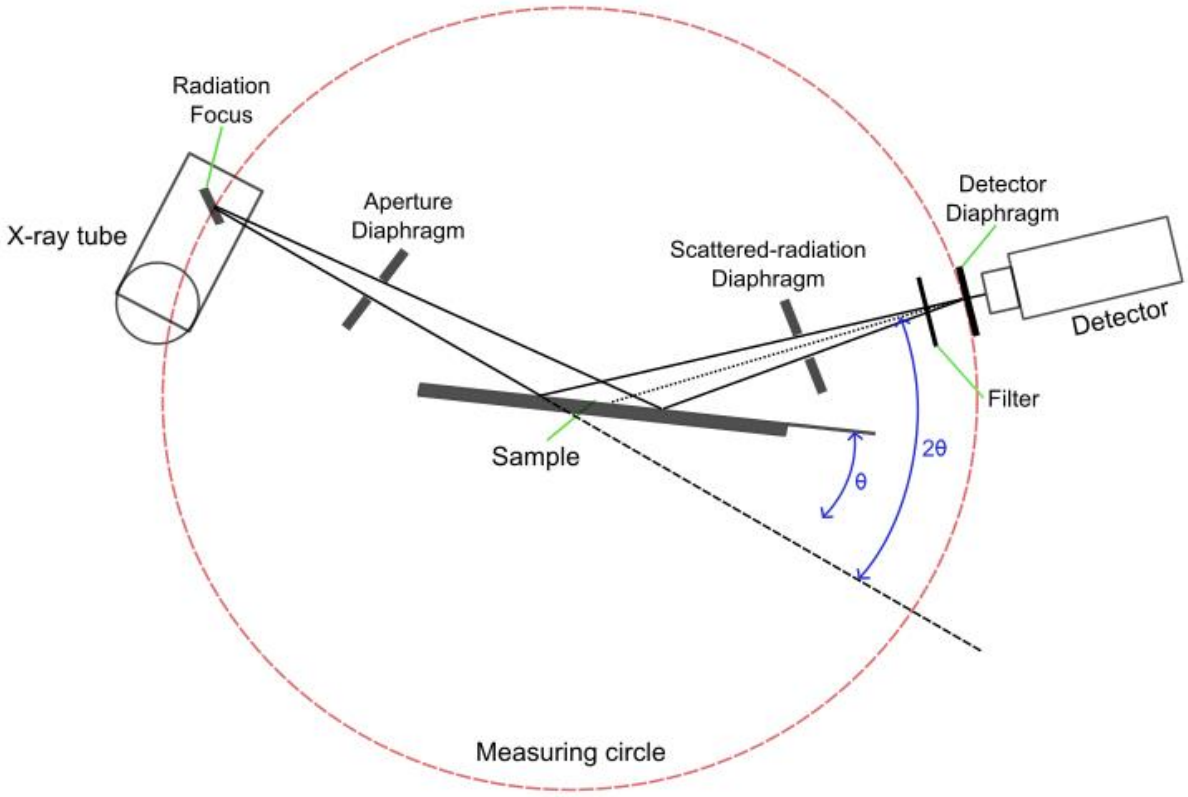

Figure 2.5 Powder X-ray diffraction diffractometer schematic

PXRD patterns were collected on a Siemens Diffractometer D5000 with Cu K_α radiation (λ = 1.5418 Å, 40 kV, 30 mA), with variable temperature experiments carried out on a Bruker D8 Diffractometer with Cu K_α radiation (λ = 1.5418 Å, 40 kV, 30 mA). All data were recorded with DIFFRAC plus XRD commander and analysed with DIFFRAC.EVA (V3.0) software suites [5].

2.3.3 Single-crystal X-ray diffraction

Single-crystal X-ray diffraction (SXD) is an analytical technique used to determine the three-dimensional structure of materials in the solid state. To do this a single-crystal, in which all of the unit cells are identical and in the same orientation in the structure, is placed at the centre of a high intensity X-ray beam. A goniometer is utilised to rotate the crystal in three-dimensions whilst retaining its position in the beam and an area detector records diffraction patterns for the crystal at different orientations; measuring the Bragg angle θ and the intensity for each *hkl* reflection.

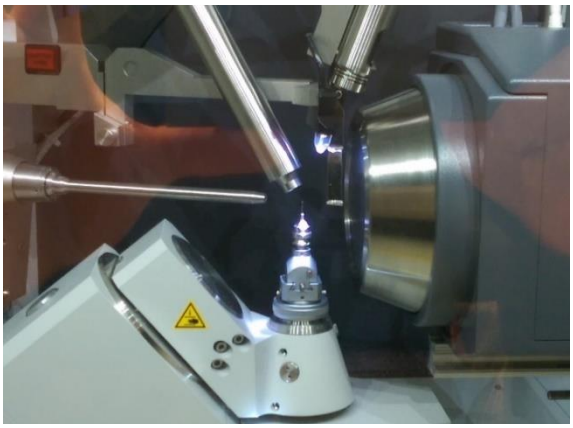

Figure 2.6 A photo of a single-crystal X-ray diffractometer taken through the observation window

The technique can be used to quickly determine the unit-cell dimensions, crystal system and space group of the single-crystal structure. These parameters can be checked against crystallographic databases to ascertain whether the crystal structure is known. From the data, if the crystal and data collection is of good quality, a complete structure determination can be accomplished with the use of computational programs to solve and refine the data to give an accurate structural model of the crystal. A good structure determination will provide definitive atomic positions and therefore accurate bond lengths and bond angles [2].

Suitable crystal → Pre-experiment → Experiment → Data reduction → Structure solution → Form a structural model → Refine structural model → Interpret results

$$\text{Diffraction Pattern} \leftarrow \xrightarrow{Fourier\ transform} \rightarrow \text{Electron Density}$$

The intensities of the diffraction pattern obtained in a single-crystal data collection are related to the arrangement of atoms in the unit cell of the structure through the structure factors, F(*hkl*). These are obtained by Fourier transformation of the electron density.

$$F(hkl) = \int_{cell} \rho(xyz)\ .\exp[2\pi i(hx+ky+lz)]dV \qquad [Eq.1]$$

Each reflection produces a structure factor with amplitude |F(*hkl*)| and a phase ø(*hkl*). The structure factor for reflection *hkl* is given by taking the value of the electron density at each point in the unit cell ρ(*x*,*y*,*z*) multiplied by the complex number exp[2πi(h*x*+k*y*+l*z*) and adding up the values integrated across the cell volume $\int_{cell} dV$ [Eq.1]. X-rays scatter in-phase in the forward direction ($2\theta = 0^o$), however, for all other angles the intensity falls off as a function of sin θ / λ. The variation of intensity with angle is called the atomic scattering factor f(θ). It is measured in units of electrons and so for f(0) the scattering factor at zero deflection is equal to the atomic number. The scattering factors of each atom and ion of all elements are known and so these unique scattering factors can utilised to identify each atomic position in the electron density map [2].

Atoms in a solid-state crystalline structure, however, are not stationary. The vibration of the atoms about their equilibrium positions in the lattice, with temperature dependent effects, influences the effective size of the electron density and increases interference effects. The atomic scattering factor falls away more rapidly as the angle increases and is typically different for atoms of the same element due to varying vibrational effects; except for symmetry-equivalent positions. For an atom which vibrates equally in all directions, known as isotropic vibration, the vibrational effect can be considered by multiplying the atomic scattering factor by a term containing an isotropic displacement parameter U [Eq.2] [2].

$$f'(\theta) = f(\theta)\ .exp\left(-\frac{8\pi^2 U sin^2\theta}{\lambda^2}\right) \qquad [Eq.2]$$

The parameter represents a mean-square amplitude of vibration of the atom; a measure of the atomic vibration. The larger the value of U, the more the curve falls away at higher Bragg angles. Taking into account all discrete atoms as a whole, the Fourier transformation relating the diffraction pattern (*via* the structure factor) to electron density takes the form given in [Eq.3].

$$F(hkl) = \sum_j f_j(\theta) \ . \ exp\left(-\frac{8\pi^2 U_j sin^2\theta}{\lambda^2}\right) . \exp\left[2\pi i\left(hx_j + ky_j + lz_j\right)\right] \qquad [Eq.3]$$

The structure factor set is formed from the sum of all atomic positions across the unit cell, each with its related atomic scattering value f_j (a function of the Bragg angle (θ)), a displacement parameter (temperature factor U_j), and coordinates of the atom positions ($x_j + y_j + z_j$) as related to the unit cell origin [2].

Determination of the electron density from the diffraction experiment (the inverse Fourier Transform of Eq.1) would reveal atomic positions and allow the structure to be determined and optimised. Each reflection has a measured amplitude, but the phases of the reflections are unknown; initial estimates of these, or a subset of them, must be obtained to allow initial structure solution. The two structure solution methods to solve the phase problem in crystallography are the Patterson synthesis method and the more commonly utilised direct methods. Direct methods are computational trial and error strategies which aim to determine approximate reflection phases from the measured intensities. This is achieved by selecting the reflections which contribute most to the Fourier transform, observing the probable relationships among the phases and attempting different phase combinations to satisfy the relationships. Fourier transforms can then be calculated from the observed amplitudes and trial phases, yielding the initial structure factors. Molecular features (atomic position) can then be identified in the resulting maps which make chemical sense, to form a structural model [2].

As shown earlier, using the Fourier transform equation, the diffraction pattern is related directly to the electron density map and *vice versa*. As a result with a model structure obtained the forward Fourier transform equation can calculate what the diffraction pattern would be given the model were correct; giving a set of calculated structure factors F_c. The overall quality of the structural model obtained from single-crystal analysis is assessed partly through the value of the residual factor of the data [Eq.4]. The value indicates a comparison between the calculated structure factor data set, with known amplitudes ($|F_c|$) and phases ($ø_c$) of F_c, and the observed structure factor set, with known amplitudes ($|F_o|$) but no phases ($ø_o$). If $|F_c|$ and $|F_c|$ structure factor data sets show a good resemblance then the R-factor value is low indicating a good agreement between model and data [2].

$$\text{Residual Factor} \quad R = \sum \left| \frac{|F_O| - |F_C|}{\sum |F_O|} \right| \qquad [Eq.4]$$

The instruments used to attain single-crystal X-ray data were:

- Agilent Supernova dual wavelength diffractometer equipped with an Oxford Cryostream, featuring a microsource with Mo K_α radiation (λ = 0.71073 Å) and Cu K_α radiation.
- Agilent Xcalibur diffractometer equipped with an Oxford Cryostream using a graphite monochromated Mo K_α (λ = 0.71073 Å) radiation source.

All crystallographic data were collected at either room temperature or at 150 K under a liquid nitrogen cryostream. Crystals were individually selected from observing the sample, suspended in an inert perfluoro polyether oil, under an optical microscope. Structures were solved using the WinGX suite of programmes [6, 7], utilising XPREP [8], SHELXS-86 [9] and SHELXL2014/7 [10]; by direct and Patterson solution methods [11]. For refinement of the structural model SHELXL2014/7 [10] was used. All non-hydrogen atomic parameters were refined anisotropically, using the F^2 least-squares method.

2.3.4 Ultraviolet/Visible spectroscopy (UV/Vis)

Ultraviolet/Visible spectroscopy is an analytical technique used to assess the absorption of electromagnetic radiation in a given range of the electromagnetic spectrum by a sample species; providing structural information on electronic transitions occurring within the specimen molecule or material. For the analysis of materials in the solid-state diffuse reflectance is used to understand the absorbance properties of the sample species with the use of the Kubelka-Munk theory.

In the setup used through the experiments undertaken, as seen in Figure 2.7, a deuterium and halogen lamp were used as radiation sources to provide the appropriate wavelength of radiation through the ultraviolet and visible regions respectively. Passing between and through a series of mirrors and aperture slits the radiation beam is collimated into a focussed beam of parallel light. A final grating disperses and selects a part of the spectrum directing the beam of monochromatic radiation through final exit aperture slit onto the sample surface. The diffuse reflectance is directed by the integrating sphere onto the detector for analysis.

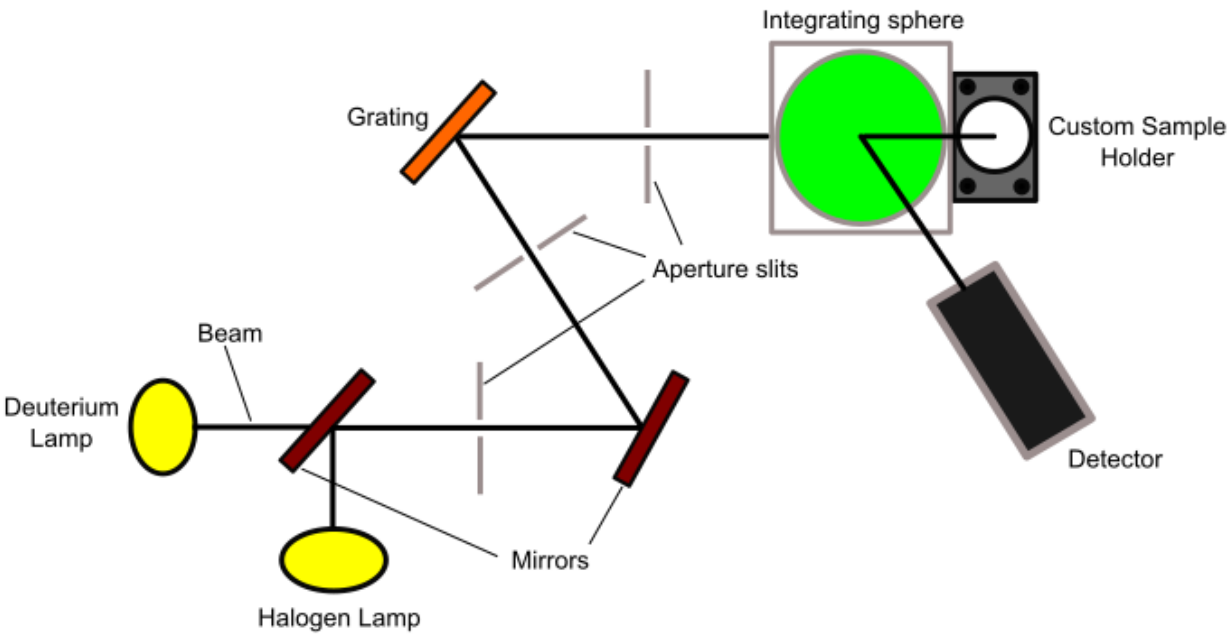

Figure 2.7 A schematic for lambda 19 spectrometer UV/Vis analysis setup

The instrument used for all ultraviolet/visible spectroscopic analysis was a Perkin Elmer UV/Vis lambda 19 spectrometer. UV/Vis spectroscopy was performed in the wavelength range of 250-1200 nm in diffuse reflectance mode. Each material was analysed in an approximate 10 wt% mixture in barium sulfate; with pure barium sulfate filled plate used as the background scan prerequisite to each compound analysis.

2.3.5 Thermogravimetric analysis (TGA)

Thermogravimetric analysis measures the weight change of a sample as temperature is ramped up through a controlled procedure. The technique is commonly utilised to study thermal stability, dehydration, phase transition, desorption and oxidation processes. Working in combination within the thermogravimetric analyser are an electronic microbalance, accurately monitoring the weight of the sample, the furnace and a programmer, adjusting the custom experiment settings over the course of the procedure as temperature and weight is constantly simultaneously measured. In conjunction with the technique, mass spectrometry is often used to analyse and identify material lost from the sample, carried by the flow gas, in real-time in tandem with thermogravimetric analysis [4].

The hardware and software used to carry out all thermogravimetric analysis was:

- A Setaram Setsys Evolution 16 TGA-DTA-DSC system with CALISTO thermal analysis software

Thermogravimetric analysis was undertaken on a number of samples with a particular focus on utilising the tool to investigate dehydration and decomposition processes of the material samples. Typically, to assess thermal stability each compound would be heated to 400 ^{o}C. Alternatively, a controlled ramp and hold procedure could be used to dehydrate a sample at a given temperature. Inert argon was used as the carrier gas with a constant flow rate through all experimentation.

2.3.6 Electron microscopy and Energy dispersive X-ray spectroscopy (EDX)

Electron microscopy and energy dispersive X-ray spectroscopy are analytical techniques often used in conjunction with one another as the theory behind their application is closely aligned. A scanning electron microscope (SEM) produces an image of a sample by bombarding the surface of the material with a relatively low energy focussed beam of electrons. Electron interaction with a structure can result in elastic scattering of the electron, a process in which the incident electron does not lose energy, or inelastic scattering, the process in which a detectable amount of energy is lost from the incident electron. The latter process is responsible for the production of the type of electron, secondary electrons (SEs), detected in SEM imaging.

Secondary electrons are generated in abundance due to the selective intensity of the ionising electron beam interacting with the atoms close to the sample material surface emitting a high count of secondary electrons for detection. Detection of the SEs can be used to produce images of the surface topography.

Similarly, energy dispersive X-ray spectroscopy (EDX) is a technique which also employs the use of electrons interacting with the sample being analysed. The high energy incident electrons excite electrons within the K-shell of the atoms to a higher electronic state. Electrons returning to the K-shell holes release excess energy in the form of X-rays. The energy of the detected X-rays is characteristic of the identity of the atom and therefore the relative intensity in the detection of the each peak can be used for quantitative analysis of the sample surface.

The instruments used in the analytic work carried out were:

- JEOL SEM6480LV for high vacuum microscope imaging
- Oxford INCA X-ray analyser for quantitative sample surface analysis

Scanning electron microscopy was performed with up to x10,000 magnification, an accelerating electron voltage of 10 kV and a vacuum pressure of 20 Pa in the chamber. Energy dispersive X-ray analysis was performed alongside SEM imaging as the detector was integrated into the 6480LV system. An approximate ~70 x 50 µm area on each crystal surface was scanned for compositional analysis using an accelerating voltage of up to 20 kV.

Chapter 3 - Hybrid halometallate materials: Part I

3.1 First 'Dalton Transactions' publication and related material

3.1.1 Precursor commentary

As discussed in the introduction to candidate materials for investigation (Chapter 1), hybrid halometallate materials and, in particular, lead-based perovskite hybrid materials have made a large impact on the emerging solar technologies research field. Of the haloplumbate hybrid salts it is methylammonium $(CH_3NH_3)^+$ and formamidinium $(CHNH_2NH_3)^+$ lead iodide, referred to as MAPI and FAPI respectively, which have garnered the most interest. Efforts to mimic the promising physical absorber properties of these materials with like-for-like substitution of the templating organic component into non-lead based alternatives have been undertaken. However, for methylammonium iodobismuthate, the three-dimensional perovskite structure of the former material is broken in favour of a much lower dimensionality. The bismuth-based hybrid material is made up for discrete zero-dimensional units of $[Bi_2I_9]^{3-}$ counterbalanced by singly charged methylammonium cations in a much more structurally disordered system. The equivalent haloantimonate structures follow a similar $A_3Sb_2X_9$ ($A = Cs^+$, MA^+; $X = I^-$, Br^-, Cl^-) low-dimensional hybrid structural system [1-6].

However, as referred to in the introduction, previously reported iodobismuthate and iodoantimonate materials exhibit a range of anionic substructure types beyond zero-dimensional interconnected structures. One- and two-dimensional network motifs have been reported with no fully three-dimensional structural connected materials stated to have been recorded in this class [1,2].

This previous work has suggested that in order to attain the highest structural and electronic connectivity for halometallate hybrid materials further research in this area is needed. This would allow improved understanding of these materials with the aim of mimicking the well-known lead iodide-based hybrid perovskite structures and subsequent material optimisation with the desired optoelectronic properties.

Investigations were thus carried out into the possible hybrid materials that could be obtained from tailored solvothermal synthesis procedures utilising the N-heterocyclic organic compounds: piperazine, 1-methylpiperazine and 1,4-dimethylpiperazine. Piperazine is the smallest saturated nitrogen-based heterocyclic compound to carry a binary charge as investigations from the literature and our own studies (Appendix A.12-13) utilising variants of five-membered imidazolium-ring based ions show a single resonance charge across the two nitrogen positions in the hybrid structures formed. As a result, it was established that piperazine ring-based organic variants would be an applicable for providing a high density of positive charge relative to their size for these hybrid materials and additionally to observe how the increased steric effects from additional alkyl groups on the organic component had an impact on firstly the resulting structural changes to the hybrid structure and thus secondly to form a relationship between these observations and the physical properties of the material.

Within the next section are the research outcomes of these initial halometallate hybrid material investigations presented in the form of a full paper submitted to the Royal Society of Chemistry journal Dalton Transactions.

3.1.2 Full paper entitled 'Synthesis and structure of pseudo-three dimensional hybrid iodobismuthate semiconductors' and associated supplementary information

Statement of Authorship

<table>
<tr><th colspan="10">This declaration concerns the article entitled:</th></tr>
<tr><td colspan="10">Synthesis and structure of pseudo-three dimensional hybrid iodobismuthate semiconductors</td></tr>
<tr><td colspan="10">Publication status (tick one)</td></tr>
<tr><td>draft manuscript</td><td></td><td>Submitted</td><td></td><td>In review</td><td></td><td>Accepted</td><td></td><td>Published</td><td>X</td></tr>
<tr><td>Publication details (reference)</td><td colspan="9">Authors: Adam J. Dennington and Mark T. Weller
Article Type: Paper
DOI: 10.1039/C6DT03602C
Citation: Dalton Trans., 2016, 45, 17974-17979</td></tr>
<tr><td>Candidate's contribution to the paper (detailed, and also given as a percentage).</td><td colspan="9">I fully developed the formulation of ideas and design of the methodology for all experimental work, carried out the synthetic work and material isolation (100%). I collected and undertook the data analysis for all single-crystal X-ray diffraction, powder X-ray diffraction, UV/Vis spectroscopy and thermogravimetric analysis presented in the work. Some acknowledged assistance was taken from Dr Mary F. Mahon to improve upon the absorption correction refinement of the SXD data for publication. Finally, I wrote the initial paper drafts, made revisions under my supervisor's guidance, and carried out all of the required referee response corrections to finalise the work to be published as a full paper.</td></tr>
<tr><td>Statement from Candidate</td><td colspan="9">This paper reports on original research I conducted during the period of my Higher Degree by Research candidature.</td></tr>
<tr><td>Signed</td><td colspan="5"></td><td>Date</td><td colspan="3"></td></tr>
</table>

Synthesis and structure of pseudo-three dimensional hybrid iodobismuthate semiconductors

A. J. Dennington[a] and M. T. Weller[b]

Abstract

The synthesis, structures and semiconducting properties of three isostructural, piperazinium-cation based iodobismuthates, $[NH_2(CH_2)_4NH_2][BiI_4]_2.4H_2O$, $[CH_3NH(CH_2)_4NH_2][BiI_4]_2.3H_2O$ and $[CH_3NH(CH_2)_4HNCH_3][BiI_4]_2.2H_2O$, are reported. The materials have pseudo-three dimensional structures consisting of infinite chains formed from edge/face sharing $[BiI_6]$ octahedra with short interchain I---I interactions of <3.8 Å. The materials have band gaps of ~1.9-2.0 eV and show variable optoelectronic properties based on the degree of methylation of the templating piperazinium ring-based organic species and the accordingly associated level of solvation in the structure.

Introduction

The emergence of metal halide perovskite photovoltaic materials over the last few years has ignited much attention towards discovering new semiconducting, organic-inorganic hybrid materials[1-3]. Lead-based materials, in particular methylammonium lead iodide (MAPI), currently dominate the field and now demonstrate solar cell efficiencies to over 22%[4]. Although commercially viable efficiencies have been validated for perovskite cells, they typically exhibit limited stability leading to concerns over for long term operation in a solar cell. Studies have been undertaken to discern and combat the issue of instability of hybrid perovskite materials when exposed to light (and/or) air;[5-7] some reports suggest an inherent thermodynamic instability of the structures resulting in a spontaneous decomposition process to the respective lead and organo-cationic halide precursor species[8]. A further key concern with these materials is that they contain toxic lead.

There is, therefore, an urgent need to discover new functional optoelectronic materials. These will need to reproduce the impressive optoelectronic properties of the lead halide perovskites but replace the toxic lead and have improved materials stability in device processing and in long-term deployment. It has been proposed that the required semiconducting properties of the lead halide perovskites derive from the fundamental electronic structure[9]. In particular, partially oxidised post transition metals with filled $5s^2$ or $6s^2$ orbitals have been shown to produce shallow defects and a dispersed valence band. As a result, the most promising metal cation candidates for further study are considered to be Sn^{2+}, Bi^{3+} and Sb^{3+}. Much initial work

focussed on the isovalent substitution of Pb^{2+} by Sn^{2+} [10-12]. However, Sn^{2+} compounds generally undergo rapid oxidation by air and decomposition through reaction with moisture[13, 14].

Bismuth is an environmentally friendly, non-toxic alternative with the potential to form materials exhibiting the required optoelectronic properties. Bulk bismuth is relatively expensive compared to lead but for thin film technologies, requiring ~4-12 g/m^2 of absorber material, the cost with bismuth, at under \$1 /m^2, is reasonable in terms of overall device cost.

Work on semiconducting metal halide materials has been extended to double perovskite systems, with general formula $A_2BB'X_6$ (X = halide) with B'= Sn, Pb. Recently, bismuth-based halide double perovskites Cs_2AgBiX_6 (X = Cl, Br) have been reported as exhibiting comparable, though larger, band gaps to their $(MA)PbX_3$ analogues[15-18]. Another route to novel hybrid semiconducting materials is to search outside of the confines of perovskite structures while aiming to maintain high structural and optoelectronic connectivity. Typically iodometallate, X = I, structures are favoured targets over other halide systems as they tend to possess smaller band gaps and lower carrier effective masses[17]. However, substitution of Pb^{2+} by Bi^{3+}, with X = I, normally yields zero- (0D) and one- dimensional (1D) iodobismuthate structures. Previously reported iodobismuthate materials demonstrate a large diversity of anionic substructures[19, 20], built from linked $[BiI_6]$ octahedra including vertex sharing, edge-sharing and face-sharing motifs. Anionic units range from discrete 0D units in $[BiI_6]^{3-}$ to $[Bi_8I_{30}]^{4-}$ motifs[21-35], through 1D chain structures[22, 36-40], including the commonly found $[BiI_4]^-_n$ and $[BiI_5]^{2-}_n$; with one reported 2D extended network, $[Bi_{2/3}I_4]^{2-}_n$[41]. To date well over 50 iodobismuthate materials have been described but three-dimensional structural, and, therefore, optoelectronic connectivity has proved elusive.

Experimental section

General

Our exploration of hybrid iodobismuthate materials has led to the discovery of three new, isostructural materials $[NH_2(CH_2)_4NH_2][BiI_4]_2.4H_2O$, $[CH_3NH(CH_2)_4NH_2][BiI_4]_2.3H_2O$ and $[CH_3NH(CH_2)_4HNCH_3][BiI_4]_2.2H_2O$. These isostructural materials have pseudo-three dimensional structures, reminiscent of the perovskite structure, where links between $[BiI_4]^-_n$ chains occur through short I---I interactions These materials also exhibit tuneable properties through the substitution of the piperazinium cation ring and, in turn, via control of solvate water molecules in the structures.

Synthetic

Crystals of the 1,4-dipiperazinium iodobismuthate tetrahydrate $[NH_2(CH_2)_4NH_2][BiI_4]_2.4H_2O$ (Compound 1) were obtained through hydrothermal reaction of $BiCl_3$ (0.2 mmol, 98% (dry wt.), Alfa Aesar), piperazine (0.15 mmol, >98%, Fluka), HI (0.5 ml, 57 wt%, no stabiliser, Sigma-Aldrich) in deionised water (6 ml). Reactants placed in a 25 ml Teflon-lined vessel, sealed in a steel autoclave and heated at 140 ^oC for 24h; with a controlled ramp up rate of 1 ^oC/min and ramp down rate of 0.1 ^oC/min. After filtration and ethanol wash, a pure phase of prismatic red block crystals of compound 1 (0.147 g) was obtained.

Deep red crystals of 1-methyl-1,4-dipiperazinium iodobismuthate trihydrate, $[CH_3NH(CH_2)_4NH_2][BiI_4]_2.3H_2O$, (Compound 2) were synthesised utilising identical conditions and procedure as described for 1 with the exception of a change of the organic templating agent to 1-methylpiperazine (0.15 mmol, 99%, Sigma-Aldrich) and an increased volume of HI (0.75 ml 57 wt%, no stabiliser, Sigma-Aldrich); these reaction conditions yielded a pure phase of millimetre-sized crystals (0.130 g).

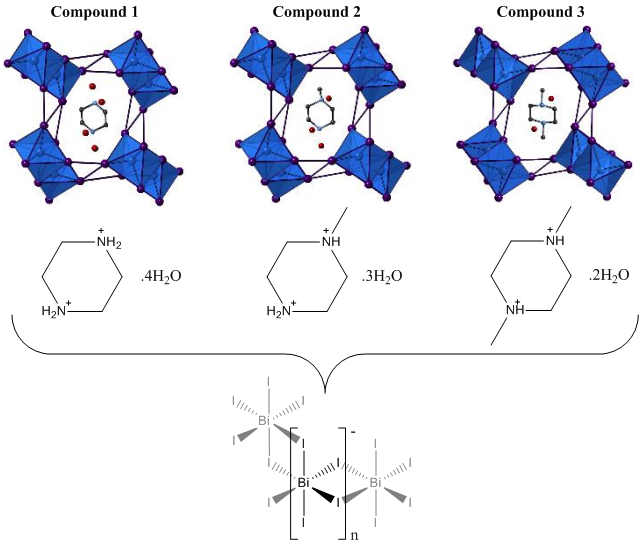

Fig. 1 A schematic illustration of the *a*-axis views of compounds **1-3**

Deep red crystals of 1,4-dimethyl-1,4-dipiperazinium iodobismuthate dihydrate, $[CH_3NH(CH_2)_4HNCH_3][BiI_4]_2.2H_2O$ (Compound 3), were attained through the hydrothermal reaction of $BiCl_3$ (0.4 mmol, 98% (dry wt.), Alfa Aesar), 1,4-dimethylpiperazine (0.15 mmol, 98%, Alfa Aesar), HI (1 ml, 57 wt%, no stabiliser, Sigma-Aldrich) in deionised water (6 ml).

Reactants were placed in a 25 ml Teflon-lined vessel, sealed in a steel autoclave and heated at 170 ºC for 24h; with a controlled ramp up rate of 1 ºC/min and ramp down rate of 0.1 ºC/min. After filtration and ethanol wash a pure phase of crystals of Compound 3 (0.206 g) was obtained.

Results and discussion

General

The structures of compounds 1-3 were solved from single crystal X-ray diffraction data (see ESI) All three compounds, $[NH_2(CH_2)_4NH_2][BiI_4]_2.4H_2O$, $[CH_3NH(CH_2)_4NH_2][BiI_4]_2.3H_2O$ and $[CH_3NH(CH_2)_4HNCH_3][BiI_4]_2.2H_2O$, crystallise in the monoclinic space group $P2_1/c$ with lattice parameters shown in Table 1. The materials are iso-structural and consist of infinite chains of the stoichiometry $[BiI_4]^-_n$ with short interchain I---I contacts. The voids delineated by the chains and inter-chain contacts are occupied by the organic cations and water molecules in a manner reminiscent of the perovskite structure, Figure 1.

	1a (150K)	1b (RT)	2a (150K)	2b (RT)	3a (150K)	3b (RT)
a =	7.3508(2)	7.4697(3)	7.5434(2)	7.6488(4)	7.7293(2)	7.7971(3)
b =	13.0215(4)	13.1773(7)	13.0515(5)	13.1532(8)	13.0336(3)	13.0868(5)
c =	13.9875(3)	13.9099(6)	13.6716(5)	13.7033(7)	13.4990(4)	13.5505(6)
β =	94.588(2)	95.109(4)	96.347(3)	96.481(5)	97.955(3)	97.925(4)
V =	1334.57(2)	1363.72(11)	1337.76(8)	1369.83(13)	1346.81(6)	1369.48(10)

Table 1 Unit cell parameters for compounds 1-3 at RT and 150 K data collections

Stability and dehydration

Thermogravimetric analysis of compound **1** displays a weight loss of 4.2% at temperature range 70 – 110 ºC corresponding to the desolvation of all four water molecules from the hydrated structure. In the same way, the tri- and di-hydrate structures of Compounds **2** & **3** exhibit dehydration steps with weight losses of 3.7% and 2.0% respectively; in close agreement with the weight percentage contributions to the unit cell. All three dehydrated structures show thermal stability to approximately 250 ºC before undergoing degradation (Figure S1-3 – see ESI).

Crystal structure analysis

In compound **1**, the dipiperazinium dications counterbalance the charge of the anionic $[BiI_4]^-_n$ chains and are located within channels extending through the *a*-axis of the structure in parallel with the sublattice. Neutral water molecules fully occupy four sites within the structure.

In Compound **2** the organic cation is disordered, adopting one of two possible orientations, and as a result the steric effect of the methyl group partially blocks the occupancy of two of the water molecule positions; previously fully occupied in Compound **1**. That is, these water molecule sites become half-filled due to the methyl group of the locally orientated 1-methyl-dipiperazinium cations occupying and so impeding the spaces. This reduces the overall hydration level in Compound **2** to give a trihydrate hybrid iodobismuthate, $[CH_3NH(CH_2)_4NH_2][BiI_4]_2.3H_2O$. Following this behaviour and trend, in compound **3**, the methyl groups of the positionally ordered 1,4-dimethyldipiperazinium cation precludes occupation of both these water molecule sites occupied in Compound **1** and this results in the formation of a dihydrate, $[CH_3NH(CH_2)_4HNCH_3][BiI_4]_2.2H_2O$. Elongated thermal parameters on the nitrogen and methyl carbon atoms in this structure indicates some possible local conformational disorder of the organic cation in the structure.

The changes to the cation and associated degree of solvation result in subtle but important changes to the anionic sub-lattice. The $[BiI_4]^-_n$ chains are formed from edge sharing individual $[BiI_6]$ octahedra, leading to 4 bridging and 2 terminal cis-related iodine atoms. The bismuth atom is slightly displaced from a central position in the $[BiI_6]$ octahedron with the shortest Bi-I interactions observed to the two terminal iodine atoms. This behaviour is in agreement with observations for other iodobismuthate materials possessing similar 1D $[BiI_4]^-_n$ chain motifs[38-40, 42, 43]. The range of Bi-I bond lengths within the octahedra decreases from compound **1** to compound **3** suggesting an increased overall regularity of the octahedra (Fig.2).

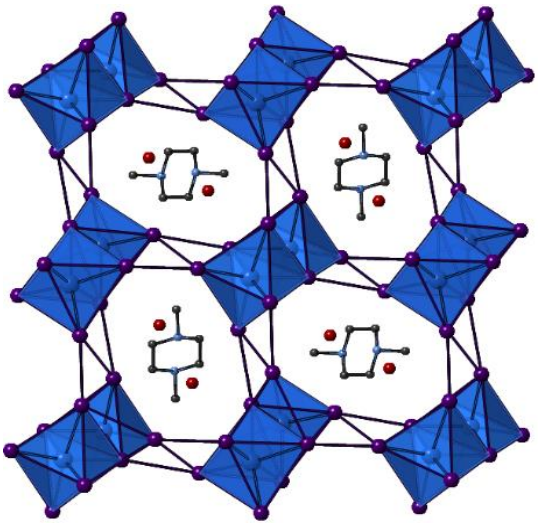

Fig. 2 *a*-axis view of compound 3

Interchain I---I interactions extend the anionic network along both the *b*- and *c*-axes of all three compounds; this can be considered as producing a degree of 3D connectivity in the materials and a potential route for electronic interactions between the $[BiI_4]^-_n$ chains. Three I---I pathways repeat regularly along the chain axis with all iodine atoms involved in interactions with adjacent chains; the longest of these being a terminal-terminal I---I interaction and the shortest two edge iodine to terminal iodine interactions. Lengths of these interactions range from 3.76-4.44 Å in the structures and the average distance of the interchain interactions decreases, 4.14 Å→4.09 Å→4.00 Å (150 K), through Compounds **1**-**3** respectively. The shortest interchain interaction is observed to exhibit minor variation through the structures 3.76 Å→3.77 Å→3.78 Å (150 K). In the series Compound **1** to Compound **3** the interchain Bi…Bi distances increase by an average of 0.05 Å as Bi-I-Bi bond angles increase beyond the octahedral angles; from 90.5°→91.9°→93.2° (150 K).

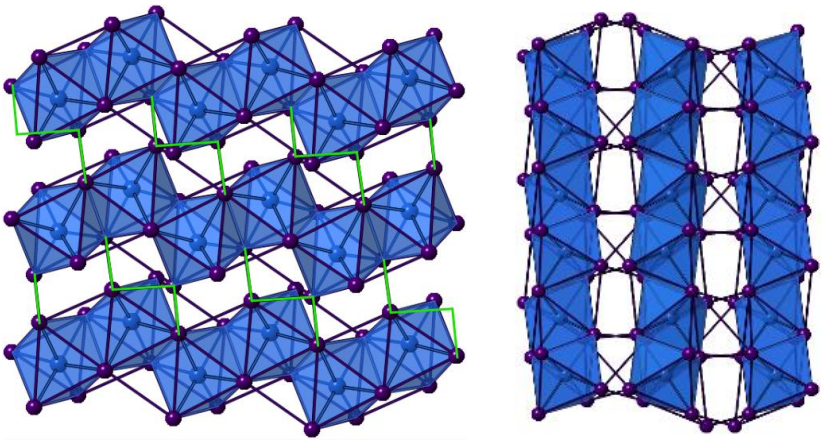

Fig. 3 Left: *b*-axis view of the anionic 1D network present in all compounds with interchain interactions highlighted (green). Right: *c*-axis view of the anionic network observed in all structures

In summary progressing from piperazinium-based, Compound **1**, through 1-methylpiperazinium-based, Compound **2**, to 1,4-dimethyldipiperazinium-based, Compound **3**, causes systematic changes within the 1D anionic chain network. These trends are observed as an extension of the distances between bismuth atom positions within the chain; Bi…Bi distances to intrachain next-but-one octahedra steadily increase 7.35 Å→7.54 Å→7.73 Å (150 K). This behaviour is accompanied by an increased level of distortion within the chains as Bi-I-Bi angles extend from 90.5°→93.2°. Simultaneously the average lengths of I---I interchain interactions decrease which increases the pseudo-3D nature of the materials. Interchain Bi…Bi distances decrease in tandem, with the average of the three closest interchain Bi…Bi distances falling from 9.20 Å→9.10 Å→8.85 Å (150K) from Compound **1** to Compound **3**. Hydrogen bonding between the solvent water molecules and the protonated amine groups and/or the iodide ions of the $[BiI_4]^-_n$ chains is likely to be present in all three compounds. However, although the hydrogen positions have been modelled to demonstrate chemical identity for the oxygen atoms located in all three structures, the true molecular orientations of the molecules could not be determined in these heavy atom structures.

Optical absorption measurements

Optical absorption spectra (250-800 nm) were collected for pure phases of Compounds **1-3** (Figure 4). Each compound shows absorption across the majority of the visible region consistent with their observed dark-red colouration. The absorption edge onset was determined from Tauc plots as 550, 560 and 575 nm which assuming a direct band gap for the strong absorption coefficients gives E_g values of 2.00 eV, 1.95 eV and 1.92 eV for Compounds **1-3**

respectively (Figure S4 – see ESI). These shifts could be attributed to the trend seen in decreasing interchain I---I distances and, therefore, increasing pseudo 3D-connectivity within these structures. Additional absorption peak features can be observed in the spectra for all three compounds at ~290 nm (4.3 eV) and ~360 nm (3.4 eV). Compound **3** also has an additional absorption peak at ~500 nm (2.5 eV). Previous studies of iodobismuthate structures have shown similar distinct bands that have been attributed to electronic transitions from the HOMO Bi(6p) orbital to the LUMO Bi(5p) orbitals [25, 38].

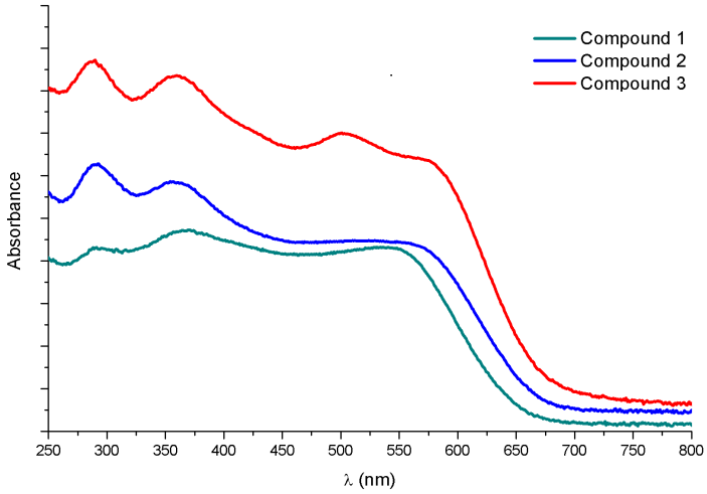

Fig. 4 UV/Vis spectra of Compounds 1-3 (10 wt% mixtures in $BaSO_4$)

Conclusions

In summary, three new, pseudo-3D piperazinium-based hybrid iodobismuthate materials have synthesised and structurally characterised. All three structures have been shown by thermogravimetric analysis to undergo dehydration processes while maintaining the integrity of the bismuth-iodide framework and semiconducting properties. Preliminary variable temperature SXD/PXRD studies indicate that the dehydration is reversible in these materials. This behaviour should be of interest in respect of depositing thin-films of these materials as it indicates that sample degradation, as seen with the lead halide perovskites, will not occur. Increased methylation of the templating piperazinium ring, tied with a decreased level of solvate within the structure, has been shown to result in average shortening of the I---I interactions between 1D $[BiI_4]^-_n$ chains in the anionic network.

Correspondingly, analysis by optical absorption indicates a shift in absorption edge in relation to this trend; with all three materials demonstrating band gap energies of ~1.9-2.0 eV; estimated from the intercept of the maximum angle of the absorption edge. Although this value is too

large for use as a highly efficient absorber materials in a single junction cell architecture, their use in tandem solar cell architectures can still be considered. The pseudo-three dimensional features of the structures of these materials, and the ability to tune them through variations in the geometry of the templating organic cation signifies a further step towards obtaining highly functional yet less toxic stable perovskite-like hybrid absorber materials for future use in solar technologies.

Acknowledgements

The authors would like to thank Dr Mary F. Mahon for assistance with the single-crystal X-ray crystallography. AJD would like to thank EPSRC for DTA studentship support.

Notes and references

‡ *Crystal data* for 1a: $C_4H_{20}N_2O_4Bi_2I_8$, M = 1593.41, monoclinic, space group *P21/c*, *a* = 7.3508(2), *b* = 13.0215(4), *c* = 13.9875(3) Å, β = 94.588(2)°, *V* = 1334.57(2)Å^3, Z = 4, crystal size: 0.506x0.232x0.114mm, T = 150.01(10)K, ρ_{calc} = 3.965gcm^{-3}, μ = 22.429mm^{-1}, 16574 reflections (4290 unique reflections), 91 parameters, 0 restraints, R1(all data) = 0.0446, wR2(all data) = 0.0889, GooF = 1.145, Further details available from CCDC 1496110

Crystal data for 1b: $C_4H_{20}N_2O_4Bi_2I_8$, M = 1593.41, monoclinic, space group *P21/c*, *a* = 7.4697(3), *b* = 13.1773(7), *c* = 13.9099(6) Å, β = 95.109(4)°, *V* = 1363.72(11)Å^3, Z = 4, crystal size: 0.358x0.260x0.0.123mm, T = 292.0(2)K, ρ_{calc} = 3.880gcm^{-3}, μ = 21.950mm^{-1}, 8961 reflections (4208 unique reflections), 91 parameters, 0 restraints, R1(all data) = 0.0634, wR2(all data) = 0.1049, GooF = 1.044, Further details available from CCDC 1496109

Crystal data for 2a: $C_5H_{20}N_2O_3Bi_2I_8$, M = 1589.27, monoclinic, space group *P21/c*, *a* = 7.5434(2), *b* = 13.0515(5), *c* = 13.6716(5) Å, β = 96.347(3)°, *V* = 1337.76(5)Å^3, Z = 4, crystal size: 0.434x0.189x0.168mm, T = 149.95(10)K, ρ_{calc} = 7.890gcm^{-3}, μ = 22.371mm^{-1}, 14198 reflections (4214 unique reflections), 109 parameters, 0 restraints, R1(all data) = 0.0381, wR2(all data) = 0.0722, GooF = 1.158, Further details available from CCDC 1496112

Crystal data for 2b: $C_5H_{20}N_2O_3Bi_2I_8$, M = 1589.27, monoclinic, space group *P21/c*, *a* = 7.6488(4), *b* = 13.1532(8), *c* = 13.7033(7) Å, β = 96.481(5)°, *V* = 1369.83(13)Å^3, Z = 4, crystal size: 0.413x0.176x0.176mm, T = 292.23(10)K, ρ_{calc} = 3.804gcm^{-3}, μ = 43.639mm^{-1}, 8333

reflections (4206 unique reflections), 109 parameters, 0 restraints, R1(all data) = 0.0590, wR2(all data) = 0.0970, GooF = 1.075, Further details available from CCDC 1496111

Crystal data for 3a: $C_6H_{20}N_2O_2Bi_2I_8$, M = 1585.43, monoclinic, space group *P21/c*, *a* = 7.7293(2), *b* = 13.0336(3), *c* = 13.4990(4) Å, β = 97.955(3)°, *V* = 1346.79(6)Å^3, Z = 4, crystal size: 0.300x0.215x0.181mm, T = 150.10(10)K, ρ_{calc} = 3.894gcm^{-3}, μ = 22.220mm^{-1}, 7814 reflections (4138 unique reflections), 91 parameters, 0 restraints, R1(all data) = 0.0402, wR2(all data) = 0.0788, GooF = 1.150, Further details available from CCDC 1496114

Crystal data for 3b: $C_6H_{20}N_2O_2Bi_2I_8$, M = 1585.43, monoclinic, space group *P21/c*, *a* = 7.7971(3), *b* = 13.0868(5), *c* = 13.5505(6) Å, β = 97.925(4)°, *V* = 1369.48(9)Å^3, Z = 4, crystal size: 0.298x0.217x0.180mm, T = 286(9)K**,** ρ_{calc} = 3.830gcm^{-3}, μ = 21.851mm^{-1}, 8720 reflections (2879 unique reflections), 91 parameters, 0 restraints, R1(all data) = 0.0654, wR2(all data) = 0.0849, GooF = 1.021, Further details available from CCDC 1496113

Single crystal data for compounds 1-3 were collected on an Agilent Xcalibur four-circle diffractometer equipped with a fine-focus ($Mo_{k\alpha}$) X-ray source and EosS2 CCD plate detector.

References

1. H. J. Snaith, *J. Phys. Chem. Lett.*, 2013, **4**, 3623-3630.

2. M. A. Green, A. Ho-Baillie and H. J. Snaith, *Nat. Photo.*, 2014, **8**, 506-514.

3. S. Kazim, M. K. Nazeeruddin, M. Gratzel and S. Ahmad, *Angew. Chem-Int. Ed.*, 2014, **53**, 2812-2824.

4. Research cell efficiency records, http://www.nrel.gov/ncpv/images/efficiency_chart.jpg (accessed July 2016)).

5. G. D. Niu, X. D. Guo and L. D. Wang, *J. Mat. Chem. A*, 2015, **3**, 8970-8980.

6. J. L. Yang, B. D. Siempelkamp, D. Y. Liu and T. L. Kelly, *ACS Nano*, 2015, **9**, 1955-1963.

7. Y. Han, S. Meyer, Y. Dkhissi, K. Weber, J. M. Pringle, U. Bach, L. Spiccia and Y. B. Cheng, *J. Mat. Chem. A*, 2015, **3**, 8139-8147.

8. A. M. Ganose, C. N. Savory and D. O. Scanlon, *J. Phys. Chem. Lett.*, 2015, **6**, 4594-4598.

9. R. E. Brandt, V. Stevanovic, D. S. Ginley and T. Buonassisi, *MRS Comm.*, 2015, **5**, 265-275.

10. N. K. Noel, S. D. Stranks, A. Abate, C. Wehrenfennig, S. Guarnera, A. A. Haghighirad, A. Sadhanala, G. E. Eperon, S. K. Pathak, M. B. Johnston, A. Petrozza, L. M. Herz and H. J. Snaith, *Energ. Environ. Sci.*, 2014, **7**, 3061-3068.

11. C. C. Stoumpos, C. D. Malliakas and M. G. Kanatzidis, *Inorg. Chem.*, 2013, **52**, 9019-9038.

12. M. Weiss, J. Horn, C. Richter and D. Schlettwein, *Phys. Stat. Solid. a-App. Mat. Sci.*, 2016, **213**, 975-981.

13. D. B. Mitzi, S. Wang, C. A. Feild, C. A. Chess and A. M. Guloy, *Sci.*, 1995, **267**, 1473-1476.

14. D. B. Mitzi, C. D. Dimitrakopoulos and L. L. Kosbar, *Chem. Mat.*, 2001, **13**, 3728-3740.

15. A. H. Slavney, T. Hu, A. M. Lindenberg and H. I. Karunadasa, *J. Amer. Chem. Soc.*, 2016, **138**, 2138-2141.

16. E. T. McClure, M. R. Ball, W. Windl and P. M. Woodward, *Chem. Mat.*, 2016, **28**, 1348-1354.

17. G. Volonakis, M. R. Filip, A. A. Haghighirad, N. Sakai, B. Wenger, H. J. Snaith and F. Giustino, *J. Phys. Chem. Lett.*, 2016, **7**, 1254-1259.

18. M. Filip, S. Hillman, A. Haghighirad, H. Snaith and F. Giustino, *J. Phys. Chem. Lett.*, 2579-2585.

19. L. M. Wu, X. T. Wu and L. Chen, *Coord. Chem. Rev.*, 2009, **253**, 2787-2804.

20. S. A. Adonin, M. N. Sokolov and V. P. Fedin, *Coord. Chem. Rev.*, 2016, **312**, 1-21.

21. A. M. Goforth, L. Peterson, M. D. Smith and H. C. zur Loye, *J. Solid State. Chem.*, 2005, **178**, 3529-3540.

22. W. H. Bi and N. Mercier, *Chem. Comm.*, 2008, 5743-5745.

23. A. M. Goforth, J. R. Gardinier, M. D. Smith, L. Peterson and H. C. Z. Loye, *Inorg. Chem. Comm.*, 2005, **8**, 684-688.

24. C. Hrizi, A. Samet, Y. Abid, S. Chaabouni, M. Fliyou and A. Koumina, *J. Mol. Struct.*, 2011, **992**, 96-101.

25. A. Samet, A. Ben Ahmed, A. Mlayah, H. Boughzala, E. K. Hlil and Y. Abid, *J. Mol. Struct.*, 2010, **977**, 72-77.

26. A. M. Goforth, M. A. Tershansy, M. D. Smith, L. Peterson, J. G. Kelley, W. J. I. DeBenedetti and H. C. zur Loye, *J. Amer. Chem. Soc.*, 2011, **133**, 603-612.

27. C. Feldmann, *J. Solid State. Chem.*, 2003, **172**, 53-58.

28. J. Heine, *Dalton Trans.*, 2015, **44**, 10069-10077.

29. H. Krautscheid, *Z. Anorg. Allge. Chem.*, 1995, **621**, 2049-2054.

30. H. Krautscheid, *Z. Anorg. Allge. Chem.*, 1999, **625**, 192-194.

31. S. A. Adonin, E. V. Peresypkina, M. N. Sokolov and V. P. Fedin, *Russ. J. Coord. Chem.*, 2014, **40**, 867-870.

32. H. Krautscheid, *Z. Anorg. Allge. Chem.*, 1994, **620**, 1559-1564.

33. K. Y. Monakhov, C. Gourlaouen, R. Pattacini and P. Braunstein, *Inorg. Chem.*, 2012, **51**, 1562-1568.

34. V. V. Sharutin, I. V. Egorova, N. N. Klepikov, E. A. Boyarkina and O. K. Sharutina, *Russ. J. Inorg. Chem.*, 2009, **54**, 1768-1778.

35. A. Okrut and C. Feldmann, *Z. Anorg. Allge. Chem.*, 2006, **632**, 409-412.

36. D. B. Mitzi and P. Brock, *Inorg. Chem.*, 2001, **40**, 2096-2104.

37. G. A. Mousdis, G. C. Papavassiliou, A. Terzis and C. P. Raptopoulou, *Z. Natur. Sec. B-a J. Chem. Sci.*, 1998, **53**, 927-931.

38. C. Hrizi, N. Chaari, Y. Abid, N. Chniba-Boudjada and S. Chaabouni, *Polyhedron*, 2012, **46**, 41-46.

39. S. Chaabouni, S. Kamoun and J. Jaud, *J. Chem. Cryst.*, 1997, **27**, 527-531.

40. N. A. Yelovik, A. V. Mironov, M. A. Bykov, A. N. Kuznetsov, A. V. Grigorieva, Z. Wei, E. V. Dikarev and A. V. Shevelkov, *Inorg. Chem.*, 2016, **55**, 4132-4140.

41. D. B. Mitzi, *Inorg. Chem.*, 2000, **39**, 6107-6113.

42. M. Erbe, D. Kohler and M. Ruck, *Z. Anorg. Allge. Chem.*, 2010, **636**, 1513-1515.

43. A. Gagor, M. Weclawik, B. Bondzior and R. Jakubas, *Crystengcomm*, 2015, **17**, 3286-3296.

Supplementary Information

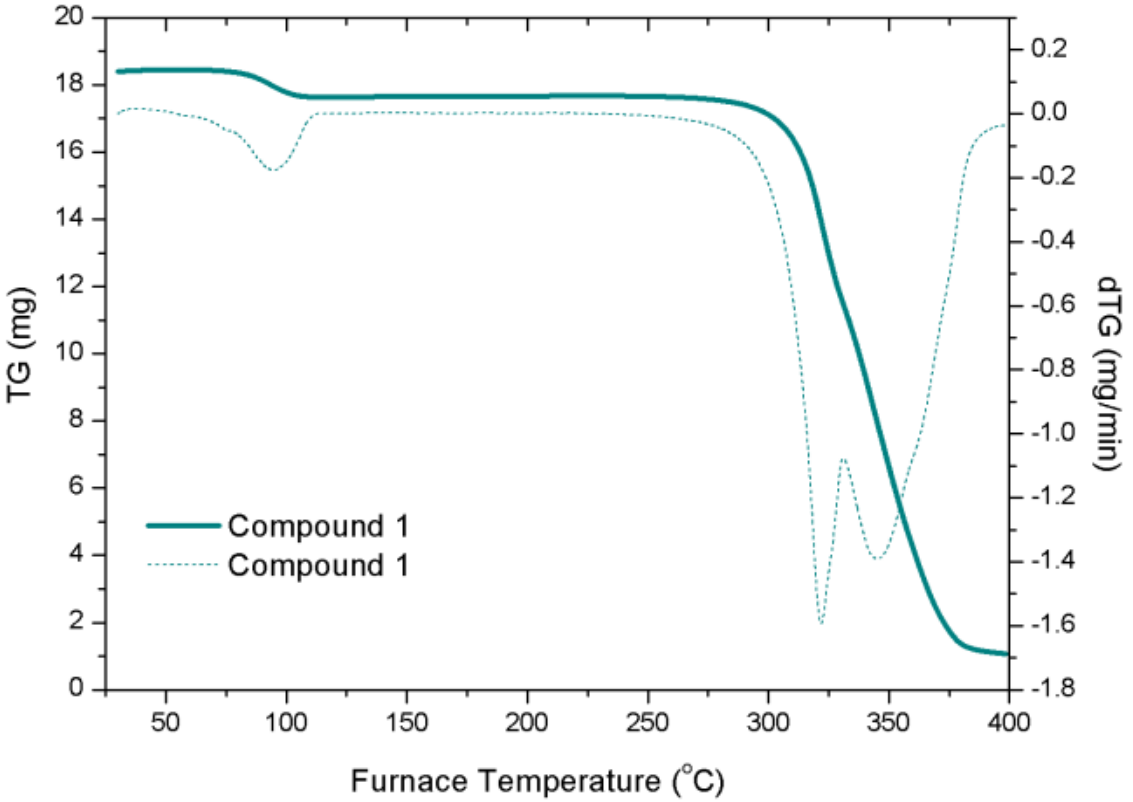

Figure S1 Thermogravimetric analysis of compound 1 (30-400ºC)

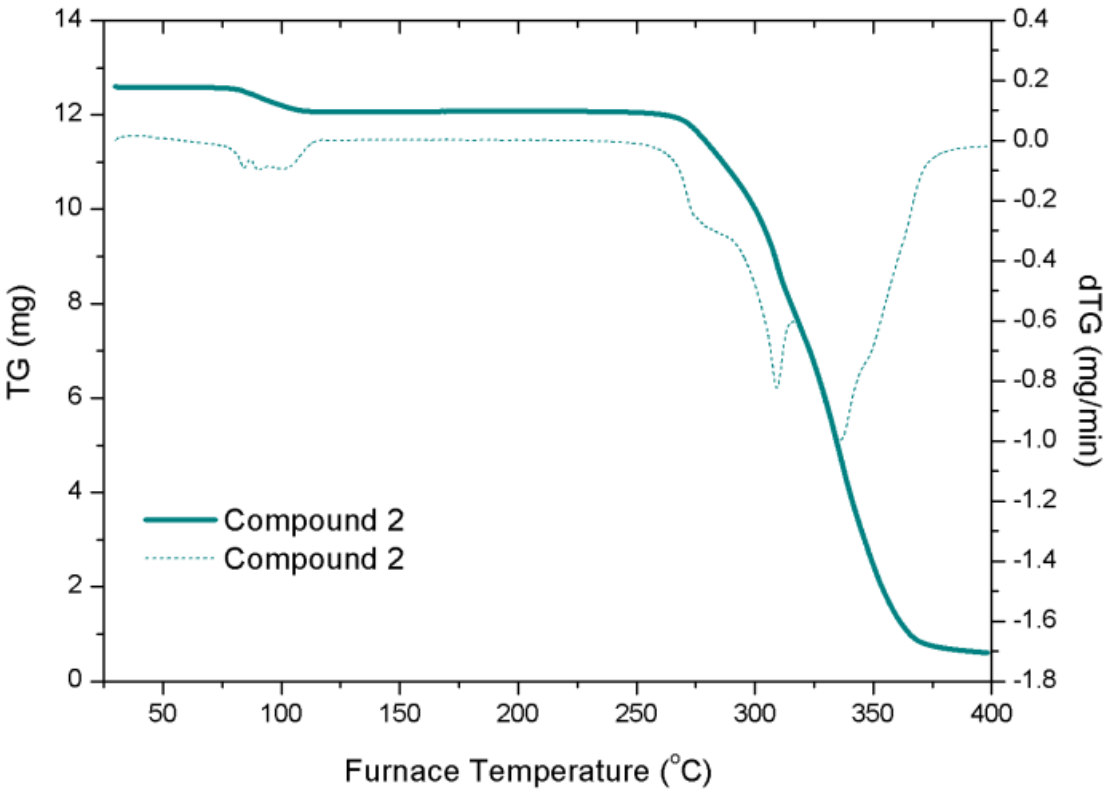

Figure S2 Thermogravimetric analysis of compound 2 (30-400ºC)

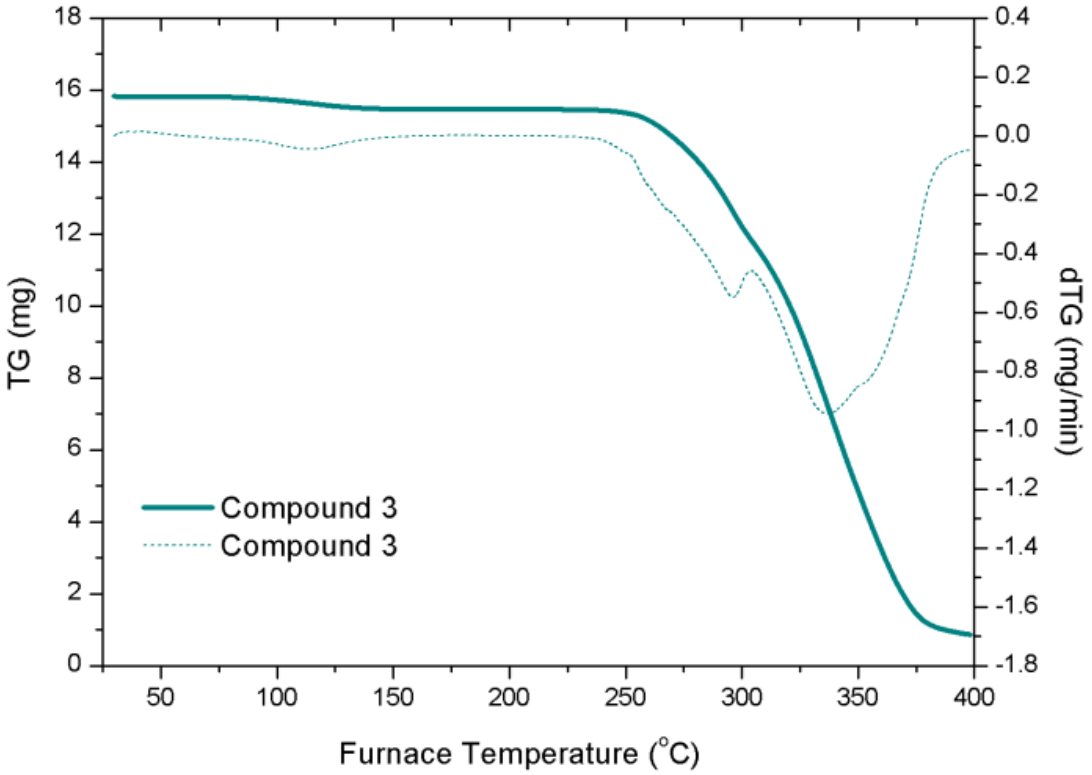

Figure S3 Thermogravimetric analysis of compound 3 (30-400ºC)

	Compound					
Parameters	1a (150K)	1b (RT)	2a (150K)	2b (RT)	3a (150K)	3b (RT)
Bi…Bi distances (Å)	4.457	4.508	4.512	4.569	4.588	4.625
	4.537	4.58	4.577	4.614	4.619	4.648
	7.351*	7.470*	7.543*	7.649*	7.729*	7.797*
Bi-I bonding interactions	2.891	2.892	2.899	2.905	2.923	2.921
	2.96	2.96	2.936	2.939	2.93	2.928
	3.058	3.065	3.045	3.061	3.056	3.064
	3.081	3.09	3.099	3.107	3.12	3.118
	3.215	3.277	3.216	3.237	3.24	3.252
	3.301	3.312	3.279	3.289	3.255	3.263
Intrachain I-I distances	4.416 (I2-I2)	4.478 (I2-I2)	4.345 (I2-I2)	4.337 (I2-I2)	4.397 (I2-I2)	4.304 (I2-I2)
	4.309 (I2-I3)	4.342 (I2-I3)	4.336 (I2-I3)	4.383 (I2-I3)	4.356 (I2-I3)	4.304 (I2-I3)
	4.325 (I2-I3)	4.377 (I2-I3)	4.416 (I2-I3)	4.448 (I2-I3)	4.492 (I2-I3)	4.378 (I2-I3)
	4.344 (I2-I3)	4.398 (I2-I3)	4.421 (I2-I3)	4.471 (I2-I3)	4.521 (I2-I3)	4.525 (I2-I3)
	4.225 (I2-I1)	4.214 (I2-I1)	4.162 (I2-I1)	4.179 (I2-I1)	4.192 (I2-I1)	4.131 (I2-I1)
	4.412 (I3-I1)	4.420 (I3-I1)	4.450 (I3-I1)	4.456 (I3-I1)	4.295 (I3-I1)	4.463 (I3-I1)
	4.554 (I3-I1)	4.348 (I3-I1)	4.494 (I3-I1)	4.483 (I3-I1)	4.351 (I3-I1)	4.499 (I3-I1)
	4.494 (I3-I3)	4.319 (I3-I3)	4.446 (I3-I3)	4.432 (I3-I3)	4.315 (I3-I3)	4.375 (I3-I3)
	4.344 (I2-I4)	4.522 (I2-I4)	4.311 (I2-I4)	4.324 (I2-I4)	4.464 (I2-I4)	4.307 (I2-I4)
	4.420 (I2-I4)	4.418 (I2-I4)	4.360 (I2-I4)	4.380 (I2-I4)	4.509 (I2-I4)	4.360 (I2-I4)
	4.250 (I1-I4)	4.263 (I1-I4)	4.284 (I1-I4)	4.295 (I1-I4)	4.343 (I1-I4)	4.338 (I1-I4)
	4.191 (I3-I4)	4.229 (I3-I4)	4.486 (I3-I4)	4.202 (I3-I4)	4.122 (I3-I4)	4.199 (I3-I4)
	4.237 (I4-I3)**	4.494 (I4-I3)**	4.316 (I4-I3)**	4.457 (I4-I3)**	4.718 (I4-I3)**	4.768 (I4-I3)**
	4.417 (I1-I2)**	4.335 (I1-I2)**	4.562 (I1-I2)**	4.634 (I1-I2)**	4.490 (I1-I2)**	4.557 (I1-I2)**
Interchain I-I interactions	3.761 (I2-I4)	4.338 (I2-I4)	3.765 (I2-I4)	3.811 (I2-I4)	4.015 (I2-I4)	3.817 (I2-I4)
	4.254 (I1-I3)	3.800 (I1-I3)	4.169 (I1-I3)	4.226 (I1-I3)	3.779 (I1-I3)	4.072 (I1-I3)
	4.396 (I1-I4)	4.436 (I1-I4)	4.324 (I1-I4)	4.357 (I1-I4)	4.210 (I1-I4)	4.244 (I1-I4)
Interchain Bi…Bi distances	8.488	8.53	8.393	8.446	8.299	8.34
	9.211	9.02	9.131	9.096	9.112	9.161
	9.914	9.202	9.782	9.168	9.146	9.167

Table S1 Interaction and bonding parameter analysis for compounds 1-3 (obtained from RT and 150K single-crystal data collections)

	Compound					
Parameters	1a (150K)	1b (RT)	2a (150K)	2b (RT)	3a (150K)	3b (RT)
I-Bi-I bond angles (o)	83.16	84.04	83.76	84.38	84.23	84.45
	85.22	85.75	87.84	87.01	86.48	85.88
	87.25	88.23	88.16	87.69	87.13	86.53
	89.15	88.49	88.34	88.26	87.18	87.26
	89.08	88.71	88.46	88.64	87.65	87.91
	89.45	89.14	88.5	88.86	88.08	88.22
	89.47	89.48	88.84	89.35	89.86	90.52
	90.55	90.41	89.52	89.6	91.45	91.73
	93.14	92.11	92.44	91.92	92.38	92.2
	93.16	93.5	94.33	94.46	93.22	93.36
	93.81	93.79	94.47	94.52	95.83	95.75
	95.93	95.77	94.98	94.92	96.46	96.25
Bi-I-Bi bond angles (o)	90.53	91.29	91.66	92.31	92.82	93.47
	90.55	91.51	92.16	92.99	93.52	94.12

Table S2 Bond angle analysis for compounds 1-3 (obtained from RT and 150K single-crystal data collections)

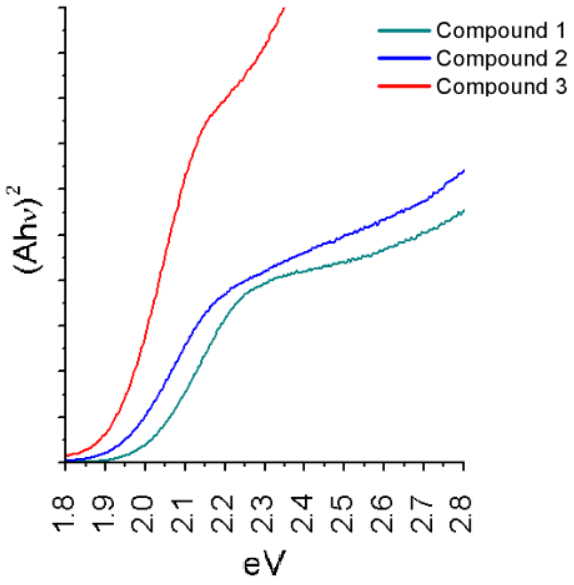

Figure S4 Tauc plot analysis of compounds 1-3

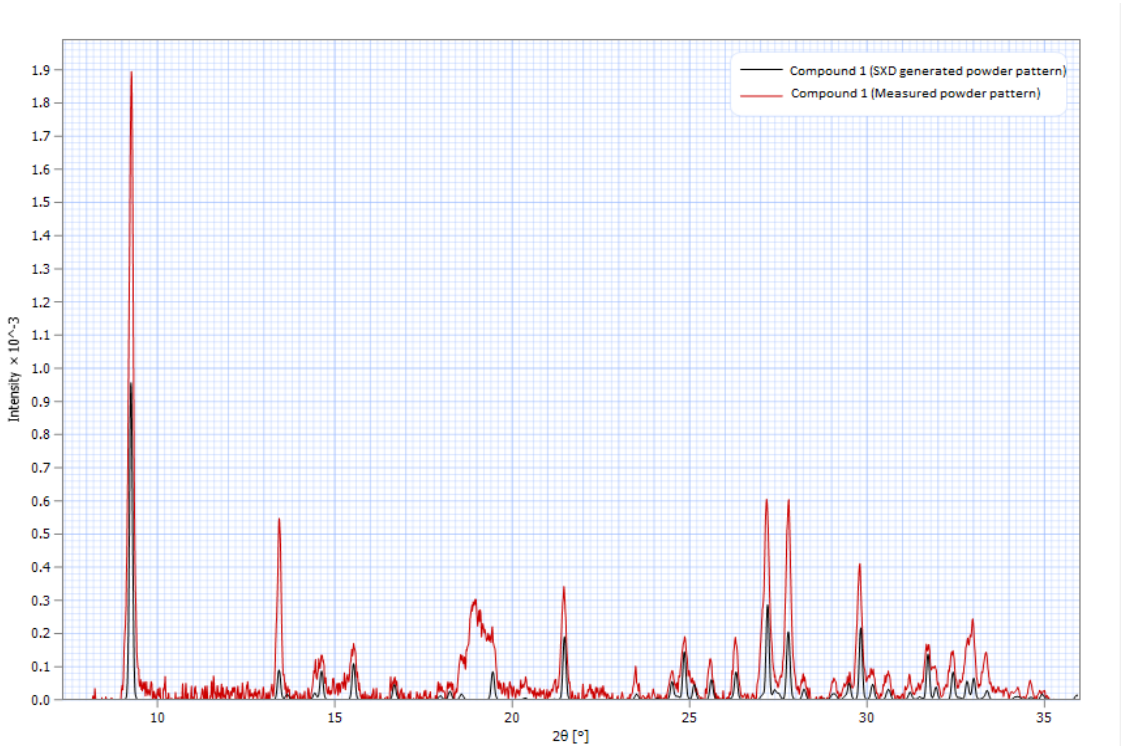

Figure S5 Compound 1 measured powder X-ray diffraction pattern compared to single-crystal data generated powder pattern (additional feature at 18.4-19.4° from sample holder)

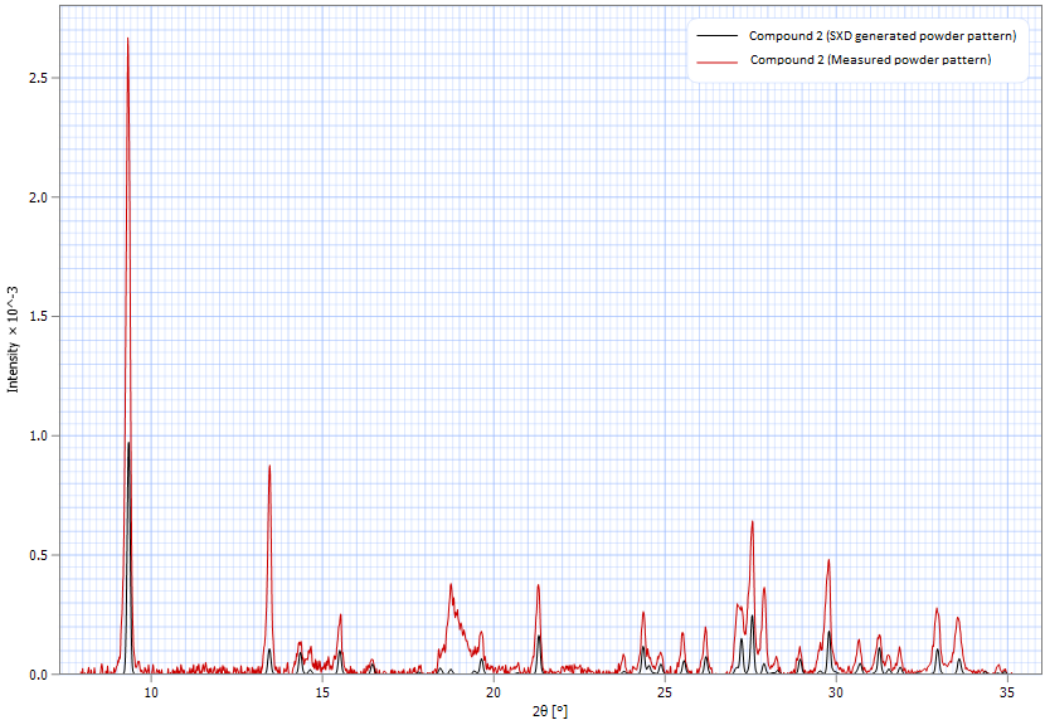

Figure S6 Compound 2 measured powder X-ray diffraction pattern compared to single-crystal data generated powder pattern (additional feature at 18.4-19.4° from sample holder)

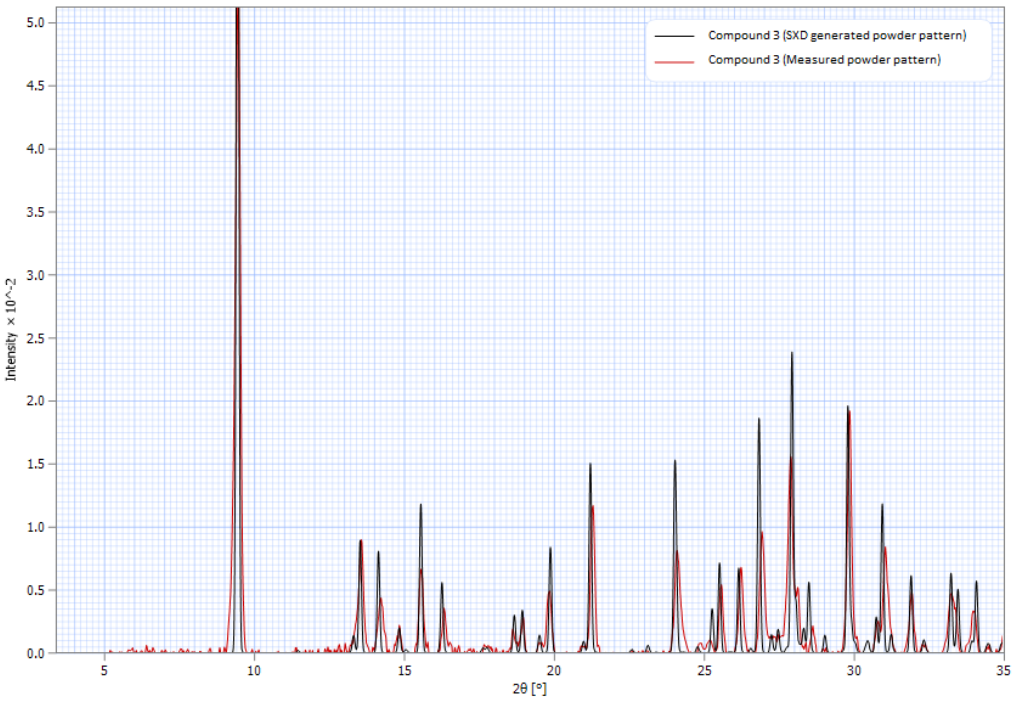

Figure S7 Compound 3 measured powder X-ray diffraction pattern compared to single-crystal data generated powder pattern

3.1.3 Afterword commentary and discussion

Following its publication this article has been cited in a number of other publications focussed also on furthering the research area of halometallate materials [7-13]. For example, the coined term pseudo-three-dimensional used to describe this class of material has been taken forward in a study looking at the role of iodine molecules and weak I---I interactions in assembling supramolecular pseudo-three-dimensional hybrid bismuth polyiodides; based around the discovery of another interesting novel organic-inorganic hybrid iodobismuthate structure [8]. The three novel hybrid materials presented in this publication are also included in a review article [12] tracking the new structural types and application areas of bismuth (III) complexes as they continue to develop [12,13].

To follow this, as mentioned within the summary to the paper, subsequent work on these materials attempted to investigate whether a material with light absorbing properties could be retained upon the dehydration of the precursor hydrated hybrid material. Thermogravimetric analysis (TGA), seen in Figures S1-S3 of the published supplementary information above, of the structures showed a dehydration step for each hybrid material at approximately 70-110 ^{o}C. Therefore, as a prerequisite to carrying out further work a preliminary TGA ramp and hold experiment at 110 ^{o}C was completed to dehydrate a sample of compound 1. The material was shown to retain its deep red colouration suggesting promisingly that the resulting structure may also be optically active as an absorber material.

Next, pure phase single-crystal samples of Compound 1 and 2 were ground to a fine powder to carry out powder X-ray diffraction analysis to explore the structural changes further. The required amount of pure phase material of Compound 3 for variable temperature dehydration analysis was not obtained for further investigation. Variable temperature (Var-T) data was taken at 10 ^{o}C increments from 30 ^{o}C to 150 ^{o}C; with scans taken at room temperature pre- and post- analysis for structural comparison.

From the powder X-ray diffraction profiles, shown in Appendix A.19-A.21, it can be seen that significant structural changes occur during variable temperature heating of the hydrated hybrid compounds. For example, the (011) plane of Compound 1 at approximately 9^{o} 2θ is observed to diminish in intensity up to around 70 ^{o}C where it becomes indistinguishable in the X-ray diffraction pattern until the final profile recorded after the resulting material was left to cool to room temperature. Through the heating of each compound multiple peaks are shown to

diminish and disappear from the structural profile with multiple new diffraction planes arising. The pre- and post- variable temperature analysis profiles, suggest that upon dehydration of each compound significant changes to the anionic framework occur in the structure; showing that the materials are not porous in the sense that the water molecules can enter and leave the structure without disrupting the structural order. They in fact play an additional part in templating the hybrid structures alongside the organic dications within the channels, likely through hydrogen bonding interactions to the electronegative halide positions of the outer substructure.

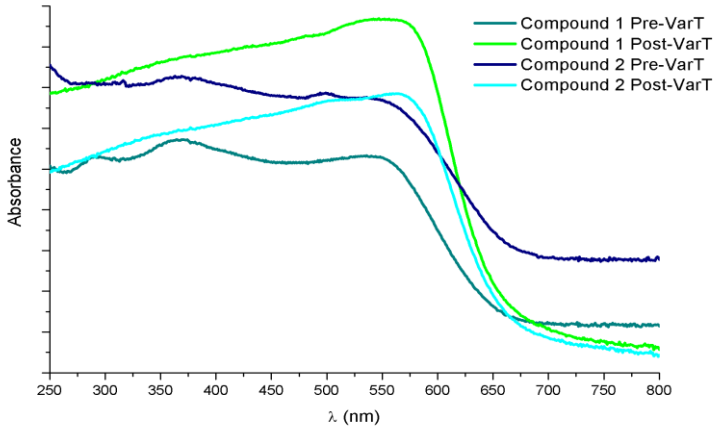

Figure 3.4 UV/Vis data on compounds 1 and 2 measured pre- and post-variable temperature powder X-ray diffraction analysis

Post-variable temperature powder X-ray diffraction analysis (Post-VarT) UV/Vis data for the 1,4-piperazinium and 1-methyl-1,4-piperazinium templated compounds 1 and 2 was obtained; as seen in figure 3.4. The post-VarT profiles of both compounds continue to possess strong absorption across the majority of the visible spectrum with absorption edge onsets shifted slightly to 575 nm from 550 and 560 nm respectively. Absorption features previously observable at ~290 nm (4.3 eV) and ~360 nm (3.4 eV), attributed to the electronic transitions from the HOMO Bi(6p) orbital to the LUMO Bi(5p) orbitals, are no longer clearly distinguishable in the spectra. Tauc plot data analysis, seen in Figure 3.5, suggests a convergence of the band gap energies of each compound to ~1.95-1.97 eV post dehydration. The Tauc plot denotes the onset of absorption in each compound and by extrapolating the linear region for each plotted data set, a useful estimate of the band gap energy of the crystalline material can be attained.

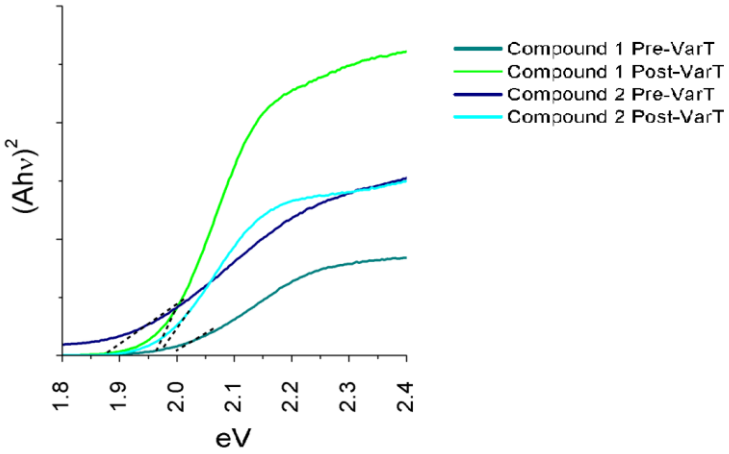

Figure 3.5 Tauc plot data on compounds 1 and 2 measured pre- and post- variable temperature powder X-ray diffraction analysis

Ultimately, the data set was not used within the published material, however, further work on full structural analysis of the powder X-ray diffraction data by Rietveld refinement analysis could yield more information on how dehydration of the structures affects the structural connectivity to give the observed changes in absorbance characteristics. As concluded from the initial investigations covered in this work, increased methylation of the templating piperazinium ring increasing the relative steric size of the dication from 1,4-dipiperazinium to 1-methyl-1,4-dipiperazinium to 1,4-dimethyl-1,4-dipiperazinium, was found to show a counterintuitive response in the series of structures as band gap energy is shown to decrease.

Contributing factors to this effect were theorised to be tied with a decreased level of solvate within the material and a structural chemistry response to the interconnections of the anionic network as the results showed an average shortening of the I---I interactions between 1D $[BiI_4]^-_n$ chains in the anionic network. This would become an important feature moving forward in the investigations and study of novel hybrid halometallate materials.
In addition to this, the work carried out showed that larger cations carrying a higher charge than commonly utilised templates such as caesium, methylammonium and formamidinium are worth exploring in greater detail to further build upon the library of hybrid materials so far considered. In doing so this would yield more understanding of how the most highly optimised absorber materials in this structural category can be obtained and made use of.
In the next section a sister compound of structure 2, templated again by the organic dication 1-methyl-1,4-dipiperazinium but with dissimilar structural and physical properties, is described before leading into the work undertaken to advance our initial halometallate hybrid material investigations further.

3.1.4 Compound 4: 1-methyl-1,4-dipiperazinium decaiododibismuthate dihydrate

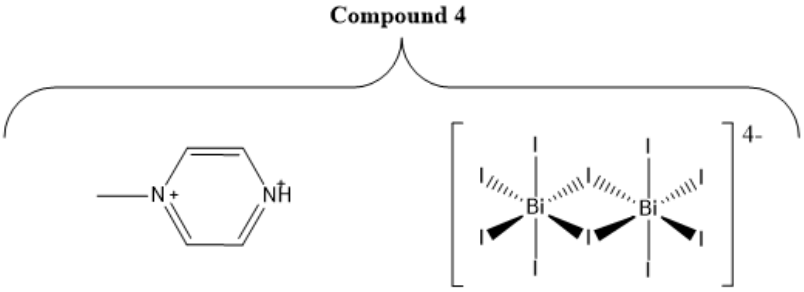

1-methyl-1,4-dipiperazinium decaiododibismuthate dihydrate
$2(C_5H_{14}N_2)Bi_2I_{10}.2(H_2O)$

Within the aforementioned published Dalton Transactions paper (DOI: 10.1039/C6DT03602C) a structure (denoted as compound 2) templated by the divalent organic cation, 1-methyl-1,4-dipiperazinium, was described in detail. To reiterate briefly on this structure, 1-methyl-1,4-dipiperazinium tetraiodobismuthate trihydrate, the novel compound was synthesised as a pure phase of red block crystals via a controlled solvothermal reaction procedure from reagents bismuth chloride (0.2 mmol), 1-methylpiperazine (0.15 mmol), hydriodic acid (0.75 ml, 57 wt% in water) in aqueous conditions (6 ml). The resultant pure phase of hybrid iodobismuthate material was determined to be templated by diprotonated 1-methyl-1,4-dipiperazinium cations, solvated with three neutral water sites and supported by an interconnected anionic substructure of one-dimensional bismuth iodide chains; founding a pseudo-three dimensional electronic network.

From an slightly altered reagent mixture ratio with an increased volume of hydriodic acid added to the reaction mixture (1 ml hydriodic acid, 57 wt% in water), increasing the acidity and volume within the Teflon® vessel, a crystallisation of two solid crystallised phases occurs. The primary phase of red block crystals (7:3 ratio) were identified from single-crystal X-ray analysis screening as being a cell match to the one-dimensional $[BiI_4]_n^-$ chain-based structure described in the published paper. However, analysis of a selected single crystal from the secondary phase of orange plate crystals revealed that it was a different material, though still a iodobismuthate hybrid structure in nature, templated again by the diprotonated cation 1-methyl-1,4-dipiperazinium, but with a much dissimilar structural form. This observation showed that the identity of the organic templating agent does not alone ultimately determine the form the hybrid material takes but is one of a number of factors influencing the formation of a structure. An organic cation, such as 1-methyl-1,4-dipiperazinium used here, can counterbalance the charge of varying anionic substructure architectures within hybrid

materials. In particular here, solvent effects influence the formation of a certain hybrid structure due to the hydrogen bonding and stabilising properties of the neutral water molecules bound within the material. This reasoning was further solidified by the previously discussed structural changes from dehydration of compounds 1 and 2 in section 3.1.3.

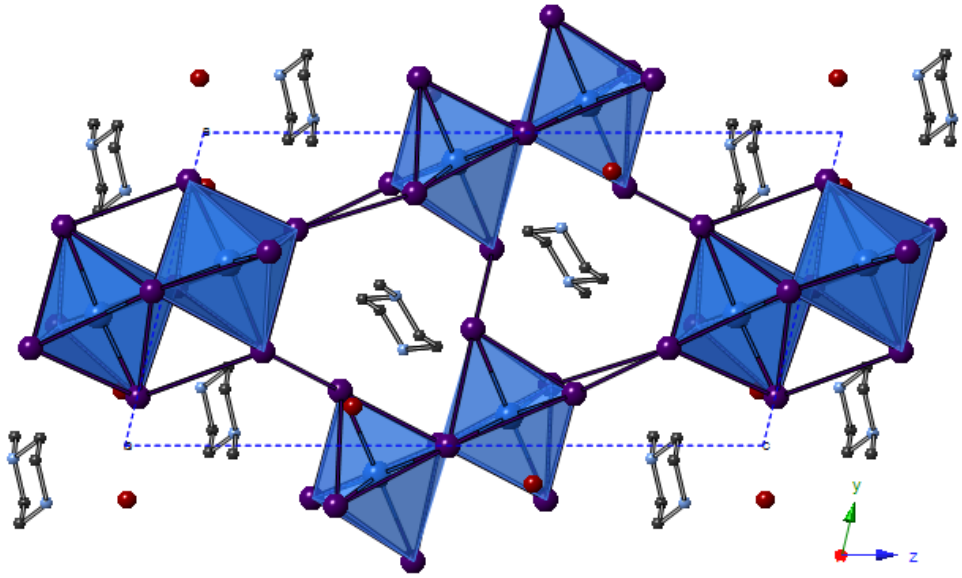

Figure 3.6 View along the *a*-axis of compound 4. Legend: [BiI_6] octahedra shaded blue; Bi atoms (blue), I atoms (purple), C atoms (dark grey), N atoms (pale blue), O atoms (red). H atoms excluded.

Hybrid structure compound 4, $2(C_5N_2H_{14})Bi_2I_{10}.2(H_2O)$, is templated by organic 1-methyl-1,4-dipiperazinium divalent charged cations. The synthetic procedure employed was found to favour the formation of a mixed phase of two hybrid structures; with the second 1-methyl-1,4-dipiperazinium templated hybrid iodobismuthate material crystallising from the reaction mixture as orange plate crystals. The identified secondary phase was determined from single-crystal X-ray analysis to have crystallised in triclinic space group *P-1*. The full structural refinement determined that the secondary phase structure was made up of an anionic substructure of interconnected $[Bi_2I_{10}]^{4-}$ units; a different structural form from the comparable one-dimensional chain network of its counterpart crystallised structure with identical templating agent (see Figures 3.6-3.8).

To further expand upon the details obtained from full structural determination, Bi-I bond distances within the bioctahedral discrete units range from 2.9682(5) - 3.2401(5) Å (Δ = 0.272 Å, Av = 3.09 Å) for the dual-Bi(1)-centred bioctahedron and 2.9516(5) - 3.2187(4) Å (Δ = 0.267 Å, Av = 3.09 Å) for the dual-Bi(2)-centred bioctahedron within each asymmetric unit cell. The regularity of the octahedra is reflected also in the I-Bi-I bonding angles with an average bonding deviation of 6.9^o from 180^o for Bi(1)-centred bioctahedron and a slightly more

distorted average measured at 8.4° from 180° for Bi(2)-centred bioctahedron. A total of twenty-six interunit interactions link the discrete anionic $[Bi_2I_{10}]^{4-}$ units into an extended conjoined network; forming a pseudo-three dimensional network. Comparably to sister structure compound 2, the inherent structural dimensionality of the conjoined octahedra in the network is reduced, however, iodide-iodide connections build an increased electronic pseudo-three dimensionality within each material. Average interaction lengths of these linking connections measure at 4.25 Å for structure 4 (0D hybrid) and at 4.09 Å for structure 2 (1D hybrid).

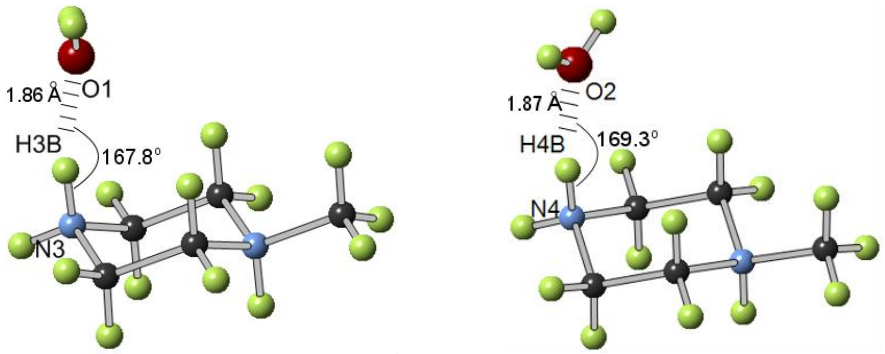

Figure 3.7 Water oxygen- organic cation hydrogen bonding interactions in compound 4

Within the hybrid structure stabilising hydrogen bonding interactions are observed between the cationic $(NH_2)^+$ ring position on both modelled 1-methyl-1,4-dipiperazinium dications to the local neutral water site positions O(1) and O(2) in turn. As seen in Figure 3.7, hydrogen bonding across positions N(3)-H(3B) … O(1) measures at a distance of 1.86 Å at an angle of 167.8° and similarly at positions N(4)-H(4B) … O(2) measuring at 1.87 Å at an angle of 169.3°.

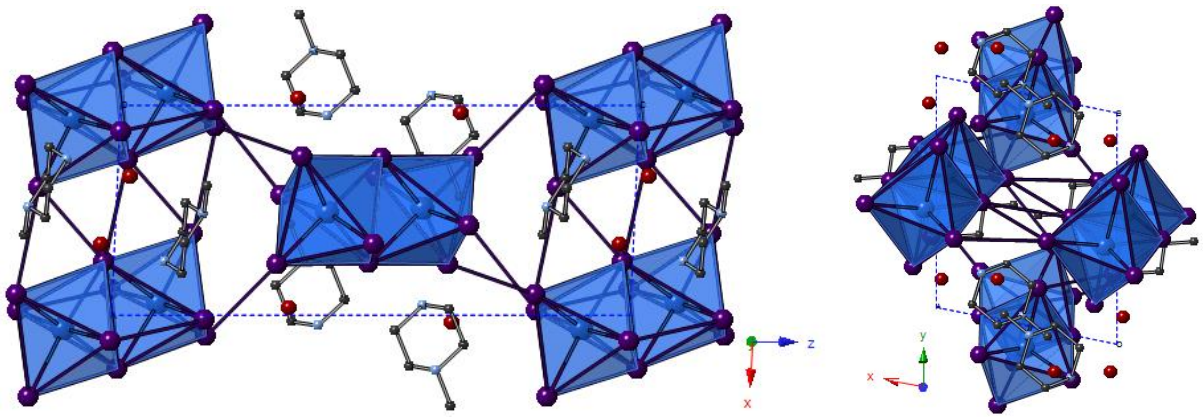

Figure 3.8 View along the *b*-axis (left) and *c*-axis (right) of compound 4. Legend as in Figure 3.6

Table 3.1 I---I interactions between discrete anionic units $[Bi_2I_{10}]$-$[Bi_2I_{10}]$ for compound 4

Bi (1) – bound iodide position	**Bi (2) – bound iodide position**	**Number of interactions**	**Interaction distance**	**Interaction type**
I(10)	I(3)	2	4.349 Å	equatorial terminal – equatorial terminal
I(10)	I(8)	2	4.306 Å	equatorial terminal – equatorial terminal
I(5)	I(1)	2	4.267 Å	axial terminal – axial terminal
I(10)-I(7)	N/A	4	4.312 Å	equatorial terminal – equatorial terminal
I(9)-I(9)	N/A	2	4.172 Å	equatorial bridging – equatorial bridging
I(2)-I(2)	N/A	2	4.279 Å	axial terminal – axial terminal
N/A	I(3)-I(8)	4	4.140 Å	equatorial terminal – equatorial terminal
N/A	I(6)-I(6)	2	4.155 Å	equatorial bridging – equatorial bridging
N/A	I(4)-I(4)	2	4.260 Å	equatorial terminal – equatorial terminal

A final structure refinement factor of 0.036, weighted refinement factor of 0.071 and goodness of fit of 1.02 was attained from the structural data analysis. Full crystallographic details of the structure solution and refinement are given in table 3.2 below.

Table 3.2 Crystal data for Compound 4	
Chemical formula	$2(C_5N_2H_{14})\cdot Bi_2I_{10}\cdot 2(H_2O)$
M_r	1927.39
Crystal system, space group	Triclinic, *P-1*
Temperature (K)	292
a, *b*, *c* (Å)	8.4128 (3), 10.8554 (3), 21.0425 (9)
α, β, γ (°)	76.131 (3), 89.833 (3), 78.764 (3)
V (Å^3)	1827.97 (12)
Z	2
F(000)	1664
D_x (Mg m^{-3})	3.502
Radiation type	Mo *K*α
No. of reflections for cell measurement	9212
θ range (°) for cell measurement	3.8–32.0
μ (mm^{-1})	18.07
Crystal shape	Plate

Colour	Orange
Data collection	
Diffractometer	Xcalibur, EosS2 diffractometer
Radiation source	fine-focus sealed X-ray tube, Enhance (Mo) X-ray Source
Monochromator	Graphite
Detector resolution (pixels mm^{-1})	8.0734
Scan method	ω scans
Absorption correction	Multi-scan *CrysAlis PRO* 1.171.38.43 (Rigaku Oxford Diffraction, 2015) Empirical absorption correction using spherical harmonics, implemented in SCALE3 ABSPACK scaling algorithm.
T_{min}, T_{max}	0.156, 1.000
No. of measured, independent and observed [$I > 2\sigma(I)$] reflections	19824, 11124, 9330
R_{int}	0.029
θ values (°)	θ_{max} = 32.0, θ_{min} = 3.4
$(\sin\theta/\lambda)_{max}$ ($Å^{-1}$)	0.746
Range of *h*, *k*, *l*	*h* = -12→12, *k* = -16→12, *l* = -30→28
Refinement	
Refinement on	F^2
$R[F^2 > 2\sigma(F^2)]$, $wR(F^2)$, *S*	0.036, 0.071, 1.02
No. of reflections	11124
No. of parameters	253
No. of restraints	0
H-atom treatment	H-atom parameters constrained
Weighting scheme	$w = 1/[\sigma^2(F_o^2) + (0.0244P)^2]$ where $P = (F_o^2 + 2F_c^2)/3$
$\Delta\rangle_{max}$, $\Delta\rangle_{min}$ (e $Å^{-3}$)	1.92, -1.94

Symmetry codes: (i) -*x*, -*y*+1, -*z*+2; (ii) -*x*+1, -*y*, -*z*+1.

Data collection: *CrysAlis PRO* 1.171.38.43 (Rigaku OD, 2015); cell refinement: *CrysAlis PRO* 1.171.38.43 (Rigaku OD, 2015); data reduction: *CrysAlis PRO* 1.171.38.43 (Rigaku OD, 2015); program(s) used to solve structure: *SHELXL2014*/7 (Sheldrick, 2014); program(s) used to refine structure: *SHELXL2014*/7 (Sheldrick, 2014); molecular graphics: Palmer, D. C. (2014). *CrystalMaker*. CrystalMaker Software Ltd, Begbroke, Oxfordshire, England.; software used to prepare material for publication: *WinGX* (Farrugia, 2012). *publCIF* [Westrip, S. P. (2010). *J. Appl. Cryst.*, **43**, 920-925] software used to generate tabulated data.

3.2 Second 'Dalton Transactions' publication and related material

3.2.1 Precursor commentary

Following the promising work on piperazinium cation based iodobismuthate hybrid material synthesis and characterisation it was considered appropriate to further explore this area by firstly attempting the synthesis of the equivalent iodoantimonate-based structures, in order to reaffirm the concept and also to allow for comparisons to be made to the bismuth-based candidate hybrid materials discovered. One aim was to seek further evidence of replication of the structural motif with identical templating agents but with a substituted metal ion identity – thereby allowing for direct comparisons of physical properties of isomorphous or similar structure types. Antimony-based structures may be found to exhibit different anionic substructures compared with their bismuth-based counterparts due to the size difference of the metal ions at the centre of each octahedra.

Results of this work would further contribute to discovering and building the library of known hybrid structures for comparison and understanding. In this work an unexpected *in-situ* solvothermal reaction also presented an interesting and exploitable opportunity to discover and analyse many more complex hybrid structures. A number of examples of how the technique was utilised are presented in the following publication and many more are presented and discussed in the following chapters.

The following paper, published in the Royal Society of Chemistry journal Dalton Transactions and entitled 'Synthesis, structure and optoelectronic properties of hybrid iodobismuthate and iodoantimonate semiconducting materials' presents the research outcomes from the in-depth investigations into halometallate hybrid material and presents comparisons of iodoantimonate and iodobismuthate structures with identical and similar organic templates. Each compound, identified by numbering scheme I-XIV, within the publication fit into the thesis numbering scheme as compounds 5-18.

3.2.2 Full paper entitled 'Synthesis, structure and optoelectronic properties of hybrid iodobismuthate and iodoantimonate semiconducting materials' and associated supplementary information

Statement of Authorship

<table>
<tr><th colspan="10">This declaration concerns the article entitled:</th></tr>
<tr><td colspan="10">Synthesis, structure and optoelectronic properties of hybrid iodobismuthate & iodoantimonate semiconducting materials</td></tr>
<tr><td colspan="10">Publication status (tick one)</td></tr>
<tr><td>draft manuscript</td><td></td><td>Submitted</td><td></td><td>In review</td><td></td><td>Accepted</td><td></td><td>Published</td><td>X</td></tr>
<tr><td>Publication details (reference)</td><td colspan="9">Authors: Adam J. Dennington and Mark T. Weller
Article Type: Paper
DOI: 10.1039/C7DT04280A
Citation: Dalton Trans., 2018, 47, 3469-3484</td></tr>
<tr><td>Candidate's contribution to the paper (detailed, and also given as a percentage).</td><td colspan="9">I fully developed the formulation of ideas and design of the methodology for all experimental work, carried out the synthetic work and material isolation (100%). I collected and undertook the data analysis for all single-crystal X-ray diffraction, powder X-ray diffraction, UV/Vis spectroscopy and thermogravimetric analysis presented in the work. Some acknowledged assistance was taken from Dr Mary F. Mahon to improve upon the structural refinement of the SXD data for compound XIII. Finally, I wrote the initial paper drafts, made revisions under my supervisor's guidance, and carried out all of the required referee response corrections to finalise the work to be published as a full paper.</td></tr>
<tr><td>Statement from Candidate</td><td colspan="9">This paper reports on original research I conducted during the period of my Higher Degree by Research candidature.</td></tr>
<tr><td>Signed</td><td colspan="5"></td><td>Date</td><td colspan="3"></td></tr>
</table>

Synthesis, structure and optoelectronic properties of hybrid iodobismuthate & iodoantimonate semiconducting materials

Adam J. Dennington[a] and Mark T. Weller[b]

Abstract

The syntheses and structures of five iodobismuthate and nine iodoantimonate hybrid materials are presented. The 1,3-dimethyl-2-oxo-2,3-dihydropyrimidinium cation has been used to template the isostructural, one-dimensional $[C_6H_9N_2O][SbI_4]$ (**I**) and $[C_6H_9N_2O][BiI_4]$ (**II**), while 4-methylmorpholinium templates the compounds, $[C_5H_{12}NO]_4[Sb_6I_{22}]$ (**III**) and $[C_5H_{12}NO]_4[Bi_4I_{16}]$ (**IV**), both containing isolated iodopnictogenide cluster anions. Five iodoantimonate compounds, templated by piperazinium cation derivatives, have been synthesised; $[C_4H_{12}N_2][SbI_4]_2.4H_2O$ (**V**), $[C_5H_{14}N_2][SbI_4]_2.3H_2O$ (**VI**), two polymorphs of $[C_6H_{16}N_2][SbI_4]_2.2H_2O$ (**VII** and **VIII**) and $[C_6H_{16}N_2][Sb_4I_{16}]_{0.5}.H_2O$ (**IX**), mainly adopting structures closely related to previously published 1D iodobismuthate hybrid materials. 1-Ethyl-2-methylbenzimidazolium cations, formed *in situ* in the reaction medium, template the isostructural 1D structures of $[C_{10}H_{13}N_2][SbI_4]$ (**X**) and $[C_{10}H_{13}N_2][BiI_4]$ (**XI**). 1,4-diazabicyclo[2.2.2]octandiium $(DABCOH_2)^{2+}$ di-cations are shown to template a hydrated iodoantimonate structure $[C_6H_{14}N_2]_2[Sb_4I_{16}].2H_2O$ (**XII**) containing $[Sb_4I_{16}]^{4-}$ complex anions and a mixed phase of two iodobismuthate materials; one phase contains, uniquely, a mixture of the complex anions $[Bi_2I_{10}]^{4-}$ and $[BiI_6]^{3-}$ in the form $[C_6H_{14}N_2]_{10}[Bi_2I_{10}]_2[BiI_6]_4.(H_2O)_8$ (**XIII**), and the second, $[C_6H_{14}N_2]_2[Bi_4I_{16}].2H_2O$ (**XIV**), contains discrete $[Bi_4I_{16}]^{4-}$ clusters. The stability and thermal decomposition routes of these phases have been determined using thermogravimetric analysis. UV-Vis spectroscopy has been used to determine band gap energy estimates which are related, for a range of iodobismuthate and iodoantimonate materials, to their structural features and potential optoelectronic applications.

Introduction

The research field of haloantimonate(III) and halobismuthate(III) hybrid organic-inorganic materials has developed over the past few decades to yield materials of interest for their non-linear dielectric and optical properties. The use of different organic cation templating species has been found to yield a large variety of structures with controlled structural dimensionality of the anionic-unit, *vide infra*. Acting as counter-ions to the anionic iodopnictogenide unit within the structure, the organic species can additionally yield various polymorphs, often by variation of the exact reactions conditions.[1-4]

Trivalent metal (M = Bi^{3+}, Sb^{3+}) hybrid halometallate materials, with general formula $[R_a]^{n+}[M_bX_{3b+a},]^{n-}$ are currently known to adopt approximately 30 variants of the anionic moiety. The most prevalent species found are oligomeric and extending polymeric structures of conjoined $[MX_6]$ octahedra but more rarely monomeric $[MX_6]$ units have been reported.[5] The ability to form $[MX_6]$ octahedra in metal-halide systems is a prerequisite to forming perovskites (corner-sharing), while adopting alternative non-perovskite structural units (edge-sharing, face-sharing or in isolation) opens up a vast library of materials with a variety of anionic substructures. For example, as demonstrated by iodobismuthate structures, the identity of the anionic inorganic component currently ranges from discrete 0D units (simple anions and clusters) in $[BiI_6]^{3-}$ to $[Bi_8I_{30}]^{6-}$ motifs [6-21], through 1D chain structures [7, 22-27], most commonly in $[BiI_4]^-_n$ or $[BiI_5]^{2-}_n$ compositions; just one 2D extended network has been reported, $[Bi_{2/3}I_4]^{2-}_n$.[28] The identity of anionic component in these hybrid materials is dependent on many different factors including the templating species, synthesis conditions and technique as well as the molar ratios of reagents used. In a similar vein, for iodoantimonate materials the anionic component can take the form of discrete units with a range of compositions and associated charges, for example, $[Sb_3I_{11}]^{2-}$, $[Sb_2I_9]^{3-}$, $[Sb_5I_{18}]^{3-}$, $[Sb_6I_{22}]^{4-}$, $[Sb_8I_{28}]^{4-}$ [5, 29, 30] as well as one-dimensional unit configurations $[SbI_4]^-_n$,[31, 32] $[SbI_5]^-_n$,[23] $[Sb_2I_7]^-_n$, [33] and $[Sb_3I_{10}]^-_n$.[34] Iodometallate materials are principally of interest in comparison with their bromo- and chloro-metallate equivalents as they tend to possess smaller band gaps and lower carrier effective masses [2, 35] – important properties for high performance optoelectronic materials.

Regarding the properties required of non-linear dielectrics, four anionic species have been identified in previous studies as having the potential to exhibit ferroelectric properties, $R_3M_2X_9$ [5], RMX_4 [36], RMX_5 [37], and $R_5M_2X_{11}$ [38, 39]; the vast majority of the compounds reported adopt the sub-lattice forms $[M_2X_9]^{3-}$ and $[M_2X_{11}]^{5-}$. It is worth noting that for $R_3M_2X_9$ four separate structural forms are known: (i) a two-dimensional layer structure, (ii) an infinite one-dimensional chain, (iii) discrete di-octahedral units, and (iv) discrete tetra-octahedral units; only the 2D layer structure form has been identified to demonstrate ferroelectric properties. Conversely, for $[M_2X_{11}]^{5-}$ the structural unit is exclusively discrete di-octahedral units with all salts exhibiting ferroelectric properties.

Also recently, and with rapidly growing traction in the last three years, hybrid organic-inorganic perovskite and perovskite-like materials have established themselves as the principal area of photovoltaic research. In particular, the leading absorber material in this field is the hybrid compound methylammonium lead iodide, MAPI, $[CH_3NH_3][PbI_3]$; with the highest

solar cell efficiencies utilising derivatives of this material reaching over 22%.[40] However, a key concern of utilising this material for commercial applications is the presence of the toxic metal, lead. Additional issues regarding the deployment of MAPI in solar cell devices concern its long-term stability; research aiming to combat this issue of instability when exposed to light (and/or) air is ongoing.[41, 42] Concurrently, other non-toxic, post transition metal-based, hybrid materials with similar functional optoelectronic properties are being explored as alternative candidates for photovoltaic applications. Such materials can offer the prospect of improved material stability, allowing simpler device processing and manufacture, and long-term cell deployment. As a result, we have been interested in exploring the synthesis, structural characterisation and studying the electrical properties of novel compounds of this type.

The desired semiconducting properties these materials have been highlighted to stem from the fundamental electronic structure of the post transition metals demonstrating the "inert pair effect" with filled $5s^2$ or $6s^2$ orbitals; these orbitals have been shown to produce shallow defects and a dispersed valence band. Prospective metal cation candidates of interest in forming semiconducting metal-halide hybrid structures are considered to be Sn^{2+}, Bi^{3+} and Sb^{3+}. Initial isovalent substitution studies with Sn^{2+} replacing Pb^{2+} in hybrid perovskite related materials have proved to be largely unsuccessful for applications, as Sn^{2+} compounds have been shown to undergo rapid oxidation by air and decompose readily through reaction with moisture. [43] Therefore the impetus has been to explore alternatives with potentially improved stability to degradation via oxidation. [44]

The stability of the Group (n-2) exhibiting the loan pair effect increases from Group 13 through Group 14 to Group 15. Thus while In^{+} and Tl^{+} are readily oxidised to the trivalent state and as mentioned previously Sn^{2+}, and to a lesser extent Pb^{2+}, can be easily oxidised, Sb^{3+} and, particularly, Bi^{3+} are both more difficult to oxidise to the Group oxidation state. This makes these species ideal for forming M(III) halocomplexes that are stable in air. With an increased level of electropositivity over tin and lead ion centres, Bi^{3+} and Sb^{3+} demonstrate a contraction of their ionic radii to 103 pm and 76 pm respectively in comparison to 119 pm (Pb^{2+}) and 102 pm (Sn^{2+}). Despite this smaller ionic radius these ionic radii are still relatively large and six coordination to halide ions remains the most common coordination geometry found for both Bi^{3+} and Sb^{3+}. However, in comparison with divalent metal hexahalides $[MX_6]^{4-}$, the formation of the higher charged metal in $[SbX_6]^{3-}$ and $[BiX_6]^{3-}$ units often results in the halide ion preferring to bridge between two metal centres and the formation of complex anions whose structures contain edge- and face- sharing octahedra. This preferred connectivity means that

three-dimensional structural, and, therefore, optoelectronic connectivity has proved elusive for iodobismuthate and iodoantimonate materials. Understanding how choice of counter cation controls structural connectivity in these iodobismuthate and iodoantimonate materials and how two and three dimensional connectivity may be induced remains a key target for producing new hybrid semiconducting materials of the Group 15 elements.

Results described in this paper develop the area of haloantimonate(III) and halobismuthate(III) hybrid materials showing how changes in the templating species and the chalcogenide allow control of the structure and band gap. These new families of hybrid materials should also allow greater tuning of the band gap and lead to new applications. One example is in low energy X-ray detectors for medical applications where nanoparticulate Bi_2S_3 has recently been shown to have high sensitivity and rapid response to dosimetric X-rays.[45]

Synthesis

Reactants and solvents were used as received from suppliers Alfa Aesar (bismuth chloride, 1,4-dimethylpiperazine), Fluka chemicals (piperazine) and Sigma-Aldrich (antimony chloride, antimony iodide, 2-aminopyrimidine, hydriodic acid, 4-methylmorpholine, 1-methylpiperazine, 1,2-benzenediamine, DABCO) at reagent grade standard or above.

Section A

Compound I $[C_6H_9N_2O][SbI_4]$ - Crystals of 1,3-dimethyl-2-oxo-2,3-dihydropyrimidinium iodoantimonate were obtained through solvothermal reaction and *in situ* methylation process from $SbCl_3$ (0.2 mmol), 2-aminopyrimidine (0.15 mmol), HI (1.0 ml, 57 wt%, no stabiliser) in methanol (6 ml). Reactants were placed in a 25 ml Teflon® vessel, sealed in a steel autoclave and heated at 140 ^oC for 24 h; with a controlled ramp up rate of 1 $^oC\ min^{-1}$ and ramp down rate of 0.1 $^oC\ min^{-1}$. A pure phase of very fine dark orange needle crystals (0.0205 g, estimated yield of 14%) was obtained after vacuum filtration and an ethanol wash.

Compound II $[C_6H_9N_2O][BiI_4]$ - The equivalent isostructural iodobismuthate hybrid compound was obtained under identical conditions except for a change of the main group metal source to bismuth trichloride (0.2 mmol). Under these conditions a pure phase of large (0.5-1 cm) red needle crystals (0.0517 g, estimated yield of 30%) was obtained following filtration and an ethanol wash.

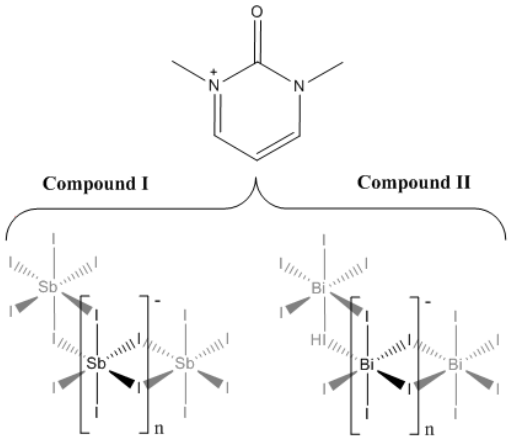

Scheme 1 Composition of compounds **I** and **II**

Section B

Compound III $[C_5H_{12}NO]_4[Sb_6I_{22}]$ - Under hydrothermal reaction conditions, a pure phase of bright orange crystals of structure **III**, was obtained from $SbCl_3$ (0.2 mmol), 4-methylmorpholine (0.15 mmol), HI (1.0 ml, 57 wt%, no stabiliser) in deionised water (6 ml). Reactants were placed in a 25 ml Teflon® vessel, sealed in a steel autoclave and heated at 140 ^oC for 24 h; with a controlled ramp up rate of 1 ^oC min^{-1} and ramp down rate of 0.1 ^oC min^{-1}. After filtration and an ethanol wash, a pure phase of crystals of 4-methylmorpholinium iodoantimonate, structure **III** (0.0773 g, estimated yield of 60%), was obtained.

Compound IV $[C_5H_{12}NO]_4[Bi_4I_{16}]$ - Changing the main group metal precursor compound to bismuth trichloride (0.2 mmol), and a reduction in the volume of hydriodic acid (0.75 ml) added to reaction mixture, produced a single phase of bright red block crystals of the related 4-methylmorpholium templated iodobismuthate; structure **IV** (0.0535 g, estimated yield of 30%).

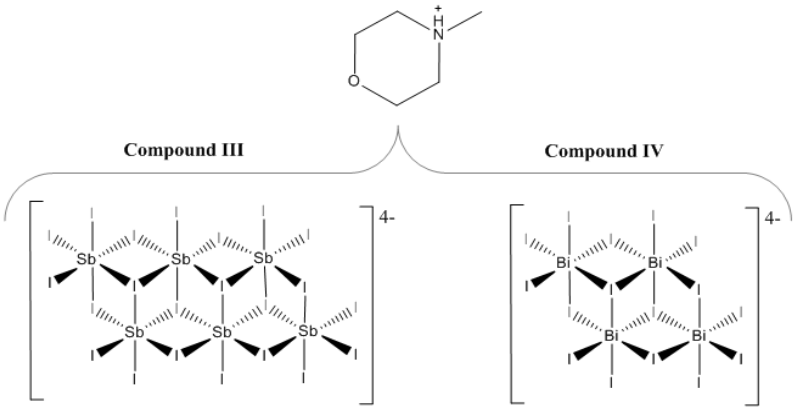

Scheme 2 Composition of compounds **III** and **IV**

Section C

Compound V $[C_4H_{12}N_2][SbI_4]_2.4H_2O$ - Crystals of 1,4-dipiperazinium iodoantimonate tetrahydrate were obtained through hydrothermal reaction of SbI_3 (0.2 mmol), piperazine (0.15 mmol), HI (1.0 ml, 57 wt%, no stabiliser) in deionised water (6 ml). Reactants were placed in a 25 ml Teflon® vessel, sealed in a steel autoclave and heated at 140 ºC for 24 h., with a controlled ramp up rate of 1ºC/min and ramp down rate of 0.1ºC/min. After filtration and ethanol wash, a pure phase of prismatic orange block crystals (0.0260 g, estimated yield - 18%) was obtained. Similarly, a pure phase of structure **V** could also be synthesised under identical conditions with a cheaper, more readily available $SbCl_3$ reagent in the place of SbI_3.

Compound VI $[C_5H_{14}N_2][SbI_4]_2.3H_2O$ - Long orange prismatic crystals of 1-methyl-1,4-dipiperazinium iodoantimonate trihydrate were synthesised in a mixed phase (with minor phase of black crystalline material). The product was obtained a hydrothermal reaction, under the same conditions as structure **V**, using the reagents SbI_3 (0.2 mmol), 1-methylpiperazine (0.15 mmol), HI (1.0 ml, 57 wt%, no stabiliser) in deionised water (6 ml). After filtration and ethanol wash, 0.0727 g of the mixed phase product (9:1 ratio by visual estimate, estimated yield of 50%) was collected.

Compounds VII $[C_6H_{16}N_2][SbI_4]_2.2H_2O$, **VIII** $[C_6H_{16}N_2][SbI_4]_2.2H_2O$ and **IX** $[C_6H_{16}N_2][Sb_4I_{16}]_{0.5}.H_2O$ - Under identical hydrothermal reaction conditions three hybrid materials, all templated by the organic di-cation 1,4-dimethyl-1,4-dipiperazinium, were synthesised in a mixed phase (10:2:1:6 ratio by visual estimate) product. This mixed phase product consisted of chunky dark orange crystals (**VII**), elongated dark orange crystals (**VIII)**

and block yellow-orange crystals (**IX)**; alongside black crystals identified to be the organic salt 1,4-dimethyl-1,4-dipiperazinium bis(tri-iodide). Reagents SbI_3 (0.2 mmol), 1,4-dimethylpiperazine (0.15 mmol), HI (1.0 ml, 57 wt%, no stabiliser) and deionised water (6 ml) were sealed in a 25 ml Teflon® vessel, sealed in a steel autoclave and heated at 140 °C for 24h; with a controlled ramp up rate of 1 °C min^{-1} and ramp down rate of 0.1 °C min^{-1}. The mixed phase product was filtered and washed with ethanol to give a total dry weight yield of 0.112 g, estimated yields of 40%(**VII**), 10%(**VIII**) and 5%(**IX**).

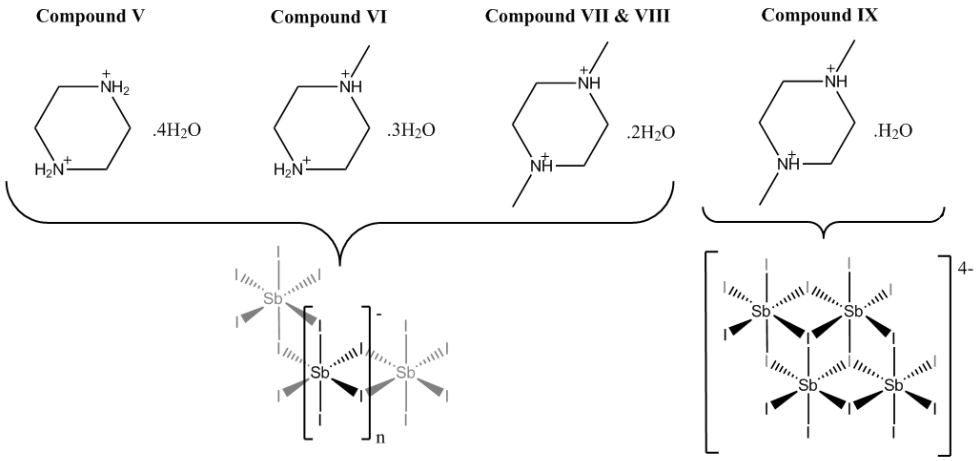

Scheme 3 Composition of compounds **V-IX**

Section D

Compound X $[C_{10}H_{13}N_2][SbI_4]$ - A mixed phase (1:9 ratio by visual estimate) of a minor impurity of semi-crystalline material alongside a major phase of transparent dark-orange elongated-plate crystals of 1-ethyl-2-methylbenzimidazolium templated structure **X** was synthesised under solvothermal conditions. The reagents $SbCl_3$ (0.2 mmol), 1,2-benzenediamine (0.15 mmol), HI (1.0 ml, 57 wt%, no stabiliser) and ethanol (6 ml) were placed in a 25 ml Teflon® vessel, sealed in a steel autoclave and heated at 140 °C for 24 h; with a controlled ramp up rate of 1 °C min^{-1} and ramp down rate of 0.1 °C min^{-1}. The product was washed with ethanol and dried by vacuum filtration to give the dry weight yield of 0.0725 g (estimated yield of 40%).

Compound XI $[C_{10}H_{13}N_2][BiI_4]$ - A major phase (4:1 ratio by visual estimate) of dark-red, prismatic needle crystals of compound **XI** was crystallised from a solvothermal reaction alongside a minor phase of crystalline orange material. The reagents $BiCl_3$ (0.2 mmol), 1,2-benzenediamine (0.15 mmol), HI (0.5 ml, 57 wt%, no stabiliser) and ethanol (6 ml) were placed in a 25 ml Teflon® vessel. The vessel was sealed within a steel autoclave and heated at 140 °C

for 24 h; with a controlled, ramp up rate of 1 ^{o}C min^{-1} and ramp down rate of 0.1 ^{o}C min^{-1}. The product was washed with ethanol and a dry weight yield (0.0434 g, estimated yield of 20%) was obtained after drying by vacuum filtration.

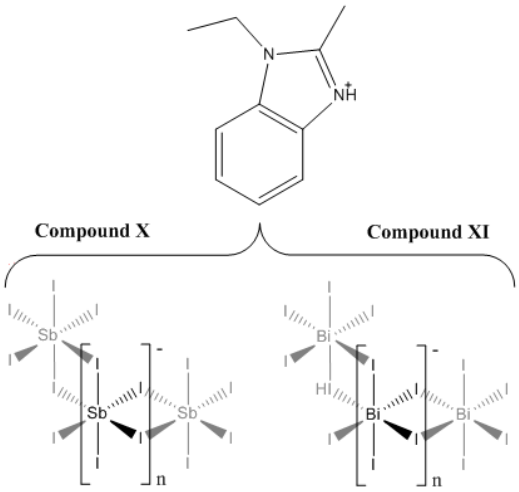

Scheme 4 Composition of compounds **X** and **XI**

Section E

Compound XII $[C_6H_{14}N_2]_2[Sb_4I_{16}].2H_2O$ - A mixed phase (1:1 ratio by visual estimate) of orange block crystals (**XII**) and black crystalline material was obtained from a hydrothermal synthesis procedure. The reagents $SbCl_3$ (0.2 mmol), DABCO (0.15 mmol), HI (0.75 ml, 57 wt%, no stabiliser) and water (6 ml) were placed in a 25 ml Teflon® vessel. In turn, the vessel was sealed within a steel autoclave and heated at 170 ^{o}C for 24 h; with a controlled ramp up rate of 1 ^{o}C min^{-1} and ramp down rate of 0.1 ^{o}C min^{-1}. The product was washed with ethanol and a total dry weight yield of 0.135 g (Estimated yield of 50%) was obtained after drying by vacuum filtration.

Compound XIII $[C_6H_{14}N_2]_{10}[Bi_2I_{10}]_2[BiI_6]_4.(H_2O)_8$ and **XIV** $[C_6H_{14}N_2]_2[Bi_4I_{16}].2H_2O$ - A mixed phase (3:2 ratio by visual estimate) of orange needle crystals (**XIII**) and red block crystals (**XIV**) was obtained from a hydrothermal synthesis procedure. Reagents $BiCl_3$ (0.2 mmol), DABCO (0.15 mmol) HI (0.75 ml, 57 wt%, no stabiliser) and water (6 ml) were sealed in a 25 ml Teflon® vessel, sealed in a steel autoclave and heated at 140 ^{o}C for 24 h; with a controlled ramp up rate of 1 ^{o}C min^{-1} and ramp down rate of 0.1 ^{o}C min^{-1}. The mixed phase

product was washed with ethanol and dried by vacuum filtration to give a combined total dry weight yield of 0.123 g (Estimated yields of 35%(**XIII**) and 30%(**XIV**)).

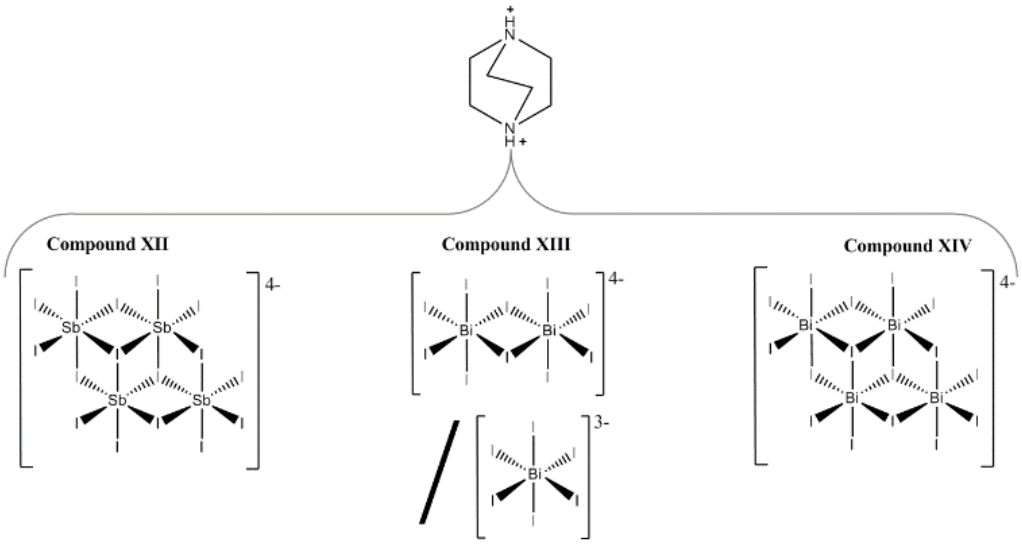

Scheme 5 Composition of compounds **XII-XIV**

Crystal structures: results and discussion

Compounds I and II

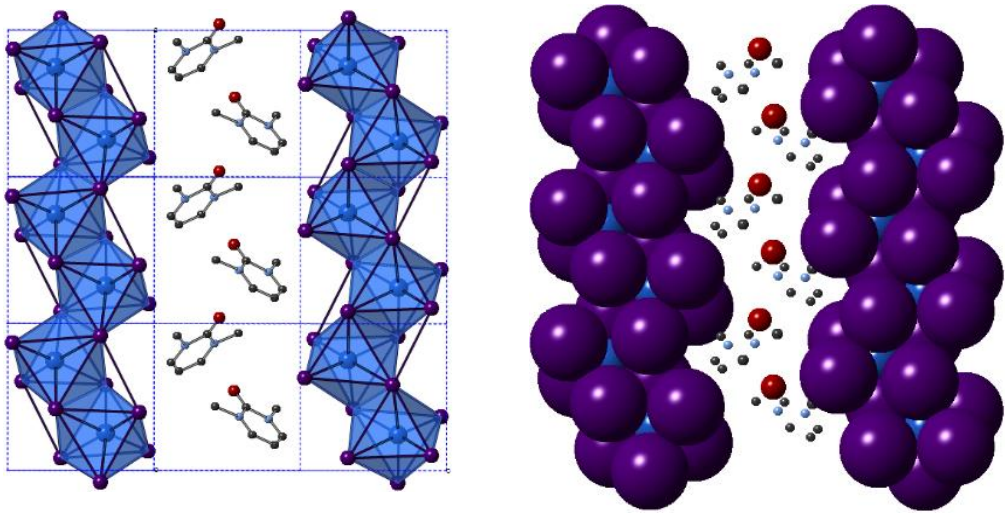

Figure 1 A single layer view of structure **II** on the *ac* plane visualised by ball and stick modelling (left) and space-filling modelling (right). [BiI_6] octahedra are shaded blue; Bi atoms (blue), I atoms (purple), C atoms (black), O atoms (red) and N atoms (pale blue)

Compounds **I** and **II**, $[C_6H_9N_2O][MI_4]$, M = Sb, Bi. The isostructural 1,3-dimethyl-2-oxo-2,3-dihydropyrimidinium templated structures **I** and **II**, were solved from single-crystal X-ray diffraction data; see Table 1 for crystallographic data comparison. In each synthetic procedure, the simpler organic amine 2-aminopyrimidine was used as a precursor reagent; however under the high temperature and pressure conditions of the solvothermal reaction, and in the presence of strong acid HI, methyl iodide forms as a transient species before undergoing alkylation of the two pyrimidine ring nitrogen positions in turn and deprotonation of the amine to form the mono-cationic organic ion 2-imino-1,3-dimethyl-2,3-dihydropyrimidium. Under the acidic aqueous conditions a further reaction occurs in-situ in which the imine is hydrolysed to a ketone functionality resulting in the templating cationic 1,3-dimethyl-2-oxo-2,3-dihydropyrimidinium species. The structures of both compounds **I** and **II** exhibit an anionic network of one-dimensional metal halide chains $[MX_4]^-_n$ interacting via weak halide-halide connections. [25, 32, 46] In the channels between the anionic network, the organic cations (counter-balancing the charge of the anionic chains) are positioned to fill the grooves of the chain structure along the *a*/*c* plane axis (see Figure 1); alternating with perpendicular orientation along the *b*-axis indicative of a herring-bone structural motif (see Figure 2 *c*-axis view).

Table 1 Unit cell parameters for compounds I and II (at 150 K)

	Compound I (Sb)	Compound II (Bi)
Space Group	Monoclinic $P2_1/c$	Monoclinic $P2_1/c$
a (Å)	10.5506(4)	10.6424(3)
b (Å)	7.6199(3)	7.6380(2)
c (Å)	19.9962(7)	20.0271(5)
β (°)	95.336(3)	94.986(2)
V (Å^3)	1600.63(10)	1621.78(7)

Weak inter-chain I---I interactions extend the anionic network asymmetrically along the *a*- and *c*-axes of both structures. A terminal-terminal I---I pathway bridges the anionic chains in, approximately, the *a*-axis direction. For structures **I** and **II**, respectively, these separations are 3.85 Å and 3.79 Å, repeating every 7.62 Å and 7.64 Å along the *b*-axis. Similarly, (for structures **I** and **II** respectively) a longer edge-terminal I---I interaction of 4.42 Å and 4.32 Å, repeating more regularly every 4.03 Å and 4.12 Å, approximately along the *c*-axis direction can be observed. The average I---I interaction distance for the iodobismuthate compound is shorter at 4.06 Å, in comparison to 4.14 Å for the iodoantimonate.

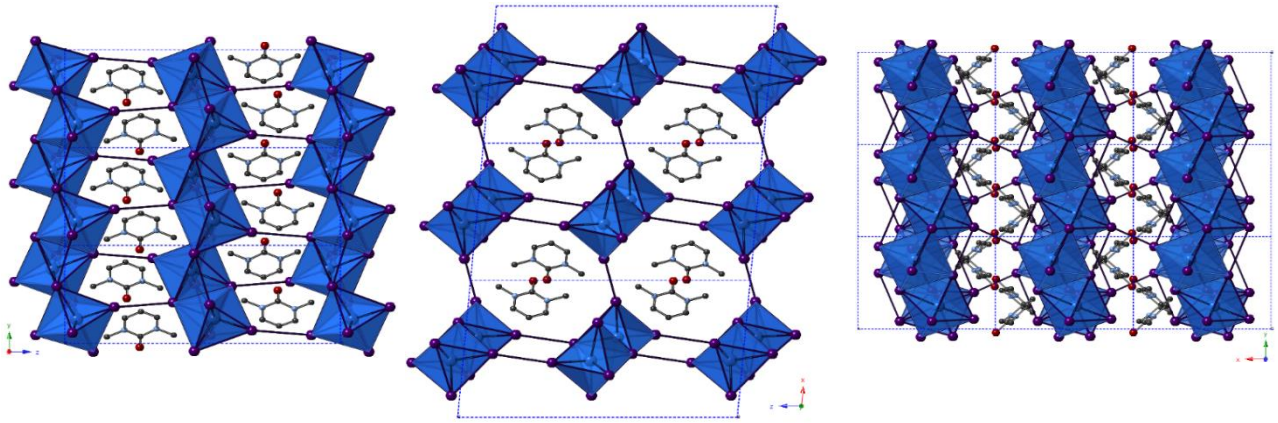

Figure 2 Visualisation of structure **II** (iso-structural with structure **I**) along *a*-axis (left), *b*-axis (centre) and *c*-axis (right); key as in Figure 1

The chain structure is formed by edge-sharing of metal iodide octahedral units along two of twelve vertices. The octahedra appear to distort away from 'perfect' regular octahedra in accordance with the known *trans* effect in halometallate structures wherein the M-X bonds across from bridging bonds are shorter (and also exhibit a higher vibrational frequency) [47, 48]. However, an additional degree of distortion may be attributed to the way in which the cations are interleaved within the grooves of the chain structure (highlighted in Figure 1). Deviation of the I-M-I bond angle away from an ideal 180 degrees within the octahedra ranges from 4.9-10.9° in structure **I** to 5.9-11.6° in structure **II**. Average bond angle deviations show distortions of 7.3° and 7.8°, respectively, away from a regular octahedron in each of the structures.

In addition to this, considering the M-I-M bond angles within the chain structures shows an average bond angle deviation from 90° of 3.9° for the $[SbI_4]^-_n$ chains in compound **I** compared to 3.5° for the $[BiI_4]^-_n$ chains in compound **II**. M-I bond distances vary by 2.83-3.27 Å (Δ = 0.44 Å) 2.92-3.29 Å (Δ = 0.37 Å) for structures **I** and **II** respectively.

Compounds III and IV

From single-crystal X-ray diffraction data, the structures of two 4-methylmorpholinium templated hybrid structures have been derived. Compound **III**, $[C_5H_{12}NO]_4[Sb_6I_{22}]$, contains clusters of four monovalent charged 4-methylmorpholinium cations charge counter-balancing discrete $[Sb_6I_{22}]^{4-}$ anions.[3] Each cation is orientated with the ring-based oxygen atom directed towards the core of the cation cluster and, thus, the positively charged protonated nitrogen atom (and attached methyl group) directed outwards from the cluster and in closer proximity to the anionic units. Each group of four cations is "encased" within an anionic sublattice formed by six $[Sb_6I_{22}]^{4-}$ units linked through weak I---I interactions. Consideration of the orientations of the four 4-methylmorpholinium cations within each cluster indicates that there are no, or extremely weak, hydrogen bonding interactions between protonated amine template cation and $[Sb_6I_{22}]^{4-}$ anions.

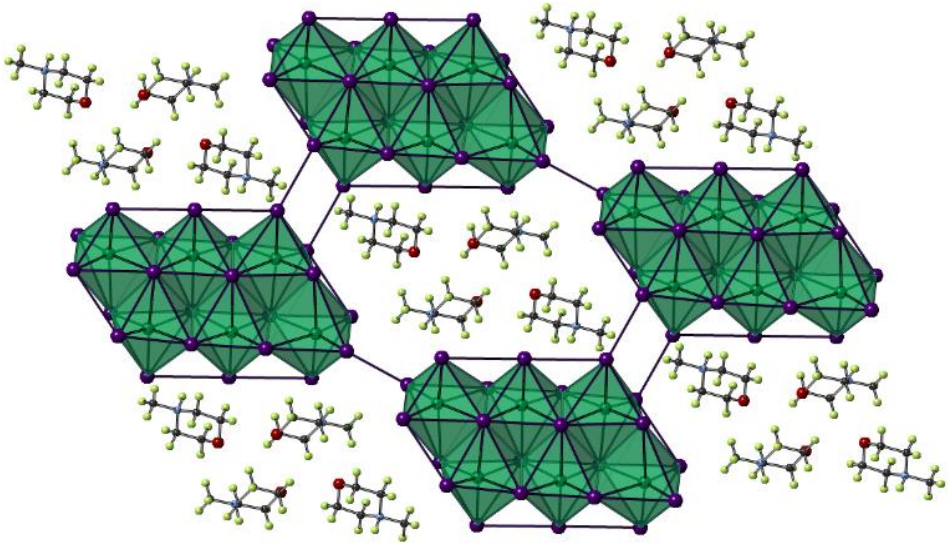

Figure 3 A single layer component of structure **III** viewed on the *ab* plane. Key as in Figure 1 aside from $[SbI_6]$ octahedra shaded teal; Sb atoms (teal), H atoms (pale green)

Further analysis of this structure shows that viewed down the *c*-axis the discrete iodoantimonate units are interconnected by weak I---I interactions of 4.64 Å between the outer Sb(1) octahedra and two I---I interactions of 4.21 Å per Sb(3) octahedra. Further weak I---I interactions interconnect each $[Sb_6I_{22}]^{4-}$ unit with a total of 38 interactions (12 repeating unique I---I distances) per unit to 12 distinct zero-dimensional $[Sb_6I_{22}]^{4-}$ units to build the anionic "network". Overall these inter-unit interactions range from 3.80-4.73 Å; with an average I---I interaction distance of 4.14 Å.

The outermost octahedra in each $[Sb_6I_{22}]^{4-}$ unit, centred by position Sb(1) with just two from twelve possible edge connections, is the most perceptibly distorted and this can be shown by considering the average deviations from 180° for the I-Sb-I angles in each $[SbI_6]$ octahedra. For the Sb(1) centred octahedra the angle was found to distort by 10.3° from 180° on average. For the Sb(3) centred octahedra, with 3/12 edge connections along its vertices, the average angle deviation from 180° for I-Sb-I is reduced to 6.7°. Lastly, with 4/12 edge connections to adjacent octahedra, the Sb(2) centred octahedra making up the core of the $[Sb_6I_{22}]^{4-}$ unit exhibits least distortion from a regular octahedron with an average deviation away from 180° of just 2.9°. Bonded Sb-I distances within each octahedra vary by 2.76-3.47 Å (Δ = 0.71 Å), 2.79-3.36 Å (Δ = 0.57 Å) and 2.79-3.35 Å (Δ = 0.56 Å) for Sb(1)-(3) respectively.

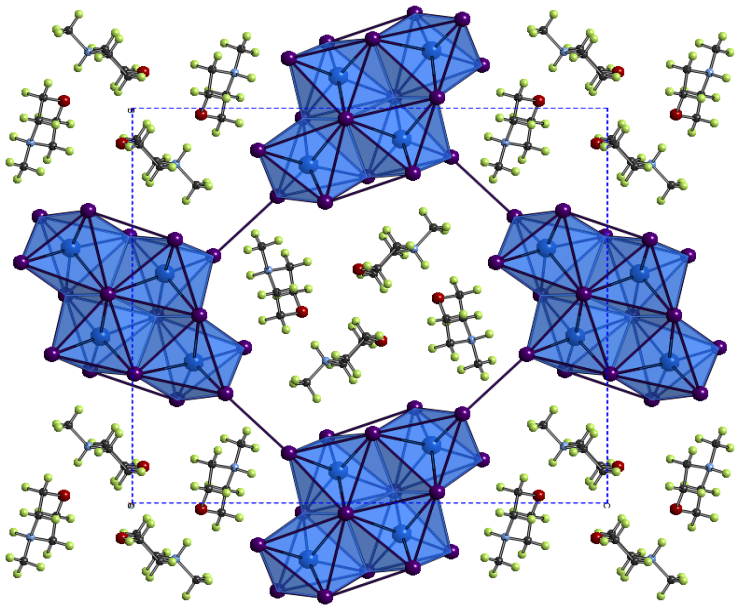

Figure 4 A cross-section of the *bc* plane of structure **IV** viewed down the *a*-axis; colour key as in Figure 1 with addition of O atoms (red) and H atoms (pale green)

Iodobismuthate hybrid material (Structure **IV**) $[C_5H_{12}NO]_4[Bi_4I_{16}]$, again templated by 4-methylmorpholinium cations, was modelled from the single-crystal X-ray diffraction data. In a similar way to its iodoantimonate counterpart, discussed previously, groups of four monovalent 4-methylmorpholinium cations are found to cluster together; again encapsulated by the anionic sublattice structure. However, here the counter-balancing tetravalent discrete anionic units take the form of $[Bi_4I_{16}]^{4-}$. [7] A total of 28 (7 repeating unique I---I distances) inter-unit I---I interactions connect each discrete bismuth iodide unit to twelve different $[Bi_4I_{16}]^{4-}$ units. Inter-unit I---I interaction distances range from 3.97-4.56 Å; with an average distance

of 4.27 Å. Orientation of the 4-methylmorpholinium suggests weak hydrogen bonding interaction between cations (N^+-H…O) may be present within the structure D-H…O (hydrogen bond distance 1.95Å with a ∟D-H--A angle of 157.6° (22.4° deviation from direct interaction) from position N(2)-H to O(1). The N(1)-H and O(2) positions are not involved in hydrogen bonding.

The outer Bi(1) centred octahedra are visibly more distorted than the central Bi(2) octahedra within each $[Bi_4I_{16}]^{4-}$ unit. Averaging the angular deviation away from 180° across all *trans* I-Bi-I motifs in the octahedra reveals a distortion of 9.8° for the Bi(1) centred outer octahedra compared to 5.4° for the core Bi(2) centred octahedra. However, the influence of the *trans* effect, wherein the M-X bonds across from bridging bonds are shorter, is similar in each octahedra with Bi-I distances varying by 2.89-3.42 Å (Δ = 0.53 Å) and 2.88-3.40 Å (Δ = 0.52 Å) for Bi(1) and Bi(2) respectively.

Table 2 Unit cell parameters for compounds III and IV (at 150 K)

	Compound III (Sb)	Compound IV (Bi)
Space Group	Triclinic *P-1*	Orthorhombic *Pbca*
a (Å)	11.3253(7)	12.7627(3)
b (Å)	13.0042(7)	20.7207(6)
c (Å)	15.2847(7)	22.7427(6)
α (°)	69.645(4)	90.000
β (°)	69.877(5)	90.000
γ (°)	64.496(6)	90.000
V (Å^3)	1853.97(17)	6014.35(3)

Compounds V - IX

The structures of Compounds **V** - **IX** were solved from single-crystal X-ray diffraction. Structures **V**, **VI**, **VII** and **VIII** $[NH_2(CH_2)_4NH_2][SbI_4]_2.4H_2O$, $[CH_3NH(CH_2)_4NH_2][SbI_4]_2.3H_2O$, and $[CH_3NH(CH_2)_4NHCH_3][SbI_4]_2.2H_2O$ (two polymorphs) were templated by 1,4-dipiperazinium, 1-methyl-1,4-dipiperazinium and 1,4-dimethyl-1,4-dipiperazinium cations respectively. The materials are iso-structural and consist of infinite one-dimensional antimony iodide $[SbI_4]^-_n$ chains with fairly short inter-chain I---I contacts.[32] Divalent charge-balancing cations are located within channels extending along the *a*-axis direction parallel with the sub-lattice of 1D $[SbI_4]^-_n$ chains.

Associated with the changes in the degree of methylation of the nitrogen positions on the piperazine ring system is a variation in the level of water incorporated into the material - which reduces as the methyl groups protrude into the space occupied by the water molecules. There is a related subtle alteration to the $[SbI_4]^-_n$ chain positions relative to each other and thus their degree of interaction via interlinking I---I connections.

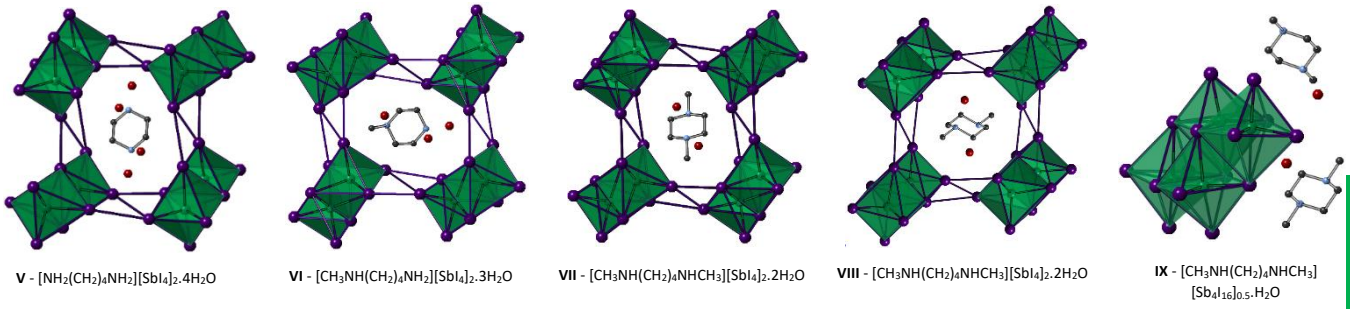

Figure 5 Left to right: Structures **V** - **VIII** viewed along the *a*-axis and the asymmetric unit cell of structure **IX**; colour key as in Figure 1 aside from Sb atoms (teal) and O atoms (red)

Similar to the equivalent iodobismuthate material described in a previous publication, [49] structure **VI** has the 1-methyl-1,4-dipiperazinium cation disordered between two orientations within the channel. An effect of this is that two of the water molecule positions within the structure become partially occupied depending on the orientation of the cation and thus the directionality and steric hindrance by the methyl (CH_3) group on these hydrated sites. Consequently, two previously fully occupied water molecule positions in structure **V** become half-filled, reducing the overall degree of hydration from a tetrahydrate (in the composition of structure **V**) to an averaged trihydrate (in the composition of structure **VI**). Continuing the trend, in the isomeric structures **VII** and **VIII**, 1,4-dimethyl-1,4-dipiperazinium ions within the channel impede occupancy of two of the would-be hydrated sites within the structure; having the effect of reducing the overall level of hydration within the material to a dihydrate composition; $[CH_3NH(CH_2)_4NHCH_3][SbI_4].2H_2O$.

The iodometallate $[MI_4]^-_n$ chains in structures **V**, **VI**, **VII** and **VIII** consist of edge sharing $[MX_6]$ octahedra; with four bridging iodine atoms along two vertices and two *cis*-related terminal iodine positions. The antimony atom position is offset from a central position within the octahedra with the shortest two Sb-I distances observed for the two *cis* terminal iodine sites. These observations are in agreement with those made for previously studied materials possessing a similar $[MX_4]^-_n$ structural motif for haloantimonates and halobismuthates exhibiting the *trans* effect; *vide supra*. Similarly, the spread of Sb-I bond lengths within the

octahedra, that interlink to form the chains, decreases from compound **V** to compound **VII** suggesting an increased overall regularity of the octahedra.

Much like their counterpart iodobismuthate hybrid structures, inter-chain I---I interactions in Compounds **V - VIII** extend the anionic network along *b*- and *c*-axes of each material. It can be considered that the pathways across this interface produces a level of pseudo-dimensionality within the anionic sublattice framework of the materials; introducing the potential electronic pathways across $[SbI_4^-]_n$ chains in addition to movement along the chain. Two edge-terminal I---I and a terminal-terminal I---I interaction repeat regularly (7.34 Å, 7.53 Å and 7.72 Å respectively) along the chain *a*-axis; with all iodide positions within the network in close enough proximity to engaged in at least one inter-chain interaction. Lengths of these interactions range from 3.80-4.46 Å in the structures and the average distance of the inter-chain interactions decreases 4.19 Å → 4.13 Å → 4.01 Å through compounds **V - VII** respectively. However, the shortest I---I interaction is shown to undergo negligible change through the structures; 3.80 Å → 3.81 Å → 3.80 Å. In response inter-chain Sb-Sb distances are observed to increase marginally by 0.05 Å and 0.08 Å in the structural pairs **V→VI** and **VI→VII** respectively. Variation in the Sb-I-Sb bond angles within the chains also sees an increase away from regular octahedral angle to 90.7° → 92.1° → 93.6° for structures **V - VII** respectively.

Table 3 Unit cell parameters for compounds V- IX (at 150 K)

	Compound V	**Compound VI**	**Compound VII**	**Compound VIII**	**Compound IX**
Space Group	Monoclinic $P2_1/c$	Monoclinic $P2_1/c$	Monoclinic $P2_1/c$	Monoclinic $P2_1/c$	Monoclinic $P2_1/n$
a (Å)	7.3391(2)	7.5306(2)	7.7213(2)	7.5751(2)	11.5391(3)
b (Å)	13.0022(5)	12.9539(4)	12.8027(3)	12.1020(3)	11.8717(4)
c (Å)	13.8121(4)	13.6147(4)	13.4527(3)	14.5071(4)	19.1648(5)
β (°)	94.550(3)	96.086(3)	97.377(2)	92.630(3)	93.705(3)
V (Å^3)	1313.86(7)	1320.64(7)	1318.84(5)	1328.52(6)	2619.87(13)

In summary as the piperazinium ring of the organic cation becomes increasingly methylated there are observable changes the anionic sub-lattice of each structure. The regular distance between repeat interactions along the chain structure in the *a*-axis direction increases (i.e. an increasingly less compressed framework along the *a*-axis) the average I---I inter-chain interaction distance decreases (4.19 Å → 4.13 Å → 4.01 Å) and the overall regularity of the

octahedra, defined by decreasing Sb-I bond length variation, increases (0.49 Å → 0.45 Å → 0.40 Å). Overall, structures **V - VII** follow similar structural trends to their iodobismuthate equivalent materials previously reported [49].

In addition to these findings on antimony iodide 1,4-dipiperazinium complexes a new polymorph of compound **VII** crystallised in the same reaction mixture, together with a third phase, *vide infra*. This first minor phase of elongated dark orange needles, identified as compound **VIII**, occurred together with the major phase of blocky, dark orange crystals of structure **VII**. The structure of compound **VIII** consists of an identical motif of interconnected $[SbI_4]^-_n$ chains as seen in structure **VII**, however, the interrelationship between the chains for **VIII** shows an offset of approximately 19° in comparison with respect to adjacent units in the sublattice network. As a result, as seen in the *a*-axis view of structure **VIII** (see figure 5), the chains become aligned in parallel. Furthermore, comparing structures **VII** and **VIII** it can be seen that the three repeating interchain I---I interactions along the chain axis are retained, however, although the regularity of recurrence of these interactions along the *a*-axis is decreased (7.72 Å → 7.58 Å) the average interaction distance sees a slight increase (4.01 Å → 4.07 Å). In addition to this, the regularity of the octahedra decreases (Δ0.40 Å → Δ0.48 Å) and the Sb-I-Sb angle within the chain decreases by 1.1° (93.6° → 92.5°). Furthermore, it can be observed that, in structure **VIII**, the di-cation positioning within the *a*-axis channel shows increased tilt with the methyl groups pointed along the propagating *a*-axis more than in the polymorph (**VII**); in which the directionality of the methyl groups is focussed more towards the interstitial interchain space.

Finally, a third 1,4-dimethyl-1,4-dipiperazinium cation templated structure $[CH_3NH(CH_2)_4NHCH_3][Sb_4I_{16}]_{0.5}.H_2O$ (compound **IX**), determined from single-crystal X-ray diffraction data, was found to crystallise in the form of yellow-orange block-shaped crystals. Comparatively to the counterpart structures (**VII** and **VIII**) it crystallised alongside, the material contains a lower dimensional Sb-I anionic sub-structure of $[Sb_4I_{16}]^{4-}$ units.[50] In each unit cell, two divalent 1,4-dimethyl-1,4-dipiperazinium cations counterbalance the anionic network of zero-dimensional $[Sb_4I_{16}]^{4-}$ units. Each anionic unit interacts with a total of 14 different adjacent units to build the substructure via 36 (10 repeating unique I---I distances) inter-linking weak I---I interactions. Distances range from 4.09-4.64 Å; with an average distance of 4.25 Å. The level of solvation within the structure is reduced with respect to structures **VII** and **VIII** from a dihydrate (1:2 dication to water molecule ratio) to a monohydrate hybrid material (1:1 ratio).

The outer Sb(2) centred octahedra of the $[Sb_4I_{16}]^{4-}$ cluster show distortion from regularity with an average angle deviation (away from 180° across I-Sb-I) in octahedra of 10.5°; compared to 4.4° for the central Sb(1) centred positions in the cluster. In accord with this observation is a larger variation in the Sb-I bonding distances within the outer octahedra compared to the inner; showing a variation covering the distance range 2.82-3.27 Å (Δ = 0.45 Å) for the Sb(1)-centred octahedron and 2.78-3.47 Å (Δ = 0.69 Å) for Sb(2).

Compounds X and XI

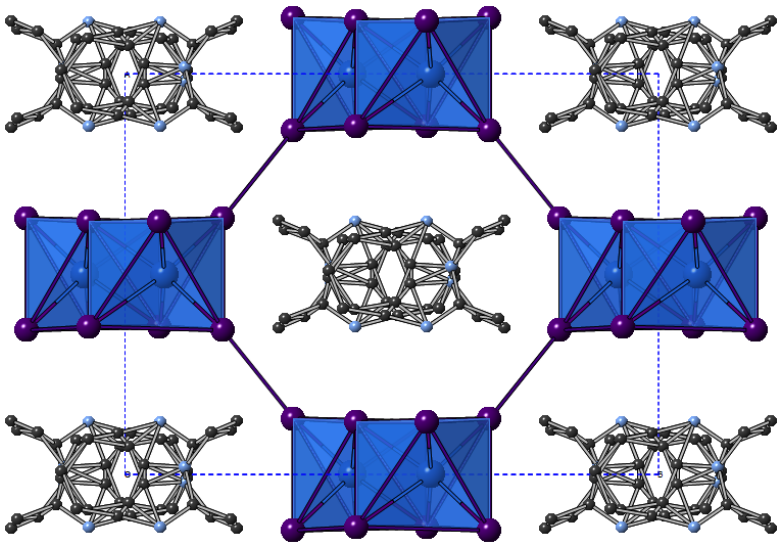

Figure 6 Structure **XI** $[C_{10}H_{13}N_2][BiI_4]$ viewed down the *c*-axis (hydrogen atoms are not shown); colour key as in Figure 1

Structures **X**, $[C_{10}H_{13}N_2][SbI_4]$, and **XI**, $[C_{10}H_{13}N_2][BiI_4]$, were solved from single-crystal X-ray diffraction data. The hybrid materials are isostructural and consist of inter-linked (through weak I---I interactions) metal iodide one-dimensional chains forming irregular sided octagonal channels in which the charge balancing organic cations are positioned. The templating cation for both isomorphs is the monovalent cation 1-ethyl-2-methylbenzimidazolium; formed *in situ* by twofold alkylation of the precursor reagent 1,2-benzenediamine via a ring-closing mechanism by reaction with ethyl iodide (formed in the reaction mixture from the solvent ethanol and HI). The materials both adopt a monoclinic crystal system, however, they crystallise in different space groups; see Table 4. This difference is related to positional changes and disorder of the organic benzimidazolium cation within the channel. Propagating along the *a*-axis, for structure **X**, and *c*-axis, for structure **XI**, the cations stack with alternating

orientations (180° rotation) with a separation of approximately 3.7 Å and an offset from the associated perpendicular structural axis of 17° and a shift of 1.6 Å. It should be noted that in the structure solution of compound **X** the organic component was modelled with PARTS instruction in order to split the ion into 55/45 occupancy over two related positions; the direction of the benzimidazolium ion alternates between these two positions, with the relationship between the two positions determined as an approximate 25° rotation in-plane of the ring system followed by a 180° 2-fold rotation through the central in-plane axis of the ion. Compound **XI**, however, was modelled in the higher symmetry monoclinic space group *C2/c*. Here, the 1-ethyl-2-methylbenzimidazolium cation lies on a glide plane running along the channel length.

Table 4 Unit cell parameters for compounds X and XI (at 150 K)

	Compound X (Sb)	Compound XI (Bi)
Space Group	Monoclinic $P2_1/n$	Monoclinic $C2/c$
a (Å)	7.5877(3)	13.3133(4)
b (Å)	17.7055(8)	17.7312(4)
c (Å)	13.2578(6)	7.6344(2)
β (°)	94.309(4)	93.450(2)
V (Å^3)	1776.07(13)	1798.92(8)

As previously mentioned, in both structures **X** and **XI,** the anionic framework is made up of one-dimensional anionic chains with the compositions $[SbI_4]^-_n$ and $[BiI_4]^-_n$ respectively.[25] In each structure the chains are aligned in parallel and consist of linked $[MI_6]$ octahedra; each octahedron has two *cis*-related terminal iodine positions with the other four iodine positions along shared edges of the octahedron. Within each octahedron the metal atom position is displaced from a central 'regular' octahedra position in the direction of the two terminal iodine positions with the two M-I(terminal) bond lengths approximately 0.5 Å shorter than to the other iodine positions. This is structural feature common to many iodobismuthate and iodoantimonate one-dimensional chain $[MI_4]^-_n$ hybrid structures. Comparing the antimonate (**X**) to the bismuthate (**XI**) structure it can be seen that the overall metal-iodide bond length range is slightly reduced (by 0.05 Å), producing more regular octahedra, and there is the expected shift to a higher average bond length (+0.05 Å) with the larger Bi. Similarly from **X**(Sb) to **XI**(Bi), the M-I-M bond angle average within the chain unit decreases from 93.5° to 93.0°. In both structures a single weak inter-chain I---I interaction is seen to repeat along the

chain axis direction; with a distance of 4.06 Å (Sb) and 3.94 Å (Bi) with a repeat distance of 7.59 Å(Sb) and 7.63 Å(Bi). Also of note, is that the one-dimensional $[MX_4]^-_n$ chain structural motif observed in these materials is reminiscent of structure **VIII**.

However, due to the increased size and reduced charge density of the monovalent 1-ethyl-2-methylbenzimidazolium cations compared to the 1,4-dimethyl-1,4-dipiperazinium divalent cations the void size accommodating the organic cations is larger; approximately 11.2 x 9.8 Å for **X** and **XI** versus 7.9 x 8.2 Å for structure **VIII**.

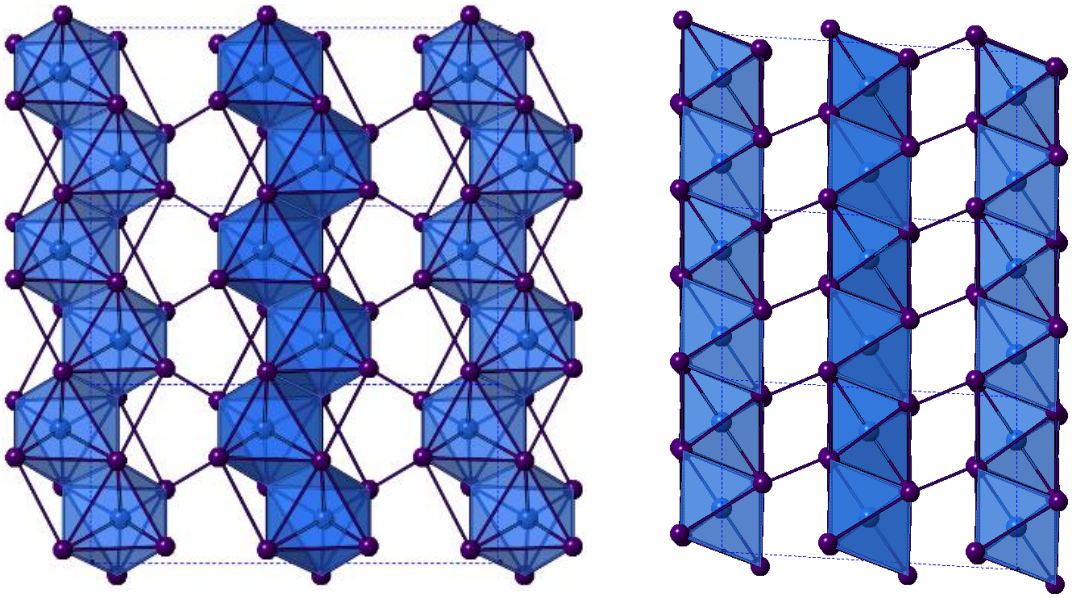

Figure 7 The $[BiI_4]^-_n$ chain units of structure **XI** viewed down the *a*-axis (left) and *b*-axis (right). Colour key as in Figure 1

Compounds XII, XIII and XIV

The iodoantimonate hybrid structure $[C_6H_{14}N_2]_2[Sb_4I_{16}].2H_2O$ (compound **XII**) was determined from single-crystal X-ray diffraction analysis. The material contains zero-dimensional tetra-octahedral $[Sb_4I_{16}]^{4-}$ anionic units which are counter-balanced by two di-protonated 1,4-diazabicyclo[2.2.2]octan-diium ($DABCOH_2$) cations (see Figure 8) alongside two sites occupied by water molecules. Within the structure each anionic $[Sb_4I_{16}]^{4-}$ structural unit interacts through weak I---I interactions, 38 (11 unique I---I bonding modes) interlinking pathways exist to a total of 12 nearby equivalent units to build the anionic "sub-lattice". I---I interaction distances range from 4.01-4.59 Å; with an average distance of 4.34 Å.

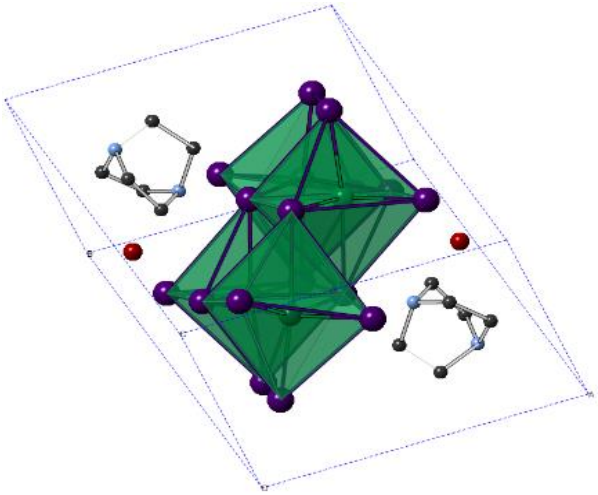

Figure 8 Symmetric unit cell of structure **XII** (hydrogen atoms excluded); colour key as in figure 5

The structure is reminiscent of structures **IV** and **IX**, each containing the 0D $[M_4I_{16}]^{4-}$ structural motif, each tetra-octahedral unit contains two equivalent central octahedra (with three shared edges) and antimony-iodide bond lengths ranging from 2.85-3.24 Å (Δ = 0.39 Å). The more distorted outer octahedra (which have two edges shared with other octahedra) show an increased metal-iodide bond length range of 2.79-3.39 Å (Δ = 0.60 Å). This variation in octahedron irregularity is also reflected in the average angle deviation from 180° of the *trans* I-Sb-I angles within the MX_6 octahedra. I-Sb-I angles have an average deviation of 5.8° from 180° for the inner octahedron centred on Sb(1), whereas the outer octahedron, centred on Sb(2), exhibits a much greater deviation of 12.3°.

In further reactions, using 1,4-diazabicyclo[2.2.2]octan-diium ($DABCOH_2$) di-cations as templating agents, a mixed phase of two new iodobismuthate hybrid material structures were obtained. Compound **XIII**, formulated as $[C_6H_{14}N_2]_{10}[Bi_2I_{10}]_2[BiI_6]_4.(H_2O)_8$ contains a unique and previously unreported combination of structural motifs, with both $[Bi_2I_{10}]^{4-}$ and $[BiI_6]^{3-}$ anionic components.[10, 51]

In each unit cell there are two di-octahedral $[Bi_2I_{10}]^{4-}$ units and four discrete $[BiI_6]^{3-}$ units generating a total anionic composition of $[Bi_8I_{44}]^{20-}$. Eight di-protonated $(DABCOH_2)^{2+}$ form the main charge-balancing organic component of the structure with positions identified within the structural model. This balancing leads to a charge deficit of 4+ per asymmetric unit cell and so to achieve an overall compositional charge neutrality to the material, it is proposed that two unrefined $(DABCOH_2)^{2+}$ dications reside within structural pores; as seen in Figure 10. This is in agreement with the results of the solvent masking algorithm utilised, detailed within the crystallographic data, suggesting that electron density within the structural pores is consistent with the presence of two additional disordered dications.

Figure 9 Thermal ellipsoid plots (Probability set at 50%) for structure **XII** (below), structure **XIII** (centre) and structure **XIV** (right). Colour key as in figure 1

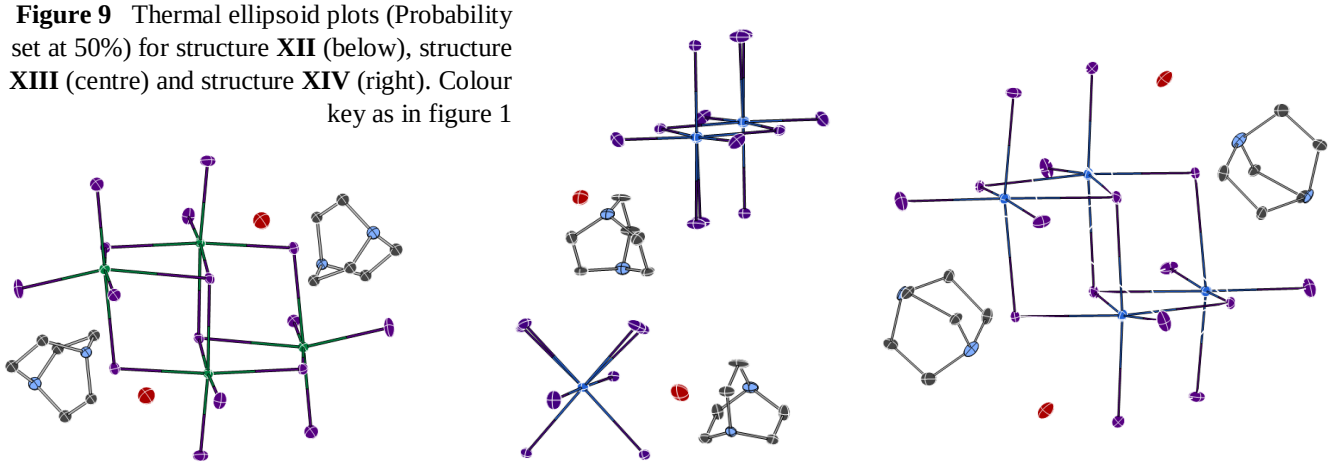

To elaborate, along the *a*-axis of compound **XIII** (see Figure 10) a large slightly irregular octahedral channel, approximately 9.0 × 8.5 Å in dimensions, propagates through the structure. In conjunction, a minor channel, approximately 4.7 × 4.2 Å in size, extends along the *c*-axis and intercepts the major channel running along *a*. Provided the weak I---I interactions are sufficiently robust this hybrid structure may have the potential for ion exchange and porosity. In addition to this eight water molecule positions have been identified within the structural model. Due to the heavy atom sites present accurately determining the orientation of bonded hydrogen atoms at each solvated sites using X-ray diffraction data is problematic.

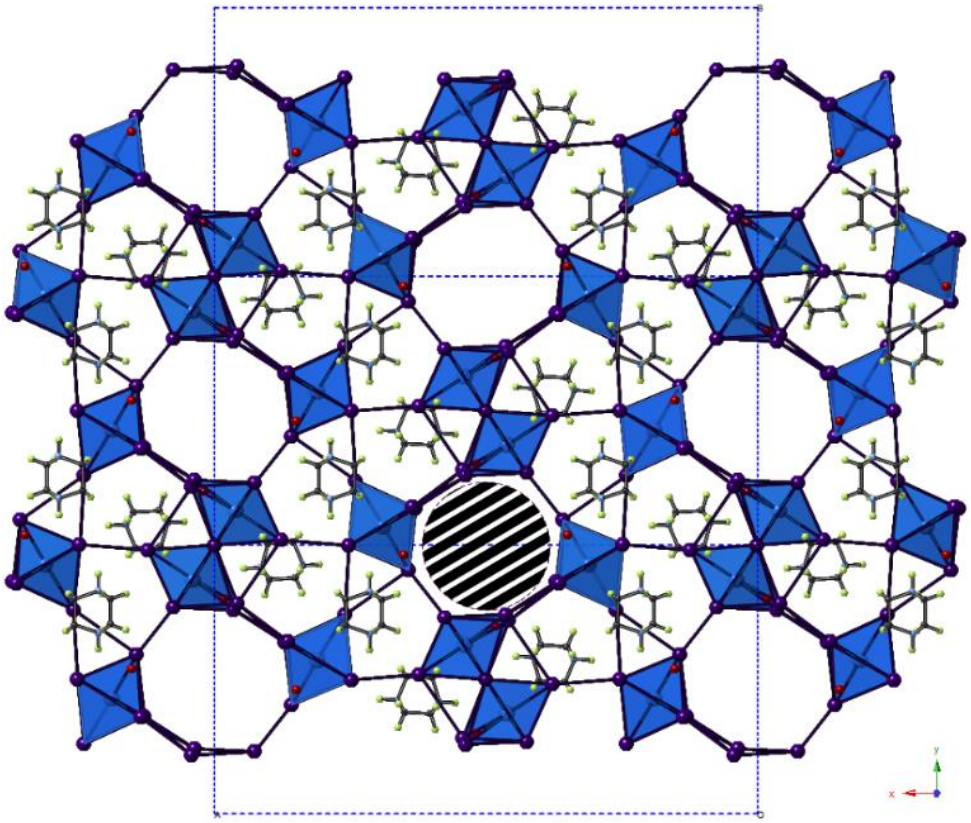

Figure 10 The structure of compound **XIII** viewed down the *a*-axis. The striped area marks one pore containing disordered DABCO di-cations; colour key as in Figure 1 with O atom sites (red) and H atoms (green)

Bi-I bond lengths within the [BiI_6] units ranges from 3.00-3.18 Å (Δ = 0.18 Å) and demonstrate only a minor deviation, of 3.1°, (*trans* I-Bi-I angles) from 180°. In comparison, within each $[Bi_2I_{10}]^{4-}$ unit the metal-iodide bond lengths ranges from 2.96-3.24 Å (Δ = 0.28 Å); the longest M-I bonds are to the edge-shared iodide positions linking the octahedra. The position of the central bismuth ion within the individual octahedra of the $[Bi_2I_{10}]^{4-}$ unit is shifted slightly towards the terminal iodide positions. Regularity of the octahedra within the di-octahedral unit is still high; with only a minor average deviation (from *trans* angles of 180°) of 4.3° observed.

As previously mentioned, a secondary phase was found to have crystallised in association with compound **XIII**. The structural analysis of this phase (compound **XIV)** showed that it was also a di-protonated DABCO templated hybrid iodobismuthate but with a differing structural composition; determined as $[C_6H_{14}N_2]_2[Bi_4I_{16}].2H_2O$.

The structure of **XIV** contains discrete tetra-octahedral $[Bi_4I_{16}]^{4-}$ unit which interact along weak I---I connections to ten adjacent $[Bi_4I_{16}]^{4-}$ units; there are a total of 34 such interactions

(9 unique bonding modes). Interaction lengths range from 4.06-4.52 Å (Δ = 0.46 Å) with an average distance of 4.31 Å. As seen in compounds (**IV**, **IX**, **XII**) the tetra-octahedral units contain two distinct Bi sites. In compound **XIV** the Bi(1) outer octahedral positions, bound to adjacent octahedra by 2 from 12 possible edge connection sites, exhibit M-I bond lengths in the range of 2.91-3.34 Å (Δ = 0.43 Å); very similar distances are seen for the Bi(2) inner octahedral positions (3/12 edge connections) with a range of 2.90-3.29 Å (Δ = 0.39 Å).

Deviation of the *trans* I-M-I angles within the octahedra from 180° shows an average of 9.5° for the outer Bi(1) site and 9.1° for Bi(2) inner site. The relatively small distortion of the outermost two octahedra within the tetra-octahedral unit may be compared to that seen previously in materials with the same anionic motif. The increased regularity found in compound **XIV** may be due to the lessened strain from reduced number of interunit I---I interactions to just ten nearby equivalent units. This compares to twelve such links seen for structures **IV** and **XII** and fourteen for structure **IX,** which saw the greatest M-I bond length range with Δ = 0.69 Å.

Table 5 Unit cell parameters for Compounds XII - XIV (at 150 K)

	Compound XII (Sb)	Compound XIII (Bi)	Compound XIV (Bi)
Space Group	Triclinic *P-1*	Orthorhombic *Pbam*	Monoclinic $P2_1/c$
a (Å)	10.8634(3)	31.9562(6)	11.0086(3)
b (Å)	10.8965(3)	15.8622(4)	15.4751(3)
c (Å)	11.2911(3)	8.6164(2)	15.3455(4)
α (°)	91.999(2)	90.000	90.000
β (°)	109.691(2)	90.000	103.001(2)
γ (°)	95.086(2)	90.000	90.000
V (Å^3)	1250.46(6)	4367.62(17)	2547.23(11)

Table 6 Structural formula list for Compounds I - XIV

Compound	Structural Formula
I	$[C_6H_9N_2O][SbI_4]$
II	$[C_6H_9N_2O][BiI_4]$
III	$[C_5H_{12}NO]_4[Sb_6I_{22}]$
IV	$[C_5H_{12}NO]_4[Bi_4I_{16}]$
V	$[C_4H_{12}N_2][SbI_4]_2.4H_2O$

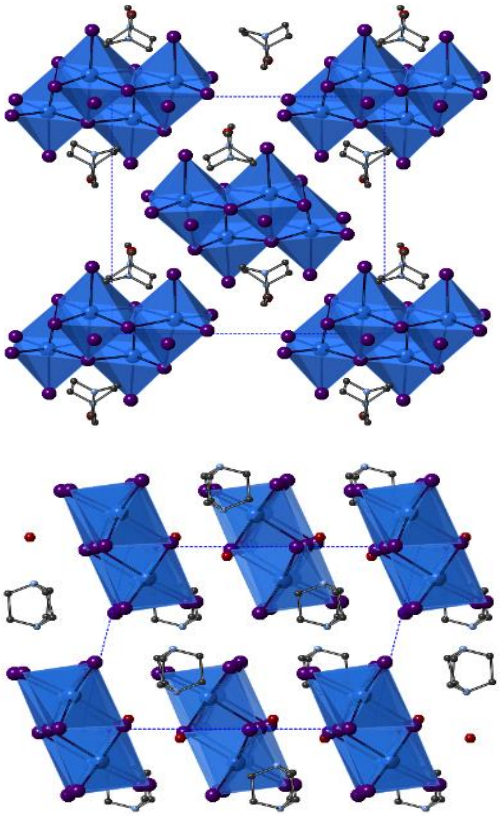

Figure 11 Structure **XIV** viewed down the *a*-axis (top) and down the *b*-axis (bottom); colour key as in figure 10

VI	$[C_5H_{14}N_2][SbI_4]_2.3H_2O$
VII	$[C_6H_{16}N_2][SbI_4]_2.2H_2O$
VIII	$[C_6H_{16}N_2][SbI_4]_2.2H_2O$
IX	$[C_6H_{16}N_2][Sb_4I_{16}]_{0.5}.H_2O$
X	$[C_{10}H_{13}N_2][SbI_4]$
XI	$[C_{10}H_{13}N_2][BiI_4]$
XII	$[C_6H_{14}N_2]_2[Sb_4I_{16}].2H_2O$
XIII	$[C_6H_{14}N_2]_{10}[Bi_2I_{10}]_2[BiI_6]_4.(H_2O)_8$
XIV	$[C_6H_{14}N_2]_2[Bi_4I_{16}].2H_2O$

Structure stability and dehydration

From thermogravimetric analysis studies (ESI – Figure S1) compound **I**, $[C_6H_9N_2O][SbI_4]$, shows a stable mass with negligible change on heating to approximately 210 ^oC, followed by a major degradation step ($\Delta m\% = -86\%$) between 210 and 320 ^oC. This is likely to be associated with complete decomposition of the amine and loss of iodine from the material; the fastest mass loss occurs from 280-300 ^oC. A further steady low rate of mass loss occurred on heating to the maximum furnace temperature of 400 ^oC; leaving residual mass (~1.2 mg) of antimony metal.

For compound **II**, $[C_6H_9N_2O][BiI_4]$, a stable thermal profile is observed up to 150 ^oC before a series of sharp, small, weight losses, equating to total loss ($\Delta m\%$) of 10%, occurs between 150 and 210 ^oC. These weight losses can be attributed rapid, possibly locally explosive decomposition of the amine. The remaining bulk mass is stable to 250 ^oC before undergoing a continuous large mass loss step ($\Delta m\% = 70\%$) on heating to 400 ^oC, with the fastest mass loss occurring between 330 and 355 ^oC. A still reducing mass of ~2.5 mg of bismuth is present at T_{max}. This weight loss corresponds to further degradation of any residual amine and its decomposition products and the loss of HI/I_2 leaving the residue of bismuth metal.

TGA studies on 4-methylmorpholium templated compounds **III** and **IV** (ESI – Figure S2) showed that each exhibits a one-step thermal degradation process. For structure **III**, a stable plateau is observed in the thermal profile up to 180 ^oC, from which point, in the temperature range of 180-320 ^oC, major degradation of the compound occurs with a total mass loss $\Delta m\% = 92\%$. The fastest rate of mass loss occurred from 260-300 ^oC, with decomposition of the amine and loss of HI/I_2, and a stable residual (~1 mg) mass of antimony metal is retained up to

the highest temperature reached of 400 °C. In comparison, the bismuth-containing structure (**IV**), with a different anionic sublattice, showed an increased stability of +60 °C over its counterpart, with a prolonged degradation of the hybrid material occurring only from 240-400 °C (Δm% = 90%); the residual mass, of approximately 2 mg, was bismuth metal.

Thermal analysis the piperazinium-based hybrid materials was carried out and the resultant traces are shown in ESI – Figure S3. Data for tetrahydrate compound **V** showed an initial expected dehydration step between 80 and 110 °C (Δm% = 5%) before a stable mass is retained up to 180 °C. From 180-260 °C (Δm% = 36%) is the first of two major degradation steps of the remaining hybrid material; followed immediately by the second step in the temperature range of 260-340 °C (Δm% = 54%). Similarly, for isolated crystals of trihydrate compound **VI**, a dehydration step 95-125 °C with a proportionately lower relative mass loss (Δm% = 3.4%) was observed. After a stable plateau, until 175 °C, further degradation between 175 and 305 °C was observed; with temperature range 290-305 °C showing the highest rate of degradation. A further slow loss of weight, likely to be due to evolution of iodine, occurred between 305 and 345 °C, at which temperature a stable residue was formed. Lastly, a mixed phase sample of structures **VII-IX** was analysed thermogravimetrically. A minor weight loss associated with dehydration of all three phases was observed in the temperature range 90-120 °C; (structures **VII** and **VIII** were determined to be dihydrates and structure **IX** a monohydrate). Following this the compounds remained stable to 175 °C until major degradation from 175-355 °C (Δm% = 96%). All three piperazinium-based templated materials were determined to remain stable to approximately the same temperature; around 175-180 °C, before major degradation. Following this simultaneous decomposition of all three phases a residue of antimony metal (~0.7 mg) was obtained with no notable mass change between 350 and 400 °C.

The nature of main degradation process of all the compounds (following loss of any water from the structure) is decomposition of the amine, and this may be associated with simultaneous loss of HI/I_2. The decomposition transitions from a clear two-step process for compound **V** to a continuous one-step process for structures **VII - IX**, presumably due to the differing stabilities of the templating cations. As the piperazinium-ring based di-cation in each structure becomes increasing methylated its effect on slowing the degradation process becomes reduced; as observed in the shift in remaining mass of each compound in temperature range 290-320 °C. This is reflected in the temperature at which maximum mass change occurs in each profile; with structure **V** indicating a maximum mass loss rate of -1.90 mg/min at 325 °C, -2.0 mg/min at 310 °C for structure **VI** and -1.65 mg/min at 285 °C for structures **VII/VIII/IX**.

Analysis of isostructural compounds **X** and **XI** shows a distinct effect of changing of metal within the hybrid material composition (ESI – Figure S4). For structure **X**, other than a minor mass loss at 185 ^{o}C, likely to derive from the 10% impurity phase of organic iodide, the thermal profile shows a stable mass to approximately 225 ^{o}C. In comparison, the equivalent bismuth compound, **XI**, demonstrates a much increased thermal stability over its counterpart, to around 280 ^{o}C. Each structure undergoes a continuous one-step degradation process, however, antimony-based structure **X** showed an increased rate of degradation with a max rate of change of mass of -2.30 mg/min occurring at 340 ^{o}C, compared to -1.65 mg/min at 385 ^{o}C for structure **XI**. As a result, a residue metal mass was left for structure **X** from temperature range 350-400 ^{o}C whereas, for structure **XI** a residue mass remained at 400 ^{o}C with a much slowed rate of mass change still occurring, as the full decomposition pathway was incomplete at this temperature.

Finally, thermogravimetric analysis was carried out on $DABCOH_2$ di-cation templated materials compound **XII** and a mixed phase of iodobismuthate compounds **XIII/XIV** (ESI – Figure S5). Iodoantimonate structure **XII** undergoes a distinct 3-step degradation process. The first and shortest step occurs at temperature range 205-230 ^{o}C; with a max *d*TG of -1.25 mg/min at 215 ^{o}C. The second at temperature range 230-280 ^{o}C; with a max *d*TG of -1.25 mg/min at 265 ^{o}C. The third and longest step occurs at temperature range 280-350 ^{o}C; with the highest *d*TG in the thermal profile of -2.15 mg/min peaking at 315 ^{o}C. A low temperature dehydration step is not observed for the material which may be attributed to the fact that the water sites are encapsulated within a zero-dimensional anionic sublattice with no open channels for rapid dehydration to occur. From 350 ^{o}C to T_{max} an expected ~1 mg metal residue mass remains. The TGA trace of the mixed phase of iodobismuthate hybrid structures **XIII** and **XIV** shows a stable thermal profile up to approximately 260 ^{o}C. From 260-400 ^{o}C degradation of the materials occurs, initially at a slow rate followed by a rapid increase to a max *d*TG of -2.15 mg/min peaking at 315 ^{o}C. Degradation of the materials then slows but continues up to T_{max} at which a still slowly degrading residual bismuth metal mass remains.

Optical absorption measurements

Optical absorption spectra (250-800 nm) were collected for Compounds **I** - **XIV** (ESI Figures S6-S10). Analysis of isostructural compounds **I** and **II** (ESI – Figure S6) shows absorbance in the ultraviolet and visible region with increasing intensity up to the absorption edge onsets at 485 nm and 540 nm respectively. An additional absorption peak feature is observed within the

ultraviolet region at 320 nm for structure **I**. Assuming a direct band gap for these materials gives E_g values of 2.13 eV and 2.05 eV; a change of -0.08 eV as a result of changing antimony to bismuth.

Similarly, analysis of 4-methylmorpholium containing compounds **III** and **IV** (ESI – figure S7) shows strong absorbance across the ultraviolet and visible regions up to the absorption edge onsets at 460 nm and 515 nm in turn. Changing the metal from antimony to bismuth and metal iodide anionic moiety from $[M_6I_{22}]$ to $[M_4I_{16}]$ results in a reduction in the estimated E_g values (assuming a direct band gap) by 0.22 eV from 2.28 eV to 2.06 eV.

The piperazinium-based structures **V** - **IX** (ESI – Figure S8) shows strong absorbance across the ultraviolet and visible regions up to absorption onsets at 480 nm, for both compounds **V** and **VI**, and at 500 nm for the mixed phase sample of structures **VII** - **IX**. As for the equivalent iodobismuthate materials studied previously, additional absorption peak features can be observed in the spectra for structure **V** (at 285 nm and 355 nm) and structure **VI** (at 290 nm and 360 nm). Features akin to this can also be observed at similar wavelengths in the spectrum obtained from the mixed phase sample (containing compounds **VII** - **IX**), although the strength of absorption is suppressed and seen as broad peaks. The estimated band gap energy reduces by 0.05 eV for the series of compounds **V** → **VI** → **VII/VIII/IX** from 2.22 eV → 2.17 eV → 2.12 eV respectively. As the templating piperazinium-ring dication becomes increasingly methylated there is an increase in the connectivity of the anionic sublattice, through weak I---I interactions, as the average $[SbI_4]^-_n$ - $[SbI_4]^-_n$ interchain distances reduce. This is likely to be the origin of the slightly reduced band gap across this series.

Isostructural compounds **X** and **XI** show absorption in the ultraviolet and visible regions with increasing absorption strength towards their respective absorption edge onsets at 470 nm and 525 nm. Both structures exhibit an identical dual pointed absorption feature (at 270 nm and 275 nm) in the ultraviolet region. An additional absorption peak can be seen at 675 nm in both spectra beyond after the main absorption edge. The commonality of this feature to both compounds **X** and **XI** suggests it can be attributed to an electronic transition occurring locally on the conjugated 2-methylbenzimidazolium cation, a component present in both the isostructural compounds. Band gap estimates from the Tauc plot show a large shift of 0.3 eV between the two 2-methylbenzimidazolium templated structures; with respective E_g values of 2.33 eV for antimony based structure **X** and 2.03 eV for bismuth based structure **XI**.

UV-Vis spectra were also collected for the $DABCOH_2$ di-cation templated hybrid materials. The iodoantimonate compound **XII** shows an absorption edge onset at 515 nm; compared to an approximate absorption edge of 520 nm for mixed phase of compounds **XIII**/**XIV**. Additional absorption features are observed in all the spectra at 375 nm and 480 nm. Band gap estimates for these materials from the Tauc plot indicates E_g values of 2.20 eV (**XII**) and 2.14 eV (mixture **XIII**/**XIV**).

Hybrid structure connectivity – band gap relationship

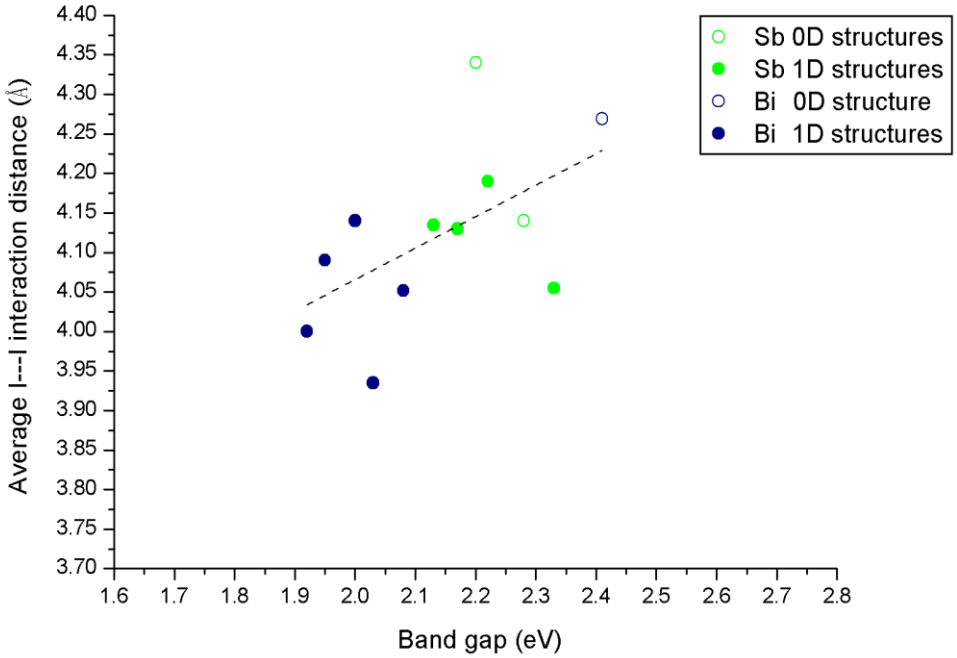

Figure 12 Effect of connectivity and dimensionality of the hybrid material anionic component, as measured through the length of weak I---I interactions, on band gap energy

The changes in the absorption edge onset, and derived bang gap, in these materials can be to some degree rationalised in terms of the structures and, specifically, the weak interactions that exist between the inorganic anions. Structural features that might control the band gap include the dimensionality of the inorganic anionic unit (0D for discrete anions or clusters through 1D chains, 2D sheets and 3D (in, for example, vertex linked perovskite structures)) and weak I---I interactions between the anionic units. In this work and our previous work the majority of the materials contain either 0D or 1D inorganic units which limits any analysis in terms of structure dimensionality alone (or the related I/M ratio).

We, therefore, analysed the variation in band gap values of the (pure phase) compounds versus the average I---I interaction distances between the 0D or 1D anionic components of the hybrid structures. This relationship is shown in Figure 12 for the structures described in this paper alongside materials from our previous publication covering piperazinium ring based hybrid bismuth structures; see reference 49.

A degree of correlation is observed with dimensionality in that 1D structures tend to have a smaller band gap than 0D; this is similar to the trends seen for lead halide systems which span a much larger dimensionality range. [46, 52]

There is also a tendency towards a reduction in the band gap energy associated with a reduction in the average I---I interaction distance. This average I---I interaction distance can be taken as a measure of the degree and strength of connectivity between the anionic "network" elements of each structure. Overall smaller band gaps in hybrid bismuth and antimony iodides can be associated with both increased inorganic anion dimensionality and reduced distances between these units.

Conclusions

In summary, five new iodobismuthate and nine new iodoantimonate hybrid materials have been synthesised and structurally characterised. Templated by cationic 1,3-dimethyl-2-oxo-2,3-dihydropyrimidium, 4-methylmorpholium, 1,4-dipiperazinium, 1-methyl-1,4-dipiperazinium, 1,4-dimethyl-1,4-dipiperazinium, 1-ethyl-2-methylbenzimidazolium and 1,4-diazabicyclo[2.2.2]octan-diium ions, the hybrid structures contain a number of structural anionic motifs including $[MI_4]^-_n$(M=Sb,Bi), $[M_4I_{16}]^{4-}$(M=Sb,Bi), $[Sb_6I_{22}]^{4-}$, and a previously unseen motif of mixed $[Bi_2I_{10}]^{4-}$ and $[BiI_6]^{3-}$ units exhibited in structure **XIII**. Also, novel in-situ alkylation reaction mechanisms, as demonstrated in the hydrothermal synthesis of structures **I**, **II, X** and **XI**, was found to be valuable and could be further utilised in this area to explore the creation of other new templating species to yield more hybrid materials.

Thermal analysis of the materials indicated the point of onset of major degradation of each hybrid material (or mixed phase) to occur in the range of 175-280 ^oC; with the iodobismuthate structures exhibiting increased thermal stability over their iodoantimonate counterparts. Band-gap estimates for the structures were determined to range from 2.03-2.33 eV; with an expected decrease in band gap energy for isomorphic materials (**I** → **II**, **X** → **XI**) measured transitioning from antimony-iodide to bismuth-iodide based structures. Although these values are too high

to be considered to compete in single junction cell architecture designs their applicability for tandem cell architectures could be considered.

Work to isolate crystals from the mixed phases for further analysis is underway; with a particular interest in comparing the 1,4-dimethyl-1,4-dipiperazinium templated polymorphic structures (**VII** and **VIII**) to observe the effect of structural change on the physical properties of the hybrid materials. The structures described here work towards building a deeper understanding of an expanding field of alternative hybrid materials in the areas of iodoantimonate and iodobismuthate chemistry. If low band gap materials (E_g ~1.5 eV) suitable for solar cell absorber layers are to be found then it is likely that new materials with 2D, and ideally 3D, connectivity will be targets. However materials with lower structural dimensionality (0D or 1D) but short I---I interactions between inorganic units should also be of interest – particularly for applications that require larger band gaps between 1.8 and 2.5 eV.

Acknowledgements

The authors would like to thank Dr Mary F. Mahon for assistance with the single-crystal X-ray crystallography. AJD would like to thank EPSRC for DTA studentship support.

Crystallographic Data

‡ *Crystal data* for **I**: $C_6H_9N_2OSbI_4$, M = 754.52, monoclinic, space group $P2_1/c$, a = 10.5506(4), b = 7.6299(3), c = 19.9962(7) Å, β = 95.336(3)°, V = 1600.63(10)Å^3, Z = 4, crystal size: 0.305x0.080x0.034mm, T = 149.9(4)K, ρ_{calc} = 3.131gcm^{-3}, μ = 9.418mm^{-1}, 4798 reflections (4798 unique reflections), 127 parameters, 0 restraints, R1(all data) = 0.0616, wR2(all data) = 0.0768, GooF = 1.048, Further details available from CCDC entry 1580940**.**

Crystal data for **II**: $C_6H_9N_2OBiI_4$, M = 841.75, monoclinic, space group $P2_1/c$, a = 10.6424(3), b = 7.6380(2), c = 20.0271(5) Å, β = 94.986(2)°, V = 1621.78(7)Å^3, Z = 4, crystal size: 0.493x0.134x0.097mm, T = 150.2(10)K, ρ_{calc} = 3.447gcm^{-3}, μ = 18.465mm^{-1}, 5140 reflections (5140 unique reflections), 128 parameters, 0 restraints, R1(all data) = 0.0454, wR2(all data) = 0.0740, GooF = 1.122, Further details available from CCDC entry 1580941.

Crystal data for **III**: $C_{20}H_{48}N_4O_4Sb_6I_{22}$, M = 3931.02, triclinic, space group *P-1*, a = 11.3253(7), b = 13.0042(7), c = 15.2847(7) Å, α = 69.645(4) °, β = 69.877(5)°, γ = 64.496(6)°,

V = 1853.97(17)Å^3, Z = 2, crystal size: 0.376x0.235x0.175mm, T = 150.01(10)K, ρ_{calc} = 3.521gcm^{-3}, μ = 11.340mm^{-1}, 11292 reflections (11292 unique reflections), 254 parameters, 0 restraints, R1(all data) = 0.0488, wR2(all data) = 0.0633, GooF = 1.044, Further details available from CCDC entry 1580942.

Crystal data for **IV**: $C_{20}H_{48}N_4O_4Bi_4I_{16}$, M = 3275.02, orthorhombic, space group *Pbca*, *a* = 12.7627(3), *b* = 20.7207(6), *c* = 22.7427(6) Å, *V* = 6014.35(3)Å^3, Z = 4, crystal size: 0.248x0.222x0.144mm, T = 150.01(10)K, ρ_{calc} = 3.617gcm^{-3}, μ = 19.909mm^{-1}, 9856 reflections (9856 unique reflections), 218 parameters, 0 restraints, R1(all data) = 0.0416, wR2(all data) = 0.0483, GooF = 1.107, Further details available from CCDC entry 1580943.

Crystal data for **V**: $C_4H_{20}N_2O_4Sb_2I_8$, M = 1418.95, monoclinic, space group *P2$_1$/c*, *a* = 7.3391(2), *b* = 13.0022(5), *c* = 13.8121(4) Å, *β* = 94.550(3)°, *V* = 1313.86(7)Å^3, Z = 4, crystal size: 0.382x0.121x0.082mm, T = 150.00(10)K, ρ_{calc} = 3.587gcm^{-3}, μ = 11.464mm^{-1}, 4084 reflections (4084 unique reflections), 91 parameters, 0 restraints, R1(all data) = 0.0359, wR2(all data) = 0.0470, GooF = 1.023, Further details available from CCDC entry 1580944.

Crystal data for **VI**: $C_5H_{20}N_2O_3Sb_2I_8$, M = 1414.96, monoclinic, space group *P2$_1$/c*, *a* = 7.5306(2), *b* = 12.9539(4), *c* = 13.6147(4) Å, *β* = 96.086(3)°, *V* = 1320.64(7)Å^3, Z = 4, crystal size: 0.346x0.0.215x0.137mm, T = 150.01(10)K**,** ρ_{calc} = 3.556gcm^{-3}, μ = 11.401mm^{-1}, 4034 reflections (4034 unique reflections), 110 parameters, 0 restraints, R1(all data) = 0.0472, wR2(all data) = 0.0711, GooF = 1.036, Further details available from CCDC entry 1580945.

Crystal data for **VII**: $C_6H_{20}N_2O_2Sb_2I_8$, M = 1410.97, monoclinic, space group *P2$_1$/c*, *a* = 7.7213(2), *b* = 12.8027(3), *c* = 13.4527(3) Å, *β* = 97.377(2)°, *V* = 1318.84(5)Å^3, Z = 4, crystal size: 0.280x0.218x0.179mm, T = 149.99(10)K**,** ρ_{calc} = 3.553gcm^{-3}, μ = 11.414mm^{-1}, 3513 reflections (3513 unique reflections), 92 parameters, 0 restraints, R1(all data) = 0.0328, wR2(all data) = 0.0563, GooF = 1.061, Further details available from CCDC entry 1580946.

Crystal data for **VIII**: $C_6H_{20}N_2O_2Sb_2I_8$, M = 1410.97, monoclinic, space group *P2$_1$/c*, *a* = 7.5751(2), *b* = 12.1020(3), *c* = 14.5071(4) Å, *β* = 92.630(3)°, *V* = 1328.52(6)Å^3, Z = 2, crystal size: 0.447x0.199x0.165mm, T = 150.00(10)K**,** ρ_{calc} = 3.527gcm^{-3}, μ = 11.331mm^{-1}, 4088 reflections (4088 unique reflections), 97 parameters, 0 restraints, R1(all data) = 0.0367, wR2(all data) = 0.0522, GooF = 1.131, Further details available from CCDC entry 1580947.

Crystal data for **IX**: $C_{12}H_{20}N_4O_2Sb_4I_{16}$, M = 2769.79, monoclinic, space group *P2$_1$/n*, *a* = 11.5391(3), *b* = 11.8717(4), *c* = 19.1648(5) Å, *β* = 93.705(3)°, *V* = 2619.87(13)Å^3, Z = 4, crystal

size: 0.293x0.242x0.193mm, T = 150.00(10)K, ρ_{calc} = 3.531gcm^{-3}, μ = 11.486mm^{-1}, 8103 reflections (8103 unique reflections), 178 parameters, 0 restraints, R1(all data) = 0.0472, wR2(all data) = 0.0578, GooF = 1.090, Further details available from CCDC entry 1580948.

Crystal data for **X**: $C_{10}H_{13}N_2SbI_4$, M = 790.58, monoclinic, space group *P2₁/n*, *a* = 7.5877(3), *b* = 17.7055(8), *c* = 13.2578(6) Å, *β* = 94.309(4)°, *V* = 1776.07(13)Å^3, Z = 4, crystal size: 0.398x0.175x0.090mm, T = 149.95(13)K, ρ_{calc} = 2.957gcm^{-3}, μ = 8.489mm^{-1}, 3104 reflections (3104 unique reflections), 266 parameters, 272 restraints, R1(all data) = 0.0760, wR2(all data) = 0.0927, GooF = 1.197, Further details available from CCDC entry 1580949.

Crystal data for **XI**: $C_{10}H_{13}N_2BiI_4$, M = 877.81, monoclinic, space group *C2/c*, *a* = 13.3133(4), *b* = 17.7312(4), *c* = 7.6344(2) Å, *β* = 93.450(2)°, *V* = 1798.92(8)Å^3, Z = 4, crystal size: 0.143x0.120x0.0.079mm, T = 150.00(10)K, ρ_{calc} = 3.237gcm^{-3}, μ = 16.650mm^{-1}, 2049 reflections (2049 unique reflections), 123 parameters, 96 restraints, R1(all data) = 0.0214, wR2(all data) = 0.0435, GooF = 1.083, Further details available from CCDC entry 1580950.

Crystal data for **XII**: $C_{12}H_{32}N_4O_2Sb_4I_{16}$, M = 2781.88, triclinic, space group *P-1*, *a* = 10.8634(3), *b* = 10.8965(3), *c* = 11.2911(3) Å, *α* = 91.999(2)°, *β* = 109.691(2)°, *γ* = 95.086(2)°, *V* = 1250.46(6)Å^3, Z = 1, crystal size: 0.392x0.325x0.324mm, T = 150.0(2)K, ρ_{calc} = 3.694gcm^{-3}, μ = 12.033mm^{-1}, 7862 reflections (4290 unique reflections), 178 parameters, 0 restraints, R1(all data) = 0.0314, wR2(all data) = 0.0602, GooF = 1.181, Further details available from CCDC entry 1580951.

Crystal data for **XIII**: $C_{60}H_{156}N_{20}O_8Bi_8I_{44}$, M = 8541.66, orthorhombic, space group *Pbam*, *a* = 31.9562(6), *b* = 15.8622(4), *c* = 8.6164(2) Å, *V* = 4367.62(17)Å^3, Z = 8, crystal size: 0.363x0.100x0.0.077mm, T = 150.00(10)K, ρ_{calc} = 3.247gcm^{-3}, μ = 15.843mm^{-1}, 7058 reflections (7058 unique reflections), 192 parameters, 0 restraints, R1(all data) = 0.0480, wR2(all data) = 0.0699, GooF = 1.164, Further details available from CCDC entry 1580952.

Crystal data for **XIV**: $C_{12}H_{32}N_4O_2Bi_4I_{16}$, M = 3130.03, monoclinic, space group *P2₁/c*, *a* = 11.0086(3), *b* = 15.4751(3), *c* = 15.3455(4) Å, *β* = 103.001(2)°, *V* = 2547.23(11)Å^3, Z = 2, crystal size: 0.312x0.295x0.0.215mm, T = 150.00(10)K, ρ_{calc} = 4.082gcm^{-3}, μ = 23.491mm^{-1}, 7829 reflections (7829 unique reflections), 178 parameters, 0 restraints, R1(all data) = 0.0474, wR2(all data) = 0.0666, GooF = 1.042, Further details available from CCDC entry 1580953.

Single crystal X-ray diffraction data collection instrumentation

Single crystal data for structures **I** - **X** and **XII** - **XIV** were collected on an Agilent Xcalibur four-circle diffractometer equipped with a fine-focus ($Mo_{k\alpha}$) X-ray source and EosS2 CCD plate detector. Single crystal data for structure **XI** was collected on an Agilent SuperNova Dual four-circle diffractometer equipped with dual fine-focus ($Mo_{k\alpha}$ and $Cu_{k\alpha}$) X-ray sources and EosS2 CCD plate detector.

References

1. S. A. Adonin, M. N. Sokolov and V. P. Fedin, *Coord. Chem. Rev.*, 2016, **312**, 1-21.

2. N. Mercier, N. Louvain and W. H. Bi, *CrystEngComm*, 2009, **11**, 720-734.

3. S. Pohl, R. Lotz, W. Saak and D. Haase, *Angew. Chem-Int. Edition in English*, 1989, **28**, 344-347.

4. G. A. Fisher, N. C. Norman, *Adv. Inorg. Chem.*, 1994, **41**, 233-272.

5. M. Weclawik, A. Gagor, R. Jakubas, A. Piecha-Bisiorek, W. Medycki, J. Baran, P. Zielinski and M. Galazka, *Inorg. Chem. Front.*, 2016, **3**, 1306-1316.

6. A. M. Goforth, L. Peterson, M. D. Smith and H. C. zur Loye, *J. Solid-State. Chem.*, 2005, **178**, 3529-3540.

7. W. H. Bi and N. Mercier, *Chem. Commun.*, 2008, 5743-5745.

8. A. M. Goforth, J. R. Gardinier, M. D. Smith, L. Peterson and H. C. Z. Loye, *Inorg. Chem. Commun.*, 2005, **8**, 684-688.

9. C. Hrizi, A. Samet, Y. Abid, S. Chaabouni, M. Fliyou and A. Koumina, *J. Mol. Struct.*, 2011, **992**, 96-101.

10. A. Samet, A. Ben Ahmed, A. Mlayah, H. Boughzala, E. K. Hlil and Y. Abid, *J. Mol. Struct.*, 2010, **977**, 72-77.

11. A. M. Goforth, M. A. Tershansy, M. D. Smith, L. Peterson, J. G. Kelley, W. J. I. DeBenedetti and H. C. zur Loye, *J. Am. Chem. Soc.*, 2011, **133**, 603-612.

12. C. Feldmann, *J. Solid-State. Chem.*, 2003, **172**, 53-58.

13. J. Heine, *Dalton Trans.*, 2015, **44**, 10069-10077.

14. H. Krautscheid, *Z. Anorg. Allg. Chem.*, 1995, **621**, 2049-2054.

15. H. Krautscheid, *Z. Anorg. Allg. Chem.*, 1999, **625**, 192-194.

16. S. A. Adonin, E. V. Peresypkina, M. N. Sokolov and V. P. Fedin, *Russ. J. Coord. Chem.*, 2014, **40**, 867-870.

17. H. Krautscheid, *Z. Anorg. Allg. Chem.*, 1994, **620**, 1559-1564.

18. K. Y. Monakhov, C. Gourlaouen, R. Pattacini and P. Braunstein, *Inorg. Chem.*, 2012, **51**, 1562-1568.

19. V. V. Sharutin, I. V. Egorova, N. N. Klepikov, E. A. Boyarkina and O. K. Sharutina, *Russ. J. Inorg. Chem.*, 2009, **54**, 1768-1778.

20. A. Okrut and C. Feldmann, *Z. Anorg. Allg. Chem.*, 2006, **632**, 409-412.

21. S. A. Adonin, M. N. Sokolov, P. A. Abramov, S. G. Kozlova, D. P. Pishchur, L. A. Sheludyakova and V. P. Fedin, *Inorg. Chim. Acta*, 2014, **419**, 19-25.

22. D. B. Mitzi and P. Brock, *Inorg. Chem.*, 2001, **40**, 2096-2104.

23. G. A. Mousdis, G. C. Papavassiliou, A. Terzis and C. P. Raptopoulou, *Zeit. Nat. Sec. B-a J. Chem. Sci.*, 1998, **53**, 927-931.

24. C. Hrizi, N. Chaari, Y. Abid, N. Chniba-Boudjada and S. Chaabouni, *Polyhedron*, 2012, **46**, 41-46.

25. S. Chaabouni, S. Kamoun and J. Jaud, *J. Chem. Cryst.*, 1997, **27**, 527-531.

26. N. A. Yelovik, A. V. Mironov, M. A. Bykov, A. N. Kuznetsov, A. V. Grigorieva, Z. Wei, E. V. Dikarev and A. V. Shevelkov, *Inorg. Chem.*, 2016, **55**, 4132-4140.

27. A. Gagor, M. Weclawik, B. Bondzior and R. Jakubas, *CrystEngComm*, 2015, **17**, 3286-3296.

28. D. B. Mitzi, *Inorg. Chem.*, 2000, **39**, 6107-6113.

29. C. J. Carmalt, L. J. Farrugia and N. C. Norman, *Z. Anorg. Allg. Chem.*, 1995, **621**, 47-56.

30. P. Szklarz, A. Pietraszko, R. Jakubas, G. Bator, P. Zielinski and M. Galazka, *J. Phys-Cond. Matt.*, 2008, **20**, 12.

31. M. Bujak and J. Zaleski, *J. Mol. Struct.*, 2003, **647**, 121-128.

32. A. Gagor, G. Banach, M. Weclawik, A. Piecha-Bisiorek and R. Jakubas, *Dalton Trans.*, 2017, **46**, 16605-16614.

33. S. Pohl, R. Lotz, D. Haase and W. Saak, *Z. Nat. Sec. B-a J. Chem. Sci.*, 1988, **43**, 1144-1150.

34. C. J. Carmalt, N. C. Norman and L. J. Farrugia, *Polyhedron*, 1994, **13**, 1655-1658.

35. G. Volonakis, M. R. Filip, A. A. Haghighirad, N. Sakai, B. Wenger, H. J. Snaith and F. Giustino, *J. Phys. Chem. Lett.*, 2016, **7**, 1254-1259.

36. W. Medycki, K. Holderna-Natkaniec, J. Swiergiel and R. Jakubas, *Solid-State. Nuc. Mag. Res.*, 2003, **24**, 209-217.

37. W. H. Bi, N. Leblanc, N. Mercier, P. Auban-Senzier and C. Pasquier, *Chem. Mat.*, 2009, **21**, 4099-4101.

38. K. Gesi, M. Iwata and Y. Ishibashi, *J. Phys. Soc. Jap.*, 1995, **64**, 2650-2655.

39. R. Jakubas, A. Piecha, A. Pietraszko and G. Bator, *Phys. Rev. B*, 2005, **72**, 8.

40. Research cell efficiency records, https://www.nrel.gov/pv/assets/images/efficiency-chart.png (accessed October 2017)).

41. A. M. Ganose, C. N. Savory and D. O. Scanlon, *J. Phys. Chem. Lett.*, 2015, **6**, 4594-4598.

42. Q. D. Tai, P. You, H. Q. Sang, Z. K. Liu, C. L. Hu, H. L. W. Chan and F. Yan, *Nat. Comm.*, 2016, **7**, 8.

43. N. K. Noel, S. D. Stranks, A. Abate, C. Wehrenfennig, S. Guarnera, A. A. Haghighirad, A. Sadhanala, G. E. Eperon, S. K. Pathak, M. B. Johnston, A. Petrozza, L. M. Herz and H. J. Snaith, *Energy & Environ. Sci.*, 2014, **7**, 3061-3068.

44. S. F. Hoefler, G. Trimmel and T. Rath, *Monat. Chem.*, 2017, **148**, 795-826.

45. X. P. Wang, T. Yan, Y. Li, Y. X. Liu, B. Du, H. M. Ma and Q. Wei, *Sci. Rep.*, 2015, **5**, 8.

46. L. M. Wu, X. T. Wu and L. Chen, *Coord. Chem. Rev.*, 2009, **253**, 2787-2804.

47. J. Laane and P. W. Jagodzinski, *Inorg. Chem.*, 1980, **19**, 44-49.

48. H. L. Sheu and J. Laane, *Inorg. Chem.*, 2013, **52**, 4244-4249.

49. A. J. Dennington and M. T. Weller, *Dalton Trans.*, 2016, **45**, 17974-17979.

50. V. V. Sharutin, A. P. Pakusina, O. K. Sharutina, O. A. Kovaleva, A. V. Gerasimenko and M. A. Pushilin, *Russ. J. Coord. Chem.*, 2004, **30**, 541-549.

51. C. Hrizi, A. Trigui, Y. Abid, N. Chniba-Boudjada, P. Bordet and S. Chaabouni, *J. Solid State Chem.*, 2011, **184**, 3336-3344.

52. M. E. Kamminga, G. A. de Wijs, R. W. A. Havenith, G. R. Blake and T. T. M. Palstra, *Inorg. Chem.*, 2017, **56**, 8408-8414.

Supplementary Information

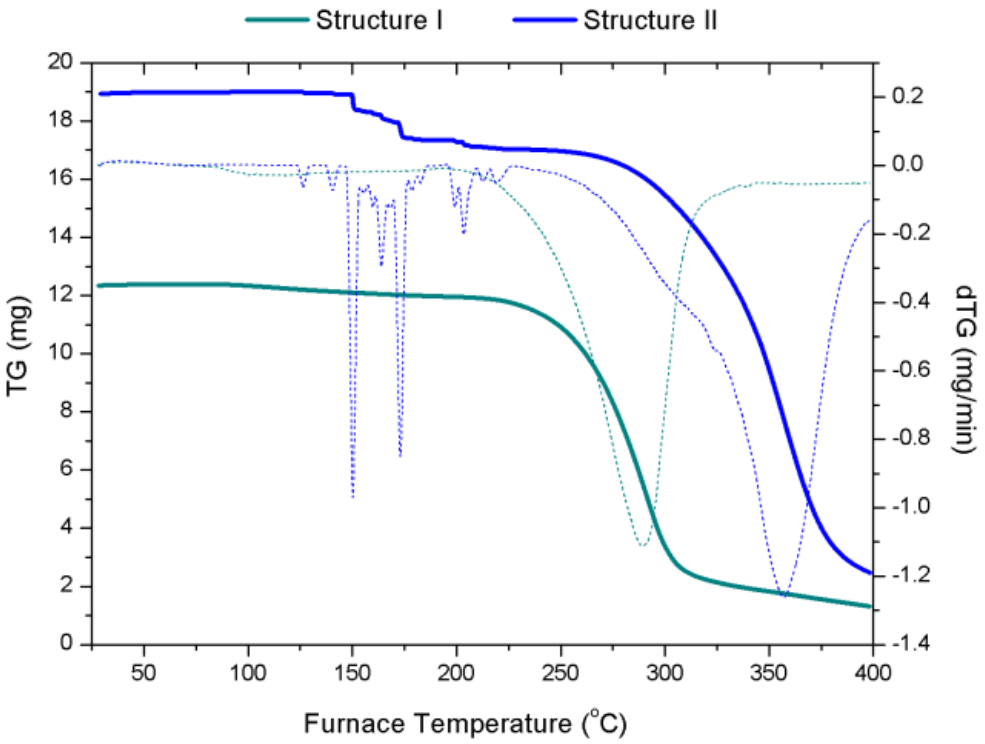

Figure S1 Thermogravimetric analysis data; comparison of compounds I and II

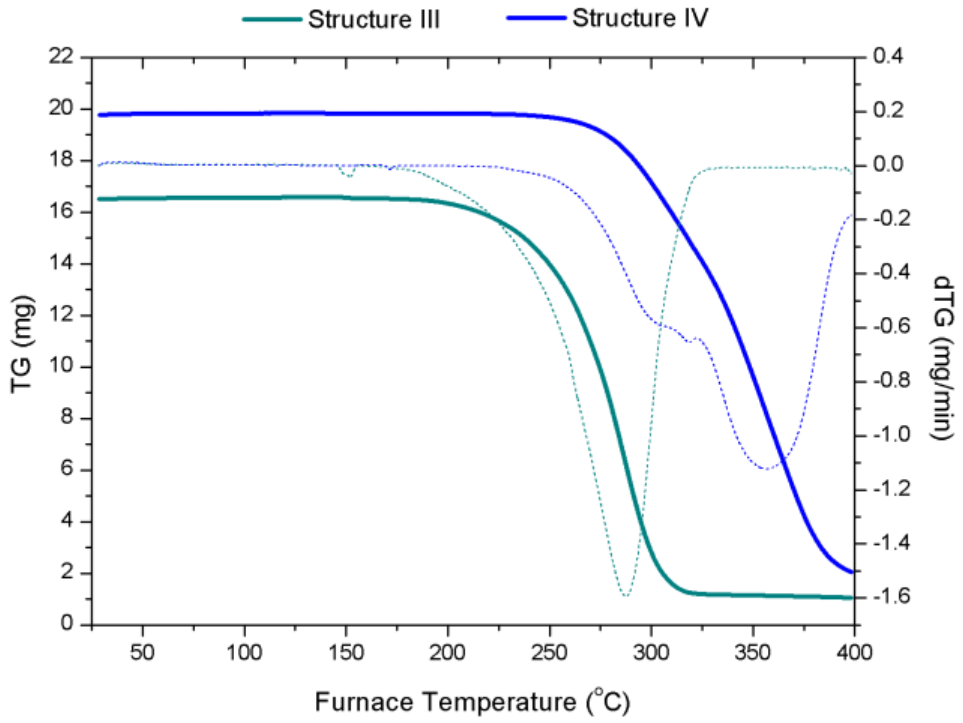

Figure S2 Thermogravimetric analysis data; comparison of compounds III and IV

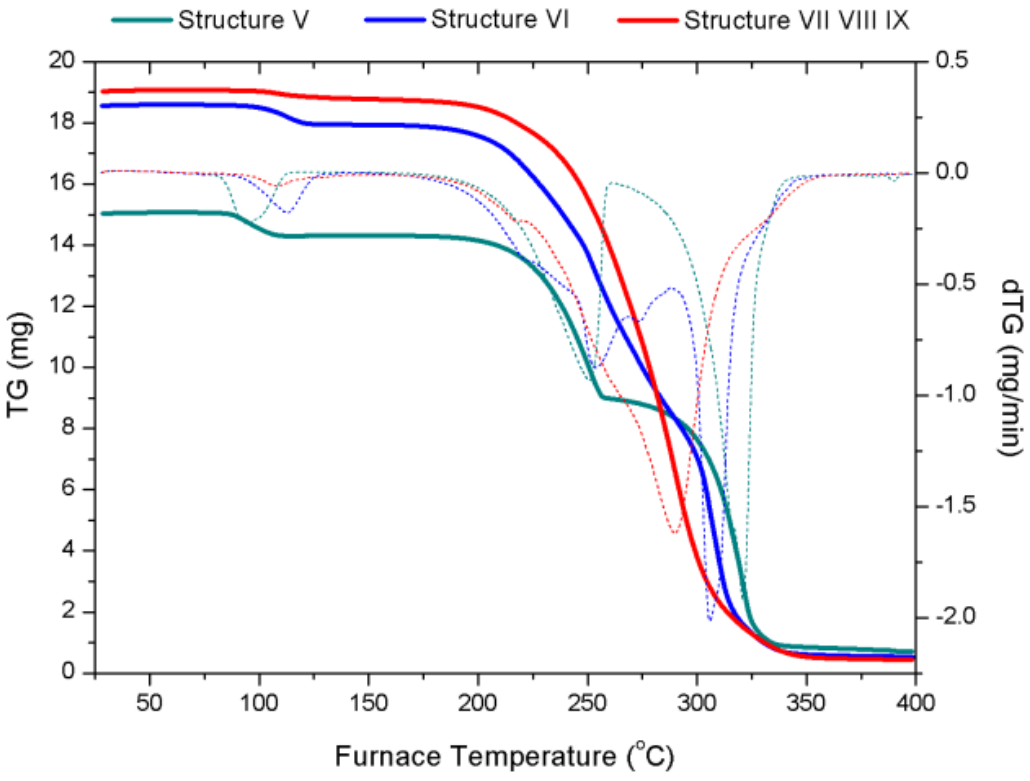

Figure S3 Thermogravimetric analysis data; comparison of structures V-IX

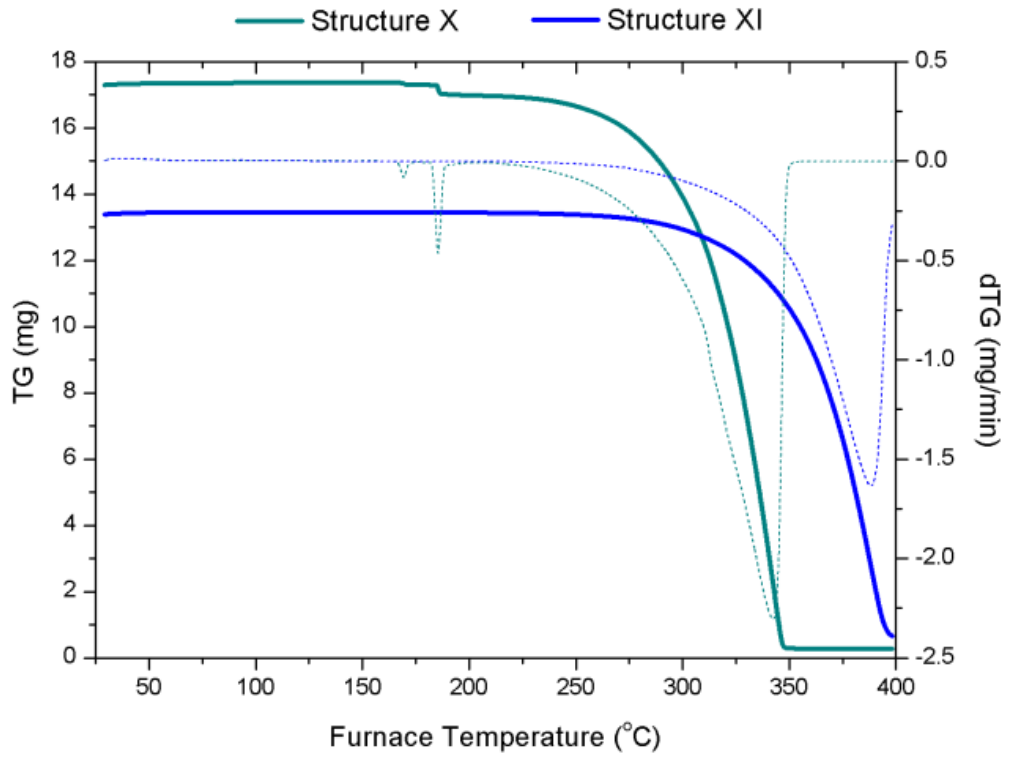

Figure S4 Thermogravimetric analysis data; comparison of compounds X and XI

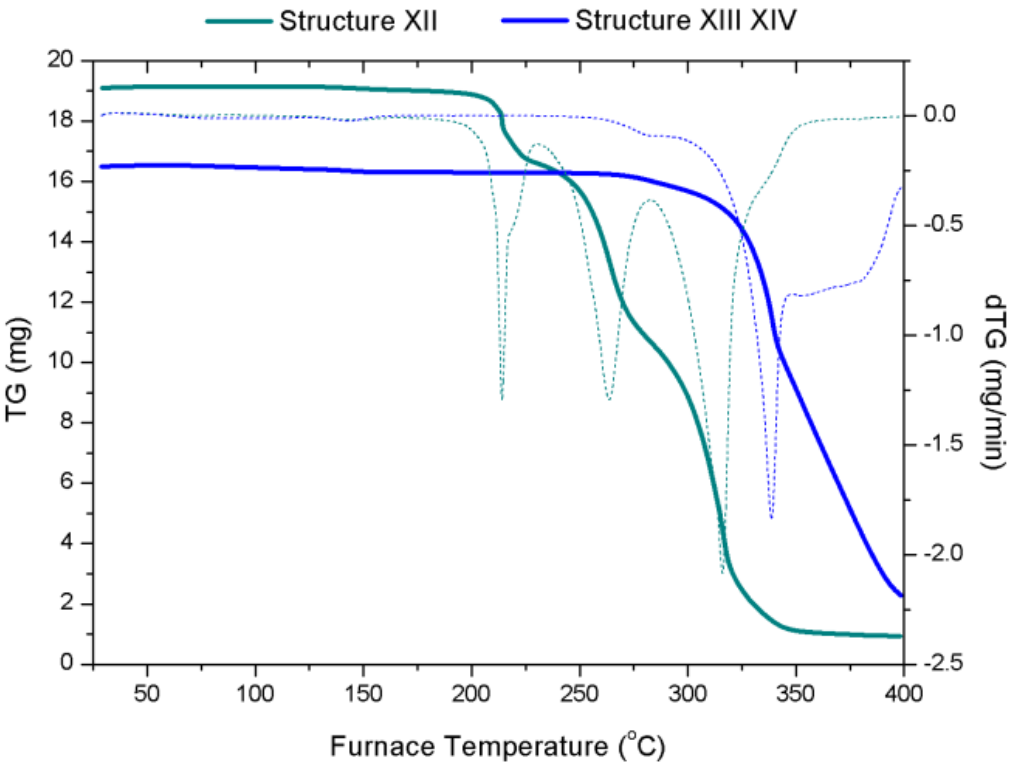

Figure S5 Thermogravimetric analysis data; comparison of compounds XII-XIV

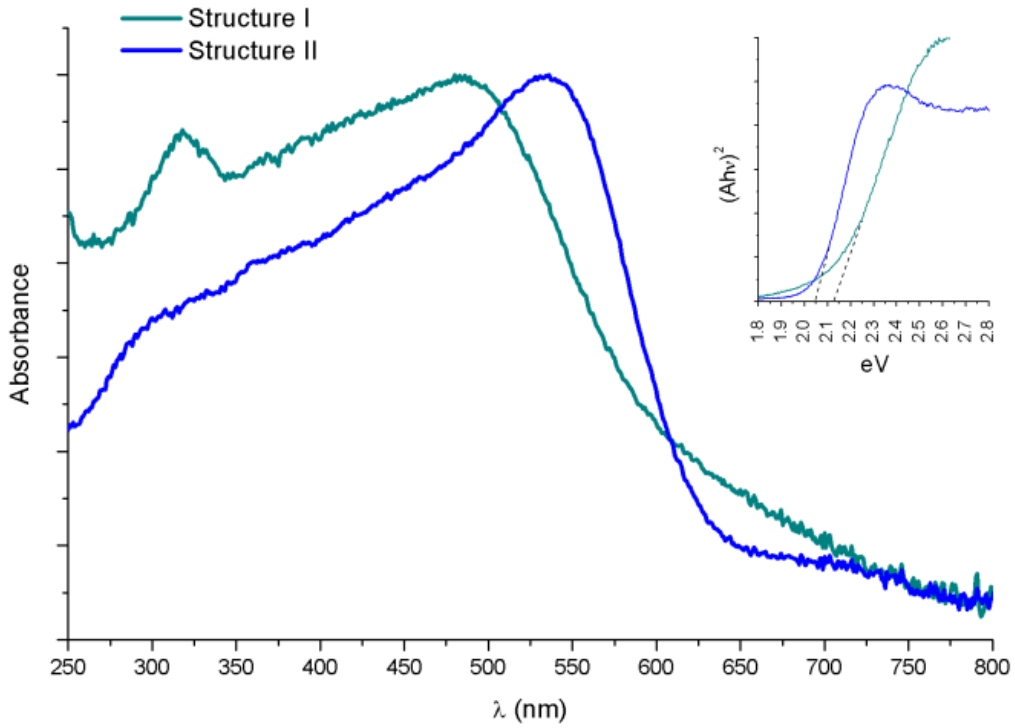

Figure S6 UV/Vis spectra of compounds I and II (10 wt% in $BaSO_4$) with related Tauc plot (inset)

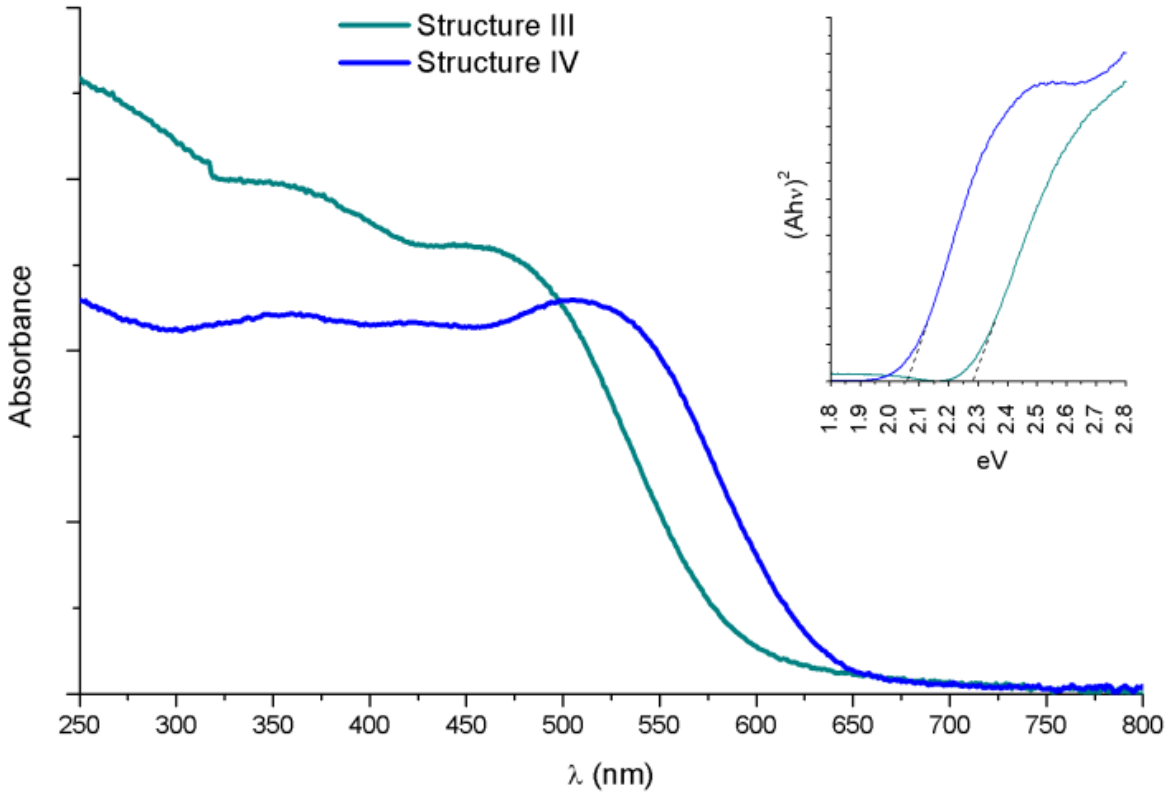

Figure S7 UV/Vis spectra of compounds III and IV (10 wt% in $BaSO_4$) with related Tauc plot (inset)

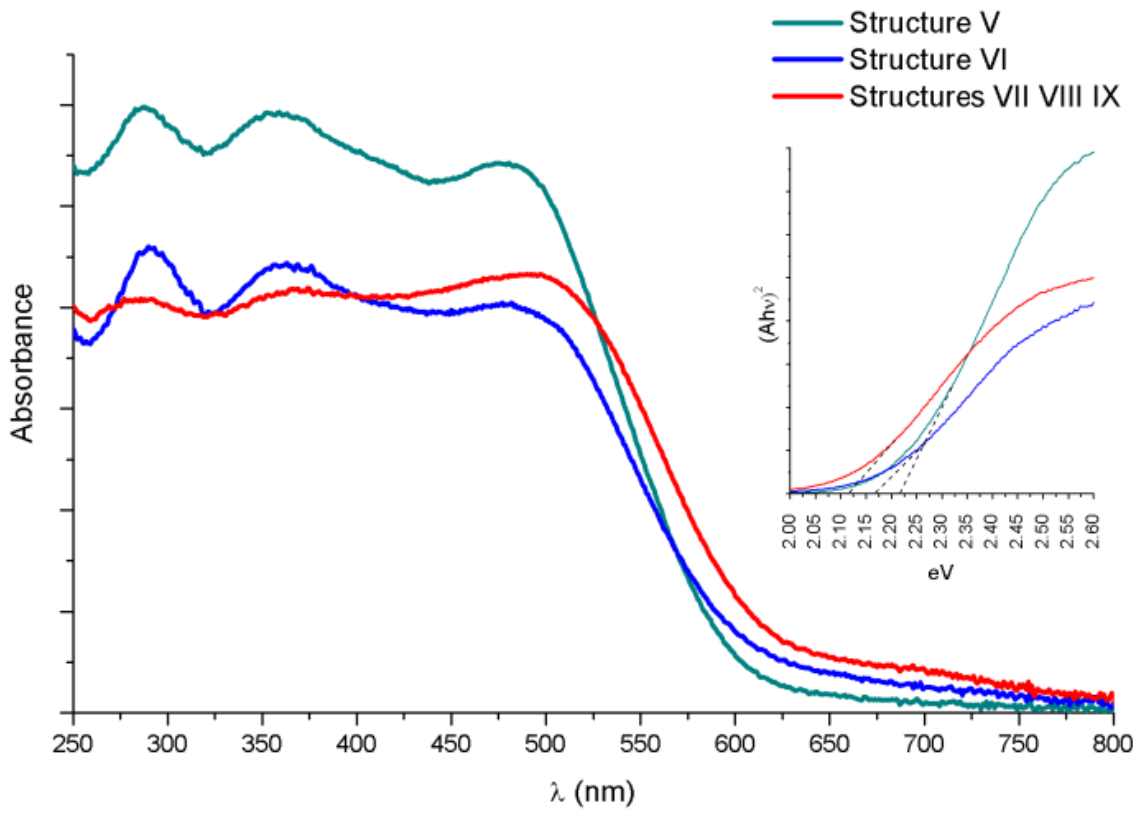

Figure S8 UV/Vis spectra of compounds V-IX (10 wt% in $BaSO_4$) with related Tauc plot (inset)

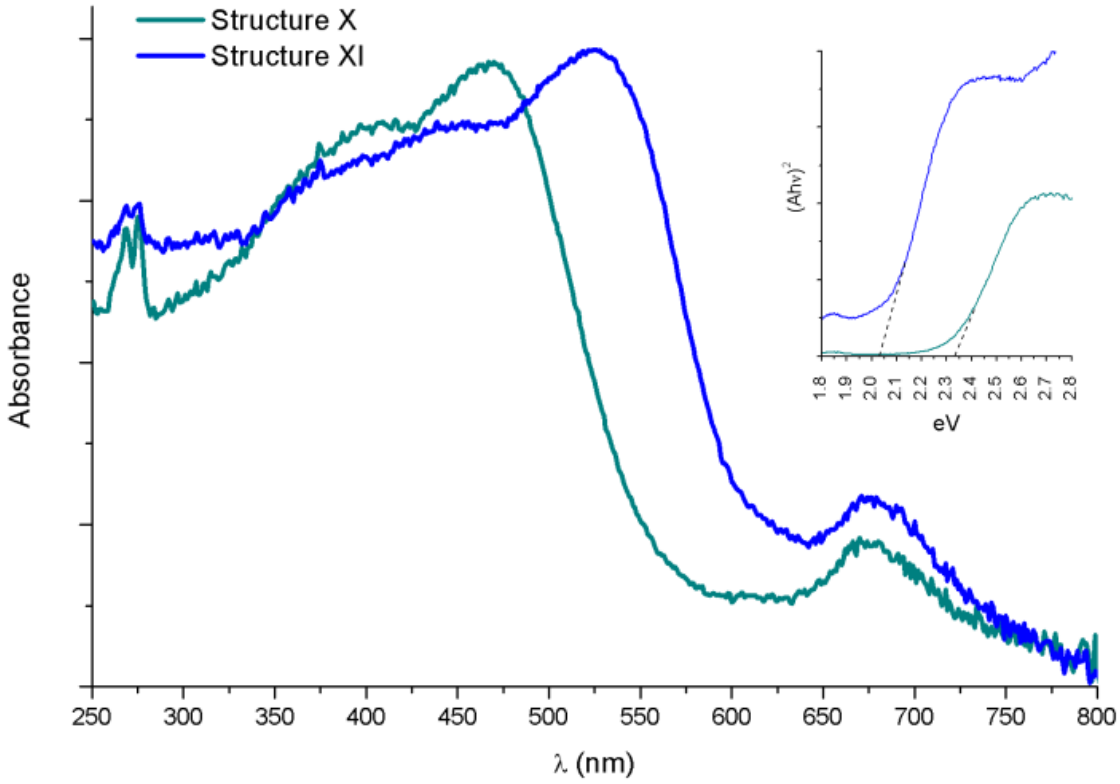

Figure S9 UV/Vis spectra of compounds X and XI (10 wt% in $BaSO_4$) with related Tauc plot (inset)

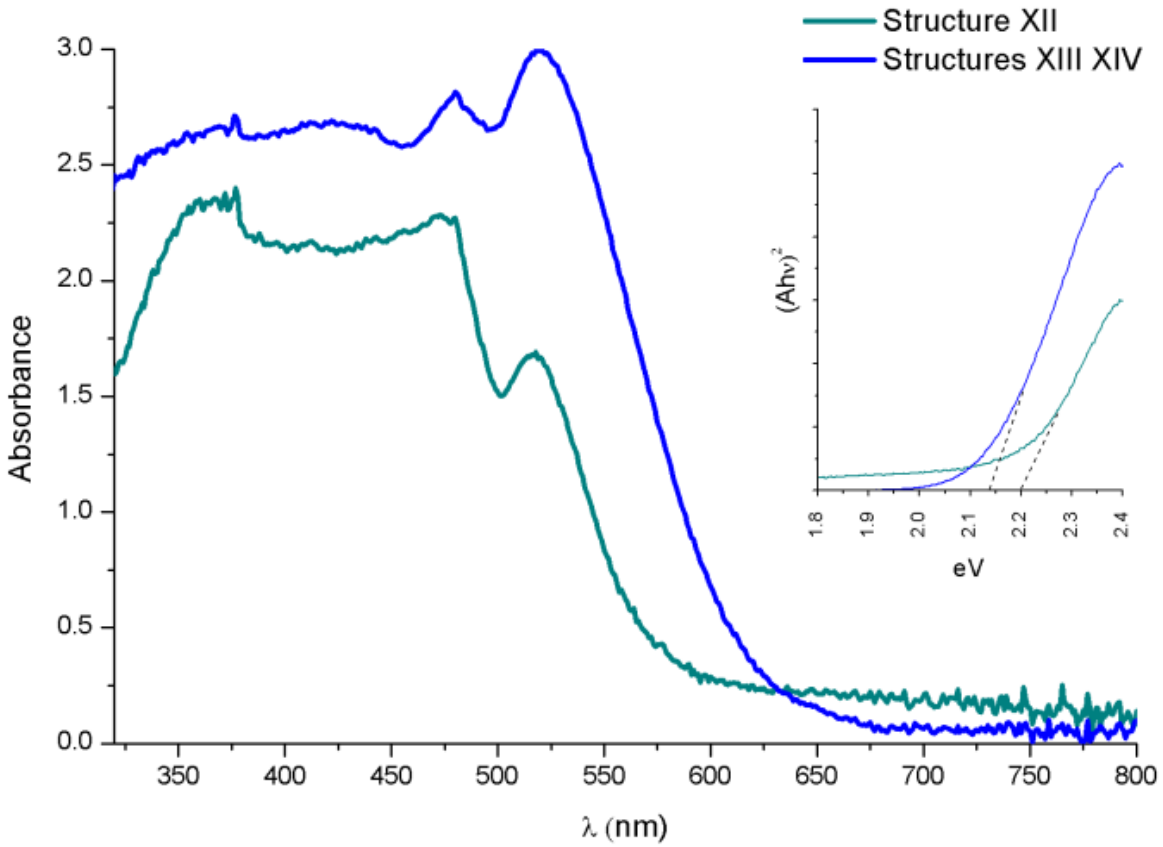

Figure S10 UV/Vis spectra of compounds XII-XIV (10 wt% in $BaSO_4$) with related Tauc plot (inset)

3.2.3 Afterword commentary and discussion

The above presented publication covered research into the discovery and characterisation of novel iodoantimonate and iodobismuthate hybrid materials with shared cationic organic templating agents; including the five novel 1,4-dipiperazinium, 1-methyl-1,4-dipiperazinium, 1,4-dimethyl-1,4-dipiperazinium ion templating iodoantimonate materials. The first three of these, structures **V**, **VI** and **VII**, show strong structural similarities to their iodobismuthate counterparts (compounds 1-3) from the first publication. Each possesses a 1D $[MI_4]^-_n$ (M = Bi, Sb) chain anionic substructure with interactions expanding on the electronic connectivity of the network. Three regularly repeating I---I interactions interconnect the chains in each structure with average I---I distances of 4.14 Å, 4.09 Å and 4.00 Å respectively for bismuth compounds 1-3 and very similar averages of 4.19 Å, 4.13 Å and 4.01 Å for antimony structures **V-VI**. Both show the trend of average interaction distance decreasing through the series with a slight increase in the range of I---I distances measured at 3.80-4.46 Å for the iodoantimonate hybrids and 3.76-4.44 Å for the iodobismuthate equivalents.

These comparisons show rather small changes in the structural chemistry of the related iodoantimonate and iodobismuthate materials. However, more obvious changes in the physical properties can be seen from the interchange of metal identity when comparing the UV/Vis data, as seen in Figure 3.9.

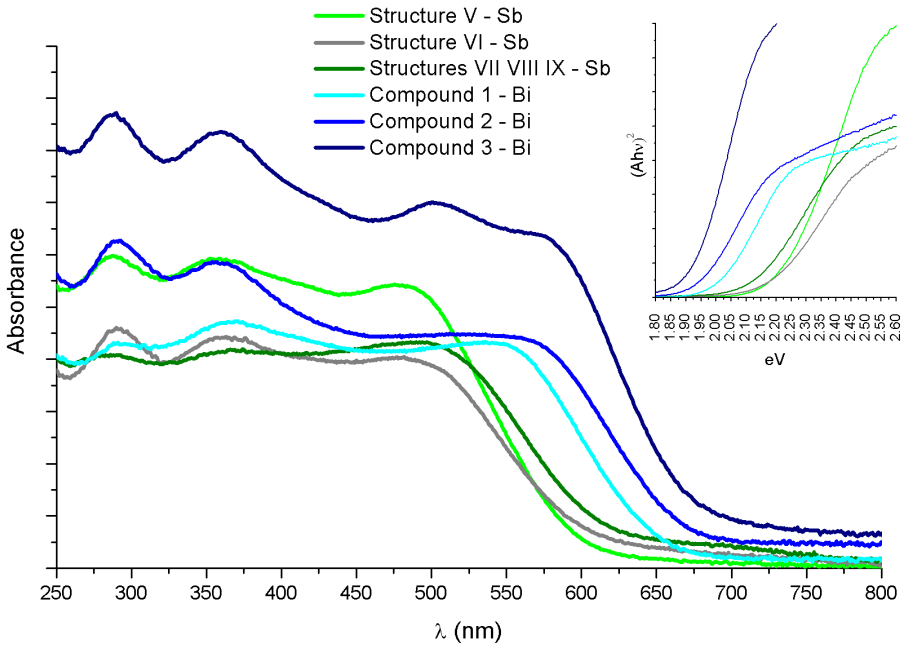

Figure 3.9 UV/Vis comparison spectra of bismuth-based compounds 1-3 alongside antimony-based structures V-IX with related Tauc plot (inset)

Comparing optical absorption spectra (250-800 nm) of bismuth compounds 1-3 alongside antimony structures **V**,**VI** and **VII** shows a clear shift in absorption edge onsets and resulting band gap energies of each material from metal interchange. Absorption edge onsets of 550 nm, 560 nm and 575 nm for compounds 1-3 respectively indicate absorption further into the visible spectrum than their antimony-based equivalents, measured at 480 nm, for structures **V** and **VI**, and 500 nm for mixed phase sample **VII-IX**. Estimated band gap energies follow a similar decreasing trend through the series of 1,4-piperazinium cation templated structures to 1,4-dimethyl-1,4-dipiperazinium cation templated structures; estimated at 2.00 eV (1), 1.95 eV (2), 1.92 eV (3), 2.22 eV (**V**), 2.17 eV (**VI**) and 2.12 eV (**VII/VIII/IX**). Absorption edge features at ~290 nm (4.3 eV) and ~360 nm (3.4 eV) attributed to electronic transitions between the HOMO Bi(6p) to the LUMO Bi (5p) orbitals and HOMO Sb (5p) to the LUMO Sb (4p) orbitals in the respective materials are observed within the absorption profiles of all recorded spectra.

As research in this area of halometallate hybrid materials garners more interest it can be observed that novel structural types can emerge as demonstrated with the unique structural motif, with a mix of discrete iodobismuthate clusters $[Bi_2I_{10}]^{4-}$/$[BiI_6]^{3-}$, seen in structure **XIII**. In close proximity to the publication of this article, another group working within the field published a paper including another mixed iodobismuthate cluster hybrid structure with a different binuclear-mononuclear mix of $[Bi_2I_9]^{3-}$/$[BiI_6]^{3-}$ units, templated by $MeDABCO^{2+}$ dications, indicating much more structural diversity is rapidly emerging through these related studies [9].

In addition, within this Dalton Transactions publication four structures (**I**, **II**, **X** and **XI**) described were discovered after utilising the novel synthetic technique of in-situ alkylation of precursor amines to develop new templating agents from more simple precursors within a one-pot synthetic procedure. The next chapter covers the initial finding which led to the identification of this technique and how it was further used outside of our published material. In conjunction, the synthesis and characterisation of other halometallate hybrid materials which do not share a common templating agent for comparison between iodoantimonate and iodobismuthate are presented and discussed.

Chapter 4 - Hybrid halometallate materials: Part II

4.1 Introduction

The work carried out on hybrid halometallate materials described in chapter 3 compared both hybrid iodoantimonate and iodobismuthate materials formed with similar, and sometimes identical, templating agents. In conjunction with that study, a number of hybrid materials unique to a specific antimonate or bismuthate halometallate system were found and fully structurally analysed. These materials are described in this chapter; starting with the origin of the in-situ solvothermal alkylation mechanism for the synthesis of novel templating agents and continuing with the utilisation of the derived mechanism in the design of a number of new complex materials. As seen in previous synthetic procedures, it was found through these studies that under relatively mild solvothermal conditions, typically at 140 ^{o}C in a 25 ml sized Teflon® vessel with a highly acidic reaction medium, such as hydriodic acid, high quality crystals of hybrid structures could be obtained for later structural and physical property analysis. However, from one of the early experiments it was found that certain simple and cheaper amine reagents could be used as precursor agents for synthesising more complex templating cationic components. Using this technique allowed the exploration of a wealth of novel templating agents previously unobtainable or only as highly priced speciality chemicals (materials that would be unsuitable and uncompetitive in the search for cheap alternatives to the current solar cell technologies). As a result, it was proposed that the in-situ synthesis of novel reagents could lead to the discovery of many novel hybrid structures with the aforementioned organic cationic templating species formed within the reaction medium.

The first example of this process was found in an initial investigation attempting to replicate the results of a low temperature solution based synthetic procedure using the templating agent *p*-phenylenediamine but under higher temperature solvothermal conditions. In the original study, published in 2011 [1], a stoichiometric reaction of bismuth nitrate, *p*-phenylenediamine and concentrated HI solution in ethanol heated to 90 ^{o}C led to the precursor amine being di-protonated to form templating p-phenylenediammonium cations and a hybrid structure of dark-red prismatic crystals, determined to be compound $[C_6H_4(NH_3)_2]_2Bi_2I_{10}$, to crystallise from the cooled reaction mixture.

Our preliminary experiment was an attempt to imitate the synthesis of high quality single crystals of this known halometallate hybrid structure but using a solvothermal procedure in a shorter synthetic time. The unexpected effect observed was that under the increased solvothermal synthesis heat and pressure, a tetra-alkylated diammonium dication formed in-situ and then acted as a templating agent source to form a stable salt with counterbalancing iodobismuthate structural units. The following section presents the structural analysis of this new compound.

4.2 Synthesis and structures from in-situ ethylation

4.2.1 Compound 19: N^1-N^1-N^4-N^4-tetraethyl-1,4-benzenediammonium decaiododibismuthate

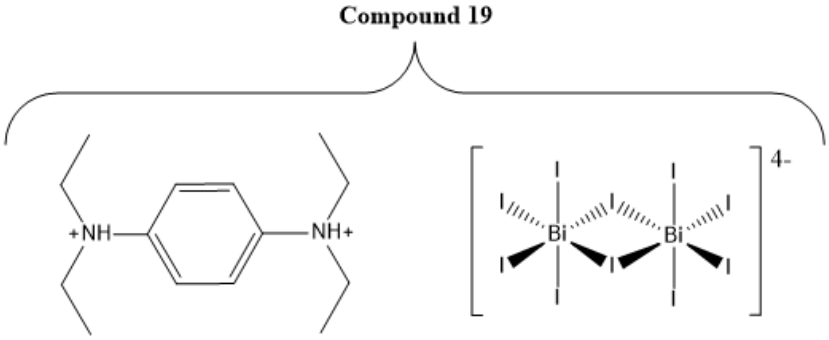

N^1,N^1,N^4,N^4-tetraethylbenzene-1,4-diaminium decaiododibismuthate

$2(C_{14}H_{26}N_2)\ Bi_2I_{10}$

The structure of a N^1-N^1-N^4-N^4-tetraethyl-1,4-benzenediammonium templated iodobismuthate material was determined from single-crystal X-ray diffraction data. The hybrid compound, $2(C_{14}N_2H_{26})\ Bi_2I_{10}$, was found to crystallise with monoclinic symmetry, in the space group $P2_1/n$, and contains discrete $[Bi_2I_{10}]^{4-}$ bioctahedral units forming the anionic substructure; these are charge counterbalanced by divalent N^1-N^1-N^4-N^4-tetraethyl-1,4-benzenediammonium cations. This cationic species was found to form in-situ under hydrothermal conditions via a fourfold alkylation mechanism wherein the primary amine 1,4-benzenediamine precursor reacts with the solvent (ethanol) under highly acidic conditions (Scheme 4.1).

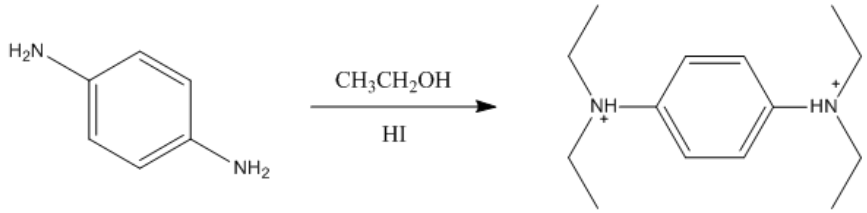

Scheme 4.1 Reaction scheme for the formation of templating "tie-fighter" cation N^1-N^1-N^4-N^4-tetraethyl-1,4-benzenediammonium via the alkylation of reagent 1,4-benzenediamine

Crystals of compound 19 were obtained from two solvothermal reaction procedures of varying acidity as follows. Reagents bismuth chloride (0.2 mmol), 1,4-benzenediamine (0.15 mmol) and hydriodic acid (1 ml, 57 wt% in water, no stabiliser) in ethanol (6 ml) were placed in a 25 ml Teflon® vessel, sealed in a steel autoclave and heated at 140 °C for 24 h; with a controlled ramp up rate of 1 °C min^{-1} and ramp down rate of 0.1 °C min^{-1}. After vacuum filtration and ethanol wash, orange needle crystals of compound 19 were obtained in a mixed phase product mixture. A single-crystal of compound 19 was selected for full structural X-ray analysis from the first procedure containing 0.75 ml of hydriodic acid in the reaction mixture. This product mixture consisted of the major phase of orange crystals (compound 19) alongside a minor phase of dark-red block crystalline material and black crystalline material; both unidentifiable from primary single-crystal screening analysis. In similar reaction procedures these additional phases were screened and identified to be either iodine or the organic cation iodide, here N^1-N^1-N^4-N^4-tetraethyl-1,4-benzenediammonium iodide, crystallising out of the reaction mixture alongside the stable hybrid material.

A final structure refinement factor of 0.029, weighted refinement factor of 0.050 and goodness of fit of 1.03 was attained from the structural data analysis. Full crystallographic details of the structure solution and refinement are shown in Table 4.1 below.

Table 4.1 Crystal data for Compound 19

Chemical formula	$Bi_2I_{10}\cdot 2(C_{14}N_2H_{26})$
M_r	2131.75
Crystal system, space group	Monoclinic, $P2_1/n$
Temperature (K)	150
a, *b*, *c* (Å)	13.3586 (2), 13.5020 (3), 14.8073 (3)
β (°)	97.529 (2)
V ($Å^3$)	2647.73 (9)
Z	2
F(000)	1888
D_x (Mg m^{-3})	2.674
Radiation type	Mo *K*α
No. of reflections for cell measurement	6152
θ range (°) for cell measurement	3.8–29.0
μ (mm^{-1})	12.49
Crystal shape	Needle
Colour	Orange

Data collection	
Diffractometer	SuperNova, Dual, Cu at zero, EosS2 diffractometer
Radiation source	SuperNova (Mo) X-ray Source
Monochromator	Mirror
Detector resolution (pixels mm^{-1})	8.1150
Scan method	ω scans
Absorption correction	Multi-scan *CrysAlis PRO*, Agilent Technologies, Version 1.171.37.35 (release 13-08-2014 CrysAlis171 .NET) (compiled Aug 13 2014,18:06:01) Empirical absorption correction using spherical harmonics, implemented in SCALE3 ABSPACK scaling algorithm.
T_{min}, T_{max}	0.575, 1.000
No. of measured, independent and observed [$I > 2\sigma(I)$] reflections	14029, 6130, 5288
R_{int}	0.033
θ values (°)	θ_{max} = 29.4, θ_{min} = 3.4
$(\sin\theta/\lambda)_{max}$ ($Å^{-1}$)	0.691
Range of *h*, *k*, *l*	*h* = -16→18, *k* = -18→17, *l* = -19→20
Refinement	
Refinement on	F^2
$R[F^2 > 2\sigma(F^2)]$, $wR(F^2)$, *S*	0.029, 0.050, 1.03
No. of reflections	6130
No. of parameters	207
No. of restraints	0
H-atom treatment	H atoms treated by a mixture of independent and constrained refinement
Weighting scheme	$w = 1/[\sigma^2(F_o^2) + (0.0082P)^2]$ where $P = (F_o^2 + 2F_c^2)/3$
$(\Delta/\sigma)_{max}$	0.198
$\Delta\rangle_{max}$, $\Delta\rangle_{min}$ (e $Å^{-3}$)	0.90, -0.92

Symmetry codes: (i) -*x*+2, -*y*, -*z*; (ii) -*x*+2, -*y*+1, -*z*+1; (iii) -*x*+1, -*y*, -*z*+1.

Software: *CrysAlis PRO* 1.171.38.43 (Rigaku OD, 2015); cell refinement: *CrysAlis PRO* 1.171.38.43 (Rigaku OD, 2015); data reduction: *CrysAlis PRO* 1.171.38.43 (Rigaku OD, 2015); program(s) used to solve structure: *SHELXL2014*/7 (Sheldrick, 2014); program(s) used to refine structure: *SHELXL2014*/7 (Sheldrick, 2014); molecular graphics: Palmer, D. C. (2014). *CrystalMaker*. CrystalMaker Software Ltd, Begbroke, Oxfordshire, England.; software used to prepare material for publication: *WinGX* (Farrugia, 2012). *publCIF* [Westrip, S. P. (2010). *J. Appl. Cryst.*, **43**, 920-925] software used for generating tabulated data.

The hybrid structure of compound 19 contains anionic $[Bi_2I_{10}]^{4-}$ discrete sub-units interacting via weak I---I interactions to form a pseudo-two-dimensional layered sublattice within the material. Each $[Bi_2I_{10}]^{4-}$ discrete sub-unit forms bridging interactions to four adjacent $[Bi_2I_{10}]^{4-}$ units; each with an I---I distance of 4.108 Å. The resultant pseudo-2D layer formed along the plane running along the *b*-axis which perfectly bisects the *ac* plane of the structure (As can be observed from the connectivity in the central *b*-axis perspective of Figure 4.1).

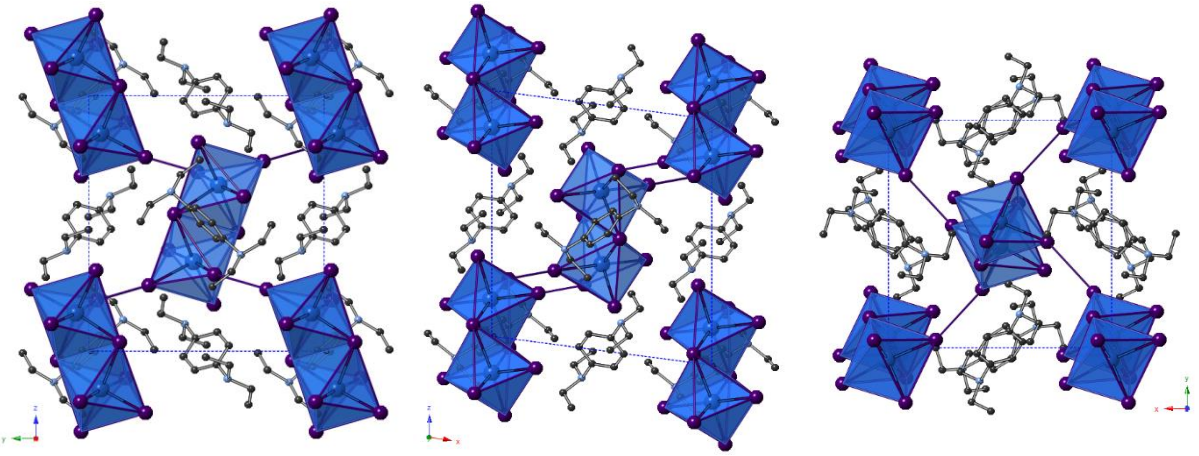

Figure 4.1 Perspectives of the *a*-axis (left), *b*-axis (central) and *c*-axis (right) of Compound 19. Legend: $[BiI_6]$ octahedra shaded blue; Bi atoms (blue), I atoms (purple), C atoms (dark grey), N atoms (pale blue). H atoms excluded for clarity.

Each bioctahedral $[Bi_2I_{10}]^{4-}$ tetraanion is made up of symmetry related positions across the edge sharing interface; formed from an inversion across Bi-I(x)-Bi^{i} , Bi-I(x)^{i}-Bi^{i} bridges (-*x*+1/2, *y*+1/2,-*z*+1/2). Accordingly, Bi-I bond distances within the unit range from 2.9186(4) - 3.2873(4) Å (Δ = 0.369 Å); with the longest bonding interactions to the bridging iodide positions. In this respect, the 'central' bismuth atom position (in one distorted BiI_6 octahedron) can be seen to be slightly shifted away from its equivalent position of the adjacent within the bioctahedra to give a Bi…Bi separation distance of 4.66 Å.

Variations in measured Bi-I bond lengths can derive from sharing the halogen in various combinations of corner, edge, and face sharing interfaces. In addition influences from intermolecular interactions to the templating cationic species, through hydrogen bonds, and weak I---I interactions can have the effect of modifying the geometry of $[MX_6]^{3-}$ octahedra [1]. As a measure of deviation away from regularity of the six-coordinate $[MX_6]^{3-}$ octahedra I-M-I angles within each octahedron component of the discrete tetranion are measured. In structure 19, I-Bi-I angles in the symmetry equivalent octahedra are measuring at 174.143(11)°, 174.734(11)° and 174.288(11)°; resulting in an average deviation of 5.6° from 180°.

4.2.2 Compound 20: N^1-N^1-N^4-N^4-tetraethyl-1,4-benzenediammonium hexadecaiodotetrabismuthate tetrahydrate

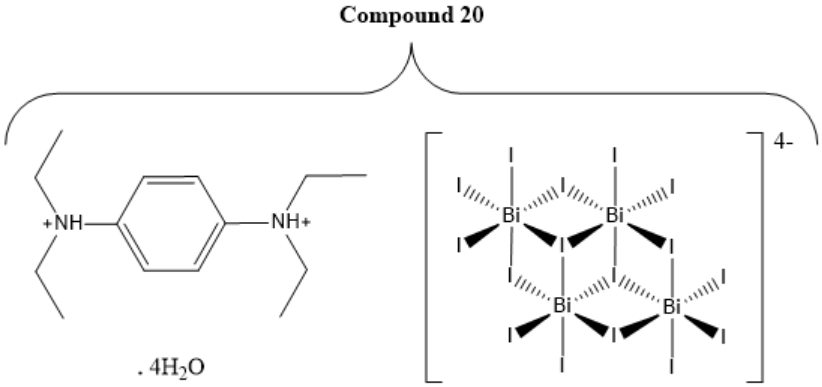

N^1,N^1,N^4,N^4-tetraethylbenzene-1,4-diaminium hexadecaiodotetrabismuthate tetrahydrate

$2(C_{14}H_{26}N_2)\ Bi_4I_{16}.4(H_2O)$

Compound 19 was not the only N^1-N^1-N^4-N^4-tetraethyl-1,4-benzenediammonium organic cation iodobismuthate hybrid structure discovered from the initial investigations undertaken in this reactant system. In an alternate hydrothermal synthesis procedure with the same reagents to those used in the synthesis of compound 19 but with an increased amount of hydriodic acid, a secondary N^1-N^1-N^4-N^4-tetraethyl-1,4-benzenediammonium templated structure (Compound 20) was obtained in a mixed phase.

Crystals of compound 20 were obtained through a solvothermal reaction of bismuth chloride (0.2 mmol), 1,4-benzenediamine (0.15 mmol) and hydriodic acid (1 ml, 57 wt% in water, no stabiliser) in ethanol (6 ml). Reactants were placed in a 25 ml Teflon® vessel, sealed in a steel autoclave and heated at 140 ^oC for 24 h; with a controlled ramp up rate of 1 $^oC\ min^{-1}$ and ramp down rate of 0.1 $^oC\ min^{-1}$. After vacuum filtration and ethanol wash, red crystals of compound 20 were obtained in a mixed phase product mixture. In this mixture it was identified by single-crystal X-ray screening that the major phase of orange crystals remained to be a match to that of the previously described compound 19, however, the previously semi-crystalline red block material was now present as bright red block single-crystals and in a greater amount in the mixed phase. Some black material was also present in the product mixture. This was commonly screened and identified to be excess iodine or the equivalent organic iodide, here N-N-N'-N'-tetraethyl-1,4-benzenediammonium iodide, crystallising out of the reaction mixture.

Crystallising as red prismatic crystals, the structure of Compound 20 was determined from single-crystal X-ray analysis to adopt the monoclinic space group $P2_1/c$. A final structure refinement factor of 0.052, weighted refinement factor of 0.106 and goodness of fit of 1.01 was attained from the structural data analysis. Full crystallographic details of the structure solution and refinement are shown in Table 4.2 below.

Table 4.2 Crystal data for Compound 20

Chemical formula	$Bi_4I_{16}\cdot 2(C_{14}N_2H_{26})\cdot 4(H_2O)$
M_r	3383.2
Crystal system, space group	Monoclinic, $P2_1/c$
Temperature (K)	150
a, b, c (Å)	11.8027 (5), 20.680 (1), 14.4900 (8)
β (°)	102.648 (5)
V (Å^3)	3450.9 (3)
Z	2
F(000)	2920
D_x (Mg m^{-3})	3.248
Radiation type	Mo $K\alpha$
No. of reflections for cell measurement	5210
θ range (°) for cell measurement	3.6–27.2
μ (mm^{-1})	17.36
Crystal shape	Prismatic
Colour	Red
Data collection	
Diffractometer	Xcalibur, EosS2 diffractometer
Radiation source	Enhance (Mo) X-ray Source
Monochromator	Graphite
Detector resolution (pixels mm^{-1})	16.1468
Scan method	ω scans
Absorption correction	Multi-scan *CrysAlis PRO*, Agilent Technologies, Version 1.171.37.35 (release 13-08-2014 CrysAlis171 .NET) (compiled Aug 13 2014,18:06:01) Empirical absorption correction using spherical harmonics, implemented in SCALE3 ABSPACK scaling algorithm.
T_{min}, T_{max}	0.598, 1.000
No. of measured, independent and observed [$I > 2\sigma(I)$] reflections	17873, 8030, 5807
R_{int}	0.034

θ values (°)	θ_{max} = 29.4, θ_{min} = 3.3
$(\sin\theta/\lambda)_{max}$ (Å^{-1})	0.691
Range of *h*, *k*, *l*	*h* = -12→15, *k* = -17→28, *l* = -19→14
Refinement	
Refinement on	F^2
$R[F^2 > 2\sigma(F^2)]$, $wR(F^2)$, *S*	0.052, 0.106, 1.01
No. of reflections	8030
No. of parameters	253
No. of restraints	0
H-atom treatment	H-atom parameters constrained
	$w = 1/[\sigma^2(F_o^2) + (0.0226P)^2 + 68.2802P]$ where $P = (F_o^2 + 2F_c^2)/3$
$(\Delta/\sigma)_{max}$	0.133
$\Delta\rangle_{max}$, $\Delta\rangle_{min}$ (e Å^{-3})	6.20, -3.92

Symmetry code: (i) -*x*+1, -*y*+1, -*z*+1.

Software: *CrysAlis PRO* 1.171.38.43 (Rigaku OD, 2015); cell refinement: *CrysAlis PRO* 1.171.38.43 (Rigaku OD, 2015); data reduction: *CrysAlis PRO* 1.171.38.43 (Rigaku OD, 2015); program(s) used to solve structure: *SHELXL2014*/7 (Sheldrick, 2014); program(s) used to refine structure: *SHELXL2014*/7 (Sheldrick, 2014); molecular graphics: Palmer, D. C. (2014). *CrystalMaker*. CrystalMaker Software Ltd, Begbroke, Oxfordshire, England.; software used to prepare material for publication: *WinGX* (Farrugia, 2012). *publCIF* [Westrip, S. P. (2010). *J. Appl. Cryst.*, **43**, 920-925] software used to generate tabulated data.

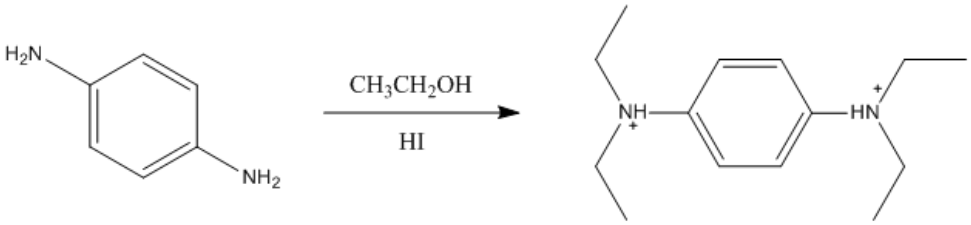

Scheme 4.2 Reaction scheme for the formation of dicationic N^1-N^1-N^4-N^4-tetraethyl-1,4-benzenediammonium ions in compound 20

Compound 20 was found to contain the aforementioned templating N^1-N^1-N^4-N^4-tetraethyl-1,4-benzenediammonium dications albeit with a slightly distorted conformation. As seen in Scheme 4.2, in comparison to the form in counterpart structure 19, one of the ($-CH_2CH_3$) ethyl groups bound to one of the two nitrogen positions is directed in an alternate conformation. Once more, the formation of the templating agent was through a fourfold in-situ alkylation of the precursor primary amine reagent, 1,4-benzenediamine, by way of the reaction solvent reacting with HI under the highly acidic conditions to form ethyl iodide. Compound 20, therefore, represents a structure with an equivalent templating dication to that found in structure 19, however, it represents an example of how the conformation of the templating agent and degree or lack of solvation of the structure can influence the structure of the templated hybrid compound.

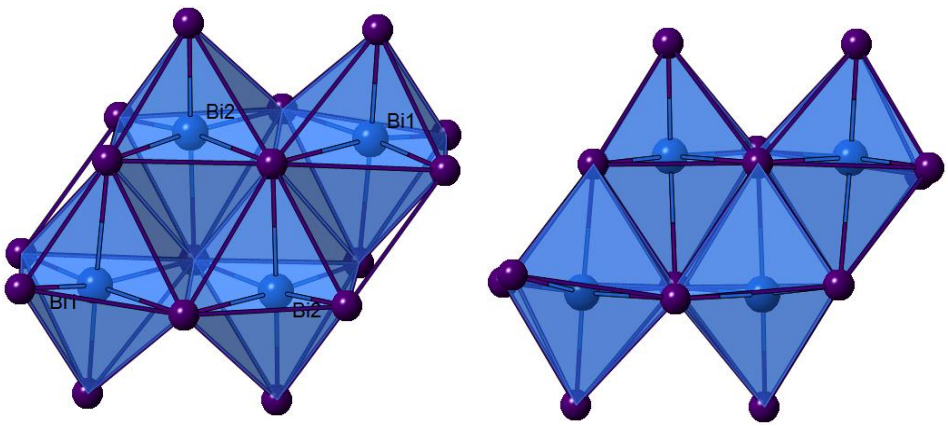

Figure 4.2 Two views of the discrete hexadexaiodotetrabismuthate $[Bi_4I_{16}]^{4-}$ tetranions present in hybrid compound 20

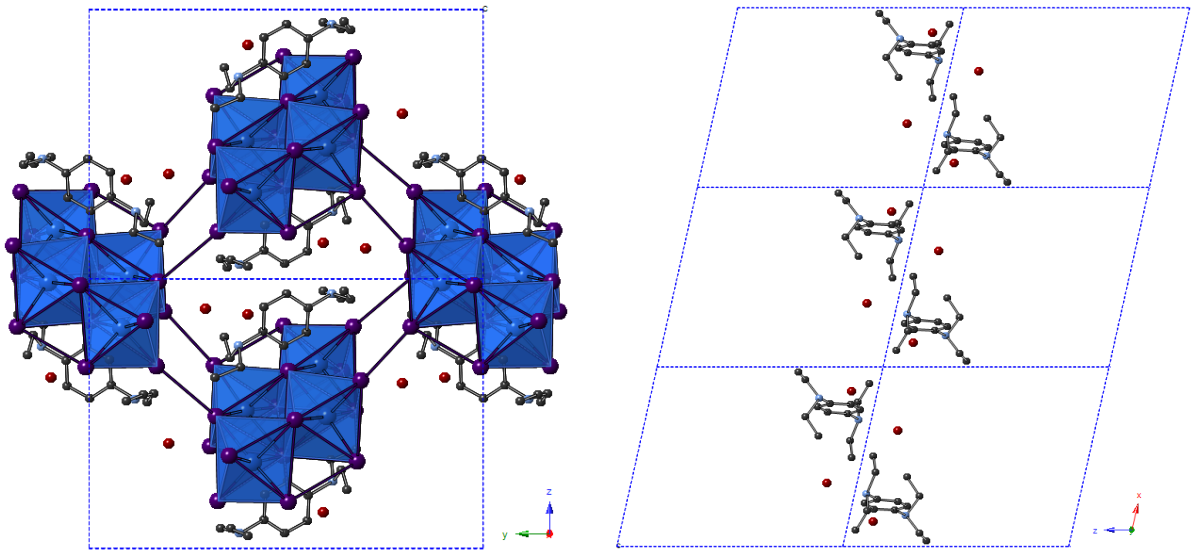

Figure 4.3 View along the *a*-axis of compound 20 (left), N^1-N^1-N^4-N^4-tetraethyl-1,4-benzenediammonium iodobismuthate tetrahydrate, and a perspective of the central stacked cations and water molecules as viewed along the *b*-axis. Legend: $[BiI_6]$ octahedra shaded blue; Bi atoms (blue), I atoms (purple), C atoms (dark grey), N atoms (pale blue), O atoms (red). Hydrogen atoms excluded for clarity.

The anionic sublattice formed in the hybrid structure, arranged around the charge balancing organic dications and neutral water molecule of crystallisation sites, is made up of discrete units of hexadexaiodotetrabismuthate $[Bi_4I_{16}]^{4-}$ tetranions (Figure 4.2) with two symmetry equivalent octahedra. Bi-I bonds within the octahedra range from 2.9050(11) - 3.3382(9) Å (Δ = 0.433 Å) for the Bi(1)-centred position and 2.8992(10) - 3.3715(9) Å (Δ = 0.472 Å) for the Bi(2)-centred position. Bi…Bi separation distances within the tetraoctahedral unit are measured at 4.75 Å, 4.81 Å and 4.92 Å. Increased distortion of the octahedra is observed (Figure 4.3) for the outer Bi(1)-centred octahedra with two shared vertices over the inner Bi(2)-centred octahedra with three shared vertices. This observation is reflected in the I-Bi-I angle measurements with an average deviation of 6.86° from 180° for the outer octahedra compared to 5.52° from 180° for the inner octahedra.

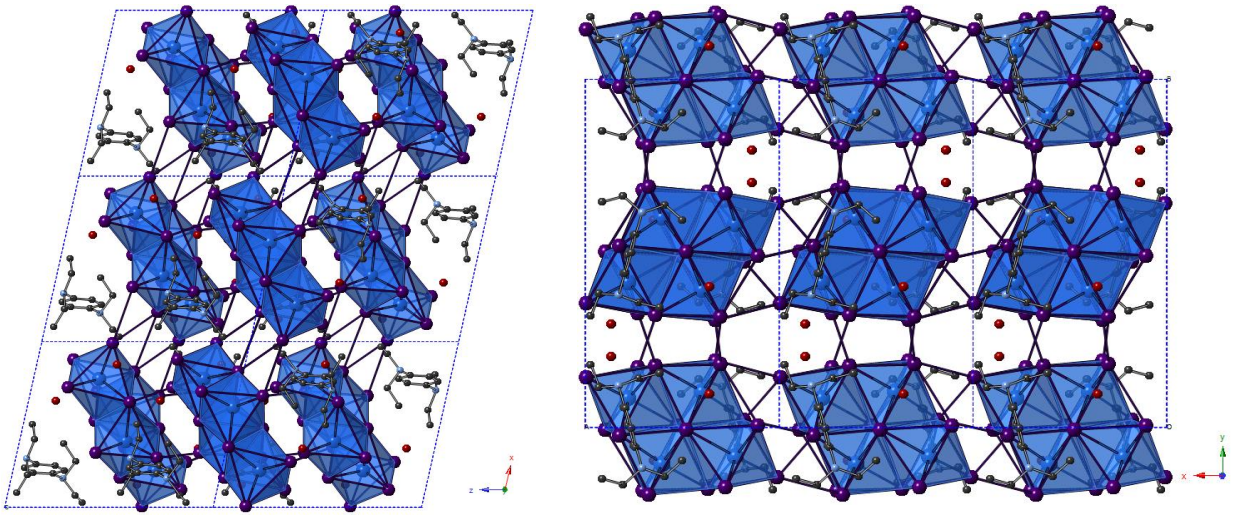

Figure 4.4 View along the *b*-axis (left) and *c*-axis of compound 20.
Legend: [BiI_6] octahedra shaded blue; Bi atoms (blue), I atoms (purple), C atoms (dark grey), N atoms (pale blue), O atoms (red). Hydrogen atoms excluded for clarity.

Interactions within the structure via weak I---I interconnections between the sub-units produce a pseudo-three dimensional network. These are formed via four fold repeating I---I interactions measured at 4.25 Å (I2-I3), 4.43 Å (I1-I4) and 3.97 Å (I3-I6) totalling twelve interactions to adjacent equivalent discrete $[Bi_4I_{16}]^{4-}$ units; with an average I---I interaction distance of 4.22 Å. When compared to compound 19, the anionic substructure changes from interlinked tetraanionic $[Bi_2I_{10}]^{4-}$ discrete units with a 1:5 (Bi:I) ratio to tetraanionic $[Bi_4I_{16}]^{4-}$ discrete units with a 1:4 (Bi:I) ratio; compound 20 is hydrated with four water molecules of crystallisation sites per asymmetric unit cell. Each water molecule is bound via hydrogen bonding interactions to adjacent N-N-N'-N'-tetraethyl-1,4-benzenediammonium dications (Figure 4.5) by distances of 1.72 Å N(1)-H(1) … O(2) (167.8º interaction angle across N1-H1-O2) and N(2)-H(2) … O(1) (171.2º interaction angle across N2-H2-O1).

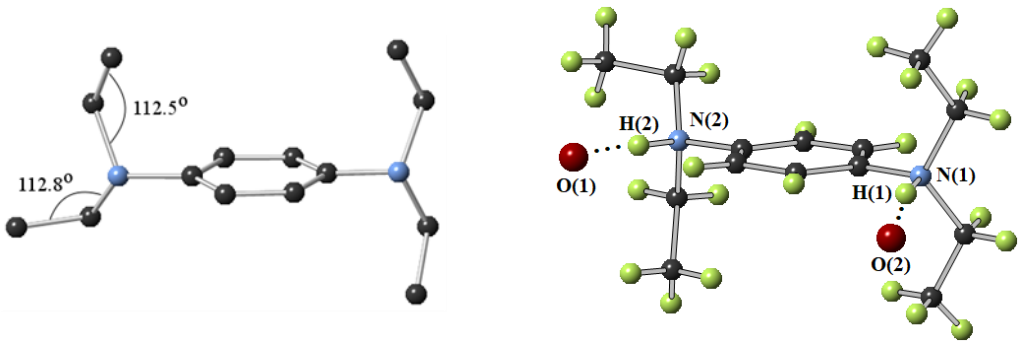

Figure 4.5 Distorted N^1-N^1-N^4-N^4-tetraethyl-1,4-benzenediammonium dications present in hybrid compound 20; showing hydrogen positions removed (left) and dication paired hydrogen bound water oxygen positions (right)

4.2.3 Compound 21: N^1-N^1-N^3-N^3-tetraethyl-1,3-benzenediammonium tetraiodobismuthate

Further systematic investigations into this type of di-substituted organic hybrid structure were focussed on alternative phenylenediamine systems. Therefore, the meta-substituted diamine precursor reagent 1,3-benzenediamine was employed to observe if and how alkylation of the amine would occur. The effect of the resulting templating agent on the potential hybrid structure formed would then be analysed and interpreted.

Compound 21

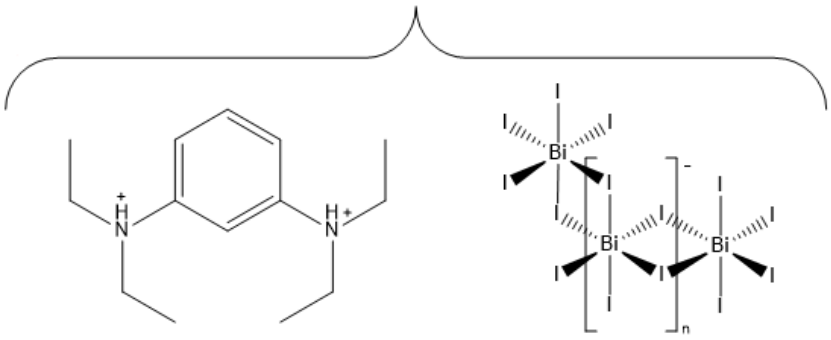

N^1,N^1,N^3,N^3-tetraethylbenzene-1,3-diaminium tetraiodobismuthate

$(C_{14}H_{26}N_2)$ $2(BiI_4)$

Crystals of compound 21 were obtained from three solvothermal reaction procedures carried out in a range of high acidity solvent media. The procedure followed a solvothermal run carried out at lower levels of acidity in the reaction mixtures with hydriodic acid (57 wt% in water, no stabiliser) volumes varying from 0.5 ml → 0.75 ml → 1 ml through the vessels (Appendix A.12). Upon analysing the products of these reactions it was observed that semi-crystalline red material was present but no single-crystal of any compound has been grown under the conditions used. Therefore, the synthesis route was optimised with an increase in volume of hydriodic acid added to the reaction vessels, thus increasing the metal:iodide ratio in mixtures. The result of this yielded analysable single-crystals of the hybrid material compound 21 from each of the three solvothermal vessels with volumes of hydriodic acid added ranging from 1.25 ml → 1.5 ml → 1.75 ml. A single-crystal of compound 21 was broken off from a larger crystal habit structure of 'feathered' sheets for full structural X-ray analysis from the first of these reaction procedures containing 1.25 ml of hydriodic acid.

Reagents bismuth chloride (0.2 mmol), 1,3-benzenediamine (0.15 mmol) and hydriodic acid (1.25 ml, 57 wt% in water, no stabiliser) in ethanol (6 ml) were placed in a 25 ml Teflon® vessel, sealed in a steel autoclave and heated at 140 ºC for 24 h; with a controlled ramp up rate of 1 ºC min^{-1} and left to cool to room temperature upon completion of the reaction dwell time. After vacuum filtration and ethanol wash red crystals of compound 21 were obtained in a mixed phase product mixture. The product contained a major phase of red crystals, compound 21, alongside a minor phase of black crystalline material, unidentifiable from single-crystal screening analysis. Again, this is commonly identified in similar reaction procedures to be either excess iodine or the equivalent organic iodide, here N-N-N'-N'-tetraethyl-1,3-benzenediammonium iodide, crystallising out of the reaction mixture.

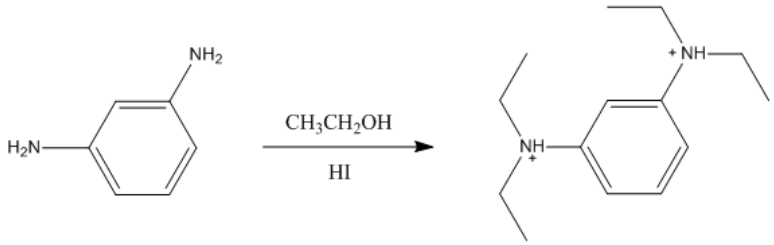

Scheme 4.3 Reaction scheme for the formation of dicationic N^1-N^1-N^3-N^3-tetraethyl-1,3-benzenediammonium ions in compound 21

The structure of compound 21 was solved from single-crystal X-ray diffraction. A final structure refinement factor of 0.052, weighted refinement factor of 0.106 and goodness of fit of 1.01 was attained from the structural data analysis. Full crystallographic details of the structure solution and refinement are shown in Table 4.3 below.

Table 4.3 Crystal data for Compound 21

Chemical formula	$2(BiI_4)\cdot C_{14}N_2H_{26}$
M_r	1655.57
Crystal system, space group	Triclinic, *P-1*
Temperature (K)	150
a, *b*, *c* (Å)	7.6515 (3), 10.0520 (4), 11.7585 (5)
α, β, γ (°)	78.328 (4), 78.761 (4), 82.680 (4)
V (Å^3)	865.04 (6)
Z	1
F(000)	738
D_x (Mg m^{-3})	3.282
Radiation type	Mo *K*α
No. of reflections for cell measurement	9421

θ range (°) for cell measurement	3.8–31.7
μ (mm^{-1})	17.31
Crystal shape	Prismatic
Colour	Red
Data collection	
Diffractometer	Xcalibur, EosS2 diffractometer
Radiation source	Enhance (Mo) X-ray Source
Monochromator	Graphite
Detector resolution (pixels mm^{-1})	8.0734
Scan method	ω scans
Absorption correction	Multi-scan *CrysAlis PRO*, Agilent Technologies, Version 1.171.37.35 (release 13-08-2014 CrysAlis171 .NET) (compiled Aug 13 2014,18:06:01) Empirical absorption correction using spherical harmonics, implemented in SCALE3 ABSPACK scaling algorithm.
T_{min}, T_{max}	0.146, 1.000
No. of measured, independent and observed [$I > 2\sigma(I)$] reflections	17191, 5465, 4864
R_{int}	0.029
θ values (°)	θ_{max} = 32.1, θ_{min} = 3.5
$(\sin\theta/\lambda)_{max}$ ($Å^{-1}$)	0.748
Range of *h*, *k*, *l*	*h* = -11→10, *k* = -13→14, *l* = -17→17
Refinement	
Refinement on	F^2
$R[F^2 > 2\sigma(F^2)]$, $wR(F^2)$, *S*	0.030, 0.077, 1.01
No. of reflections	5465
No. of parameters	122
No. of restraints	0
H-atom treatment	H-atom parameters constrained
Weighting scheme	$w = 1/[\sigma^2(F_o^2) + (0.036P)^2 + 4.4886P]$ where $P = (F_o^2 + 2F_c^2)/3$
$(\Delta/\sigma)_{max}$	3.188
$\Delta\rangle_{max}$, $\Delta\rangle_{min}$ (e $Å^{-3}$)	2.68, -2.44

Symmetry codes: (i) -*x*+2, -*y*+1, -*z*+2; (ii) -*x*+1, -*y*+1, -*z*+2; (iii) -*x*+1, -*y*, -*z*+1.

Software: *CrysAlis PRO* 1.171.38.43 (Rigaku OD, 2015); cell refinement: *CrysAlis PRO* 1.171.38.43 (Rigaku OD, 2015); data reduction: *CrysAlis PRO* 1.171.38.43 (Rigaku OD, 2015); program(s) used to solve structure: *SHELXL2014*/7 (Sheldrick, 2014); program(s) used to refine structure: *SHELXL2014*/7 (Sheldrick, 2014); molecular graphics: Palmer, D. C. (2014). *CrystalMaker*. CrystalMaker Software Ltd, Begbroke, Oxfordshire, England.; software used to prepare material for publication: *WinGX* (Farrugia, 2012). *publCIF* [Westrip, S. P. (2010). *J. Appl. Cryst.*, **43**, 920-925] software used to generate tabulated data.

Analysis of the structure obtained for Compound 21 reveals the transition from a connected zero-dimensional discrete unit anionic architecture in N-N-N'-N'-tetraethyl-1,4-benzenediammonium templated compounds 19 and 20 to an interconnected one-dimensional chain substructure in compound 21. This change in dimensionality may be the result of a steric effect involving the tetra-ethylated side groups of the N-N-N'-N'-tetraethyl-1,3-benzenediammonium cation; steric crowding of these ethyl groups is reduced in comparison with compounds 19 and 20.

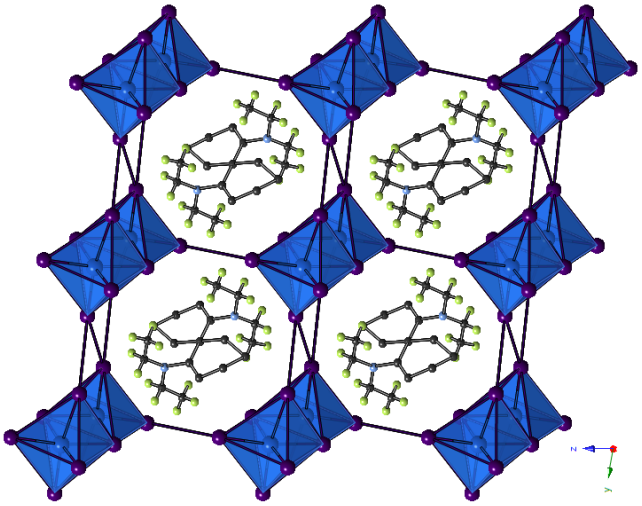

Figure 4.6 View along the *a*-axis of N^1-N^1-N^3-N^3-tetraethyl-1,3-benzenediammonium dication templated hybrid compound 21

N-N-N'-N'-tetraethyl-1,3-benzenediammonium cations counterbalance $[BiI_4]^-_n$ bismuth iodide chains in hybrid compound 21. Within the structure Bi-I bonding interactions range from 2.9252(4) - 3.2538(4) Å (Δ = 0.329 Å), Bi…Bi distances inside the chains measure at 4.57 Å and 4.60 Å. Again, as seen in previous one-dimensional chain structured compounds I---I interactions form an expanded interconnected network. In compound 21, a single 4.15 Å interaction (terminal I5 - I5 terminal), repeating every 7.65 Å along the *a*-axis, opens up connectivity approximately in the *c*-axis direction. In addition to this, an I---I interaction measured at 4.13 Å (terminal I4 – I4 terminal) repeating every 7.65 Å along the *a*-axis extends the connectivity in the *b*-axis direction in conjunction with a pair of 4.44 Å (bridging I3 – I4 terminal) I---I interactions, separated by 4.41 Å, repeating every 7.65 Å along the *a*-axis. As a result the electronic connectivity of the hybrid material, through the I---I interaction substructure network, can therefore be considered as pseudo-three dimensional with a decreasing trend in connectivity through axes *a*→*b*→*c*.

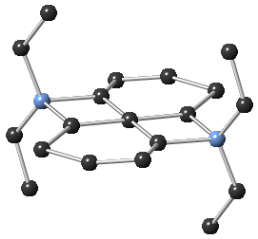

Figure 4.7 Centrosymmetric N^1-N^1-N^3-N^3-tetraethyl-1,3-benzenediammonium dication structural model present in hybrid compound 21

As seen in figure 4.6, the organic dications propagate alongside the iodobismuthate chains in the *a*-axis direction flipping in orientation between two positions. However, some distortion in the regularity of the shape of the benzene ring of the N-N-N'-N'-tetraethyl-1,3-benzenediammonium dication is observed in the structural model as the position of the dication appears to alternate with some disorder across a centrosymmetric inversion centre (*x*, *y*, *z* / -*x*, -*y*, -*z*).

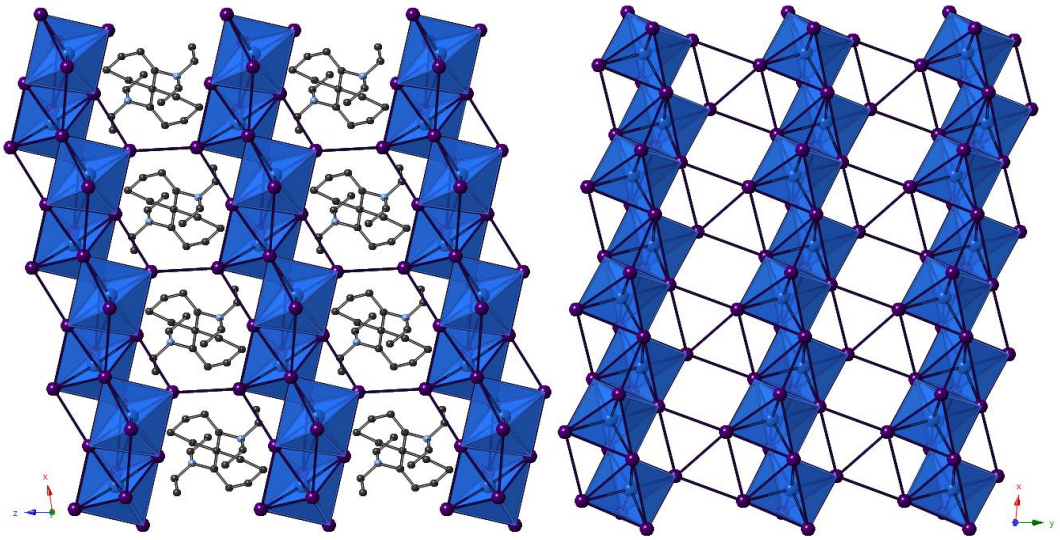

Figure 4.8 View along the *b*-axis (left) and *c*-axis (cations excluded) of compound 21. Legend: $[BiI_6]$ octahedra shaded blue; Bi atoms (blue), I atoms (purple), C atoms (dark grey), N atoms (pale blue). Hydrogen atoms excluded for clarity.

4.2.4 Compound 22: 1-ethyl-2,5-dimethylbenzimidazol-3-ium tetraiodobismuthate

Investigating the ortho-substituted phenylenediamine precursor, 1,2-benzenediamine was the next logically step in developing this series of compounds. The resultant hybrid structure was included, alongside its equivalent iodoantimonate counterpart structure, as structures X and XI in the second Dalton Transactions publication of Chapter 3. The later iodobismuthate hybrid, compound XI, was the first example obtained of alkylation of an ortho-substituted position resulting the formation of a benzimidazolium-based organic system via a ring closing mechanism; with possible further alkylation of the nitrogen positions.

Compound 22

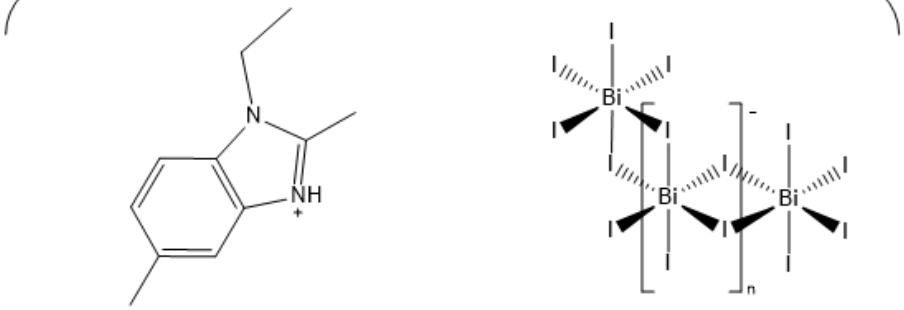

1-ethyl-2,5-dimethyl-1*H*-benzo[*d*]imidazol-3-ium tetraiodobismuthate
$(C_{11}H_{15}N_2)\ BiI_4$

To further expand on this newfound procedure it was decided that a closely related precursor reagent, 3,4-diaminotoluene, could be utilised in order to possibly compare the structural and physical property effects of adding an additional methyl group to the benzene ring to increase the steric effects of the cation in the structure.

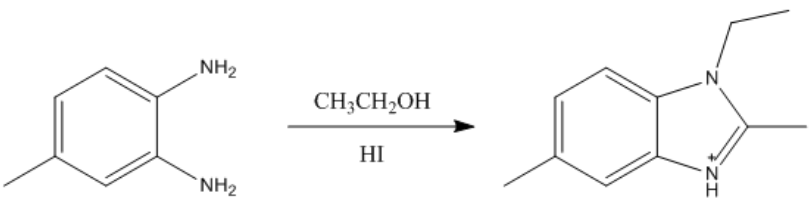

Scheme 4.4 Reaction scheme for the formation of cationic 1-ethyl-2,5-dimethylbenzimidazol-3-ium ions in compound 22

The resulting structure obtained followed a similar di-ethylation mechanism to form templating monocationic 1-ethyl-2,5-dimethylbenzimidazol-3-ium ions in-situ. This molecular compound was found to template compound 22 and counterbalance the interconnected polymeric $[BiI_4]^-_n$ chain units of the anionic sublattice.

The optimum procedure for synthesising crystals of compound 22 was found from a series of reaction mixtures with varying levels of acidity; carried out under solvothermal synthesis conditions. Reagents bismuth chloride (0.2 mmol), 3,4-diaminotoluene (0.15 mmol) and hydriodic acid (0.75 ml, 57 wt% in water, no stabiliser) in ethanol (6 ml) were placed in a 25 ml Teflon® vessel, sealed in a steel autoclave and heated at 140 °C for 24 h; with a controlled ramp up rate of 1 °C min^{-1} and ramp down rate of 0.1 °C min^{-1}. After vacuum filtration and ethanol wash, red crystals of compound 22 were obtained in a mixed phase product mixture. This product mixture contained a phase consisting of red needle crystals, compound 22, alongside a phase of orange plate crystals, compound 24 described later in this chapter, and a small amount of black crystalline material. A red needle of compound 22 was selected for analysis using single-crystal X-ray diffraction.

A final structure refinement factor of 0.068, weighted refinement factor of 0.155 and goodness of fit of 1.20 was attained from the structural data analysis. Full crystallographic details of the structure solution and refinement are shown in Table 4.4 below.

Table 4.4 Crystal data for Compound 22

Chemical formula	$C_{11}H_{15}N_2 \cdot BiI_4$
M_r	891.85
Crystal system, space group	Monoclinic, *C*2/*c*
Temperature (K)	150
a, *b*, *c* (Å)	13.4196 (10), 18.340 (2), 7.8047 (5)
β (°)	91.810 (7)
V (Å^3)	1919.9 (3)
Z	4
F(000)	2337
D_x (Mg m^{-3})	4.754
Radiation type	Mo *K*α
No. of reflections for cell measurement	1876
θ range (°) for cell measurement	3.0–28.8
μ (mm^{-1})	24.60
Crystal shape	Needle

Colour	Red
Data collection	
Diffractometer	SuperNova, Dual, Cu at zero, EosS2 diffractometer
Radiation source	SuperNova (Mo) X-ray Source
Monochromator	Mirror
Detector resolution (pixels mm^{-1})	8.1150
Scan method	ω scans
Absorption correction	Multi-scan *CrysAlis PRO*, Agilent Technologies, Version 1.171.37.35 (release 13-08-2014 CrysAlis171 .NET) (compiled Aug 13 2014,18:06:01) Empirical absorption correction using spherical harmonics, implemented in SCALE3 ABSPACK scaling algorithm.
T_{min}, T_{max}	0.918, 1.000
No. of measured, independent and observed [$I > 2\sigma(I)$] reflections	4670, 2233, 1780
R_{int}	0.034
θ values (°)	θ_{max} = 29.3, θ_{min} = 2.2
$(\sin\theta/\lambda)_{max}$ ($Å^{-1}$)	0.689
Range of *h*, *k*, *l*	*h* = -17→7, *k* = -22→24, *l* = -10→10
Refinement	
Refinement on	F^2
$R[F^2 > 2\sigma(F^2)]$, $wR(F^2)$, *S*	0.068, 0.155, 1.20
No. of reflections	2233
No. of parameters	59
No. of restraints	0
H-atom treatment	H-atom parameters not defined
	$w = 1/[\sigma^2(F_o^2) + (0.0286P)^2 + 104.4273P]$ where $P = (F_o^2 + 2F_c^2)/3$
$(\Delta/\sigma)_{max}$	5.864
$\Delta\rangle_{max}$, $\Delta\rangle_{min}$ (e $Å^{-3}$)	2.78, -3.25

Symmetry codes: (i) -*x*+1, *y*, -*z*+1/2; (ii) -*x*+1, -*y*+1, -*z*+1; (iii) *x*, -*y*+1, *z*-1/2; (iv) -*x*, *y*, -*z*+3/2.

Software: *CrysAlis PRO* 1.171.38.43 (Rigaku OD, 2015); cell refinement: *CrysAlis PRO* 1.171.38.43 (Rigaku OD, 2015); data reduction: *CrysAlis PRO* 1.171.38.43 (Rigaku OD, 2015); program(s) used to solve structure: *SHELXL2014*/7 (Sheldrick, 2014); program(s) used to refine structure: *SHELXL2014*/7 (Sheldrick, 2014); molecular graphics: Palmer, D. C. (2014). *CrystalMaker*. CrystalMaker Software Ltd, Begbroke, Oxfordshire, England.; software used to prepare material for publication: *WinGX* (Farrugia, 2012). *publCIF* [Westrip, S. P. (2010). *J. Appl. Cryst.*, **43**, 920-925] software used to generate tabulated data.

The hybrid structure of compound 22 was found to exhibit a substructure of parallel one-dimensional chains propagating along the *c*-axis of the structure alongside the stacks of cations. The cations stack with alternating ABAB orientation by 180° rotation, with a separation distance of 3.7 Å and 18.5° offset from perpendicular axis. Additionally, the cations are split between two related positions by an approximate in-plane 32° rotation and 180° 2-fold rotation through the central in-plane axis of the ion; akin to observations in related structures **X** and **XI** in Dalton Paper 2 above (Chapter 3). However, disorder in the rotation of the benzene ring system in the structural model resulted in a 7-membered ring modelled in the final refinement of the structure signifying the in-plane split position of the ion.

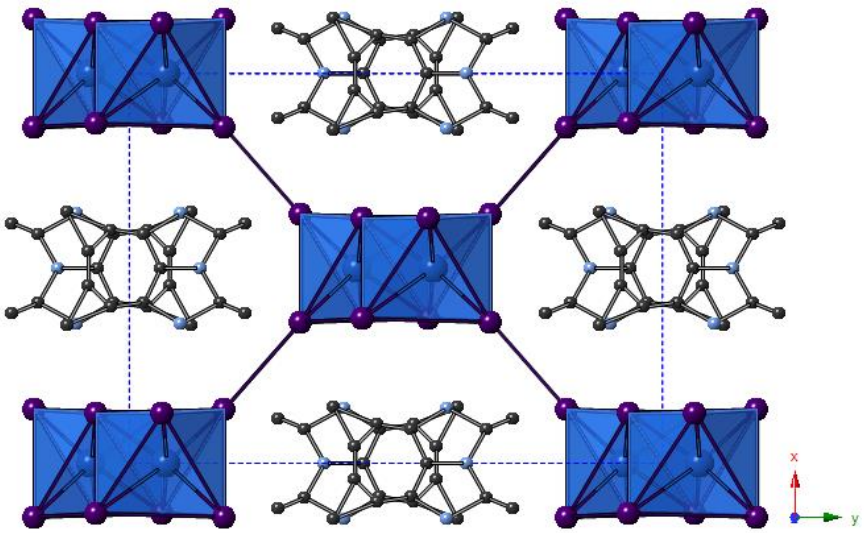

Figure 4.9 View along the *c*-axis of compound 22. Legend: [BiI_6] octahedra shaded blue; Bi atoms (blue), I atoms (purple), C atoms (dark grey), N atoms (pale blue).

Structural differences between the earlier described compound 15 and compound 22 are summarised below in Table 4.5. The effect of the additional substituted methyl group contributes to an expansion of the unit cell, increased interchain interactions distances within the anionic network and an increased channel size to accommodate the increased steric bulk of the counterbalancing monocationic 1-ethyl-2,5-dimethylbenzimidazol-3-ium ions.

Table 4.5 Structural comparison table of compound 15 (Paper 2- Structure XI) and compound 22

1-ethyl-2-methylbenzimidazol-3-ium tetraiodobismuthate	**Difference Δ**	**1-ethyl-2,5-dimethylbenzimidazol-3-ium tetraiodobismuthate**
Monoclinic *C12/c1*	-	Monoclinic *C12/c1*
a (Å) = 13.3133(4)	+ 0.1063 Å	*a* (Å) = 13.4196(10)
b (Å) = 17.7312(4)	+ 0.6087 Å	*b* (Å) = 18.3399(20)
c (Å) = 7.6344(2)	+ 0.1703 Å	*c* (Å) = 7.8047(5)
β (º) = 93.450(2)	- 1.64 Å	*β* (º) = 91.810(7)
V (Å^3) = 1798.92(8)	+ 120.97 Å^3	*V* (Å^3) = 1919.89(5)
	Bi…Bi distance	
4.632 Å	+ 0.05 Å	4.682 Å
	Bi-I bonding interactions	
2.9129(5) – 3.2875(5) Å (Δ = 0.375 Å)	Negligible	2.9071(15) – 3.2822(14) Å (Δ = 0.375 Å)
	Interchain I---I distances	
3.935 Å (repeating every 7.634 Å)	+ 0.359 Å (+0.171 Å)	4.294 Å (repeating every 7.805 Å)
	I-Bi-I angles	
172.9º (Average = 7.1º deviation)	+ 0.2º	173.1º (Average = 6.9º deviation)
	Channel size	
~11.1 x 9.7 Å	+ 0.6 x 0.1 Å	~11.7 x 9.8 Å

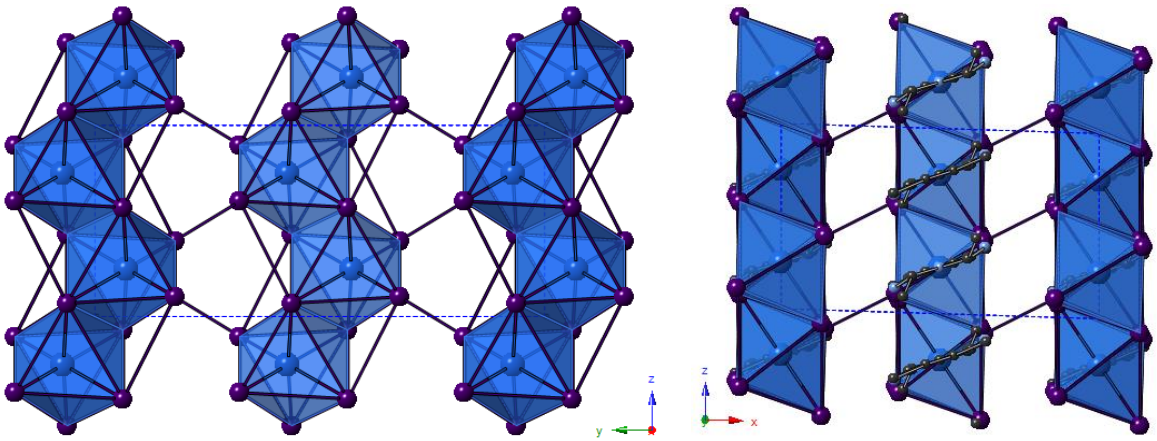

Figure 4.9 View along the *a*-axis (left) and *b*-axis (right) of compound 22.
Legend: [BiI_6] octahedra shaded blue; Bi atoms (blue), I atoms (purple), C atoms (dark grey), N atoms (pale blue).

4.2.5 Compound 23: 1,3-diethyl-2-methylbenzimidazolium nonaiododibismuthate

Compound 23

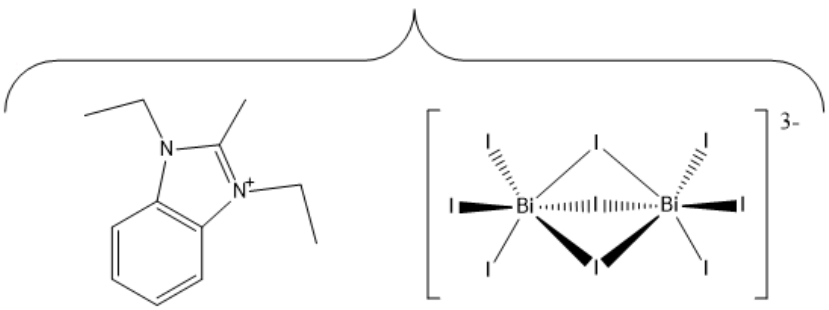

1,3-diethyl-2-methyl-1*H*-benzo[*d*]imidazol-3-ium nonaiododibismuthate

$3(C_{12}H_{17}N_2)\ Bi_2I_9$

The next compound analysed in the series of novel hybrid compounds formed from in-situ ethylated precursor amines is the first example of ribbon-like pseudo 1D chains of $[Bi_2I_9]^{3-}$ trivalent anionic clusters. From single-crystal X-ray diffraction data, the structure of a 1,3-diethyl-2-methyl-benzimidazol-3-ium templated iodobismuthate material was determined. This templating species was found to form in-situ under hydrothermal conditions via a threefold alkylation mechanism. Under increasingly acidic conditions, the structure was found to crystallise as a secondary phase alongside counterpart 1-ethyl-2-methyl-benzimidazolium templated compound 15. Here the precursor primary amine 1,2-benzenediamine, utilised as a reaction reagent, again reacts with the reaction solvent (ethanol) under highly acidic conditions to form 1,3-diethyl-2-methyl-benzimidazol-3-ium cations in-situ.

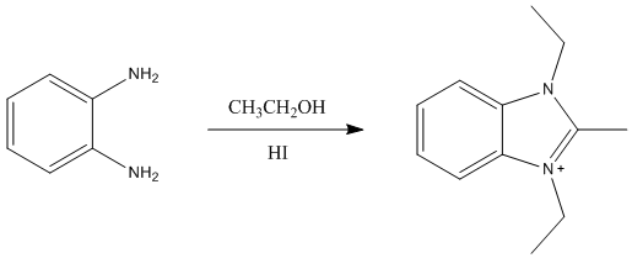

Scheme 4.5 Reaction scheme for the formation of templating cation 1,3-diethyl-2-methylbenzimidazolium via the alkylation of reagent 1,2-diaminobenzene

The reagents bismuth chloride (0.2 mmol), 1,2-benzenediamine (0.15 mmol) and hydriodic acid (1.0 ml, 57 wt% in water, no stabiliser) in ethanol (6.0 ml) were placed in a 25 ml Teflon® vessel, sealed in a steel autoclave and heated at 140 °C for 24 h; with a controlled ramp up rate of 1 °C min^{-1} and ramp down rate of 0.1 °C min^{-1}. After vacuum filtration and ethanol wash,

orange crystals of compound 23 were obtained in a mixed phase product mixture. In this product mixture, it was identified that the phase of thin red plate-like needle crystals was that of the previously described novel compound 15, published in the second Dalton Transactions paper (Chapter 3), alongside a secondary phase of the here described orange wedge-shaped crystals of compound 23. Increasing the volume of HI in the reaction mixture from 0.5 ml to 1.0 ml had the effect of increased alkylation of the organic component, crystallising high quality crystals of compound 23 for analysis (see Appendices A.12). An orange wedge shaped crystal was selected for analysis using single-crystal X-ray diffraction.

A final structure refinement factor of 0.076, weighted refinement factor of 0.169 and goodness of fit of 1.30 was attained from the structural data analysis. Full crystallographic details of the structure solution and refinement are shown in Table 4.6 below.

Table 4.6 Crystal data for Compound 23

Chemical formula	$3(C_{12}N_2H_{17})\cdot Bi_2I_9$
M_r	2127.94
Crystal system, space group	Orthorhombic, *Cmcm*
Temperature (K)	150
a, *b*, *c* (Å)	14.8492 (19), 16.747 (3), 22.056 (5)
V (Å^3)	5484.9 (16)
Z	4
F(000)	3652
D_x (Mg m^{-3})	2.544
Radiation type	Mo *K*α
No. of reflections for cell measurement	2057
θ range (°) for cell measurement	3.3–28.7
μ (mm^{-1})	11.50
Crystal shape	Wedge
Colour	Orange
Data collection	
Diffractometer	SuperNova, Dual, Cu at zero, EosS2 diffractometer
Radiation source	SuperNova (Mo) X-ray Source
Monochromator	Mirror
Detector resolution (pixels mm^{-1})	8.1150
Scan method	ω scans
Absorption correction	Multi-scan *CrysAlis PRO*, Agilent Technologies, Version 1.171.37.35 (release 13-08-2014 CrysAlis171 .NET) (compiled Aug 13 2014,18:06:01) Empirical absorption correction using

	spherical harmonics, implemented in SCALE3 ABSPACK scaling algorithm.
T_{min}, T_{max}	0.714, 1.000
No. of measured, independent and observed [$I > 2\sigma(I)$] reflections	22766, 3593, 3179
R_{int}	0.092
θ values (°)	θ_{max} = 29.3, θ_{min} = 2.4
$(\sin\theta/\lambda)_{max}$ (Å^{-1})	0.689
Range of *h*, *k*, *l*	*h* = -19→18, *k* = -23→20, *l* = -27→23
Refinement	
Refinement on	F^2
$R[F^2 > 2\sigma(F^2)]$, $wR(F^2)$, *S*	0.076, 0.169, 1.30
No. of reflections	3593
No. of parameters	166
No. of restraints	0
H-atom treatment	H-atom parameters not defined
	$w = 1/[\sigma^2(F_o^2) + 651.1779P]$ where $P = (F_o^2 + 2F_c^2)/3$
$(\Delta/\sigma)_{max}$	0.324
$\Delta\rangle_{max}$, $\Delta\rangle_{min}$ (e Å^{-3})	2.80, -2.25

Symmetry codes: (i) -*x*, *y*, *z*; (ii) -*x*, *y*, -*z*+1/2; (iii) *x*, *y*, -*z*+1/2; (iv) -*x*-1, *y*, *z*.

Software: *CrysAlis PRO* 1.171.38.43 (Rigaku OD, 2015); cell refinement: *CrysAlis PRO* 1.171.38.43 (Rigaku OD, 2015); data reduction: *CrysAlis PRO* 1.171.38.43 (Rigaku OD, 2015); program(s) used to solve structure: *SHELXL2014*/7 (Sheldrick, 2014); program(s) used to refine structure: *SHELXL2014*/7 (Sheldrick, 2014); molecular graphics: Palmer, D. C. (2014). *CrystalMaker*. CrystalMaker Software Ltd, Begbroke, Oxfordshire, England.; software used to prepare material for publication: *WinGX* (Farrugia, 2012). *publCIF* [Westrip, S. P. (2010). *J. Appl. Cryst.*, **43**, 920-925] software used to generate tabulated data.

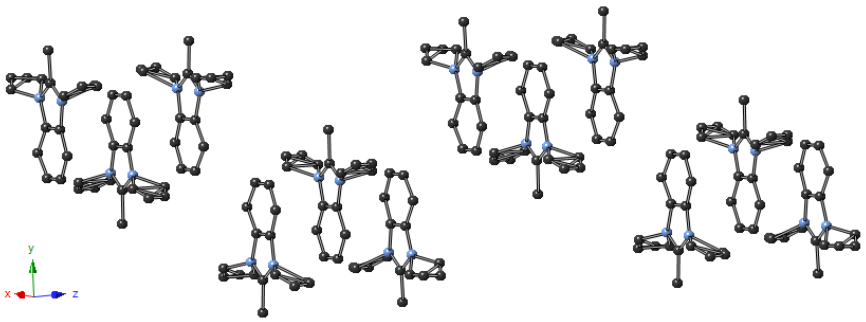

Figure 4.10 1,3-diethyl-2-methylbenzimidazolium cations present in hybrid compound 23

An obvious observable structural effect of the increased size of the counterbalancing monocationic templating species from an increased degree of alkylation is that the one-dimensional (pseudo-3D) anionic substructures of the associated 1-ethyl-2-methylbenzimidazolium cation templated structures (X and XI in Dalton Paper 2 above) is broken in favour of a structure of lower structural and electronic dimensionality. Compound 23 exhibits discrete zero-dimensional nonaiododibismuthate units linked to form a pseudo-one dimensional network (Figure 4.11/4.13).

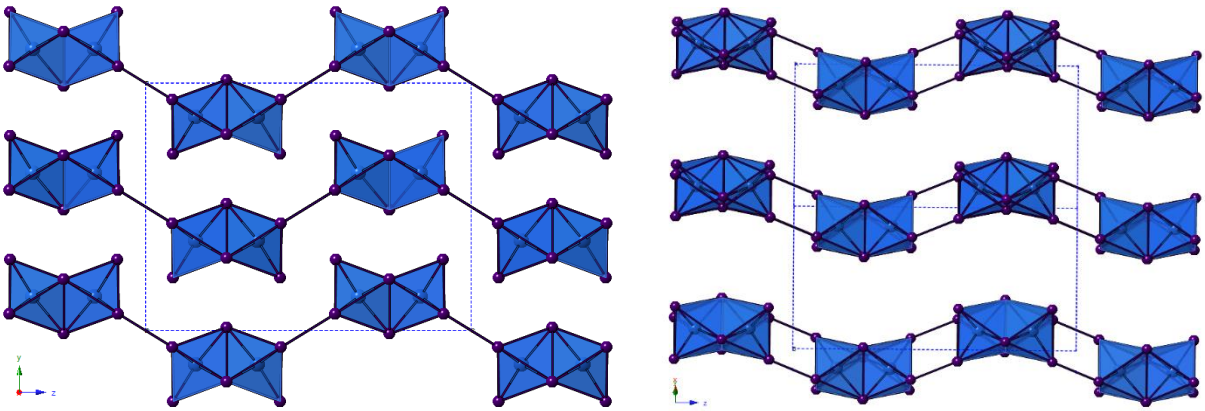

Figure 4.11 Graphic showing the *a*-axis view (left) and *ab* plane view (right) showing the interlinked $[Bi_2I_9]^{3-}$ units in compound 23 (cations excluded)

The anionic substructure of the hybrid material consists of discrete face-sharing bioctahedral $[Bi_2I_9]^{3-}$ units. Within each unit Bi-I bonds range from 2.9523(18) - 3.2734(18) Å (Δ = 0.32 Å, Average = 3.10 Å), the longest of which are to the iodide positions forming the face-sharing connection between the octahedra measuring at 3.2428(13) Å, 3.2429(13) Å and 3.2734(18) Å respectively. Bi…Bi bonding distance within the bioctahedral cluster measures at 4.18 Å. The monovalent cations, as seen in Figure 4.10, cluster in groups of three and follow a similar wave-like form through the structure as found in the anionic counterpart. Each group counterbalances the trivalent charge of the anionic units, with a separation distance of approximately 3.57 Å between cations. Therefore, each cation is related by an 180° rotation on the *ab* plane, a +2.25 Å translation along the *b*-axis and a 3.65 Å translation along the *c*-axis; with likely a degree of pi-stacking stabilising interactions between the cations in the group. The effect of the anionic substructure structural connectivity changes on crystal colour can be observed in the optical microscope image comparison below in Figure 4.12.

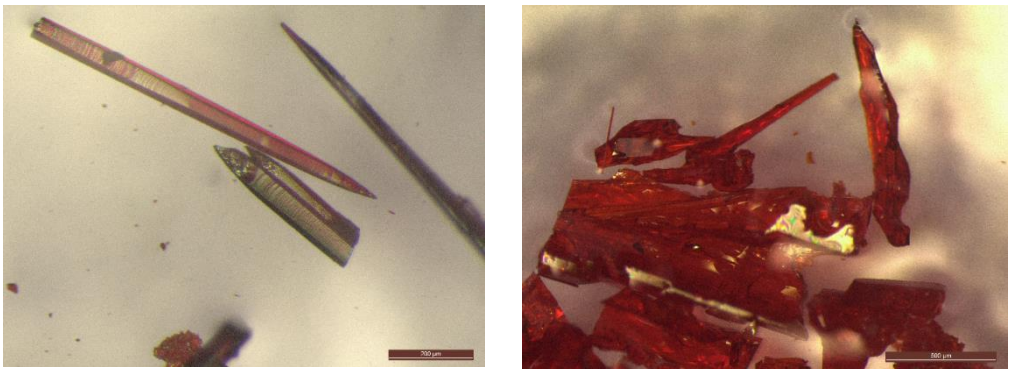

Figure 4.12 Optical microscope image comparison of dark-red crystals of compound 15 (Paper 2 – Structure XI) (left – 200 µm scale) alongside counterpart orange crystals of compound 23 (right – 500 µm scale)

As previously mentioned, interunit interactions between the clusters connect the discrete units to a form a pseudo-one-dimensional chain network within the hybrid material. A total of four I---I interactions each measured at 4.27 Å (terminal I4 – I4 terminal) connect the bioctahedral units to form the observed ribbon-like chain motif propagating along the *c*-axis of the structure.

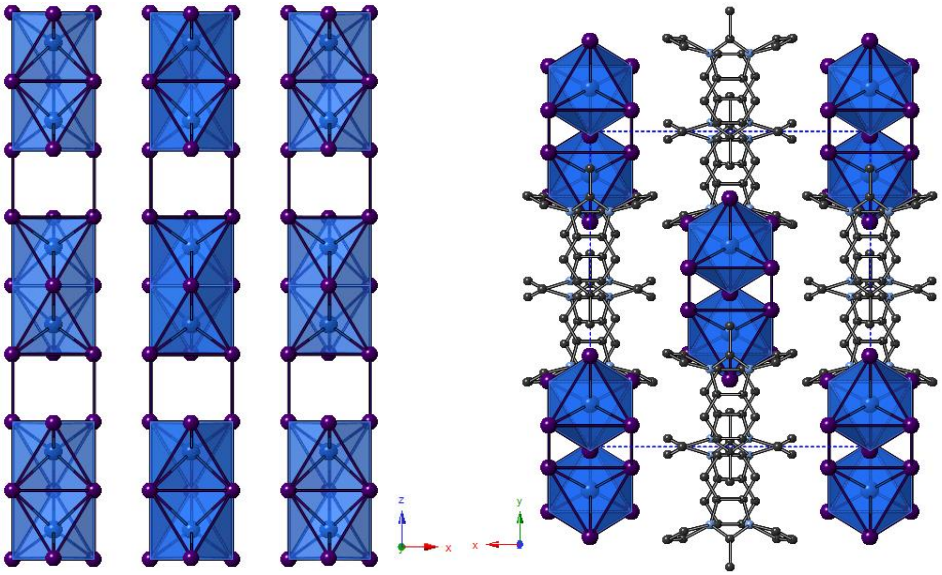

Figure 4.13 View along the *b*-axis (left) (cations excluded) and *c*-axis (right) of compound 23

4.2.6 Compound 24: 1,3-diethyl-2,5-dimethylbenzimidazolium nonaiododibismuthate

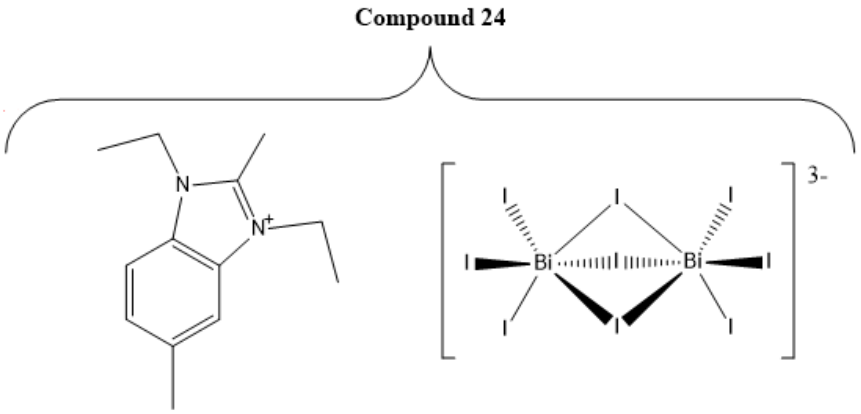

1,3-diethyl-2,5-dimethyl-1*H*-benzo[*d*]imidazol-3-ium nonaiododibismuthate
$3(C_{13}H_{19}N_2)\ Bi_2I_9$

Crystallising from the solvothermal reaction mixture alongside the previously described dark red needle crystals of compound 22 was a phase of orange plate crystals. Once again, from single-crystal X-ray structural analysis it was determined that a secondary iodobismuthate hybrid material had crystallised from the reaction mixture again templated by a derivative of the precursor organic reagent used in the synthesis, 3,4-diaminotoluene. However, here an additional ethylation of the diamine, via a threefold alkylation of the precursor diamine, formed the monovalent templating cation 1,3-diethyl-2,5-dimethylbenzimidazolium. From single-crystal X-ray diffraction analysis the resulting structure was determined to have crystallised with orthorhombic symmetry in space group *Cmcm*.

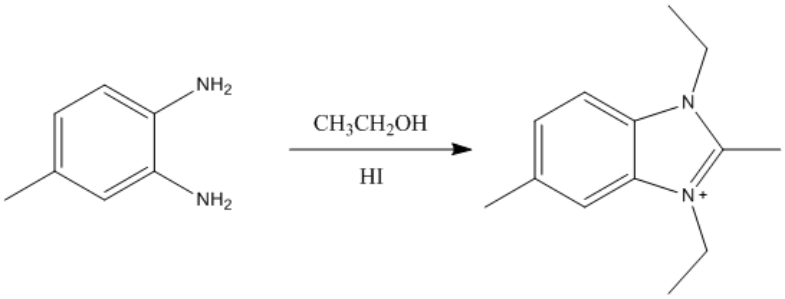

Scheme 4.6 Reaction scheme for the formation of templating cation 1,3-diethyl-2,5-dimethylbenzimidazolium via the alkylation of reagent 3,4-diaminotoluene

The optimal procedure for synthesising crystals of compound 24 was found from a series of reaction mixtures with varying levels of acidity; carried out under solvothermal synthesis conditions. Reagents bismuth chloride (0.2 mmol), 3,4-diaminotoluene (0.15 mmol) and hydriodic acid (0.75 ml, 57 wt% in water, no stabiliser) in ethanol (6 ml) were placed in a 25 ml Teflon® vessel, sealed in a steel autoclave and heated at 140 °C for 24 h; with a controlled

ramp up rate of 1 ^{o}C min^{-1} and ramp down rate of 0.1 ^{o}C min^{-1}. After vacuum filtration and ethanol wash, orange plate crystals of compound 24 were obtained in a mixed phase product mixture. In this product mixture it was identified that the phase of red needle crystals was that of the previously described novel compound 22 alongside a phase of the here described orange plate crystals of compound 24 and a small amount of black crystalline material.

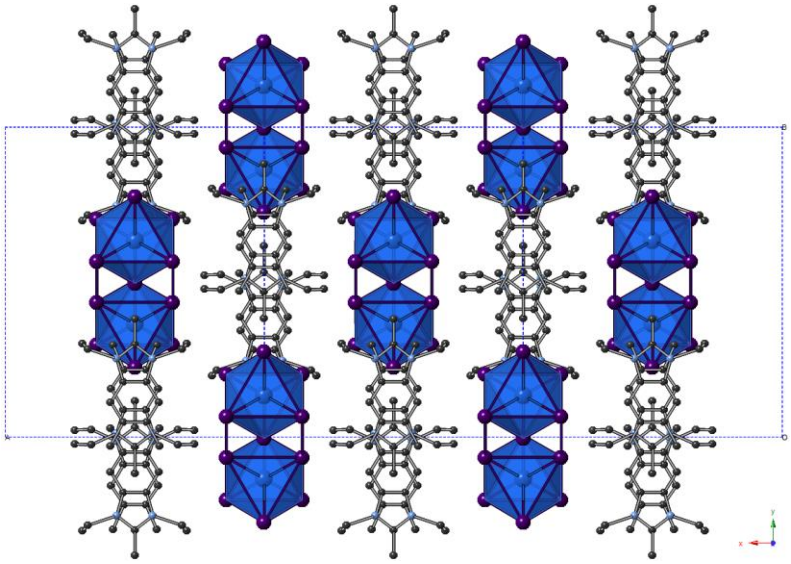

Figure 4.14 View along the *c*-axis of compound 24.
Legend: [BiI_6] octahedra shaded blue; Bi atoms (blue), I atoms (purple), C atoms (dark grey), N atoms (pale blue)

Within the structure, templated by monovalent 1,3-diethyl-2,5-dimethylbenzimidazolium cations, is an unusual anionic sublattice substructure made up of adjoining discrete units of $[Bi_2I_9]^{3-}$ clusters; analogous with the motif observed in previous compound 23. Each $[Bi_2I_9]^{3-}$ unit consists of two face-sharing octahedra with Bi-I bonding distances of 2.9537(16) - 3.2412(12) Å (Δ = 0.29 Å, Average = 3.10 Å); the longest of which (3.2326(15) Å, 3.2411(12) Å and 3.2412(12) Å) are found to be across the bridging iodides within the bioctahedral cluster. The monovalent cations are again found in clusters of three, counterbalancing the trivalent anionic units, with a separation distance of approximately 3.65 Å between cations. Therefore, each cation is related by an 180^{o} rotation on the *ab* plane, a +1.47 Å translation along the *b*-axis and a 3.65 Å translation along the *c*-axis; with again a degree of pi-stacking stabilising interactions between the cations in the group.

Each $[Bi_2I_9]^{3-}$ is linked to two adjacent $[Bi_2I_9]^{3-}$ units via four terminal-terminal I---I (I3-I3) interunit interactions; forming a pseudo-1D chain motif substructure unique to structures 23 and 24. To expand, two I3---I3 interactions occur in parallel, 4.34 Å apart, at each side of the

$[Bi_2I_9]^{3-}$ unit. The ribbon-like chains formed from these I---I interactions propagate the anionic network along the *c*-axis of the hybrid material. In comparison to compound 23, the length of the I---I interactions linking the units is observed to increase slightly from 4.27 Å to 4.36 Å.

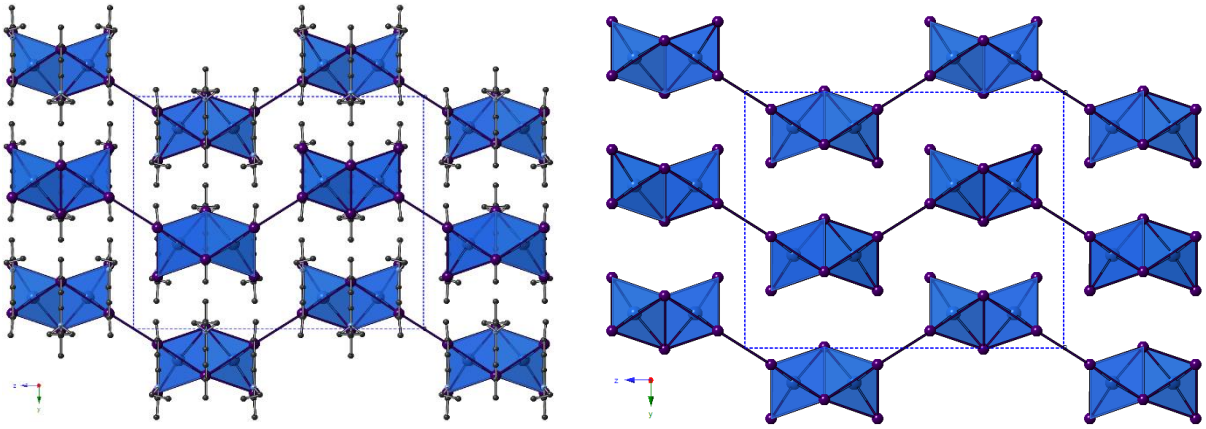

Figure 4.15 a-axis view of structure 24 showing the ribbon-like motif of adjoining $[Bi_2I_9]^{3-}$ units. 1,3-diethyl-2,5-dimethylbenzimidazolium cations shown in left image, removed for clarity in right. Legend: $[BiI_6]$ octahedra shaded blue; Bi atoms (blue), I atoms (purple), C atoms (dark grey), N atoms (pale blue)

A final structure refinement factor of 0.060, weighted refinement factor of 0.131 and goodness of fit of 1.07 was attained from the structural data analysis. Full crystallographic details of the structure solution and refinement are shown in Table 4.7 below.

Table 4.7 Crystal data for Compound 24	
Chemical formula	$3(C_{13}N_2H_{19})\cdot Bi_2I_9$
M_r	2170.02
Crystal system, space group	Orthorhombic, *Cmcm*
Temperature (K)	150
a, *b*, *c* (Å)	14.7835 (9), 17.6895 (8), 22.095 (3)
V (Å^3)	5778.2 (8)
Z	4
F(000)	3796
D_x (Mg m^{-3})	2.497
Radiation type	Mo *K*α
No. of reflections for cell measurement	2368
θ range (°) for cell measurement	3.8–25.3
μ (mm^{-1})	10.92

Crystal shape	Plate
Colour	Orange
Data collection	
Diffractometer	Xcalibur, EosS2 diffractometer
Radiation source	Enhance (Mo) X-ray Source
Monochromator	Graphite
Detector resolution (pixels mm^{-1})	16.1468
Scan method	ω scans
Absorption correction	Multi-scan *CrysAlis PRO*, Agilent Technologies, Version 1.171.37.35 (release 13-08-2014 CrysAlis171 .NET) (compiled Aug 13 2014,18:06:01) Empirical absorption correction using spherical harmonics, implemented in SCALE3 ABSPACK scaling algorithm.
T_{min}, T_{max}	0.760, 1.000
No. of measured, independent and observed [$I > 2\sigma(I)$] reflections	9709, 3541, 2072
R_{int}	0.036
θ values (°)	θ_{max} = 29.3, θ_{min} = 3.6
$(\sin\theta/\lambda)_{max}$ ($Å^{-1}$)	0.689
Range of *h*, *k*, *l*	*h* = -18→18, *k* = -24→14, *l* = -23→30
Refinement	
Refinement on	F^2
$R[F^2 > 2\sigma(F^2)]$, $wR(F^2)$, *S*	0.060, 0.131, 1.07
No. of reflections	3541
No. of parameters	160
No. of restraints	0
H-atom treatment	H-atom parameters not defined
	$w = 1/[\sigma^2(F_o^2) + (0.0152P)^2 + 238.8884P]$ where $P = (F_o^2 + 2F_c^2)/3$
$\Delta\rangle_{max}$, $\Delta\rangle_{min}$ (e $Å^{-3}$)	2.06, -1.24

Symmetry codes: (i) *x*, *y*, -*z*+1/2; (ii) -*x*, *y*, *z*; (iii) -*x*, *y*, -*z*+1/2.

Software: *CrysAlis PRO* 1.171.38.43 (Rigaku OD, 2015); cell refinement: *CrysAlis PRO* 1.171.38.43 (Rigaku OD, 2015); data reduction: *CrysAlis PRO* 1.171.38.43 (Rigaku OD, 2015); program(s) used to solve structure: *SHELXL2014*/7 (Sheldrick, 2014); program(s) used to refine structure: *SHELXL2014*/7 (Sheldrick, 2014); molecular graphics: Palmer, D. C. (2014). *CrystalMaker*. CrystalMaker Software Ltd, Begbroke, Oxfordshire, England.; software used to prepare material for publication: *WinGX* (Farrugia, 2012). *publCIF* [Westrip, S. P. (2010). *J. Appl. Cryst.*, **43**, 920-925] software used to generate tabulated data.

4.3 An exception to the trend - compound 25: 2,3-diaminophenazin-5-ium hexadecaiodotetrabismuthate

An unexpected hybrid structure was synthesised from a hydrothermal synthetic procedure with templating ions, determined from single-crystal X-ray analysis of the structure to be phenazine-2,3-benzenediammonium monocations. It stands as another example of a new templating organic agent synthesised in-situ from a precursor reagent, in this case from 1,2-benzenediamine under aqueous conditions at high pressure. From single-crystal X-ray diffraction analysis of the black single crystals of compound 25 it was determined that the structure crystallises in the triclinic crystal system, in space group *P-1*. Counterbalancing the cations is an anionic sublattice of hexadecaiodotetrabismuthate $[Bi_4I_{16}]^{4-}$ anions.

Compound 25

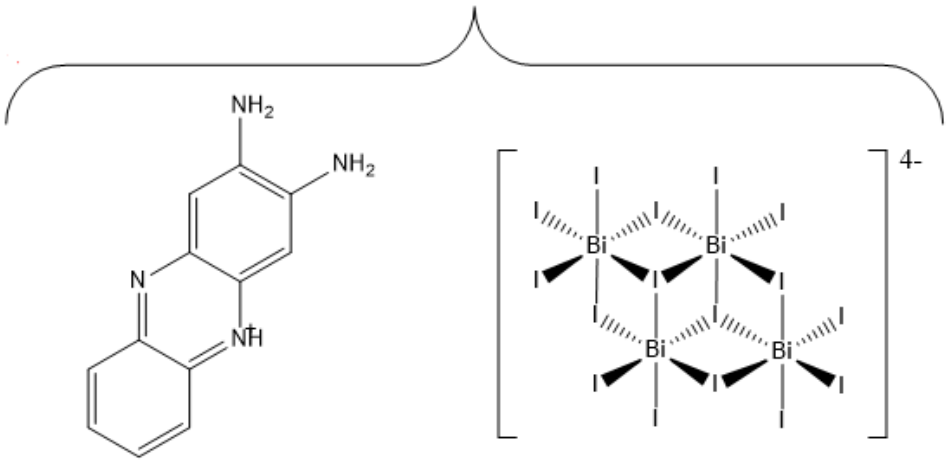

2,3-diaminophenazin-5-ium hexadecaiodotetrabismuthate

$4(C_{12}H_{11}N_4)\ Bi_4I_{16}$

The conjugated benzene ring compound is formed from homodimerisation fusing of two 1,2-benzenediamine molecules in the reaction mixture. It can be theorised that a highly reactive intermediate may form from the deprotonation of 1,2-diaminobenzene under the highly acidic and pressurised hydrothermal conditions to drive dimerization of the molecule in situ and form the templating monocationic 2,3-diaminophenazin-5-ium species.

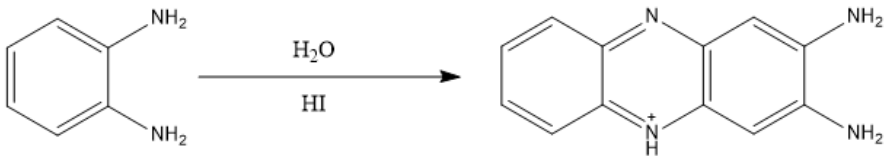

Scheme 4.7 Reaction scheme for the formation of templating cation 2,3-diaminophenzan-5-ium via an in-situ dimerisation reaction of precursor reagent 1,2-diaminobenzene

Compound 25 was formed in the reaction between bismuth chloride (0.2 mmol), 1,2-benzenediamine (0.15 mmol) and hydriodic acid (0.5 ml, 57 wt% in water, no stabiliser) in water (6 ml) placed in a 25 ml Teflon® vessel, sealed in a steel autoclave and heated at 140 ºC for 24 h; with a controlled ramp up rate of 1 ºC min^{-1} and ramp down rate of 0.1 ºC min^{-1}. After vacuum filtration and an aqueous wash black crystals of compound 25 were obtained in a mixed phase product mixture. In this product mixture it was identified that the phase of black crystals was that of the new compound 25 alongside a minor phase of a non-crystalline reddish/brown powder. Single-crystal X-ray diffraction data was collected from a selected black crystal.

A final structure refinement factor of 0.039, weighted refinement factor of 0.131 and goodness of fit of 1.12 was attained from the structural data analysis. Full crystallographic details of the structure solution and refinement are given in Table 4.8 below.

Table 4.8 Crystal data for Compound 25

Chemical formula	$4(C_{12}N_4H_{11})\cdot Bi_4I_{16}$
M_r	3711.38
Crystal system, space group	Triclinic, *P-1*
Temperature (K)	292
a, *b*, *c* (Å)	11.8856 (12), 13.1561 (13), 14.0216 (10)
α, β, γ (°)	70.264 (8), 79.492 (7), 64.968 (10)
V ($Å^3$)	1867.9 (3)
Z	1
F(000)	1628
D_x (Mg m^{-3})	3.303
Radiation type	Mo *K*α
No. of reflections for cell measurement	8627
θ range (°) for cell measurement	3.7–31.5
μ (mm^{-1})	16.05

Crystal shape	Needle
Colour	Black
Data collection	
Diffractometer	Xcalibur, EosS2 diffractometer
Radiation source	Enhance (Mo) X-ray Source
Monochromator	Graphite
Detector resolution (pixels mm^{-1})	16.1468
Scan method	ω scans
Absorption correction	Multi-scan *CrysAlis PRO*, Agilent Technologies, Version 1.171.37.35 (release 13-08-2014 CrysAlis171 .NET) (compiled Aug 13 2014,18:06:01) Empirical absorption correction using spherical harmonics, implemented in SCALE3 ABSPACK scaling algorithm.
T_{min}, T_{max}	0.392, 1.000
No. of measured, independent and observed [$I > 2\sigma(I)$] reflections	21138, 11346, 9280
R_{int}	0.027
θ values (°)	θ_{max} = 32.0, θ_{min} = 3.2
$(\sin\theta/\lambda)_{max}$ ($Å^{-1}$)	0.746
Range of *h*, *k*, *l*	*h* = -17→10, *k* = -18→17, *l* = -20→19
Refinement	
Refinement on	F^2
$R[F^2 > 2\sigma(F^2)]$, $wR(F^2)$, *S*	0.039, 0.131, 1.12
No. of reflections	11346
No. of parameters	374
No. of restraints	0
H-atom treatment	H-atom parameters constrained
Weighting scheme	$w = 1/[\sigma^2(F_o^2) + (0.065P)^2 + 6.0997P]$ where $P = (F_o^2 + 2F_c^2)/3$
$\Delta\rangle_{max}$, $\Delta\rangle_{min}$ (e $Å^{-3}$)	2.34, -2.25

Symmetry code: (i) -*x*+1, -*y*+2, -*z*+1.

Software: *CrysAlis PRO* 1.171.38.43 (Rigaku OD, 2015); cell refinement: *CrysAlis PRO* 1.171.38.43 (Rigaku OD, 2015); data reduction: *CrysAlis PRO* 1.171.38.43 (Rigaku OD, 2015); program(s) used to solve structure: *SHELXL2014*/7 (Sheldrick, 2014); program(s) used to refine structure: *SHELXL2014*/7 (Sheldrick, 2014); molecular graphics: Palmer, D. C. (2014). *CrystalMaker*. CrystalMaker Software Ltd, Begbroke, Oxfordshire, England.; software used to prepare material for publication: *WinGX* (Farrugia, 2012). *publCIF* [Westrip, S. P. (2010). *J. Appl. Cryst.*, **43**, 920-925] software used to generate tabulated data.

As previously mentioned, within the hybrid structure $[Bi_4I_{16}]^{4-}$ discrete anionic units counterbalance the highly conjugated singly charged cations. Symmetry equivalent octahedra across an inversion centre forms each unit in the structural model. Bi-I bonding distances are measured at 2.8562(7) - 3.3902(8) Å (Δ = 0.534 Å) for both Bi1-centred inner octahedra and outer Bi2-centred octahedra positions; with Bi…Bi distances of 5.06 Å (Bi1-Bi1), 4.73 Å and 4.83 Å (Bi1-Bi2). A similar distortion from regularity is observed in both octahedra sites with average I-Bi-I bond angles of 172.4^o (Bi1) and 172.5^o (Bi2).

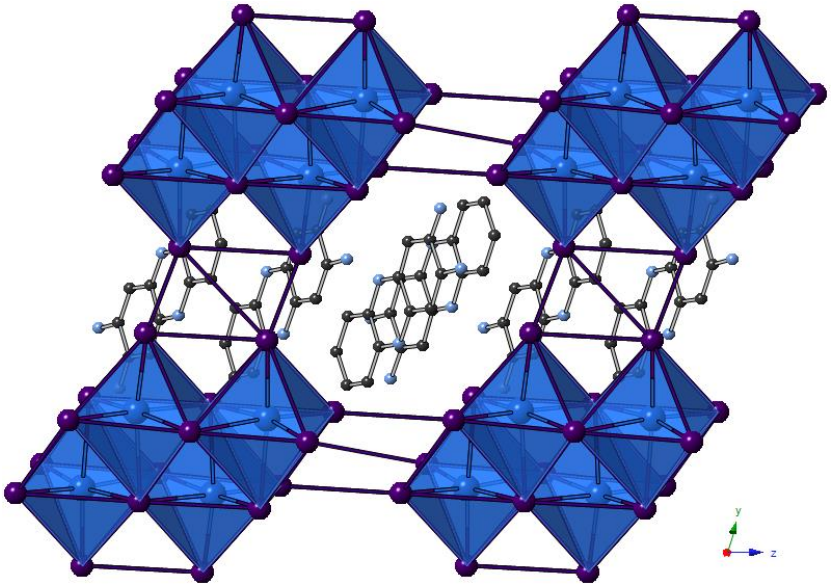

Figure 4.16 View along the *a*-axis of compound 25, 4($C_{12}N_4H_{11}$) Bi_4I_{16}.
Legend: [BiI_6] octahedra shaded blue; Bi atoms (blue), I atoms (purple), C atoms (dark grey), N atoms (pale blue). H atoms excluded for clarity.

A total of ten interunit $[Bi_4I_{16}]$----$[Bi_4I_{16}]$ interactions connect the structural units to six adjacent $[Bi_4I_{16}]^{4-}$ units within the structure to enhance electron mobility within the material. Interunit I---I interaction distances range from 3.70 - 4.39 Å (Δ = 0.69 Å); consisting of four repeating interactions measured at 3.70 Å (terminal I6-I8 terminal), four 4.33 Å (terminal I7-I9 terminal) connections and two 4.39 Å (terminal I10-I10 terminal) interactions.

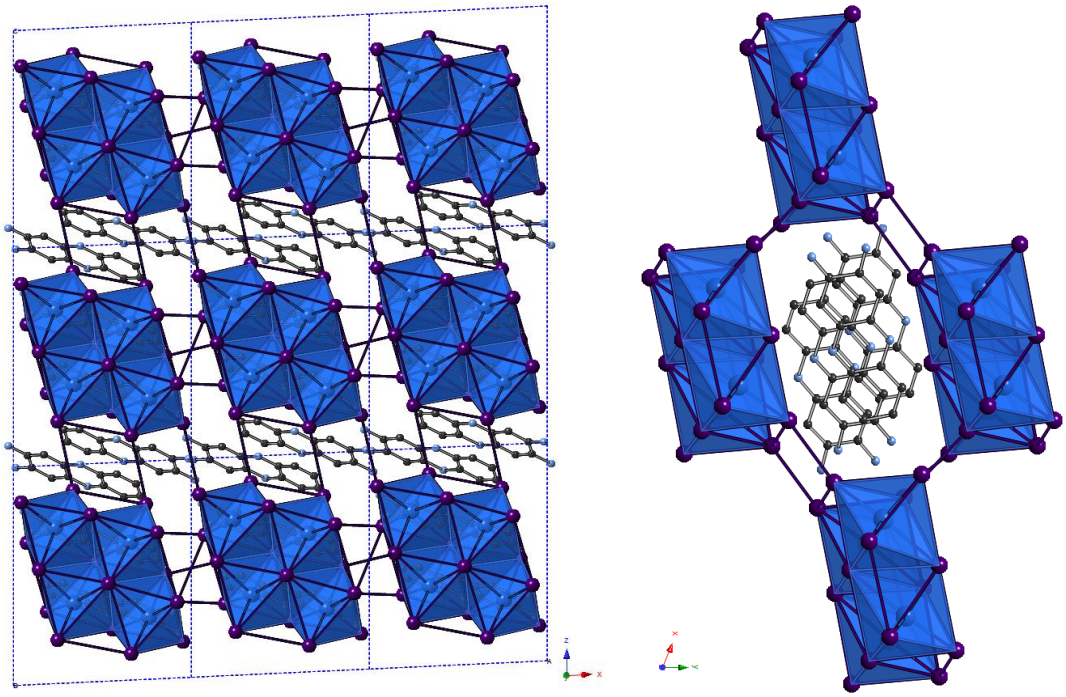

Figure 4.17 A wide *b*-axis view (left) and isolated *c*-axis stack view (right) of compound 25. Legend: [BiI_6] octahedra shaded blue; Bi atoms (blue), I atoms (purple), C atoms (dark grey), N atoms (pale blue). H atoms excluded for clarity.

Singly charged 2,3-diaminophenazin-5-ium cations stack and propagate through the hybrid structure zig-zagging in groups of four with AABB alternating orientations. Each cation is separated by 3.20 Å with pi-stacking between the highly conjugated planar ions likely increasing the stabilisation of the hybrid structure.

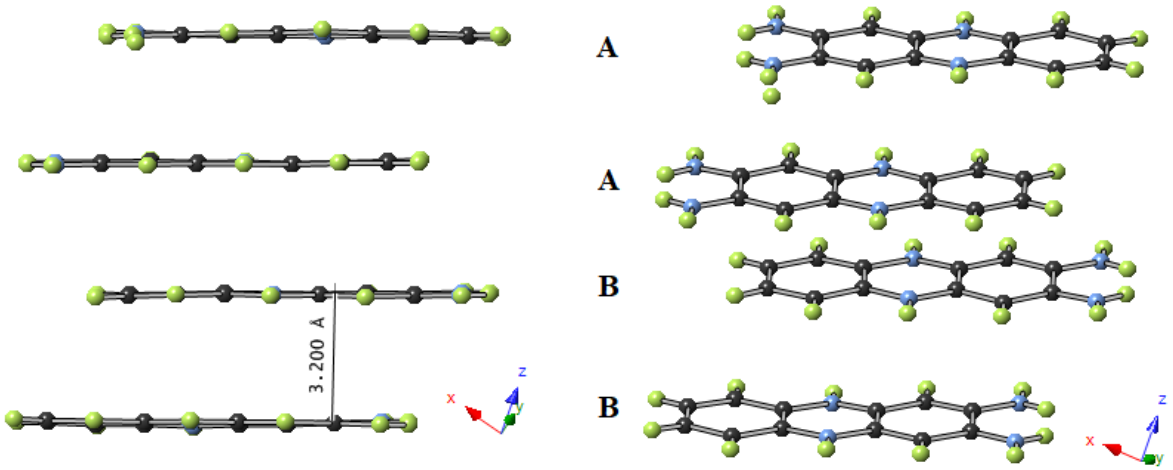

Figure 4.18 AABB stacking of 2,3-diaminophenzin-5-ium cations in compound 25. Legend: C atoms (dark grey), N atoms (pale blue), H atoms (light green)

4.4 Synthesis and structures from in-situ methylation

4.4.1 Compound 26: N^1,N^1,N^1,N^4,N^4,N^4-hexamethylbenzene-1,4-diaminium tetraiodobismuthate

Another line of investigation within the study of novel hybrid halometallate materials was to investigate varying the reaction solvent from the previously used ethanol to methanol. This was expected to lead to methylation of the benzene-diamine precursors and experiments were initiated with para-substituted ring systems to mirror the start point and progression of the ethanol/ethylation results.

Compound 26

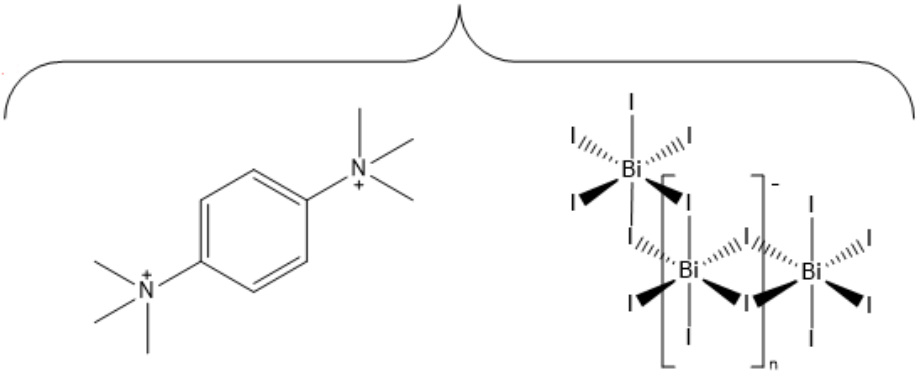

N^1,N^1,N^1,N^4,N^4,N^4-hexamethylbenzene-1,4-diaminium tetraiodobismuthate

$(C_{12}H_{22}N_2)\ 2(BiI_4)$

Primary diamine p-phenylenediamine was utilised as a precursor reagent in the solvothermal procedure carried out with the synthetic details as follows:

Reagents bismuth chloride (0.2 mmol), 1,4-benzenediamine (0.15 mmol), and hydriodic acid (1.00 ml, 57 wt% in water, no stabiliser) in methanol (6 ml) were placed in a 25 ml Teflon® vessel, sealed in a steel autoclave and heated at 140 ^{o}C for 24 h; with a controlled ramp up rate of 1 ^{o}C min^{-1} and ramp down rate of 0.1 ^{o}C min^{-1}. After vacuum filtration and methanol wash, thin orange plate crystals of compound 26 were obtained in a mixed phase product mixture. In this product mixture it was identified that the phase of thin orange plate crystals was of the novel compound 26 alongside a phase of dark orange/brown flaky crystalline material. Orange plate crystals of compound 26, isolated for examination by single-crystal X-ray diffraction analysis, were found to crystallise with triclinic symmetry in space group *P-1*.

A final structure refinement factor of 0.043, weighted refinement factor of 0.102 and goodness of fit of 1.03 was attained from the structural data analysis. Full crystallographic details of the structure solution and refinement are given in Table 4.9 below.

Table 4.9 Crystal data for Compound 26

Chemical formula	$C_{12}N_2H_{22}\cdot 2(BiI_4)$
M_r	1627.52
Crystal system, space group	Triclinic, *P-1*
Temperature (K)	150
a, *b*, *c* (Å)	7.7789 (6), 10.2077 (8), 11.1130 (11)
α, β, γ (°)	71.951 (8), 88.194 (7), 68.618 (7)
V (Å^3)	777.94 (12)
Z	1
F(000)	698
D_x (Mg m^{-3})	3.474
Radiation type	Mo *K*α
No. of reflections for cell measurement	2968
θ range (°) for cell measurement	3.8–28.3
μ (mm^{-1})	19.23
Crystal shape	Prismatic
Colour	Orange
Data collection	
Diffractometer	Xcalibur, EosS2 diffractometer
Radiation source	Enhance (Mo) X-ray Source
Monochromator	Graphite
Detector resolution (pixels mm^{-1})	8.0734
Scan method	ω scans
Absorption correction	Multi-scan *CrysAlis PRO*, Agilent Technologies, Version 1.171.37.35 (release 13-08-2014 CrysAlis171 .NET) (compiled Aug 13 2014,18:06:01) Empirical absorption correction using spherical harmonics, implemented in SCALE3 ABSPACK scaling algorithm.
T_{min}, T_{max}	0.595, 1.000
No. of measured, independent and observed [$I > 2\sigma(I)$] reflections	6941, 3554, 2921
R_{int}	0.042
θ values (°)	θ_{max} = 29.4, θ_{min} = 3.4
$(\sin\theta/\lambda)_{max}$ (Å^{-1})	0.691

Range of *h*, *k*, *l*	*h* = -10→9, *k* = -13→12, *l* = -12→14
Refinement	
Refinement on	F^2
$R[F^2 > 2\sigma(F^2)]$, $wR(F^2)$, *S*	0.043, 0.102, 1.03
No. of reflections	3554
No. of parameters	112
No. of restraints	0
H-atom treatment	H-atom parameters constrained
Weighting scheme	$w = 1/[\sigma^2(F_o^2) + (0.0398P)^2]$ where $P = (F_o^2 + 2F_c^2)/3$
$\Delta\rangle_{max}$, $\Delta\rangle_{min}$ (e Å^{-3})	2.34, -2.43

Symmetry codes: (i) -*x*+1, -*y*+1, -*z*+1; (ii) -*x*, -*y*+1, -*z*+1; (iii) -*x*, -*y*+2, -*z*.

Software: *CrysAlis PRO* 1.171.38.43 (Rigaku OD, 2015); cell refinement: *CrysAlis PRO* 1.171.38.43 (Rigaku OD, 2015); data reduction: *CrysAlis PRO* 1.171.38.43 (Rigaku OD, 2015); program(s) used to solve structure: *SHELXL2014*/7 (Sheldrick, 2014); program(s) used to refine structure: *SHELXL2014*/7 (Sheldrick, 2014); molecular graphics: Palmer, D. C. (2014). *CrystalMaker*. CrystalMaker Software Ltd, Begbroke, Oxfordshire, England.; software used to prepare material for publication: *WinGX* (Farrugia, 2012). *publCIF* [Westrip, S. P. (2010). *J. Appl. Cryst.*, **43**, 920-925] software used to generate tabulated data.

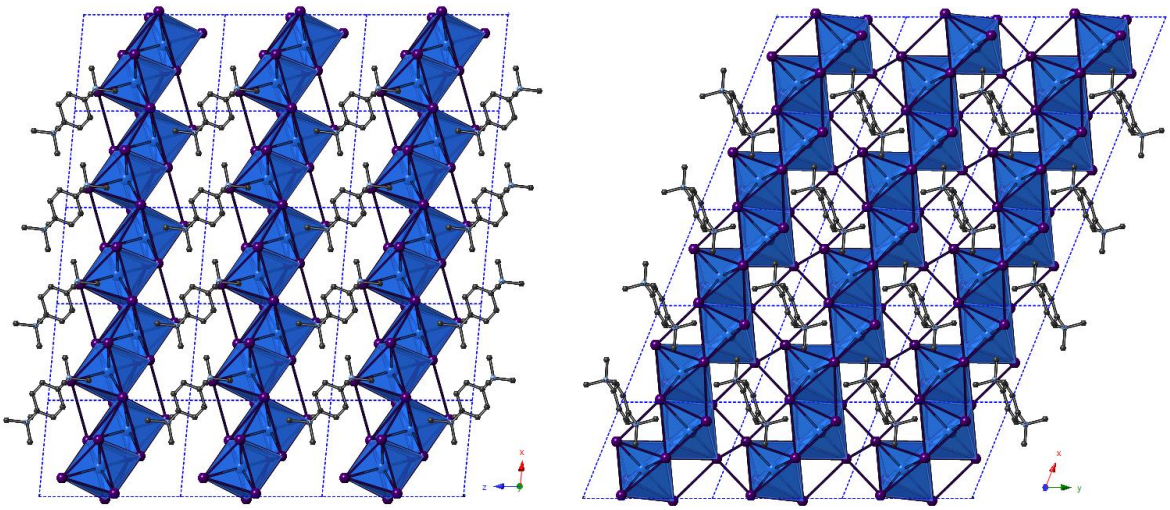

Figure 4.19 Graphic showing the *b*-axis view (left) and *c*-axis view (right) of compound 26, $(C_{12}N_2H_{22})$ $2(BiI_4)$ Legend: $[BiI_6]$ octahedra shaded blue; Bi atoms (blue), I atoms (purple), C atoms (dark grey), N atoms (pale blue). H atoms excluded for clarity.

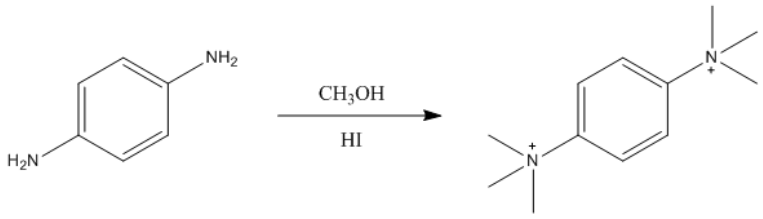

Scheme 4.8 Reaction scheme for the formation of templating cation N^1,N^1,N^1,N^4,N^4,N^4-hexamethylbenzene-1,4-diammonium via the alkylation of reagent 1,4-diaminobenzene

As seen in reaction scheme 4.8, primary diamine 1,4-benzenediamine undergoes methylation at both side groups under the acidic solvothermal procedure conditions to form hexamethylated quaternary diammonium cations. The in-situ formation of this dicationic species leads to the formation of a hybrid materials counterbalanced by previously seen one-dimensional $[BiI_4]^-_n$ chain structures.

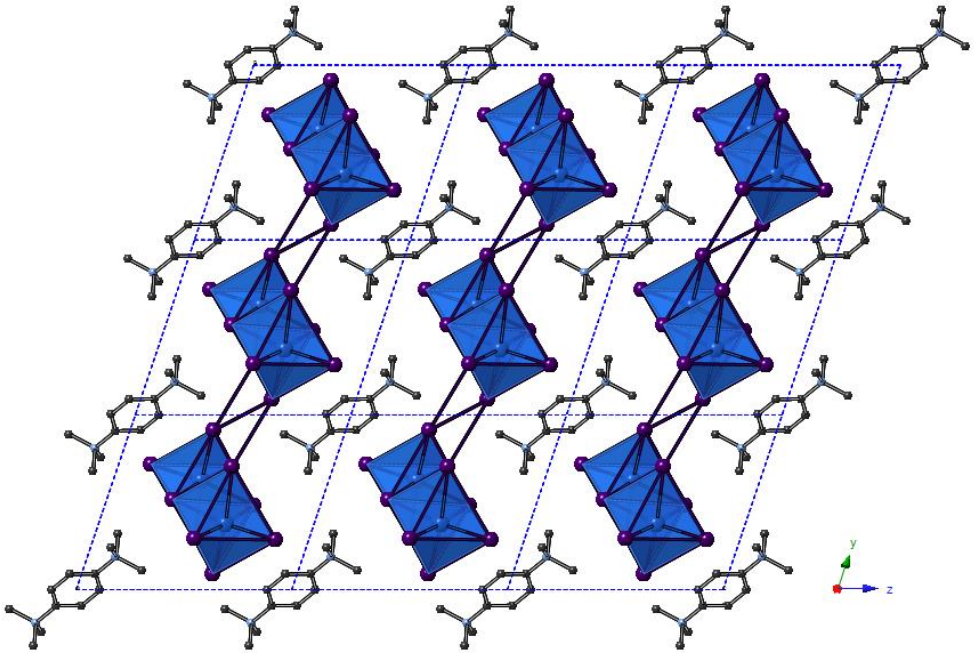

Figure 4.20 View along the *a*-axis of compound 26, $(C_{12}N_2H_{22})$ $2(BiI_4)$
Legend: $[BiI_6]$ octahedra shaded blue; Bi atoms (blue), I atoms (purple), C atoms (dark grey), N atoms (pale blue). H atoms excluded for clarity.

The structure of compound 26 is shown in Figures 4.19 and 4.20. Bi-I bonding distances in the anionic substructure range from 2.9062(9) - 3.3071(9) Å (Δ = 0.401 Å) and Bi-Bi distances of 4.63 Å and 4.67 Å. Three repeating I---I interactions occur along the chain axis repeating every 7.78 Å; the "groove" separation distance. The interactions interconnecting the bismuth iodide chains in the *b*-axis direction, opening up pathways for electronic pseudo-two dimensionality in the structure, measured at 4.28 Å (I3---I4)(x2) and 4.05 Å (I4---I4).

4.4.2 Compound 27: N,N,N-trimethylbenzaminium nonaiododibismuthate

Compound 27

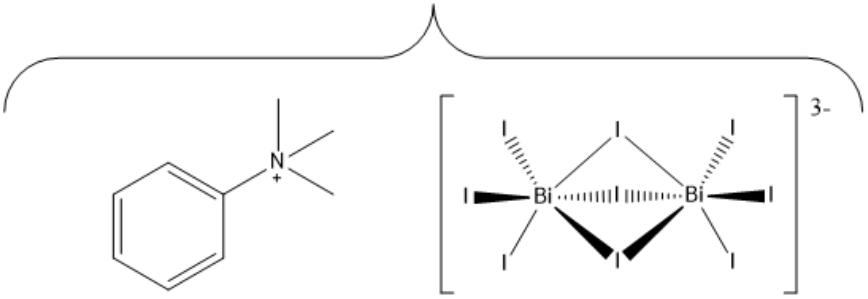

N,N,N-trimethylbenzenaminium nonaiododibismuthate
$3(C_9H_{14}N)\ Bi_2I_9$

In subsequent experimental studies, a closely related organic amine, aniline, was used as a mono-substituted equivalent of the previously studied para-, meta- and ortho-phenylenediamines. Solvents ethanol, methanol and water were used in different procedures in a series of solvothermal experiments but only the methylated organic component led to a stable hybrid compound product crystallising under the conditions investigated. Further variation of the solvothermal synthetic conditions by maximum temperature, reagent ratios, dwell time and cooling procedures could be expected to lead to the synthesis of comparable hybrid materials by ethylation or under aqueous hydrothermal reaction conditions.

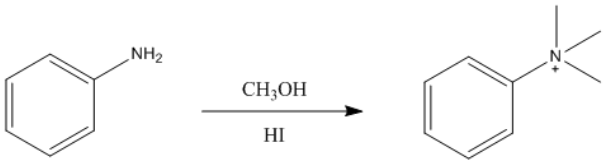

Scheme 4.9 Reaction scheme for the formation of templating cation N,N,N-trimethylbenzaminium via the alkylation of reagent aminobenzene

The reaction conditions used in the solvothermal procedure to obtain and isolate crystals of compound 27 were as follows:

Reagents bismuth chloride (0.2 mmol), aniline (0.15 mmol), and hydriodic acid (1.00 ml, 57 wt% in water, no stabiliser) in methanol (6 ml) were placed in a 25 ml Teflon® vessel, sealed in a steel autoclave and heated at 140 ^{o}C for 24 h; with a controlled ramp up rate of 1 ^{o}C min^{-1} and ramp down rate of 0.1 ^{o}C min^{-1}. After vacuum filtration and methanol wash, orange needle crystals of compound 27 were obtained in a mixed phase product mixture. In this product mixture it was identified that the phase of orange needle crystals was that of novel compound

27 alongside a phase of deep red needle crystals; from which a high-quality single-crystal required for full structural analysis could not be found.

A final structure refinement factor of 0.162, weighted refinement factor of 0.423 and goodness of fit of 1.16 was attained from the structural data analysis. Full crystallographic details of the structure solution and refinement are given in Table 4.10 below.

Table 4.10 Crystal data for Compound 27	
Chemical formula	$3(C_9H_{14}N)\cdot Bi_2I_9$
M_r	1968.75
Crystal system, space group	Monoclinic, *P*2/*m*
Temperature (K)	150
a, *b*, *c* (Å)	9.8611 (3), 34.8853 (14), 14.3734 (5)
β (°)	93.670 (3)
V (Å^3)	4934.4 (3)
Z	4
F(000)	3060
D_x (Mg m^{-3})	2.429
Radiation type	Mo *K*α
No. of reflections for cell measurement	11581
θ range (°) for cell measurement	2.5–29.0
μ (mm^{-1})	12.76
Crystal shape	Needle
Colour	Orange
Data collection	
Diffractometer	SuperNova, Dual, Cu at zero, EosS2 diffractometer
Radiation source	SuperNova (Mo) X-ray Source
Monochromator	Mirror
Detector resolution (pixels mm^{-1})	16.2300
Scan method	ω scans
Absorption correction	Multi-scan *CrysAlis PRO*, Agilent Technologies, Version 1.171.37.35 (release 13-08-2014 CrysAlis171 .NET) (compiled Aug 13 2014,18:06:01) Empirical absorption correction using spherical harmonics, implemented in SCALE3 ABSPACK scaling algorithm.
T_{min}, T_{max}	0.644, 1.000
No. of measured, independent and observed [$I > 2\sigma(I)$] reflections	23061, 11374, 10372

R_{int}	0.035
θ values (°)	θ_{max} = 29.4, θ_{min} = 2.2
$(\sin\theta/\lambda)_{max}$ (Å^{-1})	0.691
Range of *h*, *k*, *l*	*h* = -13→9, *k* = -47→30, *l* = -19→18
Refinement	
Refinement on	F^2
$R[F^2 > 2\sigma(F^2)]$, $wR(F^2)$, *S*	0.162, 0.423, 1.16
No. of reflections	11374
No. of parameters	180
No. of restraints	0

Software: *CrysAlis PRO* 1.171.38.43 (Rigaku OD, 2015); cell refinement: *CrysAlis PRO* 1.171.38.43 (Rigaku OD, 2015); data reduction: *CrysAlis PRO* 1.171.38.43 (Rigaku OD, 2015); program(s) used to solve structure: *SHELXL2014*/7 (Sheldrick, 2014); program(s) used to refine structure: *SHELXL2014*/7 (Sheldrick, 2014); molecular graphics: Palmer, D. C. (2014). *CrystalMaker*. CrystalMaker Software Ltd, Begbroke, Oxfordshire, England.; software used to prepare material for publication: *WinGX* (Farrugia, 2012). *publCIF* [Westrip, S. P. (2010). *J. Appl. Cryst.*, **43**, 920-925] software used to generate tabulated data.

From the structural analysis, although not of the highest quality, it was determined that the structure of the hybrid compound formed consisted of an anionic substructure of trivalent face-sharing bioctahedral $[Bi_2I_9]^{3-}$ units counterbalanced by N,N,N-trimethylbenzaminium cations formed in-situ in the reaction from the threefold methylation of the primary precursor amine to a quaternary ammonium cation. Similar discrete units were found and discussed for compounds 23 and 24 where it was found that interconnections between the units formed a wave-like chain formation through the structure. Here, however, the shortest interunit distance is measured to be approximately 5.96 Å and so no determinable significant I---I interactions between the units are present in compound 27. As a result, the hybrid material is an example of a true zero-dimensional hybrid structure.

A bioctahedral $[Bi_2I_9]^{3-}$ unit, with four symmetry equivalent positions in the unit cell, is formed of Bi-I bonding interactions with a range of 2.949(3) - 3.256(3) Å (Δ = 0.307 Å) (Bi1-centred) and 2.935(3) - 3.305(3) Å (Δ = 0.370 Å) (Bi2-centred) respectively; with a Bi…Bi separation distance of 4.15 Å. Forming the face-sharing interface within the bioctahedron are three Bi-I-Bi links with bonding angles of 79.3°, 80°, and 80.2°. As a measure of distortion from regularity, it can be observed that I-Bi-I angles deviate from 180° by an average of 9° (Bi1-centred) and 8.2° (Bi2-centred).

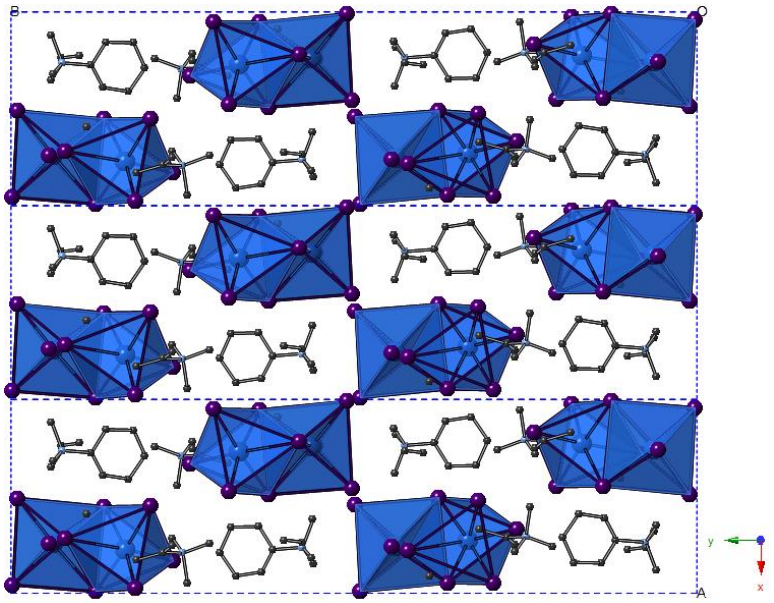

Figure 4.21 View along the *c*-axis of compound 27, 3($C_9H_{14}N$) Bi_2I_9. Legend: [BiI_6] octahedra shaded blue; Bi atoms (blue), I atoms (purple), C atoms (dark grey), N atoms (pale blue).

Each unit cell contains four discrete $[Bi_2I_9]^{3-}$ units totalling a 12- anionic charge. Due to disorder in the structure solution and refinement of the organic cations within the hybrid structure, four fully modelled (C_9N^+) N,N,N-trimethylbenzaminium cations have been identified alongside four partially modelled (C_6N^+) structural components. Also, three disordered carbon atom positions, repeating four times each within the cell, are predicted to be a part of the missing four remaining monocations in the electron density map to make up the remaining 4(+) charge currently missing from the structural model to balance the hybrid salt structure to a state of stable charge neutrality.

4.4.3 Compound 28: N,N,N,4-tetramethylbenzaminium nonaiododibismuthate

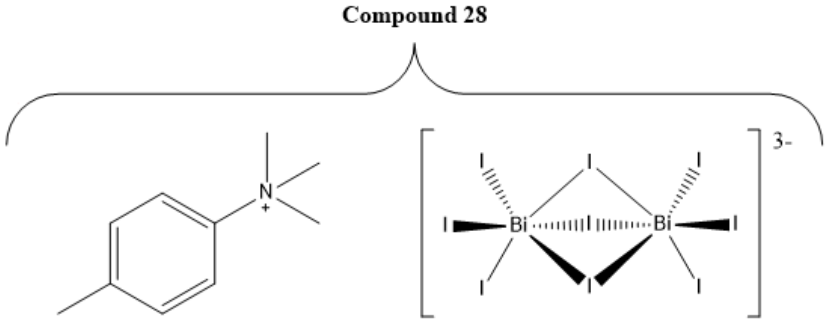

N,N,N,4-tetramethylbenzenaminium nonaiododibismuthate
$3(C_{10}H_{16}N)\ Bi_2I_9$

Subsequently in the study, p-toluidine was used as a comparison to the aniline-based equivalent hybrid structure previously described as compound 27. Again, reaction procedures were undertaken in different reaction mediums, ethanol, methanol and water. However, the comparable methylated structure, similar to the process for previously described structure 27, was the procedure found to produce a stable hybrid structure under the conditions investigated.

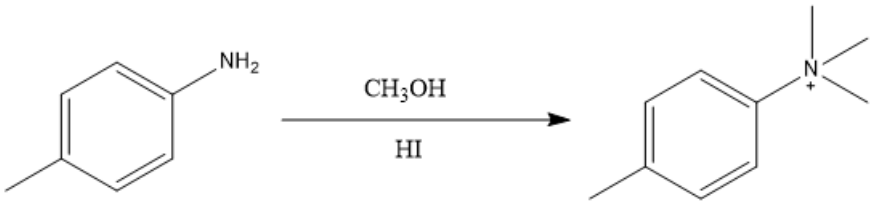

Scheme 4.10 Reaction scheme for the formation of templating cation N,N,N,4-tetramethylbenzenaminium via the alkylation of reagent p-toluidine

Crystals of compound 28 were isolated from a solvothermal synthesis procedure using p-toluidine as the precursor reagent as described next. Reagents bismuth chloride (0.2 mmol), p-toluidine (0.15 mmol), and hydriodic acid (0.75 ml, 57 wt% in water, no stabiliser) in methanol (6 ml) were placed in a 25 ml Teflon® vessel, sealed in a steel autoclave and heated at 140 ^{o}C for 24 h; with a controlled ramp up rate of 1 ^{o}C min^{-1} and ramp down rate of 0.1 ^{o}C min^{-1}. After vacuum filtration and methanol wash, orange needle crystals of compound 28 were obtained in a mixed phase product mixture. In this product mixture it was identified that the phase of orange needle crystals was of the novel compound 28, crystallising in triclinic space group *P-1*, alongside a phase of orange non-crystalline powder. One orange needle was selected for analysis using single-crystal X-ray diffraction.

A final structure refinement factor of 0.138, weighted refinement factor of 0.349 and goodness of fit of 1.15 was attained from the structural data analysis. Full crystallographic details of the structure solution and refinement are given in Table 4.11 below.

Table 4.11 Crystal data for Compound 28	
Chemical formula	$C_{30}H_{48}Bi_2I_9N_3$
M_r	2010.83
Crystal system, space group	Triclinic, *P-1*
Temperature (K)	150
a, *b*, *c* (Å)	9.7286 (2), 16.1917 (5), 17.1512 (7)
α, β, γ (°)	102.615 (3), 92.353 (2), 101.483 (2)
V (Å^3)	2573.59 (15)
Z	2
F(000)	3368
D_x (Mg m^{-3})	5.077
Radiation type	Mo *K*α
No. of reflections for cell measurement	18712
θ range (°) for cell measurement	2.5–31.6
μ (mm^{-1})	25.67
Crystal shape	Needle
Colour	Orange
Data collection	
Diffractometer	SuperNova, Dual, Cu at zero, EosS2 diffractometer
Radiation source	SuperNova (Mo) X-ray Source
Monochromator	Mirror
Detector resolution (pixels mm^{-1})	16.2300
Scan method	ω scans
Absorption correction	Multi-scan *CrysAlis PRO*, Agilent Technologies, Version 1.171.37.35 (release 13-08-2014 CrysAlis171 .NET) (compiled Aug 13 2014,18:06:01) Empirical absorption correction using spherical harmonics, implemented in SCALE3 ABSPACK scaling algorithm.
T_{min}, T_{max}	0.195, 1.000
No. of measured, independent and observed [$I > 2\sigma(I)$] reflections	51725, 16355, 12987
R_{int}	0.057
θ values (°)	θ_{max} = 32.1, θ_{min} = 2.2
$(\sin\theta/\lambda)_{max}$ (Å^{-1})	0.747

Range of *h*, *k*, *l*	h = -14→13, k = -24→23, l = -24→25
Refinement	
Refinement on	F^2
$R[F^2 > 2\sigma(F^2)]$, $wR(F^2)$, S	0.138, 0.349, 1.15
No. of reflections	16355
No. of parameters	380
No. of restraints	0
H-atom treatment	H-atom parameters constrained
	$w = 1/[\sigma^2(F_o^2) + (0.0512P)^2 + 699.931P]$ where $P = (F_o^2 + 2F_c^2)/3$
$\Delta\rangle_{max}$, $\Delta\rangle_{min}$ (e Å^{-3})	6.49, -5.50

Software: *CrysAlis PRO* 1.171.38.43 (Rigaku OD, 2015); cell refinement: *CrysAlis PRO* 1.171.38.43 (Rigaku OD, 2015); data reduction: *CrysAlis PRO* 1.171.38.43 (Rigaku OD, 2015); program(s) used to solve structure: *SHELXL2014*/7 (Sheldrick, 2014); program(s) used to refine structure: *SHELXL2014*/7 (Sheldrick, 2014); molecular graphics: Palmer, D. C. (2014). *CrystalMaker*. CrystalMaker Software Ltd, Begbroke, Oxfordshire, England.; software used to prepare material for publication: *WinGX* (Farrugia, 2012). *publCIF* [Westrip, S. P. (2010). *J. Appl. Cryst.*, **43**, 920-925] software used to generate tabulated data.

The structure of compound 28 (Figure 4.22), again determined at moderate quality, consists of an anionic substructure of trivalent $[Bi_2I_9]^{3-}$ nonaiododibismuthate anions with counterbalancing monocations of N,N,N,4-tetramethylbenzaminium. This organic species was formed from the related trimethylation of precursor reagent, p-toluidine, in-situ under the highly acidic solvothermal reaction conditions. Comparably to structure 27, the $[Bi_2I_9]$-$[Bi_2I_9]$ interunit distance is only reduced to approximately 4.71 Å and therefore additional electronic connectivity between the discrete anionic units is likely very weak.

Each anionic unit is formed of bismuth iodide octahedra with Bi-I bonding distances of 2.954(2) - 3.225(2) Å (Δ = 0.271 Å) (Bi1-centred) and 2.898(2) - 3.286(2) Å (Δ = 0.388 Å) (Bi2-centred); with an intraunit Bi…Bi separation distance of 4.16 Å. Across the face-sharing bioctahedron interface Bi-I-Bi angles are measured at 79.5°, 80.1° and 80.7° with some irregularity observed in the average deviation from 180° for the I-Bi-I internal bonding angles; measured at 6.8° (Bi1-centred) and 10.1° (Bi2-centred).

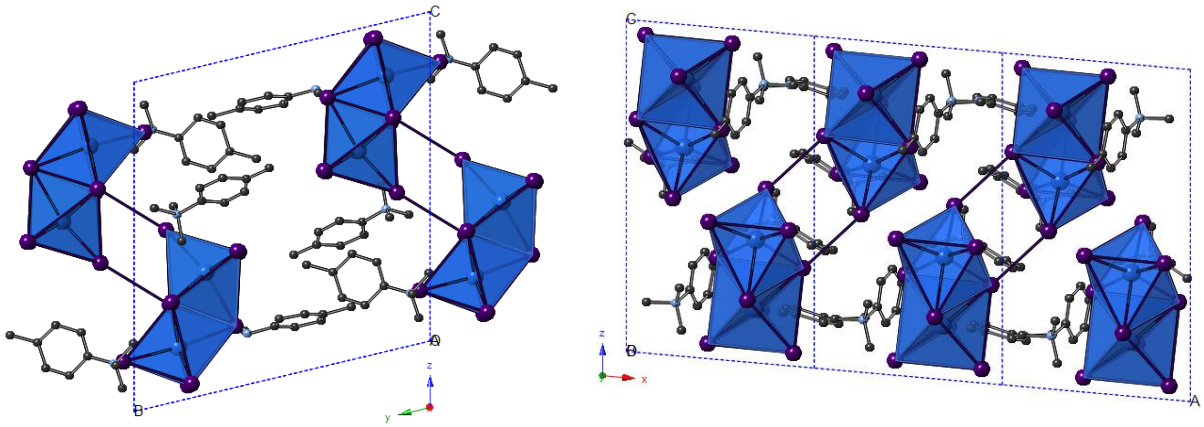

Figure 4.22 View of the *a*-axis (left) and *b*-axis (right) of compound 28.
Legend: $[BiI_6]$ octahedra shaded blue; Bi atoms (blue), I atoms (purple), C atoms (dark grey), N atoms (pale blue). H atoms excluded for clarity.

In compound 28, each unit cell contains a symmetry equivalent pair of $[Bi_2I_9]^{3-}$ anions totalling a negative charge of 6(-). Again, in the structure solution and refinement of the data obtained it was difficult to fully map the electron density of the organic cations within the cell. Four out of six ($C_{10}N^+$) N,N,N,4-tetramethylbenzaminium cations were fully modelled in final refinement, however, two of the cations which make up the remaining cationic charge to obtain charge neutrality were partially modelled as (C_8N^+) with two missing carbon positions on the charged nitrogen atom.

4.4.4 Compound 29: 1,3-dimethylbenzimidazol-3-ium tetraiodobismuthate

Compound 29

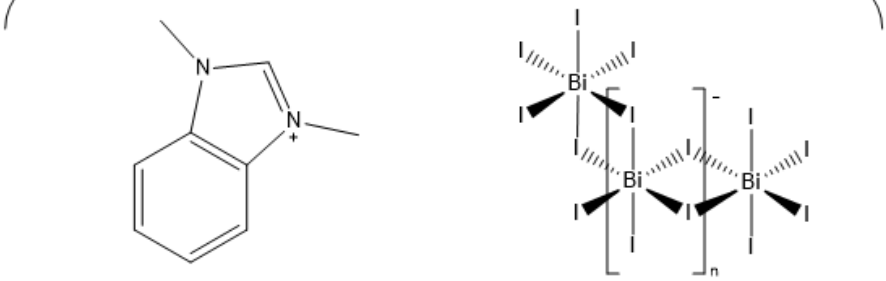

1,3-dimethyl-1*H*-benzo[*d*]imidazol-3-ium tetraiodobismuthate
$(C_9H_{11}N_2)\ BiI_4$

Following the preceding investigations on the effects of alkylation on para- and meta-substituted diamine group positions of benzene ring based organic cations, it was logical to apply a similar technique utilising the ortho-substituted equivalent benzene diamine as a precursor reagent. Due to the proximity of the two amino groups, steric effects would be likely to play a significant role in determining the templating species formed. Here, 1,2-diaminobenzene was utilised as a precursor reagent in the solvothermal reaction mixture. Reacting with methyl iodide formed in-situ under the highly acidic conditions in methanol, 1,2-diaminobenzene was found to undergo an initial ring closing reaction to form an intermediary benzimidazolium structural unit before undergoing further methylation of each of the nitrogen positions to form the templating species (see Scheme 4.11) of the hybrid structure crystallised from the reaction mixture; 1,3-methylbenzimidazolium iodobismuthate.

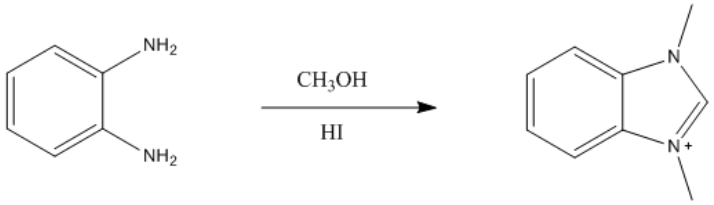

Scheme 4.11 Reaction scheme for the formation of templating cation 1,3-dimethylbenzimidazolium via the alkylation of reagent 1,2-diaminobenzene

In the synthetic procedure, reagents bismuth chloride (0.2 mmol), 1,2-benzenediamine (0.15 mmol), and hydriodic acid (1.00 ml, 57 wt% in water, no stabiliser) in methanol (6 ml) were placed in a 25 ml Teflon® vessel, sealed in a steel autoclave and heated at 140 ^{o}C for 24 h; with a controlled ramp up rate of 1 ^{o}C min^{-1} and ramp down rate of 0.1 ^{o}C min^{-1}.

After vacuum filtration and methanol wash deep red crystals of compound 29 were obtained in a mixed phase product mixture. In this product mixture it was identified that the phase of deep-red crystals was of the novel compound 29 alongside a phase of reddish/brown powder.

A final structure refinement factor of 0.030, weighted refinement factor of 0.064 and goodness of fit of 1.10 was attained from the structural data analysis. Full crystallographic details of the structure solution and refinement are given in Table 4.12 below.

Table 4.12 Crystal data for Compound 29

Chemical formula	$C_9H_{11}N_2 \cdot BiI_4$
M_r	863.80
Crystal system, space group	Triclinic, *P-1*
Temperature (K)	292
a, *b*, *c* (Å)	7.5533 (3), 10.7486 (5), 11.4658 (4)
α, β, γ (°)	80.088 (4), 79.679 (3), 72.107 (4)
V (Å^3)	864.68 (7)
Z	2
F(000)	748
D_x (Mg m^{-3})	3.318
Radiation type	Mo *K*α
No. of reflections for cell measurement	5160
θ range (°) for cell measurement	3.9–31.4
μ (mm^{-1})	17.32
Crystal shape	Prismatic
Colour	Red
Data collection	
Diffractometer	Xcalibur, EosS2 diffractometer
Radiation source	Enhance (Mo) X-ray Source
Monochromator	Graphite
Detector resolution (pixels mm^{-1})	8.0734
Scan method	ω scans
Absorption correction	Multi-scan *CrysAlis PRO*, Agilent Technologies, Version 1.171.37.35 (release 13-08-2014 CrysAlis171 .NET) (compiled Aug 13 2014,18:06:01) Empirical absorption correction using spherical harmonics, implemented in SCALE3 ABSPACK scaling algorithm.
T_{min}, T_{max}	0.272, 1.000
No. of measured, independent and	9450, 5244, 4683

observed [$I > 2\sigma(I)$] reflections	
R_{int}	0.022
θ values (°)	θ_{max} = 31.9, θ_{min} = 3.6
$(\sin\theta/\lambda)_{max}$ (Å^{-1})	0.743
Range of *h*, *k*, *l*	*h* = -10→10, *k* = -15→15, *l* = -16→15
Refinement	
Refinement on	F^2
$R[F^2 > 2\sigma(F^2)]$, $wR(F^2)$, *S*	0.030, 0.064, 1.10
No. of reflections	5244
No. of parameters	145
No. of restraints	0
H-atom treatment	H-atom parameters constrained
Weighting scheme	$w = 1/[\sigma^2(F_o^2) + (0.0179P)^2 + 2.1173P]$ where $P = (F_o^2 + 2F_c^2)/3$
$\Delta\rangle_{max}$, $\Delta\rangle_{min}$ (e Å^{-3})	1.46, -1.24

Symmetry codes: (i) -*x*, -*y*, -*z*; (ii) -*x*+1, -*y*, -*z*.

Software: *CrysAlis PRO* 1.171.38.43 (Rigaku OD, 2015); cell refinement: *CrysAlis PRO* 1.171.38.43 (Rigaku OD, 2015); data reduction: *CrysAlis PRO* 1.171.38.43 (Rigaku OD, 2015); program(s) used to solve structure: *SHELXL2014*/7 (Sheldrick, 2014); program(s) used to refine structure: *SHELXL2014*/7 (Sheldrick, 2014); molecular graphics: Palmer, D. C. (2014). *CrystalMaker*. CrystalMaker Software Ltd, Begbroke, Oxfordshire, England.; software used to prepare material for publication: *WinGX* (Farrugia, 2012). *publCIF* [Westrip, S. P. (2010). *J. Appl. Cryst.*, **43**, 920-925] software used to generate tabulated data.

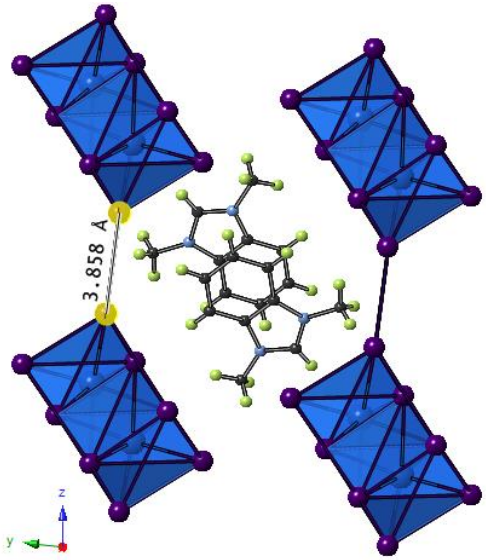

Figure 4.23 View along the *a*-axis of structure 29, ($C_9H_{11}N_2$) BiI_4.
Legend: [BiI_6] octahedra shaded blue; Bi atoms (blue), I atoms (purple), C atoms (dark grey), N atoms (pale blue), H atoms (pale green)

Compound 29 contains edge connecting octahedral [BiI_6] units in a one-dimensional $[BiI_4]^-_n$ chain structural motif. Interlinking I---I interactions between $[BiI_4]^-_n$ chains extend the anionic network into a pseudo-two-dimensional layered sublattice. These interactions occur in line with the *c*-axis measuring at 3.86 Å; repeating every 7.53 Å along the chain axis (Figure 4.23) and are the only repeating interchain connections within the anionic sublattice of the structure. The closest interchain distance in the *b*-axis direction to potentially increase the electronic dimensionality of the material with further connections is measured at 4.78 Å; this is considerably outside of the range of interaction based on twice the Shannon ionic radius of the iodide ions (220 pm) and therefore discounted as an associated interunit I---I link. Interlaced within the pseudo-2D layered network are charge balancing templating counterions of 1,3-dimethylbenzimidazolium. Propagating along *a*-axis in parallel with their anionic chain counterparts, the singly-charged cations can be considered as repeating stacked pairs for, as seen in figure 4.24, the more closely related "paired" cations are associated to each other by a separation distance of 3.3 Å with respect to the plane of each ion and similarly mimic the staggered arrangement of the $[BiI_4]^-_n$ chains. The cations are seen to be offset from one another by a rotation of 180° and a translation within the plane of the ion of approximately 1.5 Å along the length of the cation.

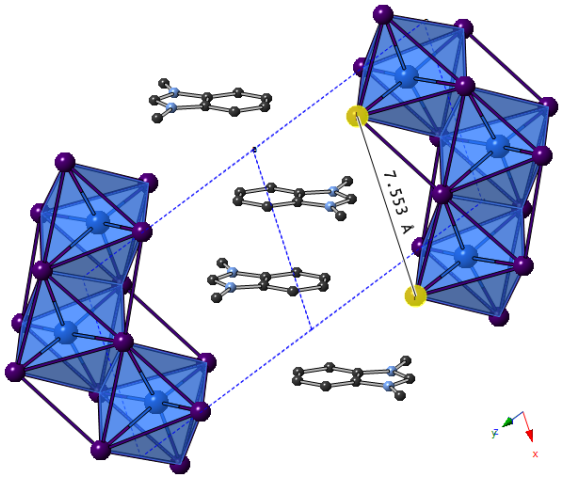

Figure 4.24 Interleaving of stacked cations towards the grooves of the $[BiI_4]_n^-$ chain motif. Legend: $[BiI_6]$ octahedra shaded blue; Bi atoms (blue), I atoms (purple), C atoms (dark grey), N atoms (pale blue), H atoms excluded for clarity

As a result, the methylated imidazolium part of the cation, carrying the single charge, is directed toward the anionic chain; interleaving within the grooves of the chain linked octahedra (Figure 4.24). Consequently from this arrangement there is likely to be a degree pi-pi stacking stabilisation between the slightly offset unsaturated benzene ring systems of each cation. The association of each cation with its secondary adjacent cation within the stack outside of the "pair" shows an increased offset and therefore weaker interlinking interaction. To expand, the ions are again related by a separation distance 3.3 Å and a rotation of 180° with respect to the plane of the ions with the addition of an increased translation distance of 3.5 Å in the direction of the length of the cation plus a translational offset perpendicular to the aforementioned translation of 2.0 Å. As a result of this increased misalignment of stacking through the sublattice channel, the interrelationship here is expected to be much weaker than the "paired" positions as only the pi-orbitals of carbon atoms C(4) and C(7) within the benzene-ring system are in close enough proximity for pi-pi interactions. The irregular hexagonal shaped channel along the *a*-axis, as seen in Figure 4.25, in which the templating cations are retained within in the hybrid structure is measured to be approximately 7.8 Å x 7.6 Å x 3.9 Å in size. Within the $[BiI_6]$ octahedra M-I bonding ranges from 2.9192(4) - 3.2748(4) Å (Δ = 0.356 Å), with the shortest bonds to the terminal iodide positions I(1) and I(4). The earlier mentioned repeating interchain interaction of 3.858 Å between chains to form the pseudo-2D layers occur from position I(1)-I(1)* with the shortest M-I bond to the central bismuth position of 2.9192(4) Å. Within the octahedra opposite I-Bi-I angles have an average deviation from regularity (180°) of approximately 6.8°; with Bi-I-Bi angles across the octahedra edge connections of 92.7° and 93.0°.

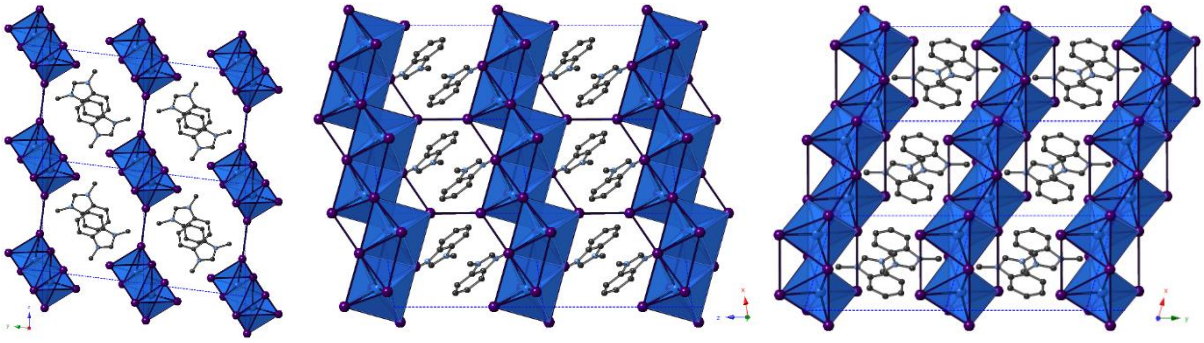

Figure 4.25 Structure 29 *a*-axis view (left), *b*-axis view (centre), *c*-axis view (right). Legend: [BiI_6] octahedra shaded blue; Bi atoms (blue), I atoms (purple), C atoms (dark grey), N atoms (pale blue), H atoms excluded for clarity.

4.4.5 Compound 30: 1,3,5-trimethylbenzimidazol-3-ium tetraiodobismuthate

Compound 30

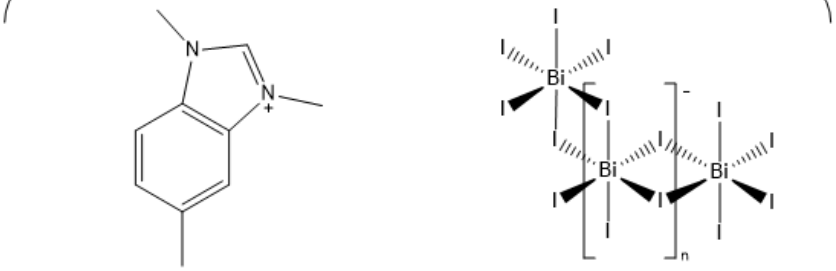

1,3,5-trimethyl-1*H*-benzo[*d*]imidazol-3-ium tetraiodobismuthate

$(C_{10}H_{13}N_2)\ BiI_4$

In response to the earlier described investigation into the effects of in-situ methylation on the ortho-substituted ring based precursor reagent, 1,2-diaminobenzene, it was considered of interest to look at what structural effects would occur on the hybrid material if the cation was slightly modified. To increase the cation size the precursor reagent 3,4-diaminotoluene was utilised in the synthesis.

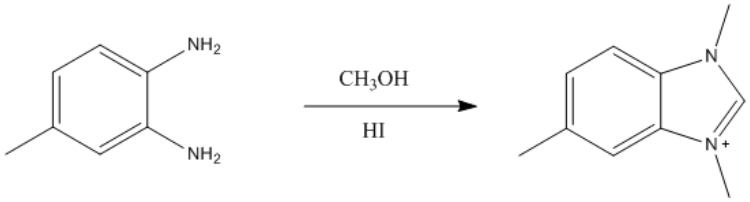

Scheme 4.12 Reaction scheme for the formation of templating cation 1,3,5-trimethylbenzimidazolium via the alkylation of reagent 3,4-diaminotoluene

Crystals of compound 30 were isolated from a solvothermal synthesis procedure using 3,4-diaminotoluene as the precursor reagent. Reagents bismuth chloride (0.2 mmol), 3,4-diaminotoluene (0.15 mmol), and hydriodic acid (1.00 ml, 57 wt% in water, no stabiliser) in methanol (6 ml) were placed in a 25 ml Teflon® vessel, sealed in a steel autoclave and heated at 140 °C for 24 h; with a controlled ramp up rate of 1 °C min^{-1} and ramp down rate of 0.1 °C min^{-1}. After vacuum filtration and methanol wash, deep red needle crystals of compound 30 were obtained in a mixed phase product mixture. In this product mixture it was identified that the phase of deep red needle crystals was of the novel compound 30, alongside a minor phase of orange powder. Full crystallographic details of the structure solution from single-crystal X-ray diffraction data and refinement are given in Table 4.13 below. A final structure refinement factor of 0.061, weighted refinement factor of 0.109 and goodness of fit of 1.11 was attained from the structural data analysis.

Table 4.13 Crystal data for Compound 30

Chemical formula	$C_{10}H_{13}N_2 \cdot BiI_4$
M_r	877.82
Crystal system, space group	Monoclinic, $P2_1$
Temperature (K)	292
a, *b*, *c* (Å)	7.6537 (2), 33.8824 (11), 13.9995 (5)
β (°)	90.399 (4)
V (Å^3)	3630.3 (2)
Z	8
F(000)	3056
D_x (Mg m^{-3})	3.212
Radiation type	Mo *K*α
No. of reflections for cell measurement	5581
θ range (°) for cell measurement	3.8–31.5
μ (mm^{-1})	16.50
Crystal shape	Needle
Colour	Red
Data collection	
Diffractometer	Xcalibur, EosS2 diffractometer
Radiation source	Enhance (Mo) X-ray Source
Monochromator	Graphite
Detector resolution (pixels mm^{-1})	16.1468

Scan method	ω scans
Absorption correction	Multi-scan *CrysAlis PRO*, Agilent Technologies, Version 1.171.37.35 (release 13-08-2014 CrysAlis171 .NET) (compiled Aug 13 2014,18:06:01) Empirical absorption correction using spherical harmonics, implemented in SCALE3 ABSPACK scaling algorithm.
T_{min}, T_{max}	0.274, 1.000
No. of measured, independent and observed [$I > 2\sigma(I)$] reflections	17265, 13485, 12200
R_{int}	0.032
θ values (°)	θ_{max} = 32.1, θ_{min} = 3.3
$(\sin\theta/\lambda)_{max}$ (Å^{-1})	0.747
Range of *h*, *k*, *l*	*h* = -11→11, *k* = -42→47, *l* = -17→20
Refinement	
Refinement on	F^2
$R[F^2 > 2\sigma(F^2)]$, $wR(F^2)$, *S*	0.061, 0.109, 1.11
No. of reflections	13485
No. of parameters	613
No. of restraints	1
H-atom treatment	H-atom parameters constrained
	$w = 1/[\sigma^2(F_o^2) + (0.0063P)^2 + 117.9887P]$ where $P = (F_o^2 + 2F_c^2)/3$
$(\Delta/\sigma)_{max}$	0.463
$\Delta\rangle_{max}$, $\Delta\rangle_{min}$ (e Å^{-3})	7.31, -5.22
Absolute structure	Refined as a perfect inversion twin.
Absolute structure parameter	0.5

Symmetry codes: (i) *x*+1, *y*, *z*; (ii) *x*-1, *y*, *z*.

Software: *CrysAlis PRO* 1.171.38.43 (Rigaku OD, 2015); cell refinement: *CrysAlis PRO* 1.171.38.43 (Rigaku OD, 2015); data reduction: *CrysAlis PRO* 1.171.38.43 (Rigaku OD, 2015); program(s) used to solve structure: *SHELXL2014*/7 (Sheldrick, 2014); program(s) used to refine structure: *SHELXL2014*/7 (Sheldrick, 2014); molecular graphics: Palmer, D. C. (2014). *CrystalMaker*. CrystalMaker Software Ltd, Begbroke, Oxfordshire, England.; software used to prepare material for publication: *WinGX* (Farrugia, 2012). *publCIF* [Westrip, S. P. (2010). *J. Appl. Cryst.*, **43**, 920-925] software used to generate tabulated data.

From this, following a comparable three-fold alkylation reaction process of the ortho-substituted diamine positions, the templating cation 1,3,5-trimethylbenzimidazolium forms in the reaction mixture. With the increased steric effect of an additional methyl group on the benzene ring system, whilst retaining the analogous single charge and benzimidazolium component, it was hypothesised that the structural conformation and interconnectivity of the anionic structure would be shifted to some extent whilst also modifying the interrelationship between the cations.

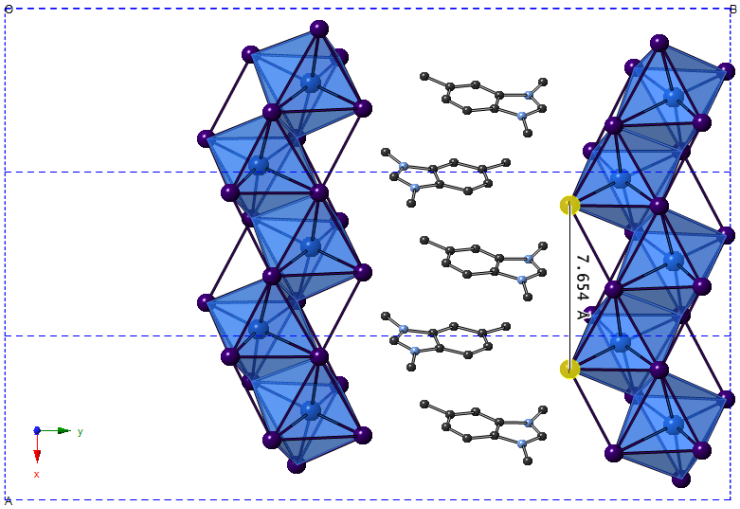

Figure 4.26 Interleaving of stacked cations towards the grooves of the $[BiI_4]^-_n$ chain motif. Legend: $[BiI_6]$ octahedra shaded blue; Bi atoms (blue), I atoms (purple), C atoms (dark grey), N atoms (pale blue), H atoms excluded for clarity

---

In compound 30, in comparison to the previously described compound 29, the anionic network component, the $[BiI_4]_n^-$ chain, is retained; however, as predicted, altering the templating agent modifies its position and alignment and, therefore, the interconnectivity between the chains. As seen previously in compound 29, the cations appear in a stacking arrangement propagating along the *a*-axis channels of the hybrid material alongside their bismuth iodide chain counterparts (Figure 4.26 - 4.27). However, there are two unique stacked column arrangements of cations within the structure. One set of cations are directed in orientation within the structure towards being interleaved into the primary 1^o chain containing metal positions Bi(1) and Bi(2); these are observed to be separated by 3.3 Å, with a 160^o rotation in the plane of the ion and a 180^o rotation along the length of the cation axis with a translational offset of ~2.5 Å. Interleaving into the secondary 2^o chain structure (Bi(3) and (Bi(4)) the relationship of the cations in the second stack is determined to be slightly different with a separation again of 3.3 Å but with a 171^o rotation offset, a 180^o rotation along the length of the cation axis and a larger translational offset of ~3.0 Å.

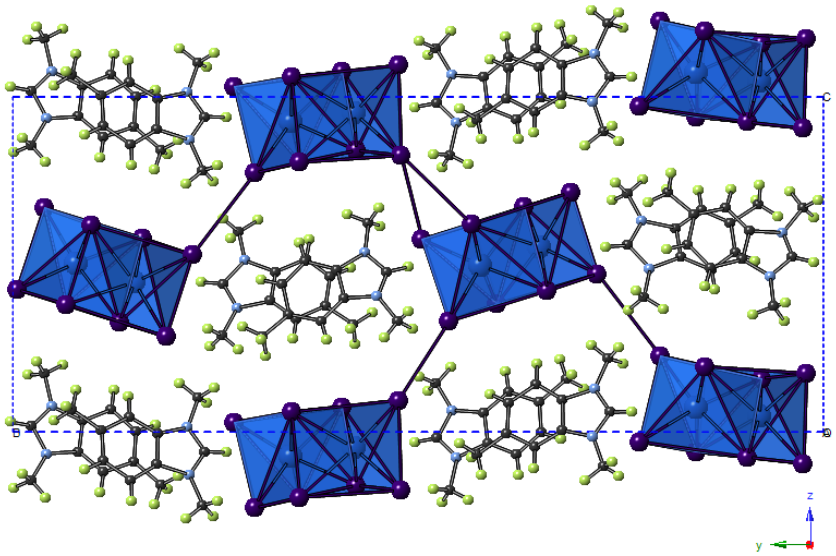

Figure 4.27 View along the *a*-axis of compound 30, $(C_{10}H_{13}N_2)BiI_4$. Legend: $[BiI_6]$ octahedra shaded blue; Bi atoms (blue), I atoms (purple), C atoms (dark grey), N atoms (pale blue), H atoms (pale green).

4.5 Conclusions

Twelve novel iodobismuthate hybrid halometallate materials have been presented and discussed with full structural analysis in this chapter. Compounds 19-24 covered structures discovered containing organic mono- and di-ammonium cations components formed in-situ by varying degrees of ethylation; resulting in templating species N-N-N'-N'-tetraethyl-1,4-benzenediammonium (19,20), N-N-N'-N'-tetraethyl-1,3-benzenediammonium (21), 1-ethyl-2,5-dimethylbenzimidazol-3-ium (22), 1,3-diethyl-2-methylbenzimidazol-3-ium (23) and 1,3-diethyl-2,5-dimethylbenzimidazol-3-ium (24) respectively within each hybrid structure. Compound 25, an example of a templating species formed by dimerisation of the precursor diamine reagent, in the form of 2,3-diaminophenazin-5-ium monocations, revealed a novel structure with enhanced conjugation and pi-stacking orbital interactions between the organic component within a pseudo-3D connected sublattice anionic network.

Compounds 26-30 further exhibited the utilisation of in-situ alkylation with the use of methanol as a solvothermal reaction solvent to form a range of novel iodobismuthate hybrid compounds; containing as-synthesised templating organic species N^1,N^1,N^1,N^4,N^4,N^4-hexamethylbenzene-1,4-diaminium (26), N,N,N-trimethylbenzaminium (27), N,N,N,4-tetramethylbenzaminium (28), 1,3-dimethylbenzimidazol-3-ium (29) and 1,3,5-trimethylbenzimidazol-3-ium (30) respectively.

Overall, zero- and one-dimensional structurally connected materials, with a range of 1-3D electronic pseudo-connectivity, were attained with four types of anionic sublattice motifs represented in the form of decaiododibismuthate $[Bi_2I_{10}]^{4-}$ tetraanionic units, hexadecaiodotetrabismuthate $[Bi_4I_{16}]^{4-}$ tetraanionic units, tetraiodobismuthate $[BiI_4]^-_n$ polymeric monocationic chain units, and nonaiododibismuthate $[Bi_2I_9]^{3-}$ trianionic discrete units. Due to the high turnaround time of running controlled temperature solvothermal procedures, not all of the novel hybrid iodobismuthate structures obtained through this research could be synthesised as pure phases for further optoelectronic characterisation analysis as achieved for those halometallates described and discussed in the published material presented in Chapter 3.

Within the next chapter is the final part of the research undertaken on halometallate hybrid structures in which an unusual and unique three-dimensional structurally connected iodoantimonate perovskite material is introduced and characterised.

Chapter 5 - Hybrid halometallate materials: Part III

5.1 Introduction

Through the previous work, a range of novel heterocyclic piperazinium ring-based templated hybrid iodoantimonate and iodobismuthate materials have been discovered and structurally characterised. Resulting from further investigation, utilising the primary diamine (±)2-methylpiperazine, a structure with a unique three-dimensional network motif is presented here with preliminary data analysis, including single-crystal X-ray diffraction and SEM/EDX analysis. It is noted that the current quality of the structural determination is below the expected standard, however, the primary results analysed suggest that the compound may contain a unique and very interesting structural motif; and so its inclusion as provisional information is warranted on this basis.

The results presented show the synthesis and characterisation of a novel three-dimensional iodoantimonate perovskite material, given the name compound Z. Early observations indicate that the structure could contain a unique structural motif made up of $[Sb_6I_{18}X]$ halometallate superoctahedra, of six bound octahedral units, interconnected by corner-sharing $[SbI_6]$ units at each point vertex. With further work and confirmation this would be of great significance as such a structural motif is currently unobserved throughout the family of halometallate material chemistry.

Outside of the field, in published literature, the cluster structure is observed to mimic a high symmetry manganese oxide $[Mn^{III}_{18}O_{14}]^{26+}$ superoctahedron [1], however, a metal-halide framework exhibiting this motif and in particular a structure in which corner-sharing octahedral metal iodide units link the superoctahedral clusters into a three-dimensionally connected perovskite-like structure is unseen presently.

5.2 Synthesis, results and discussion related to a unique superoctahedral-octahedral three-dimensional iodoantimonate perovskite structure

Crystals of compound Z were obtained as a by-product phase of red crystals from two separate hydrothermal procedures. In detail, the synthesis reagents antimony chloride (0.2 mmol), (±)2-methylpiperazine (0.15 mmol) and hydriodic acid (1.0 ml, 57 wt% in water, no stabiliser) in water (6 ml) were placed in a 25 ml Teflon® vessel, sealed in a steel autoclave and heated at 170 ^{o}C for 24 h; with a controlled ramp up rate of 1 ^{o}C min^{-1} and ramp down rate of 0.1 ^{o}C min^{-1}. After vacuum filtration and an aqueous wash, a minor phase of red crystals of compound Z were obtained in a mixed phase product mixture alongside a major phase of large chunky brick red/orange crystals. Alternatively, as mentioned a secondary procedure run simultaneously with an increased amount of reagent antimony chloride (0.3 mmol) also produced a very similar phase mixture; with red crystals again identified to be novel compound Z (see Appendix A.13).

From the preliminary single-crystal X-ray diffraction data analysis, of a selected small red prismatic crystal, it is proposed that compound Z most likely crystallises in cubic space group *Pm-3m* (#221) with approximate cell dimensions of 18.0743(4) Å ($a = b = c$). An iodoantimonate [$Sb_6I_{18}X$] motif linked by [SbI_6] octahedra to build a three-dimensional network has been identified from the best structural model and refinement. Within the superoctahedron structure Sb-I bonding interactions range from between 2.736(12) - 3.218(6) Å (Δ = 0.48Å) with each Sb^{3+} metal ion position visibly distorted away from the high-valence central site of the cluster; with Sb-I bond distances of 3.067(4) - 3.071(4) Å for the Sb(1)-centred cluster linking [SbI_6] octahedra. At the central iodide position of each vertex edge of the [$Sb_6I_{18}X$] superoctahedron twelve I(3)---I(4) interactions, measured at 4.12Å, interconnect each cluster to a total of twelve adjacent superoctahedra positions (Figure 5.1). It is currently not elucidated from the structural data whether the designated 'Site X' at the centre of tier three of the superoctahedron at its core is occupied by an iodide atom with a very high bond valence of 2.0936 (Δ = +1.0936 over standard value) or possibly occupied by a smaller high-valence anion, such as sulphur (S^{2-}). A final structure refinement factor of 0.247, weighted refinement factor of 0.764 and goodness of fit of 2.54 was attained from the structural data analysis, indicating the preliminary nature of the structural conclusions drawn for this material. Full crystallographic details of the structure solution and refinement are given in Table 5.1 below.

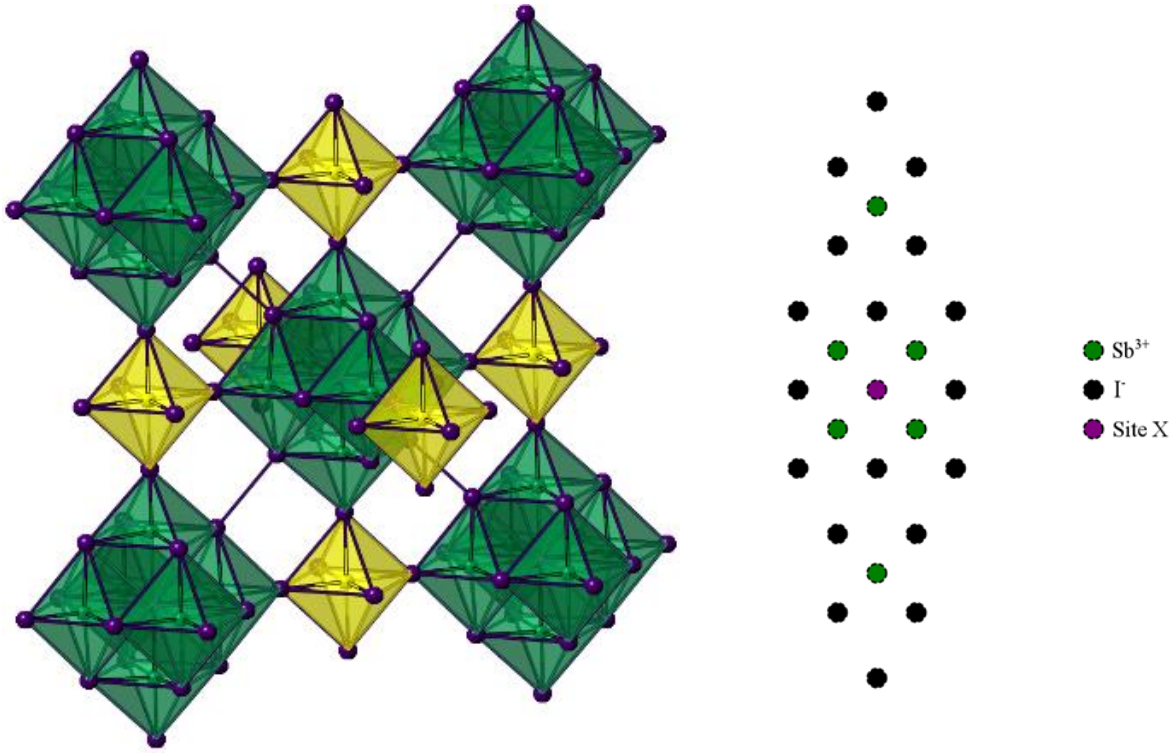

Figure 5.1 The structural iodoantimonate sublattice model of compound Z (left). Superoctahedral units are highlighted in green with octahedral linking units in yellow. Legend: Antimony (Green/Yellow), Iodine (Purple). A cross sectional stacked arrangement schematic of the superoctadral unit (right)

Table 5.1 Crystal data for Compound Z	
Chemical formula	$Sb_9I_{18}X{\cdot}SbI_6$
M_r	13566.00
Crystal system, space group	Cubic, $P4_2/\,n\bar{3}2/\,m$ (*Originat* $\bar{1}$)
Temperature (K)	150
a (Å)	18.0743 (4)
V (Å^3)	5904.5 (4)
Z	8
F(000)	4784
D_x (Mg m^{-3})	3.156
Radiation type	Mo *K*α
No. of reflections for cell measurement	1277
θ range (°) for cell measurement	3.9–29.0
μ (mm^{-1})	10.20
Crystal shape	Prismatic
Colour	Red

Data collection	
Diffractometer	Xcalibur, EosS2 diffractometer
Radiation source	fine-focus sealed X-ray tube, Enhance (Mo) X-ray Source
Monochromator	Graphite
Detector resolution (pixels mm^{-1})	16.1468
Scan method	ω scans
Absorption correction	Multi-scan *CrysAlis PRO* 1.171.38.46 (Rigaku Oxford Diffraction, 2015) Empirical absorption correction using spherical harmonics, implemented in SCALE3 ABSPACK scaling algorithm.
T_{min}, T_{max}	0.316, 1.000
No. of measured, independent and observed [$I > 2\sigma(I)$] reflections	12208, 1845, 743
R_{int}	0.054
θ values (°)	θ_{max} = 31.3, θ_{min} = 3.4
$(\sin\theta/\lambda)_{max}$ ($Å^{-1}$)	0.731
Range of *h*, *k*, *l*	*h* = -16→21, *k* = -14→23, *l* = -9→25
Refinement	
Refinement on	F^2
$R[F^2 > 2\sigma(F^2)]$, $wR(F^2)$, *S*	0.247, 0.764, 2.54
No. of reflections	1845
No. of parameters	44
No. of restraints	0
Weighting scheme	$w = 1/[\sigma^2(F_o^2) + (0.2P)^2]$ where $P = (F_o^2 + 2F_c^2)/3$
$(\Delta/\sigma)_{max}$	2.559
$\Delta\rangle_{max}$, $\Delta\rangle_{min}$ (e $Å^{-3}$)	25.91, -7.79

Symmetry codes: (i) *y*, *x*, -*z*+1; (ii) *x*, *y*, -*z*+1; (iii) -*x*, *y*, -*z*+1; (iv) *z*, -*x*+1, -*y*+1; (v) *z*, *x*, *y*; (vi) *y*, *z*, *x*; (vii) -*x*, -*z*+1, *y*; (viii) *x*, *z*, -*y*+1; (ix) -*x*, -*y*+1, -*z*+1; (x) *y*, *x*, *z*; (xi) -*y*, -*x*, *z*; (xii) -*x*, -*y*, *z*; (xiii) -*x*, -*y*, -*z*+1.

Software: *CrysAlis PRO* 1.171.38.43 (Rigaku OD, 2015); cell refinement: *CrysAlis PRO* 1.171.38.43 (Rigaku OD, 2015); data reduction: *CrysAlis PRO* 1.171.38.43 (Rigaku OD, 2015); program(s) used to solve structure: *SHELXL2014*/7 (Sheldrick, 2014); program(s) used to refine structure: *SHELXL2014*/7 (Sheldrick, 2014); molecular graphics: Palmer, D. C. (2014). *CrystalMaker*. CrystalMaker Software Ltd, Begbroke, Oxfordshire, England.; software used to prepare material for publication: *WinGX* (Farrugia, 2012). *publCIF* [Westrip, S. P. (2010). *J. Appl. Cryst.*, **43**, 920-925] software used to generate tabulated data.

Scanning electron microscope (SEM) and Energy dispersive X-ray (EDX) analysis was undertaken to assess the crystal quality and analyse the composition stoichiometry with surface analysis. The study was targeted towards the minor phase of red crystals, designated as compound Z, in the mixed phase product mixture. Crystal images and EDX analysis by surface etching was carried out under high vacuum using a JEOL SEM6480LV scanning electron microscope twinned with an Oxford INCA X-ray analyser for energy dispersive X-ray spectroscopy, as described in Chapter 2. Imaging was taken with 10 kV acceleration voltage. From the images an average prismatic crystal size of 75 x 75 x 25 µm was determined and it was observed that the surface was coated in small particles of material, as seen in the Figure 5.2 close-up magnification, to be taken into consideration in the surface etching EDX analysis.

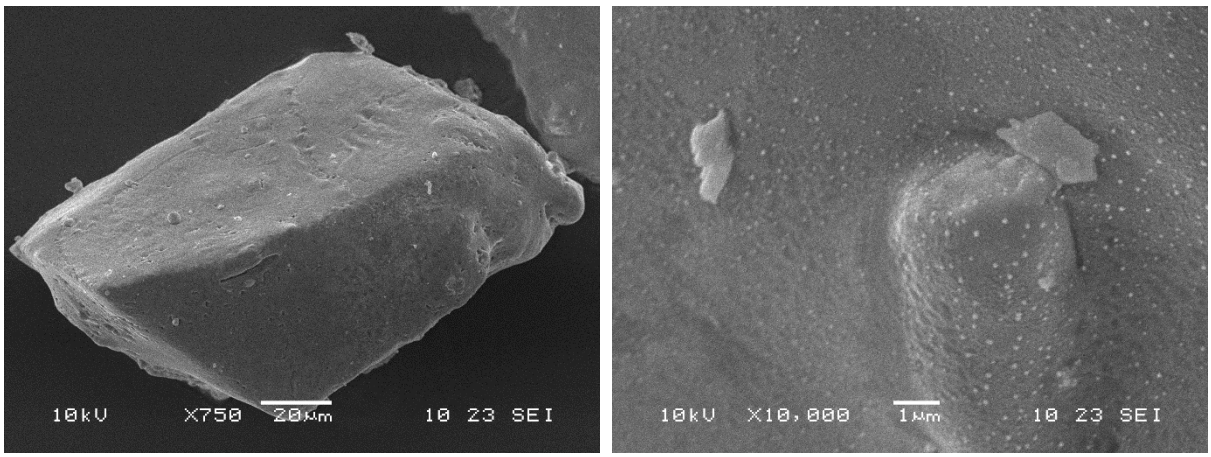

Figure 5.2 Scanning electron microscope images of compound Z crystals at x750 magnification (left) and a surface close-up at x10,000 magnification (right) at 10 kV acceleration voltage

Table 5.2 Sb:I ratios determined from EDX surface analysis

Atom								
Sb	Weight %	37.8	17.89	17.42	19.65	18.50	16.59	17.54
I	Weight %	47.66	67.92	63.92	59.61	68.21	59.75	63.60
	Ratio	1:1.3	1:3.8	1:3.7	1:3.0	1:3.7	1:3.6	1:3.6

The determined Sb:I ratio, see Table 5.2 above, ranges from (1:3.0)-(1:3.8), average 1:3.56 (excluding initial anomalous result), suggesting a high iodide content structural architecture in close agreement to a $[Sb_{28}I_{76}]^{8+}[I]^{8-}$ inorganic stoichiometry for compound Z with a 1:3 Sb:I content ratio. Chlorine peaks (average at 0.1 wt%) were observed, however, it is likely that chlorine is not present in the bulk material but is only present as a surface coating on the crystal as the peak rapidly decreases after a few seconds of electron bombardment as the high intensity electron beam at (~20 kV) continues to etch into the crystal surface through the atomic analysis. Hypothetically, with a sulphur-containing $[Sb_{28}I_{72}S_4]^{4+}[I]^{4-}$ inorganic structural model for compound Z, the weight percentage of sulphur at <1 wt% content may have been at the limit of detection for identification and confirmation by EDX analysis.

5.3 Conclusions

Additional efforts were undertaken through a series of solvothermal procedures to replicate the synthesis of the novel cubic phase originally obtained and characterised as outlined in the reaction procedures presented in the Appendix (A.13 85J-X). A number of adjustments to reagent ratios, reaction temperature and dwell time, ramp down rate were made in an attempt to replicate or possibly optimise the reaction conditions in favour of the minor phase red crystals identified as compound Z. Additionally, thiourea was used as a possible S^{2-} ion dopant source as the unidentified central position within the superoctahedra architecture was theorised to possibly contain sulphur ions appropriate for the size of the cavity and could have been sourced from low-level contamination of the Teflon® cell walls.

However, after the initial mixed phase products contained the red crystals of compound Z in two separate reaction mixture procedures, an optimised route to obtain the target material in an increased amount and with improved quality of crystal for analysis could not be achieved within the time available.

Initial photoluminescence work was carried out on the red crystals of compound Z; however, the data were inconclusive, indicating only a possible weak peak observed at 540-500 nm (2.25 - 2.29 eV) close in proximity to the green filter edge (535 – 540 nm) of the setup used. It is theorised that surface defects on the small crystals used in the analysis may also contribute to dampening photoluminescence activity, however, as mentioned synthesising larger high quality single-crystals in a pure phase was not ultimately achieved and so further analysis work in this area is required.

Due to difficulties in the degree of structural refinement that could be obtained from the current quality of the crystals of this material, alternative approaches could be attempted in order to gain information on this material given the impact the novel structural motif would have to the research community. The further work would attempt to gain a greater understanding of this compound possibly utilising alternative synthetic methodologies or optimised solvothermal synthetic procedures. This would be carried out with the aim of yielding the material of interest in a great enough quality and quantity in order that an improved structural determination and interpretation could then be carried out; either by single-crystal or powder (Rietveld refinement) methods. This brief discussion of this novel material was included in order to ignite interest and awareness that further work optimising the synthetic route to this unique material should be undertaken in the future.

Within the next chapter initial investigations into utilising bismuth in solvothermal synthesis procedures to produce novel metal-organic frameworks are introduced alongside research on bismuth chalcohalide materials and how pseudohalides and their precursor complexes may have a future role in alternative absorber materials.

Chapter 6 – Coordination polymer, pseudohalide and bismuth chalcohalide materials

6.1 Introduction

In conjunction with the work on alternative hybrid halometallate materials presented and discussed throughout the previous results chapters, a number of separate investigations were undertaken into developing novel coordination polymer, pseudohalide-containing complexes and bismuth chalcohalide materials. Development of the use of bismuth in solvothermal procedures for the synthesis of novel metal-ion centred supramolecular structures in the pursuit of increasingly structurally and electronically connected materials was undertaken firstly.

Initial investigations were carried out in the attempt to find novel bismuth-carboxylic acid based structures through a systematic series of solvothermal reaction procedures that were performed with over 140 products screened for crystals which could be analysed by single-crystal X-ray diffraction. Procedures were varied by changing experimental parameters such as the bismuth precursor reagent used, the carboxylic acid(s) used in the reaction, molar ratios of reagents, solvent type, reaction temperature, dwell time at T_{max}, cooling procedure employed and the templating/pH adjusting agent used. To give an example, the experiment shown in Table 6.1 below was carried out with bismuth (III) nitrate pentahydrate as the bismuth reagent with many variables kept constant as shown in the table.

Table 6.1 Experiment Code AD011A procedure details

Experiment Code	Temperature	Solvent	Carboxylic Acid	Product Code	Crystals Obtained	Cooling procedure employed	Bismuth:Carboxylic Acid Ratio (mmol)	Templating/pH adjusting agent / Notes
AD011A	180 °C	Water (10 ml)	1,3-adamantanedicarboxylic acid	AD011A P1	Y	0.1 °C/min	0.1:0.3	KOH (0.1 mmol) Crystals (Cubic Appearance) Sandy coloured (s15mtw031 & e15mtw06)
			1,3-adamantanedicarboxylic acid	AD011A P2	Y	0.1 °C/min	0.1:0.3	KOH (0.2 mmol) Small crystals
			1,3-adamantanedicarboxylic acid	AD011A P3	N	0.1 °C/min	0.1:0.3	KOH (0.3 mmol)
			1,3-adamantanedicarboxylic acid	AD011A P4	N	0.1 °C/min	0.1:0.3	Ethylenediamine (a few drops below neutral pH i.e. slightly acidic)
			1,3-adamantanedicarboxylic acid	AD011A P5	N	0.1 °C/min	0.1:0.3	Ethylenediamine (adjusted to neutral pH dropwise)
			1,3-adamantanedicarboxylic acid	AD011A P6	N	0.1 °C/min	0.1:0.3	Ethylenediamine (a few drops above neutral pH i.e. slightly basic)

The variable changed between each autoclave was the templating agent used (KOH or Ethylenediamine) and the amount of agent used. The result was that products P1 & P2 were found to contain crystals; with the P1 cubic crystals found to be appropriate for analysis by single-crystal X-ray diffraction in an attempt to determine a three-dimensional structure of the material.

In the following solvothermal procedure, as shown in Table 6.2 below, the reaction temperature and solvent type were modified with respect to AD011A.

Table 6.2 Experiment code AD011B procedure details

Experiment Code	Temperature	Solvent	Carboxylic Acid	Product Code	Crystals Obtained	Cooling procedure employed	Bismuth:Carboxylic Acid Ratio (mmol)	Templating/pH adjusting agent / Notes
AD011B	100 °C	DMF (5 ml)	1,3-Adamantanedicarboxylic acid	AD011B P1	N	0.1 °C/min	0.1:0.3	KOH (0.1 mmol)
			1,3-Adamantanedicarboxylic acid	AD011B P2	Y	0.1 °C/min	0.1:0.3	KOH (0.2 mmol) Jagged white crystals. (s15mtw030 & s15mtw034)
			1,3-Adamantanedicarboxylic acid	AD011B P3	Y	0.1 °C/min	0.1:0.3	KOH (0.3 mmol) White crystals. (s15mtw033)
			1,3-Adamantanedicarboxylic acid	AD011B P4	N	0.1 °C/min	0.1:0.3	Ethylenediamine (1 drop)
			1,3-Adamantanedicarboxylic acid	AD011B P5	N	0.1 °C/min	0.1:0.3	Ethylenediamine (2 drops)
			1,3-Adamantanedicarboxylic acid	AD011B P6	N	0.1 °C/min	0.1:0.3	Ethylenediamine (3 drops)

The templating/pH adjusting agent used and the amount of agent used for each autoclave were modified in the same way as experiment procedure AD011A. Results here showed crystals to be present in products P2 & P3, and following this both were analysed by single-crystal X-ray diffraction in an attempt to determine the structure. A full list of experiment procedures carried out related to finding novel bismuth-carboxylic acid structures can be found in the Appendices (See A.1-A.7). Experiments accounted in A.4-A.7 employed both rigid aromatic and flexible alkyl chain carboxylic acids in the synthesis procedures.

In order to replicate and develop procedures for synthesising bismuth sulphide iodide, experiments were carried out as seen in the Appendices A.8-A.9; as well as subsequent reactions with the as-synthesised BiSI product under solvothermal and under reflux conditions to investigate where an $XBiSI_2$ (where X = Cs, Na) or similar phase could be formed. Literature methods for synthesising BiSI with a solvothermal methodology typically involve reacting bismuth (III) chloride with thiourea and iodine in aqueous conditions to give a mixed phase product with a major phase of black BiSI needles with a minor phase of orange BiOI plates.

6.2 Synthetic procedures

Procedure 1. Synthesis of [Bi_2(2,6-pyridinedicarboxylic acid)$_4$] (AD010B P2)

A mixture of $Bi(NO_3)_3.5H_2O$ (0.485 g, 1.0 mmol) and 2,6-pyridinedicarboxylic acid (2,6-pydc) (0.201 g, 1.2 mmol) suspended in dimethylformamide (10 ml) was sealed in a 25 ml Teflon® vessel placed in a stainless steel autoclave and heated at 120 ºC for 3 days with a ramp up and ramp down rate of 1 ºC/min. Product washed with DMF and dried in oven overnight. Product Appearance- Clear crystals with a secondary dark grey/black powder phase.

Procedure 2. Synthesis of [Bi(1,3,5-Benzenetricarboxylic acid)(DMF)] (AD010A P3)

A mixture of $Bi(NO_3)_3.5H_2O$ (0.485 g, 1.0 mmol) and 1,3,5-benzenedicarboxylic acid (1,3,5-BTC) (0.252 g, 1.2 mmol) suspended in dimethylformamide (5 ml) was sealed in a 25 ml Teflon® vessel placed in a stainless steel autoclave and heated at 120 ºC for 3 days with a ramp up and ramp down rate of 1 ºC/min. Product washed with DMF and dried in oven overnight. Product Appearance- Single uniform phase of white crystals.

Procedure 3. Synthesis of [Bi(1,3,5-benzenetricarboxylic acid)(DMF)*x*] (AD010B P6)

A mixture of $Bi(NO_3)_3.5H_2O$ (0.485 g, 1.0 mmol) and 1,3,5-benzenedicarboxylic acid (1,3,5-BTC) (0.252 g, 1.2 mmol) suspended in dimethylformamide (10 ml) was sealed in a 25 ml Teflon® vessel placed in a stainless steel autoclave and heated at 120 ºC for 3 days with a ramp up and ramp down rate of 1 ºC/min. Product washed with DMF and dried in oven overnight. Product Appearance- White crystals with dark streaks (crystal analysed) with secondary phase of clusters of dark grey crystals.

Procedure 4. Synthesis of [Bi_9O_8(1,3-adamantanedicarboxylic acid)$_6$.*x*H_2O] (AD011A P1)

A mixture of $Bi(NO_3)_3.5H_2O$ (0.049 g, 0.1 mmol), 1,3-adamantanedicarboxylic acid (1,3-ADC) (0.067 g, 0.3 mmol) and KOH (0.0056 g, 0.1 mmol) suspended in water (10 ml) was sealed in a 25 ml Teflon® vessel placed in a stainless steel autoclave and heated at 180 ºC for 3 days with a ramp up rate of 1 ºC/min and a ramp down rate of 0.1 ºC/min. Product washed

with DMF and dried in oven overnight. Product Appearance- Single phase of sandy coloured cubic crystals of irregular size.

Procedure 5. Synthesis of [$Bi_2K_2(DMF)_4$(1,3-adamantanedicarboxylic acid)$_4$] (AD011B P3)

A mixture of $Bi(NO_3)_3.5H_2O$ (0.049 g, 0.1 mmol), 1,3-adamantanedicarboxylic acid (1,3-ADC) (0.067 g, 0.3 mmol) and KOH (0.0168 g, 0.3 mmol) suspended in dimethylformamide (5 ml) was sealed in a 25 ml Teflon® vessel placed in a stainless steel autoclave and heated at 100 ºC for 3 days with a ramp up rate of 1 ºC/min and a ramp down rate of 0.1 ºC/min. Product washed with DMF and dried in oven overnight. Product Appearance- Uniform phase of white crystals.

Procedure 6. Synthesis of [$Bi_{12}O_{22}$(2,6-pyridinedicarboxylic acid)$_{10}$(1,4-butanedicarboxylic acid)$_2$] (AD019A P1)

A mixture of $BiCl_3$ (0.063 g, 0.2 mmol), 2,6-pyridinedicarboxylic acid (2,6-pydc) (0.1 g, 0.6 mmol), 1,4-butanedicarboxylic acid (0.087 g, 0.6 mmol) and KOH (0.028 g, 0.5 mmol) suspended in water (10 ml) was sealed in a 25 ml Teflon® vessel placed in a stainless steel autoclave and heated at 180 ºC for 3 days with a ramp up rate of 1 ºC/min and a ramp down rate of 0.1 ºC/min. Product washed with DMF and dried in oven overnight. Product Appearance- White needle crystals with a secondary phase of grey crystalline powder in clusters.

Procedure 7. Synthesis of BiSI (AD023A, AD023B, AD023C)

A mixture of $BiCl_3$ (3.153 g, 10 mmol), thiourea ($SC(NH_2)_2$) (0.720 g, 10 mmol) and iodine (I_2) (2.538 g, 10 mmol) was ground to mix uniformly and was placed in a 25 ml Teflon® vessel placed in a stainless steel autoclave with water (16 ml). The vessel was sealed and heated at 160 ºC for 30 h with a ramp up rate of 1 ºC/min. The autoclave was removed from the oven and left to cool to room temperature. The product was washed with copious amounts of water, rinsed with ethanol, and dried in oven overnight. Product appearance – Major phase of long black needle crystals with a secondary minor phase of orange plates.

Procedure 8. Synthesis of BiSI (AD023D)

A mixture of $BiCl_3$ (3.153 g, 10 mmol), thiourea ($SC(NH_2)_2$) (0.720 g, 10 mmol) and iodine (I_2) (2.538 g, 10 mmol) was ground to mix uniformly and was placed in a 25 ml Teflon® vessel placed in a stainless steel autoclave with water (16 ml). The vessel was sealed and heated at 200 ^oC for 24 h with a ramp up rate of 1 ^oC/min. The autoclave was removed from the oven and left to cool to room temperature. The product was washed with copious amounts of water, rinsed with ethanol, and dried in oven overnight. Product appearance – Major phase of black needle crystals with a secondary minor phase of large hexagonal orange plates.

Procedure 9. Exploratory syntheses of bismuth caesium sulphide iodide/ bismuth sodium sulphide iodide phases (AD036)

A mixture of BiSl (AD023A,B,C) (P1-P6) (0.368 g, 1 mmol) and caesium iodide (CsI) (P1-P3) (0.2598 g, 1 mmol)/ sodium iodide (NaI) (P4-P6) (0.1499 g, 1 mmol) was placed in a 25 ml Teflon® vessel placed in a stainless steel autoclave with γ-butyrolactone (P1, P4) (10 ml)/ dimethylsulfoxide (DMSO) (P2,P5) (10 ml)/ N,N-dimethylformamide (DMF) (P3, P6) (10 ml). The vessels were sealed and heated at 180 ^oC for 3 days with a ramp up rate of 1 ^oC/min and a ramp down rate of 0.1 ^oC/min to RT. The products were washed with copious amounts of water, rinsed with ethanol, and dried in an oven overnight. Product appearances – P1 (Very fine reflective dark grey/ black needle crystals), P2 (Product not obtained, sealed in bomb), P3 (Fine grey needles with large black needles), P4 (Very fine reflective dark grey/ black needle crystals), P5 (Mixed black and red crystalline phases), P6 (Fine grey needles with large black needles).

Procedure 10. Exploratory synthesis of bismuth caesium sulphide iodide ($CsBiSI_2$) or similar phase (AD032)

A mixture of aqueous hydroiodic acid (HI) (57 wt% in water) (6.8 ml, 7.58 M) and aqueous hypophosphorous acid solution (50 wt% in water) (1.7 ml) was degassed with a flow of nitrogen; and kept under a nitrogen flow throughout the experiment. BiSI (AD023A,B,C) (0.368 g, 1 mmol) was dissolved in the mixture heated to ~120 ^{o}C under stirring. Caesium iodide (CsI) (0.2598 g, 1 mmol) was added to the solution and heated under reflux for 1 h. Solution allowed to cool to RT. The mother liquor was left for 24 h for crystal growth. The product was washed with copious amounts of ethanol. Product Appearance – Large red plate crystals with a secondary red powder phase.

Procedure 11. Exploratory synthesis of bismuth caesium sulphide iodide ($CsBiSI_2$) or similar phase (AD033)

A mixture of aqueous hydroiodic acid (HI) (57 wt% in water) (6.8 ml, 7.58 M) and aqueous hypophosphorous acid solution (50 wt% in water) (1.7 ml) was degassed with a flow of nitrogen; and kept under a nitrogen flow throughout the experiment. BiSI (AD023A,B,C) (0.368 g, 1 mmol) was dissolved in the mixture heated to ~120 ^{o}C under stirring. Caesium iodide (CsI) (0.3897 g, 1.5 mmol) was added to the solution and heated under reflux for 1 h. Solution allowed to cool to RT. The mother liquor was left for 24 h for crystal growth. The product was washed with copious amounts of ethanol. Product Appearance – Red powder phase with a small red plate crystals.

6.3 Novel bismuth-carboxylic acid coordination polymers

From a systematic series of solvothermal experiments (Appendices A1-A7) changing experimental parameters such as reaction temperature, reaction dwell time, solvent type, solvent volume, bismuth precursor reagent, organic linker reagent, templating agent, molar ratios of reagents, and cooling procedures a number of novel bismuth-carboxylic acid structures were obtained and analysed by single-crystal X-ray diffraction (SXD).

6.3.1 [Bi_2(2,6-pyridinedicarboxylic acid)$_4$]

The first of the novel structures described here was synthesised through solvothermal methods (Procedure 1) from bismuth (III) nitrate pentahydrate reacting with 2,6-pyridinedicarboxylic acid in DMF forming a crystallised structure of [Bi_2(2,6-pyridinedicarboxylic acid)$_4$] clusters. Structural determination was carried out by selecting a crystal for analysis by SXD from the products obtained from the synthesis; clear crystals with a secondary dark grey/black powder phase. The crystallographic information was gathered using the Agilent Xcalibur diffractometer with a Mo K_α (λ = 0.71073 Å) radiation source and is as follows:

Crystal System - Monoclinic, Space Group - $P2_1/n$, Cell axes (Å) a = 10.8674(3)
b = 7.1219(2) c = 22.2108(6), Cell angles (^{o}) α = 90 β = 93.959(2) γ = 90,
V (Å^3) = 1714.94(8), R-factor - 0.0325 (3.25%), GooF - 1.059

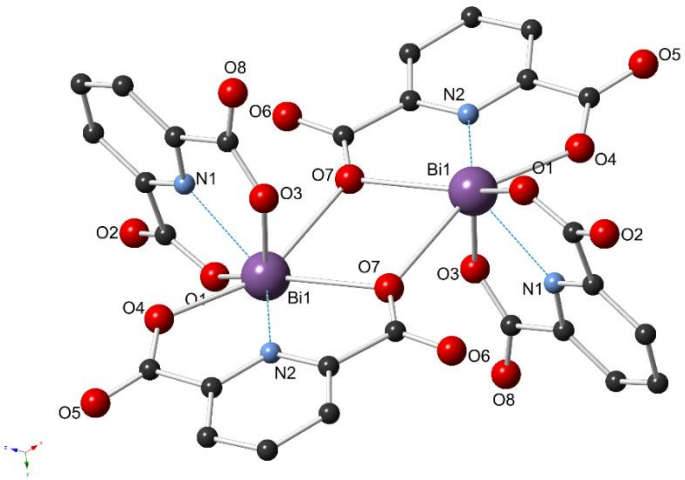

Figure 6.1 Ball and stick model of the structure showing the coordination around symmetry equivalent bismuth positions

After obtaining a structural model by direct methods it was refined to a residual factor of 3.25% with a goodness of fit close to unity showing good agreement between the observed and calculated data; and therefore can be accepted as a satisfactory structure determination.

From the single-crystal X-ray analysis a symmetric structure was found (Figure 6.1, 6.2) to form from the binding of four 2,6-pyridinedicarboxylic acid ligands to two bismuth sites in each cluster. Monodentate carboxyl oxygen binding bond lengths (Bi1-O1, Bi1-O3, Bi1-O4) range from 2.261(5)-2.497(5) Å. Oxygen site (O7) acts as a μ-oxo bridge between the bismuth ions with Bi-O bond lengths of 2.663(5) Å and 2.589(5) Å. The lone pair of electrons on the nitrogen of the pyridine ring also acts as an additional coordination node in the formation of this complex with bond lengths of 2.381(6) Å and 2.472(6) Å to bismuth.

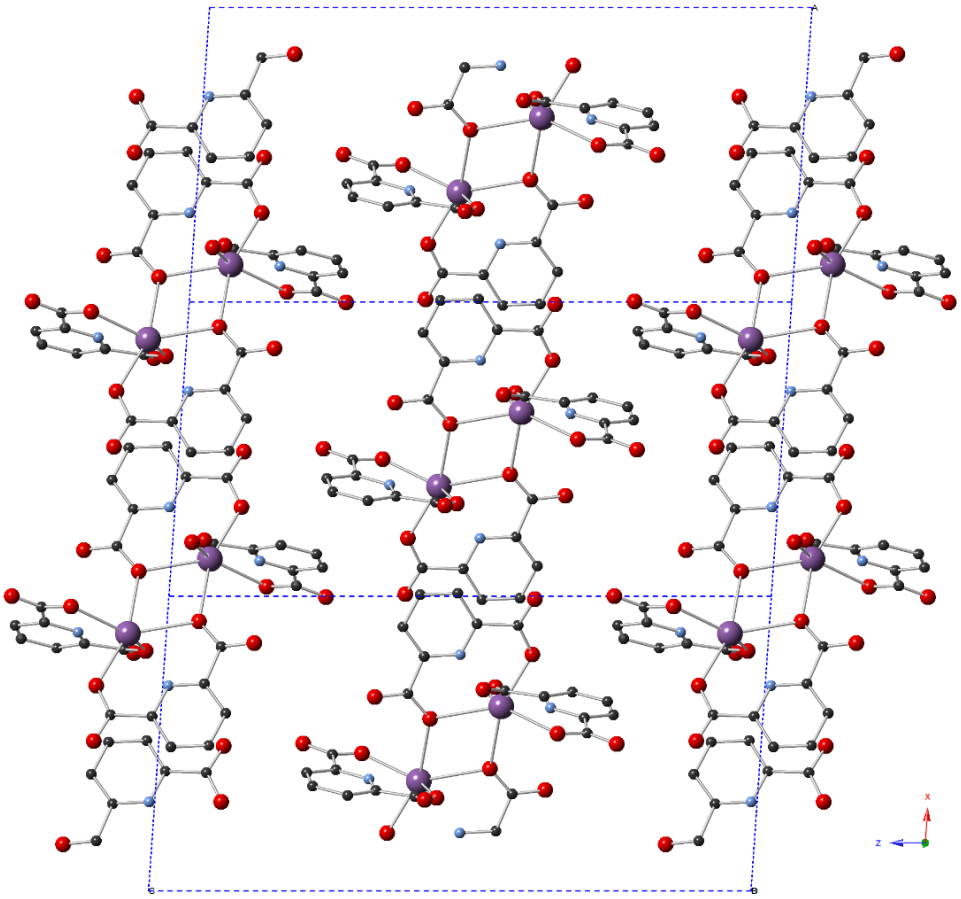

Figure 6.2 View along the *b*-axis of the crystal structure of Bi_2(2,6-pyridinedicarboxylic acid)$_4$

6.3.2 [Bi(1,3,5-benzenetricarboxylic acid)(DMF)]

A novel 3-dimensional coordination framework was synthesised from bismuth (III) nitrate pentahydrate and 1,3,5-benzenetricarboxylic acid in DMF in a solvothermal synthesis procedure (Procedure 2) to give a uniform single phase sample of white crystals; from which an appropriate crystal was selected for structural determination by SXD. The crystallographic information was gathered using the Agilent Xcalibur diffractometer with a Mo K_α (λ = 0.71073 Å) radiation source and is as follows:

Crystal System - Monoclinic, Space Group - $P2_1/n$, Cell axes (Å) a = 10.1586(4)
b = 14.5944(4) c = 11.5180(5), Cell angles (°) α = 90 β = 100.486(4) γ = 90,
V (Å^3) = 1679.12(13), R-factor - 0.0564 (5.64%), GooF - 1.160

After obtaining a structural model by direct methods it was refined to a residual factor of 5.64% with a goodness of fit showing good agreement between the observed and calculated data. Although slightly above a residual factor of 5%, the structural model can be regarded as reliable, though could perhaps be improved through data collection from a higher quality crystal.

From single-crystal X-ray analysis (Figure 6.3, 6.4) the structural formula of the framework was determined to be [Bi(1,3,5-benzenetricarboxylic acid)(DMF)].

The coordination polymer is comprised of symmetric pairs of bismuth (III) ions, separated by a distance of 3.78 Å, with a coordination number of 9. One of the carboxyl groups (O1, O2) is bound bidentate to bismuth with bond lengths of 2.268(8) Å and 2.499(9) Å respectively. The carboxyl group with oxygens (O3, O4) are bound via μ-oxo bridge (O3), with bond lengths of approximately 2.77 Å and 2.78 Å, and monodentate binding from O4 with a shorter bond length of 2.268(8) Å. Similarly, the third carboxyl group (O5, O6) of the 1,3,5-BTC ligand is bound via a μ-oxo bridge (O6), with comparatively weaker bridging bond lengths of 2.82 Å and 2.93 Å. Analysis of the structure has also shown the DMF molecules are bound to bismuth in the framework, with a Bi-O bond length of 2.413(12) Å.

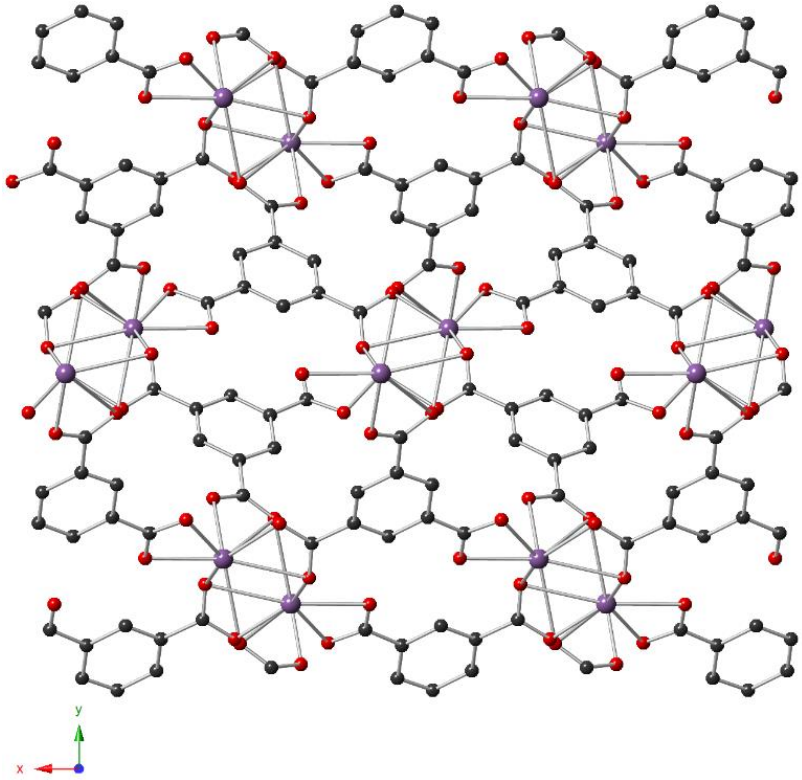

Figure 6.3 View along the *c*-axis of the framework of structure [Bi(1,3,5-benzenetricarboxylic acid)(DMF)] (DMF excluded)

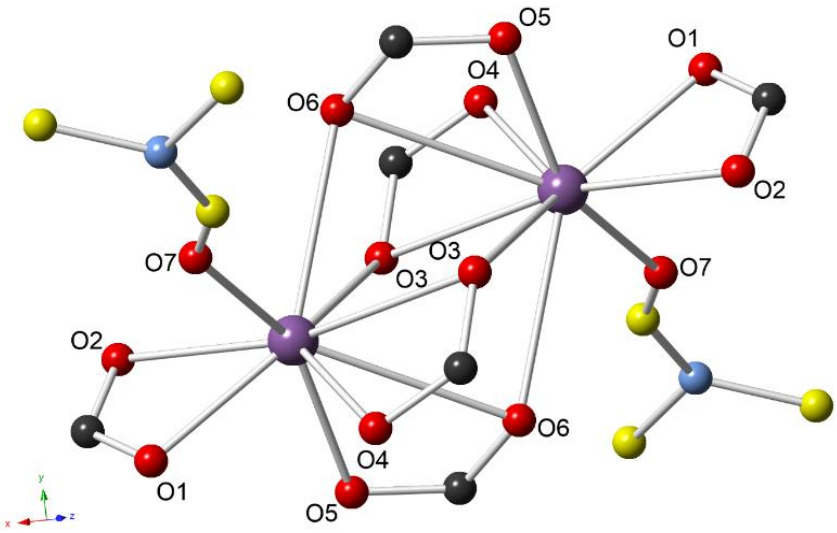

Figure 6.4 Ball and stick model of coordination around bismuth in the framework (DMF shown with carbon atoms in yellow)

When observing the framework down the *a*-axis (Figure 6.5) it can be seen that the bound DMF molecules are situated in channels propagating through the structure. Removing DMF from the imaging shows this more clearly. The pore size of the desolvated channels has been determined to be approximately 11 Å x 7 Å. More studies are required to determine whether DMF can be evacuated from the structure whilst retaining a stable framework; which could be assessed for potential applications such as gas adsorption (H_2, CH_4) or absorptive removal of hazardous materials (Azo dyes); for example.

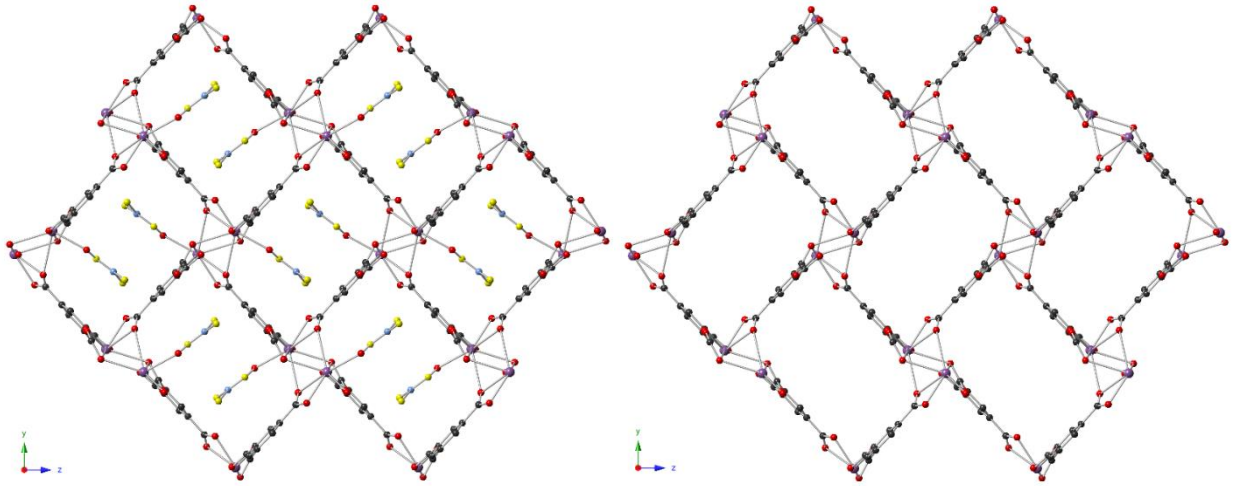

Figure 6.5 Graphic showing the *a*-axis of framework (DMF included – Left, DMF excluded – Right)

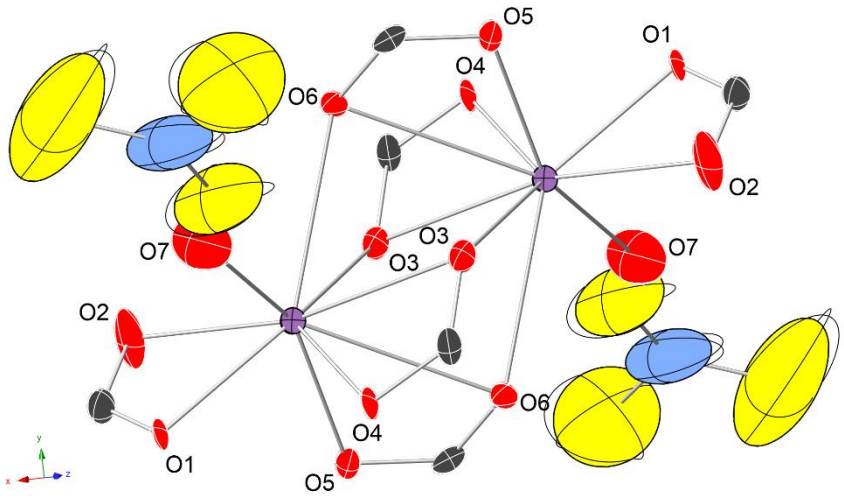

Figure 6.6 Thermal ellipsoid model of coordination around bismuth in the framework [Bi(1,3,5-benzenetricarboxylic acid)(DMF)] (DMF shown with carbon atoms in yellow)

By examining the thermal parameters of the atom positions of the structure (Figure 6.6) it can be seen that the thermal ellipsoids of the atoms constituting the DMF molecules are much larger than those of the 1,3,5-BTC ligand atoms and bismuth positions. This suggests that DMF is more weakly bound and more mobile in the channels and therefore could be susceptible to ligand exchange or removal from the structure. Additionally, this analysis shows how the proximity of the bound DMF molecules to oxygen position (2) in the bidentate bound carboxyl group appears to enlarge the thermal ellipsoid of the position explaining why the bond length is a weaker 2.499(9) Å in comparison to the Bi-O1 bond length of 2.268(8) Å. Removal of the DMF may lead to a strengthening of the 1,3,5-BTC carboxyl group bindings resulting in a stable solvent free coordination polymer.

6.3.3 [Bi(1,3,5-benzenetricarboxylic acid)(DMF)$_x$]

By manipulating the synthetic procedure slightly with an increased volume of DMF in Teflon® bomb (Procedure 3) in comparison to the synthesis of structure [Bi(1,3,5-benzenetricarboxylic acid)(DMF)], alterations in the framework structure are observed. Structural determination was carried out by selecting a crystal for analysis by SXD from the products obtained from the synthesis; white crystals with dark streaks (crystal analysed) with secondary phase of clusters of dark grey crystals. The crystallographic information was gathered using the Agilent Xcalibur diffractometer with a Mo K_α (λ = 0.71073 Å) radiation source and is as follows:

Crystal System - Monoclinic, Space Group - $P2_1$, Cell axes (Å) a = 9.9966(4)
b = 10.2258(4) c = 18.6404(10), Cell angles (°) α = 90 β = 101.848(4) γ =90,
V (Å^3) = 1864.89(16), R-factor - 0.0978 (9.78%), GooF - 1.268

After obtaining a structural model by direct methods it was refined to a residual factor of 9.78% with a goodness of fit deviated slightly from unity and therefore does not fully assure agreement of the observed and calculated data. To refine the residual factor of the structure below 5%, to obtain a more reliable structural model determination, may require a data collection from a higher quality crystal with a longer run to determine all atom positions.

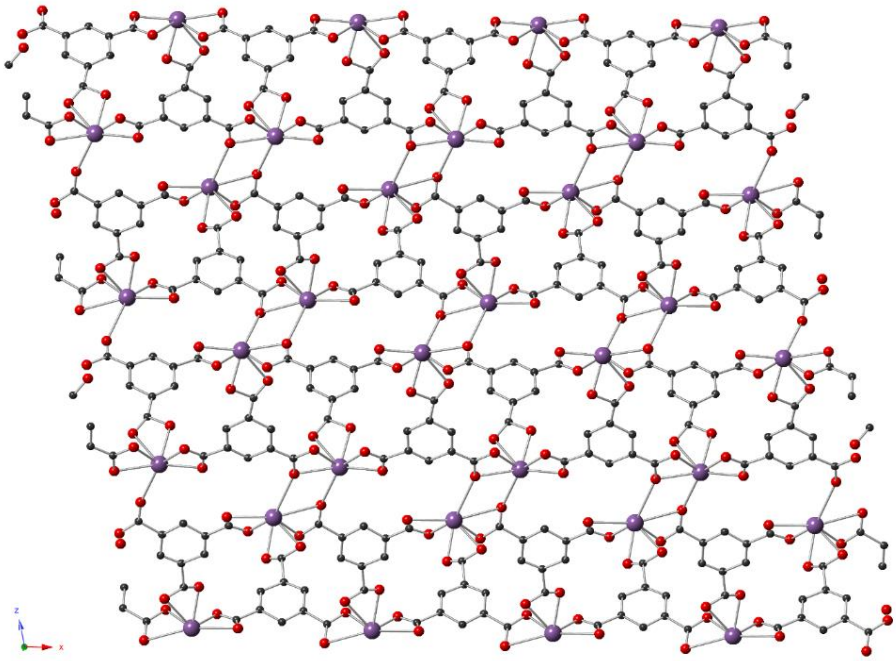

Figure 6.7 View along the *b*-axis of framework [Bi(1,3,5-benzenetricarboxylic acid)$(DMF)_x$] (DMF excluded)

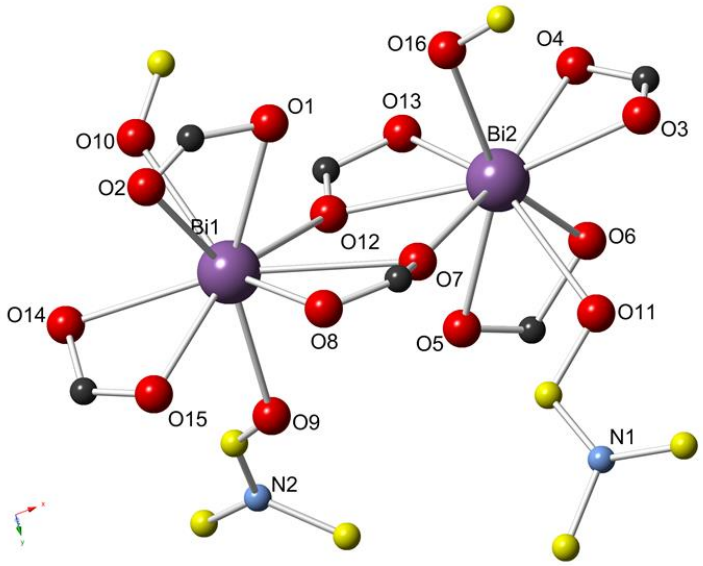

Figure 6.8 Ball and stick model of coordination around bismuth in the framework (DMF shown with carbon atoms in yellow)

From single-crystal X-ray analysis of the structure (Figure 6.7, 6.8), the bonding and atom positions of the 1,3,5-BTC ligand atoms bound to bismuth can be determined, however, from the data obtained with the examined crystal all atom positions on the electron density map could not be resolved.

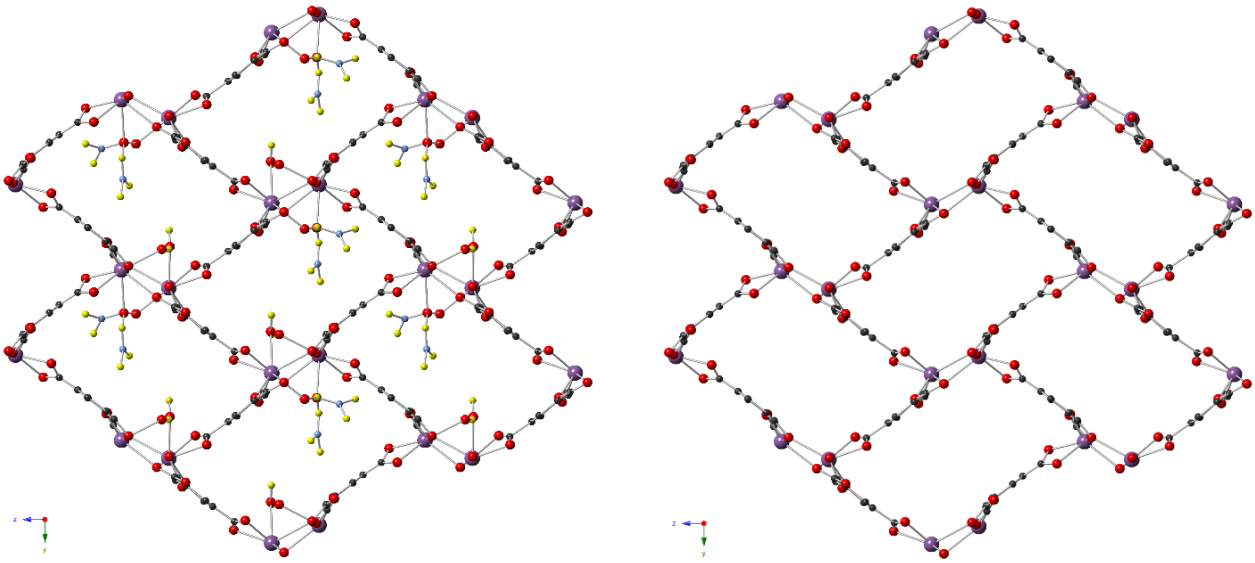

Figure 6.9 View along the *a*-axis of framework [Bi(1,3,5-benzenetricarboxylic acid)(DMF)$_x$] (DMF/fragments included – Left, DMF/fragments excluded – Right)

The coordination number of the bismuth atoms is retained as nine, but the coordination of the carboxyl groups of the 1,3,5-BTC ligands has changed. For bismuth atom (Bi1) two carboxyl groups are bound bidentate (Bi1-O1 = 2.59(4) Å, Bi1-O2 = 2.47(3) Å, Bi1-O14 = 2.61(2) Å, Bi1-O15 = 2.37(4) Å), with the third bound with a monodentate oxygen (Bi1-O8 = 2.31(3) Å) and a µ-oxo bridge oxygen measured at (Bi1-O7 = 2.78 Å). A second µ-oxo bridge (Bi1-O12) has a bond distance of approximately 2.99 Å. A fully resolved DMF molecule is bound to bismuth (Bi1-O9 = 2.55(2) Å) with a marginally stronger bond than an unresolved DMF molecule/fragment (Bi1-010 = 2.62(3) Å).

Correspondingly, for bismuth atom (Bi2) two carboxyl groups are bound bidentate (Bi2-O3 = 2.378(19) Å, Bi2-O4 = 2.29(3) Å, Bi2-O5 = 2.61(4) Å, Bi2-O6 = 2.29(2) Å), with the third bound with a monodentate oxygen (Bi2-O13 = 2.31(3) Å) and a µ-oxo bridge oxygen (Bi2-O12 = 2.55(3) Å). A second weaker µ-oxo bridge (Bi2-O7) has a bond distance of approximately 2.86 Å. A fully resolved DMF molecule is bound to bismuth (Bi2-O11 = 2.75(4) Å) with a marginally stronger bond than an unresolved DMF molecule/fragment (Bi1-O16 = 2.72(4) Å).

Although a full structure determination cannot be reliably obtained for the framework it can be shown that an increased amount of solvent in the synthetic procedure has increased the total solvent uptake into the crystallised structure. This has had the effect of altering the coordination of the 1,3,5-BTC carboxyl groups around the bismuth positions. In comparison to the previous related framework the Bi...Bi distance has also increased by almost 1 Å from 3.78 Å to 4.74 Å. The distorted desolvated channels has been determined to be approximately 12.2 Å x 7 Å and the cell volume has increased to 1864.89(16) $Å^3$ in comparison to the cell volume of structure (6.3.2) of 1679.12(13) $Å^3$.

6.3.4 [Bi_9O_8(1,3-adamantanedicarboxylic acid)$_6$.xH_2O]

From a hydrothermal synthesis procedure (Procedure 4) a novel coordination polymer was synthesised made up of Bi-oxo clusters (Bi_9O_8) connected by 1,3-adamantanedicarboxylic acid linkers. Structural determination was carried out by selecting a crystal for analysis by SXD from the product obtained from the synthesis; a single phase of sandy coloured cubic crystals of irregular size.

The crystallographic information was gathered using the Agilent Xcalibur diffractometer with a Mo Kα (λ = 0.71073 Å) radiation source and is as follows:

Crystal System - Trigonal, Space Group - *R3*, Cell axes (Å) *a* = 17.8945(25) *b* = 17.8945(25) *c* = 24.8811(50), Cell angles (°) α = 90 β = 90 γ = 120, *V* (Å^3) = 6899.85(19), R-factor - 0.0456 (4.56%), GooF - 1.026

After obtaining a structural model (Figure 6.10, 6.11) by direct methods it was refined to a residual factor of 4.56% with a goodness of fit close to unity showing good agreement between the observed and calculated data; and therefore can be accepted as a satisfactory structure determination.

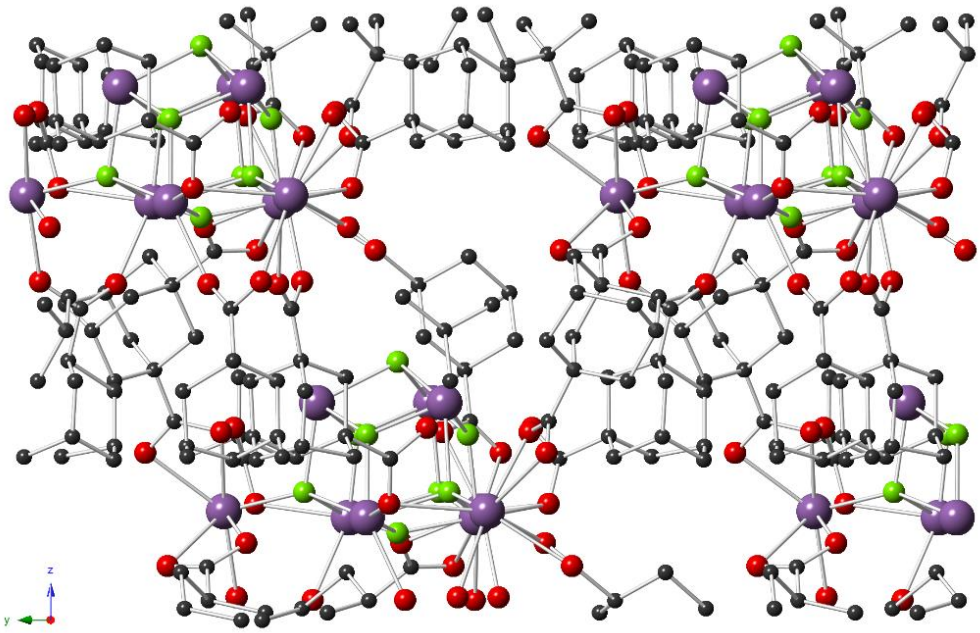

Figure 6.10 View along the *a*-axis of the crystal structure [Bi_9O_8(1,3-adamantanedicarboxylic acid)$_6$.xH_2O] (oxygen atoms in Bi-oxo cluster shown in green) (Solvent excluded)

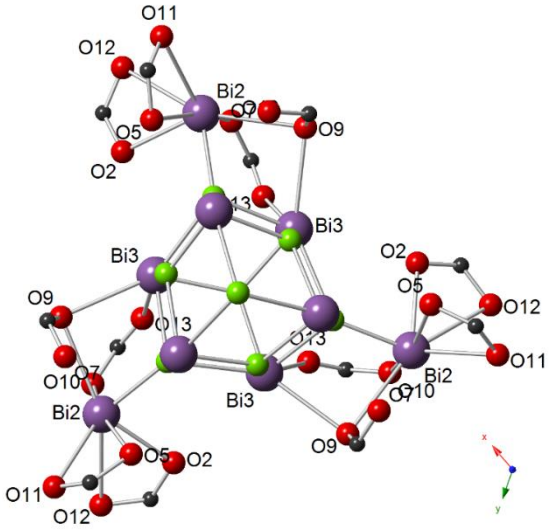

Figure 6.11 Ball and stick model view along the *c*-axis showing coordination around Bi-oxo cluster (Solvent excluded)

The *c*-axis view through the apex of the cluster (Figure 6.11) reveals the trigonal crystal system characteristic single threefold axis. Bismuth atom (Bi2) protrudes from the bismuth-oxo cage (Figure 6.12) and is involved in the majority of the Bi-O coordination to construct the framework. To elaborate, two adamantanedicarboxylic acid carboxyl groups are bound bidentate to bismuth atom (Bi2) with bond lengths of 2.426(15) Å (Bi2-O5), 2.654(17) Å (Bi2-O11), 2.335(13) Å (Bi2-O2) and 2.690(17) Å (Bi2-O12). For carboxyl group (O7, O9) oxygen (9) is μ-oxo bridge between Bi3 (Bi3-O9 = 2.589(17) Å) and Bi2 (Bi2-O9 = 2.641(17) Å). Lastly, there is a carboxyl group bridge (Bi-O-C-O-Bi) between bismuth atoms Bi3 and Bi2 (Bi3-O13 = 2.44(2) Å, O13-C = 1.13(5) Å, C-O10 = 1.31(3) Å, O10-Bi2 = 2.378(10) Å) below the cluster.

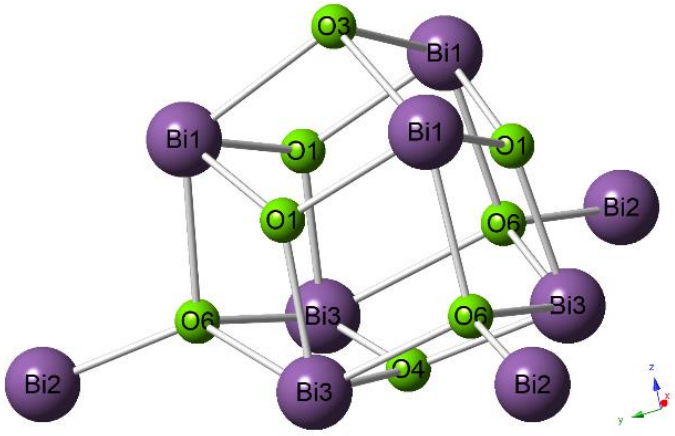

Figure 6.12 Close up view of the Bi-oxo cluster in the crystal structure (Solvent excluded)

Regarding the bonding within the Bi-oxo cluster itself (Figure 6.13), due to the threefold axis there are four unique oxygen atom positions. Oxygen position (O1) has three equivalents with Bi3-O1 bond lengths of 2.185(14) Å and Bi1-O1 bond lengths of 2.144(12) Å and 2.259(14) Å. Oxygen atom (O3) positioned at the apex of the cluster has three equal bonds to bismuth atom (Bi1) with a distance of 2.376(16) Å. Correspondingly, at the base of the cluster oxygen atom (O4) has three equivalent bonds to bismuth atom (Bi3) with an average distance of 2.15 Å; the shortest Bi-O bond length within the cluster. Finally, oxygen (O6) is bonded to bismuth atom (Bi3) with bond lengths of 2.259(14) Å and 2.524(14) Å, to bismuth atom (Bi1) with a bond length of 2.376(16) Å and to bismuth atom (Bi2) with a bond length of 2.185(14) Å.

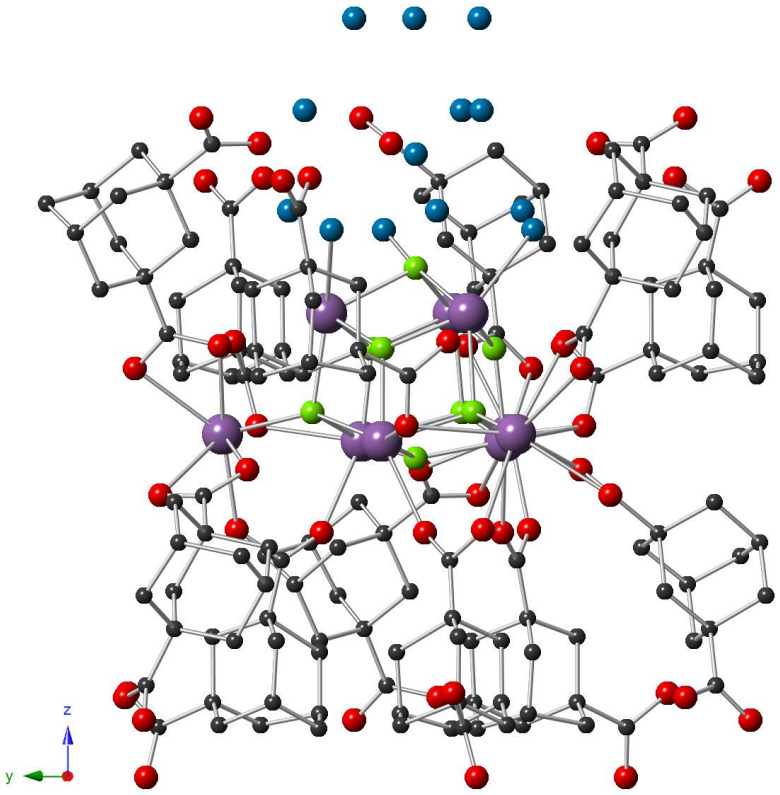

Figure 6.13 Close up view of bonding interactions around one Bi-oxo cluster in the crystal structure (Solvent included – Water oxygen atoms shown in blue)

Above the apex of the cluster there is a region of disordered solvent molecules (oxygen atoms in water shown in blue). The closest water molecule is bound to bismuth atom (Bi1) with a distance of 2.690(17) Å. Several water molecules are likely hydrogen bonded to one another in this area, however, from the single-crystal X-ray analysis it cannot be reliably determined with the data obtained due to the level of disorder of the molecule positions and orientations.

6.3.5 [$Bi_2K_2(DMF)_4$(1,3-adamantanedicarboxylic acid)$_4$]

In an alternate synthesis procedure (Procedure 5) with a change of solvent from water (10 ml) to DMF (5 ml) and a temperature change from 180 ^oC to 100 ^oC another, but dissimilar, framework structure with 1,3-adamantanedicarboxylic acid as the organic linker was formed (Figure 6.14). The procedure gave a uniform single phase of white crystals; from which an appropriate crystal was selected for structural determination by SXD.

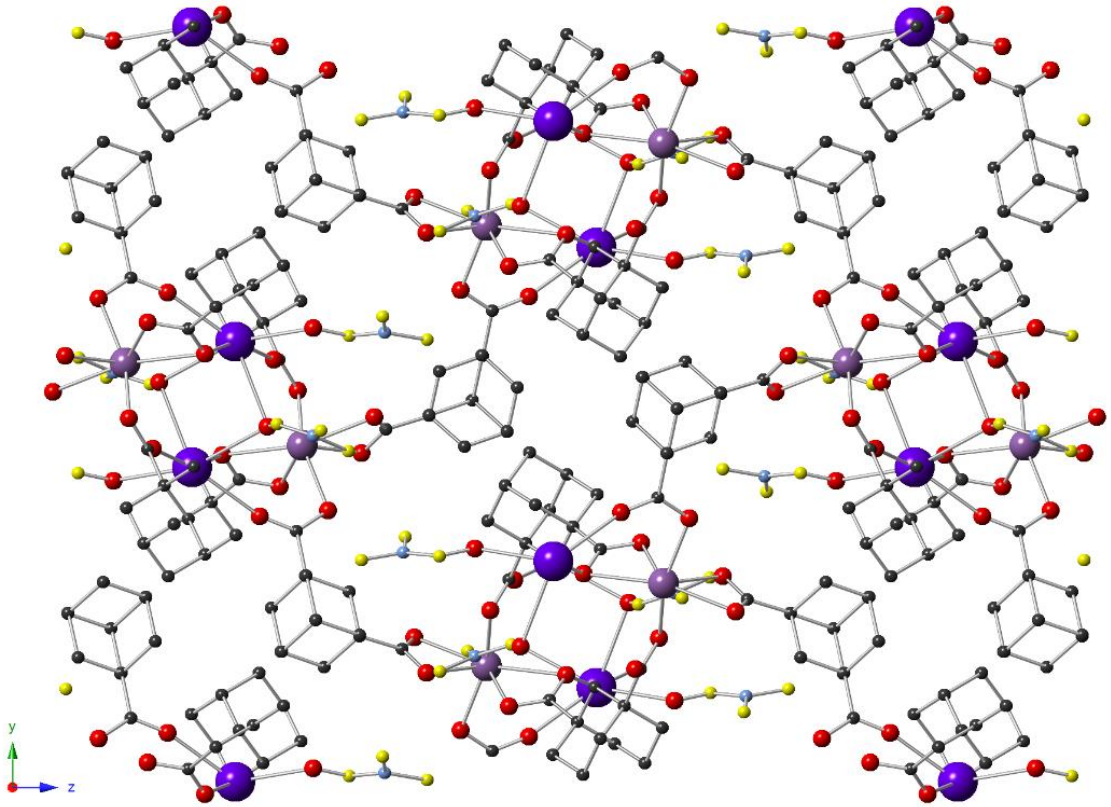

Figure 6.14 View along the *a*-axis of the framework of compound [$Bi_2K_2(DMF)_4$(1,3-adamantanedicarboxylic acid)$_4$]

The crystallographic information was gathered using the Agilent Supernova diffractometer with a Mo K_α (λ = 0.71073 Å) radiation source and is as follows:

Crystal System - Monoclinic, Space Group - $P2_1/n$, Cell axes (Å) a = 10.6289(4) b = 13.7844(4) c = 22.9834(7), Cell angles(^{o}) α = 90 β = 99.846(3) γ = 90, V (Å^3) = 3317.77(18), R-factor - 0.0640 (6.40%), GooF - 1.027

After obtaining a structural model by direct methods it was refined down to a residual factor of 6.40% with a goodness of fit close to unity. This shows fairly good agreement between the observed and calculated data, however, to refine below 5% to give a more reliable determination of the whole crystal structure may require a higher quality data collection.

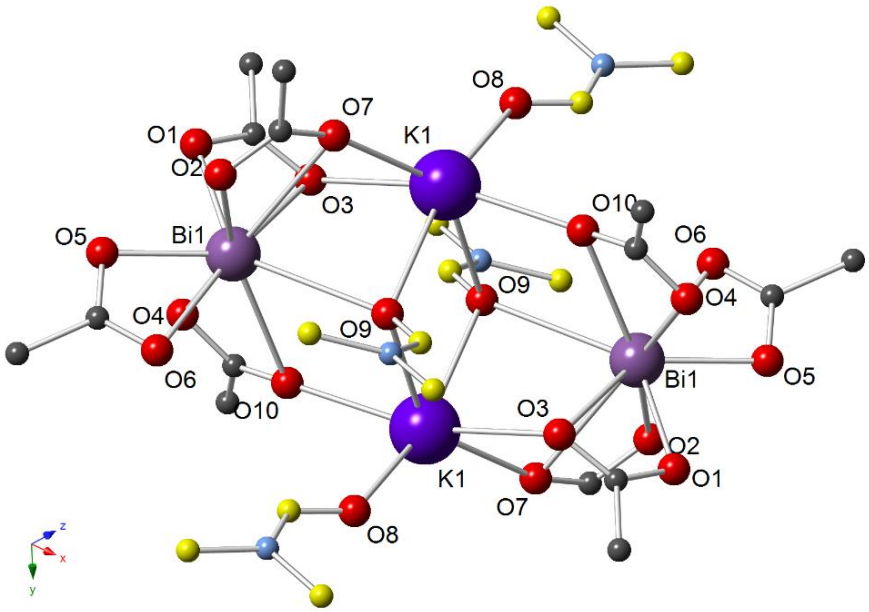

Figure 6.15 Close-up view of the bonding interactions around bismuth and potassium sites in the structure

The crystallised structure, solved by single-crystal X-ray analysis, is made up of symmetric units of $Bi_2K_2(DMF)_4$ interconnected by 1,3-adamantanedicarboxylic acid bound to both K^+ and Bi^{3+} ions. KOH was used as a reducing agent, changing the pH of the reaction mixture, with a possible structural directing role for many of the solvothermal procedures. However, this was the only crystallised product obtained where potassium ions were found to be incorporated into the structure itself.

More specifically, oxygen atoms (O5, O6; Figure 6.15) are solely bound bidentate to bismuth with bond distances of 2.261(4) Å and 2.503(4) Å. Furthermore, carboxyl group (O1, O3) can be seen as bridging between Bi1 and K1 with monodentate binding from O1 to Bi1 (BD = 2.267(4) Å) and O3 acting as a μ-oxo bridge between Bi1 (Bi1-O3 = 2.662(4) Å) and K1 (K1-O3 = 2.708(5) Å). Likewise, carboxyl group (O2, O7) bridges between atom positions Bi1 and

K1 with monodentate binding of O2 to Bi1 (BD = 2.322(4) Å) and O7 has a μ-oxo bridge bonding mode between Bi1 (Bi1-O7 = 2.886(5) Å) and K1 (K1-O7 = 2.638(4) Å). The last of the carboxyl group binding sites in the structure (O4, O10) also bridges positions Bi1 and K1 with a monodentate binding from O4 to Bi1 (BD = 2.369(4) Å) and O10 acts as a third μ-oxo bridge between Bi1 (Bi1-O10 = 2.819(6) Å) and K1 (K1-O10 = 2.572(5) Å).

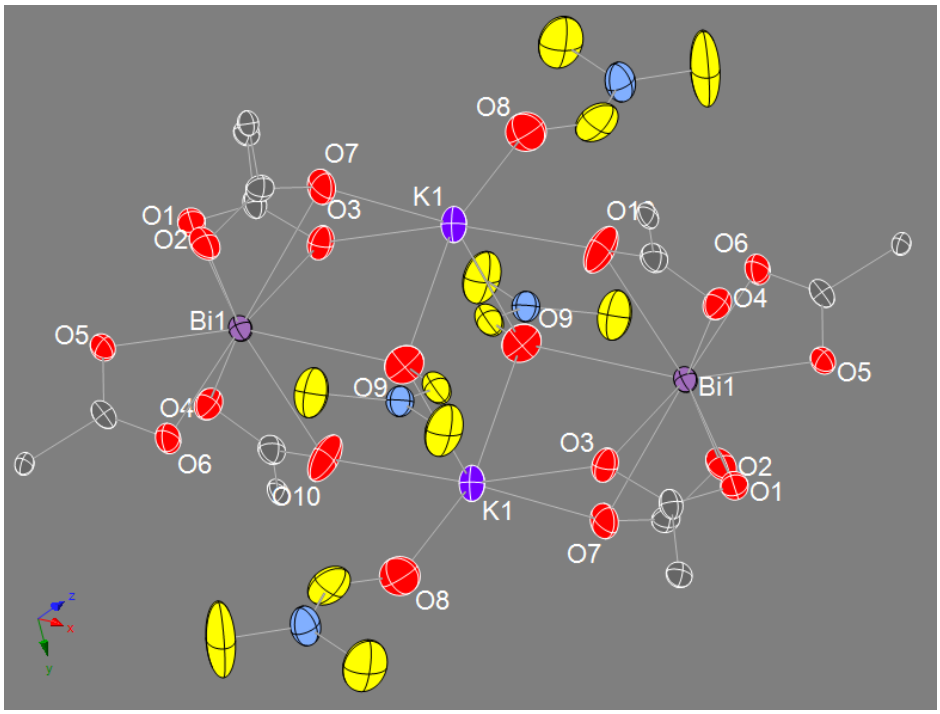

Figure 6.16 Thermal ellipsoid model of a close-up view of the bonding interactions around bismuth and potassium sites in the structure $[Bi_2K_2(DMF)_4(1,3\text{-adamantanedicarboxylic acid})_4]$ indicating higher thermal parameter values for the bound DMF molecule atomic positions

From single-crystal X-ray analysis it was also determined that at each $Bi_2K_2(DMF)_4$ cluster in the structure, one DMF molecule is bound to each potassium atom position via monodentate binding from the carbonyl oxygen (O8) in DMF (K1-O8 = 2.686(5) Å; Figure 6.16). Two more DMF molecules are bound in identical symmetric positions in the cluster; carbonyl oxygen (O9) bridges between the potassium ions with bond distances of 2.886(5) Å and 2.935(5) Å with a potential weak interaction to Bi1 with a bond distance of 3.07 Å. The coordination numbers of the bismuth and potassium atom positions in the structure are nine and six, respectively. The metal nodes are separated by distances of 4.23 Å (K…K), 7.33 Å (Bi…Bi), 3.88 Å and 4.56 Å (Bi-K).

6.3.6 [$Bi_{12}O_{22}$(2,6-pyridinedicarboxylic acid)$_{10}$(1,4-butanedicarboxylic acid)$_2$]

The last of the novel bismuth-carboxylic acid structures obtained was from a solvothermal procedure (Procedure 6) with both a rigid aromatic organic linker (2,6-pyridinedicarboxylic acid) and a flexible alkyl chain organic linker (1,4-butanedicarboxylic acid) as reagents in the synthesis. It was hypothesised that by employing both rigid aromatic and flexible alkyl chain linkers in the synthesis both could be incorporated into the structure with the possibility that rigid units of bismuth atoms bound to rigid linkers in the framework may be interconnected by flexible linkers to form a novel stable coordination network with pore spaces or channels; for example.

Structural determination was carried out by selecting a crystal for analysis by SXD from the product obtained from the synthesis; white needle crystals with a secondary phase of grey crystalline powder in clusters. The crystallographic information was gathered using the Agilent Supernova diffractometer with a Mo K_α (λ = 0.71073 Å) radiation source and is as follows:

Crystal System - Triclinic, Space Group - *P-1*, Cell axes (Å) a = 10.6596(14) b = 18.8676(18) c = 19.0976(22), Cell angles (^{o}) α = 65.359(10) β = 74.163(11) γ = 77.961(10), V (Å^3) = 3338.85(188), R-factor - 0.1045 (10.45%), GooF - 1.085

The structure was solved by direct methods and was refined with SHELX to a residual factor of 10.45% with a goodness of fit close to unity. In order to improve upon the current structural model may require adjustments to the synthetic procedure and crystallisation of the product; with the intention of reducing disorder in the atomic positions to improve the quality of data collected by X-ray crystallography.

A structure obtained from the procedure and analysed by single-crystal X-ray crystallography appears to show a two-dimensional layered coordination polymer (Figure 6.17, 6.18, 6.19). A complete structure determination has not been accomplished as it can be seen that there is disorder in the atomic positions and site occupancies of a number of bismuth atoms.

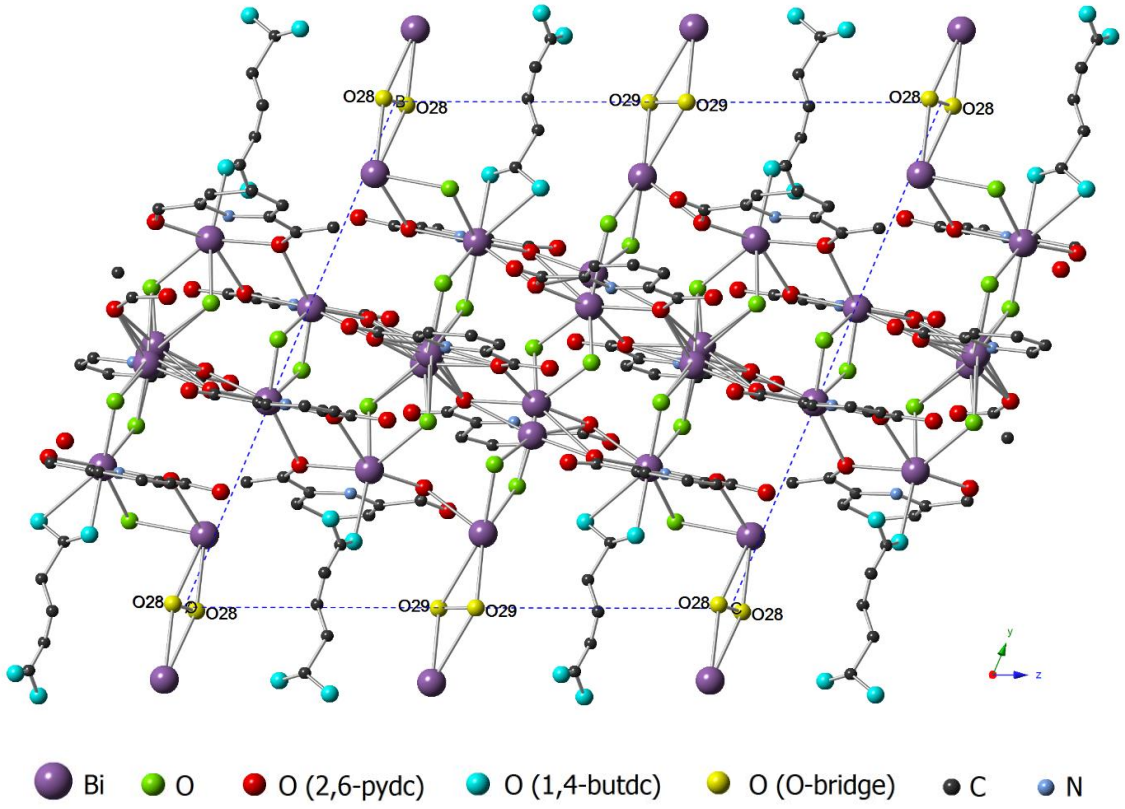

Figure 6.17 View along the *a*-axis of crystal structural model attained

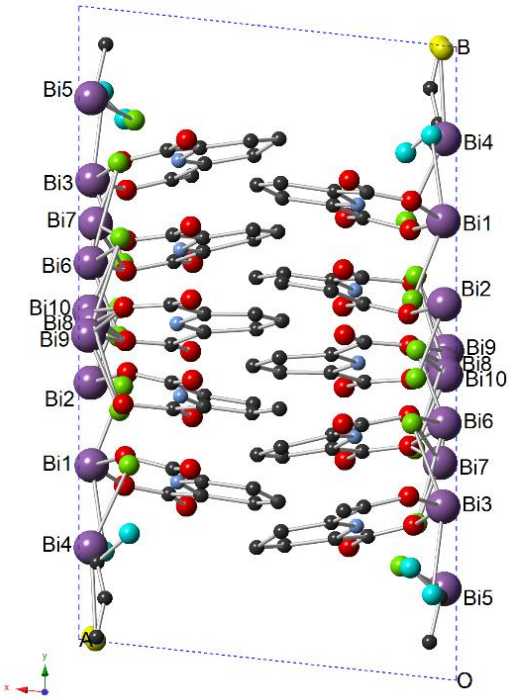

Figure 6.18 View along the *c*-axis of the unit cell with bismuth atom labels

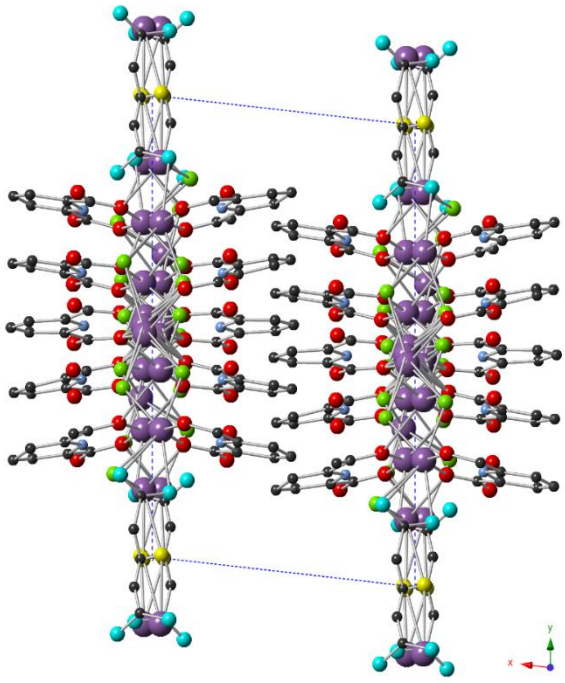

Figure 6.19 View along the *c*-axis of the layered structure

Two disordered positions, where electron density is delocalised around an atomic site, can be observed for Bi8 (Site occupancy = 0.4), Bi9 (Site occupancy = 0.3), Bi10 (Site occupancy = 0.3) in close proximity and for Bi6, Bi7 (0.07) 1.076 Å apart. Accounting for this, there are approximately 14 bismuth atom sites in the unit cell, however, two of the bismuth atoms Bi4 and Bi5 have site occupancies of 0.555 and 0.535, respectively.

Within the layers, Bi-oxo units (approximately $Bi_{12}O_{18}$ per unit cell) with bound 2,6-pyridine carboxylic acid ligands (10 per unit cell) propagate down the *c*-axis of the structure. Intralayer bonding between the ($Bi_{12}O_{18}$(2,6-pydc)$_{10}$) units consists of two 1,4-butanedicarboxylic acid linkers per unit cell (although only five carbon atoms appear in the refinement of the alkyl chain), bound bidentate to Bi1 and monodentate to Bi3, and two (μ^2-η^2,η^2) oxygen bridges (O28, O29) bound to Bi5 and Bi4 respectively (when the positions are occupied). The intra-layer bonding extends the coordination polymer in 2D down the *b*-axis.

Interlayer interactions consist of interleaving aromatic rings of the bound 2,6-pyridinedicarboxylic acid ligands down the *c*-axis, with the absence of pi-pi stacking interactions as the rings are offset (Figure 6.20)

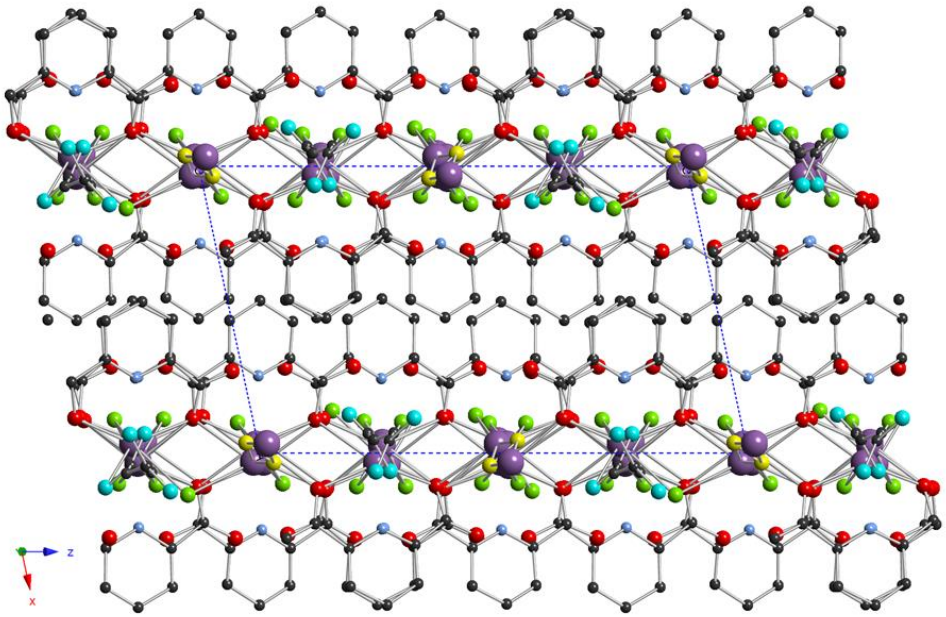

Figure 6.20 View along the *b*-axis of the layered structure

6.4 Bismuth sulphide iodide studies

With bismuth sulphide iodide (BiSI) identified as an interesting semiconducting material for photovoltaic applications, literature procedures for solvothermal synthesis of the material were researched and replicated. From this, further work was undertaken into controlling the morphology of the BiSI crystals synthesised and to explore reacting BiSI in solution-based procedures to introduce dopants or create novel semiconducting phases; which could in turn be investigated for photoactivity.

6.4.1 Hydrothermal synthesis of BiSI

Following a procedure (Procedure 7) for the facile and clean synthesis of BiSI crystals, a product with a major phase of black needle crystals and a minor secondary phase of orange plates was synthesised. Structural determination was carried out by selecting a needle crystal for analysis by SXD and UV/Vis spectroscopy analysis was carried out on the obtained product (see Appendix A.18). The crystallographic information was gathered using the Agilent Xcalibur diffractometer with a Mo K_α (λ = 0.71073 Å) radiation source and is as follows:

Crystal System - Orthorhombic, Space Group - *Pna2₁*, Cell axes (Å) a = 8.4799(5) b = 10.2221(10) c = 4.1626(3), Cell angles (°) α = 90 β = 90 γ = 90, V (Å^3) = 360.82(0), R-factor - 0.0663 (6.63%), GooF - 1.096

After obtaining a structural model by direct methods it was refined to a residual factor of 6.63% with a goodness of fit close to unity showing good agreement between the observed and calculated data. The crystallographic measurements match those stored for BiSI in the Inorganic Crystal Structure Database (ICSD).

A similar literature procedure [1] in which stoichiometric amounts of $BiCl_3$, thiourea and iodine in water (70 ml) are reacted under hydrothermal conditions in a Teflon® autoclave (100 ml) at 200 °C and a reduced reaction T_{max} dwell time (24 h) gives a mixed phase product of 1-D BiSI and 2-D BiOI nanostructures. The procedure was modified (Procedure 8) and scaled to a 23 ml autoclave. The product synthesised remained as a major phase of black needle crystals and a secondary minor phase orange plates; both products on the microstructure scale. However, the conditions had resulted in shorter crystal growth for the black needles, identified

as BiSI, and much larger hexagonal-shaped crystalline orange plates, suggested but not identified as BiOI; in comparison to procedure 7.

6.4.2 Solution-based reactions undertaken with as-synthesised BiSI

Several reactions have been undertaken (Appendix A.9) under reflux conditions with as-synthesised BiSI with an intent to explore whether caesium iodide could react with BiSI in solution-based conditions to form a $CsBiSI_2$ or similar phase.

A solution-based technique (Procedure 10), inspired by a solution synthesis method by Stompous et al. [2], for the formation of $CH_3NH_3SnI_3$ and $CH_3NH_3PbI_3$ perovskite materials was carried out. BiSI was found to dissolve in the HI/H_3PO_2 solution at high temperature. Upon addition of caesium iodide to the mixture, a dark precipitate instantly formed in solution. After heating under reflux for an hour, the solution was allowed to cool to RT and the product was left in solution for 24 h. From the product obtained, large red plate crystals with a red powder phase, an appropriate crystal was selected for analysis by SXD. A pre-experiment data collection was run and the unit cell was checked against the data in the ICSD. The structure was found to match that of $Cs_3Bi_2I_9$ [3]. The high concentration of iodide ions in solution is thought to have driven the reaction towards the formation of a stable $Cs_3Bi_2I_9$ phase. Under reaction conditions (Procedure 11) with an increased molar ratio of CsI to BiSI a similar product mixture to Procedure 10 was obtained, however, with smaller crystals and a major red powder phase.

With related reaction conditions with N,N-Dimethylformamide (DMF) and γ-Butyrolactone (GBL) used respectively as solvents, BiSI was found not to react with CsI and remained in the needle solid-state form.

In order to investigate whether BiSI would react with CsI/NaI in DMF, GBL and Dimethylsulfoxide (DMSO) respectively in a solvothermal process, under increased pressure and temperature, a procedure was undertaken (Procedure 9) (Appendix A.8). From the products obtained PXRD analysis was performed for AD036 P1, P3, P4 & P6.

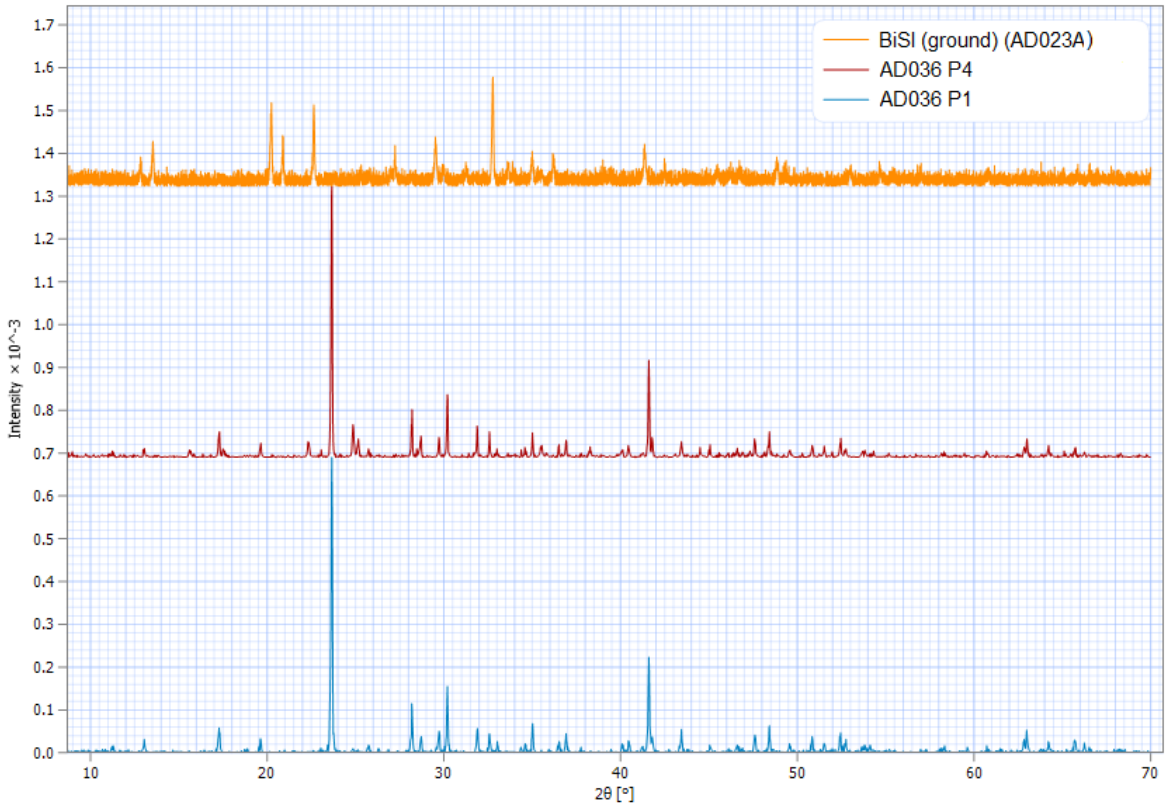

Figure 6.21 PXRD pattern comparison between BiSI (ground) and products AD036 P1/ AD036 P4

As seen in Figure 6.21, following the reaction of as-synthesised BiSI with CsI(P1)/NaI(P4) respectively in the solvothermal process carried out in γ-Butyrolactone (GBL), the products show changes in the crystalline structure. Both patterns for the products are similar and show additional peaks with higher intensities in comparison to the starting BiSI material. At this stage, a suitable crystal for SXD analysis to determine structural information for the fine needle structures in the products has not been achieved.

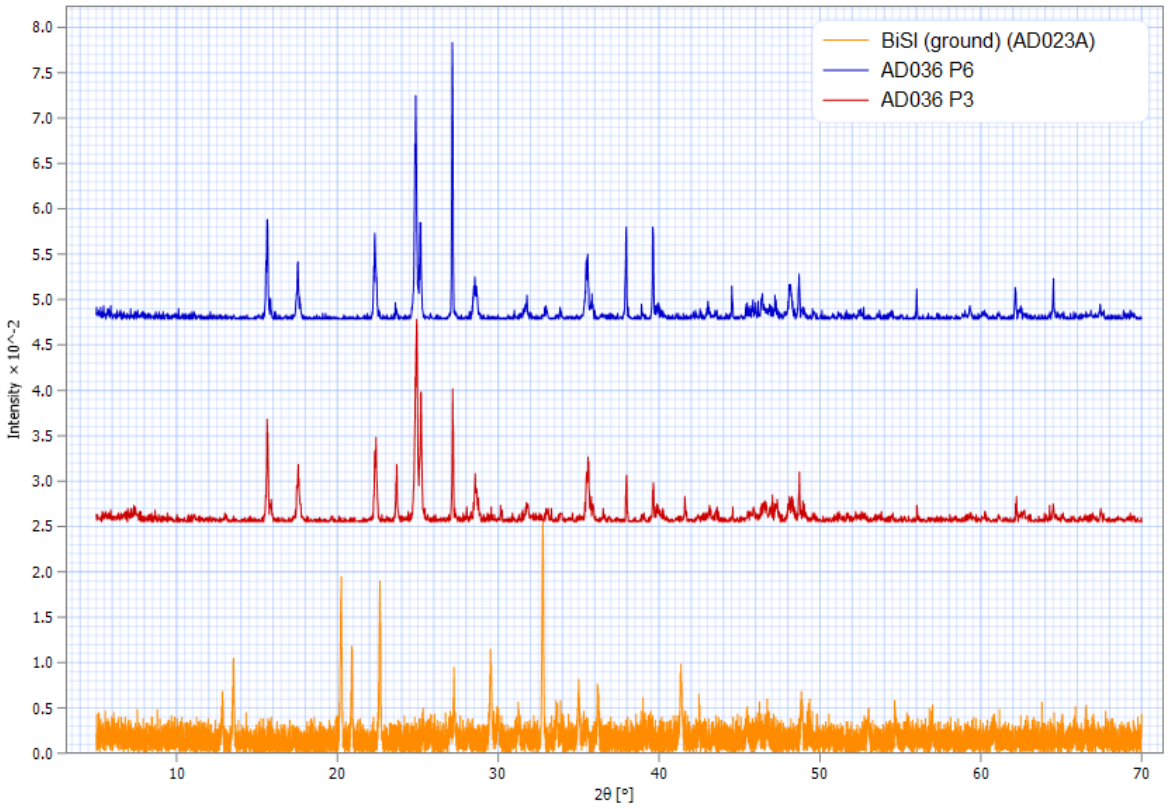

Figure 6.22 PXRD pattern comparison between BiSI (ground) and products AD036 P3/ AD036 P6

Dissimilar PXRD patterns (Figure 6.22), in comparison to P1/P4, were found for reactions carried out in analogous conditions apart from a change of solvent to DMF. Here fine grey needles and black needles were found in both products; AD036 P3 and AD036 P6. Again, the crystalline structure of the material has changed with respect to that of BiSI. An appropriate crystal, a fine grey needle from sample AD036 P6, was found for analysis by SXD. A pre-experiment data collection was run and the unit cell was checked against the data in the ICSD. The structure was found to match that of Bi_2S_3.

6.5 Pseudohalide-based studies

Another area of interest for investigation was considered in a transitory study carried out here into the integration of a pseudohalogen species into hybrid halometallate photovoltaic absorbers. As alluded to in the introduction to candidate materials, pseudohalogen doping of lead-based perovskite materials has been studied for their ability to increase the stability of the structures and develop the moisture tolerance of the absorber layer to degradation and thus loss of function. Under certain stoichiometries, thiocyanate doped $MAPbI_3$ frameworks were shown to exhibit an optical band gap shift and an enhanced photoluminescence emission quantum yield for the material [4-9].

The thiocyanate anion (SCN^-) is a suitable substitute for a halide in these materials as it has an effective ionic radius of ~217 pm, very similar to that of iodine (I^-) ~220 pm, and its ambidentate binding modes to bismuth metal centre positions in complexes means it can be utilised to possibly replace iodine connectivity in iodometallate structures. In the synthesis of bismuth (III) thiocyanate and selenocyanate complexes it has been demonstrated that through N- and S- bonding modes of thiocyanate ions bonding links can be formed; and can also act as a hydrogen bond interaction acceptor. In the literature [10], a $[NH_4(18\text{-crown-}6)][BiCl_3(SCN)]$ complex was found to exhibit a polymeric anionic chain structure made up of bridging chlorides and thiocyanates; formed of $(BiCl_4(NCS)_2)$ octahedra bonded through two Bi-NCS-Bi and two Bi-Cl-Bi edge-sharing bridging links. As a result, work began on attempting to synthesise precursor reagents which could bind thiocyanate and heterocyclic amines together.

Following a procedure related to the synthesis of a zinc thiocyanate complex, $(HTen)_2[Zn(NCS)_4]$, in which zinc binds to four thiocyanate ligands via N-donor coordination in a distorted tetrahedral geometry in a complex salt counterbalanced by two singly charged 1,4-diazabicyclo(2,2,2)octane $(HTen)^+$ cations [11]. A related solution-based synthetic reaction procedure was carried out with piperazine as a precursor amine; following earlier success in its utilisation in the synthesis of multiple novel hybrid halometallate materials.

In the synthesis, reagents zinc oxide (0.410 g, 0.005 mol), ammonium thiocyanate (1.42 g, 0.019 mmol) and piperazine (0.8614 g, 0.01 mol) were placed in a round-bottomed flask with acetonitrile (20 cm^3). The reaction flask was heated to boiling (~90-100 ^oC) as the mixture was stirred for 2-3 minutes to complete solution of the oxide. The resulting mixture was removed from the oil bath and left to cool slowly to room temperature.

After several days of slow solvent evaporation crystals were observed to have crystallised and the mixture was filtered by gravity to obtain a mixed phase of clear needle crystals and multi-millimetre sized clear block crystals.

Analysis of a selected needle crystal from the sample by single-crystal X-ray analysis revealed that the structure was made up of a simple salt structure of balanced monovalent ions; determined to be piperazinium thiocyanate (Figure 6.23). The structure was found to crystallise in orthorhombic space group *Pbcm*; with four balancing ions of the organic salt per unit cell.

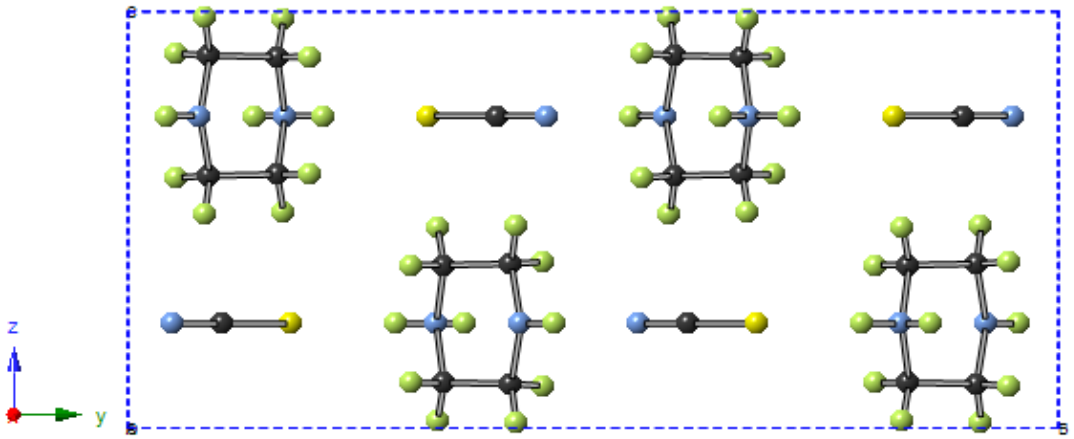

Figure 6.23 View along the *a*-axis of simple organic salt piperazinium thiocyanate

A final structure refinement factor of 0.044, weighted refinement factor of 0.114 and goodness of fit of 1.07 was attained from the structural data analysis. Full crystallographic details of the structure solution and refinement are given in Table 6.3 below.

Table 6.3 Crystal data of structure $C_4N_2H_{11}$·SCN	
Chemical formula	$C_4N_2H_{11}$·SCN
M_r	145.22
Crystal system, space group	Orthorhombic, *Pbcm*
Temperature (K)	150
a, *b*, *c* (Å)	4.5098 (3), 19.1437 (11), 8.5562 (7)
V (Å^3)	738.69 (9)
Z	4
F(000)	312
D_x (Mg m^{-3})	1.306
Radiation type	Mo *K*α

No. of reflections for cell measurement	2173
θ range (°) for cell measurement	4.2–31.1
μ (mm^{-1})	0.36
Crystal shape	Needle
Colour	Clear
Data collection	
Diffractometer	Xcalibur, EosS2 diffractometer
Radiation source	fine-focus sealed X-ray tube, Enhance (Mo) X-ray Source
Monochromator	Graphite
Detector resolution (pixels mm^{-1})	8.0734
Scan method	ω scans
Absorption correction	Multi-scan *CrysAlis PRO* 1.171.38.43 (Rigaku Oxford Diffraction, 2015) Empirical absorption correction using spherical harmonics, implemented in SCALE3 ABSPACK scaling algorithm.
T_{min}, T_{max}	0.668, 1.000
No. of measured, independent and observed [$I > 2\sigma(I)$] reflections	7141, 1257, 1039
R_{int}	0.038
θ values (°)	θ_{max} = 32.0, θ_{min} = 4.3
$(\sin\theta/\lambda)_{max}$ ($Å^{-1}$)	0.746
Range of *h*, *k*, *l*	*h* = -6→6, *k* = -28→25, *l* = -12→11
Refinement	
Refinement on	F^2
$R[F^2 > 2\sigma(F^2)]$, $wR(F^2)$, *S*	0.044, 0.114, 1.07
No. of reflections	1257
No. of parameters	52
No. of restraints	0
H-atom treatment	H atoms treated by a mixture of independent and constrained refinement
Weighting scheme	$w = 1/[\sigma^2(F_o^2) + (0.0504P)^2 + 0.4941P]$ where $P = (F_o^2 + 2F_c^2)/3$
$\Delta\rangle_{max}$, $\Delta\rangle_{min}$ (e $Å^{-3}$)	0.78, -0.76

Symmetry code: (i) *x*, *y*, -*z*+1/2.

Software: *CrysAlis PRO* 1.171.38.43 (Rigaku OD, 2015); cell refinement: *CrysAlis PRO* 1.171.38.43 (Rigaku OD, 2015); data reduction: *CrysAlis PRO* 1.171.38.43 (Rigaku OD, 2015); program(s) used to solve structure: *SHELXL2014*/7 (Sheldrick, 2014); program(s) used to refine structure: *SHELXL2014*/7 (Sheldrick, 2014); molecular graphics: Palmer, D. C. (2014). *CrystalMaker*. CrystalMaker Software Ltd, Begbroke, Oxfordshire, England.; software used to prepare material for publication: *WinGX* (Farrugia, 2012). *publCIF* [Westrip, S. P. (2010). *J. Appl. Cryst.*, **43**, 920-925] software used to generate tabulated data.

Crystallising alongside the needle crystals of organic salt, piperazinium thiocyanate, large clear block crystals crystallised as the major product. From single-crystal X-ray structural analysis, the structure of these block crystals was determined to be a novel zinc-containing coordination complex, dipiperazinium piperazin-1-yl zinc trithiocyanate; crystallising in the monoclinic space group $P2_1/n$. Within the complex zinc is bonded in a distorted tetrahedral geometry to three thiocyanate anions via nitrogen atom coordination and a single piperazine ring again via nitrogen coordination to the metal centre; forming a "virus-shaped" complex as seen in Figure 6.24 with a 1- charge.

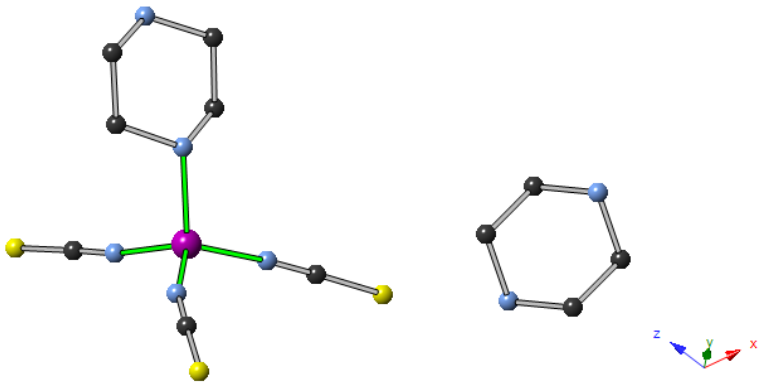

Figure 6.24 An isolated view of novel complex dipiperazinium piperazin-1-yl zinc trithiocyanate as determined by SXD analysis

---

Divalent diprotonated piperazinium cations form the counterbalancing charged units in the structure to give net neutrality with two equivalent ionic zinc complex positions per unit cell. It is notable that the bonding distance of Zn-N1(Pip) 2.0639(14) Å to the bound heterocyclic amine is slightly larger than the near equal Zinc-thiocyanate bond distances of Zn-N3(SCN) 1.9468(16) Å, Zn-N4(SCN) 1.9697(16) Å and Zn-N5(SCN) 1.9388(15) Å within the structure. N-Zn-N angles are in the range 101.79(6)-114.83(7)°; marginally more distorted than comparable examples [12]. Thiocyanate ligands are observed to be near linear with bond angles of 178.23(17)°, 178.34(17)° and 178.80(17)°; with the largest Zn-N-C deviation from linearity of 163.96(15)°. With adjustment to the reagent molar ratios it may be possible to attain a pure

phase of the zinc ionic complex, without excess piperazinium thiocyanate, as the reaction product. A final structure refinement factor of 0.029, weighted refinement factor of 0.071 and goodness of fit of 1.04 was attained from the structural data analysis. Full crystallographic details of the structure solution and refinement are given in Table 6.4 below.

Table 6.4 Crystal data for structure $C_4N_2H_{12}\cdot2((C_4N_2H_9)Zn(NCS)_3)$

Chemical formula	$C_4N_2H_{12}\cdot2((C_4N_2H_9)Zn(NCS)_3)$
M_r	725.67
Crystal system, space group	Monoclinic, $P2_1/n$
Temperature (K)	150
a, b, c (Å)	12.3854 (5), 8.6868 (3), 15.0359 (5)
β (°)	111.663 (4)
V (Å^3)	1503.45 (10)
Z	2
F(000)	752
D_x (Mg m^{-3})	1.625
Radiation type	Mo $K\alpha$
No. of reflections for cell measurement	7565
θ range (°) for cell measurement	3.7–31.6
μ (mm^{-1})	2.05
Crystal shape	Block
Colour	Clear
Data collection	
Diffractometer	Xcalibur, EosS2 diffractometer
Radiation source	fine-focus sealed X-ray tube, Enhance (Mo) X-ray Source
Monochromator	Graphite
Detector resolution (pixels mm^{-1})	8.0734
Scan method	ω scans
Absorption correction	Multi-scan *CrysAlis PRO* 1.171.38.43 (Rigaku Oxford Diffraction, 2015) Empirical absorption correction using spherical harmonics, implemented in SCALE3 ABSPACK scaling algorithm.
T_{min}, T_{max}	0.840, 1.000
No. of measured, independent and observed [$I > 2\sigma(I)$] reflections	16124, 4722, 4090
R_{int}	0.028

θ values (°)	θ_{max} = 31.9, θ_{min} = 3.5
$(\sin\theta/\lambda)_{max}$ (Å^{-1})	0.744
Range of *h*, *k*, *l*	*h* = -18→15, *k* = -12→12, *l* = -21→19
Refinement	
Refinement on	F^2
$R[F^2 > 2\sigma(F^2)]$, $wR(F^2)$, *S*	0.029, 0.071, 1.04
No. of reflections	4722
No. of parameters	221
No. of restraints	0
H-atom treatment	H atoms treated by a mixture of independent and constrained refinement
Weighting scheme	$w = 1/[\sigma^2(F_o^2) + (0.0274P)^2 + 1.1045P]$ where $P = (F_o^2 + 2F_c^2)/3$
$(\Delta/\sigma)_{max}$	1.137
$\Delta\rangle_{max}$, $\Delta\rangle_{min}$ (e Å^{-3})	0.97, -0.66
Extinction method	*SHELXL2014*/7 (Sheldrick 2014, $Fc^*=kFc[1+0.001xFc^2\lambda^3/\sin(2\theta)]^{-1/4}$
Extinction coefficient	0.0026 (3)

Symmetry code: (i) -*x*+1, -*y*+1, -*z*.

Software: *CrysAlis PRO* 1.171.38.43 (Rigaku OD, 2015); cell refinement: *CrysAlis PRO* 1.171.38.43 (Rigaku OD, 2015); data reduction: *CrysAlis PRO* 1.171.38.43 (Rigaku OD, 2015); program(s) used to solve structure: *SHELXL2014*/7 (Sheldrick, 2014); program(s) used to refine structure: *SHELXL2014*/7 (Sheldrick, 2014); molecular graphics: Palmer, D. C. (2014). *CrystalMaker*. CrystalMaker Software Ltd, Begbroke, Oxfordshire, England.; software used to prepare material for publication: *WinGX* (Farrugia, 2012). *publCIF* [Westrip, S. P. (2010). *J. Appl. Cryst.*, **43**, 920-925] software used to generate tabulated data.

A number of other exploratory pseudohalide-based experiments were undertaken under solvothermal synthetic conditions, as seen in Appendix A.15, with combinations of bismuth precursor, thiocyanate precursor and organic/inorganic halide salt precursor reagents in the effort to induce a possible bismuth halometallate hybrid structure with halide-pseudohalide connectivity but with no significant results. Going forward from the work carried out here, the novel thiocyanate complexes described previously could be utilised as precursor reagents in similar solvothermal reaction procedures in a further attempt to yield a bismuth/antimony-based halide-pseudohalide with high structural and electronic connectivity. Studies of similar complexes have also found relevance for the design of drugs [12].

6.6 Conclusions

To summarise, as a result of a methodical series of solvothermal procedures altering a range of experimental parameters, six novel bismuth-carboxylic acid structures were found and analysed by single-crystal X-ray analysis with over 140 products synthesised and screened. Of particular interest from these metal-organic structures is the framework [Bi(1,3,5-benzenetricarboxylic acid)(DMF)] (AD010A P3) due to the nature of whether the channels solvated with bound DMF molecules within the structure can undergo solvent exchange processes or removal from the structure whilst retaining the coordination framework. Gas adsorption (BET) analysis could then also be considered. Concurrently with this study, however, a research team in China also discovered and later published this Bi-BTC framework of interest alongside optical and photocatalytic property data [13].

Although further work studying the physical properties of these new frameworks was not undertaken after these early project results, a developed understanding of the synthesis of bismuth-based metal-organic complexes under solvothermal conditions was then applied to the design and synthesis of more sustainable novel alterative inorganic-organic hybrid materials.

Solvothermal procedures have also been carried out to synthesise BiSI needle crystal structures with a secondary minor BiOI phase. Initial solution-based techniques were utilised in an attempt to find novel semiconducting materials, with an $XBiSI_2$ type structure (where X = Cs, Na), from as-synthesised BiSI as a reagent. With further follow-up investigations doping BiSI through solid-state synthetic procedures (Appendix A.11) yielding known phases of no further interest. A number of other exploratory synthetic procedures in the areas of bismuth-halide double perovskite and bromometallate hybrid materials were undertaken (Appendix A.16-A17), however, no significant results of note were attained from this work.

From the utilisation of thiocyanate in preliminary investigations a novel zinc-thiocyanate coordination complex has been discovered and could be taken forward into future inorganic-organic hybrid framework studies or into other relevant applications; with the possibility of yielding Zn-N-C-S-Bi/Bi-N-C-S-Bi connections within alternative Zn(II)/Bi(III)-based coordination frameworks expanding upon the current knowledge and understanding in the field.

Chapter 7 – Conclusions and future look

7.1 Conclusions

In the search for alternative lead-free semiconducting absorber materials a foundation understanding of structures and the synthetic routes to obtain them is of great importance to be able to build structure-property relationships from the library of stable structures discovered and determine potential applications for those materials. The work undertaken through my research has been directed to a large extent on alternative bismuth- and antimony-based organic-inorganic hybrid structures. From this research, three novel piperazinium cation-based hybrid iodobismuthate materials were discovered, fully structurally characterised and probed for their inherent optical properties and stability to degradation; with the results presented as a full paper (Chapter 3). These isostructural pseudo-three dimensional hybrid materials showed how control of the degree of methylation and steric effects of the organic cation could influence the solvation of the structure and influence the tunability of the band gap through changes to interactions between chains within the anionic substructure; and have been included in a review article on the evolving field of Bi(III) complexes.

A solvothermal synthetic technique to develop templating unique cationic species in-situ in the one-pot reaction procedures was identified and utilised to great effect to contribute to the expansion of known iodometallate (M = Bi, Sb) organic-inorganic hybrid materials; more complex organic structures such as benzimidazolium-related species could be formed from simpler, cheaper and more accessible starting reagents. A total of four compounds (I, II, X and XI) synthesised through in-situ solvothermal high acidity and pressure induced alkylation were included in the second published paper included in Chapter 3; with eleven further structures discovered using the technique described in chapter four. Compound XIII was found to exhibit mixed component architecture with $[Bi_2I_{10}]^{4-}$ and $[BiI_6]^{3-}$ anionic units; not previously reported in the literature and alongside other related studies suggests much more information on the diversity of these structures is yet to be uncovered and understood.

A total of fourteen novel iodometallate structures were included in the more extensive follow-up publication (the second published paper presented in Chapter 3), describing the synthesis, full structural model interpretation and analysis, thermogravimetric stability studies and optical absorption measurements; these included the first four compounds (I, II, X and XI) from in-situ solvothermal high acidity, temperature and pressure induced alkylation, along with ten other hybrid materials synthesised using standard hydrothermal methods. From this series of fourteen compounds a structure-property relationship study of the hybrid structures was identified exhibiting the influence of increased connectivity within the anionic sublattice of hybrid halometallates through weak halogen-halogen interactions as well as structural dimensionality of the anionic component has the effect of a reduction in the band gap energy value of the resulting material. Band gap energies of the pure phases of novel hybrid halometallate materials were observed to be in the range of 1.92 - 2.33 eV; these are not optimal for a single-junction solar cell architectures but are possible alternatives for inclusion in tandem cell designs or in applications requiring semiconducting materials with a large band gap energy.

A unique three-dimensional iodoantimonate superoctahedral-octahedral structural motif has been identified by single-crystal structural analysis and included in chapter 5. The novel motif could be of much interest to the halometallate absorber material community and from this preliminary work it would be expected that further work to achieve full structural analysis of the structure and optimisation of the synthetic route to obtain a pure phase of the material should be undertaken for additional physical property analysis. Although only outline analysis of the structure is presented, the partial structural analysis introduces an unexpected perovskite motif as a new structural class within metal-halide frameworks. Our results reinforce the fact that the area of halometallate materials is underexplored for potential new novel materials with high structural and electronic connectivity and could lead to further interesting results in the search and identification of alternative photovoltaic absorber materials.

7.2 Future look

As alluded to in the presented work, optimisation of certain synthetic procedures to obtain pure phases of each photovoltaic candidate material discovered would be desirable. From this, full physical property determination may be achieved and contribute to a greater understanding of the structure-property trends observed in these materials. It is known that the organic component alone exhibits structure-directing properties, however, manipulation of the synthetic conditions can yield a variety of hybrid structures. For example, different solvate structural forms, polymorphs, and often compounds with different anionic substructure identities can be synthesised. Greater understanding and control of these systems may lead in the future to the synthesis of predictable structures with properties tuned to the desired application.

Bibliography

Chapter 1 – Introduction

1. W. A. Hermann, *Energy*, 2006, **31**, 1685-1702.
2. *https://pureenergies.com/us/home-solar/how-solar-works/solar-energy-facts/*
3. G. K. Singh, *Energy*, 2013, **53**, 1-13.
4. Inorganic Chemistry, 5th Edition, *Shriver & Atkins et al*, 2009, ISBN 978-0199236176
5. W. Shockley and H. J. Queisser, *Journal of Applied Physics*, 1961, **32**, 510.
6. *http://ec.europa.eu/clima/policies/eccp/index_en.htm*
7. *https://www.gov.uk/government/news/controlling-the-cost-of-renewable-energy*
8. *http://energyinformative.org/solar-energy-pros-and-cons/*
9. T. M. Razykov, C. S. Ferekides, D. Morel, E. Stefanakos, H. S. Ullal and H. M. Upadhyaya, *Solar Energy*, 2011, **85**, 1580-1608.
10. B. Parida, S. Iniyan and R. Goic, *Renewable & Sustainable Energy Reviews*, 2011, **15**, 1625-1636.
11. M. A. Green, *J Mat Electron*, 2007, **18**, S15-S19.
12. Z. J. Ning, H. P. Dong, Q. Zhang, O. Voznyy and E. H. Sargent, *ACS Nano*, 2014, **8**, 10321-10327.
13. L. El Chaar, L. A. Lamont and N. El Zein, *Renewable & Sustainable Energy Reviews*, 2011, **15**, 2165-2175.
14. S. D. Stranks and H. J. Snaith, *Nature Nanotechnology*, 2015, **10**, 391-402.
15. T. P. Dhakal, C. Y. Peng, R. R. Tobias, R. Dasharathy and C. R. Westgate, *Solar Energy*, 2014, **100**, 23-30.
16. J. Patel, F. Mighri, A. Ajji, D. Tiwari and T. K. Chaudhuri, *Applied Physics a-Materials Science & Processing*, 2014, **117**, 1791-1799.
17. J. Burschka, N. Pellet, S. J. Moon, R. Humphry-Baker, P. Gao, M. K. Nazeeruddin and M. Gratzel, *Nature*, 2013, **499**, 316.
18. M. D. Xiao, F. Z. Huang, W. C. Huang, Y. Dkhissi, Y. Zhu, J. Etheridge, A. Gray-Weale, U. Bach, Y. B. Cheng and L. Spiccia, *Angewandte Chemie-International Edition*, 2014, **53**, 9898-9903.
19. M. Z. Liu, M. B. Johnston and H. J. Snaith, *Nature*, 2013, **501**, 395.
20. D. Y. Liu and T. L. Kelly, *Nature Photonics*, 2014, **8**, 133-138.
21. Y. Kutes, L. H. Ye, Y. Y. Zhou, S. P. Pang, B. D. Huey and N. P. Padture, *Journal of Physical Chemistry Letters*, 2014, **5**, 3335-3339.
22. D. Perednis and L. J. Gauckler, *Journal of Electroceramics*, 2005, **14**, 103-111.

23. W. Wang, S. Y. Wang and M. Liu, *Materials Research Bulletin*, 2005, **40**, 1781-1786.
24. N. T. Hahn, A. J. E. Rettie, S. K. Beal, R. R. Fullon and C. B. Mullins, *Journal of Physical Chemistry C*, 2012, **116**, 24878-24886.
25. H. Suzuki and Y. Matano, *Organobismuth Chemistry*, 2001, ISBN 978-0444205285
26. X. Xiao and W. D. Zhang, *Journal of Materials Chemistry*, 2010, **20**, 5866-5870.
27. X. Zhang, Z. H. Ai, F. L. Jia and L. Z. Zhang, *Journal of Physical Chemistry C*, 2008, **112**, 747-753.
28. Y. Y. Li, J. S. Wang, B. Liu, L. Y. Dang, H. C. Yao and Z. J. Li, *Chemical Physics Letters*, 2011, **508**, 102-106.
29. K. Zhao, X. Zhang and L. Z. Zhang, *Electrochemistry Communications*, 2009, **11**, 612-615.
30. J. Lee, B. K. Min, I. Cho and Y. Sohn, *Bulletin of the Korean Chemical Society*, 2013, **34**, 773-776.
31. S. Meng, X. Zhang, G. H. Zhang, Y. M. Wang, H. Zhang and F. Q. Huang, *Inorganic Chemistry*, 2015, **54**, 5768-5773.
32. Y. Mizuguchi, H. Fujihisa, Y. Gotoh, K. Suzuki, H. Usui, K. Kuroki, S. Demura, Y. Takano, H. Izawa and O. Miura, *Physical Review B*, 2012, **86**, 5.
33. S. K. Singh, A. Kumar, B. Gahtori, Shruti, G. Sharma, S. Patnaik and V. P. S. Awana, *Journal of the American Chemical Society*, 2012, **134**, 16504-16507.
34. X. Zhang, Y. F. Liu, G. H. Zhang, Y. Q. Wang, H. Zhang and F. Q. Huang, *ACS Applied Materials & Interfaces*, 2015, **7**, 4442-4448.
35. H. M. Cui, H. Liu, X. Li, J. Y. Wang, F. Han, X. D. Zhang and R. I. Boughton, *Journal of Solid State Chemistry*, 2004, **177**, 4001-4006.
36. X. B. Zhao, X. H. Ji, Y. H. Zhang, T. J. Zhu, J. P. Tu and X. B. Zhang, *Applied Physics Letters*, 2005, **86**, 3.
37. C. B. Satterthwaite and R. W. Ure, *Physical Review*, 1957, **108**, 1164-1170.
38. G. L. Sun, X. Y. Qin, D. Li, J. Zhang, B. J. Ren, T. H. Zou, H. X. Xin, S. B. Paschen and X. L. Yan, *Journal of Alloys and Compounds*, 2015, **639**, 9-14.
39. H. C. Liao, M. C. Wu, M. H. Jao, C. M. Chuang, Y. F. Chen and W. F. Su, *CrystEngcomm*, 2012, **14**, 3645-3652.
40. M. Salavati-Niasari, Z. Behfard, O. Amiri, E. Khosravifard and S. M. Hosseinpour-Mashkani, *Journal of Cluster Science*, 2013, **24**, 349-363.
41. M. B. Sigman and B. A. Korgel, *Chemistry of Materials*, 2005, **17**, 1655-1660.
42. H. Wang, J. J. Zhu, J. M. Zhu and H. Y. Chen, *Journal of Physical Chemistry B*, 2002, **106**, 3848-3854.
43. V. Kaltenhauser, T. Rath, W. Haas, A. Torvisco, S. K. Muller, B. Friedel, B. Kunert, R. Saf, F. Hofer and G. Trimmel, *Journal of Materials Chemistry C*, 2013, **1**, 7825-7832.

44. Q. F. Han, J. Chen, X. J. Yang, L. Lu and X. Wang, *Journal of Physical Chemistry C*, 2007, **111**, 14072-14077.
45. Y. W. Koh, C. S. Lai, A. Y. Du, E. R. T. Tiekink and K. P. Loh, *Chemistry of Materials*, 2003, **15**, 4544-4554.
46. L. Y. Zhu, Y. Xie, X. W. Zheng, X. Yin and X. B. Tian, *Inorganic Chemistry*, 2002, **41**, 4560-4566.
47. A. Audzijonis, G. Gaigalas, L. Zigas, A. Pauliukas, R. Zaltauskas, A. Cerskus, J. Narusis and A. Kvedaravicius, *Physica B-Condensed Matter*, 2007, **391**, 22-27.
48. A. Audzijonis, R. Zaltauskas, R. Sereika, L. Zigas and A. Reza, *Journal of Physics and Chemistry of Solids*, 2010, **71**, 884-891.
49. J. Horak, K Cemak, *Czech J Phys*, 1965, 536-538
50. N. T. Hahn, J. L. Self and C. B. Mullins, *Journal of Physical Chemistry Letters*, 2012, **3**, 1571-1576.
51. S. Kazim, M. K. Nazeeruddin, M. Gratzel and S. Ahmad, *Angewandte Chemie-International Edition*, 2014, **53**, 2812-2824.
52. C. C. Stoumpos, C. D. Malliakas and M. G. Kanatzidis, *Inorganic Chemistry*, 2013, **52**, 9019-9038.
53. J. P. Correa-Baena, M. Saliba, T. Buonassisi, M. Gratzel, A. Abate, W. Tress and A. Hagfeldt, *Science*, 2017, **358**, 739-744.
54. P. P. Boix, S. Agarwala, T. M. Koh, N. Mathews and S. G. Mhaisalkar, *Journal of Physical Chemistry Letters*, 2015, **6**, 898-907.
55. Q. L. Jiang, D. Rebollar, J. Gong, E. L. Piacentino, C. Zheng and T. Xu, *Angewandte Chemie-International Edition*, 2015, **54**, 7617-7620.
56. A. Halder, R. Chulliyil, A. S. Subbiah, T. Khan, S. Chattoraj, A. Chowdhury and S. K. Sarkar, *Journal of Physical Chemistry Letters*, 2015, **6**, 3483-3489.
57. R. E. Brandt, V. Stevanovic, D. S. Ginley and T. Buonassisi, *MRS Communications*, 2015, **5**, 265-275.
58. Z. W. Xiao, W. W. Meng, J. B. Wang, D. B. Mitzi and Y. F. Yan, *Materials Horizons*, 2017, **4**, 206-216.
59. J. M. Frost, K. T. Butler, F. Brivio, C. H. Hendon, M. van Schilfgaarde and A. Walsh, *Nano Letters*, 2014, **14**, 2584-2590.
60. N. K. Noel, S. D. Stranks, A. Abate, C. Wehrenfennig, S. Guarnera, A. A. Haghighirad, A. Sadhanala, G. E. Eperon, S. K. Pathak, M. B. Johnston, A. Petrozza, L. M. Herz and H. J. Snaith, *Energy & Environmental Science*, 2014, **7**, 3061-3068.
61. M. Weiss, J. Horn, C. Richter and D. Schlettwein, *Physica Status Solidi a-Applications and Materials Science*, 2016, **213**, 975-981.

62. C. C. Stoumpos, L. Frazer, D. J. Clark, Y. S. Kim, S. H. Rhim, A. J. Freeman, J. B. Ketterson, J. I. Jang and M. G. Kanatzidis, *Journal of the American Chemical Society*, 2015, **137**, 6804-6819.
63. D. B. Mitzi, S. Wang, C. A. Feild, C. A. Chess and A. M. Guloy, *Science*, 1995, **267**, 1473-1476.
64. D. B. Mitzi, C. D. Dimitrakopoulos and L. L. Kosbar, *Chemistry of Materials*, 2001, **13**, 3728-3740.
65. K. Eckhardt, V. Bon, J. Getzschmann, J. Grothe, F. M. Wisser and S. Kaskel, *Chemical Communications*, 2016, **52**, 3058-3060.
66. Y. N. Ivanov, A. A. Sukhovskii, V. V. Lisin and I. P. Aleksandrova, *Inorganic Materials*, 2001, **37**, 623-627.
67. P. Szklarz, A. Pietraszko, R. Jakubas, G. Bator, P. Zielinski and M. Galazka, *Journal of Physics-Condensed Matter*, 2008, **20**, 12.
68. R. L. Z. Hoye, R. E. Brandt, A. Osherov, V. Stevanovic, S. D. Stranks, M. W. B. Wilson, H. Kim, A. J. Akey, J. D. Perkins, R. C. Kurchin, J. R. Poindexter, E. N. Wang, M. G. Bawendi, V. Bulovic and T. Buonassisi, *Chemistry-a European Journal*, 2016, **22**, 2605-2610.
69. B. W. Park, B. Philippe, X. L. Zhang, H. Rensmo, G. Boschloo and E. M. J. Johansson, *Advanced Materials*, 2015, **27**, 6806.
70. F. X. Wei, Z. Y. Deng, S. J. Sun, F. Xie, G. Kieslich, D. M. Evans, M. A. Carpenter, P. D. Bristowe and A. K. Cheetham, *Materials Horizons*, 2016, **3**, 328-332.
71. E. T. McClure, M. R. Ball, W. Windl and P. M. Woodward, *Chemistry of Materials*, 2016, **28**, 1348-1354.
72. A. H. Slavney, T. Hu, A. M. Lindenberg and H. I. Karunadasa, *Journal of the American Chemical Society*, 2016, **138**, 2138-2141.
73. G. Volonakis, M. R. Filip, A. A. Haghighirad, N. Sakai, B. Wenger, H. J. Snaith and F. Giustino, *Journal of Physical Chemistry Letters*, 2016, **7**, 1254-1259.
74. S. L. Li and Q. Xu, *Energy & Environmental Science*, 2013, **6**, 1656-1683.
75. M. Feyand, E. Mugnaioli, F. Vermoortele, B. Bueken, J. M. Dieterich, T. Reimer, U. Kolb, D. de Vos and N. Stock, *Angewandte Chemie-International Edition*, 2012, **51**, 10373-10376.
76. J. P. Lei, R. C. Qian, P. H. Ling, L. Cui and H. X. Ju, *Trac-Trends in Analytical Chemistry*, 2014, **58**, 71-78.
77. Q. L. Zhu, T. L. Sheng, R. B. Fu, S. M. Hu, J. S. Chen, S. C. Xiang, C. J. Shen and X. T. Wu, *Crystal Growth & Design*, 2009, **9**, 5128-5134.
78. X. P. Zhang, D. G. Wang, Y. Su, H. R. Tian, J. J. Lin, Y. L. Fenga and J. W. Cheng, *Dalton Transactions*, 2013, **42**, 10384-10387.
79. M. Savage, S. H. Yang, M. Suyetin, E. Bichoutskaia, W. Lewis, A. J. Blake, S. A. Barnett and M. Schroder, *Chemistry-a European Journal*, 2014, **20**, 8024-8029.

80. E. Bichoutskaia, M. Suyetin, M. Bound, Y. Yan and M. Schroder, *Journal of Physical Chemistry C*, 2014, **118**, 15573-15580.
81. D. Banerjee, A. J. Cairns, J. Liu, R. K. Motkuri, S. K. Nune, C. A. Fernandez, R. Krishna, D. M. Strachan and P. K. Thallapally, *Accounts of Chemical Research*, 2015, **48**, 211-219.
82. P. Horcajada, C. Serre, M. Vallet-Regi, M. Sebban, F. Taulelle and G. Ferey, *Angewandte Chemie-International Edition*, 2006, **45**, 5974-5978.
83. E. Haque, J. E. Lee, I. T. Jang, Y. K. Hwang, J. S. Chang, J. Jegal and S. H. Jhung, *Journal of Hazardous Materials*, 2010, **181**, 535-542.
84. X. Zhang, W Wang, *Coord Chem Rev*, **284**, 2015, 206-235
85. A. C. Wibowo, M. D. Smith and H. C. zur Loye, *Chemical Communications*, 2011, **47**, 7371-7373.
86. A. C. Wibowo, M. D. Smith and H. C. zur Loye, *CrystEngcomm*, 2011, **13**, 426-429.
87. A. Thirumurugan and A. K. Cheetham, *European Journal of Inorganic Chemistry*, 2010, 3823-3828.
88. A. Thirumurugan, W. Li and A. K. Cheetham, *Dalton Transactions*, 2012, **41**, 4126-4134.
89. M. Feyand, M. Koppen, G. Friedrichs and N. Stock, *Chemistry-a European Journal*, 2013, **19**, 12537-12546.
90. A. C. Wibowo, S. A. Vaughn, M. D. Smith and H. C. zur Loye, *Inorganic Chemistry*, 2010, **49**, 11001-11008.
91. A. C. Wibowo, M. D. Smith and H. C. zur Loye, *Crystal Growth & Design*, 2011, **11**, 4449-4457.
92. M. E. Lines, A. M. Glass, *Principles and applications of ferroelectrics and related materials*, 1977.
93. M. Bujak and J. Zaleski, *Journal of Molecular Structure*, 2003, **647**, 121-128.
94. B. Kulicka, R. Jakubas, A. Pietraszko, W. Medycki and J. Swiergiel, *Journal of Molecular Structure*, 2006, **783**, 88-95.
95. W. Medycki, K. Holderna-Natkaniec, J. Swiergiel and R. Jakubas, *Solid State Nuclear Magnetic Resonance*, 2003, **24**, 209-217.
96. M. Wojtas and R. Jakubas, *Journal of Physics-Condensed Matter*, 2004, **16**, 7521-7534.
97. I. Plowas, G. Bator, R. Jakubas and J. Baran, *Vibrational Spectroscopy*, 2012, **62**, 121-132.
98. P. Szklarz, J. Zaleski, R. Jakubas, G. Bator, W. Medycki and K. Falinska, *Journal of Physics-Condensed Matter*, 2005, **17**, 2509-2528.
99. G. A. Mousdis, G. C. Papavassiliou, A. Terzis and C. P. Raptopoulou, *Zeitschrift Fur Naturforschung Section B-a Journal of Chemical Sciences*, 1998, **53**, 927-931.
100. S. K. Batabyal, C. Basu, A. R. Das and G. S. Sanyal, *Materials Letters*, 2006, **60**, 2582-2585.
101. A. Chaudhuri, S. Mitra, M. Mandal and K. Mandal, *Journal of Alloys and Compounds*, 2010, **491**, 703-706.

102. X. Yang, Y. F. Zhang, G. Xu, X. Wei, Z. H. Ren, G. Shen and G. R. Han, *Materials Research Bulletin*, 2013, **48**, 1694-1699.

103. M. Bella, C. Rivero, S. Blayac, H. Basti, M. C. Record and P. Boulet, *Materials Research Bulletin*, 2017, **90**, 188-194.

104. W. D. Shi, J. B. Yu, H. S. Wang and H. J. Zhang, *Journal of the American Chemical Society*, 2006, **128**, 16490-16491.

105. W. D. Shi, L. Zhou, S. Y. Song, J. H. Yang and H. J. Zhang, *Advanced Materials*, 2008, **20**, 1892.

106. R. C. Jin, G. Chen, Q. Wang, J. X. Sun and Y. Wang, *Journal of Materials Chemistry*, 2011, **21**, 6628-6635.

107. S. X. Zhou, Y. X. Ke, J. M. Li and S. M. Lu, *Materials Letters*, 2003, **57**, 2053-2055.

108. A. C. Mera, Y. Moreno, J. Y. Pivan, O. Pena and H. D. Mansilla, *Journal of Photochemistry and Photobiology a-Chemistry*, 2014, **289**, 7-13.

109. X. Su, G. Zhang, T. Liu, Y. Liu, J. G. Qin and C. T. Chen, *Russian Journal of Inorganic Chemistry*, 2006, **51**, 1864-1868.

110. C. R. Wang, K. B. Tang, Q. Yang, B. Hai, G. Z. Shen, C. H. An, W. C. Yu and Y. T. Qian, *Inorganic Chemistry Communications*, 2001, **4**, 339-341.

Chapter 2 – Experimental Techniques

1. E. A. Moore, L. E. Smart, *Solid State Chemistry: An Introduction*, **2012**, ISBN 978-1-4398-4790-9

2. W. Clegg, *Crystal Structure Determination*, Oxford Chemistry Primer, 0-19-855907-1

3. www.nobelprize.org/prizes/physics/1915/summary/

4. *Inorganic Chemistry, 5th Edition*, Shriver & Atkins et al, **2009**, ISBN 978-0199236176

5. S. Grazulis, D. Chateigner, R. T. Downs, A. T. Yokochi, M. Quirós, L. Lutterotti, E. Manakova, J. Butkus, P. Moeck and A. Le Bail: "Crystallography Open Database - an open-access collection of crystal structures", J. Appl. Cryst. **2009**, 42, 726-729.

6. L. J. Farrugia, *Journal of Applied Crystallography*, **2012**, 45, 849-854.

7. L. J. Farrugia, *Journal of Applied Crystallography*, **1999**, 32, 837-838.

8. G. M. Sheldrick, XPREP. *Space Group Determination and Reciprocal Space Plots*, **1991**.

9. G. M. Sheldrick, *Program for Crystal structure solution*, Institut fur Anorganische Chemie der Universitat, Tammanstrasse 4, D-3400, Gottingen, Germany, **1986**.

10. G. M. Sheldrick, SHELXL 2014/7, *Program for crystal structure solution and refinement*, **2014**.

11. G. M. Sheldrick, *Acta Crystallogr, Sect.A: Fundam.Crystallogr*, **2008**, A64, 112-122.

Chapter 3 – Hybrid halometallate materials: Part I

1. H. Hu, B. H. Dong and W. Zhang, *Journal of Materials Chemistry A*, **2017**, 5, 11436-11449.

2. S. F. Hoefler, G. Trimmel and T. Rath, *Monatshefte Fur Chemie*, **2017**, 148, 795-826.

3. B. Saparov, F. Hong, J. P. Sun, H. S. Duan, W. W. Meng, S. Cameron, I. G. Hill, Y. F. Yan and D. B. Mitzi, *Chemistry of Materials*, **2015**, 27, 5622-5632.

4. P. Szklarz, A. Pietraszko, R. Jakubas, G. Bator, P. Zielinski and M. Galazka, *Journal of Physics-Condensed Matter*, **2008**, 20, 12.

5. G. Bator, J. Baran, R. Jakubas and L. Sobczyk, *Journal of Molecular Structure*, **1998**, 450, 89-100.

6. A. J. Lehner, D. H. Fabini, H. A. Evans, C. A. Hebert, S. R. Smock, J. Hu, H. B. Wang, J. W. Zwanziger, M. L. Chabinyc and R. Seshadri, *Chemistry of Materials*, **2015**, 27, 7137-7148.

7. V. Y. Kotov, A. B. Ilyukhin, A. E. Baranchikov, R. I. Ishmetova, G. L. Rusinov and S. A. Kozyukhin, *Journal of Molecular Structure*, **2018**, 1151, 186-190.

8. T. A. Shestimerova, N. A. Golubev, N. A. Yelavik, M. A. Bykov, A. V. Grigorieva, Z. Wei, E. V. Dikarev and A. V. Shevelkov, *Crystal Growth & Design*, **2018**, 18, 2572-2578.

9. Z. P. Zhang, Q. Y. Feng, Q. L. Wang, X. Y. Huang, D. Chen and J. Zhou, *Journal of Cluster Science*, **2018**, 29, 367-374.

10. Z. P. Zhang, Q. Y. Feng, Y. L. Wei, Z. Y. Gao, Z. W. Wang and Y. M. Wang, *Journal of Cluster Science*, **2018**, 29, 725-735.

11. V. Y. Kotov, A. B. Ilyukhin, A. A. Korlyukov, A. F. Smol'yakov and S. A. Kozyukhin, *New Journal of Chemistry*, **2018**, 42, 6354-6363.

12. S. A. Adonin, M. N. Sokolov and V. P. Fedin, *Russian Journal of Inorganic Chemistry*, **2017**, 62, 1789-1796.

13. T. A. Shestimerova, N. A. Yelavik, A. V. Mironov, A. N. Kuznetsov, M. A. Bykov, A. V. Grigorieva, V. V. Utochnikova, L. S. Lepnev and A. V. Shevelkov, *Inorganic Chemistry*, **2018**, 57, 4077-4087.

14. S. A. Adonin, M. N. Sokolov and V. P. Fedin, *Coordination Chemistry Reviews*, **2016**, 312, 1-21.

Chapter 4 – Hybrid halometallate materials: Part II

1. C. Hrizi, A. Trigui, Y. Abid, N. Chniba-Boudjada, P. Bordet and S. Chaabouni, *Journal of Solid State Chemistry*, **2011**, 184, 3336-3344.

Chapter 5 – Hybrid halometallate materials: Part III

1. A. J. Zhou, J. D. Leng, J. S. Hu and M. L. Tong, *Dalton Transactions*, **2013**, 42, 9428-9431.

Chapter 6 – Coordination polymer, pseudohalide and bismuth chalcohalide materials

1. J. Lee, B. K. Min, I. Cho and Y. Sohn, *Bulletin of the Korean Chemical Society*, **2013**, 34, 773-776.

2. C. C. Stoumpos, C. D. Malliakas and M. G. Kanatzidis, *Inorganic Chemistry*, **2013**, 52, 9019-9038.

3. O. Lindqvis, *Acta Chemica Scandinavica*, **1968**, 22, 2943.

4. A. Halder, R. Chulliyil, A. S. Subbiah, T. Khan, S. Chattoraj, A. Chowdhury and S. K. Sarkar, *Journal of Physical Chemistry Letters*, **2015**, 6, 3483-3489.

5. Q. L. Jiang, D. Rebollar, J. Gong, E. L. Piacentino, C. Zheng and T. Xu, *Angewandte Chemie-International Edition*, **2015**, 54, 7617-7620.

6. A. Toma, C. I. Rat, A. Silvestru, T. Ruffer, H. Lang and M. Mehring, *Journal of Organometallic Chemistry*, **2013**, 745, 71-79.

7. Y. N. Chen, B. B. Li, W. Huang, D. Q. Gao and Z. Q. Liang, *Chemical Communications*, **2015**, 51, 11997-11999.

8. M. Daub and H. Hillebrecht, *Angewandte Chemie-International Edition*, **2015**, 54, 11016-11017.

9. A. M. Ganose, C. N. Savory and D. O. Scanlon, *Journal of Physical Chemistry Letters*, **2015**, 6, 4594-4598.

10. A. Crispini, R. J. Errington, G. A. Fisher, F. J. Funke, N. C. Norman, A. G. Orpen, S. E. Stratford and O. Struve, *Journal of the Chemical Society-Dalton Transactions*, **1994**, 1327-1335.

11. S. R. Petrusenko, V. N. Kokozay and I. O. Fritsky, *Polyhedron*, **1997**, 16, 267-274.

12. K. Balasubramani, P. Devi, M. Hemamalini, P. T. Muthiah and R. J. Butcher, *Journal of Chemical Crystallography*, **2011**, 41, 1894-1900.

13. G. Z. Wang, Y. Y. Liu, B. B. Huang, X. Y. Qin, X. Y. Zhang and Y. Dai, *Dalton Transactions*, **2015**, 44, 16238-16241.

A. Appendices

A.1. Bismuth Nitrate Pentahydrate- Carboxylic Acid Solvothermal Synthetic Procedures

Experiment Code	Temperature	Solvent	Carboxylic Acid	Product Code	Crystals Obtained	Cooling procedure employed	Bismuth:Carboxylic Acid Ratio (mmol)	Notes
AD002 & AD005	180ºC	Water	1,4-Benzenedicarboxylic acid	AD002 P1	Y	Y	0.5:1.7	
			1,2,4,5-Benzenetetracarboxylic acid	AD002 P2	Y	Y	1.0:1.2	
			1,3,5-Benzenetricarboxylic acid	AD005 P1	Y	Y	1.0:1.2	
			2,6-Naphthalenedicarboxylic acid	AD005 P2	N	Y	1.0:1.2	
			1,4,5,8-Napthalenetetracarboxylic acid	AD005 P3	N	Y	1.0:1.2	
AD005B	180ºC	Water	3,5-Pyridinedicarboxylic acid	AD005B P1	N	N	1.0:1.2	
			2,6-Pyridinedicarboxylic acid	AD005B P2	Y	N	1.0:1.2	
			2,3-Pyridinedicarboxylic acid	AD005B P3	Y	N	1.0:1.2	
			3,4-Pyridinedicarboxylic acid	AD005B P4	N	N	1.0:1.2	
			2,5-Pyridinedicarboxylic acid	AD005B P5	Y	N	1.0:1.2	
AD009A	180ºC	Dimethylformamide	1,4-Benzenedicarboxylic acid	AD009A P1	N	N	1.0:1.2	
			1,2,4,5-Benzenetetracarboxylic acid	AD009A P2	N	N	1.0:1.2	
			1,3,5-Benzenetricarboxylic acid	AD009A P3	N	N	1.0:1.2	
			2,6-Naphthalenedicarboxylic acid	AD009A P4	N	N	1.0:1.2	
			1,4,5,8-Napthalenetetracarboxylic acid	AD009A P5	N	N	1.0:1.2	
AD009B	180ºC	Dimethylformamide	3,5-Pyridinedicarboxylic acid	AD009B P1	N	N	1.0:1.2	
			2,6-Pyridinedicarboxylic acid	AD009B P2	Y	N	1.0:1.2	
			2,3-Pyridinedicarboxylic acid	AD009B P3	N	N	1.0:1.2	

			3,4-Pyridinedicarboxylic acid	AD009B P4	N	N	1.0:1.2	
			2,5-Pyridinedicarboxylic acid	AD009B P5	N	N	1.0:1.2	
AD010A	120ºC	Dimethylformamide	1,4-Benzenedicarboxylic acid	AD010A P1	N	N	1.0:1.2	
		(5ml)	1,2,4,5-Benzenetetracarboxylic acid	AD010A P2	N	N	1.0:1.2	
			1,3,5-Benzenetricarboxylic acid	AD010A P3	Y	N	1.0:1.2	
			2,6-Naphthalenedicarboxylic acid	AD010A P4	N	N	1.0:1.2	
			1,4,5,8-Napthalenetetracarboxylic acid	AD010A P5	N	N	1.0:1.2	
AD010B	120ºC	Dimethylformamide	3,5-Pyridinedicarboxylic acid	AD010B P1	N	N	1.0:1.2	
		(10ml)	2,6-Pyridinedicarboxylic acid	AD010B P2	Y	N	1.0:1.2	
			2,3-Pyridinedicarboxylic acid	AD010B P3	N	N	1.0:1.2	
			3,4-Pyridinedicarboxylic acid	AD010B P4	N	N	1.0:1.2	
			2,5-Pyridinedicarboxylic acid	AD010B P5	Y	N	1.0:1.2	
			1,3,5-Benzenetricarboxylic acid	AD010B P6	Y	N	1.0:1.2	
AD011A	180ºC	Water (10ml)	1,3-Adamantanedicarboxylic acid	AD011A P1	Y	0.1ºC/min	0.1:0.3	KOH (0.1mmol) Crystals (Cubic Appearance) Sandy coloured (s15mtw031 & e15mtw06)
			1,3-Adamantanedicarboxylic acid	AD011A P2	Y	0.1ºC/min	0.1:0.3	KOH (0.2mmol) Small crystals
			1,3-Adamantanedicarboxylic acid	AD011A P3	N	0.1ºC/min	0.1:0.3	KOH (0.3mmol)
			1,3-Adamantanedicarboxylic acid	AD011A P4	N	0.1ºC/min	0.1:0.3	Ethylenediamine (a few drops below neutral pH i.e. slightly acidic)
			1,3-Adamantanedicarboxylic acid	AD011A P5	N	0.1ºC/min	0.1:0.3	Ethylenediamine (adjusted to neutral pH dropwise)
			1,3-Adamantanedicarboxylic acid	AD011A P6	N	0.1ºC/min	0.1:0.3	Ethylenediamine (a few drops

								above neutral pH i.e. slightly basic)
AD011B	100ºC	DMF (5ml)	1,3-Adamantanedicarboxylic acid	AD011B P1	N	0.1ºC/min	0.1:0.3	KOH (0.1mmol)
			1,3-Adamantanedicarboxylic acid	AD011B P2	Y	0.1ºC/min	0.1:0.3	KOH (0.2mmol) Jagged white crystals. (s15mtw030 & s15mtw034)
			1,3-Adamantanedicarboxylic acid	AD011B P3	Y	0.1ºC/min	0.1:0.3	KOH (0.3mmol) White crystals. (s15mtw033)
			1,3-Adamantanedicarboxylic acid	AD011B P4	N	0.1ºC/min	0.1:0.3	Ethylenediamine (1 drop)
			1,3-Adamantanedicarboxylic acid	AD011B P5	N	0.1ºC/min	0.1:0.3	Ethylenediamine (2 drops)
			1,3-Adamantanedicarboxylic acid	AD011B P6	N	0.1ºC/min	0.1:0.3	Ethylenediamine (3 drops)
AD012A	180ºC	Water (10ml)	Diphenic Acid (Biphenyl-2,2'-dicarboxylic acid)	AD012A P1	N	0.1ºC/min	1.0:1.2	KOH (0.5mmol)
			Diphenic Acid (Biphenyl-2,2'-dicarboxylic acid)	AD012A P2	N	0.1ºC/min	1.0:1.2	KOH (1.0mmol)
			Diphenic Acid (Biphenyl-2,2'-dicarboxylic acid)	AD012A P3	N	0.1ºC/min	1.0:1.2	KOH (1.5mmol)
			Diphenic Acid (Biphenyl-2,2'-dicarboxylic acid)	AD012A P4	N	0.1ºC/min	1.0:1.2	Ethylenediamine (adjust dropwise to slightly below neutral pH i.e. slighty acidic)
			Diphenic Acid (Biphenyl-2,2'-dicarboxylic acid)	AD012A P5	N	0.1ºC/min	1.0:1.2	Ethylenediamine (adjust dropwise to neutral pH)
			Diphenic Acid (Biphenyl-2,2'-dicarboxylic acid)	AD012A P6	N	0.1ºC/min	1.0:1.2	Ethylenediamine (adjust dropwise to slightly above neutral pH i.e. slighty basic)
AD012B	100ºC	DMF (5ml)	Diphenic Acid (Biphenyl-2,2'-dicarboxylic acid)	AD012B P1	N	0.1ºC/min	0.5:0.6	KOH (0.5mmol)
			Diphenic Acid (Biphenyl-2,2'-dicarboxylic acid)	AD012B P2	N	0.1ºC/min	0.5:0.6	KOH (1.0mmol)

			Diphenic Acid (Biphenyl-2,2'-dicarboxylic acid)	AD012B P3	Y	0.1°C/min	0.5:0.6	KOH (1.5mmol) Long large crystals determined as Potassium Carbonate
			Diphenic Acid (Biphenyl-2,2'-dicarboxylic acid)	AD012B P4	N	0.1°C/min	0.5:0.6	Ethylenediamine (adjust dropwise to slightly below neutral pH i.e. slighty acidic)
			Diphenic Acid (Biphenyl-2,2'-dicarboxylic acid)	AD012B P5	N	0.1°C/min	0.5:0.6	Ethylenediamine (adjust dropwise to neutral pH)
			Diphenic Acid (Biphenyl-2,2'-dicarboxylic acid)	AD012B P6	N	0.1°C/min	0.5:0.6	Ethylenediamine (adjust dropwise to slightly above neutral pH i.e. slighty basic)
AD027	120oC	DMF (5ml)	1,3,5-Benzenetricarboxylic Acid	AD027 P1		1°C/min	1.0:1.2	No KOH
		DMF (5ml)	1,3,5-Benzenetricarboxylic Acid	AD027 P2		1°C/min	1.0:1.2	No KOH

A.2. Bismuth Oxychloride - Carboxylic Acid Solvothermal Synthetic Procedures

Experiment Code	Temperature	Solvent	Carboxylic Acid	Product Code	Crystals Obtained	Extended cooling procedure employed	Bismuth:Carboxylic Acid Ratio (mmol)	Notes
AD006A	180°C	Water	1,4-Benzenedicarboxylic acid	AD006A P1	Y	Y	1.0:1.2	Cream polycrystalline powder + colourless crystals. Crystallised Carboxylic Acid Obtained
			1,2,4,5-Benzenetetracarboxylic acid	AD006A P2	N	Y	1.0:1.2	
			1,3,5-Benzenetricarboxylic acid	AD006A P3	N	Y	1.0:1.2	Solvent Evaporated
			2,6-Naphthalenedicarboxylic acid	AD006A P4	N	Y	1.0:1.2	Solvent Evaporated
			1,4,5,8-Napthalenetetracarboxylic acid	AD006A P5	N	Y	1.0:1.2	Solvent Evaporated
AD006B	180°C	Water	3,5-Pyridinedicarboxylic acid	AD006B P1	Y	N	1.0:1.2	Crystallised Carboxylic Acid Obtained
			2,6-Pyridinedicarboxylic acid	AD006B P2	N	N	1.0:1.2	

			2,3-Pyridinedicarboxylic acid	AD006B P3	N	N	1.0:1.2	
			3,4-Pyridinedicarboxylic acid	AD006B P4	N	N	1.0:1.2	
			2,5-Pyridinedicarboxylic acid	AD006B P5	N	N	1.0:1.2	Solvent Evaporated
AD007A	180ºC	Ethylene Glycol	1,4-Benzenedicarboxylic acid	AD007A P1	N	N	1.0:1.2	
			1,2,4,5-Benzenetetracarboxylic acid	AD007A P2	N	N	1.0:1.2	
			1,3,5-Benzenetricarboxylic acid	AD007A P3	N	N	1.0:1.2	
			2,6-Naphthalenedicarboxylic acid	AD007A P4	N	N	1.0:1.2	
			1,4,5,8-Napthalenetetracarboxylic acid	AD007A P5	N	N	1.0:1.2	
AD007B	180ºC	Ethylene Glycol	3,5-Pyridinedicarboxylic acid	AD007B P1	N	N	1.0:1.2	
			2,6-Pyridinedicarboxylic acid	AD007B P2	N	N	1.0:1.2	
			2,3-Pyridinedicarboxylic acid	AD007B P3	N	N	1.0:1.2	
			3,4-Pyridinedicarboxylic acid	AD007B P4	N	N	1.0:1.2	
			2,5-Pyridinedicarboxylic acid	AD007B P5	N	N	1.0:1.2	

A.3. Bismuth Chloride - Carboxylic Acid Solvothermal Synthetic Procedures

Experiment Code	Temperature	Solvent	Carboxylic Acid	Product Code	Crystals Obtained	Extended cooling procedure employed	Bismuth:Carboxylic Acid Ratio (mmol)	Notes
AD027	120ºC	Water (10ml)	2,3-Pyrazinedicarboxylic Acid	AD027 P3	N	1ºC/min	1.0:1.2	KOH (0.5mmol)
		Water (10ml)	2,3-Pyrazinedicarboxylic Acid	AD027 P4	N	1ºC/min	1.0:1.2	No KOH
		DMF (5ml)	2,3-Pyrazinedicarboxylic Acid	AD027 P5	N	1ºC/min	1.0:1.2	KOH (0.5mmol)
		DMF (5ml)	2,3-Pyrazinedicarboxylic Acid	AD027 P6	N	1ºC/min	1.0:1.2	No KOH

A.4. Bismuth Nitrate Pentahydrate – Rigid & Flexible Carboxylic Acid Solvothermal Synthetic Procedures

Experiment Code	Rigid Carboxylic Acid	Flexible Carboxylic Acid	pH adjusting template	Bi : CA(Rigid) : CA(Flex) : Template (mmol)	Solvent Mixture	Ramp Rate (°C/min)	Temperature (°C)	Cooling Rate (°C/min)	Dwell Time (h)	Product Code	Crystals Obtained	Additional Notes
AD013A	1,4-Benzenedicarboxylic Acid	Succinic Acid	KOH	0.2 : 0.6 : 0.85 : 0.5	Water (10ml)	1	180	0.1	72	AD013A P1	N	
	1,4-Benzenedicarboxylic Acid	Succinic Acid	KOH	0.4 : 0.6 : 0.85 : 0.5	Water (10ml)	1	180	0.1	72	AD013A P2	N	
	1,4-Benzenedicarboxylic Acid	Succinic Acid	KOH	0.6 : 0.6 : 0.85 : 0.5	Water (10ml)	1	180	0.1	72	AD013A P3	N	
	1,4-Benzenedicarboxylic Acid	Succinic Acid	KOH	0.8 : 0.6 : 0.85 : 0.5	Water (10ml)	1	180	0.1	72	AD013A P4	N	
	1,4-Benzenedicarboxylic Acid	Succinic Acid	KOH	1.0 : 0.6 : 0.85 : 0.5	Water (10ml)	1	180	0.1	72	AD013A P5	N	
	1,4-Benzenedicarboxylic Acid	Succinic Acid	KOH	1.2 : 0.6 : 0.85 : 0.5	Water (10ml)	1	180	0.1	72	AD013A P6	N	
AD016A	2,5-Pyridinedicarboxylic Acid	Adipic Acid	KOH	0.2 : 0.6 : 0.85 : 0.5	Water (10ml)	1	180	0.1	72	AD016A P1	N	
	2,5-Pyridinedicarboxylic Acid	Adipic Acid	KOH	0.4 : 0.6 : 0.85 : 0.5	Water (10ml)	1	180	0.1	72	AD016A P2	Y	Known structure cell match
	2,5-Pyridinedicarboxylic Acid	Adipic Acid	KOH	0.6 : 0.6 : 0.85 : 0.5	Water (10ml)	1	180	0.1	72	AD016A P3	N	
	2,5-Pyridinedicarboxylic Acid	Adipic Acid	KOH	0.8 : 0.6 : 0.85 : 0.5	Water (10ml)	1	180	0.1	72	AD016A P4	N	
	2,5-Pyridinedicarboxylic Acid	Adipic Acid	KOH	1.0 : 0.6 : 0.85 : 0.5	Water (10ml)	1	180	0.1	72	AD016A P5	N	
	2,5-Pyridinedicarboxylic Acid	Adipic Acid	KOH	1.2 : 0.6 : 0.85 : 0.5	Water (10ml)	1	180	0.1	72	AD016A P6	Y	Aurivillius phase

A.5. Bismuth Chloride – Rigid & Flexible Carboxylic Acid Solvothermal Synthetic Procedures

Experiment Code	Rigid Carboxylic Acid	Flexible Carboxylic Acid	pH adjusting template	Bi : CA(Rigid) : CA(Flex) : Template (mmol)	Solvent Mixture	Ramp Rate (°C/min)	Temperature (°C)	Cooling Rate (°C/min)	Dwell Time (h)	Product Code	Crystals Obtained	Additional Notes
AD018A	2,5-Pyridinedicarboxylic Acid	Adipic Acid	KOH	0.2 : 0.6 : 0.6 : 0.5	Water (10ml)	1	180	0.1	72	AD018A P1	N	
	2,5-Pyridinedicarboxylic Acid	Adipic Acid	KOH	0.4 : 0.6 : 0.6 : 0.5	Water (10ml)	1	180	0.1	72	AD018A P2	N	
	2,5-Pyridinedicarboxylic Acid	Adipic Acid	KOH	0.6 : 0.6 : 0.6 : 0.5	Water (10ml)	1	180	0.1	72	AD018A P3	N	
	2,5-Pyridinedicarboxylic Acid	Adipic Acid	KOH	0.8 : 0.6 : 0.6 : 0.5	Water (10ml)	1	180	0.1	72	AD018A P4	N	
	2,5-Pyridinedicarboxylic Acid	Adipic Acid	KOH	1.0 : 0.6 : 0.6 : 0.5	Water (10ml)	1	180	0.1	72	AD018A P5	N	
	2,5-Pyridinedicarboxylic Acid	Adipic Acid	KOH	1.2 : 0.6 : 0.6 : 0.5	Water (10ml)	1	180	0.1	72	AD018A P6	N	
AD018B	2,5-Pyridinedicarboxylic Acid	Adipic Acid	KOH	0.2 : 0.6 : 0.6 : 0.5	DMF (5ml)	1	100	0.1	72	AD018B P1	N	
	2,5-Pyridinedicarboxylic Acid	Adipic Acid	KOH	0.4 : 0.6 : 0.6 : 0.5	DMF (5ml)	1	100	0.1	72	AD018B P2	N	
	2,5-Pyridinedicarboxylic Acid	Adipic Acid	KOH	0.6 : 0.6 : 0.6 : 0.5	DMF (5ml)	1	100	0.1	72	AD018B P3	N	
	2,5-Pyridinedicarboxylic Acid	Adipic Acid	KOH	0.8 : 0.6 : 0.6 : 0.5	DMF (5ml)	1	100	0.1	72	AD018B P4	N	
	2,5-Pyridinedicarboxylic Acid	Adipic Acid	KOH	1.0 : 0.6 : 0.6 : 0.5	DMF (5ml)	1	100	0.1	72	AD018B P5	N	
	2,5-Pyridinedicarboxylic Acid	Adipic Acid	KOH	1.2 : 0.6 : 0.6 : 0.5	DMF (5ml)	1	100	0.1	72	AD018B P6	N	
AD019A	2,6-Pyridinedicarboxylic Acid	Adipic Acid	KOH	0.2 : 0.6 : 0.6 : 0.5	Water (10ml)	1	180	0.1	72	AD019A P1	Y	
	2,6-Pyridinedicarboxylic Acid	Adipic Acid	KOH	0.4 : 0.6 : 0.6 : 0.5	Water (10ml)	1	180	0.1	72	AD019A P2	N	
	2,6-Pyridinedicarboxylic Acid	Adipic Acid	KOH	0.6 : 0.6 : 0.6 : 0.5	Water (10ml)	1	180	0.1	72	AD019A P3	N	
	2,6-Pyridinedicarboxylic Acid	Adipic Acid	KOH	0.8 : 0.6 : 0.6 : 0.5	Water (10ml)	1	180	0.1	72	AD019A P4	N	
	2,6-Pyridinedicarboxylic Acid	Adipic Acid	KOH	1.0 : 0.6 : 0.6 : 0.5	Water (10ml)	1	180	0.1	72	AD019A P5	N	
	2,6-Pyridinedicarboxylic Acid	Adipic Acid	KOH	1.2 : 0.6 : 0.6 : 0.5	Water (10ml)	1	180	0.1	72	AD019A P6	N	

AD019B	2,6-Pyridinedicarboxylic Acid	Adipic Acid	KOH	0.2 : 0.6 : 0.6 : 0.5	DMF (5ml)	1	100	0.1	72	AD019B P1	N	
	2,6-Pyridinedicarboxylic Acid	Adipic Acid	KOH	0.4 : 0.6 : 0.6 : 0.5	DMF (5ml)	1	100	0.1	72	AD019B P2	N	
	2,6-Pyridinedicarboxylic Acid	Adipic Acid	KOH	0.6 : 0.6 : 0.6 : 0.5	DMF (5ml)	1	100	0.1	72	AD019B P3	N	
	2,6-Pyridinedicarboxylic Acid	Adipic Acid	KOH	0.8 : 0.6 : 0.6 : 0.5	DMF (5ml)	1	100	0.1	72	AD019B P4	N	
	2,6-Pyridinedicarboxylic Acid	Adipic Acid	KOH	1.0 : 0.6 : 0.6 : 0.5	DMF (5ml)	1	100	0.1	72	AD019B P5	N	
	2,6-Pyridinedicarboxylic Acid	Adipic Acid	KOH	1.2 : 0.6 : 0.6 : 0.5	DMF (5ml)	1	100	0.1	72	AD019B P6	N	
AD020A	2,5-Pyridinedicarboxylic Acid	Glutaric Acid	KOH	0.2 : 0.6 : 0.6 : 0.5	Water (10ml)	1	180	0.1	72	AD020A P1	N	
	2,5-Pyridinedicarboxylic Acid	Glutaric Acid	KOH	0.4 : 0.6 : 0.6 : 0.5	Water (10ml)	1	180	0.1	72	AD020A P2	N	
	2,5-Pyridinedicarboxylic Acid	Glutaric Acid	KOH	0.6 : 0.6 : 0.6 : 0.5	Water (10ml)	1	180	0.1	72	AD020A P3	N	
	2,5-Pyridinedicarboxylic Acid	Glutaric Acid	KOH	0.8 : 0.6 : 0.6 : 0.5	Water (10ml)	1	180	0.1	72	AD020A P4	N	
	2,5-Pyridinedicarboxylic Acid	Glutaric Acid	KOH	1.0 : 0.6 : 0.6 : 0.5	Water (10ml)	1	180	0.1	72	AD020A P5	N	
	2,5-Pyridinedicarboxylic Acid	Glutaric Acid	KOH	1.2 : 0.6 : 0.6 : 0.5	Water (10ml)	1	180	0.1	72	AD020A P6	N	
AD021A	2,6-Pyridinedicarboxylic Acid	Glutaric Acid	KOH	0.2 : 0.6 : 0.6 : 0.5	Water (10ml)	1	180	0.1	72	AD021A P1	Y	BiOCl crystals
	2,6-Pyridinedicarboxylic Acid	Glutaric Acid	KOH	0.4 : 0.6 : 0.6 : 0.5	Water (10ml)	1	180	0.1	72	AD021A P2	Y	BiOCl crystals
	2,6-Pyridinedicarboxylic Acid	Glutaric Acid	KOH	0.6 : 0.6 : 0.6 : 0.5	Water (10ml)	1	180	0.1	72	AD021A P3	Y	BiOCl crystals
	2,6-Pyridinedicarboxylic Acid	Glutaric Acid	KOH	0.8 : 0.6 : 0.6 : 0.5	Water (10ml)	1	180	0.1	72	AD021A P4	N	
	2,6-Pyridinedicarboxylic Acid	Glutaric Acid	KOH	1.0 : 0.6 : 0.6 : 0.5	Water (10ml)	1	180	0.1	72	AD021A P5	N	
	2,6-Pyridinedicarboxylic Acid	Glutaric Acid	KOH	1.2 : 0.6 : 0.6 : 0.5	Water (10ml)	1	180	0.1	72	AD021A P6	N	
AD026A	Diphenic Acid (Biphenyl-2,2’-dicarboxylic acid)	Glutaric Acid	KOH	0.2 : 0.6 : 0.6 : 0.5	Water (10ml)	1	180	0.1	72	AD026A P1	N	
	Diphenic Acid (Biphenyl-2,2’-dicarboxylic acid)	Glutaric Acid	KOH	0.4 : 0.6 : 0.6 : 0.5	Water (10ml)	1	180	0.1	72	AD026A P2	N	

	Diphenic Acid (Biphenyl-2,2'-dicarboxylic acid)	Glutaric Acid	KOH	0.6 : 0.6 : 0.6 : 0.5	Water (10ml)	1	180	0.1	72	AD026A P3	N	
	Diphenic Acid (Biphenyl-2,2'-dicarboxylic acid)	Glutaric Acid	KOH	0.8 : 0.6 : 0.6 : 0.5	Water (10ml)	1	180	0.1	72	AD026A P4	N	
	Diphenic Acid (Biphenyl-2,2'-dicarboxylic acid)	Glutaric Acid	KOH	1.0 : 0.6 : 0.6 : 0.5	Water (10ml)	1	180	0.1	72	AD026A P5	N	
	Diphenic Acid (Biphenyl-2,2'-dicarboxylic acid)	Glutaric Acid	KOH	1.2 : 0.6 : 0.6 : 0.5	Water (10ml)	1	180	0.1	72	AD026A P6	N	
AD026B	Diphenic Acid (Biphenyl-2,2'-dicarboxylic acid)	Succinic Acid	KOH	0.2 : 0.6 : 0.6 : 0.5	Water (10ml)	1	180	0.1	72	AD026B P1	N	
	Diphenic Acid (Biphenyl-2,2'-dicarboxylic acid)	Succinic Acid	KOH	0.4 : 0.6 : 0.6 : 0.5	Water (10ml)	1	180	0.1	72	AD026B P2	N	
	Diphenic Acid (Biphenyl-2,2'-dicarboxylic acid)	Succinic Acid	KOH	0.6 : 0.6 : 0.6 : 0.5	Water (10ml)	1	180	0.1	72	AD026B P3	N	
	Diphenic Acid (Biphenyl-2,2'-dicarboxylic acid)	Succinic Acid	KOH	0.8 : 0.6 : 0.6 : 0.5	Water (10ml)	1	180	0.1	72	AD026B P4	N	
	Diphenic Acid (Biphenyl-2,2'-dicarboxylic acid)	Succinic Acid	KOH	1.0 : 0.6 : 0.6 : 0.5	Water (10ml)	1	180	0.1	72	AD026B P5	N	
	Diphenic Acid (Biphenyl-2,2'-dicarboxylic acid)	Succinic Acid	KOH	1.2 : 0.6 : 0.6 : 0.5	Water (10ml)	1	180	0.1	72	AD026B P6	N	

A.6. Bismuth Nitrate Pentahydrate – Rigid & Flexible Carboxylic Acid Reflux + Slow Evaporation Synthetic Procedures

Experiment Code	**Rigid Carboxylic Acid**	**Flexible Carboxylic Acid**	**pH adjusting template**	**Bi : CA(Rigid) : CA(Flex) : Template (mmol)**	**Solvent Mixture**	**Temperature (ºC)**	**Cooling Rate**	**Dwell Time (h)**	**Product Code**	**Crystals Obtained**
AD014	N/A	Succinic Acid	KOH	1.0 : 0 : 1.2 : 1.2	DMF (10ml)	~100-110ºC	Left to cool	6	AD014A	N
	N/A	Succinic Acid	KOH	1.0 : 0 : 1.2 : 1.2	DMF (10ml)	~100-110ºC	Left to cool	24	AD014B	N
AD015	N/A	Adipic Acid	KOH	1.0 : 0 : 1.2 : 1.2	DMF (10ml)	~100-110ºC	Left to cool	48	AD015	N

A.7. Bismuth Chloride – Rigid & Flexible Carboxylic Acid Reflux + Slow Evaporation Synthetic Procedures

Experiment Code	Rigid Carboxylic Acid	Flexible Carboxylic Acid	pH adjusting template	Bi : CA(Rigid) : CA(Flex) : Template (mmol)	Solvent Mixture	Temperature (ºC)	Cooling Rat	Dwell Time (h)	Product Code	Crystals Obtained
AD017	Pyridine-2,5-dicarboxylic Acid	Glutaric Acid	KOH	1.0 : 0.6 : 0.6 : 1.2	DMF (10ml)	~100-110ºC	Left to cool	48h	AD017	N
AD022	Pyridine-2,6-dicarboxylic Acid	Glutaric Acid	KOH	1.0 : 0.6 : 0.6 : 1.2	DMF (10ml)	~100-110ºC	Left to cool	48h	AD022	N

A.8. Bismuth sulphide iodide (BiSI) Solvothermal Synthetic Procedures

Experiment Code	Bismuth(III) Chloride (mmol)	Thiourea (mmol)	Iodine (mmol)	Solvent Mixture	Ramp Rate (ºC/min)	Temperature (ºC)	Cooling Rate (ºC/min)	Dwell Time (h)	Product Code(s)	Notes
AD023	10	10	10	Water (16ml)	1	160	Removed from oven, left to cool	30	AD023A, AD023B, AD023C	Synthesis of BiSI crystals - Literature method (A Facile and Clean Synthesis of Pure Bismuth Sulfide Iodide Crystals, Russian Journal of Inorganic Chemistry, 2006, Vol 51, No 12, pp1864-1868)
	10	10	10	Water (16ml)	1	200	Removed from oven, left to cool	24	AD023D	Synthesis of BiSI crystals – Modified Literature method (Synthesis and Characterisation of 1-D BiSI and 2-D BiOI Nanostructures)
AD024	Bismuth(III) Chloride (mmol)	Thiourea (mmol)	Caesium Iodide (mmol)	Solvent Mixture	Ramp Rate (ºC/min)	Temperature (ºC)	Cooling Rate (ºC/min)	Dwell Time (h)	Product Code	Notes
	10	10	10	Water (16ml)	1	160	Quench rapidly in water	30	AD024	BiSI needles, Cs not incorporated into structure

				Solvent Mixture	Ramp Rate (ºC/min)	Temperature (ºC)	Cooling Rate (ºC/min)	Dwell Time (h)	Product Code	Notes
AD036	BiSI (1mmol)	Caesium Iodide (1mmol)		GBL (10ml)	1	180	0.1	72	AD036 P1	Very fine reflective dark grey/ black needle crystals
	BiSI (1mmol)	Caesium Iodide (1mmol)		DMSO (10ml)	1	180	0.1	72	AD036 P2	Product not obtained, sealed in bomb
	BiSI (1mmol)	Caesium Iodide (1mmol)		DMF (10ml)	1	180	0.1	72	AD036 P3	Fine grey needles with large black needles
	BiSI (1mmol)	Sodium Iodide (1mmol)		GBL (10ml)	1	180	0.1	72	AD036 P4	Very fine reflective dark grey/ black needle crystals
	BiSI (1mmol)	Sodium Iodide (1mmol)		DMSO (10ml)	1	180	0.1	72	AD036 P5	Mixed black and red crystalline phases
	BiSI (1mmol)	Sodium Iodide (1mmol)		DMF (10ml)	1	180	0.1	72	AD036 P6	Fine grey needles with large black needles

A.9. Bismuth sulphide iodide (BiSI) Reflux Synthetic Procedures

Experiment Code	**Bismuth Sulfide Iodide (mmol) (AD023 product)**	**Caesium Iodide (mmol)**	**Solvent Mixture**	**Temperature (ºC)**	**Cooling Rate**	**Dwell Time (h)**	**Product Code**	**Notes**
AD025	0.1	0.1	DMF (10ml)	160	Slow cool to RT	16	AD025A	BiSI needle remain
AD032	1	1	HI (6.8ml)/ H3PO2 (1.7ml)	120	Slow cool to RT	1h	AD032	Large Red Plate Crystals + Powder
AD033	1	1.5	HI (6.8ml)/ H3PO2 (1.7ml)	120	Slow cool to RT	1h	AD033	Much smaller and fewer plate crystals than AD032
AD034	1	1	DMF (15ml)	160	Slow cool to RT		AD034	BiSI needles (additional peaks in PXRD possibly from powder coating needles)
AD035	1	1	GBL (10ml)	110-120	Slow cool to RT		AD035	BiSI needle remain

A.10. Bismuth selendide iodide (BiSeI) Solvothermal Synthetic Procedures

Experiment Code	Bismuth (III) Chloride (mmol)	Selenium Powder (mmol)	Sodium Iodide (mmol)	Solvent Mixture	Ramp Rate (°C/min)	Temperature (°C)	Cooling Rate (°C/min)	Dwell Time (h)	Product Code	Notes
AD040	1	1	1	Ethanol (16ml)	1	200	0.1	12	AD040A	Modified literature procedure (A Mild Solution Route to Bismuth Selenoiodide Rod-like crystals (L.Zhu, X.Zheng, X. Yin et al)) Clear crystals (BiOCl from SXD) and Needle crystals BiSeI from SXD) Only pre-exps run
	1	1	1	Ethanol (16ml)	1	200	0.1	24	AD040B	Dwell Time Increased
	1	1	1	Ethanol (16ml)	1	200	0.1	12	AD040C	Repeat of AD040A procedure + 2M HCl Wash (2x250ml)

A.11. Bismuth sulphide iodide – Solid State Pyrex Tube Procedures

Experiment Code	Bismuth Precursor	Iodide Salt	Pyrex Tube	Temperature (°C)	Dwell Time (h)	Observations
AD057A	BiSI (1mmol)	CsI (1mmol)	1x10cm	250	24	Redish tinge around half way of tube, possibly a small amount of iodine
	BiSI (1mmol)	CsI (1mmol)	1x10cm	300	24	No other change in appearance
	BiSI (1mmol)	CsI (1mmol)	1x10cm	350	24	No other change in appearance
	BiSI (1mmol)	CsI (1mmol)	1x10cm	375	24	No other change in appearance
	BiSI (1mmol)	CsI (1mmol)	1x10cm	400	24	No other change in appearance
	BiSI (1mmol)	CsI (1mmol)	1x10cm	425	24	No other change in appearance
	BiSI (1mmol)	CsI (1mmol)	1x10cm	450	24	No other change in appearance
	BiSI (1mmol)	CsI (1mmol)	1x10cm	475	24	Darkening around compound at far end of tube but BiSI needle-like crystals still present
	BiSI (1mmol)	CsI (1mmol)	1x10cm	500	24	Red crystalline material present within the bulk material - Possible dispropotionation to BiI3 Bi2S3?
	BiSI (1mmol)	CsI (1mmol)	1x10cm	500	72	Ramp to 500oC for a longer period - End of tube exploded,recovered material for analysis (Cs3Bi2I9 crystal cell match)
AD057B	BiSI (1mmol)	RbI (1mmol)	1x10cm	475	36	Ramped to lower temperature than 57A, similarly crystal cell match to Rb3Bi2I9 present in mixture

A.12. Bismuth halometallate hybrid materials Solvothermal Synthetic Procedures

Experiment Code	Bismuth Precursor	Amine Precursor	Solvent Mixture	Ramp up Rate (°C/min)	Dwell Temperature (°C)	Dwell Time (h)	Ramp down Rate (°C/min)	Product Code	Notes
AD051A	$BiCl_3$ (0.2mmol)	1,4-benzenediamine (0.15mmol)	Ethanol (6ml), Hydriodic Acid (57% in water) (0.5ml)	1	140	24	0.1	AD051A P1	Shiny dark crystalline material coated in an orangey/brown powder
	$BiCl_3$ (0.2mmol)	1,4-benzenediamine (0.15mmol)	Ethanol (6ml), Hydriodic Acid (57% in water) (0.75ml)	1	140	24	0.1	AD051A P2	Major phase of orange needle crystals (s15mtw080), dark red chunky crystalline blocks (Minor) and shiny black balls(iodine?).
	$BiCl_3$ (0.2mmol)	1,4-benzenediamine (0.15mmol)	Ethanol (6ml), Hydriodic Acid (57% in water) (1ml)	1	140	24	0.1	AD051A P3	Major phase of orange crystals, Mix of bright red crystals (e15mtw053) deep red and black crystalline material. Shiny black balls again present
AD051B	$BiCl_3$ (0.2mmol)	1,3-benzenediamine (0.15mmol)	Ethanol (6ml), Hydriodic Acid (57% in water) (0.5ml)	1	140	24	0.1	AD051B P1	Large shiny black hemispheres with flat bottoms (varying sizes)
	$BiCl_3$ (0.2mmol)	1,3-benzenediamine (0.15mmol)	Ethanol (6ml), Hydriodic Acid (57% in water) (0.75ml)	1	140	24	0.1	AD051B P2	Dark red crystalline balls
	$BiCl_3$ (0.2mmol)	1,3-benzenediamine (0.15mmol)	Ethanol (6ml), Hydriodic Acid (57% in water) (1ml)	1	140	24	0.1	AD051B P3	Dark red crystalline balls
AD051C	$BiCl_3$ (0.2mmol)	1,2-benzenediamine (0.15mmol)	Ethanol (6ml), Hydriodic Acid (57% in water) (0.5ml)	1	140	24	0.1	AD051C P1	Deep dark red, almost black, prismatic needle crystals (Major)(s15mtw82)(formed as clusters nucleating out from a common point in some cases). Minor phase of crystalline orange/red material also present
	$BiCl_3$ (0.2mmol)	1,2-benzenediamine (0.15mmol)	Ethanol (6ml), Hydriodic Acid (57% in water) (0.75ml)	1	140	24	0.1	AD051C P2	V.large mm scale blood orange crystals (require breaking down for analysis by SXD) with a minor phase of orange crystalline material
	$BiCl_3$ (0.2mmol)	1,2-benzenediamine (0.15mmol)	Ethanol (6ml), Hydriodic Acid (57% in water) (1ml)	1	140	24	0.1	AD051C P3	Mixed Phases of crystals - Long but thin plate-like needles (Red)(again appearing in clusters) with a secondary phase of orange crystals (s15mtw83)(Wedges)

AD051D	$BiCl_3$ (0.2mmol)	1,4-benzenediamine (0.15mmol)	Ethanol (6ml), Hydriodic Acid (57% in water) (0.5ml)	1	180	24	0.1	AD051D P1	Light brown crystalline balls with dark crystalline (semi-porous) crystalline interior
	$BiCl_3$ (0.2mmol)	1,4-benzenediamine (0.15mmol)	Ethanol (6ml), Hydriodic Acid (57% in water) (0.75ml)	1	180	24	0.1	AD051D P2	Chunky red/brown semi-porous crystalline material
	$BiCl_3$ (0.2mmol)	1,4-benzenediamine (0.15mmol)	Ethanol (6ml), Hydriodic Acid (57% in water) (1ml)	1	180	24	0.1	AD051D P3	Chunky red/brown semi-porous crystalline material
AD051E	$BiCl_3$ (0.2mmol)	1,3-benzenediamine (0.15mmol)	Ethanol (6ml), Hydriodic Acid (57% in water) (1.25ml)	1	140	24	Left to cool in oven to RT	AD051E P1	Red crystals (e15mtw056/e15mtw058) growing as 'feathered' sheets - require breaking for single crystal. Minor amount of black crystalline material also present
	$BiCl_3$ (0.2mmol)	1,3-benzenediamine (0.15mmol)	Ethanol (6ml), Hydriodic Acid (57% in water) (1.5ml)	1	140	24	Left to cool in oven to RT	AD051E P2	V.similar to P1 product
	$BiCl_3$ (0.2mmol)	1,3-benzenediamine (0.15mmol)	Ethanol (6ml), Hydriodic Acid (57% in water) (1.75ml)	1	140	24	Left to cool in oven to RT	AD051E P3	Deep red crystals with some dark crystalline material
AD051F	$BiCl_3$ (0.2mmol)	1,4-benzenediamine (0.15mmol)	Methanol (6ml), Hydriodic Acid (57% in water) (0.5ml)	1	140	24	0.1	AD051F P1	Dark orange/brown flaky crystalline material
	$BiCl_3$ (0.2mmol)	1,4-benzenediamine (0.15mmol)	Methanol (6ml), Hydriodic Acid (57% in water) (0.75ml)	1	140	24	0.1	AD051F P2	Dark orange/brown flaky crystalline material
	$BiCl_3$ (0.2mmol)	1,4-benzenediamine (0.15mmol)	Methanol (6ml), Hydriodic Acid (57% in water) (1ml)	1	140	24	0.1	AD051F P3	Dark orange/brown flaky crystalline material, orange crystal isolated (e15mtw057)
AD051G	$BiCl_3$ (0.2mmol)	1,3-benzenediamine (0.15mmol)	Methanol (6ml), Hydriodic Acid (57% in water) (1.25ml)	1	140	24	Left to cool in oven to RT	AD051G P1	Flaky orange/brown non-crystalline material with one black non-crystalline material
	$BiCl_3$ (0.2mmol)	1,3-benzenediamine (0.15mmol)	Methanol (6ml), Hydriodic Acid (57% in water) (1.5ml)	1	140	24	Left to cool in oven to RT	AD051G P2	Pure phase of flaky orange non-crystalline material
	$BiCl_3$ (0.2mmol)	1,3-benzenediamine (0.15mmol)	Methanol (6ml), Hydriodic Acid (57% in water) (1.75ml)	1	140	24	Left to cool in oven to RT	AD051G P3	Same as P1

AD051H	$BiCl_3$ (0.2mmol)	1,2-benzenediamine (0.15mmol)	Methanol (6ml), Hydriodic Acid (57% in water) (0.5ml)	1	140	24	0.1	AD051H P1	Minor phase of dark red/black crystals coated with a major phase of reddish/brown non-crystalline powder
	$BiCl_3$ (0.2mmol)	1,2-benzenediamine (0.15mmol)	Methanol (6ml), Hydriodic Acid (57% in water) (0.75ml)	1	140	24	0.1	AD051H P2	Black crystals with a reddish/brown powder phase
	$BiCl_3$ (0.2mmol)	1,2-benzenediamine (0.15mmol)	Methanol (6ml), Hydriodic Acid (57% in water) (1ml)	1	140	24	0.1	AD051H P3	Deep red/black crystals (e15mtw061) with a reddish/brown powder phase
AD051I	$BiCl_3$ (0.2mmol)	1,2-benzenediamine (0.15mmol)	Water (6ml), Hydriodic Acid (57% in water) (0.5ml)	1	140	24	0.1	AD051I P1	Major phase of black needle crystals with a minor phase of reddish/brown powder
	$BiCl_3$ (0.2mmol)	1,2-benzenediamine (0.15mmol)	Water (6ml), Hydriodic Acid (57% in water) (0.75ml)	1	140	24	0.1	AD051I P2	Mix of black needle crystals with a reddish/brown non-crystalline powder
	$BiCl_3$ (0.2mmol)	1,2-benzenediamine (0.15mmol)	Water (6ml), Hydriodic Acid (57% in water) (1ml)	1	140	24	0.1	AD051I P3	Black needle crystals with a v.dark red/brown powder phase
AD052A	$BiCl_3$ (0.2mmol)	2-Ethylaniline (0.15mmol)	Ethanol (6ml), Hydriodic Acid (57% in water) (0.5ml)	1	140	24	0.1	AD052A P1	Dark red/black sticky crystalline material, semi-porous looking, expanded and crystallised upon heating in drying oven.
	$BiCl_3$ (0.2mmol)	2-Ethylaniline (0.15mmol)	Ethanol (6ml), Hydriodic Acid (57% in water) (0.75ml)	1	140	24	0.1	AD052A P2	Dark red/black sticky crystalline material, semi-porous looking, expanded and crystallised upon heating in drying oven.
	$BiCl_3$ (0.2mmol)	2-Ethylaniline (0.15mmol)	Ethanol (6ml), Hydriodic Acid (57% in water) (1ml)	1	140	24	0.1	AD052A P3	Dark red/black sticky crystalline material, semi-porous looking, expanded and crystallised upon heating in drying oven.
AD053A	$BiCl_3$ (0.2mmol)	3,4-Diaminotoluene (0.15mmol)	Ethanol (6ml), Hydriodic Acid (57% in water) (0.5ml)	1	140	24	0.1	AD053A P1	V. dark red clusters of crystals nucleating outwards from a common point. Have a dark orange tinge when broken off cluster. Minor phase of black balls
	$BiCl_3$ (0.2mmol)	3,4-Diaminotoluene (0.15mmol)	Ethanol (6ml), Hydriodic Acid (57% in water) (0.75ml)	1	140	24	0.1	AD053A P2	Mixed phase - Dark red needle crystals with orange plate-like crystals (Red needle - s15mtw088)(Orange crystal - e15mtw055), and black crystalline material

	$BiCl_3$ (0.2mmol)	3,4-Diaminotoluene (0.15mmol)	Ethanol (6ml), Hydriodic Acid (57% in water) (1ml)	1	140	24	0.1	AD053A P3	Mixed phases of orange crystalline structures and black crystalline material. High pressure in bomb
AD053B	$BiCl_3$ (0.2mmol)	3,4-Diaminotoluene (0.15mmol)	Methanol (6ml), Hydriodic Acid (57% in water) (0.5ml)	1	140	24	0.1	AD053B P1	Mix of non-crystalline black and orange powders
	$BiCl_3$ (0.2mmol)	3,4-Diaminotoluene (0.15mmol)	Methanol (6ml), Hydriodic Acid (57% in water) (0.75ml)	1	140	24	0.1	AD053B P2	Dark red/black crystalline material with a secondary powder phase
	$BiCl_3$ (0.2mmol)	3,4-Diaminotoluene (0.15mmol)	Methanol (6ml), Hydriodic Acid (57% in water) (1ml)	1	140	24	0.1	AD053B P3	Deep red needle crystals (e15mtw063/e15mtw065), some coated in minor orange powder phase
AD053C	$BiCl_3$ (0.2mmol)	3,4-Diaminotoluene (0.15mmol)	Water (6ml), Hydriodic Acid (57% in water) (0.5ml)	1	140	24	0.1	AD053C P1	Black non-crystalline material (uniform)
	$BiCl_3$ (0.2mmol)	3,4-Diaminotoluene (0.15mmol)	Water (6ml), Hydriodic Acid (57% in water) (0.75ml)	1	140	24	0.1	AD053C P2	Black non-crystalline material (uniform)
	$BiCl_3$ (0.2mmol)	3,4-Diaminotoluene (0.15mmol)	Water (6ml), Hydriodic Acid (57% in water) (1ml)	1	140	24	0.1	AD053C P3	Black non-crystalline material (uniform)
AD054A	$BiCl_3$ (0.2mmol)	Aniline (0.15mmol)	Ethanol (6ml), Hydriodic Acid (57% in water) (0.5ml)	1	140	24	0.1	AD054A P1	Deep red crystalline balls (Lenton oven)
	$BiCl_3$ (0.2mmol)	Aniline (0.15mmol)	Ethanol (6ml), Hydriodic Acid (57% in water) (0.75ml)	1	140	24	0.1	AD054A P2	Red crystalline material (stuck/clumped together) (Lenton oven)
	$BiCl_3$ (0.2mmol)	Aniline (0.15mmol)	Ethanol (6ml), Hydriodic Acid (57% in water) (1ml)	1	140	24	0.1	AD054A P3	Red crystalline material (stuck/clumped together) (Lenton oven)
AD054B	$BiCl_3$ (0.2mmol)	Aniline (0.15mmol)	Methanol (6ml), Hydriodic Acid (57% in water) (0.5ml)	1	140	24	0.1	AD054B P1	Red crystalline needles (non single-crystal by sight) (Lenton)
	$BiCl_3$ (0.2mmol)	Aniline (0.15mmol)	Methanol (6ml), Hydriodic Acid (57% in water) (0.75ml)	1	140	24	0.1	AD054B P2	Deep red crystalline needles (possibly single-crystal)
	$BiCl_3$ (0.2mmol)	Aniline (0.15mmol)	Methanol (6ml), Hydriodic Acid (57% in water) (1ml)	1	140	24	0.1	AD054B P3	Deep red needle crystals and orange needle crystals (s15mtw091)

AD054C	$BiCl_3$ (0.2mmol)	Aniline (0.15mmol)	Water (6ml), Hydriodic Acid (57% in water) (0.5ml)	1	140	24	0.1	AD054C P1	V small amount of dark red crystalline material (Lenton)
	$BiCl_3$ (0.2mmol)	Aniline (0.15mmol)	Water (6ml), Hydriodic Acid (57% in water) (0.75ml)	1	140	24	0.1	AD054C P2	No product
	$BiCl_3$ (0.2mmol)	Aniline (0.15mmol)	Water (6ml), Hydriodic Acid (57% in water) (1ml)	1	140	24	0.1	AD054C P3	No product
AD055A	$BiCl_3$ (0.2mmol)	2-Aminopyrimidine (0.15mmol)	Ethanol (6ml), Hydriodic Acid (57% in water) (0.5ml)	1	140	24	0.1	AD055A P1	Major phase of orangey red crystals/crystalline material with a minor phase of v.small black crystalline balls
	$BiCl_3$ (0.2mmol)	2-Aminopyrimidine (0.15mmol)	Ethanol (6ml), Hydriodic Acid (57% in water) (0.75ml)	1	140	24	0.1	AD055A P2	Same as P1 but the orange/red crystalline material is increasingly the major phase
	$BiCl_3$ (0.2mmol)	2-Aminopyrimidine (0.15mmol)	Ethanol (6ml), Hydriodic Acid (57% in water) (1ml)	1	140	24	0.1	AD055A P3	Largely bulk phase of fine orange crystalline material with a secondary phase of black crystalline balls
AD055B	$BiCl_3$ (0.2mmol)	2-Aminopyrimidine (0.15mmol)	Methanol (6ml), Hydriodic Acid (57% in water) (0.5ml)	1	140	24	0.1	AD055B P1	~2 large 1-2cm elongated deep red prismatic needle crystals with many smaller red crystals of a similar shape. Secondary minor phase of black crystalline material
	$BiCl_3$ (0.2mmol)	2-Aminopyrimidine (0.15mmol)	Methanol (6ml), Hydriodic Acid (57% in water) (0.75ml)	1	140	24	0.1	AD055B P2	V.close to a pure phase elongated red prismatic needle crystals, v.small amount of black material present
	$BiCl_3$ (0.2mmol)	2-Aminopyrimidine (0.15mmol)	Methanol (6ml), Hydriodic Acid (57% in water) (1ml)	1	140	24	0.1	AD055B P3	Pure phase of elongated red prismatic needle crystals (e15mtw060) (many 0.5-1cm in length)
AD055C	$BiCl_3$ (0.2mmol)	2-Aminopyrimidine (0.15mmol)	Water (6ml), Hydriodic Acid (57% in water) (0.5ml)	1	140	24	Left to cool in oven to RT	AD055C P1	Major phase of v.small prismatic red crystals with a minor phase of chunky orangey/brown crystals
	$BiCl_3$ (0.2mmol)	2-Aminopyrimidine (0.15mmol)	Water (6ml), Hydriodic Acid (57% in water) (0.75ml)	1	140	24	Left to cool in oven to RT	AD055C P2	Major phase of fine red needle crystals (e15mtw064) with a minor phase of black crystalline material
	$BiCl_3$ (0.2mmol)	2-Aminopyrimidine (0.15mmol)	Water (6ml), Hydriodic Acid (57% in water) (1ml)	1	140	24	Left to cool in oven to RT	AD055C P3	Pure phase of fine red needle crystals

AD055D	$BiCl_3$ (0.2mmol)	2-Aminopyrimidine (0.15mmol)	Methanol (6ml), Hydriodic Acid (57% in water) (1ml)	1	140	24	0.1	AD055D P1	Large masses of fine needle crystals. Mixed phase of bright orangey-red needle crystals (major) and a minor phase of deep red/ black needle crystals
	$BiCl_3$ (0.2mmol)	2-Aminopyrimidine (0.15mmol)	Methanol (6ml), Hydriodic Acid (57% in water) (1ml)	1	140	24	0.1	AD055D P2	Major phase of large deep red prismatic needle crystals with a minor phase of black crystalline material
	$BiCl_3$ (0.2mmol)	2-Aminopyrimidine (0.15mmol)	Methanol (6ml), Hydriodic Acid (57% in water) (1ml)	1	140	24	0.1	AD055D P3	V.similar to P2
AD055E	$BiCl_3$ (0.2mmol)	2-Aminopyrimidine (0.15mmol)	Methanol (6ml), Hydriodic Acid (57% in water) (1ml)	1	140	24	0.1	AD055E P1	No product
	$BiCl_3$ (0.2mmol)	2-Aminopyrimidine (0.15mmol)	Methanol (6ml), Hydriodic Acid (57% in water) (1ml)	1	140	24	0.1	AD055E P2	No product
	$BiCl_3$ (0.2mmol)	2-Aminopyrimidine (0.15mmol)	Methanol (6ml), Hydriodic Acid (57% in water) (1ml)	1	140	24	0.1	AD055E P3	No product
AD055F	n/a	2-Aminopyrimidine (0.15mmol)	Methanol (6ml), Hydriodic Acid (57% in water) (1ml)	1	140	24	0.1	AD055F P1	No product
	n/a	2-Aminopyrimidine (0.15mmol)	Methanol (6ml), Hydriodic Acid (57% in water) (1ml)	1	140	24	0.1	AD055F P2	No product
	n/a	2-Aminopyrimidine (0.15mmol)	Methanol (6ml), Hydriodic Acid (57% in water) (1ml)	1	140	24	0.1	AD055F P3	No product
AD058A	$BiCl_3$ (0.2mmol)	p-Toluidine (0.15mmol)	Ethanol (6ml), Hydriodic Acid (57% in water) (0.5ml)	1	140	24	0.1	AD058A P1	Lenton 2 - Product not found
	$BiCl_3$ (0.2mmol)	p-Toluidine (0.15mmol)	Ethanol (6ml), Hydriodic Acid (57% in water) (0.75ml)	1	140	24	0.1	AD058A P2	Lenton 2 - Product not found
	$BiCl_3$ (0.2mmol)	p-Toluidine (0.15mmol)	Ethanol (6ml), Hydriodic Acid (57% in water) (1ml)	1	140	24	0.1	AD058A P3	Lenton 2 - Product not found
AD058B	$BiCl_3$ (0.2mmol)	p-Toluidine (0.15mmol)	Methanol (6ml), Hydriodic Acid (57% in water) (0.5ml)	1	140	24	0.1	AD058B P1	Large mass of reddish brown crystalline material with some visibly larger crystals present

	$BiCl_3$ (0.2mmol)	p-Toluidine (0.15mmol)	Methanol (6ml), Hydriodic Acid (57% in water) (0.75ml)	1	140	24	0.1	AD058B P2	Mixed phase of orange needle crystals (s15mtw092) with a minor phase of orange non-crystalline powder
	$BiCl_3$ (0.2mmol)	p-Toluidine (0.15mmol)	Methanol (6ml), Hydriodic Acid (57% in water) (1ml)	1	140	24	0.1	AD058B P3	Similar to P1 - less larger crystals visible
AD058C	$BiCl_3$ (0.2mmol)	p-Toluidine (0.15mmol)	Water (6ml), Hydriodic Acid (57% in water) (0.5ml)	1	140	24	0.1	AD058C P1	Neligibly small/ no product obtained
	$BiCl_3$ (0.2mmol)	p-Toluidine (0.15mmol)	Water (6ml), Hydriodic Acid (57% in water) (0.75ml)	1	140	24	0.1	AD058C P2	Neligibly small/ no product obtained
	$BiCl_3$ (0.2mmol)	p-Toluidine (0.15mmol)	Water (6ml), Hydriodic Acid (57% in water) (1ml)	1	140	24	0.1	AD058C P3	Neligibly small/ no product obtained

Experiment Code	**Bismuth Precursor**	**Amine Precursor**	**Solvent Mixture**	**Ramp up Rate (ºC/min)**	**Dwell Temperature (ºC)**	**Dwell Time (h)**	**Ramp down Rate (ºC/min)**	**Product Code**	**Notes**
AD059A	$BiCl_3$ (0.2mmol)	Imidazole (0.15mmol)	Ethanol (6ml), Hydriodic Acid (57% in water) (0.5ml)	1	140	24	0.1	AD059A P1	No product
	$BiCl_3$ (0.2mmol)	Imidazole (0.15mmol)	Ethanol (6ml), Hydriodic Acid (57% in water) (0.75ml)	1	140	24	0.1	AD059A P2	No product
	$BiCl_3$ (0.2mmol)	Imidazole (0.15mmol)	Ethanol (6ml), Hydriodic Acid (57% in water) (1ml)	1	140	24	0.1	AD059A P3	No product
AD059B	$BiCl_3$ (0.2mmol)	Imidazole (0.15mmol)	Methanol (6ml), Hydriodic Acid (57% in water) (0.5ml)	1	140	24	0.1	AD059B P1	Negligable amount of non-crystalline product
	$BiCl_3$ (0.2mmol)	Imidazole (0.15mmol)	Methanol (6ml), Hydriodic Acid (57% in water) (0.75ml)	1	140	24	0.1	AD059B P2	Negligable amount of non-crystalline product
	$BiCl_3$ (0.2mmol)	Imidazole (0.15mmol)	Methanol (6ml), Hydriodic Acid (57% in water) (1ml)	1	140	24	0.1	AD059B P3	Negligable amount of non-crystalline product
AD059C	$BiCl_3$ (0.2mmol)	Imidazole (0.15mmol)	Water (6ml), Hydriodic Acid (57% in water) (0.5ml)	1	140	24	0.1	AD059C P1	No product

	$BiCl_3$ (0.2mmol)	Imidazole (0.15mmol)	Water (6ml), Hydriodic Acid (57% in water) (0.75ml)	1	140	24	0.1	AD059C P2	No product
	$BiCl_3$ (0.2mmol)	Imidazole (0.15mmol)	Water (6ml), Hydriodic Acid (57% in water) (1ml)	1	140	24	0.1	AD059C P3	No product
AD059D	$BiCl_3$ (0.2mmol)	Imidazole (0.15mmol)	Methanol (6ml), Hydriodic Acid (57% in water) (0.5ml)	1	180	24	0.1	AD059D P1	Black needle (non-crystalline) phase with large clear chunky khaki green/grey crystals (e16mtw022)(identified as Bi2O3, possibly tetragonal beta phase although alpha phase should form on cooling)
	$BiCl_3$ (0.2mmol)	Imidazole (0.15mmol)	Methanol (6ml), Hydriodic Acid (57% in water) (0.75ml)	1	180	24	0.1	AD059D P2	Pure phase of bright red crystals (hex bipyramids non-tapered)
	$BiCl_3$ (0.2mmol)	Imidazole (0.15mmol)	Methanol (6ml), Hydriodic Acid (57% in water) (1ml)	1	180	24	0.1	AD059D P3	Mixed phase of hexagonal bipyramid red crystals (untapered) and a coating of orange crystalline powder product
AD059E	$BiCl_3$ (0.2mmol)	Imidazole (0.15mmol)	Water (6ml), Hydriodic Acid (57% in water) (0.5ml)	1	180	24	0.1	AD059E P1	Pure phase of bright red crystalline material. Many clearly shaped as red hexagonal/ distorted irregular hexagonal face plate crystals (crystal quality looks good by eye but low quality diffraction observed on screening in SXD)
	$BiCl_3$ (0.2mmol)	Imidazole (0.15mmol)	Water (6ml), Hydriodic Acid (57% in water) (0.75ml)	1	180	24	0.1	AD059E P2	Pure phase of bright red hexagonal plate crystalline material. Increasingly large hexagonal plate-like crystals present (crystal quality looks good by eye but low quality diffraction observed on screening in SXD)
	$BiCl_3$ (0.2mmol)	Imidazole (0.15mmol)	Water (6ml), Hydriodic Acid (57% in water) (1ml)	1	180	24	0.1	AD059E P3	No product
AD062A	$BiCl_3$ (0.2mmol)	DABCO (0.15mmol)	Water (6ml), Hydriodic Acid (57% in water) (0.5ml)	1	140	24	0.1	AD062A P1	Mixed phase of disordered dark red & orange crystalline material
	$BiCl_3$ (0.2mmol)	DABCO (0.15mmol)	Water (6ml), Hydriodic Acid (57% in water) (0.75ml)	1	140	24	0.1	AD062A P2	Mixed phase of orange needle crystals (e16mtw002/e16mtw010) and orangey-red block crystals (e16mtw007)

	$BiCl_3$ (0.2mmol)	DABCO (0.15mmol)	Water (6ml), Hydriodic Acid (57% in water) (1ml)	1	140	24	0.1	AD062A P3	Large masses of bright yellow needle crystals in clumps mixed with a major phase of small chunky orange crystals
AD062B	$BiCl_3$ (0.2mmol)	DABCO (0.15mmol) + MAI (0.15mmol)	Water (6ml), Hydriodic Acid (57% in water) (0.5ml)	1	140	24	0.1	AD062B P1	Mixed phase of deep red/ black crystalline material
	$BiCl_3$ (0.2mmol)	DABCO (0.15mmol) + MAI (0.15mmol)	Water (6ml), Hydriodic Acid (57% in water) (0.75ml)	1	140	24	0.1	AD062B P2	Mixed phase of long prismatic deep red crystals(e15mtw069) with long black hollow crystalline structures
	$BiCl_3$ (0.2mmol)	DABCO (0.15mmol) + MAI (0.15mmol)	Water (6ml), Hydriodic Acid (57% in water) (1ml)	1	140	24	0.1	AD062B P3	V.large orange block crystal(e16mtw001) & Orange rod crystal (e16mtw008). V similar to 62A P3 but with larger chunky orange crystals
AD067A	$BiCl_3$ (0.2mmol)	Piperazine (0.15mmol)	Water (6ml), Hydriodic Acid (57% in water) (0.5ml)	1	140	24	0.1	AD067A P1	Deep red block crystals (e16mtw006/e16mtw030)
	$BiCl_3$ (0.2mmol)	Piperazine (0.15mmol)	Water (6ml), Hydriodic Acid (57% in water) (0.75ml)	1	140	24	0.1	AD067A P2	Deep red block crystals (cell match in SXD to P1 crystal structure)
	$BiCl_3$ (0.2mmol)	Piperazine (0.15mmol)	Water (6ml), Hydriodic Acid (57% in water) (1ml)	1	140	24	0.1	AD067A P3	Deep red block crystals (cell match in SXD to P1 crystal structure)
AD067B	$BiCl_3$ (0.2mmol)	Piperazine (0.15mmol) + MAI (0.15mmol)	Water (6ml), Hydriodic Acid (57% in water) (0.5ml)	1	140	24	0.1	AD067B P1	No product
	$BiCl_3$ (0.2mmol)	Piperazine (0.15mmol) + MAI (0.15mmol)	Water (6ml), Hydriodic Acid (57% in water) (0.75ml)	1	140	24	0.1	AD067B P2	No product
	$BiCl_3$ (0.2mmol)	Piperazine (0.15mmol) + MAI (0.15mmol)	Water (6ml), Hydriodic Acid (57% in water) (1ml)	1	140	24	0.1	AD067B P3	No product
AD067C	$BiCl_3$ (0.2mmol)	Piperazine (0.15mmol)	Water (6ml), Hydriodic Acid (57% in water) (0.5ml)	1	140	24	0.1	AD067C P1	Repeat conditions of (AD067A P1) for more product
	$BiCl_3$ (0.2mmol)	Piperazine (0.15mmol)	Water (6ml), Hydriodic Acid (57% in water) (0.5ml)	1	140	24	0.1	AD067C P2	Repeat conditions of (AD067A P1) for more product

	$BiCl_3$ (0.2mmol)	Piperazine (0.15mmol)	Water (6ml), Hydriodic Acid (57% in water) (0.5ml)	1	140	24	0.1	AD067C P3	Repeat conditions of (AD067A P1) for more product
AD067D	$BiCl_3$ (0.2mmol)	Piperazine (0.15mmol)	Water (6ml), Hydriodic Acid (57% in water) (0.5ml)	1	200	24	0.1	AD067D P1	No product
	$BiCl_3$ (0.2mmol)	Piperazine (0.15mmol)	Water (6ml), Hydriodic Acid (57% in water) (0.5ml)	1	200	24	0.1	AD067D P2	No product
	$BiCl_3$ (0.2mmol)	Piperazine (0.15mmol)	Water (6ml), Hydriodic Acid (57% in water) (0.5ml)	1	200	24	0.1	AD067D P3	No product
AD073A	$BiCl_3$ (0.2mmol)	1-Methylpiperazine (0.15mmol)	Water (6ml), Hydriodic Acid (57% in water) (0.5ml)	1	140	24	0.1	AD073A P1	No product
	$BiCl_3$ (0.2mmol)	1-Methylpiperazine (0.15mmol)	Water (6ml), Hydriodic Acid (57% in water) (0.75ml)	1	140	24	0.1	AD073A P2	Deep red block crystals (e16mtw021/e16mtw031)
	$BiCl_3$ (0.2mmol)	1-Methylpiperazine (0.15mmol)	Water (6ml), Hydriodic Acid (57% in water) (1ml)	1	140	24	0.1	AD073A P3	Red block crystals & Orange plate crystal (e16mtw034)
AD073B	$BiCl_3$ (0.2mmol)	1-Methylpiperazine (0.15mmol)	Water (6ml), Hydriodic Acid (57% in water) (0.75ml)	1	140	24	0.1	AD073B P1	Repeat conditions of (AD073A P2) for more product
	$BiCl_3$ (0.2mmol)	1-Methylpiperazine (0.15mmol)	Water (6ml), Hydriodic Acid (57% in water) (0.75ml)	1	140	24	0.1	AD073B P2	Repeat conditions of (AD073A P2) for more product
	$BiCl_3$ (0.2mmol)	1-Methylpiperazine (0.15mmol)	Water (6ml), Hydriodic Acid (57% in water) (0.75ml)	1	140	24	0.1	AD073B P3	Repeat conditions of (AD073A P2) for more product
AD073C	$BiCl_3$ (0.2mmol)	1-Methylpiperazine (0.15mmol)	Water (6ml), Hydriodic Acid (57% in water) (0.5ml)	1	200	24	0.1	AD073C P1	No product
	$BiCl_3$ (0.2mmol)	1-Methylpiperazine (0.15mmol)	Water (6ml), Hydriodic Acid (57% in water) (0.75ml)	1	200	24	0.1	AD073C P2	No product
	$BiCl_3$ (0.2mmol)	1-Methylpiperazine (0.15mmol)	Water (6ml), Hydriodic Acid (57% in water) (1ml)	1	200	24	0.1	AD073C P3	No product

AD074A	$BiCl_3$ (0.4mmol)	Pyrrole (0.3mmol)	Water (6ml), Hydriodic Acid (57% in water) (0.5ml)	1	140	24	0.1	AD074A P1	Standard molar quantities doubled (to allow for more accurate measuring of pyrrole)
	$BiCl_3$ (0.4mmol)	Pyrrole (0.3mmol)	Water (6ml), Hydriodic Acid (57% in water) (0.75ml)	1	140	24	0.1	AD074A P2	Standard molar quantities doubled (to allow for more accurate measuring of pyrrole)
	$BiCl_3$ (0.4mmol)	Pyrrole (0.3mmol)	Water (6ml), Hydriodic Acid (57% in water) (1ml)	1	140	24	0.1	AD074A P3	Standard molar quantities doubled (to allow for more accurate measuring of pyrrole)
AD075A	$BiCl_3$ (0.4mmol)	Ethylenediamine (0.3mmol)	Water (6ml), Hydriodic Acid (57% in water) (0.5ml)	1	140	24	0.1	AD075A P1	No product obtained from synthesis, Standard molar quantities doubled
	$BiCl_3$ (0.4mmol)	Ethylenediamine (0.3mmol)	Water (6ml), Hydriodic Acid (57% in water) (0.75ml)	1	140	24	0.1	AD075A P2	No product obtained from synthesis, Standard molar quantities doubled
	$BiCl_3$ (0.4mmol)	Ethylenediamine (0.3mmol)	Water (6ml), Hydriodic Acid (57% in water) (1ml)	1	140	24	0.1	AD075A P3	No product obtained from synthesis, Standard molar quantities doubled
AD075B	$BiCl_3$ (0.4mmol)	Ethylenediamine (0.3mmol)	Water (6ml), Hydriodic Acid (57% in water) (0.5ml)	1	180	24	0.1	AD075B P1	No product
	$BiCl_3$ (0.4mmol)	Ethylenediamine (0.3mmol)	Water (6ml), Hydriodic Acid (57% in water) (0.75ml)	1	180	24	0.1	AD075B P2	No product
	$BiCl_3$ (0.4mmol)	Ethylenediamine (0.3mmol)	Water (6ml), Hydriodic Acid (57% in water) (1ml)	1	180	24	0.1	AD075B P3	No product
AD076A	$BiCl_3$ (0.2mmol)	Indole (0.15mmol)	Water (6ml), Hydriodic Acid (57% in water) (0.5ml)	1	140	24	0.1	AD076A P1	No product
	$BiCl_3$ (0.2mmol)	Indole (0.15mmol)	Water (6ml), Hydriodic Acid (57% in water) (0.75ml)	1	140	24	0.1	AD076A P2	No product
	$BiCl_3$ (0.2mmol)	Indole (0.15mmol)	Water (6ml), Hydriodic Acid (57% in water) (1ml)	1	140	24	0.1	AD076A P3	No product
AD076B	$BiCl_3$ (0.2mmol)	Indole (0.15mmol)	Water (6ml), Hydriodic Acid (57% in water) (0.5ml)	1	180	24	0.1	AD076B P1	No product
	$BiCl_3$ (0.2mmol)	Indole (0.15mmol)	Water (6ml), Hydriodic Acid (57% in water) (0.75ml)	1	180	24	0.1	AD076B P2	No product

	$BiCl_3$ (0.2mmol)	Indole (0.15mmol)	Water (6ml), Hydriodic Acid (57% in water) (1ml)	1	180	24	0.1	AD076B P3	No product
AD076C	$BiCl_3$ (0.3mmol)	Indole (0.15mmol)	Water (6ml), Hydriodic Acid (57% in water) (0.5ml)	1	140	24	0.1	AD076C P1	Boltgun grey metallic-lustre crystalline material mostly spherical in shape
	$BiCl_3$ (0.3mmol)	Indole (0.15mmol)	Water (6ml), Hydriodic Acid (57% in water) (0.75ml)	1	140	24	0.1	AD076C P2	Boltgun grey metallic-lustre crystalline material mostly spherical in shape
	$BiCl_3$ (0.3mmol)	Indole (0.15mmol)	Water (6ml), Hydriodic Acid (57% in water) (1ml)	1	140	24	0.1	AD076C P3	Boltgun grey metallic-lustre crystalline material mostly spherical in shape
AD077A	$BiCl_3$ (0.2mmol)	1,4-dimethylpiperazine (0.15mmol)	Water (6ml), Hydriodic Acid (57% in water) (0.5ml)	1	140	24	0.1	AD077A P1	No product
	$BiCl_3$ (0.2mmol)	1,4-dimethylpiperazine (0.15mmol)	Water (6ml), Hydriodic Acid (57% in water) (0.75ml)	1	140	24	0.1	AD077A P2	Red block crystal(e16mtw033/e16mtw037)
	$BiCl_3$ (0.2mmol)	1,4-dimethylpiperazine (0.15mmol)	Water (6ml), Hydriodic Acid (57% in water) (1ml)	1	140	24	0.1	AD077A P3	No product
AD077B	$BiCl_3$ (0.2mmol)	1,4-dimethylpiperazine (0.15mmol)	Water (6ml), Hydriodic Acid (57% in water) (0.5ml)	1	200	24	0.1	AD077B P1	No product
	$BiCl_3$ (0.2mmol)	1,4-dimethylpiperazine (0.15mmol)	Water (6ml), Hydriodic Acid (57% in water) (0.75ml)	1	200	24	0.1	AD077B P2	No product
	$BiCl_3$ (0.2mmol)	1,4-dimethylpiperazine (0.15mmol)	Water (6ml), Hydriodic Acid (57% in water) (1ml)	1	200	24	0.1	AD077B P3	No product
AD077C	$BiCl_3$ (0.2mmol)	1,4-dimethylpiperazine (0.15mmol)	Water (6ml), Hydriodic Acid (57% in water) (0.5ml)	1	170	24	0.1	AD077C P1	No product

	$BiCl_3$ (0.2mmol)	1,4-dimethylpiperazine (0.15mmol)	Water (6ml), Hydriodic Acid (57% in water) (0.75ml)	1	170	24	0.1	AD077C P2	No product
	$BiCl_3$ (0.2mmol)	1,4-dimethylpiperazine (0.15mmol)	Water (6ml), Hydriodic Acid (57% in water) (1ml)	1	170	24	0.1	AD077C P3	No product
AD077D	$BiCl_3$ (0.2mmol)	1,4-dimethylpiperazine (0.15mmol)	Water (6ml), Hydriodic Acid (57% in water) (0.5ml)	1	170	36	0.1	AD077D P1	No product
	$BiCl_3$ (0.2mmol)	1,4-dimethylpiperazine (0.15mmol)	Water (6ml), Hydriodic Acid (57% in water) (0.75ml)	1	170	36	0.1	AD077D P2	No product
	$BiCl_3$ (0.2mmol)	1,4-dimethylpiperazine (0.15mmol)	Water (6ml), Hydriodic Acid (57% in water) (1ml)	1	170	36	0.1	AD077D P3	No product
	$BiCl_3$ (0.3mmol)	1,4-dimethylpiperazine (0.15mmol)	Water (6ml), Hydriodic Acid (57% in water) (0.5ml)	1	170	36	0.1	AD077D P4	Pure phase of red crystalline material (no black crystallites), however, crystal quality is poor does not look single
	$BiCl_3$ (0.3mmol)	1,4-dimethylpiperazine (0.15mmol)	Water (6ml), Hydriodic Acid (57% in water) (0.75ml)	1	170	36	0.1	AD077D P5	Pure phase of red crystalline material (no black crystallites), crystal quality looks better but may need further optimisation for a pure single crystal phase
	$BiCl_3$ (0.3mmol)	1,4-dimethylpiperazine (0.15mmol)	Water (6ml), Hydriodic Acid (57% in water) (1ml)	1	170	36	0.1	AD077D P6	Deep red crystals and large black crystals (Di-Methyl-Pip iodide)
AD077E	$BiCl_3$ (0.3mmol)	1,4-dimethylpiperazine (0.15mmol)	Water (6ml), Hydriodic Acid (57% in water) (0.75ml)	1	140	36	0.1		Repeat of AD077D P5 to obtain more material (but at lower T 140oC)
	$BiCl_3$ (0.3mmol)	1,4-dimethylpiperazine (0.15mmol)	Water (6ml), Hydriodic Acid (57% in water) (0.75ml)	1	140	36	0.1		Repeat of AD077D P5 to obtain more material (but at lower T 140oC)
	$BiCl_3$ (0.3mmol)	1,4-dimethylpiperazine (0.15mmol)	Water (6ml), Hydriodic Acid (57% in water) (0.75ml)	1	140	36	0.1		Repeat of AD077D P5 to obtain more material (but at lower T 140oC)

AD077F	$BiCl_3$ (0.3mmol)	1,4-dimethylpiperazine (0.15mmol)	Water (6ml), Hydriodic Acid (57% in water) (0.5ml)	1	170	24	0.1	AD077F P1	No product
	$BiCl_3$ (0.3mmol)	1,4-dimethylpiperazine (0.15mmol)	Water (6ml), Hydriodic Acid (57% in water) (0.75ml)	1	170	24	0.1	AD077F P2	No product
	$BiCl_3$ (0.3mmol)	1,4-dimethylpiperazine (0.15mmol)	Water (6ml), Hydriodic Acid (57% in water) (1ml)	1	170	24	0.1	AD077F P3	No product
	$BiCl_3$ (0.4mmol)	1,4-dimethylpiperazine (0.15mmol)	Water (6ml), Hydriodic Acid (57% in water) (0.5ml)	1	170	24	0.1	AD077F P4	No product
	$BiCl_3$ (0.4mmol)	1,4-dimethylpiperazine (0.15mmol)	Water (6ml), Hydriodic Acid (57% in water) (0.75ml)	1	170	24	0.1	AD077F P5	No product
	$BiCl_3$ (0.4mmol)	1,4-dimethylpiperazine (0.15mmol)	Water (6ml), Hydriodic Acid (57% in water) (1ml)	1	170	24	0.1	AD077F P6	Pure phase of red block crystals
AD077G	$BiCl_3$ (0.4mmol)	1,4-dimethylpiperazine (0.15mmol)	Water (6ml), Hydriodic Acid (57% in water) (1ml)	1	170	24	0.1	AD077G P1	Repeat of AD077F P6 for more pure phase material
	$BiCl_3$ (0.4mmol)	1,4-dimethylpiperazine (0.15mmol)	Water (6ml), Hydriodic Acid (57% in water) (1ml)	1	170	24	0.1	AD077G P2	Repeat of AD077F P6 for more pure phase material
	$BiCl_3$ (0.4mmol)	1,4-dimethylpiperazine (0.15mmol)	Water (6ml), Hydriodic Acid (57% in water) (1ml)	1	170	24	0.1	AD077G P3	Repeat of AD077F P6 for more pure phase material
AD078A	$BiCl_3$ (0.4mmol)	Pyrrolidine (0.3mmol)	Water (6ml), Hydriodic Acid (57% in water) (0.5ml)	1	140	24	0.1	AD078A P1	No product
	$BiCl_3$ (0.4mmol)	Pyrrolidine (0.3mmol)	Water (6ml), Hydriodic Acid (57% in water) (0.75ml)	1	140	24	0.1	AD078A P2	No product
	$BiCl_3$ (0.4mmol)	Pyrrolidine (0.3mmol)	Water (6ml), Hydriodic Acid (57% in water) (1ml)	1	140	24	0.1	AD078A P3	No product

AD078B	$BiCl_3$ (0.4mmol)	Pyrrolidine (0.3mmol)	Water (6ml), Hydriodic Acid (57% in water) (0.5ml)	1	170	24	0.1	AD078B P1	No product
	$BiCl_3$ (0.4mmol)	Pyrrolidine (0.3mmol)	Water (6ml), Hydriodic Acid (57% in water) (0.75ml)	1	170	24	0.1	AD078B P2	No product
	$BiCl_3$ (0.4mmol)	Pyrrolidine (0.3mmol)	Water (6ml), Hydriodic Acid (57% in water) (1ml)	1	170	24	0.1	AD078B P3	No product
AD078C	$BiCl_3$ (0.4mmol)	Pyrrolidine (0.3mmol)	Water (6ml), Hydriodic Acid (57% in water) (0.5ml)	1	200	24	0.1	AD078C P1	No product
	$BiCl_3$ (0.4mmol)	Pyrrolidine (0.3mmol)	Water (6ml), Hydriodic Acid (57% in water) (0.75ml)	1	200	24	0.1	AD078C P2	No product
	$BiCl_3$ (0.4mmol)	Pyrrolidine (0.3mmol)	Water (6ml), Hydriodic Acid (57% in water) (1ml)	1	200	24	0.1	AD078C P3	No product
AD079A	$BiCl_3$ (0.2mmol)	2-Methylpiperidine (0.3mmol)	Water (6ml), Hydriodic Acid (57% in water) (0.5ml)	1	140	24	0.1	AD079A P1	No product
	$BiCl_3$ (0.2mmol)	2-Methylpiperidine (0.3mmol)	Water (6ml), Hydriodic Acid (57% in water) (0.75ml)	1	140	24	0.1	AD079A P2	No product
	$BiCl_3$ (0.2mmol)	2-Methylpiperidine (0.3mmol)	Water (6ml), Hydriodic Acid (57% in water) (1ml)	1	140	24	0.1	AD079A P3	No product
AD079B	$BiCl_3$ (0.2mmol)	2-Methylpiperidine (0.3mmol)	Water (6ml), Hydriodic Acid (57% in water) (0.5ml)	1	200	24	0.1	AD079B P1	No product
	$BiCl_3$ (0.2mmol)	2-Methylpiperidine (0.3mmol)	Water (6ml), Hydriodic Acid (57% in water) (0.75ml)	1	200	24	0.1	AD079B P2	No product
	$BiCl_3$ (0.2mmol)	2-Methylpiperidine (0.3mmol)	Water (6ml), Hydriodic Acid (57% in water) (1ml)	1	200	24	0.1	AD079B P3	No product
AD084A	$BiCl_3$ (0.2mmol)	2-Methylpiperazine (0.15mmol)	Water (6ml), Hydriodic Acid (57% in water) (0.5ml)	1	140	24	0.1	AD084A P1	No product
	$BiCl_3$ (0.2mmol)	2-Methylpiperazine (0.15mmol)	Water (6ml), Hydriodic Acid (57% in water) (0.75ml)	1	140	24	0.1	AD084A P2	No product

	$BiCl_3$ (0.2mmol)	2-Methylpiperazine (0.15mmol)	Water (6ml), Hydriodic Acid (57% in water) (1ml)	1	140	24	0.1	AD084A P3	No product
AD084B	$BiCl_3$ (0.2mmol)	2-Methylpiperazine (0.15mmol)	Water (6ml), Hydriodic Acid (57% in water) (0.5ml)	1	170	24	0.1	AD084B P1	Deep red block crystals
	$BiCl_3$ (0.2mmol)	2-Methylpiperazine (0.15mmol)	Water (6ml), Hydriodic Acid (57% in water) (0.75ml)	1	170	24	0.1	AD084B P2	Deep red red crystals (more irregular shapes - likely twinned)
	$BiCl_3$ (0.2mmol)	2-Methylpiperazine (0.15mmol)	Water (6ml), Hydriodic Acid (57% in water) (1ml)	1	170	24	0.1	AD084B P3	No product
AD084C	$BiCl_3$ (0.3mmol)	2-Methylpiperazine (0.15mmol)	Water (6ml), Hydriodic Acid (57% in water) (0.5ml)	1	170	24	0.1	AD084C P1	Deep red crystals (clustered into large plate structures formed of many crystals)
	$BiCl_3$ (0.3mmol)	2-Methylpiperazine (0.15mmol)	Water (6ml), Hydriodic Acid (57% in water) (0.75ml)	1	170	24	0.1	AD084C P2	Mix of pinky-red (matte-lustre) prismatic block crystals with two large clusters of deep red crystals
	$BiCl_3$ (0.3mmol)	2-Methylpiperazine (0.15mmol)	Water (6ml), Hydriodic Acid (57% in water) (1ml)	1	170	24	0.1	AD084C P3	Mixed phases of deep red crystals with amorphous dark grey/black material
AD086A	$BiCl_3$ (0.2mmol)	4-Methylmorpholine (0.15mmol)	Water (6ml), Hydriodic Acid (57% in water) (0.5ml)	1	140	24	0.1	AD086A P1	Major phase of black (orangey/brown powder coated) crystalline material with a minor phase of red crystals (agglomerated as chunks)
	$BiCl_3$ (0.2mmol)	4-Methylmorpholine (0.15mmol)	Water (6ml), Hydriodic Acid (57% in water) (0.75ml)	1	140	24	0.1	AD086A P2	Pure phase of bright red crystals/ crystalline material (e16mtw063 - Isolated red crystal)
	$BiCl_3$ (0.2mmol)	4-Methylmorpholine (0.15mmol)	Water (6ml), Hydriodic Acid (57% in water) (1ml)	1	140	24	0.1	AD086A P3	Small amount of v.chunky dark red/black crystalline material
AD086B	$BiCl_3$ (0.3mmol)	4-Methylmorpholine (0.15mmol)	Water (6ml), Hydriodic Acid (57% in water) (0.5ml)	1	140	24	0.1	AD086B P1	Pure phase of deep red (orangey/ brown powder coated) crystalline material
	$BiCl_3$ (0.3mmol)	4-Methylmorpholine (0.15mmol)	Water (6ml), Hydriodic Acid (57% in water) (0.75ml)	1	140	24	0.1	AD086B P2	Mixed phase of black (orangey/brown powder coated) crystalline material with a phase of bright red crystals
	$BiCl_3$ (0.3mmol)	4-Methylmorpholine (0.15mmol)	Water (6ml), Hydriodic Acid (57% in water) (1ml)	1	140	24	0.1	AD086B P3	Mixed phase of bright red crystals with deep red/black crystalline material

AD086C	$BiCl_3$ (0.2mmol)	4-Methylmorpholine (0.15mmol)	Water (6ml), Hydriodic Acid (57% in water) (0.75ml)	1	140	24	0.1	AD086C P1	(Repeat of AD086A P2 synthesis for more pure phase material)
	$BiCl_3$ (0.2mmol)	4-Methylmorpholine (0.15mmol)	Water (6ml), Hydriodic Acid (57% in water) (0.75ml)	1	140	24	0.1	AD086C P2	(Repeat of AD086A P2 synthesis for more pure phase material)
	$BiCl_3$ (0.2mmol)	4-Methylmorpholine (0.15mmol)	Water (6ml), Hydriodic Acid (57% in water) (0.75ml)	1	140	24	0.1	AD086C P3	(Repeat of AD086A P2 synthesis for more pure phase material)
AD087A	$BiCl_3$ (0.2mmol)	Azetidinium Iodide (0.15mmol)	Water (6ml), Hydriodic Acid (57% in water) (0.5ml)	1	140	24	0.1	AD087A P1	No product
	$BiCl_3$ (0.2mmol)	Azetidinium Iodide (0.15mmol)	Water (6ml), Hydriodic Acid (57% in water) (0.75ml)	1	140	24	0.1	AD087A P2	No product
	$BiCl_3$ (0.2mmol)	Azetidinium Iodide (0.15mmol)	Water (6ml), Hydriodic Acid (57% in water) (1ml)	1	140	24	0.1	AD087A P3	No product
AD087B	$BiCl_3$ (0.1mmol)	Azetidinium Iodide (0.075mmol)	Water (6ml), Hydriodic Acid (57% in water) (0.5ml)	1	170	24	0.1	AD087B P1	No product
	$BiCl_3$ (0.1mmol)	Azetidinium Iodide (0.075mmol)	Water (6ml), Hydriodic Acid (57% in water) (0.75ml)	1	170	24	0.1	AD087B P2	No product
	$BiCl_3$ (0.1mmol)	Azetidinium Iodide (0.075mmol)	Water (6ml), Hydriodic Acid (57% in water) (1ml)	1	170	24	0.1	AD087B P3	No product

A.13. Antimony halometallate hybrid materials Solvothermal Synthetic Procedures

Experiment Code	**Antimony Precursor**	**Amine Precursor**	**Solvent Mixture**	**Ramp up Rate (ºC/min)**	**Dwell Temperature (ºC)**	**Dwell Time (h)**	**Ramp down Rate (ºC/min)**	**Product Code**	**Notes**
AD082A	SbI3 (0.2mmol)	Piperazine (0.15mmol)	Water (6ml), Hydriodic Acid (0.5ml)	1	140	24	0.1	AD082A P1	Brown non-crystalline powder
	SbI3 (0.2mmol)	Piperazine (0.15mmol)	Water (6ml), Hydriodic Acid (0.75ml)	1	140	24	0.1	AD082A P2	Mixed phase of brown non-crystalline powder and large chunky orange prismatic crystals

	SbI3 (0.2mmol)	Piperazine (0.15mmol)	Water (6ml), Hydriodic Acid (1ml)	1	140	24	0.1	AD082A P3	Pure phase of chunky block orange prismatic crystals (e16mtw057)(better quality by eye)
AD082B	SbI3 (0.2mmol)	1-Methylpiperazine (0.15mmol)	Water (6ml), Hydriodic Acid (0.5ml)	1	140	24	0.1	AD082B P1	Black/brown non-crystalline powder
	SbI3 (0.2mmol)	1-Methylpiperazine (0.15mmol)	Water (6ml), Hydriodic Acid (0.75ml)	1	140	24	0.1	AD082B P2	Mixed phase of black/brown powder material and long orange prismatic crystals
	SbI3 (0.2mmol)	1-Methylpiperazine (0.15mmol)	Water (6ml), Hydriodic Acid (1ml)	1	140	24	0.1	AD082B P3	Long orange prismatic crystals (e16mtw058)(some chunky but hollow), Minor phase of black crystalline material
AD082C	SbI3 (0.2mmol)	1,4-Dimethylpiperazine (0.15mmol)	Water (6ml), Hydriodic Acid (0.5ml)	1	140	24	0.1	AD082C P1	Chunky black crystals with a minor phase orange/brown non-crystalline powder
	SbI3 (0.2mmol)	1,4-Dimethylpiperazine (0.15mmol)	Water (6ml), Hydriodic Acid (0.75ml)	1	140	24	0.1	AD082C P2	Mixed phase of black crystals and orange crystals (Black crystals likely Organic-iodide salt and Orange the SbI-hybrid material)
	SbI3 (0.2mmol)	1,4-Dimethylpiperazine (0.15mmol)	Water (6ml), Hydriodic Acid (1ml)	1	140	24	0.1	AD082C P3	Mixed phase like P2, Possibly orange crystals are the major phase(e16mtw059), black crystals (e17mtw024). Further investigation showed show two polymorphs of orange crystals; block orange crystal [Sb4I16]4- structure and elongated orange crystal a [SbI4]-n polymorph(e17mtw023).
AD083A	SbCl3 (0.2mmol)	Piperazine (0.15mmol)	Water (6ml), Hydriodic Acid (0.5ml)	1	140	24	0.1	AD083A P1	Small amount of mustard yellow powder (non-crystalline)
	SbCl3 (0.2mmol)	Piperazine (0.15mmol)	Water (6ml), Hydriodic Acid (0.75ml)	1	140	24	0.1	AD083A P2	Small amount of brown powder with a few small orange crystals (likely the SbI hybrid structure)
	SbCl3 (0.2mmol)	Piperazine (0.15mmol)	Water (6ml), Hydriodic Acid (1ml)	1	140	24	0.1	AD083A P3	Pure phase of large orange block crystals
AD083B	SbCl3 (0.2mmol)	1-Methylpiperazine (0.15mmol)	Water (6ml), Hydriodic Acid (0.5ml)	1	140	24	0.1	AD083B P1	Black/yellow non-crystalline powder material

	SbCl3 (0.2mmol)	1-Methylpiperazine (0.15mmol)	Water (6ml), Hydriodic Acid (0.75ml)	1	140	24	0.1	AD083B P2	Black crystalline material with small orange crystals on surface
	SbCl3 (0.2mmol)	1-Methylpiperazine (0.15mmol)	Water (6ml), Hydriodic Acid (1ml)	1	140	24	0.1	AD083B P3	Bulk (long orange prismatic crystals), Minor phase of deep red/black crystalline material
AD083C	SbCl3 (0.2mmol)	1,4-Dimethylpiperazine (0.15mmol)	Water (6ml), Hydriodic Acid (0.5ml)	1	140	24	0.1	AD083C P1	Large chunky prismatic black crystals with a secondary yellow powder phase
	SbCl3 (0.2mmol)	1,4-Dimethylpiperazine (0.15mmol)	Water (6ml), Hydriodic Acid (0.75ml)	1	140	24	0.1	AD083C P2	Major phase of black crystals with a small amount of orange powder
	SbCl3 (0.2mmol)	1,4-Dimethylpiperazine (0.15mmol)	Water (6ml), Hydriodic Acid (1ml)	1	140	24	0.1	AD083C P3	Mixed phase of orange crystals and black crystals (Further investigation shows orange crystals are a mix of three polymorphs; Elongated dark orange crystal (matched to e17mtw023 1D chain structure), chunky lighter yellow-orange crystals (match to [Sb4I16]4- e16mtw059 structure) and dark orange chunky crystal (match to e17mtw013 1D chain structure).
AD083D	SbCl3 (0.2mmol)	2-Methylpiperazine (0.15mmol)	Water (6ml), Hydriodic Acid (57% in water) (0.5ml)	1	170	24	0.1	AD083D P1	Mixed phase of long prismatic orange crystals (dull lustre) with a non-crystallin beige powder phase
	SbCl3 (0.2mmol)	2-Methylpiperazine (0.15mmol)	Water (6ml), Hydriodic Acid (57% in water) (0.75ml)	1	170	24	0.1	AD083D P2	A small amount of non-crystalline cream coloured solid
	SbCl3 (0.2mmol)	2-Methylpiperazine (0.15mmol)	Water (6ml), Hydriodic Acid (57% in water) (1ml)	1	170	24	0.1	AD083D P3	Mixed phase of brick red chunky prismatic crystals with a minor phase of orange semi-crystalline solid
AD083E	SbCl3 (0.3mmol)	2-Methylpiperazine (0.15mmol)	Water (6ml), Hydriodic Acid (57% in water) (0.5ml)	1	170	24	0.1	AD083E P1	Small amount of non-crystalline cream coloured solid
	SbCl3 (0.3mmol)	2-Methylpiperazine (0.15mmol)	Water (6ml), Hydriodic Acid (57% in water) (0.75ml)	1	170	24	0.1	AD083E P2	Small amount of non-crystalline brown solid

	SbCl3 (0.3mmol)	2-Methylpiperazine (0.15mmol)	Water (6ml), Hydriodic Acid (57% in water) (1ml)	1	170	24	0.1	AD083E P3	Mixed phase of brick red block crystals with a small amount of orange non-crystalline solid
AD083F	SbCl3 (0.2mmol)	1,4-Dimethylpiperazine (0.15mmol)	Water (6ml), Hydriodic Acid (0.5ml)	1	170	24	0.1	AD083F P1	Mixed phase of large shiny black crystals and a brown non-crystalline solid
	SbCl3 (0.2mmol)	1,4-Dimethylpiperazine (0.15mmol)	Water (6ml), Hydriodic Acid (0.75ml)	1	170	24	0.1	AD083F P2	Mixed phase of chunky orange crystals and deep black crystalline material
	SbCl3 (0.2mmol)	1,4-Dimethylpiperazine (0.15mmol)	Water (6ml), Hydriodic Acid (1ml)	1	170	24	0.1	AD083F P3	Mixed phase of v.large (multi mm) sized orange block crystals with a v.minor phase of black crystalline solid
AD083G	SbCl3 (0.2mmol)	1,4-Dimethylpiperazine (0.15mmol)	Water (6ml), Hydriodic Acid (1ml)	1	140	24	0.1	AD083G P1	Repeat of AD083C P3 for more material.
	SbCl3 (0.2mmol)	1,4-Dimethylpiperazine (0.15mmol)	Water (6ml), Hydriodic Acid (1ml)	1	140	24	0.1	AD083G P2	Repeat of AD083C P3 for more material.
	SbCl3 (0.2mmol)	1,4-Dimethylpiperazine (0.15mmol)	Water (6ml), Hydriodic Acid (1ml)	1	140	24	0.1	AD083G P3	Repeat of AD083C P3 for more material.
AD085A	SbCl3 (0.2mmol)	1,4-benzenediamine (0.15mmol)	Ethanol (6ml), Hydriodic Acid (57% in water) (0.5ml)	1	140	24	0.1	AD085A P1	Major phase of orange crystalline material with a minor phase of shiny black balls
(der. AD051A)	SbCl3 (0.2mmol)	1,4-benzenediamine (0.15mmol)	Ethanol (6ml), Hydriodic Acid (57% in water) (0.75ml)	1	140	24	0.1	AD085A P2	Major phase of orange crystalline material with a minor phase of shiny black balls
	SbCl3 (0.2mmol)	1,4-benzenediamine (0.15mmol)	Ethanol (6ml), Hydriodic Acid (57% in water) (1ml)	1	140	24	0.1	AD085A P3	Major phase of orange crystalline material with a minor phase of shiny black balls. Balls seen dispersed in the growing sheets of orange crystalline material
AD085B	SbCl3 (0.2mmol)	1,2-benzenediamine (0.15mmol)	Ethanol (6ml), Hydriodic Acid (57% in water) (0.5ml)	1	140	24	0.1	AD085B P1	No product

(der. AD051C)	SbCl3 (0.2mmol)	1,2-benzenediamine (0.15mmol)	Ethanol (6ml), Hydriodic Acid (57% in water) (0.75ml)	1	140	24	0.1	AD085B P2	Dark orangey/brown elongated plate crystals with a minor phase of black crystalline material
	SbCl3 (0.2mmol)	1,2-benzenediamine (0.15mmol)	Ethanol (6ml), Hydriodic Acid (57% in water) (1ml)	1	140	24	0.1	AD085B P3	Dark orange elongated plate crystals - mix of crystalline and transparent single crystal material
AD085C	SbCl3 (0.2mmol)	2-Aminopyrimidine (0.15mmol)	Methanol (6ml), Hydriodic Acid (57% in water) (0.5ml)	1	140	24	0.1	AD085C P1	No product
(der. AD055B)	SbCl3 (0.2mmol)	2-Aminopyrimidine (0.15mmol)	Methanol (6ml), Hydriodic Acid (57% in water) (0.75ml)	1	140	24	0.1	AD085C P2	No product
	SbCl3 (0.2mmol)	2-Aminopyrimidine (0.15mmol)	Methanol (6ml), Hydriodic Acid (57% in water) (1ml)	1	140	24	0.1	AD085C P3	V. fine dark orange needle crystals
AD085C2	SbCl3 (0.2mmol)	2-Aminopyrimidine (0.15mmol)	Methanol (6ml), Hydriodic Acid (57% in water) (1ml)	1	140	24	0.1	AD085C2 P1	No product
	SbCl3 (0.2mmol)	2-Aminopyrimidine (0.15mmol)	Methanol (6ml), Hydriodic Acid (57% in water) (1ml)	1	140	24	0.1	AD085C2 P2	No product
	SbCl3 (0.2mmol)	2-Aminopyrimidine (0.15mmol)	Methanol (6ml), Hydriodic Acid (57% in water) (1ml)	1	140	24	0.1	AD085C2 P3	No product
AD085D	SbCl3 (0.2mmol)	DABCO (0.15mmol)	Water (6ml), Hydriodic Acid (0.5ml)	1	140	24	0.1	AD085D P1	Large chunky grey-lustre crystals with a non-crystalline yellow powder phase
(der. AD062A)	SbCl3 (0.2mmol)	DABCO (0.15mmol)	Water (6ml), Hydriodic Acid (0.75ml)	1	140	24	0.1	AD085D P2	Large chunky grey-lustre crystals with a non-crystalline light borwn powder phase
	SbCl3 (0.2mmol)	DABCO (0.15mmol)	Water (6ml), Hydriodic Acid (1ml)	1	140	24	0.1	AD085D P3	Mixed phase of black crystals (elongated prismatic) with an orange crystalline phase
AD085D2	SbCl3 (0.2mmol)	DABCO (0.15mmol)	Water (6ml), Hydriodic Acid (0.5ml)	1	170	24	0.1	AD085D2 P1	
	SbCl3 (0.2mmol)	DABCO (0.15mmol)	Water (6ml), Hydriodic Acid (0.75ml)	1	170	24	0.1	AD085D2 P2	
	SbCl3 (0.2mmol)	DABCO (0.15mmol)	Water (6ml), Hydriodic Acid (1ml)	1	170	24	0.1	AD085D2 P3	

AD085E	SbCl3 (0.2mmol)	DABCO (0.15mmol)	Methanol (6ml), Hydriodic Acid (57% in water) (0.5ml)	1	140	24	0.1	AD085E P1	Flaky black plate crystalline material
	SbCl3 (0.2mmol)	DABCO (0.15mmol)	Methanol (6ml), Hydriodic Acid (57% in water) (0.75ml)	1	140	24	0.1	AD085E P2	Major phase of black needles with a minor phase of orange/brown powder coating many crystals
	SbCl3 (0.2mmol)	DABCO (0.15mmol)	Methanol (6ml), Hydriodic Acid (57% in water) (1ml)	1	140	24	0.1	AD085E P3	Mix of v.fine red needle crystals with a bulk phase of black needles/crystalline material
AD085F	SbCl3 (0.2mmol)	3,4-Diaminotoluene (0.15mmol)	Ethanol (6ml), Hydriodic Acid (57% in water) (0.5ml)	1	140	24	0.1	AD085F P1	-
(der. AD053A)	SbCl3 (0.2mmol)	3,4-Diaminotoluene (0.15mmol)	Ethanol (6ml), Hydriodic Acid (57% in water) (0.75ml)	1	140	24	0.1	AD085F P2	-
	SbCl3 (0.2mmol)	3,4-Diaminotoluene (0.15mmol)	Ethanol (6ml), Hydriodic Acid (57% in water) (1ml)	1	140	24	0.1	AD085F P3	
AD085G	SbCl3 (0.2mmol)	3,4-Diaminotoluene (0.15mmol)	Methanol (6ml), Hydriodic Acid (57% in water) (0.5ml)	1	140	24	0.1	AD085G P1	-
(der. AD053B)	SbCl3 (0.2mmol)	3,4-Diaminotoluene (0.15mmol)	Methanol (6ml), Hydriodic Acid (57% in water) (0.75ml)	1	140	24	0.1	AD085G P2	-
	SbCl3 (0.2mmol)	3,4-Diaminotoluene (0.15mmol)	Methanol (6ml), Hydriodic Acid (57% in water) (1ml)	1	140	24	0.1	AD085G P3	-
AD085H	SbCl3 (0.2mmol)	4-Methylmorpholine (0.15mmol)	Water (6ml), Hydriodic Acid (57% in water) (0.5ml)	1	140	24	0.1	AD085H P1	-
(der. AD086A)	SbCl3 (0.2mmol)	4-Methylmorpholine (0.15mmol)	Water (6ml), Hydriodic Acid (57% in water) (0.75ml)	1	140	24	0.1	AD085H P2	
	SbCl3 (0.2mmol)	4-Methylmorpholine (0.15mmol)	Water (6ml), Hydriodic Acid (57% in water) (1ml)	1	140	24	0.1	AD085H P3	-
AD085H B2	SbCl3 (0.2mmol)	4-Methylmorpholine (0.15mmol)	Water (6ml), Hydriodic Acid (57% in water) (1ml)	1	140	24	0.1	AD085H B2 P1	(Repeat synthesis of AD085H P3 for more material)
	SbCl3 (0.2mmol)	4-Methylmorpholine (0.15mmol)	Water (6ml), Hydriodic Acid (57% in water) (1ml)	1	140	24	0.1	AD085H B2 P2	(Repeat synthesis of AD085H P3 for more material)

	SbCl3 (0.2mmol)	4-Methylmorpholine (0.15mmol)	Water (6ml), Hydriodic Acid (57% in water) (1ml)	1	140	24	0.1	AD085H B2 P3	(Repeat synthesis of AD085H P3 for more material)
AD085I	SbCl3 (0.2mmol)	Imidazole (0.15mmol)	Methanol (6ml), Hydriodic Acid (57% in water) (0.5ml)	1	180	24	0.1	AD085I P1	-
(der. AD059D)	SbCl3 (0.2mmol)	Imidazole (0.15mmol)	Methanol (6ml), Hydriodic Acid (57% in water) (0.75ml)	1	180	24	0.1	AD085I P2	
	SbCl3 (0.2mmol)	Imidazole (0.15mmol)	Methanol (6ml), Hydriodic Acid (57% in water) (1ml)	1	180	24	0.1	AD085I P3	-
AD085J	SbCl3 (0.2mmol)	2-Methylpiperazine (0.15mmol)	Water (6ml), Hydriodic Acid (57% in water) (0.5ml)	1	170	24	0.1	AD085J P1	Neglible amount of material synthesised
(der. AD084B)	SbCl3 (0.2mmol)	2-Methylpiperazine (0.15mmol)	Water (6ml), Hydriodic Acid (57% in water) (0.75ml)	1	170	24	0.1	AD085J P2	Mixed phase of long prismatic deep orange crystals and deep red/black crystalline material
	SbCl3 (0.2mmol)	2-Methylpiperazine (0.15mmol)	Water (6ml), Hydriodic Acid (57% in water) (1ml)	1	170	24	0.1	AD085J P3	Mixed phase of large chunky orange crystals (major) and small crystalline deep red crystals (minor)
AD085K	$SbCl_3$ (0.3mmol)	2-Methylpiperazine (0.15mmol)	Water (6ml), Hydriodic Acid (57% in water) (0.5ml)	1	170	24	0.1	AD085K P1	V.small amount of non-crystalline brown material
(der. AD084C)	$SbCl_3$ (0.3mmol)	2-Methylpiperazine (0.15mmol)	Water (6ml), Hydriodic Acid (57% in water) (0.75ml)	1	170	24	0.1	AD085K P2	Mixed phase of large brick red crystalline material, yellowy/orange non-crystalline material and deep red/black possibly crystalline solids
	$SbCl_3$ (0.3mmol)	2-Methylpiperazine (0.15mmol)	Water (6ml), Hydriodic Acid (57% in water) (1ml)	1	170	24	0.1	AD085K P3	Mixed phase of brick red/orange crystalline blocks with a small amount of deep red/black crystal phase
AD085M	SbCl3 (0.1mmol)	2-Methylpiperazine (0.075mmol)	Water (6ml), Hydriodic Acid (57% in water) (0.5ml)	1	170	24	0.1	AD085M P1	-
	SbCl3 (0.1mmol)	2-Methylpiperazine (0.075mmol)	Water (6ml), Hydriodic Acid (57% in water) (0.75ml)	1	170	24	0.1	AD085M P2	-

	SbCl3 (0.1mmol)	2-Methylpiperazine (0.075mmol)	Water (6ml), Hydriodic Acid (57% in water) (1ml)	1	170	24	0.1	AD085MP3	-
AD085N	SbCl3 (0.2mmol)	2-Methylpiperazine (0.15mmol)	Water (6ml), Hydriodic Acid (57% in water) (1ml)	1	170	24	0.1	AD085NP1	-
	SbCl3 (0.2mmol)	2-Methylpiperazine (0.15mmol)	Water (6ml), Hydriodic Acid (57% in water) (1.25ml)	1	170	24	0.1	AD085NP2	-
	SbCl3 (0.2mmol)	2-Methylpiperazine (0.15mmol)	Water (6ml), Hydriodic Acid (57% in water) (1.5ml)	1	170	24	0.1	AD085NP3	-
	SbI3 (0.2mmol)	2-Methylpiperazine (0.15mmol)	Water (6ml), Hydriodic Acid (57% in water) (1ml)	1	170	24	0.1	AD085NP4	-
	SbI3 (0.2mmol)	2-Methylpiperazine (0.15mmol)	Water (6ml), Hydriodic Acid (57% in water) (1.25ml)	1	170	24	0.1	AD085NP5	-
	SbI3 (0.2mmol)	2-Methylpiperazine (0.15mmol)	Water (6ml), Hydriodic Acid (57% in water) (1.5ml)	1	170	24	0.1	AD085NP6	-
AD085O	SbCl3 (0.2mmol)	2-Methylpiperazine (0.15mmol)	Water (6ml), Hydriodic Acid (57% in water) (1ml)	1	200	24	0.05	AD085OP1	-
	SbCl3 (0.2mmol)	2-Methylpiperazine (0.15mmol)	Water (6ml), Hydriodic Acid (57% in water) (1.25ml)	1	200	24	0.05	AD085OP2	-
	SbCl3 (0.2mmol)	2-Methylpiperazine (0.15mmol)	Water (6ml), Hydriodic Acid (57% in water) (1.5ml)	1	200	24	0.05	AD085OP3	-
	SbI3 (0.2mmol)	2-Methylpiperazine (0.15mmol)	Water (6ml), Hydriodic Acid (57% in water) (1ml)	1	200	24	0.05	AD085OP4	-
	SbI3 (0.2mmol)	2-Methylpiperazine (0.15mmol)	Water (6ml), Hydriodic Acid (57% in water) (1.25ml)	1	200	24	0.05	AD085OP5	-
	SbI3 (0.2mmol)	2-Methylpiperazine (0.15mmol)	Water (6ml), Hydriodic Acid (57% in water) (1.5ml)	1	200	24	0.05	AD085OP6	-
AD085P	SbCl3 (0.2mmol)	2-Methylpiperazine (0.15mmol)	Water (6ml), Hydriodic Acid (57% in water) (1ml)	1	170	24	0.1	AD085PP1	-

	SbCl3 (0.2mmol)	2-Methylpiperazine (0.15mmol)	Water (6ml), Hydriodic Acid (57% in water) (1ml)	1	170	24	0.1	AD085P P2	-
	SbCl3 (0.2mmol)	2-Methylpiperazine (0.15mmol)	Water (6ml), Hydriodic Acid (57% in water) (1ml)	1	170	24	0.1	AD085P P3	-
	SbCl3 (0.3mmol)	2-Methylpiperazine (0.15mmol)	Water (6ml), Hydriodic Acid (57% in water) (1ml)	1	170	24	0.1	AD085P P4	-
	SbCl3 (0.3mmol)	2-Methylpiperazine (0.15mmol)	Water (6ml), Hydriodic Acid (57% in water) (1ml)	1	170	24	0.1	AD085P P5	-
	SbCl3 (0.3mmol)	2-Methylpiperazine (0.15mmol)	Water (6ml), Hydriodic Acid (57% in water) (1ml)	1	170	24	0.1	AD085P P6	-
AD085Q	SbCl3 (0.2mmol)/ BiCl3(0.05mmol)	2-Methylpiperazine (0.15mmol)	Water (6ml), Hydriodic Acid (57% in water) (0.5ml)	1	170	24	0.1	AD085Q P1	-
	SbCl3 (0.2mmol)/ BiCl3(0.05mmol)	2-Methylpiperazine (0.15mmol)	Water (6ml), Hydriodic Acid (57% in water) (0.75ml)	1	170	24	0.1	AD085Q P2	-
	SbCl3 (0.2mmol)/ BiCl3(0.05mmol)	2-Methylpiperazine (0.15mmol)	Water (6ml), Hydriodic Acid (57% in water) (1ml)	1	170	24	0.1	AD085Q P3	-
AD085R	SbCl3 (0.2mmol)	2-Methylpiperazine (0.15mmol)	Water (6ml), Hydriodic Acid (57% in water) (0.5ml)	1	140	72	0.1	AD085R P1	-
	SbCl3 (0.2mmol)	2-Methylpiperazine (0.15mmol)	Water (6ml), Hydriodic Acid (57% in water) (0.75ml)	1	140	72	0.1	AD085R P2	-
	SbCl3 (0.2mmol)	2-Methylpiperazine (0.15mmol)	Water (6ml), Hydriodic Acid (57% in water) (1ml)	1	140	72	0.1	AD085R P3	-
AD085S	SbCl3 (0.3mmol)	2-Methylpiperazine (0.15mmol)	Water (6ml), Hydriodic Acid (57% in water) (0.5ml)	1	140	72	0.1	AD085S P1	-
	SbCl3 (0.3mmol)	2-Methylpiperazine (0.15mmol)	Water (6ml), Hydriodic Acid (57% in water) (0.75ml)	1	140	72	0.1	AD085S P2	-

	SbCl3 (0.3mmol)	2-Methylpiperazine (0.15mmol)	Water (6ml), Hydriodic Acid (57% in water) (1ml)	1	140	72	0.1	AD085S P3	-
AD085T	SbCl3 (0.2mmol)	2-Methylpiperazine (0.15mmol)	Water (6ml), Hydriodic Acid (57% in water) (0.5ml)	1	170	4	0.1	AD085T P1	-
	SbCl3 (0.2mmol)	2-Methylpiperazine (0.15mmol)	Water (6ml), Hydriodic Acid (57% in water) (0.75ml)	1	170	4	0.1	AD085T P2	-
	SbCl3 (0.2mmol)	2-Methylpiperazine (0.15mmol)	Water (6ml), Hydriodic Acid (57% in water) (1ml)	1	170	4	0.1	AD085T P3	-
AD085U	SbCl3 (0.2mmol)	No Organic Template	Water (6ml), Hydriodic Acid (57% in water) (0.5ml)	1	170	24	0.1	AD085U P1	-
	SbCl3 (0.2mmol)	No Organic Template	Water (6ml), Hydriodic Acid (57% in water) (0.75ml)	1	170	24	0.1	AD085U P2	-
	SbCl3 (0.2mmol)	No Organic Template	Water (6ml), Hydriodic Acid (57% in water) (1ml)	1	170	24	0.1	AD085U P3	-
AD085V	SbCl3 (0.2mmol)	2-Methylpiperazine (0.15mmol)	Water (6ml), Hydriodic Acid (57% in water) (0.5ml)	1	170	24	0.1	AD085V P1	Repeat of 85J (No wash procedure). Autoclave sealed as tightly as possible.
	SbCl3 (0.2mmol)	2-Methylpiperazine (0.15mmol)	Water (6ml), Hydriodic Acid (57% in water) (0.75ml)	1	170	24	0.1	AD085V P2	Repeat of 85J (No wash procedure). Autoclave sealed as tightly as possible.
	SbCl3 (0.2mmol)	2-Methylpiperazine (0.15mmol)	Water (6ml), Hydriodic Acid (57% in water) (1ml)	1	170	24	0.1	AD085V P3	Repeat of 85J (No wash procedure). Autoclave sealed as tightly as possible.
AD085X	SbCl3 (0.2mmol) + Thiourea (0.1mmol)	2-Methylpiperazine (0.15mmol)	Water (6ml), Hydriodic Acid (57% in water) (0.5ml)	1	170	24	0.1	AD085X P1	Identical to 85J but with a dopant of thiourea (sulphide ion source) (0.1mmol)
	SbCl3 (0.2mmol) + Thiourea (0.1mmol)	2-Methylpiperazine (0.15mmol)	Water (6ml), Hydriodic Acid (57% in water) (0.75ml)	1	170	24	0.1	AD085X P2	Identical to 85J but with a dopant of thiourea (sulphide ion source) (0.1mmol)
	SbCl3 (0.2mmol) + Thiourea (0.1mmol)	2-Methylpiperazine (0.15mmol)	Water (6ml), Hydriodic Acid (57% in water) (1ml)	1	170	24	0.1	AD085X P3	Identical to 85J but with a dopant of thiourea (sulphide ion source) (0.1mmol)

AD088A	SbCl3 (0.2mmol)	(R)-(-)-2-Methylpiperazine (0.15mmol)	Water (6ml), Hydriodic Acid (57% in water) (0.5ml)	1	170	24	0.1	AD088A P1	-
	SbCl3 (0.2mmol)	(R)-(-)-2-Methylpiperazine (0.15mmol)	Water (6ml), Hydriodic Acid (57% in water) (0.75ml)	1	170	24	0.1	AD088A P2	-
	SbCl3 (0.2mmol)	(R)-(-)-2-Methylpiperazine (0.15mmol)	Water (6ml), Hydriodic Acid (57% in water) (1ml)	1	170	24	0.1	AD088A P3	
AD088B	SbCl3 (0.2mmol)	(R)-(-)-2-Methylpiperazine (0.15mmol)	Water (6ml), Hydriodic Acid (57% in water) (1ml)	1	170	24	0.05	AD088B P1	-
	SbCl3 (0.2mmol)	(R)-(-)-2-Methylpiperazine (0.15mmol)	Water (6ml), Hydriodic Acid (57% in water) (1.1ml)	1	170	24	0.05	AD088B P2	-
	SbCl3 (0.2mmol)	(R)-(-)-2-Methylpiperazine (0.15mmol)	Water (6ml), Hydriodic Acid (57% in water) (1.2ml)	1	170	24	0.05	AD088B P3	-
AD088D	SbCl3 (0.2mmol)	(R)-(-)-2-Methylpiperazine (0.15mmol)	Water (6ml), Hydriodic Acid (57% in water) (0.5ml)	1	200	24	0.1	AD088D P1	Mixed phases of crystalline orange material and non-crystalline beige material
	SbCl3 (0.2mmol)	(R)-(-)-2-Methylpiperazine (0.15mmol)	Water (6ml), Hydriodic Acid (57% in water) (0.75ml)	1	200	24	0.1	AD088D P2	Red crystals coated with orange powder (likely tarnished from the ethanol wash) underneath red crystal quality is retained in some cases
	SbCl3 (0.2mmol)	(R)-(-)-2-Methylpiperazine (0.15mmol)	Water (6ml), Hydriodic Acid (57% in water) (1ml)	1	200	24	0.1	AD088D P3	P2 sensitive to wash so P3 was filtered but not washed. Some crystals retained in mother liquor. Bright red crystals with smaller orangey-red crystals on surface (possibly a different phase)

A.14. Pseudohalide-based Reflux Synthetic Procedures

Experiment Code	Bismuth thiocyanate source	Isolated thiocyanate	Metal/Ammonium salt	Reaction Solvent	Temperature (ºC)	Notes
AD060	Bi(NO3)3.5H2O 1:3 KSCN	Y (Orange solid)	Methylammonium Iodide (MAI)	DMF	60-70	Solid filtered from reaction. Filtrate cooled in ice, further precipitate present
	Bi(NO3)3.5H2O 1:3 KSCN	N (Yellow solution in THF)	Methylammonium Iodide (MAI)	THF	60-70	Hexane (10ml) added to orange solution after heating + cooling. Oily fraction at bottom of flask extracted. Cold diethyl ether (2ml) added, immisible with the oil. Solid product precitating from oil over a period of days - Red hexagonal plate crystals obtained (Cell match to hexagonal MA3Bi2I9 phase from SXD pre-exp)
AD061	Bi(NO3)3.5H2O 1:3 KSCN	N (Yellow solution in THF)	Caesium Iodide	THF	60-70	Red product isolated, powder product
AD063	Bi(NO3)3.5H2O 1:3 KSeCN	No		THF		Synthesis of BiSeCN crystals – No crystals could be isolated
AD090	Ammonium Thiocyanate (NH4SCN) + Zinc Oxide (ZnO) + Triethylenediamine (Ten/DABCO)			Acetonitrile	90	Synthesis of (HTen)2[Zn(NCS)4] from literature method (Direct synthesis and crystal structure of zinc thiocyanate complexes with 1,4-diazabicyclo(2,2,2)octane)
AD091	Ammonium Thiocyanate (NH4SCN) + Zinc Oxide (ZnO) + Piperazine			Acetonitrile	90	Product of very large chunky clear crystals (e17mtw001) and clear needle crystals (e16mtw069)

A.15. Pseudohalide-based Solvothermal Synthetic Procedures

Experiment Code	Bismuth Precursor	Pseudohalide Precursor	Amine Precursor	Solvent Mixture	Ramp up Rate (ºC/min)	Dwell Temperature (ºC)	Dwell Time (h)	Ramp down Rate (ºC/min)	Product Code
AD069A	Bi(NO3)3.5H2O (0.784mmol)	KSCN (2.350mmol)	Methylammonium Iodide (0.125mmol)	DMF (10ml)	1	140	24	0.1	AD069A P1
	(Split to 3 autoclaves)	(Split to 3 autoclaves)	Methylammonium Iodide (0.250mmol)	DMF (10ml)	1	140	24	0.1	AD069A P2

	(Split to 3 autoclaves)	(Split to 3 autoclaves)	Methylammonium Iodide (0.375mmol)	DMF (10ml)	1	140	24	0.1	AD069A P3
AD069B	Bi(NO3)3.5H2O (0.784mmol)	KSCN (2.350mmol)	Methylammonium Iodide (0.125mmol)	DMF (10ml)	1	100	24	0.1	AD069B P1
	(Split to 3 autoclaves)	(Split to 3 autoclaves)	Methylammonium Iodide (0.250mmol)	DMF (10ml)	1	100	24	0.1	AD069B P2
	(Split to 3 autoclaves)	(Split to 3 autoclaves)	Methylammonium Iodide (0.375mmol)	DMF (10ml)	1	100	24	0.1	AD069B P3
AD069C	BiCl3 (0.784mmol)	KSCN (2.350mmol)	Methylammonium Iodide (0.125mmol)	DMF (10ml)	1	140	24	0.1	AD069C P1
	(Split to 3 autoclaves)	(Split to 3 autoclaves)	Methylammonium Iodide (0.250mmol)	DMF (10ml)	1	140	24	0.1	AD069C P2
	(Split to 3 autoclaves)	(Split to 3 autoclaves)	Methylammonium Iodide (0.375mmol)	DMF (10ml)	1	140	24	0.1	AD069C P3
AD070A	Bi(NO3)3.5H2O (0.784mmol)	KSCN (2.350mmol)	Caesium Iodide (0.125mmol)	DMF (10ml)	1	140	24	0.1	AD070A P1
	(Split to 3 autoclaves)	(Split to 3 autoclaves)	Caesium Iodide (0.250mmol)	DMF (10ml)	1	140	24	0.1	AD070A P2
	(Split to 3 autoclaves)	(Split to 3 autoclaves)	Caesium Iodide (0.375mmol)	DMF (10ml)	1	140	24	0.1	AD070A P3
AD070B	Bi(NO3)3.5H2O (0.784mmol)	KSCN (2.350mmol)	Caesium Iodide (0.125mmol)	DMF (10ml)	1	100	24	0.1	AD070B P1
	(Split to 3 autoclaves)	(Split to 3 autoclaves)	Caesium Iodide (0.250mmol)	DMF (10ml)	1	100	24	0.1	AD070B P2
	(Split to 3 autoclaves)	(Split to 3 autoclaves)	Caesium Iodide (0.375mmol)	DMF (10ml)	1	100	24	0.1	AD070B P3
AD070C	BiCl3 (0.784mmol)	KSCN (2.350mmol)	Caesium Iodide (0.125mmol)	DMF (10ml)	1	140	24	0.1	AD070C P1

	(Split to 3 autoclaves)	(Split to 3 autoclaves)	Caesium Iodide (0.250mmol)	DMF (10ml)	1	140	24	0.1	AD070C P2
	(Split to 3 autoclaves)	(Split to 3 autoclaves)	Caesium Iodide (0.375mmol)	DMF (10ml)	1	140	24	0.1	AD070C P3
AD071A	Bi(NO3)3.5H2O (0.250mmol)	KSCN (0.750mmol)	Methylammonium Iodide (0.125mmol)	Water (6ml)	N/A	140	24	N/A	AD071A P1
	Bi(NO3)3.5H2O (0.250mmol)	KSCN (0.750mmol)	Methylammonium Iodide (0.250mmol)	Water (6ml)	N/A	140	24	N/A	AD071A P2
	Bi(NO3)3.5H2O (0.250mmol)	KSCN (0.750mmol)	Methylammonium Iodide (0.375mmol)	Water (6ml)	N/A	140	24	N/A	AD071A P3
AD071B	BiCl3 (0.250mmol)	KSCN (0.750mmol)	Methylammonium Iodide (0.125mmol)	Water (6ml)	N/A	140	24	N/A	AD071B P1
	BiCl3 (0.250mmol)	KSCN (0.750mmol)	Methylammonium Iodide (0.250mmol)	Water (6ml)	N/A	140	24	N/A	AD071B P2
	BiCl3 (0.250mmol)	KSCN (0.750mmol)	Methylammonium Iodide (0.375mmol)	Water (6ml)	N/A	140	24	N/A	AD071B P3
AD072A	Bi(NO3)3.5H2O (0.250mmol)	KSCN (0.750mmol)	Caesium Iodide (0.125mmol)	Water (6ml)	N/A	140	24	N/A	AD072A P1
	Bi(NO3)3.5H2O (0.250mmol)	KSCN (0.750mmol)	Caesium Iodide (0.250mmol)	Water (6ml)	N/A	140	24	N/A	AD072A P2
	Bi(NO3)3.5H2O (0.250mmol)	KSCN (0.750mmol)	Caesium Iodide (0.375mmol)	Water (6ml)	N/A	140	24	N/A	AD072A P3

A.16. Bismuth halide Double Perovskite Solvothermal synthesis procedures

Experiment Code	A-site Precursor	B-site Precursor	C-site Precursor	Solvent Mixture	Ramp up Rate (°C/min)	Dwell Temperature (°C)	Dwell Time (h)	Ramp down Rate (°C/min)	Product Code	Notes
AD080A	Caesium Iodide (1.2mmol)	Copper Iodide (0.6mmol)	Bismuth Chloride (0.6mmol)	Water (6ml), Hydriodic Acid (57wt% in water) (0.5ml)	1	140	24	0.1	AD080A P1	No product crystallised
	Caesium Iodide (1.2mmol)	Copper Iodide (0.6mmol)	Bismuth Chloride (0.6mmol)	Water (6ml), Hydriodic Acid (57wt% in water) (0.75ml)	1	140	24	0.1	AD080A P2	No product crystallised
	Caesium Iodide (1.2mmol)	Copper Iodide (0.6mmol)	Bismuth Chloride (0.6mmol)	Water (6ml), Hydriodic Acid (57wt% in water) (1.0ml)	1	140	24	0.1	AD080A P3	No product crystallised
AD080B	Caesium Iodide (1.2mmol)	Silver Iodide (0.6mmol)	Bismuth Chloride (0.6mmol)	Water (6ml), Hydriodic Acid (57wt% in water) (0.5ml)	1	140	24	0.1	AD080B P1	No product crystallised
	Caesium Iodide (1.2mmol)	Silver Iodide (0.6mmol)	Bismuth Chloride (0.6mmol)	Water (6ml), Hydriodic Acid (57wt% in water) (0.75ml)	1	140	24	0.1	AD080B P2	No product crystallised
	Caesium Iodide (1.2mmol)	Silver Iodide (0.6mmol)	Bismuth Chloride (0.6mmol)	Water (6ml), Hydriodic Acid (57wt% in water) (1.0ml)	1	140	24	0.1	AD080B P3	No product crystallised

A.17. Bismuth and Antimony bromometallate hybrid material Solvothermal synthesis procedures

Experiment Code	Bismuth Precursor	Amine Precursor	Solvent Mixture	Ramp up Rate (°C/min)	Dwell Temperature (°C)	Dwell Time (h)	Ramp down Rate (°C/min)	Product Code	Notes
AD100	$BiCl_3$ (0.2mmol)	Piperazine (0.15mmol)	Water (6ml), Hydrobromic Acid (57% in water) (0.5ml)	1	140	24	0.1	AD100 P1	No product crystallised
	$BiCl_3$ (0.2mmol)	Piperazine (0.15mmol)	Water (6ml), Hydrobromic Acid (57% in water) (0.75ml)	1	140	24	0.1	AD100 P2	No product crystallised
	$BiCl_3$ (0.2mmol)	Piperazine (0.15mmol)	Water (6ml), Hydrobromic Acid (57% in water) (1ml)	1	140	24	0.1	AD100 P3	No product crystallised
AD101A	$BiCl_3$ (0.2mmol)	4-methylmorpholine (0.15mmol)	Water (6ml), Hydrobromic Acid (57% in water) (0.5ml)	1	140(1st), 200(2nd)	24	0.1	AD101A P1	No product crystallised

	$BiCl_3$ (0.2mmol)	4-methylmorpholine (0.15mmol)	Water (6ml), Hydrobromic Acid (57% in water) (0.75ml)	1	140(1st), 200(2nd)	24	0.1	AD101A P2	No product crystallised
	$BiCl_3$ (0.2mmol)	4-methylmorpholine (0.15mmol)	Water (6ml), Hydrobromic Acid (57% in water) (1ml)	1	140(1st), 200(2nd)	24	0.1	AD101A P3	No product crystallised
AD101B	$SbCl_3$ (0.2mmol)	4-methylmorpholine (0.15mmol)	Water (6ml), Hydrobromic Acid (57% in water) (0.5ml)	1	140(1st), 200(2nd)	24	0.1	AD101B P1	No product crystallised
	$SbCl_3$ (0.2mmol)	4-methylmorpholine (0.15mmol)	Water (6ml), Hydrobromic Acid (57% in water) (0.75ml)	1	140(1st), 200(2nd)	24	0.1	AD101B P2	No product crystallised
	$SbCl_3$ (0.2mmol)	4-methylmorpholine (0.15mmol)	Water (6ml), Hydrobromic Acid (57% in water) (1ml)	1	140(1st), 200(2nd)	24	0.1	AD101B P3	No product crystallised

A.18. UV/Vis spectrum of as-synthesised bismuth sulphide iodide needle crystals

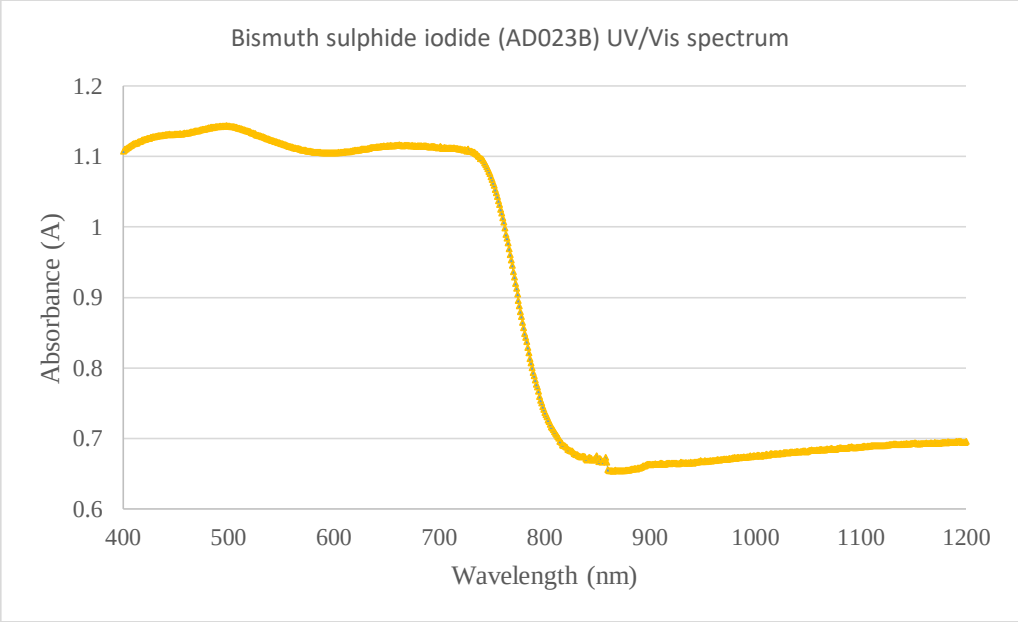

A.19. Powder X-ray diffraction data taken for compounds 1 and 2 at room temperature pre- and post- variable temperature powder X-ray diffraction analysis

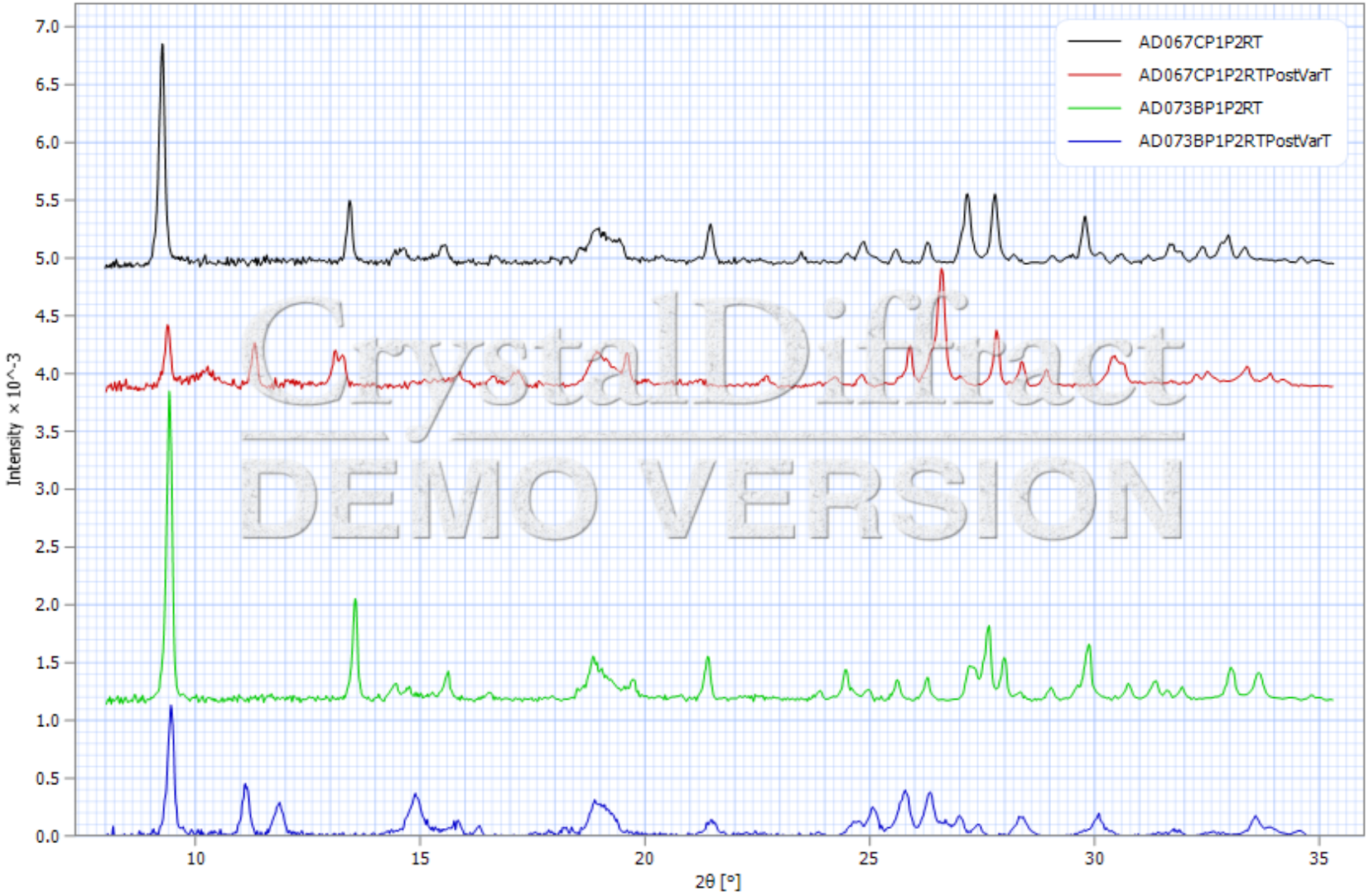

A.20. Variable temperature powder X-ray diffraction data for compound 1. Legend: 1st scan (bottom) Pre-VarT RT, 2nd-15th scans 30-150 °C, 16th scan (top) Post-VarT RT

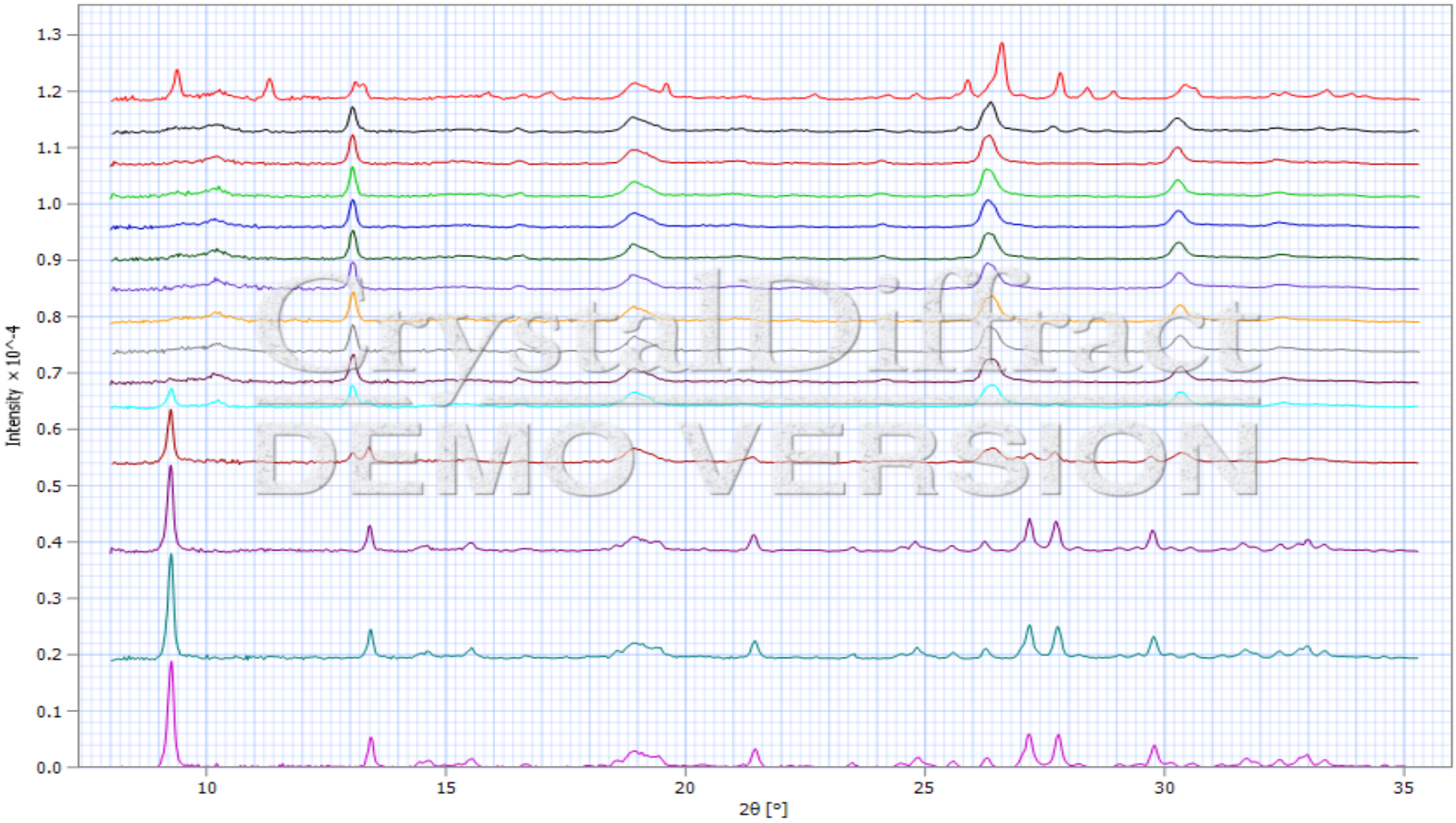

A.21. Variable temperature powder X-ray diffraction data for compound 2. Legend: 1st scan (bottom) Pre-VarT RT, 2nd-15th scans 30-150 °C, 16th scan (top) Post-VarT RT

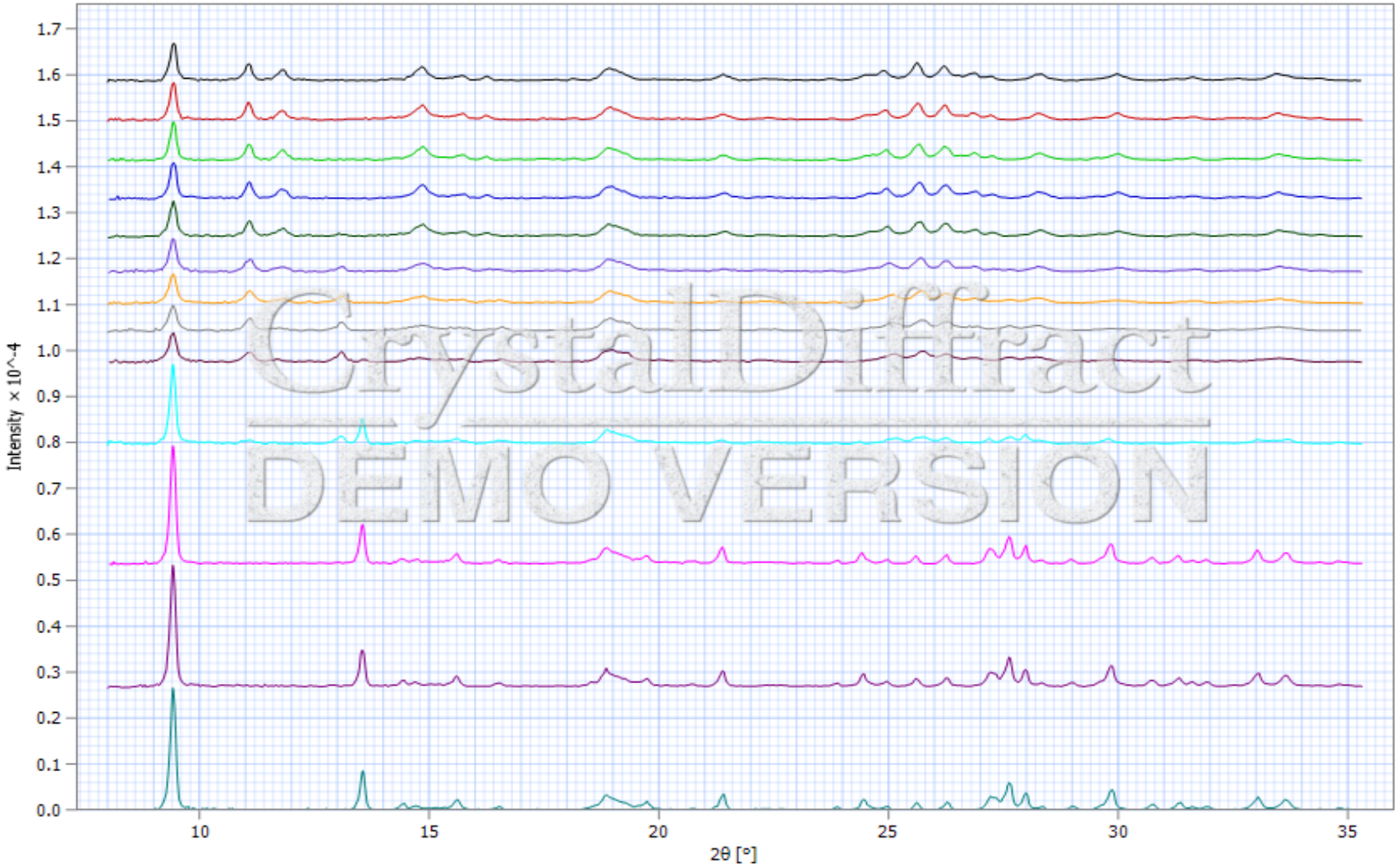

Dalton Transactions

PAPER

View Article Online
View Journal

Cite this: DOI: 10.1039/c6dt03602c

Synthesis and structure of pseudo-three dimensional hybrid iodobismuthate semiconductors†

Adam J. Dennington and Mark T. Weller*

Received 16th September 2016,
Accepted 18th October 2016

DOI: 10.1039/c6dt03602c

www.rsc.org/dalton

The synthesis, structures and semiconducting properties of three isostructural, piperazinium-cation based iodobismuthates, $[NH_2(CH_2)_4NH_2][BiI_4]_2{\cdot}4H_2O$, $[CH_3NH(CH_2)_4NH_2][BiI_4]_2{\cdot}3H_2O$ and $[CH_3NH(CH_2)_4HNCH_3][BiI_4]_2{\cdot}2H_2O$, are reported. The materials have pseudo-three dimensional structures consisting of infinite chains formed from edge/face sharing $[BiI_6]$ octahedra with short interchain I···I interactions of <3.8 Å. The materials have band gaps of ~1.9–2.0 eV and show variable optoelectronic properties based on the degree of methylation of the templating piperazinium ring-based organic species and the accordingly associated level of solvation in the structure.

Introduction

The emergence of metal halide perovskite photovoltaic materials over the last few years has ignited much attention towards discovering new semiconducting, organic–inorganic hybrid materials.[1–3] Lead-based materials, in particular methylammonium lead iodide (MAPI), currently dominate the field and now demonstrate solar cell efficiencies of over 22%.[4] Although commercially viable efficiencies have been validated for perovskite cells, they typically exhibit limited stability leading to concerns over long term operation in a solar cell. Studies have been undertaken to discern and combat the issue of instability of hybrid perovskite materials when exposed to light and/or air;[5–7] some reports suggest the inherent thermodynamic instability of the structures resulting in a spontaneous decomposition process to the respective lead and organo-cationic halide precursor species.[8] A further key concern with these materials is that they contain toxic lead.

There is, therefore, an urgent need to discover new functional optoelectronic materials. These will need to reproduce the impressive optoelectronic properties of the lead halide perovskites but replace the toxic lead and have improved material stability in device processing and in long-term deployment. It has been proposed that the required semiconducting properties of the lead halide perovskites derive from the fundamental electronic structure.[9] In particular, partially oxidised post transition metals with filled $5s^2$ or $6s^2$ orbitals have been shown to produce shallow defects and a dispersed valence band. As a result, the most promising metal cation candidates for further study are considered to be Sn^{2+}, Bi^{3+} and Sb^{3+}. Much initial work focussed on the isovalent substitution of Pb^{2+} by Sn^{2+}.[10–12] However, Sn^{2+} compounds generally undergo rapid oxidation by air and decomposition through reaction with moisture.[13,14]

Bismuth is an environmentally friendly, non-toxic alternative with the potential to form materials exhibiting the required optoelectronic properties. Bulk bismuth is relatively expensive compared to lead but for thin film technologies, requiring ~4–12 g m^{-2} of the absorber material, the cost of bismuth, at under $1 per m^2, is reasonable in terms of the overall device cost.

Work on semiconducting metal halide materials has been extended to double perovskite systems, with the general formula $A_2BB'X_6$ (X = halide) with B′ = Sn, Pb. Recently, bismuth-based halide double perovskites Cs_2AgBiX_6 (X = Cl, Br) have been reported as exhibiting comparable, though larger, band gaps to their $(MA)PbX_3$ analogues.[15–18] Another route to novel hybrid semiconducting materials is to search outside of the confines of perovskite structures while aiming to maintain high structural and optoelectronic connectivity. Typically iodometallate, X = I, structures are favoured targets over other halide systems as they tend to possess smaller band gaps and lower carrier effective masses.[17] However, substitution of Pb^{2+} by Bi^{3+}, with X = I, normally yields zero- (0D) and one-dimensional (1D) iodobismuthate structures. Previously reported iodobismuthate materials demonstrate a large diversity of anionic substructures,[19,20] built from linked $[BiI_6]$ octahedra including vertex sharing, edge-sharing and face-sharing motifs. Anionic units range from discrete 0D units in $[BiI_6]^{3-}$ to $[Bi_8I_{30}]^{4-}$ motifs,[21–35] through 1D chain structures,[22,36–40] including the commonly found $[BiI_4]^-_n$ and $[BiI_5]^{2-}_n$, with one reported 2D extended network, $[Bi_{2/3}I_4]^{2-}_n$.[41]

The University of Bath – Department of Chemistry, Bath, Claverton Down BA2 7AY, UK

† Electronic supplementary information (ESI) available. CCDC 1496109–1496114. For ESI and crystallographic data in CIF or other electronic format see DOI: 10.1039/c6dt03602c

To date well over 50 iodobismuthate materials have been described but three-dimensional structural, and, therefore, optoelectronic connectivity has proved elusive.

Experimental section

General

Our exploration of hybrid iodobismuthate materials has led to the discovery of three new, isostructural materials $[NH_2(CH_2)_4NH_2][BiI_4]_2{\cdot}4H_2O$, $[CH_3NH(CH_2)_4NH_2][BiI_4]_2{\cdot}3H_2O$ and $[CH_3NH(CH_2)_4HNCH_3][BiI_4]_2{\cdot}2H_2O$. These isostructural materials have pseudo-three dimensional structures, reminiscent of the perovskite structure, where links between $[BiI_4^-]_n$ chains occur through short I···I interactions. These materials also exhibit tuneable properties through the substitution of the piperazinium cation ring and, in turn, *via* control of solvate water molecules in the structures.

Synthesis

Crystals of 1,4-dipiperazinium iodobismuthate tetrahydrate $[NH_2(CH_2)_4NH_2][BiI_4]_2{\cdot}4H_2O$ (compound **1**) were obtained through a hydrothermal reaction of $BiCl_3$ (0.2 mmol, 98% (dry wt), Alfa Aesar), piperazine (0.15 mmol, >98%, Fluka), and HI (0.5 ml, 57 wt%, no stabiliser, Sigma-Aldrich) in deionised water (6 ml). Reactants were placed in a 25 ml Teflon-lined vessel, sealed in a steel autoclave and heated at 140 °C for 24 h, with a controlled ramp up rate of 1 °C min^{-1} and a ramp down rate of 0.1 °C min^{-1}. After filtration and ethanol wash, a pure phase of prismatic red block crystals of compound **1** (0.147 g) was obtained.

Deep red crystals of 1-methyl-1,4-dipiperazinium iodobismuthate trihydrate, $[CH_3NH(CH_2)_4NH_2][BiI_4]_2{\cdot}3H_2O$ (compound **2**), were synthesised utilising identical conditions and the procedure as described for **1** with the exception of a change of the organic templating agent to 1-methylpiperazine (0.15 mmol, 99%, Sigma-Aldrich) and an increased volume of HI (0.75 ml, 57 wt%, no stabiliser, Sigma-Aldrich); these reaction conditions yielded a pure phase of millimetre-sized crystals (0.130 g).

Deep red crystals of 1,4-dimethyl-1,4-dipiperazinium iodobismuthate dihydrate, $[CH_3NH(CH_2)_4HNCH_3][BiI_4]_2{\cdot}2H_2O$ (compound **3**), were attained through the hydrothermal reaction of $BiCl_3$ (0.4 mmol, 98% (dry wt), Alfa Aesar), 1,4-dimethylpiperazine (0.15 mmol, 98%, Alfa Aesar), and HI (1 ml, 57 wt%, no stabiliser, Sigma-Aldrich) in deionised water (6 ml).

Reactants were placed in a 25 ml Teflon-lined vessel, sealed in a steel autoclave and heated at 170 °C for 24 h, with a controlled ramp up rate of 1 °C min^{-1} and a ramp down rate of 0.1 °C min^{-1}. After filtration and ethanol wash a pure phase of crystals of compound **3** (0.206 g) was obtained.

Crystal data for **1a**: $C_4H_{20}N_2O_4Bi_2I_8$, M = 1593.41, monoclinic space group $P21/c$, a = 7.3508(2), b = 13.0215(4), c = 13.9875(3) Å, β = 94.588(2)°, V = 1334.57(2) $Å^3$, Z = 4, crystal size: 0.506 × 0.232 × 0.114 mm, T = 150.01(10) K, ρ_{calc} = 3.965 g cm^{-3}, μ = 22.429 mm^{-1}, 16 574 reflections (4290 unique reflections), 91 parameters, 0 restraints, R_1 (all data) = 0.0446, wR_2 (all data) = 0.0889, GooF = 1.145, further details available from CCDC 1496110.

Crystal data for **1b**: $C_4H_{20}N_2O_4Bi_2I_8$, M = 1593.41, monoclinic space group $P21/c$, a = 7.4697(3), b = 13.1773(7), c = 13.9099(6) Å, β = 95.109(4)°, V = 1363.72(11) $Å^3$, Z = 4, crystal size: 0.358 × 0.260 × 0.0.123 mm, T = 292.0(2) K, ρ_{calc} = 3.880 g cm^{-3}, μ = 21.950 mm^{-1}, 8961 reflections (4208 unique reflections), 91 parameters, 0 restraints, R_1 (all data) = 0.0634, wR_2 (all data) = 0.1049, GooF = 1.044, further details available from CCDC 1496109.

Crystal data for **2a**: $C_5H_{20}N_2O_3Bi_2I_8$, M = 1589.27, monoclinic space group $P21/c$, a = 7.5434(2), b = 13.0515(5), c = 13.6716(5) Å, β = 96.347(3)°, V = 1337.76(5) $Å^3$, Z = 4, crystal size: 0.434 × 0.189 × 0.168 mm, T = 149.95(10) K, ρ_{calc} = 7.890 g cm^{-3}, μ = 22.371 mm^{-1}, 14 198 reflections (4214 unique reflections), 109 parameters, 0 restraints, R_1 (all data) = 0.0381, wR_2 (all data) = 0.0722, GooF = 1.158, further details available from CCDC 1496112.

Crystal data for **2b**: $C_5H_{20}N_2O_3Bi_2I_8$, M = 1589.27, monoclinic space group $P21/c$, a = 7.6488(4), b = 13.1532(8), c = 13.7033(7) Å, β = 96.481(5)°, V = 1369.83(13) $Å^3$, Z = 4, crystal size: 0.413 × 0.176 × 0.176 mm, T = 292.23(10) K, ρ_{calc} = 3.804 g cm^{-3}, μ = 43.639 mm^{-1}, 8333 reflections (4206 unique reflections), 109 parameters, 0 restraints, R_1 (all data) = 0.0590, wR_2 (all data) = 0.0970, GooF = 1.075, further details available from CCDC 1496111.

Crystal data for **3a**: $C_6H_{20}N_2O_2Bi_2I_8$, M = 1585.43, monoclinic space group $P21/c$, a = 7.7293(2), b = 13.0336(3), c = 13.4990(4) Å, β = 97.955(3)°, V = 1346.79(6) $Å^3$, Z = 4, crystal size: 0.300 × 0.215 × 0.181 mm, T = 150.10(10) K, ρ_{calc} = 3.894 g cm^{-3}, μ = 22.220 mm^{-1}, 7814 reflections (4138 unique reflections), 91 parameters, 0 restraints, R_1 (all data) = 0.0402, wR_2 (all data) = 0.0788, GooF = 1.150, further details available from CCDC 1496114.

Crystal data for **3b**: $C_6H_{20}N_2O_2Bi_2I_8$, M = 1585.43, monoclinic space group $P21/c$, a = 7.7971(3), b = 13.0868(5), c = 13.5505(6) Å, β = 97.925(4)°, V = 1369.48(9) $Å^3$, Z = 4, crystal size: 0.298 × 0.217 × 0.180 mm, T = 286(9) K, ρ_{calc} = 3.830 g cm^{-3}, μ = 21.851 mm^{-1}, 8720 reflections (2879 unique reflections), 91 parameters, 0 restraints, R_1 (all data) = 0.0654, wR_2 (all data) = 0.0849, GooF = 1.021, further details available from CCDC 1496113.

Single crystal data for compounds **1–3** were obtained on an Agilent Xcalibur four-circle diffractometer equipped with a fine-focus (MoK_α) X-ray source and EosS2 CCD plate detector.

Results and discussion

General

The structures of compounds **1–3** were solved from single crystal X-ray diffraction data (see the ESI†) All three compounds, $[NH_2(CH_2)_4NH_2][BiI_4]_2{\cdot}4H_2O$, $[CH_3NH(CH_2)_4NH_2][BiI_4]_2{\cdot}3H_2O$ and $[CH_3NH(CH_2)_4HNCH_3][BiI_4]_2{\cdot}2H_2O$, crystallise in the

Table 1 Unit cell parameters for compounds **1–3** at RT and 150 K data collections

	1a (150 K)	**1b** (RT)	**2a** (150 K)	**2b** (RT)	**3a** (150 K)	**3b** (RT)
a (Å)	7.3508(2)	7.4697(3)	7.5434(2)	7.6488(4)	7.7293(2)	7.7971(3)
b (Å)	13.0215(4)	13.1773(7)	13.0515(5)	13.1532(8)	13.0336(3)	13.0868(5)
c (Å)	13.9875(3)	13.9099(6)	13.6716(5)	13.7033(7)	13.4990(4)	13.5505(6)
β (°)	94.588(2)	95.109(4)	96.347(3)	96.481(5)	97.955(3)	97.925(4)
V (Å^3)	1334.57(2)	1363.72(11)	1337.76(8)	1369.83(13)	1346.81(6)	1369.48(10)

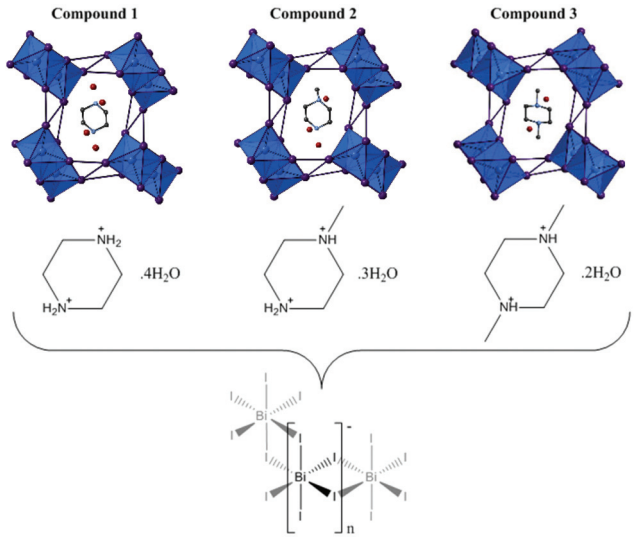

Fig. 1 A schematic illustration of the a-axis views of compounds **1–3**.

monoclinic space group $P2_1/c$ with lattice parameters shown in Table 1. The materials are iso-structural and consist of infinite chains of the stoichiometry $[BiI_4^-]_n$ with short interchain I···I contacts. The voids delineated by the chains and inter-chain contacts are occupied by the organic cations and water molecules in a manner reminiscent of the perovskite structure, (Fig. 1).

Stability and dehydration

Thermogravimetric analysis of compound **1** displays a weight loss of 4.2% in the temperature range of 70–110 °C corresponding to the desolvation of all four water molecules from the hydrated structure. In the same way, the tri- and di-hydrate structures of compounds **2** and **3** exhibit dehydration steps with weight losses of 3.7% and 2.0% respectively, in close agreement with the weight percentage contributions to the unit cell. All three dehydrated structures show thermal stability to approximately 250 °C before undergoing degradation (Fig. S1–S3 – see the ESI†).

Crystal structure analysis

In compound **1**, the dipiperazinium dications counterbalance the charge of the anionic $[BiI_4^-]_n$ chains and are located within channels extending through the a-axis of the structure in parallel with the sublattice. Neutral water molecules fully occupy four sites within the structure.

In compound **2** the organic cation is disordered, adopting one of two possible orientations, and as a result the steric effect of the methyl group partially blocks the occupancy of two of the water molecule positions, previously fully occupied in compound **1**. That is, these water molecule sites become half-filled due to the methyl group of the locally orientated 1-methyl-dipiperazinium cations occupying and so impeding the spaces. This reduces the overall hydration level in compound **2** to give a trihydrate hybrid iodobismuthate, $[CH_3NH(CH_2)_4NH_2][BiI_4]_2{\cdot}3H_2O$. Following this behaviour and trend, in compound **3**, the methyl groups of the positionally ordered 1,4-dimethyldipiperazinium cation preclude the occupation of both these water molecule sites occupied in compound **1** and this results in the formation of a dihydrate, $[CH_3NH(CH_2)_4HNCH_3][BiI_4]_2{\cdot}2H_2O$. Elongated thermal parameters on the nitrogen and methyl carbon atoms in this structure indicate some possible local conformational disorder of the organic cation in the structure.

The changes to the cation and the associated degree of solvation result in subtle but important changes to the anionic sub-lattice. The $[BiI_4^-]_n$ chains are formed from edge sharing individual $[BiI_6]$ octahedra, leading to 4 bridging and 2 terminal *cis*-related iodine atoms. The bismuth atom is slightly displaced from a central position in the $[BiI_6]$ octahedron with the shortest Bi–I interactions observed for the two terminal iodine atoms. This behaviour is in agreement with observations for other iodobismuthate materials possessing similar 1D $[BiI_4^-]_n$ chain motifs.[38–40,42,43] The range of Bi–I bond lengths within the octahedra decreases from compound **1** to compound **3** suggesting an increased overall regularity of the octahedra (Fig. 2).

Interchain I···I interactions extend the anionic network along both the b- and c-axes of all three compounds; this can be considered as producing a degree of 3D connectivity in the materials and a potential route for electronic interactions between the $[BiI_4^-]_n$ chains. Three I···I pathways repeat regularly along the chain axis with all iodine atoms involved in interactions with adjacent chains; the longest of these being a terminal–terminal I···I interaction and the shortest two edge iodine to terminal iodine interactions. Lengths of these interactions range from 3.76–4.44 Å in the structures and the average distance of the interchain interactions decreases, 4.14 Å → 4.09 Å → 4.00 Å (150 K), through compounds **1–3** respectively (Fig. 3). The shortest interchain interaction is observed to exhibit minor variation through the structures 3.76 Å → 3.77 Å → 3.78 Å (150 K). In the series of compound **1** to compound **3** the interchain Bi···Bi distances increase by an

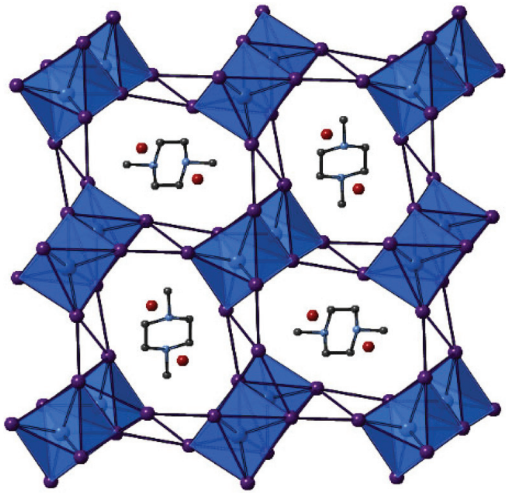

Fig. 2 View down the *a*-axis of compound **3** highlighting the inter chain I···I interactions.

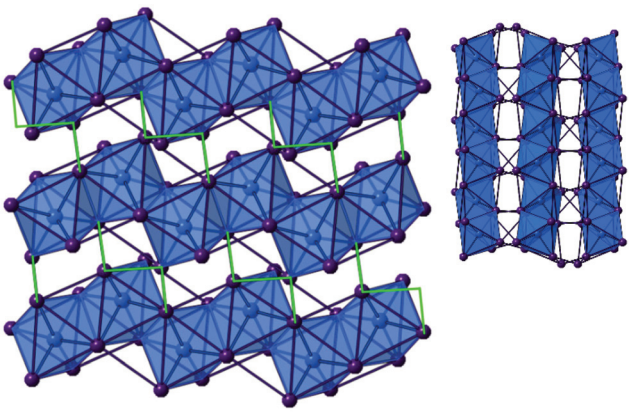

Fig. 3 Left: *a*-axis view of the anionic 1D network present in all compounds with interchain interactions highlighted (green). Right: *c*-axis view of the anionic network observed in all structures.

average of 0.05 Å as the Bi–I–Bi bond angles increase beyond the octahedral angles, from 90.5° → 91.9° → 93.2° (150 K).

In summary progressing from piperazinium-based, compound **1**, through 1-methylpiperazinium-based, compound **2**, to 1,4-dimethyldipiperazinium-based, compound **3**, causes systematic changes within the 1D anionic chain network. These trends are observed as an extension of the distances between bismuth atom positions within the chain; Bi···Bi distances to intrachain next-but-one octahedra steadily increase 7.35 Å → 7.54 Å → 7.73 Å (150 K). This behaviour is accompanied by an increased level of distortion within the chains as the Bi–I–Bi angles extend from 90.5° → 93.2°. Simultaneously the average lengths of I···I interchain interactions decrease which increases the pseudo-3D nature of the materials. Interchain Bi···Bi distances decrease in tandem, with the average of the three closest interchain Bi···Bi distances falling from 9.20 Å → 9.10 Å → 8.85 Å (150 K) from compound **1** to compound **3**.

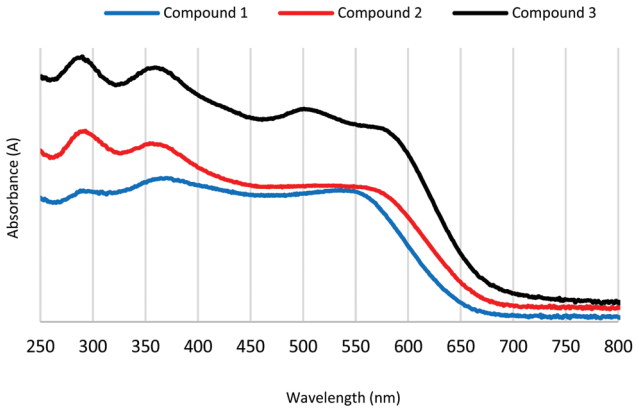

Fig. 4 UV/Vis spectra of compounds **1–3** (10 wt% mixtures in $BaSO_4$).

Hydrogen bonding between the solvent water molecules and the protonated amine groups and/or the iodide ions of the $[BiI_4^-]_n$ chains is likely to be present in all three compounds. Note that while hydrogen positions with the water molecules were modelled in all three structures, the true molecular orientations of the molecules could not be determined in these heavy atom compounds.

Optical absorption measurements

Optical absorption spectra (250–800 nm) were collected for the pure phases of compounds **1–3** (Fig. 4). Each compound shows absorption across the majority of the visible region consistent with their observed dark red colouration. The absorption edge onset was determined from Tauc plots as 550, 560 and 575 nm which assuming a direct band gap for the strong absorption coefficients gives E_g values of 2.00 eV, 1.95 eV and 1.92 eV for compounds **1–3** respectively (Fig. S4 – see the ESI†). These shifts could be attributed to the trend seen in decreasing interchain I···I distances and, therefore, increasing pseudo 3D-connectivity within these structures. Additional absorption peak features can be observed in the spectra for all three compounds at ~290 nm (4.3 eV) and ~360 nm (3.4 eV). Compound **3** also has an additional absorption peak at ~500 nm (2.5 eV). Previous studies of iodobismuthate structures have shown similar distinct bands that have been attributed to the electronic transitions from the HOMO Bi(6p) orbital to the LUMO Bi(5p) orbitals.[25,38]

Conclusions

In summary, three new, pseudo-3D piperazinium-based hybrid iodobismuthate materials have been synthesised and structurally characterised. All three structures have been shown by thermogravimetric analysis to undergo dehydration processes while maintaining the integrity of the bismuth-iodide framework and semiconducting properties. Preliminary variable temperature SXD/PXRD studies indicate that the dehydration is reversible in these materials. This behaviour should be of

interest in respect of depositing thin-films of these materials as it indicates that sample degradation, as seen with the lead halide perovskites, will not occur. Increased methylation of the templating piperazinium ring, tied with a decreased level of solvate within the structure, has been shown to result in average shortening of the I···I interactions between 1D $[BiI_4^-]_n$ chains in the anionic network.

Correspondingly, analysis by optical absorption indicates a shift in the absorption edge in relation to this trend, with all three materials demonstrating band gap energies of ~1.9–2.0 eV, estimated from the intercept of the maximum angle of the absorption edge. Although this value is too large for use as highly efficient absorber materials in a single junction cell architecture, their use in tandem solar cell architectures can still be considered. The pseudo-three dimensional features of the structures of these materials, and the ability to tune them through variations in the geometry of the templating organic cation signify a further step towards obtaining highly functional yet less toxic stable perovskite-like hybrid absorber materials for future use in solar technologies.

Acknowledgements

The authors would like to thank Dr Mary F. Mahon for assistance with the single crystal X-ray crystallography. AJD would like to thank EPSRC for DTA studentship support.

Notes and references

1 H. J. Snaith, *J. Phys. Chem. Lett.*, 2013, **4**, 3623–3630.
2 M. A. Green, A. Ho-Baillie and H. J. Snaith, *Nat. Photonics*, 2014, **8**, 506–514.
3 S. Kazim, M. K. Nazeeruddin, M. Gratzel and S. Ahmad, *Angew. Chem., Int. Ed.*, 2014, **53**, 2812–2824.
4 . Research cell efficiency records, http://www.nrel.gov/ncpv/images/efficiency_chart.jpg (accessed July 2016).
5 G. D. Niu, X. D. Guo and L. D. Wang, *J. Mater. Chem. A*, 2015, **3**, 8970–8980.
6 J. L. Yang, B. D. Siempelkamp, D. Y. Liu and T. L. Kelly, *ACS Nano*, 2015, **9**, 1955–1963.
7 Y. Han, S. Meyer, Y. Dkhissi, K. Weber, J. M. Pringle, U. Bach, L. Spiccia and Y. B. Cheng, *J. Mater. Chem. A*, 2015, **3**, 8139–8147.
8 A. M. Ganose, C. N. Savory and D. O. Scanlon, *J. Phys. Chem. Lett.*, 2015, **6**, 4594–4598.
9 R. E. Brandt, V. Stevanovic, D. S. Ginley and T. Buonassisi, *MRS Commun.*, 2015, **5**, 265–275.
10 N. K. Noel, S. D. Stranks, A. Abate, C. Wehrenfennig, S. Guarnera, A. A. Haghighirad, A. Sadhanala, G. E. Eperon, S. K. Pathak, M. B. Johnston, A. Petrozza, L. M. Herz and H. J. Snaith, *Energy Environ. Sci.*, 2014, **7**, 3061–3068.
11 C. C. Stoumpos, C. D. Malliakas and M. G. Kanatzidis, *Inorg. Chem.*, 2013, **52**, 9019–9038.
12 M. Weiss, J. Horn, C. Richter and D. Schlettwein, *Phys. Status Solidi A*, 2016, **213**, 975–981.
13 D. B. Mitzi, S. Wang, C. A. Feild, C. A. Chess and A. M. Guloy, *Sci.*, 1995, **267**, 1473–1476.
14 D. B. Mitzi, C. D. Dimitrakopoulos and L. L. Kosbar, *Chem. Mater.*, 2001, **13**, 3728–3740.
15 A. H. Slavney, T. Hu, A. M. Lindenberg and H. I. Karunadasa, *J. Am. Chem. Soc.*, 2016, **138**, 2138–2141.
16 E. T. McClure, M. R. Ball, W. Windl and P. M. Woodward, *Chem. Mater.*, 2016, **28**, 1348–1354.
17 G. Volonakis, M. R. Filip, A. A. Haghighirad, N. Sakai, B. Wenger, H. J. Snaith and F. Giustino, *J. Phys. Chem. Lett.*, 2016, **7**, 1254–1259.
18 M. Filip, S. Hillman, A. Haghighirad, H. Snaith and F. Giustino, *J. Phys. Chem. Lett.*, 2016, 2579–2585.
19 L. M. Wu, X. T. Wu and L. Chen, *Coord. Chem. Rev.*, 2009, **253**, 2787–2804.
20 S. A. Adonin, M. N. Sokolov and V. P. Fedin, *Coord. Chem. Rev.*, 2016, **312**, 1–21.
21 A. M. Goforth, L. Peterson, M. D. Smith and H. C. Zur Loye, *J. Solid State Chem.*, 2005, **178**, 3529–3540.
22 W. H. Bi and N. Mercier, *Chem. Commun.*, 2008, 5743–5745.
23 A. M. Goforth, J. R. Gardinier, M. D. Smith, L. Peterson and H. C. Z. Loye, *Inorg. Chem. Commun.*, 2005, **8**, 684–688.
24 C. Hrizi, A. Samet, Y. Abid, S. Chaabouni, M. Fliyou and A. Koumina, *J. Mol. Struct.*, 2011, **992**, 96–101.
25 A. Samet, A. Ben Ahmed, A. Mlayah, H. Boughzala, E. K. Hlil and Y. Abid, *J. Mol. Struct.*, 2010, **977**, 72–77.
26 A. M. Goforth, M. A. Tershansy, M. D. Smith, L. Peterson, J. G. Kelley, W. J. I. DeBenedetti and H. C. Zur Loye, *J. Am. Chem. Soc.*, 2011, **133**, 603–612.
27 C. Feldmann, *J. Solid State Chem.*, 2003, **172**, 53–58.
28 J. Heine, *Dalton Trans.*, 2015, **44**, 10069–10077.
29 H. Krautscheid, *Z. Anorg. Allg. Chem.*, 1995, **621**, 2049–2054.
30 H. Krautscheid, *Z. Anorg. Allg. Chem.*, 1999, **625**, 192–194.
31 S. A. Adonin, E. V. Peresypkina, M. N. Sokolov and V. P. Fedin, *Russ. J. Coord. Chem.*, 2014, **40**, 867–870.
32 H. Krautscheid, *Z. Anorg. Allg. Chem.*, 1994, **620**, 1559–1564.
33 K. Y. Monakhov, C. Gourlaouen, R. Pattacini and P. Braunstein, *Inorg. Chem.*, 2012, **51**, 1562–1568.
34 V. V. Sharutin, I. V. Egorova, N. N. Klepikov, E. A. Boyarkina and O. K. Sharutina, *Russ. J. Inorg. Chem.*, 2009, **54**, 1768–1778.
35 A. Okrut and C. Feldmann, *Z. Anorg. Allg. Chem.*, 2006, **632**, 409–412.
36 D. B. Mitzi and P. Brock, *Inorg. Chem.*, 2001, **40**, 2096–2104.
37 G. A. Mousdis, G. C. Papavassiliou, A. Terzis and C. P. Raptopoulou, *Z. Naturforsch., B: Chem. Sci.*, 1998, **53**, 927–931.
38 C. Hrizi, N. Chaari, Y. Abid, N. Chniba-Boudjada and S. Chaabouni, *Polyhedron*, 2012, **46**, 41–46.
39 S. Chaabouni, S. Kamoun and J. Jaud, *J. Chem. Crystallogr.*, 1997, **27**, 527–531.

40 N. A. Yelovik, A. V. Mironov, M. A. Bykov, A. N. Kuznetsov, A. V. Grigorieva, Z. Wei, E. V. Dikarev and A. V. Shevelkov, *Inorg. Chem.*, 2016, **55**, 4132–4140.
41 D. B. Mitzi, *Inorg. Chem.*, 2000, **39**, 6107–6113.
42 M. Erbe, D. Kohler and M. Ruck, *Z. Anorg. Allg. Chem.*, 2010, **636**, 1513–1515.
43 A. Gagor, M. Weclawik, B. Bondzior and R. Jakubas, *CrystEngComm*, 2015, **17**, 3286–3296.

Dalton Transactions

PAPER

View Article Online
View Journal

Cite this: DOI: 10.1039/c7dt04280a

Synthesis, structure and optoelectronic properties of hybrid iodobismuthate & iodoantimonate semiconducting materials†

Adam J. Dennington and Mark T. Weller *

The syntheses and structures of five iodobismuthate and nine iodoantimonate hybrid materials are presented. The 1,3-dimethyl-2-oxo-2,3-dihydropyrimidinium cation has been used to template the isostructural, one-dimensional $[C_6H_9N_2O][SbI_4]$ (**I**) and $[C_6H_9N_2O][BiI_4]$ (**II**), while 4-methylmorpholinium templates the compounds, $[C_5H_{12}NO]_4[Sb_6I_{22}]$ (**III**) and $[C_5H_{12}NO]_4[Bi_4I_{16}]$ (**IV**), both containing isolated iodopnictogenide cluster anions. Five iodoantimonate compounds, templated by piperazinium cation derivatives, have been synthesised; $[C_4H_{12}N_2][SbI_4]_2{\cdot}4H_2O$ (**V**), $[C_5H_{14}N_2][SbI_4]_2{\cdot}3H_2O$ (**VI**), two polymorphs of $[C_6H_{16}N_2][SbI_4]_2{\cdot}2H_2O$ (**VII** and **VIII**) and $[C_6H_{16}N_2][Sb_4I_{16}]_{0.5}{\cdot}H_2O$ (**IX**), mainly adopting structures closely related to previously published 1D iodobismuthate hybrid materials. 1-Ethyl-2-methylbenzimidazolium cations, formed *in situ* in the reaction medium, template the isostructural 1D structures of $[C_{10}H_{13}N_2][SbI_4]$ (**X**) and $[C_{10}H_{13}N_2][BiI_4]$ (**XI**). 1,4-Diazabicyclo[2.2.2]octandiium $(DABCOH_2)^{2+}$ dications are shown to template a hydrated iodoantimonate structure $[C_6H_{14}N_2]_2[Sb_4I_{16}]{\cdot}2H_2O$ (**XII**) containing $[Sb_4I_{16}]^{4-}$ complex anions and a mixed phase of two iodobismuthate materials; one phase contains, uniquely, a mixture of the complex anions $[Bi_2I_{10}]^{4-}$ and $[BiI_6]^{3-}$ in the form $[C_6H_{14}N_2]_{10}[Bi_2I_{10}]_2[BiI_6]_4{\cdot}(H_2O)_8$ (**XIII**), and the second, $[C_6H_{14}N_2]_2[Bi_4I_{16}]{\cdot}2H_2O$ (**XIV**), contains discrete $[Bi_4I_{16}]^{4-}$ clusters. The stability and thermal decomposition routes of these phases have been determined using thermogravimetric analysis. UV-vis spectroscopy has been used to determine band gap energy estimates which are related, for a range of iodobismuthate and iodoantimonate materials, to their structural features and potential optoelectronic applications.

Received 13th November 2017,
Accepted 30th January 2018

DOI: 10.1039/c7dt04280a

rsc.li/dalton

Introduction

The research field of haloantimonate(III) and halobismuthate(III) hybrid organic–inorganic materials has developed over the past few decades to yield materials of interest for their non-linear dielectric and optical properties. The use of different organic cation templating species has been found to yield a large variety of structures with controlled structural dimensionality of the anionic-unit, *vide infra*. Acting as counter-ions to the anionic iodopnictogenide unit within the structure, the organic species can additionally yield various polymorphs, often by variation of the exact reaction conditions.[1–4]

Trivalent metal (M = Bi^{3+}, Sb^{3+}) hybrid halometallate materials, with general formula $[R_a]^{n+}[M_bX_{3b+a}]^{n-}$ are currently known to adopt approximately 30 variants of the anionic moiety. The most prevalent species found are oligomeric and extending polymeric structures of conjoined $[MX_6]$ octahedra but more rarely monomeric $[MX_6]$ units have been reported.[5] The ability to form $[MX_6]$ octahedra in metal–halide systems is a prerequisite to forming perovskites (corner-sharing), while adopting alternative non-perovskite structural units (edge-, face-sharing or in isolation) opens up a vast library of materials with a variety of anionic substructures. For example as demonstrated by iodobismuthate structures, the identity of the anionic inorganic component currently ranges from discrete 0D units (simple anions and clusters) in $[BiI_6]^{3-}$ to $[Bi_8I_{30}]^{6-}$ motifs,[6–21] through 1D chain structures,[7,22–27] most commonly in $[BiI_4]_n^{-}$ or $[BiI_5]_n^{2-}$ compositions; just one 2D extended network has been reported, $[Bi_{2/3}I_4]_n^{2-}$.[28] The identity of anionic component in these hybrid materials is dependent on many different factors including the templating species, synthesis conditions and technique as well as the molar ratios of reagents used. In a similar vein, for iodoantimonate materials the anionic component can take the form of discrete units with a range of compositions and associated charges, for example, $[Sb_3I_{11}]^{2-}$, $[Sb_2I_9]^{3-}$, $[Sb_5I_{18}]^{3-}$, $[Sb_6I_{22}]^{4-}$, $[Sb_8I_{28}]^{4-}$ [5,29,30] as well as one-

Department of Chemistry, University of Bath, BA2 7AY, UK.
E-mail: M.T.Weller@bath.ac.uk

†Electronic supplementary information (ESI) available: UV-vis spectra and thermogravimetric data. CCDC 1580940–1580953. For ESI and crystallographic data in CIF or other electronic format see DOI: 10.1039/c7dt04280a

dimensional unit configurations $[SbI_4]_n^-$,[31,32] $[SbI_5]_n^-$,[23] $[Sb_2I_7]_n^-$,[33] and $[Sb_3I_{10}]_n^-$.[34] Iodometallate materials are principally of interest in comparison with their bromo- and chlorometallate equivalents as they tend to possess smaller band gaps and lower carrier effective masses[2,35] – important properties for high performance optoelectronic materials.

Regarding the properties required of non-linear dielectrics, four anionic species have been identified in previous studies as having the potential to exhibit ferroelectric properties, $R_3M_2X_9$,[5] RMX_4,[36] RMX_5,[37] and $R_5M_2X_{11}$;[38,39] the vast majority of the compounds reported adopt the sub-lattice forms $[M_2X_9]^{3-}$ and $[M_2X_{11}]^{5-}$. It is worth noting that for $R_3M_2X_9$ four separate structural forms are known: (i) a two-dimensional layer structure, (ii) an infinite one-dimensional chain, (iii) discrete di-octahedral units, and (iv) discrete tetra-octahedral units; only the 2D layer structure form has been identified to demonstrate ferroelectric properties. Conversely, for $[M_2X_{11}]^{5-}$ the structural unit is exclusively discrete di-octahedral units with all salts exhibiting ferroelectric properties.

Also recently, and with rapidly growing traction in the last three years, hybrid organic–inorganic perovskite and perovskite-like materials have established themselves as the principal area of photovoltaic research. In particular, the leading absorber material in this field is the hybrid compound methylammonium lead iodide, MAPI, $[CH_3NH_3][PbI_3]$; with the highest solar cell efficiencies utilising derivatives of this material reaching over 22%.[40] However, a key concern of utilising this material for commercial applications is the presence of the toxic metal lead. Additional issues regarding the deployment of MAPI in solar cell devices concern its long-term stability; research aiming to combat this issue of instability when exposed to light (and/or) air is ongoing.[41,42] Concurrently, other non-toxic, post transition metal-based, hybrid materials with similar functional optoelectronic properties are being explored as alternative candidates for photovoltaic applications. Such materials can offer the prospect of improved material stability, allowing simpler device processing and manufacture, and long-term cell deployment. As a result, we have been interested in exploring the synthesis, structural characterisation and studying the electrical properties of novel compounds of this type.

The desired semiconducting properties these materials have has been highlighted to stem from the fundamental electronic structure of the post transition metals demonstrating the "inert pair effect" with filled $5s^2$ or $6s^2$ orbitals; these orbitals have been shown to produce shallow defects and a dispersed valence band. Prospective metal cation candidates of interest in forming semiconducting metal–halide hybrid structures are considered to be Sn^{2+}, Bi^{3+} and Sb^{3+}. Initial isovalent substitution studies with Sn^{2+} replacing Pb^{2+} in hybrid perovskite related materials have proved to be largely unsuccessful for applications, as Sn^{2+} compounds have been shown to undergo rapid oxidation by air and decompose readily through reaction with moisture.[43] Therefore the impetus has been to explore alternatives with potentially improved stability to degradation *via* oxidation.[44]

The stability of the Group (n-2) exhibiting the loan pair effect increases from Group 13 through Group 14 to Group 15. Thus while In^+ and Tl^+ are readily oxidised to the trivalent state and as mentioned previously Sn^{2+}, and to a lesser extent Pb^{2+}, can be easily oxidised, Sb^{3+} and, particularly, Bi^{3+} are both more difficult to oxidise to the Group oxidation state. This makes these species ideal for forming M(III) halocomplexes that are stable in air. With an increased level of electropositivity over tin and lead ion centres, Bi^{3+} and Sb^{3+} demonstrate a contraction of their ionic radii to 103 pm and 76 pm respectively in comparison to 119 pm (Pb^{2+}) and 102 pm (Sn^{2+}). Despite this smaller ionic radius these ionic radii are still relatively large and six coordination to halide ions remains the most common coordination geometry found for both Bi^{3+} and Sb^{3+}. However, in comparison with divalent metal hexahalides $[MX_6]^{4-}$, the formation of the higher charged metal in $[SbX_6]^{3-}$ and $[BiX_6]^{3-}$ units often results in the halide ion preferring to bridge between two metal centres and the formation of complex anions whose structures contain edge- and face-sharing octahedra. This preferred connectivity means that three-dimensional structural, and, therefore, optoelectronic connectivity has proved elusive for iodobismuthate and iodoantimonate materials. Understanding how choice of counter cation controls structural connectivity in these iodobismuthate and iodoantimonate materials and how two and three dimensional connectivity may be induced remains a key target for producing new hybrid semiconducting materials of the Group 15 elements.

Results described in this paper develop the area of haloantimonate(III) and halobismuthate(III) hybrid materials showing how changes in the templating species and the chalcogenide allow control of the structure and band gap. These new families of hybrid materials should also allow greater tuning of the band gap and lead to new applications. One example is in low energy X-ray detectors for medical applications where nanoparticulate Bi_2S_3 has recently been shown to have high sensitivity and rapid response to dosimetric X-rays.[45]

Synthesis

Reactants and solvents were used as received from suppliers Alfa Aesar (bismuth chloride, 1,4-dimethylpiperazine), Fluka chemicals (piperazine) and Sigma-Aldrich (antimony chloride, antimony iodide, 2-aminopyrimidine, hydriodic acid, 4-methylmorpholine, 1-methylpiperazine, 1,2-benzenediamine, DABCO) at reagent grade standard or above.

Section A

Compound I $[C_6H_9N_2O][SbI_4]$ – crystals of 1,3-dimethyl-2-oxo-2,3-dihydropyrimidinium iodoantimonate were obtained through solvothermal reaction and *in situ* methylation process from $SbCl_3$ (0.2 mmol), 2-aminopyrimidine (0.15 mmol), HI (1.0 ml, 57 wt%, no stabiliser) in methanol (6 ml). Reactants were placed in a 25 ml Teflon® vessel, sealed in a steel autoclave and heated at 140 °C for 24 h; with a controlled ramp up

rate of 1 °C min^{-1} and ramp down rate of 0.1 °C min^{-1}. A pure phase of very fine dark orange needle crystals (0.0205 g, estimated yield of 14%) was obtained after vacuum filtration and an ethanol wash.

Compound II $[C_6H_9N_2O][BiI_4]$ – the equivalent isostructural iodobismuthate hybrid compound was obtained under identical conditions except for a change of the main group metal source to bismuth trichloride (0.2 mmol). Under these conditions a pure phase of large (0.5–1 cm) red needle crystals (0.0517 g, estimated yield of 30%) was obtained following filtration and an ethanol wash.

Section B

Compound III $[C_5H_{12}NO]_4[Sb_6I_{22}]$ – under hydrothermal reaction conditions, a pure phase of bright orange crystals of structure **III**, was obtained from $SbCl_3$ (0.2 mmol), 4-methylmorpholine (0.15 mmol), HI (1.0 ml, 57 wt%, no stabiliser) in deionised water (6 ml). Reactants were placed in a 25 ml Teflon® vessel, sealed in a steel autoclave and heated at 140 °C for 24 h; with a controlled ramp up rate of 1 °C min^{-1} and ramp down rate of 0.1 °C min^{-1}. After filtration and an ethanol wash a pure phase of crystals of 4-methylmorpholinium iodoantimonate, structure **III** (0.0773 g, estimated yield of 60%), was obtained.

Compound IV $[C_5H_{12}NO]_4[Bi_4I_{16}]$ – changing the main group metal precursor compound to bismuth trichloride (0.2 mmol), and a reduction in the volume of hydriodic acid (0.75 ml) added to reaction mixture, produced a single phase of bright red block crystals of the related 4-methylmorpholium templated iodobismuthate; structure **IV** (0.0535 g, estimated yield of 30%) (Scheme 2).

Section C

Compound V $[C_4H_{12}N_2][SbI_4]_2{\cdot}4H_2O$ – crystals of 1,4-dipiperazinium iodoantimonate tetrahydrate were obtained through hydrothermal reaction of SbI_3 (0.2 mmol), piperazine (0.15 mmol), HI (1.0 ml, 57 wt%, no stabiliser) in deionised water (6 ml). Reactants were placed in a 25 ml Teflon® vessel, sealed in a steel autoclave and heated at 140 °C for 24 h., with a controlled ramp up rate of 1 °C min^{-1} and ramp down rate of 0.1 °C min^{-1}. After filtration and ethanol wash, a pure phase of prismatic orange block crystals (0.0260 g, estimated yield – 18%) was obtained. Similarly, a pure phase of structure **V** could also be synthesised under identical conditions with a cheaper, more readily available $SbCl_3$ reagent in the place of SbI_3 (Scheme 1).

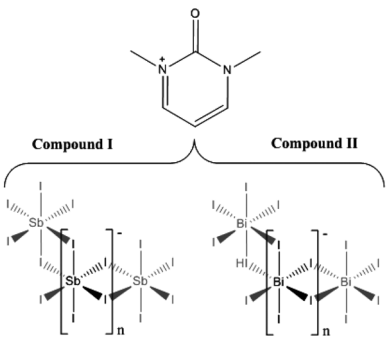

Scheme 1 Composition of compounds I and II.

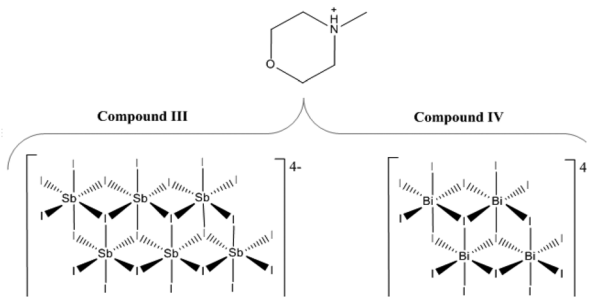

Scheme 2 Composition of compounds III and IV.

Compound VI $[C_5H_{14}N_2][SbI_4]_2{\cdot}3H_2O$ – long orange prismatic crystals of 1-methyl-1,4-dipiperazinium iodoantimonate trihydrate were synthesised in a mixed phase (with minor phase of black crystalline material). The product was obtained a hydrothermal reaction, under the same conditions as structure **V**, using the reagents SbI_3 (0.2 mmol), 1-methylpiperazine (0.15 mmol), HI (1.0 ml, 57 wt%, no stabiliser) in deionised water (6 ml). After filtration and ethanol wash, 0.0727 g of the mixed phase product (9 : 1 ratio by visual estimate, estimated yield of 50%) was collected.

Compounds VII $[C_6H_{16}N_2][SbI_4]_2{\cdot}2H_2O$, **VIII** $[C_6H_{16}N_2][SbI_4]_2{\cdot}2H_2O$ and **IX** $[C_6H_{16}N_2][Sb_4I_{16}]_{0.5}{\cdot}H_2O$ – under identical hydrothermal reaction conditions three hybrid materials, all templated by the organic di-cation 1,4-dimethyl-1,4-dipiperazinium, were synthesised in a mixed phase (10 : 2 : 1 : 6 ratio by visual estimate) product. This mixed phase product consisted of chunky dark orange crystals (**VII**), elongated dark orange crystals (**VIII**) and block yellow-orange crystals (**IX**); alongside black crystals identified to be the organic salt 1,4-dimethyl-1,4-dipiperazinium bis(tri-iodide). Reagents SbI_3 (0.2 mmol), 1,4-dimethylpiperazine (0.15 mmol), HI (1.0 ml, 57 wt%, no stabiliser) and deionised water (6 ml) were sealed in a 25 ml Teflon® vessel, sealed in a steel autoclave and heated at 140 °C for 24 h; with a controlled ramp up rate of 1 °C min^{-1} and ramp down rate of 0.1 °C min^{-1}. The mixed phase product was filtered and washed with ethanol to give a total dry weight yield of 0.112 g, estimated yields of 40% (**VII**), 10% (**VIII**) and 5% (**IX**) (Scheme 3).

Section D

Compound X $[C_{10}H_{13}N_2][SbI_4]$ – a mixed phase (1 : 9 ratio by visual estimate) of a minor impurity of semi-crystalline material alongside a major phase of transparent dark-orange elongated-plate crystals of 1-ethyl-2-methylbenzimidazolium templated structure **X** was synthesised under solvothermal conditions. The reagents $SbCl_3$ (0.2 mmol), 1,2-benzenediamine (0.15 mmol), HI (1.0 ml, 57 wt%, no stabiliser) and ethanol (6 ml) were placed in a 25 ml Teflon® vessel, sealed in

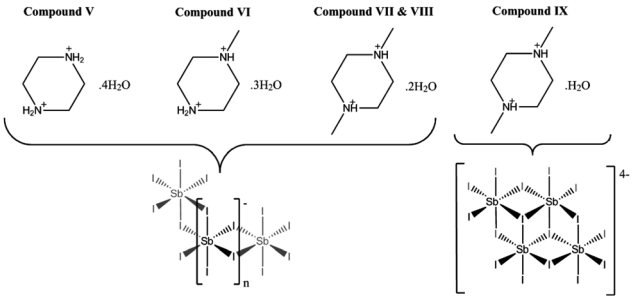

Scheme 3 Composition of compounds **V–IX**.

a steel autoclave and heated at 140 °C for 24 h; with a controlled ramp up rate of 1 °C min^{-1} and ramp down rate of 0.1 °C min^{-1}. The product was washed with ethanol and dried by vacuum filtration to give the dry weight yield of 0.0725 g (estimated yield of 40%) (Scheme 4).

Compound XI $[C_{10}H_{13}N_2][BiI_4]$ – a major phase (4 : 1 ratio by visual estimate) of dark-red, prismatic needle crystals of compound **XI** was crystallised from a solvothermal reaction alongside a minor phase of crystalline orange material. The reagents $BiCl_3$ (0.2 mmol), 1,2-benzenediamine (0.15 mmol), HI (0.5 ml, 57wt%, no stabiliser) and ethanol (6 ml) were placed in a 25 ml Teflon® vessel. The vessel was sealed within a steel autoclave and heated at 140 °C for 24 h; with a controlled, ramp up rate of 1 °C min^{-1} and ramp down rate of 0.1 °C min^{-1}. The product was washed with ethanol and a dry weight yield (0.0434 g, estimated yield of 20%) was obtained after drying by vacuum filtration.

Section E

Compound XII $[C_6H_{14}N_2]_2[Sb_4I_{16}]\cdot 2H_2O$ – a mixed phase (1 : 1 ratio by visual estimate) of orange block crystals (**XII**) and black crystalline material was obtained from a hydrothermal synthesis procedure. The reagents $SbCl_3$ (0.2 mmol), DABCO (0.15 mmol), HI (0.75 ml, 57 wt%, no stabiliser) and water (6 ml) were placed in a 25 ml Teflon® vessel. In turn, the vessel was sealed within a steel autoclave and heated at 170 °C for 24 h; with a controlled ramp up rate of 1 °C min^{-1} and ramp down rate of 0.1 °C min^{-1}. The product was washed with

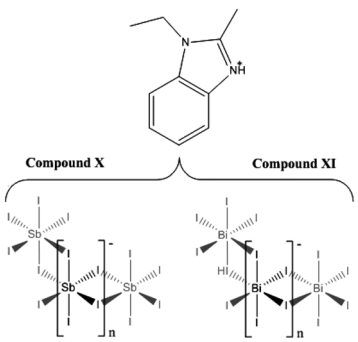

Scheme 4 Composition of compounds **X** and **XI**.

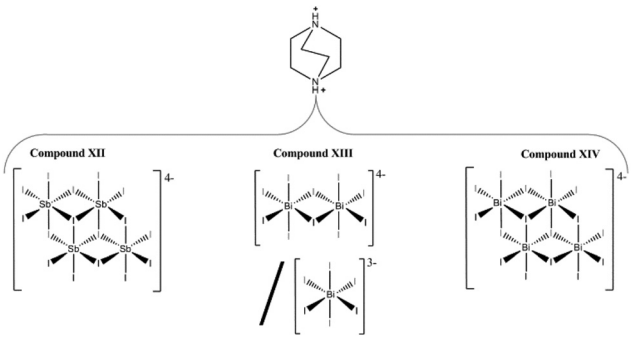

Scheme 5 Composition of compounds **XII–XIV**.

ethanol and a total dry weight yield of 0.135 g (estimated yield of 50%) was obtained after drying by vacuum filtration.

Compound XIII $[C_6H_{14}N_2]_{10}[Bi_2I_{10}]_2[BiI_6]_4\cdot(H_2O)_8$ and **XIV** $[C_6H_{14}N_2]_2[Bi_4I_{16}]\cdot 2H_2O$ – a mixed phase (3 : 2 ratio by visual estimate) of orange needle crystals (**XIII**) and red block crystals (**XIV**) was obtained from a hydrothermal synthesis procedure. Reagents $BiCl_3$ (0.2 mmol), DABCO (0.15 mmol) HI (0.75 ml, 57wt%, no stabiliser) and water (6 ml) were sealed in a 25 ml Teflon® vessel, sealed in a steel autoclave and heated at 140 °C for 24 h; with a controlled ramp up rate of 1 °C min^{-1} and ramp down rate of 0.1 °C min^{-1}. The mixed phase product was washed with ethanol and dried by vacuum filtration to give a combined total dry weight yield of 0.123 g (estimated yields of 35% (**XIII**) and 30% (**XIV**)) (Scheme 5).

Crystal structures: results and discussion

Compounds I and II

Compounds **I** and **II**, $[C_6H_9N_2O][MI_4]$, M = Sb, Bi. The isostructural 1,3-dimethyl-2-oxo-2,3-dihydropyrimidinium templated structures **I** and **II**, were solved from single crystal X-ray diffraction data; see Table 1 for crystallographic data comparison. In each synthetic procedure the simpler organic amine 2-aminopyrimidine was used as a precursor reagent; however under the high temperature and pressure conditions of the solvothermal reaction, and in the presence of strong acid HI, methyl iodide forms as a transient species before undergoing alkylation of the two pyrimidine ring nitrogen positions in turn and deprotonation of the amine to form the monocationic organic ion 2-imino-1,3-dimethyl-2,3-dihydropyrimi-

Table 1 Unit cell parameters for compounds I and II (at 150 K)

	Compound **I** (Sb)	Compound **II** (Bi)
Space group	Monoclinic $P2_1/c$	Monoclinic $P2_1/c$
a (Å)	10.5506(4)	10.6424(3)
b (Å)	7.6199(3)	7.6380(2)
c (Å)	19.9962(7)	20.0271(5)
β (°)	95.336(3)	94.986(2)
V (Å^3)	1600.63(10)	1621.78(7)

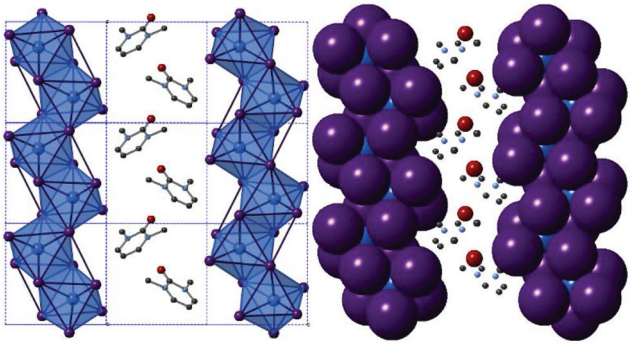

Fig. 1 A single layer view of structure **II** on the *ac* plane visualised by ball and stick modelling (left) and space-filling modelling (right). [BiI_6] octahedra are shaded blue; Bi atoms (blue), I atoms (purple), C atoms (black) and N atoms (pale blue).

dium. Under the acidic aqueous conditions a further reaction occurs *in situ* in which the imine is hydrolysed to a ketone functionality resulting in the templating cationic 1,3-dimethyl-2-oxo-2,3-dihydropyrimidinium species. The structures of both compounds **I** and **II** exhibit an anionic network of one-dimensional metal halide chains $[MX_4]_n^-$ interacting *via* weak halide–halide connections.[25,32,46] In the channels between the anionic network, the organic cations (counter-balancing the charge of the anionic chains) are positioned to fill the grooves of the chain structure along the *a*/*c* plane axis (see Fig. 1); alternating with perpendicular orientation along the *b*-axis indicative of a herring-bone structural motif (see Fig. 2 *c*-axis view).

Weak inter-chain I···I interactions extend the anionic network asymmetrically along the *a*- and *c*-axes of both structures. A terminal-terminal I···I pathway bridges the anionic chains in, approximately, the *a*-axis direction. For structures **I** and **II**, respectively, these separations are 3.85 Å and 3.79 Å, repeating every 7.62 Å and 7.64 Å along the *b*-axis. Similarly, (for structures **I** and **II** respectively) a longer edge-terminal I···I interaction of 4.42 Å and 4.32 Å, repeating more regularly every 4.03 Å and 4.12 Å, approximately along the *c*-axis direction can be observed. The average I···I interaction distance for the iodobismuthate compound is shorter at 4.06 Å, in comparison to 4.14 Å for the iodoantimonate.

The chain structure is formed by edge-sharing of metal iodide octahedral units along two of twelve vertices. The octahedra appear to distort away from 'perfect' regular octahedra in accordance with the known *trans* effect in halometallate structures wherein the M–X bonds across from bridging bonds are shorter (and also exhibit a higher vibrational frequency).[47,48] However, an additional degree of distortion may be attributed to the way in which the cations are interleaved within the grooves of the chain structure (highlighted in Fig. 1). Deviation of the I–M–I bond angle away from an ideal 180 degrees within the octahedra ranges from 4.9–10.9° in structure **I** to 5.9–11.6° in structure **II**. Average bond angle deviations show distortions of 7.3° and 7.8°, respectively, away from a regular octahedron in each of the structures.

In addition to this, considering the M–I–M bond angles within the chain structures shows an average bond angle deviation from 90° of 3.9° for the $[SbI_4]_n^-$ chains in compound **I** compared to 3.5° for the $[BiI_4]_n^-$ chains in compound **II**. M–I bond distances vary by 2.83–3.27 Å (Δ = 0.44 Å) 2.92–3.29 Å (Δ = 0.37 Å) for structures **I** and **II** respectively.

Compounds III and IV

From single crystal X-ray diffraction data, the structures of two 4-methylmorpholinium templated hybrid structures have been derived. Compound **III**, $[C_5H_{12}NO]_4[Sb_6I_{22}]$, contains clusters of four monovalent charged 4-methylmorpholinium cations charge counter-balancing discrete $[Sb_6I_{22}]^{4-}$ anions.[3] Each cation is orientated with the ring-based oxygen atom directed towards the core of the cation cluster and, thus, the positively charged protonated nitrogen atom (and attached methyl group) directed outwards from the cluster and in closer proximity to the anionic units. Each group of four cations is "encased" within an anionic sublattice formed by six $[Sb_6I_{22}]^{4-}$ units linked through weak I···I interactions. Consideration of the orientations of the four 4-methylmorpholinium cations

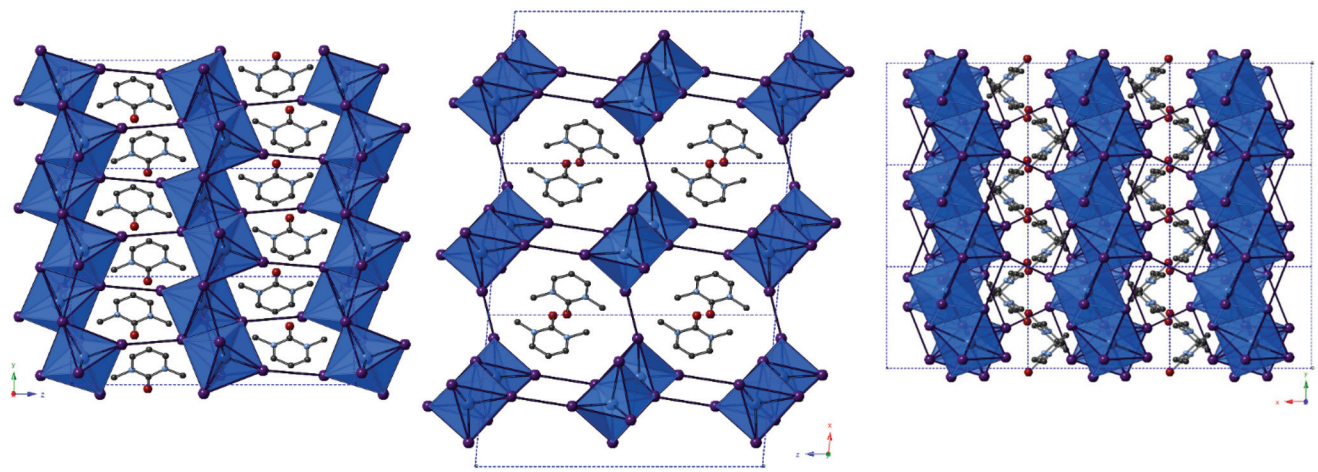

Fig. 2 Visualisation of structure **II** (iso-structural with structure **I**) along *a*-axis (left), *b*-axis (centre) and *c*-axis (right); key as in Fig. 1.

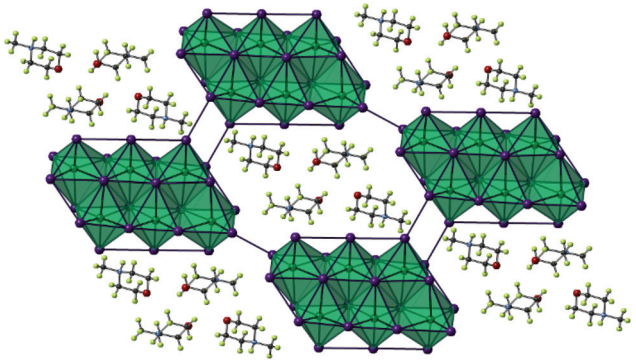

Fig. 3 A single layer component of structure **III** viewed on the *ab* plane. Key as in Fig. 1 aside from [SbI_6] octahedra shaded teal; Sb atoms (teal), H atoms (pale green).

within each cluster indicates that there are no, or extremely weak, hydrogen bonding interactions between protonated amine template cation and $[Sb_6I_{22}]^{4-}$ anions (Fig. 3).

Further analysis of this structure shows that viewed down the *c*-axis the discrete iodoantimonate units are interconnected by weak I···I interactions of 4.64 Å between the outer Sb(1) octahedra and two I···I interactions of 4.21 Å per Sb(3) octahedra. Further weak I···I interactions interconnect each $[Sb_6I_{22}]^{4-}$ unit with a total of 38 interactions (12 repeating unique I···I distances) per unit to 12 distinct zero-dimensional $[Sb_6I_{22}]^{4-}$ units to build the anionic "network". Overall these inter-unit interactions range from 3.80–4.73 Å; with an average I···I interaction distance of 4.14 Å.

The outermost octahedra in each $[Sb_6I_{22}]^{4-}$ unit, centred by position Sb(1) with just two from twelve possible edge connections, is the most perceptibly distorted and this can be shown by considering the average deviations from 180° for the I–Sb–I angles in each [SbI_6] octahedra. For the Sb(1) centred octahedra the angle was found to distort by 10.3° from 180° on average. For the Sb(3) centred octahedra, with 3/12 edge connections along its vertices, the average angle deviation from 180° for I–Sb–I is reduced to 6.7°. Lastly, with 4/12 edge connections to adjacent octahedra, the Sb(2) centred octahedra making up the core of the $[Sb_6I_{22}]^{4-}$ unit exhibits least distortion from a regular octahedron with an average deviation away from 180° of just 2.9°. Bonded Sb–I distances within each octahedra vary by 2.76–3.47 Å (Δ = 0.71 Å), 2.79–3.36 Å (Δ = 0.57 Å) and 2.79–3.35 Å (Δ = 0.56 Å) for Sb(1)–(3) respectively (Fig. 4).

Iodobismuthate hybrid material (structure **IV**) $[C_5H_{12}NO]_4[Bi_4I_{16}]$, again templated by 4-methylmorpholinium cations, was modelled from the single crystal X-ray diffraction data. In a similar way to its iodoantimonate counterpart, discussed previously, groups of four monovalent 4-methylmorpholinium cations are found to cluster together; again encapsulated by the anionic sublattice structure. However, here the counter-balancing tetravalent discrete anionic units take the form of $[Bi_4I_{16}]^{4-}$.[7] A total of 28 (7 repeating unique I···I distances) inter-unit I···I interactions connect each discrete bismuth iodide unit to twelve different $[Bi_4I_{16}]^{4-}$ units.

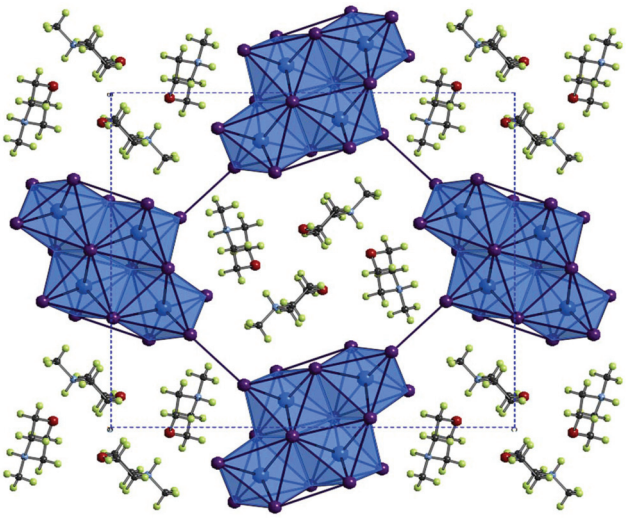

Fig. 4 A cross-section of the *bc* plane of structure **IV** viewed down the *a*-axis; colour key as in Fig. 1 with addition of O atoms (red) and H atoms (pale green).

Inter-unit I···I interaction distances range from 3.97–4.56 Å; with an average distance of 4.27 Å. Orientation of the 4-methylmorpholinium suggests weak hydrogen bonding interaction between cations (N^+–H···O) may be present within the structure D–H···O (hydrogen bond distance 1.95 Å with a ∠D–H···A angle of 157.6° (22.4° deviation from direct interaction)) from position N(2)–H to O(1). The N(1)–H and O(2) positions are not involved in hydrogen bonding (Table 2).

The outer Bi(1) centred octahedra are visibly more distorted than the central Bi(2) octahedra within each $[Bi_4I_{16}]^{4-}$ unit. Averaging the angular deviation away from 180° across all *trans* I–Bi–I motifs in the octahedra reveals a distortion of 9.8° for the Bi(1) centred outer octahedra compared to 5.4° for the core Bi(2) centred octahedra. However, the influence of the *trans* effect, wherein the M–X bonds across from bridging bonds are shorter, is similar in each octahedra with Bi–I distances varying by 2.89–3.42 Å (Δ = 0.53 Å) and 2.88–3.40 Å (Δ = 0.52 Å) for Bi(1) and Bi(2) respectively.

Compounds V–IX

The structures of Compounds **V–IX** were solved from single crystal X-ray diffraction. Structures **V**, **VI**, **VII** and **VIII** $[NH_2(CH_2)_4NH_2][SbI_4]_2{\cdot}4H_2O$, $[CH_3NH(CH_2)_4NH_2][SbI_4]_2{\cdot}3H_2O$,

Table 2 Unit cell parameters for compounds III and IV (at 150 K)

	Compound **III** (Sb)	Compound **IV** (Bi)
Space group	Triclinic *P*-1	Orthorhombic *Pbca*
a (Å)	11.3253(7)	12.7627(3)
b (Å)	13.0042(7)	20.7207(6)
c (Å)	15.2847(7)	22.7427(6)
α (°)	69.645(4)	90.000
β (°)	69.877(5)	90.000
γ (°)	64.496(6)	90.000
V (Å^3)	1853.97(17)	6014.35(3)

and $[CH_3NH(CH_2)_4NHCH_3][SbI_4]_2{\cdot}2H_2O$ (two polymorphs) were templated by 1,4-dipiperazinium, 1-methyl-1,4-dipiperazinium and 1,4-dimethyl-1,4-dipiperazinium cations respectively. The materials are iso-structural and consist of infinite one-dimensional antimony iodide $[SbI_4]_n^-$ chains with fairly short inter-chain I···I contacts.[32] Divalent charge-balancing cations are located within channels extending along the *a*-axis direction parallel with the sub-lattice of 1D $[SbI_4]_n^-$ chains. Associated with the changes in the degree of methylation of the nitrogen positions on the piperazine ring system is a variation in the level of water incorporated into the material – which reduces as the methyl groups protrude into the space occupied by the water molecules. There is a related subtle alteration to the $[SbI_4]_n^-$ chain positions relative to each other and thus their degree of interaction *via* interlinking I···I connections (Table 3).

Similar to the equivalent iodobismuthate material described in a previous publication,[49] structure **VI** has the 1-methyl-1,4-dipiperazinium cation disordered between two orientations within the channel. An effect of this is that two of the water molecule positions within the structure become partially occupied depending on the orientation of the cation and thus the directionality and steric hindrance by the methyl (CH_3) group on these hydrated sites. Consequently, two previously fully occupied water molecule positions in structure **V** become half-filled, reducing the overall degree of hydration from a tetrahydrate (in the composition of structure **V**) to an averaged trihydrate (in the composition of structure **VI**). Continuing the trend, in the isomeric structures **VII** and **VIII**, 1,4-dimethyl-1,4-dipiperazinium ions within the channel impede occupancy of two of the would-be hydrated sites within the structure; having the effect of reducing the overall level of hydration within the material to a dihydrate composition; $[CH_3NH(CH_2)_4NHCH_3][SbI_4]{\cdot}2H_2O$.

The iodometallate $[MI_4]_n^-$ chains in structures **V**, **VI**, **VII** and **VIII** consist of edge sharing $[MX_6]$ octahedra; with four bridging iodine atoms along two vertices and two *cis*-related terminal iodine positions. The antimony atom position is offset from a central position within the octahedra with the shortest two Sb–I distances observed for the two *cis* terminal iodine sites. These observations are in agreement with those made for previously studied materials possessing a similar $[MX_4]_n^-$ structural motif for haloantimonates and halobismuthates exhibiting the *trans* effect; *vide supra*. Similarly, the spread of Sb–I bond lengths within the octahedra, that interlink to form the chains, decreases from compound **V** to compound **VII** suggesting an increased overall regularity of the octahedra.

Much like their counterpart iodobismuthate hybrid structures, inter-chain I···I interactions in Compounds **V–VIII** extend the anionic network along *b*- and *c*-axes of each material. It can be considered that the pathways across this interface produces a level of pseudo-dimensionality within the anionic sublattice framework of the materials; introducing the potential electronic pathways across $[SbI_4^-]_n$ chains in addition to movement along the chain. Two edge-terminal I···I and a terminal-terminal I···I interaction repeat regularly (7.34 Å, 7.53 Å and 7.72 Å respectively) along the chain *a*-axis; with all iodide positions within the network in close enough proximity to engaged in at least one inter-chain interaction. Lengths of these interactions range from 3.80–4.46 Å in the structures and the average distance of the inter-chain interactions decreases 4.19 Å → 4.13 Å → 4.01 Å through compounds **V–VII** respectively. However, the shortest I···I interaction is shown to undergo negligible change through the structures; 3.80 Å → 3.81 Å → 3.80 Å. In response inter-chain Sb–Sb distances are observed to increase marginally by 0.05 Å and 0.08 Å in the structural pairs **V** → **VI** and **VI** → **VII** respectively. Variation in the Sb–I–Sb bond angles within the chains also sees an increase away from regular octahedral angle to 90.7° → 92.1° → 93.6° for structures **V–VII** respectively.

In summary as the piperazinium ring of the organic cation becomes increasingly methylated there are observable changes the anionic sub-lattice of each structure. The regular distance between repeat interactions along the chain structure in the *a*-axis direction increases (*i.e.* an increasingly less compressed framework along the *a*-axis) the average I···I inter-chain interaction distance decreases (4.19 Å → 4.13 Å → 4.01 Å) and the overall regularity of the octahedra, defined by decreasing Sb–I bond length variation, increases (0.49 Å → 0.45 Å → 0.40 Å). Overall, structures **V–VII** follow similar structural trends to their iodobismuthate equivalent materials previously reported.[49]

In addition to these findings on antimony iodide 1,4-dipiperazinium complexes a new polymorph of compound **VII** crystallised in the same reaction mixture, together with a third phase, *vide infra*. This first minor phase of elongated dark orange needles, identified as compound **VIII**, occurred together with the major phase of blocky, dark orange crystals of structure **VII**. The structure of compound **VIII** consists of an identical motif of interconnected $[SbI_4]_n^-$ chains as seen in structure **VII**, however, the interrelationship between the chains for **VIII** shows an offset of approximately 19° in com-

Table 3 Unit cell parameters for compounds **V–IX** (at 150 K)

	Compound **V**	Compound **VI**	Compound **VII**	Compound **VIII**	Compound **IX**
Space group	Monoclinic $P2_1/c$	Monoclinic $P2_1/c$	Monoclinic $P2_1/c$	Monoclinic $P2_1/c$	Monoclinic $P2_1/n$
a (Å)	7.3391(2)	7.5306(2)	7.7213(2)	7.5751(2)	11.5391(3)
b (Å)	13.0022(5)	12.9539(4)	12.8027(3)	12.1020(3)	11.8717(4)
c (Å)	13.8121(4)	13.6147(4)	13.4527(3)	14.5071(4)	19.1648(5)
β (°)	94.550(3)	96.086(3)	97.377(2)	92.630(3)	93.705(3)
V (Å^3)	1313.86(7)	1320.64(7)	1318.84(5)	1328.52(6)	2619.87(13)

parison with respect to adjacent units in the sublattice network. As a result, as seen in the *a*-axis view of structure **VIII** (see Fig. 5), the chains become aligned in parallel. Furthermore, comparing structures **VII** and **VIII** it can be seen that the three repeating interchain I···I interactions along the chain axis are retained, however, although the regularity of recurrence of these interactions along the *a*-axis is decreased (7.72 Å → 7.58 Å) the average interaction distance sees a slight increase (4.01 Å → 4.07 Å). In addition to this, the regularity of the octahedra decreases (*Δ* 0.40 Å → *Δ* 0.48 Å) and the Sb–I–Sb angle within the chain decreases by 1.1° (93.6° → 92.5°). Furthermore, it can be observed that, in structure **VIII**, the dication positioning within the *a*-axis channel shows increased tilt with the methyl groups pointed along the propagating *a*-axis more than in the polymorph (**VII**); in which the directionality of the methyl groups is focussed more towards the interstitial interchain space.

Finally, a third 1,4-dimethyl-1,4-dipiperazinium cation templated structure $[CH_3NH(CH_2)_4NHCH_3][Sb_4I_{16}]_{0.5}{\cdot}H_2O$ (compound **IX**), determined from single crystal X-ray diffraction data, was found to crystallise in the form of yellow-orange block-shaped crystals. Comparatively to the counterpart structures (**VII** and **VIII**) it crystallised alongside, the material contains a lower dimensional Sb–I anionic sub-structure of $[Sb_4I_{16}]^{4-}$ units.[50] In each unit cell, two divalent 1,4-dimethyl-1,4-dipiperazinium cations counterbalance the anionic network of zero-dimensional $[Sb_4I_{16}]^{4-}$ units. Each anionic unit interacts with a total of 14 different adjacent units to build the substructure *via* 36 (10 repeating unique I···I distances) inter-linking weak I···I interactions. Distances range from 4.09–4.64 Å; with an average distance of 4.25 Å. The level of solvation within the structure is reduced with respect to structures **VII** and **VIII** from a dihydrate (1 : 2 dication to water molecule ratio) to a monohydrate hybrid material (1 : 1 ratio).

The outer Sb(2) centred octahedra of the $[Sb_4I_{16}]^{4-}$ cluster show distortion from regularity with an average angle deviation (away from 180° across I–Sb–I) in octahedra of 10.5°; compared to 4.4° for the central Sb(1) centred positions in the cluster. In accord with this observation is a larger variation in the Sb–I bonding distances within the outer octahedra compared to the inner; showing a variation covering the distance range 2.82–3.27 Å (*Δ* = 0.45 Å) for the Sb(1)-centred octahedron and 2.78–3.47 Å (*Δ* = 0.69 Å) for Sb(2) (Fig. 6).

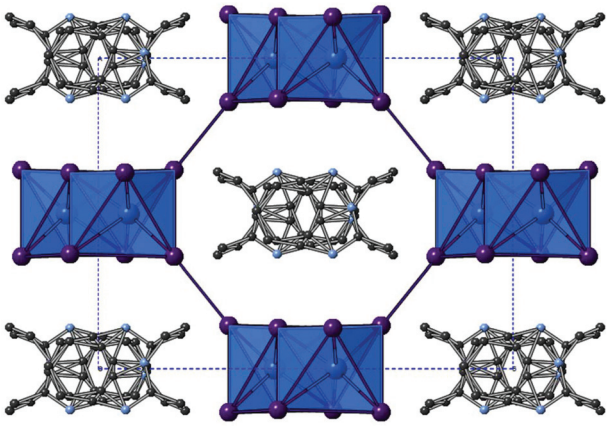

Fig. 6 Structure **XI** $[C_{10}H_{13}N_2][BiI_4]$ viewed down the *c*-axis (hydrogen atoms are not shown); colour key as in Fig. 1.

Compounds X and XI

Structures **X**, $[C_{10}H_{13}N_2][SbI_4]$, and **XI**, $[C_{10}H_{13}N_2][BiI_4]$, were solved from single crystal X-ray diffraction data. The hybrid materials are isostructural and consist of inter-linked (through weak I···I interactions) metal iodide one-dimensional chains forming irregular sided octagonal channels in which the charge balancing organic cations are positioned. The templating cation for both isomorphs is the monovalent cation 1-ethyl-2-methylbenzimidazolium; formed *in situ* by twofold alkylation of the precursor reagent 1,2-benzenediamine *via* a ring-closing mechanism by reaction with ethyl iodide (formed in the reaction mixture from the solvent ethanol and HI). The materials both adopt a monoclinic crystal system, however, they crystallise in different space groups; see Table 4. This difference is related positional changes and disorder of the organic benzimidazolium cation within the channel. Propagating along the *a*-axis, for structure **X**, and *c*-axis, for structure **XI**, the cations stack with alternating orientations (180° rotation) with a separation of approximately 3.7 Å and an offset from the associated perpendicular structural axis of 17° and a shift of 1.6 Å. It should be noted that in the structure solution of compound **X** the organic component was modelled with PARTS instruction in order to split the ion into 55/45 occupancy over two related positions; the direction of the

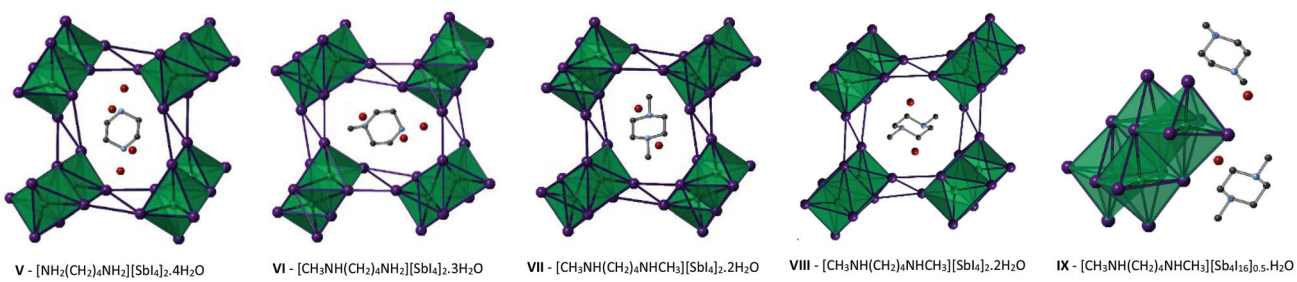

Fig. 5 Left to right: Structures **V–VIII** viewed along the *a*-axis and the asymmetric unit cell of structure **IX**; colour key as in Fig. 1 aside from Sb atoms (teal) and O atoms (red).

Table 4 Unit cell parameters for compounds X and XI (at 150 K)

	Compound **X** (Sb)	Compound **XI** (Bi)
Space group	Monoclinic $P2_1/n$	Monoclinic $C2/c$
a (Å)	7.5877(3)	13.3133(4)
b (Å)	17.7055(8)	17.7312(4)
c (Å)	13.2578(6)	7.6344(2)
β (°)	94.309(4)	93.450(2)
V (Å^3)	1776.07(13)	1798.92(8)

benzimidazolium ion alternates between these two positions, with the relationship between the two positions determined as an approximate 25° rotation in-plane of the ring system followed by a 180° 2-fold rotation through the central in-plane axis of the ion. Compound **XI**, however, was modelled in the higher symmetry monoclinic space group $C2/c$. Here, the 1-ethyl-2-methylbenzimidazolium cation lies on a glide plane running along the channel length.

As previously mentioned, in both structures **X** and **XI** the anionic framework is made up of one-dimensional anionic chains with the compositions $[SbI_4]_n^-$ and $[BiI_4]_n^-$ respectively.[25] In each structure the chains are aligned in parallel and consist of linked $[MI_6]$ octahedra; each octahedron has two *cis*-related terminal iodine positions with the other four iodine positions along shared edges of the octahedron. Within each octahedron the metal atom position is displaced from a central 'regular' octahedra position in the direction of the two terminal iodine positions with the two M–I(terminal) bond lengths approximately 0.5 Å shorter than to the other iodine positions. This is structural feature common to many iodobismuthate and iodoantimonate one-dimensional chain $[MI_4]_n^-$ hybrid structures. Comparing the antimonate (**X**) to the bismuthate (**XI**) structure it can be seen that the overall metal–iodide bond length range is slightly reduced (by 0.05 Å), producing more regular octahedra, and there is the expected shift to a higher average bond length (+0.05 Å) with the larger Bi. Similarly from **X**(Sb) to **XI**(Bi), the M–I–M bond angle average within the chain unit decreases from 93.5° to 93.0°. In both structures a single weak inter-chain I···I interaction is seen to repeat along the chain axis direction; with a distance of 4.06 Å (Sb) and 3.94 Å (Bi) with a repeat distance of 7.59 Å(Sb) and 7.63 Å(Bi).

Also of note, is that the one-dimensional $[MX_4]_n^-$ chain structural motif observed in these materials is reminiscent of structure **VIII**. However, due to the increased size and reduced charge density of the monovalent 1-ethyl-2-methylbenzimidazolium cations compared to the 1,4-dimethyl-1,4-dipiperazinium divalent cations the void size accommodating the organic cations is larger; approximately 11.2 × 9.8 Å for **X** and **XI** *versus* 7.9 × 8.2 Å for structure **VIII** (Fig. 7).

Compounds XII, XIII and XIV

The iodoantimonate hybrid structure $[C_6H_{14}N_2]_2[Sb_4I_{16}]\cdot 2H_2O$ (compound **XII**) was determined from single-crystal X-ray diffraction analysis. The material contains zero-dimensional tetra-octahedral $[Sb_4I_{16}]^{4-}$ anionic units which are counter-balanced

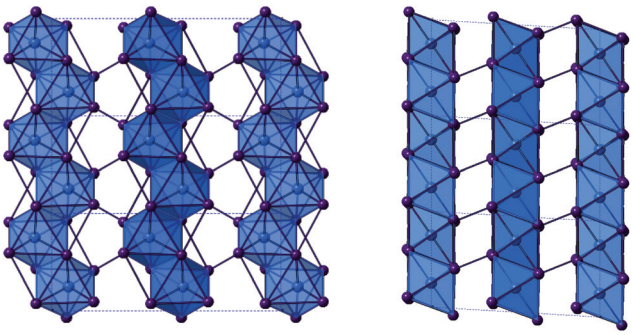

Fig. 7 The $[BiI_4]_n^-$ chain units of structure **XI** viewed down the a-axis (left) and b-axis (right). Colour key as in Fig. 1.

by two di-protonated 1,4-diazabicyclo[2.2.2]octan-diium ($DABCOH_2$) cations (see Fig. 8) alongside two sites occupied by water molecules. Within the structure each anionic $[Sb_4I_{16}]^{4-}$ structural unit interacts through weak I···I interactions, 38 (11 unique I···I bonding modes) interlinking pathways exist to a total of 12 nearby equivalent units to build the anionic "sublattice". I···I interaction distances range from 4.01–4.59 Å; with an average distance of 4.34 Å.

The structure is reminiscent of structures **IV** and **IX**, each containing the 0D $[M_4I_{16}]^{4-}$ structural motif, each tetra-octahedral unit contains two equivalent central octahedra (with three shared edges) and antimony–iodide bond lengths ranging from 2.85–3.24 Å (Δ = 0.39 Å). The more distorted outer octahedra (which have two edges shared with other octahedra) show an increased metal–iodide bond length range of 2.79–3.39 Å (Δ = 0.60 Å). This variation in octahedron irregularity is also reflected in the average angle deviation from 180° of the *trans* I–Sb–I angles within the MX_6 octahedra. I–Sb–I angles have an average deviation of 5.8° from 180° for the inner octahedron centred on Sb(1), whereas the outer octahedron, centred on Sb(2), exhibits a much greater deviation of 12.3°.

In further reactions, using 1,4-diazabicyclo[2.2.2]octan-diium ($DABCOH_2$) di-cations as templating agents, a mixed phase of two new iodobismuthate hybrid material structures were obtained. Compound **XIII**, formulated as $[C_6H_{14}N_2]_{10}[Bi_2I_{10}]_2[BiI_6]_4\cdot(H_2O)_8$ contains a unique and previously unreported com-

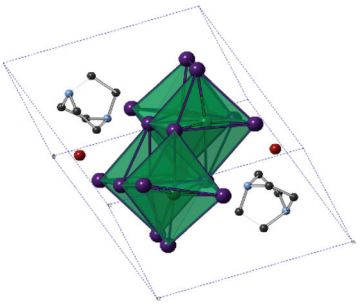

Fig. 8 Symmetric unit cell of structure **XII** (hydrogen atoms excluded); colour key as in Fig. 5.

bination of structural motifs, with both $[Bi_2I_{10}]^{4-}$ and $[BiI_6]^{3-}$ anionic components.[10,51]

In each unit cell there are two di-octahedral $[Bi_2I_{10}]^{4-}$ units and four discrete $[BiI_6]^{3-}$ units generating a total anionic composition of $[Bi_8I_{44}]^{20-}$. Eight di-protonated $(DABCOH_2)^{2+}$ form the main charge-balancing organic component of the structure with positions identified within the structural model. This balancing leads to a charge deficit of 4+ per asymmetric unit cell and so to achieve an overall compositional charge neutrality to the material it is proposed that two unrefined $(DABCOH_2)^{2+}$ dications reside within structural pores; as seen in Fig. 10. This is in agreement with the results of the solvent masking algorithm utilised, detailed within the crystallographic data, suggesting that electron density within the structural pores is consistent with the presence of two additional disordered dications (Fig. 9).

To elaborate, along the *a*-axis of compound **XIII** (see Fig. 10) a large slightly irregular octahedral channel, approximately 9.0 × 8.5 Å in dimensions, propagates through the structure. In conjunction, a minor channel, approximately 4.7 × 4.2 Å in size, extends along the *c*-axis and intercepts the major channel running along *a*. Provided the weak I···I interactions are sufficiently robust this hybrid structure may have the potential for ion exchange and porosity. In addition to this eight water molecule positions have been identified within the structural model. Due to the heavy atom sites present accurately determining the orientation of bonded hydrogen atoms at each solvated sites using X-ray diffraction data is problematic (Table 5).

Bi–I bond lengths within the $[BiI_6]$ units ranges from 3.00–3.18 Å (Δ = 0.18 Å) and demonstrate only a minor deviation, of 3.1°, (*trans* I–Bi–I angles) from 180°. In comparison, within each $[Bi_2I_{10}]^{4-}$ unit the metal–iodide bond lengths ranges from 2.96–3.24 Å (Δ = 0.28 Å); the longest M–I bonds are to the edge-shared iodide positions linking the octahedra. The position of the central bismuth ion within the individual octahedra of the $[Bi_2I_{10}]^{4-}$ unit is shifted slightly towards the terminal iodide positions. Regularity of the octahedra within the di-octahedral unit is still high; with only a minor average deviation (from *trans* angles of 180°) of 4.3° observed.

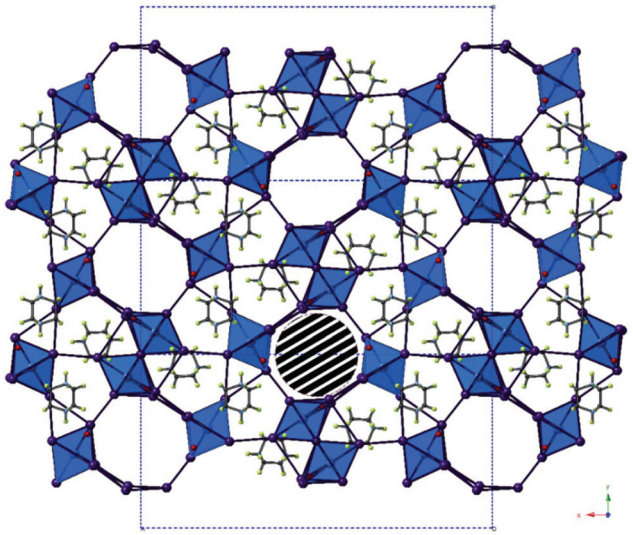

Fig. 10 The structure of compound **XIII** viewed down the *a*-axis. The striped area marks one pore containing disordered DABCO di-cations; colour key as in Fig. 1 with O atom sites (red) and H atoms (green).

Table 5 Unit cell parameters for compounds **XII**–**XIV** (at 150 K)

	Compound **XII** (Sb)	Compound **XIII** (Bi)	Compound **XIV** (Bi)
Space group	Triclinic $P\bar{1}$	Orthorhombic *Pbam*	Monoclinic $P2_1/c$
a (Å)	10.8634(3)	31.9562(6)	11.0086(3)
b (Å)	10.8965(3)	15.8622(4)	15.4751(3)
c (Å)	11.2911(3)	8.6164(2)	15.3455(4)
α (°)	91.999(2)	90.000	90.000
β (°)	109.691(2)	90.000	103.001(2)
γ (°)	95.086(2)	90.000	90.000
V (Å^3)	1250.46(6)	4367.62(17)	2547.23(11)

As previously mentioned, a secondary phase was found to have crystallised in association with compound **XIII**. The structural analysis of this phase (compound **XIV**) showed that it was also a di-protonated DABCO templated hybrid iodobismuthate

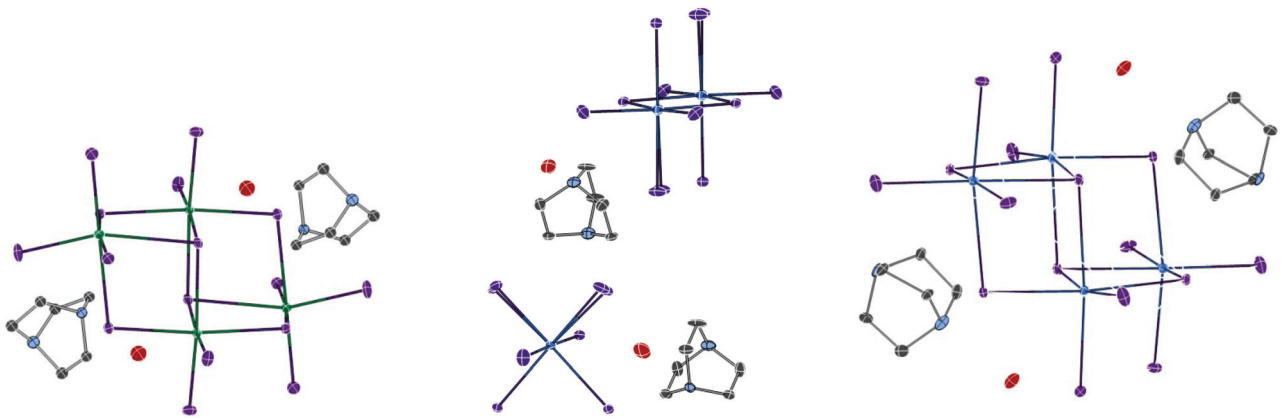

Fig. 9 Thermal ellipsoid plots (probability set at 50%) for structure **XII** (below), structure **XIII** (centre) and structure **XIV** (right).

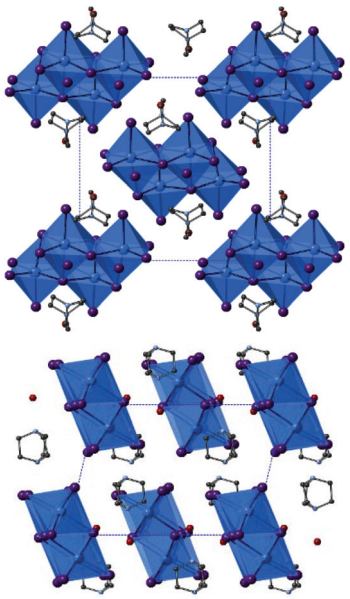

Fig. 11 Structure **XIV** viewed down the *a*-axis (top) and down the *b*-axis (bottom); colour key as in Fig. 10.

but with a differing structural composition; determined as $[C_6H_{14}N_2]_2[Bi_4I_{16}]\cdot 2H_2O$ (Fig. 11).

The structure of **XIV** contains discrete tetra-octahedral $[Bi_4I_{16}]^{4-}$ unit which interact along weak I···I connections to ten adjacent $[Bi_4I_{16}]^{4-}$ units; there are a total of 34 such interactions (9 unique bonding modes). Interaction lengths range from 4.06–4.52 Å (Δ = 0.46 Å) with an average distance of 4.31 Å. As seen in compounds (**IV**, **IX**, **XII**) the tetra-octahedral units contain two distinct Bi sites. In compound **XIV** the Bi(1) outer octahedral positions, bound to adjacent octahedra by 2 from 12 possible edge connection sites, exhibit M–I bond lengths in the range of 2.91–3.34 Å (Δ = 0.43 Å); very similar distances are seen for the Bi(2) inner octahedral positions (3/12 edge connections) with a range of 2.90–3.29 Å (Δ = 0.39 Å).

Deviation of the *trans* I–M–I angles within the octahedra from 180° shows an average of 9.5° for the outer Bi(1) site and 9.1° for Bi(2) inner site. The relatively small distortion of the outermost two octahedra within the tetra-octahedral unit may be compared to that seen previously in materials with the same anionic motif. The increased regularity found in compound **XIV** may be due to the lessened strain from reduced number of interunit I···I interactions to just ten nearby equivalent units. This compares to twelve such links seen for structures **IV** and **XII** and fourteen for structure **IX**, which saw the greatest M–I bond length range with Δ = 0.69 Å (Table 6).

Structure stability and dehydration

From thermogravimetric analysis studies (ESI – Fig. S1†) compound **I**, $[C_6H_9N_2O][SbI_4]$, shows a stable mass with negligible change on heating to approximately 210 °C, followed by a major degradation step (Δm% = −86%) between 210 and 320 °C. This is likely to be associated with complete decomposition of the amine and loss of iodine from the material; the fastest mass loss occurs from 280–300 °C. A further steady low rate of mass loss occurred on heating to the maximum furnace temperature of 400 °C; leaving residual mass (~1.2 mg) of antimony metal.

Table 6 Structural formula of compounds **I**–**XIV**

Compound	Structural formula
I	$[C_6H_9N_2O][SbI_4]$
II	$[C_6H_9N_2O][BiI_4]$
III	$[C_5H_{12}NO]_4[Sb_6I_{22}]$
IV	$[C_5H_{12}NO]_4[Bi_4I_{16}]$
V	$[C_4H_{12}N_2][SbI_4]_2\cdot 4H_2O$
VI	$[C_5H_{14}N_2][SbI_4]_2\cdot 3H_2O$
VII	$[C_6H_{16}N_2][SbI_4]_2\cdot 2H_2O$
VIII	$[C_6H_{16}N_2][SbI_4]_2\cdot 2H_2O$
IX	$[C_6H_{16}N_2][Sb_4I_{16}]_{0.5}\cdot H_2O$
X	$[C_{10}H_{13}N_2][SbI_4]$
XI	$[C_{10}H_{13}N_2][BiI_4]$
XII	$[C_6H_{14}N_2]_2[Sb_4I_{16}]\cdot 2H_2O$
XIII	$[C_6H_{14}N_2]_{10}[Bi_2I_{10}]_2[BiI_6]_4\cdot(H_2O)_8$
XIV	$[C_6H_{14}N_2]_2[Bi_4I_{16}]\cdot 2H_2O$

For compound **II**, $[C_6H_9N_2O][BiI_4]$, a stable thermal profile is observed up to 150 °C before a series of sharp, small, weight losses, equating to total loss (Δm%) of 10%, occurs between 150 and 210 °C. These weight losses can be attributed rapid, possibly locally explosive decomposition of the amine. The remaining bulk mass is stable to 250 °C before undergoing a continuous large mass loss step (Δm% = 70%) on heating to 400 °C, with the fastest mass loss occurring between 330 and 355 °C. A still reducing mass of ~2.5 mg of bismuth is present at T_{max}. This weight loss corresponds to further degradation of any residual amine and its decomposition products and the loss of HI/I_2 leaving the residue of bismuth metal.

TGA studies on 4-methylmorpholium templated compounds **III** and **IV** (ESI – Fig. S2†) showed that each exhibits a one-step thermal degradation process. For structure **III**, a stable plateau is observed in the thermal profile up to 180 °C, from which point, in the temperature range of 180–320 °C, major degradation of the compound occurs with a total mass loss Δm% = 92%. The fastest rate of mass loss occurred from 260–300 °C, with decomposition of the amine and loss of HI/I_2, and a stable residual (~1 mg) mass of antimony metal is retained up to the highest temperature reached of 400 °C. In comparison, the bismuth-containing structure (**IV**), with a different anionic sublattice, showed an increased stability of +60 °C over its counterpart, with a prolonged degradation of the hybrid material occurring only from 240–400 °C (Δm% = 90%); the residual mass, of approximately 2 mg, was bismuth metal.

Thermal analysis the piperazinium-based hybrid materials was carried out and the resultant traces are shown in ESI – Fig. S3.† Data for tetrahydrate compound **V** showed an initial expected dehydration step between 80 and 110 °C (Δm% = 5%) before a stable mass is retained up to 180 °C. From 180–260 °C (Δm% = 36%) is the first of two major degradation steps of the remaining hybrid material; followed immediately by the second step in the temperature range of 260–340 °C

($\Delta m\%$ = 54%). Similarly, for isolated crystals of trihydrate compound **VI**, a dehydration step 95–125 °C with a proportionately lower relative mass loss ($\Delta m\%$ = 3.4%) was observed. After a stable plateau, until 175 °C, further degradation between 175 and 305 °C was observed; with temperature range 290–305 °C showing the highest rate of degradation. A further slow loss of weight, likely to be due to evolution of iodine, occurred between 305 and 345 °C, at which temperature a stable residue was formed. Lastly, a mixed phase sample of structures **VII–IX** was analysed thermogravimetrically. A minor weight loss associated with dehydration of all three phases was observed in the temperature range 90–120 °C; (structures **VII** and **VIII** were determined to be dihydrates and structure **IX** a monohydrate). Following this the compounds remained stable to 175 °C until major degradation from 175–355 °C ($\Delta m\%$ = 96%). All three piperazinium-based templated materials were determined to remain stable to approximately the same temperature; around 175–180 °C, before major degradation. Following this simultaneous decomposition of all three phases a residue of antimony metal (~0.7 mg) was obtained with no notable mass change between 350 and 400 °C.

The nature of main degradation process of all the compounds (following loss of any water from the structure) is decomposition of the amine, and this may be associated with simultaneous loss of HI/I_2. The decomposition transitions from a clear two-step process for compound **V** to a continuous one-step process for structures **VII–IX**, presumably due to the differing stabilities of the templating cations. As the piperazinium-ring based di-cation in each structure becomes increasing methylated its effect on slowing the degradation process becomes reduced; as observed in the shift in remaining mass of each compound in temperature range 290–320 °C. This is reflected in the temperature at which maximum mass change occurs in each profile; with structure **V** indicating a maximum mass loss rate of −1.90 mg min^{-1} at 325 °C, −2.0 mg min^{-1} at 310 °C for structure **VI** and −1.65 mg min^{-1} at 285 °C for structures **VII/VIII/IX**.

Analysis of isostructural compounds **X** and **XI** shows a distinct effect of changing of metal within the hybrid material composition (ESI – Fig. S4†). For structure **X**, other than a minor mass loss at 185 °C, likely to derive from the 10% impurity phase of organic iodide, the thermal profile shows a stable mass to approximately 225 °C. In comparison, the equivalent bismuth compound, **XI**, demonstrates a much increased thermal stability over its counterpart, to around 280 °C. Each structure undergoes a continuous one-step degradation process, however, antimony-based structure **X** showed an increased rate of degradation with a max rate of change of mass of −2.30 mg min^{-1} occurring at 340 °C, compared to −1.65 mg min^{-1} at 385 °C for structure **XI**. As a result, a residue metal mass was left for structure **X** from temperature range 350–400 °C whereas, for structure **XI** a residue mass remained at 400 °C with a much slowed rate of mass change still occurring, as the full decomposition pathway was incomplete at this temperature.

Finally, thermogravimetric analysis was carried out on $DABCOH_2$ di-cation templated materials compound **XII** and a mixed phase of iodobismuthate compounds **XIII**/**XIV** (ESI – Fig. S5†). Iodoantimonate structure **XII** undergoes a distinct 3-step degradation process. The first and shortest step occurs at temperature range 205–230 °C; with a max *d*TG of −1.25 mg min^{-1} at 215 °C. The second at temperature range 230–280 °C; with a max *d*TG of −1.25 mg min^{-1} at 265 °C. The third and longest step occurs at temperature range 280–350 °C; with the highest *d*TG in the thermal profile of −2.15 mg min^{-1} peaking at 315 °C. A low temperature dehydration step is not observed for the material which may be attributed to the fact that the water sites are encapsulated within a zero-dimensional anionic sublattice with no open channels for rapid dehydration to occur. From 350 °C to T_{max} an expected ~1 mg metal residue mass remains. The TGA trace of the mixed phase of iodobismuthate hybrid structures **XIII** and **XIV** shows a stable thermal profile up to approximately 260 °C. From 260–400 °C degradation of the materials occurs, initially at a slow rate followed by a rapid increase to a max *d*TG of −2.15 mg min^{-1} peaking at 315 °C. Degradation of the materials then slows but continues up to T_{max} at which a still slowly degrading residual bismuth metal mass remains.

Optical absorption measurements

Optical absorption spectra (250–800 nm) were collected for Compounds **I–XIV** (ESI Fig. S6–S10†). Analysis of isostructural compounds **I** and **II** (ESI – Fig. S6†) shows absorbance in the ultraviolet and visible region with increasing intensity up to the absorption edge onsets at 485 nm and 540 nm respectively. An additional absorption peak feature is observed within the ultraviolet region at 320 nm for structure **I**. Assuming a direct band gap for these materials gives E_g values of 2.13 eV and 2.05 eV; a change of −0.08 eV as a result of changing antimony to bismuth.

Similarly, analysis of 4-methylmorpholium containing compounds **III** and **IV** (ESI – Fig. S7†) shows strong absorbance across the ultraviolet and visible regions up to the absorption edge onsets at 460 nm and 515 nm in turn. Changing the metal from antimony to bismuth and metal iodide anionic moiety from $[M_6I_{22}]$ to $[M_4I_{16}]$ results in a reduction in the estimated E_g values (assuming a direct band gap) by 0.22 eV from 2.28 eV to 2.06 eV.

The piperazinium-based structures **V–IX** (ESI – Fig. S8†) shows strong absorbance across the ultraviolet and visible regions up to absorption onsets at 480 nm, for both compounds **V** and **VI**, and at 500 nm for the mixed phase sample of structures **VII–IX**. As for the equivalent iodobismuthate materials studied previously, additional absorption peak features can be observed in the spectra for structure **V** (at 285 nm and 355 nm) and structure **VI** (at 290 nm and 360 nm). Features akin to this can also be observed at similar wavelengths in the spectrum obtained from the mixed phase sample (containing compounds **VII–IX**), although the strength of absorption is suppressed and seen as broad peaks. The estimated band gap energy reduces by 0.05 eV for the series of compounds **V** → **VI** → **VII/VIII/IX** from 2.22 eV → 2.17 eV → 2.12 eV respectively. As the templating piperazinium-ring dica-

tion becomes increasingly methylated there is an increase in the connectivity of the anionic sublattice, through weak I···I interactions, as the average $[SbI_4]_n^-$–$[SbI_4]_n^-$ interchain distances reduce. This is likely to be the origin of the slightly reduced band gap across this series.

Isostructural compounds **X** and **XI** show absorption in the ultraviolet and visible regions with increasing absorption strength towards their respective absorption edge onsets at 470 nm and 525 nm. Both structures exhibit an identical dual pointed absorption feature (at 270 nm and 275 nm) in the ultraviolet region. An additional absorption peak can be seen at 675 nm in both spectra beyond after the main absorption edge. The commonality of this feature to both compounds **X** and **XI** suggests it can be attributed to an electronic transition occurring locally on the conjugated 2-methylbenzimidazolium cation, a component present in both the isostructural compounds. Band gap estimates from the Tauc plot show a large shift of 0.3 eV between the two 2-methylbenzimidazolium templated structures; with respective E_g values of 2.33 eV for antimony based structure **X** and 2.03 eV for bismuth based structure **XI**.

UV-vis spectra were also collected for the $DABCOH_2$ dication templated hybrid materials. The iodoantimonate compound **XII** shows an absorption edge onset at 515 nm; compared to an approximate absorption edge of 520 nm for mixed phase of compounds **XIII**/**XIV**. Additional absorption features are observed in all the spectra at 375 nm and 480 nm. Band gap estimates for these materials from the Tauc plot indicates E_g values of 2.20 eV (**XII**) and 2.14 eV (mixture **XIII**/**XIV**).

Hybrid structure connectivity – band gap relationship

The changes in the absorption edge onset, and derived bang gap, in these materials can be to some degree rationalised in terms of the structures and, specifically, the weak interactions that exist between the inorganic anions. Structural features that might control the band gap include the dimensionality of the inorganic anionic unit (0D for discrete anions or clusters through 1D chains, 2D sheets and 3D (in, for example, vertex linked perovskite structures)) and weak I···I interactions between the anionic units. In this work and our previous work the majority of the materials contain either 0D or 1D inorganic units which limits any analysis in terms of structure dimensionality alone (or the related I/M ratio).

We, therefore, analysed the variation in band gap values of the (pure phase) compounds *versus* the average I···I interaction distances between the 0D or 1D anionic components of the hybrid structures. This relationship is shown in Fig. 12 for the structures described in this paper alongside materials from our previous publication covering piperazinium ring based hybrid bismuth structures; see ref. 49.

A degree of correlation is observed with dimensionality in that 1D structures tend to have a smaller band gap than 0D; this is similar to the trends seen for lead halide systems which span a much larger dimensionality range.[46,52]

There is also a tendency towards a reduction in the band gap energy associated with a reduction in the average I···I interaction distance. This average I···I interaction distance can be taken as a measure of the degree and strength of connectivity between the anionic "network" elements of each structure. Overall smaller band gaps in hybrid bismuth and antimony iodides can be associated with both increased inorganic anion dimensionality and reduced distances between these units.

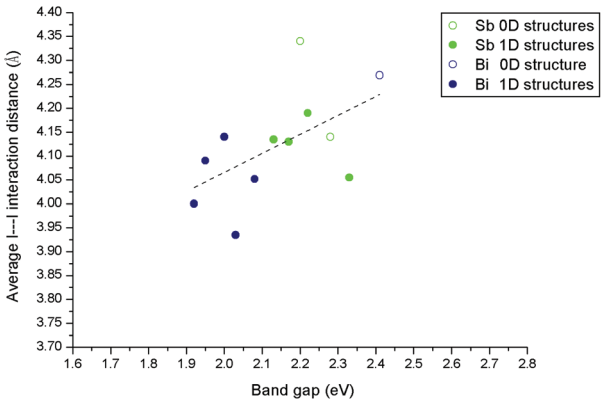

Fig. 12 Effect of connectivity and dimensionality of the hybrid material anionic component, as measured through the length of weak I···I interactions, on band gap energy.

Conclusions

In summary, five new iodobismuthate and nine new iodoantimonate hybrid materials have been synthesised and structurally characterised. Templated by cationic 1,3-dimethyl-2-oxo-2,3-dihydropyrimidium, 4-methylmorpholium, 1,4-dipiperazinium, 1-methyl-1,4-dipiperazinium, 1,4-dimethyl-1,4-dipiperazinium, 1-ethyl-2-methylbenzimidazolium and 1,4-diazabicyclo[2.2.2]octan-diium ions the hybrid structures contain a number of structural anionic motifs including $[MI_4]_n^-$(M = Sb, Bi), $[M_4I_{16}]^{4-}$(M = Sb, Bi), $[Sb_6I_{22}]^{4-}$, and a previously unseen motif of mixed $[Bi_2I_{10}]^{4-}$ and $[BiI_6]^{3-}$ units exhibited in structure **XIII**. Also, novel *in situ* alkylation reaction mechanisms, as demonstrated in the hydrothermal synthesis of structures **I**, **II**, **X** and **XI**, was found to be valuable and could be further utilised in this area to explore the creation of other new templating species to yield more hybrid materials.

Thermal analysis of the materials indicated the point of onset of major degradation of each hybrid material (or mixed phase) to occur in the range of 175–280 °C; with the iodobismuthate structures exhibiting increased thermal stability over their iodoantimonate counterparts. Band gap estimates for the structures were determined to range from 2.03–2.33 eV; with an expected decrease in band gap energy for isomorphic materials (**I** → **II**, **X** → **XI**) measured transitioning from antimony-iodide to bismuth-iodide based structures. Although these values are too high to be considered to compete in single junction cell architecture designs their applicability for tandem cell architectures could be considered.

Work to isolate crystals from the mixed phases for further analysis is underway; with a particular interest in comparing the 1,4-dimethyl-1,4-dipiperazinium templated polymorphic structures (**VII** and **VIII**) to observe the effect of structural change on the physical properties of the hybrid materials. The structures described here work towards building a deeper understanding of an expanding field of alternative hybrid materials in the areas of iodoantimonate and iodobismuthate chemistry. If low band gap materials ($E_g \sim 1.5$ eV) suitable for solar cell absorber layers are to be found then it is likely that new materials with 2D, and ideally 3D, connectivity will be targets. However materials with lower structural dimensionality (0D or 1D) but short I···I interactions between inorganic units should also be of interest – particularly for applications that require larger band gaps between 1.8 and 2.5 eV.

Crystallographic data

Crystal data for I

$C_6H_9N_2OSbI_4$, M = 754.52, monoclinic, space group $P2_1/c$, a = 10.5506(4), b = 7.6299(3), c = 19.9962(7) Å, β = 95.336(3)°, V = 1600.63(10) Å^3, Z = 4, crystal size: 0.305 × 0.080 × 0.034 mm, T = 149.9(4) K, ρ_{calc} = 3.131 g cm^{-3}, μ = 9.418 mm^{-1}, 4798 reflections (4798 unique reflections), 127 parameters, 0 restraints, R_1 (all data) = 0.0616, wR_2 (all data) = 0.0768, GooF = 1.048, further details available from CCDC entry 1580940.†

Crystal data for II

$C_6H_9N_2OBiI_4$, M = 841.75, monoclinic, space group $P2_1/c$, a = 10.6424(3), b = 7.6380(2), c = 20.0271(5) Å, β = 94.986(2)°, V = 1621.78(7) Å^3, Z = 4, crystal size: 0.493 × 0.134 × 0.097 mm, T = 150.2(10) K, ρ_{calc} = 3.447 g cm^{-3}, μ = 18.465 mm^{-1}, 5140 reflections (5140 unique reflections), 128 parameters, 0 restraints, R_1 (all data) = 0.0454, wR_2 (all data) = 0.0740, GooF = 1.122, further details available from CCDC entry 1580941.†

Crystal data for III

$C_{20}H_{48}N_4O_4Sb_6I_{22}$, M = 3931.02, triclinic, space group $P\bar{1}$, a = 11.3253(7), b = 13.0042(7), c = 15.2847(7) Å, α = 69.645(4)°, β = 69.877(5)°, γ = 64.496(6)°, V = 1853.97(17) Å^3, Z = 2, crystal size: 0.376 × 0.235 × 0.175 mm, T = 150.01(10) K, ρ_{calc} = 3.521 g cm^{-3}, μ = 11.340 mm^{-1}, 11 292 reflections (11 292 unique reflections), 254 parameters, 0 restraints, R_1 (all data) = 0.0488, wR_2(all data) = 0.0633, GooF = 1.044, further details available from CCDC entry 1580942.†

Crystal data for IV

$C_{20}H_{48}N_4O_4Bi_4I_{16}$, M = 3275.02, orthorhombic, space group $Pbca$, a = 12.7627(3), b = 20.7207(6), c = 22.7427(6) Å, V = 6014.35(3) Å^3, Z = 4, crystal size: 0.248 × 0.222 × 0.144 mm, T = 150.01(10) K, ρ_{calc} = 3.617 g cm^{-3}, μ = 19.909 mm^{-1}, 9856 reflections (9856 unique reflections), 218 parameters, 0 restraints, R_1 (all data) = 0.0416, wR_2 (all data) = 0.0483, GooF = 1.107, further details available from CCDC entry 1580943.†

Crystal data for V

$C_4H_{20}N_2O_4Sb_2I_8$, M = 1418.95, monoclinic, space group $P2_1/c$, a = 7.3391(2), b = 13.0022(5), c = 13.8121(4) Å, β = 94.550(3)°, V = 1313.86(7) Å^3, Z = 4, crystal size: 0.382 × 0.121 × 0.082 mm, T = 150.00(10) K, ρ_{calc} = 3.587 g cm^{-3}, μ = 11.464 mm^{-1}, 4084 reflections (4084 unique reflections), 91 parameters, 0 restraints, R_1 (all data) = 0.0359, wR_2 (all data) = 0.0470, GooF = 1.023, further details available from CCDC entry 1580944.†

Crystal data for VI

$C_5H_{20}N_2O_3Sb_2I_8$, M = 1414.96, monoclinic, space group $P2_1/c$, a = 7.5306(2), b = 12.9539(4), c = 13.6147(4) Å, β = 96.086(3)°, V = 1320.64(7) Å^3, Z = 4, crystal size: 0.346 × 0.0.215 × 0.137 mm, T = 150.01(10) K, ρ_{calc} = 3.556 g cm^{-3}, μ = 11.401 mm^{-1}, 4034 reflections (4034 unique reflections), 110 parameters, 0 restraints, R_1 (all data) = 0.0472, wR_2 (all data) = 0.0711, GooF = 1.036, further details available from CCDC entry 1580945.†

Crystal data for VII

$C_6H_{20}N_2O_2Sb_2I_8$, M = 1410.97, monoclinic, space group $P2_1/c$, a = 7.7213(2), b = 12.8027(3), c = 13.4527(3) Å, β = 97.377(2)°, V = 1318.84(5) Å^3, Z = 4, crystal size: 0.280 × 0.218 × 0.179 mm, T = 149.99(10) K, ρ_{calc} = 3.553 g cm^{-3}, μ = 11.414 mm^{-1}, 3513 reflections (3513 unique reflections), 92 parameters, 0 restraints, R_1 (all data) = 0.0328, wR_2 (all data) = 0.0563, GooF = 1.061, further details available from CCDC entry 1580946.†

Crystal data for VIII

$C_6H_{20}N_2O_2Sb_2I_8$, M = 1410.97, monoclinic, space group $P2_1/c$, a = 7.5751(2), b = 12.1020(3), c = 14.5071(4) Å, β = 92.630(3)°, V = 1328.52(6) Å^3, Z = 2, crystal size: 0.447 × 0.199 × 0.165 mm, T = 150.00(10) K, ρ_{calc} = 3.527 g cm^{-3}, μ = 11.331 mm^{-1}, 4088 reflections (4088 unique reflections), 97 parameters, 0 restraints, R_1 (all data) = 0.0367, wR_2 (all data) = 0.0522, GooF = 1.131, further details available from CCDC entry 1580947.†

Crystal data for IX

$C_{12}H_{20}N_4O_2Sb_4I_{16}$, M = 2769.79, monoclinic, space group $P2_1/n$, a = 11.5391(3), b = 11.8717(4), c = 19.1648(5) Å, β = 93.705(3)°, V = 2619.87(13) Å^3, Z = 4, crystal size: 0.293 × 0.242 × 0.193 mm, T = 150.00(10) K, ρ_{calc} = 3.531 g cm^{-3}, μ = 11.486 mm^{-1}, 8103 reflections (8103 unique reflections), 178 parameters, 0 restraints, R_1 (all data) = 0.0472, wR_2 (all data) = 0.0578, GooF = 1.090, further details available from CCDC entry 1580948.†

Crystal data for X

$C_{10}H_{13}N_2SbI_4$, M = 790.58, monoclinic, space group $P2_1/n$, a = 7.5877(3), b = 17.7055(8), c = 13.2578(6) Å, β = 94.309(4)°, V = 1776.07(13) Å^3, Z = 4, crystal size: 0.398 × 0.175 × 0.090 mm, T = 149.95(13) K, ρ_{calc} = 2.957 g cm^{-3}, μ = 8.489 mm^{-1}, 3104 reflections (3104 unique reflections), 266 parameters, 272 restraints, R_1 (all data) = 0.0760, wR_2 (all data) = 0.0927, GooF = 1.197, further details available from CCDC entry 1580949.†

Crystal data for XI

$C_{10}H_{13}N_2BiI_4$, M = 877.81, monoclinic, space group $C2/c$, a = 13.3133(4), b = 17.7312(4), c = 7.6344(2) Å, β = 93.450(2)°, V = 1798.92(8) Å^3, Z = 4, crystal size: 0.143 × 0.120 × 0.0.079 mm, T = 150.00(10) K, ρ_{calc} = 3.237 g cm^{-3}, μ = 16.650 mm^{-1}, 2049 reflections (2049 unique reflections), 123 parameters, 96 restraints, R_1 (all data) = 0.0214, wR_2 (all data) = 0.0435, GooF = 1.083, further details available from CCDC entry 1580950.†

Crystal data for XII

$C_{12}H_{32}N_4O_2Sb_4I_{16}$, M = 2781.88, triclinic, space group $P\bar{1}$, a = 10.8634(3), b = 10.8965(3), c = 11.2911(3) Å, α = 91.999(2)°, β = 109.691(2)°, γ = 95.086(2)°, V = 1250.46(6) Å^3, Z = 1, crystal size: 0.392 × 0.325 × 0.324 mm, T = 150.0(2) K, ρ_{calc} = 3.694 g cm^{-3}, μ = 12.033 mm^{-1}, 7862 reflections (4290 unique reflections), 178 parameters, 0 restraints, R_1 (all data) = 0.0314, wR_2 (all data) = 0.0602, GooF = 1.181, further details available from CCDC entry 1580951.†

Crystal data for XIII

$C_{60}H_{156}N_{20}O_8Bi_8I_{44}$, M = 8541.66, orthorhombic, space group $Pbam$, a = 31.9562(6), b = 15.8622(4), c = 8.6164(2) Å, V = 4367.62(17) Å^3, Z = 8, crystal size: 0.363 × 0.100 × 0.0.077 mm, T = 150.00(10) K, ρ_{calc} = 3.247 g cm^{-3}, μ = 15.843 mm^{-1}, 7058 reflections (7058 unique reflections), 192 parameters, 0 restraints, R_1 (all data) = 0.0480, wR_2 (all data) = 0.0699, GooF = 1.164, further details available from CCDC entry 1580952.†

Crystal data for XIV

$C_{12}H_{32}N_4O_2Bi_4I_{16}$, M = 3130.03, monoclinic, space group $P2_1/c$, a = 11.0086(3), b = 15.4751(3), c = 15.3455(4) Å, β = 103.001(2)°, V = 2547.23(11) Å^3, Z = 2, crystal size: 0.312 × 0.295 × 0.0.215 mm, T = 150.00(10) K, ρ_{calc} = 4.082 g cm^{-3}, μ = 23.491 mm^{-1}, 7829 reflections (7829 unique reflections), 178 parameters, 0 restraints, R_1 (all data) = 0.0474, wR_2 (all data) = 0.0666, GooF = 1.042, further details available from CCDC entry 1580953.†

Single crystal X-ray diffraction data collection instrumentation

Single crystal data for structures **I–X** and **XII–XIV** were collected on an Agilent Xcalibur four-circle diffractometer equipped with a fine-focus ($Mo_{k\alpha}$) X-ray source and EosS2 CCD plate detector. Single crystal data for structure **XI** was collected on an Agilent SuperNova Dual four-circle diffractometer equipped with dual fine-focus ($Mo_{k\alpha}$ and $Cu_{k\alpha}$) X-ray sources and EosS2 CCD plate detector.

Conflicts of interest

There are no conflicts to declare.

Acknowledgements

The authors would like to thank Dr Mary F. Mahon for assistance with the single crystal X-ray crystallography. AJD would like to thank EPSRC for DTA studentship support.

References

1 S. A. Adonin, M. N. Sokolov and V. P. Fedin, *Coord. Chem. Rev.*, 2016, **312**, 1–21.
2 N. Mercier, N. Louvain and W. H. Bi, *CrystEngComm*, 2009, **11**, 720–734.
3 S. Pohl, R. Lotz, W. Saak and D. Haase, *Angew. Chem., Int. Ed. Engl.*, 1989, **28**, 344–347.
4 G. A. Fisher and N. C. Norman, *Adv. Inorg. Chem.*, 1994, **41**, 233–272.
5 M. Weclawik, A. Gagor, R. Jakubas, A. Piecha-Bisiorek, W. Medycki, J. Baran, P. Zielinski and M. Galazka, *Inorg. Chem. Front.*, 2016, **3**, 1306–1316.
6 A. M. Goforth, L. Peterson, M. D. Smith and H. C. zur Loye, *J. Solid State Chem.*, 2005, **178**, 3529–3540.
7 W. H. Bi and N. Mercier, *Chem. Commun.*, 2008, 5743–5745.
8 A. M. Goforth, J. R. Gardinier, M. D. Smith, L. Peterson and H. C. Z. Loye, *Inorg. Chem. Commun.*, 2005, **8**, 684–688.
9 C. Hrizi, A. Samet, Y. Abid, S. Chaabouni, M. Fliyou and A. Koumina, *J. Mol. Struct.*, 2011, **992**, 96–101.
10 A. Samet, A. Ben Ahmed, A. Mlayah, H. Boughzala, E. K. Hlil and Y. Abid, *J. Mol. Struct.*, 2010, **977**, 72–77.
11 A. M. Goforth, M. A. Tershansy, M. D. Smith, L. Peterson, J. G. Kelley, W. J. I. DeBenedetti and H. C. zur Loye, *J. Am. Chem. Soc.*, 2011, **133**, 603–612.
12 C. Feldmann, *J. Solid State Chem.*, 2003, **172**, 53–58.
13 J. Heine, *Dalton Trans.*, 2015, **44**, 10069–10077.
14 H. Krautscheid, *Z. Anorg. Allg. Chem.*, 1995, **621**, 2049–2054.
15 H. Krautscheid, *Z. Anorg. Allg. Chem.*, 1999, **625**, 192–194.
16 S. A. Adonin, E. V. Peresypkina, M. N. Sokolov and V. P. Fedin, *Russ. J. Coord. Chem.*, 2014, **40**, 867–870.
17 H. Krautscheid, *Z. Anorg. Allg. Chem.*, 1994, **620**, 1559–1564.
18 K. Y. Monakhov, C. Gourlaouen, R. Pattacini and P. Braunstein, *Inorg. Chem.*, 2012, **51**, 1562–1568.
19 V. V. Sharutin, I. V. Egorova, N. N. Klepikov, E. A. Boyarkina and O. K. Sharutina, *Russ. J. Inorg. Chem.*, 2009, **54**, 1768–1778.
20 A. Okrut and C. Feldmann, *Z. Anorg. Allg. Chem.*, 2006, **632**, 409–412.
21 S. A. Adonin, M. N. Sokolov, P. A. Abramov, S. G. Kozlova, D. P. Pishchur, L. A. Sheludyakova and V. P. Fedin, *Inorg. Chim. Acta*, 2014, **419**, 19–25.
22 D. B. Mitzi and P. Brock, *Inorg. Chem.*, 2001, **40**, 2096–2104.
23 G. A. Mousdis, G. C. Papavassiliou, A. Terzis and C. P. Raptopoulou, *Z. Naturforsch., B: J. Chem. Sci.*, 1998, **53**, 927–931.

24 C. Hrizi, N. Chaari, Y. Abid, N. Chniba-Boudjada and S. Chaabouni, *Polyhedron*, 2012, **46**, 41–46.
25 S. Chaabouni, S. Kamoun and J. Jaud, *J. Chem. Crystallogr.*, 1997, **27**, 527–531.
26 N. A. Yelovik, A. V. Mironov, M. A. Bykov, A. N. Kuznetsov, A. V. Grigorieva, Z. Wei, E. V. Dikarev and A. V. Shevelkov, *Inorg. Chem.*, 2016, **55**, 4132–4140.
27 A. Gagor, M. Weclawik, B. Bondzior and R. Jakubas, *CrystEngComm*, 2015, **17**, 3286–3296.
28 D. B. Mitzi, *Inorg. Chem.*, 2000, **39**, 6107–6113.
29 C. J. Carmalt, L. J. Farrugia and N. C. Norman, *Z. Anorg. Allg. Chem.*, 1995, **621**, 47–56.
30 P. Szklarz, A. Pietraszko, R. Jakubas, G. Bator, P. Zielinski and M. Galazka, *J. Phys.: Condens. Matter*, 2008, **20**, 12.
31 M. Bujak and J. Zaleski, *J. Mol. Struct.*, 2003, **647**, 121–128.
32 A. Gagor, G. Banach, M. Weclawik, A. Piecha-Bisiorek and R. Jakubas, *Dalton Trans.*, 2017, **46**, 16605–16614.
33 S. Pohl, R. Lotz, D. Haase and W. Saak, *Z. Naturforsch., B: J. Chem. Sci.*, 1988, **43**, 1144–1150.
34 C. J. Carmalt, N. C. Norman and L. J. Farrugia, *Polyhedron*, 1994, **13**, 1655–1658.
35 G. Volonakis, M. R. Filip, A. A. Haghighirad, N. Sakai, B. Wenger, H. J. Snaith and F. Giustino, *J. Phys. Chem. Lett.*, 2016, **7**, 1254–1259.
36 W. Medycki, K. Holderna-Natkaniec, J. Swiergiel and R. Jakubas, *Solid State Nucl. Magn. Reson.*, 2003, **24**, 209–217.
37 W. H. Bi, N. Leblanc, N. Mercier, P. Auban-Senzier and C. Pasquier, *Chem. Mater.*, 2009, **21**, 4099–4101.
38 K. Gesi, M. Iwata and Y. Ishibashi, *J. Phys. Soc. Jpn.*, 1995, **64**, 2650–2655.
39 R. Jakubas, A. Piecha, A. Pietraszko and G. Bator, *Phys. Rev. B: Condens. Matter Mater. Phys.*, 2005, **72**, 8.
40 Research cell efficiency records, https://www.nrel.gov/pv/assets/images/efficiency-chart.png (accessed October 2017).
41 A. M. Ganose, C. N. Savory and D. O. Scanlon, *J. Phys. Chem. Lett.*, 2015, **6**, 4594–4598.
42 Q. D. Tai, P. You, H. Q. Sang, Z. K. Liu, C. L. Hu, H. L. W. Chan and F. Yan, *Nat. Commun.*, 2016, **7**, 8.
43 N. K. Noel, S. D. Stranks, A. Abate, C. Wehrenfennig, S. Guarnera, A. A. Haghighirad, A. Sadhanala, G. E. Eperon, S. K. Pathak, M. B. Johnston, A. Petrozza, L. M. Herz and H. J. Snaith, *Energy Environ. Sci.*, 2014, **7**, 3061–3068.
44 S. F. Hoefler, G. Trimmel and T. Rath, *Monatsh. Chem.*, 2017, **148**, 795–826.
45 X. P. Wang, T. Yan, Y. Li, Y. X. Liu, B. Du, H. M. Ma and Q. Wei, *Sci. Rep.*, 2015, **5**, 8.
46 L. M. Wu, X. T. Wu and L. Chen, *Coord. Chem. Rev.*, 2009, **253**, 2787–2804.
47 J. Laane and P. W. Jagodzinski, *Inorg. Chem.*, 1980, **19**, 44–49.
48 H. L. Sheu and J. Laane, *Inorg. Chem.*, 2013, **52**, 4244–4249.
49 A. J. Dennington and M. T. Weller, *Dalton Trans.*, 2016, **45**, 17974–17979.
50 V. V. Sharutin, A. P. Pakusina, O. K. Sharutina, O. A. Kovaleva, A. V. Gerasimenko and M. A. Pushilin, *Russ. J. Coord. Chem.*, 2004, **30**, 541–549.
51 C. Hrizi, A. Trigui, Y. Abid, N. Chniba-Boudjada, P. Bordet and S. Chaabouni, *J. Solid State Chem.*, 2011, **184**, 3336–3344.
52 M. E. Kamminga, G. A. de Wijs, R. W. A. Havenith, G. R. Blake and T. T. M. Palstra, *Inorg. Chem.*, 2017, **56**, 8408–8414.

